frontiers | Research Topics

Vegetation-soil-hydrology interactions and ecohydrological processes

Edited by
Jing Liu, Jing Zhang and Xudong Huang

Published in
Frontiers in Environmental Science

ISSN 1664-8714
ISBN 978-2-8325-6731-9
DOI 10.3389/978-2-8325-6731-9

Generative AI statement
Any alternative text (Alt text) provided alongside figures in the articles in this ebook has been generated by Frontiers with the support of artificial intelligence and reasonable efforts have been made to ensure accuracy, including review by the authors wherever possible. If you identify any issues, please contact us.

About Frontiers

Frontiers is more than just an open access publisher of scholarly articles: it is a pioneering approach to the world of academia, radically improving the way scholarly research is managed. The grand vision of Frontiers is a world where all people have an equal opportunity to seek, share and generate knowledge. Frontiers provides immediate and permanent online open access to all its publications, but this alone is not enough to realize our grand goals.

Frontiers journal series

The Frontiers journal series is a multi-tier and interdisciplinary set of open-access, online journals, promising a paradigm shift from the current review, selection and dissemination processes in academic publishing. All Frontiers journals are driven by researchers for researchers; therefore, they constitute a service to the scholarly community. At the same time, the *Frontiers journal series* operates on a revolutionary invention, the tiered publishing system, initially addressing specific communities of scholars, and gradually climbing up to broader public understanding, thus serving the interests of the lay society, too.

Dedication to quality

Each Frontiers article is a landmark of the highest quality, thanks to genuinely collaborative interactions between authors and review editors, who include some of the world's best academicians. Research must be certified by peers before entering a stream of knowledge that may eventually reach the public - and shape society; therefore, Frontiers only applies the most rigorous and unbiased reviews. Frontiers revolutionizes research publishing by freely delivering the most outstanding research, evaluated with no bias from both the academic and social point of view. By applying the most advanced information technologies, Frontiers is catapulting scholarly publishing into a new generation.

What are Frontiers Research Topics?

Frontiers Research Topics are very popular trademarks of the *Frontiers journals series*: they are collections of at least ten articles, all centered on a particular subject. With their unique mix of varied contributions from Original Research to Review Articles, Frontiers Research Topics unify the most influential researchers, the latest key findings and historical advances in a hot research area.

Find out more on how to host your own Frontiers Research Topic or contribute to one as an author by contacting the Frontiers editorial office: frontiersin.org/about/contact

Vegetation-soil-hydrology interactions and ecohydrological processes

Topic editors
Jing Liu — University of Birmingham, United Kingdom
Jing Zhang — North China University of Water Conservancy and Electric Power, China
Xudong Huang — North China University of Water Conservancy and Electric Power, China

Citation
Liu, J., Zhang, J., Huang, X., eds. (2025). *Vegetation-soil-hydrology interactions and ecohydrological processes*. Lausanne: Frontiers Media SA.
doi: 10.3389/978-2-8325-6731-9

Table of contents

frontiers | Frontiers in Environmental Science

TYPE Editorial
PUBLISHED 29 September 2025
DOI 10.3389/fenvs.2025.1705595

OPEN ACCESS

EDITED AND REVIEWED BY
Angela Helen Arthington,
Griffith University, Australia

*CORRESPONDENCE
Xu-Dong Huang,
✉ huangxudong@ncwu.edu.cn

RECEIVED 15 September 2025
ACCEPTED 18 September 2025
PUBLISHED 29 September 2025

CITATION
Huang X-D, Luo G-M, Han P-P, Liu J and Zhang J (2025) Editorial: Vegetation–soil–hydrology interactions and ecohydrological processes.
Front. Environ. Sci. 13:1705595.
doi: 10.3389/fenvs.2025.1705595

Editorial: Vegetation–soil–hydrology interactions and ecohydrological processes

Xu-Dong Huang[1,2]*, Guang-Mei Luo[1], Pei-Pei Han[3], Jing Liu[1,2,4] and Jing Zhang[1,2]

[1]College of Water Resources, North China University of Water Resources and Electric Power, Zhengzhou, China, [2]Henan Key Laboratory of Water Resources Conservation and Intensive Utilization in the Yellow River Basin, Zhengzhou, China, [3]Henan Yellow River Hydrological Survey and Design Institute, Zhengzhou, China, [4]School of Geography, Earth, and Environmental Sciences, University of Birmingham, Birmingham, United Kingdom

KEYWORDS

vegetation, soil structures, hydrological response, ecohydrological processes, multiple interactions and models

Editorial on the Research Topic
Vegetation–soil–hydrology interactions and ecohydrological processes

1 Introduction

The many complex interactions among vegetation, soil, and hydrological processes generate important feedbacks between different spheres that make up the Earth system (Steffen et al., 2020). Vegetation influences the land surface's biophysical characteristics by modifying surface roughness, albedo, and interception of precipitation, which together ultimately affect local hydrological processes. These changes further modulate regional climatic factors, such as rainfall regime and near-surface air temperature, which in turn affect vegetation growth (Forzier et al., 2017). Soil not only provides water and nutrients essential for the growth and development of plants, but also serves as a crucial link connecting the atmosphere, hydrosphere, biosphere, and lithosphere. In addition, soil constitutes the primary medium for numerous biological, physical, and chemical processes, while water acts as the main vector of the exchange of matter and energy between these layers (Li, 2011). However, under the dual pressure of climate change and human activities, pressing challenges like water scarcity, soil functional degradation, and extreme meteorological events are increasing in both frequency and magnitude are demanding even more from our conventional understanding of hydrology and ecological management. Therefore, a deeper understanding of how the ecohydrological ecosystem interacts with both hydrological and geochemical processes is now imperative for advancing ecological restoration, enhancing water-use efficiency, and addressing environmental risks.

2 Overview of this special issue

This Special Issue focuses on the central theme of vegetation–soil–hydrology interactions and consists of 16 papers. The specific topics include hydrological modeling and disaster risk prediction; mechanisms of preferential flow; aeolian landforms and water regulation in grassland ecosystems; the evolution of soil functions; groundwater stress and its ecological risks; the ecological regulation of lakes and reservoirs; and drought dynamics.

As extreme meteorological events increase in both frequency and magnitude, enhancing hydrological modeling capabilities, including risk prediction, is particularly crucial for disaster prevention and mitigation. Chai et al. introduced the M-Copula function to construct a multidimensional joint distribution of critical rainfall. By calculating critical rainfall under different risk combinations, they proposed two-tier warning thresholds of "preparation transfer" and "immediate transfer". The findings contribute to the prevention and control of flash flood disasters. Wang et al. combined HEC–HMS with LSTM to develop a hybrid la-LSTM model, which enhanced the accuracy of rainfall-runoff simulations. Such modeling results can be used to improve flood forecasting and water resources management. In another study, Li et al. used the HEC-HMS model to evaluate the effects of soil water content and different rainfall patterns on flash flood evolution in small watersheds. The corresponding results can provide support for the simulation and early warning of mountain flood disasters. In the domain of agricultural water resources management, Chen et al. optimized maize irrigation strategies under various water deficit scenarios to enhance water use efficiency while maintaining yield. This study offers guidance for mitigating regional water scarcity, enhancing the efficiency of irrigation, and tackling challenges arising from rigid water resource constraints. Additionally, Schwamback et al. devised an innovative tipping-bucket flow meter, providing an efficient and low-cost solution for continuous runoff monitoring.

A study on preferential flow is included. Du et al. conducted dye tracer experiments on typical slopes at different positions in the Miyun Reservoir Basin. Their results revealed the preferential flow infiltration mechanisms that operate at various slopes and their interactions with soil properties, enriching our understanding of hydrological processes governing the migration and distribution of water, nutrients, and contaminants in the ecosystem.

Aeolian landforms are widely distributed in arid and semi-arid regions, representing a concentrated manifestation of regional ecological vulnerability and land degradation. Huang et al. combined the revised wind erosion equation and partial least-squares regression model to uncover the spatial patterns and driving factors of soil erosion dynamics in a wind erosion region. Bao et al. demonstrated that, at microtopographic scales, the sand deposition zones within wind-eroded pits harbor a certain water storage capacity under rainfall conditions; however, that water retention capacity is limited, and moisture is prone to rapid loss. These research findings provide empirical support for the management of wind-eroded pits and the restoration of grassland vegetation.

Soil acts as a nexus linking vegetation dynamics and hydrological processes (Shu et al., 2025), and its physicochemical properties and ecological functions continually evolve in the face of external disturbances. When Zha et al. compared different soil profiles in the Yangshao Village cultural relic site, they found that ancient humans were able to enhance the fertility of soil via various practices, such as slash-and-burn activity, habitation, and the application of human and animal feces. However, these activities also disrupted the original soil voids and structure, which prevented the downward leaching or precipitation of soil particles and minerals, thereby hindering soil development overall. Melkani et al. discovered in a subtropical nature reserve that wet and dry seasons, along with different land cover types, can regulate its hydrolytic enzyme activities and organic matter decomposition, thereby influencing both the carbon cycle and soil nutrient cycling. Saline-alkali land is an important and abundant land resource in China, but its high salinity and low fertility severely constrain agricultural productivity. Through field experiments carried out on saline-alkali land in Xinjiang, Chen et al. found that an appropriate application of FGD gypsum and aeolian sand is able to improve the physicochemical properties of saline-alkali soils and effectively inhibit greenhouse gas emissions. Overall, among the treatments used, the application of aeolian sand at 30 t/ha was the most effective improvement measure. This finding provides a key technological pathway for not only the reclamation of saline-alkali land but also the reduction of carbon emissions.

Groundwater, a vital water resource in arid and semi-arid regions, also faces dual pressure from intensified human activities and climate change. To address the ecological problems caused by groundwater overexploitation, Xiao et al. employed numerical modeling, finding that under overexploitation, the discharge of the BL Spring located in Xilin Gol League continues to decline, which could eventually lead to the spring's exhaustion and ecological degradation. Using 50 years of hydrological data, Zhang et al. analyzed the long-term evolution of surface water and groundwater interactions in the secondary perched reach of the lower Yellow River. They found that both river water and groundwater levels show a significant downward trend, while the recharge from river water to groundwater has markedly weakened and exhibits a notable time lag.

Lakes and reservoirs serve as nodes for regional water security and ecological conservation. Work by Liu et al. demonstrated that, while external water replenishment can improve the water quality of Ulansuhai Lake, its long-term enhancement still depends on pollution source control and protection of lake water ecology. Yang and Liu, focusing on ecological protection objectives, established an ecological operation model of sediment-laden river reservoirs for wetland protection. This model successfully balanced multiple objective requirements, including water supply, ecological, sediment transport, power generation, and flood control in the Xiaolangdi Reservoir. This study shows that an equilibrium between economic benefits and ecological protection is indeed achievable.

Finally, drought, among the most destructive natural disasters, is happening more frequently under the influence of climate change. Wan et al. revealed the propagation law and stage response relationship between meteorological elements and hydrological drought in the Xiangtan area, thus providing a scientific basis for bolstering drought mitigation and drought risk assessment there.

3 Conclusion

This Special Issue centers on "vegetation–soil–hydrology interactions" and features a collection of 16 representative research articles, covering an array of timely topics: hydrological modeling and disaster risk prediction, preferential flow mechanisms, soil-water processes in wind erosion regions, the evolution of soil functions, groundwater security, ecological regulation of lakes and reservoirs, and drought evolution. These studies entail advances not only in theoretical modeling, experimental observation, and methodological approaches, but also in practical applications such as agricultural water conservation, ecological restoration, and disaster prevention and control. Overall, their collective findings deepen our understanding of the complex feedback mechanisms among vegetation, soil, and hydrological processes, while providing a scientific foundation and practical references for water resource optimization and ecosystem sustainability.

Author contributions

X-DH: Funding acquisition, Writing – original draft, Writing – review and editing. G-ML: Writing – review and editing. P-PH: Writing – review and editing. JL: Writing – review and editing. JZ: Writing – review and editing.

Funding

The author(s) declare that financial support was received for the research and/or publication of this article. This work is supported by the Natural Science Foundation of China (grant numbers 42207100).

Conflict of interest

The authors declare that the research was conducted in the absence of any commercial or financial relationships that could be construed as a potential conflict of interest.

Generative AI statement

The author(s) declare that no Generative AI was used in the creation of this manuscript.

Any alternative text (alt text) provided alongside figures in this article has been generated by Frontiers with the support of artificial intelligence and reasonable efforts have been made to ensure accuracy, including review by the authors wherever possible. If you identify any issues, please contact us.

Publisher's note

References

Forzier, G., Alkama, R., Miralles, D. G., and Cescatti, A. (2017). Satellites reveal contrasting responses of regional climate to the widespread greening of Earth. *Science* 356, 1180–1184. doi:10.1126/science.aal1727

Li, X. Y. (2011). Mechanism of coupling, response and adaptation between soil, vegetation and hydrology in arid and semiarid regions. *J. Sci. Sin. Terrae* 41 (12), 1721–1730. doi:10.1360/zd-2011-41-12-1721

Shu, Z., Zhang, B., Yu, L., and Zhao, X. (2025). Reconciling plant water stress response using vegetation and soil moisture data assimilation for vegetation-soil-hydrology interaction estimation over the Chinese Loess Plateau. *J. Agric. For. Meteorology* 369, 110581. doi:10.1016/j.agrformet.2025.110581

Steffen, W., Richardson, K., Rockström, J., Schellnhuber, H. J., Dube, O. P., Dutreuil, S., et al. (2020). The emergence and evolution of Earth System science. *J. Nat. Rev. Earth Environ.* 1, 54–63. doi:10.1038/s43017-019-0005-6

frontiers | Frontiers in Environmental Science

TYPE Original Research
PUBLISHED 11 May 2023
DOI 10.3389/fenvs.2023.1207032

OPEN ACCESS

EDITED BY
Xudong Huang,
North China University of Water Conservancy and Electric Power, China

REVIEWED BY
Han Xiaole,
Hohai University, China
Dawei Zhang,
China Institute of Water Resources and Hydropower Research, China
Jinshu Li,
Stantec, United States

*CORRESPONDENCE
Yichen Yang,
hhuinnanjing@163.com

RECEIVED 17 April 2023
ACCEPTED 02 May 2023
PUBLISHED 11 May 2023

CITATION
Yang Y and Liu B (2023), Reservoir ecological operation on sediment-laden river considering wetland protection.
Front. Environ. Sci. 11:1207032.
doi: 10.3389/fenvs.2023.1207032

Reservoir ecological operation on sediment-laden river considering wetland protection

Yichen Yang[1]* and Bojun Liu[2]

[1]State Key Laboratory of Water Resources Engineering and Management, Wuhan University, Wuhan, China, [2]Yellow River Engineering Consulting Co., Ltd., Zhengzhou, China

Reservoir ecological operation has become an important means of ecological protection and restoration. The operation of reservoirs on sediment-laden rivers with water supply, sediment transport, flood control, wetland protection, and power generation as the primary objectives is a challenge in water resources management. Currently, most studies on reservoir ecological operation models involve a single ecological objective, and the inadequacy of the corresponding ecological constraint conditions makes it difficult to optimize reservoir ecological operation. To address these challenges, this study considers comprehensive water shortage, ecological water shortage, effective sediment transport in the river, and reservoir power generation as objective functions to establish an ecological operation model of sediment-laden river reservoirs for wetland protection. In this model, the ecological flow at key sections and water quantity discharged into the ocean are added as the constraint conditions to generate optimal operation schemes that reflect ecological benefits. The case study of the Xiaolangdi Reservoir (XLDR) on the Yellow River, China shows that with this model, the multi-objective requirements of water supply, ecology, sediment transport, flood control, and power generation in the XLDR could be met synergistically by optimizing the average daily discharge of the reservoir. Although the generated ecological operation schemes consider the demand for wetland protection, the reservoir flood control, sediment transport and power generation were not affected, and the latter two even showed improvement. In addition, this model has stronger applicability for large reservoirs. In dry years, small and medium reservoirs require water transfer, water-saving, and other measures required to alleviate water shortage.

KEYWORDS

ecological operation, reservoir, optimal operation scheme, wetland protection, Xiaolangdi reservoir, Yellow River

1 Introduction

Reservoir construction is an important method of exploiting river water resources (Sawakuchi et al., 2021). The operation and storage functions of a reservoir offer great economic benefits to society (Maskey et al., 2022); however, they have an impact on river hydrology, hydrodynamics, and water ecology (Ngor et al., 2018; Maavara et al., 2020), especially in causing unnatural flow patterns (Grill et al., 2019). For maintaining the ecological health of rivers and adapting river flow processes subjected to the influence of reservoirs, the concept of ecological operation has been proposed (Zhou and Guo, 2013; Valeria and Alberto, 2015). The core of ecological operation is to meet both the social and economic water requirements and maintain the ecological health of the river. Ecological protection and restoration have gradually become some of the important objectives of reservoir operation (Suwal et al., 2020), and this concept has enabled the field of water-resource management to develop immensely (Wang et al., 2015; Ai et al., 2022). To date, the primary scientific problem faced in the ecological operation of reservoirs is the optimization of the operation to reconstruct the ecological flow and hydrodynamic processes of the river (Acreman et al., 2014; Poff, 2018); that is, to create hydrological regime and hydrodynamic conditions favorable to ecological protection and water environment improvement downstream of the reservoir and to provide water flow process for river-beach forest and grass irrigation, wetland ecology, and fish habitat using pulsed discharge from the reservoir (Huang et al., 2018; Deng et al., 2020; Katrien et al., 2020).

Currently, the ecological protection role of reservoir has received considerable attention (Baumgartner et al., 2020; Deng et al., 2020). Through the ecological operation of reservoirs, an artificial flow process is created to improve the ecological environment quality downstream, which has been studied with respect to the operations of many reservoirs (Gillespie et al., 2015). Sale et al. (1982) investigated the relationship between biological flow demand and river water intake using mathematical methods, and the concept of ecological operation was explored. Ecological operation concepts have been implemented in the Glen Canyon Dam and Colorado River Reservoir in the United States, and the combined objectives of river sediment transport, habitat restoration, and fish protection were attained (Chen et al., 2019; Dobson et al., 2019). Babel et al. (2005) developed a reservoir operation optimization model to maximize the total economic benefits, and this model met the water requirements of different departments including living, production, and ecology to the greatest extent and guaranteed the ecological water demand downstream. Shiau and Wu (2007) studied the ecological flow rates of the river over different years and used an optimization algorithm to determine the balance between economy and ecology. Several scholars have considered the calculated minimum ecological flow rate of a river as the constraint condition in reservoir (group) operation optimization models to realize their ecological benefits. In some studies, the power generation in hydropower stations under different ecological flow conditions were investigated to optimize the trade-off between ecology and power generation objectives (Castellitti et al., 2008; Hu et al., 2008; Steinschneider et al., 2014; Nyatsanza et al., 2015).

In 2017, a reservoir operation model that coupled the structural differences in the river runoff regime was proposed, and a runoff mode was designed to ensure the ecological integrity of the Mekong River and socio-economic demand in this model (Sabo et al., 2017). Since 1999, operations on the Yellow River in China have been unified. Ecological operation based on water and sediment in the lower reaches of the Yellow River was carried out, and this practice improved the biodiversity of the Yellow River Delta (Li, 2006). Yan et al. (2021) constructed a reservoir operation model with two defined ecological objectives of water quantity level and hydrological alteration with the economic objective of hydropower production. Li et al. (2022) constructed an operation model of the Three Gorges and Gezhouba reservoir groups, and the ecological demand of representative fishes in the Yangtze River was involved in this model. Based on a refined reservoir discharge strategy, appropriate conditions for fish spawning were created. The realization of a win-win situation for economic development and ecological protection by incorporating these into reservoir operations is at the cutting edge of research (Margaret and Albert, 2019), but in general, the ecological operations of reservoirs have been less studied (Poff and Schmidt, 2016; You et al., 2021).

A number of studies have confirmed the feasibility of ecological operation, but most of the current ecological operations have the characteristic of "high-flow-rate discharge in the flood period" (Lan et al., 2022). With the increase in ecological protection awareness, the fulfillment of ecological demand at a high level has become an important goal (Niu et al., 2021), and ecological operation has expanded from the guarantee of ecological base flow of a single section to considering the ecological water demand of the area downstream (Tsai et al., 2015; Zeng et al., 2022). Because different rivers have different hydrological, water-sediment, and hydro-ecological characteristics that are affected by the operation and storage capacity of the reservoir itself, an obvious antagonistic effect exists between the benefit and ecological objectives. Optimized, refined, dynamic, and operable ecological operations have become a challenge. Meanwhile, studies on ecological operation in China focus on the Yangtze River (Huang et al., 2019; Jiang et al., 2019), and few studies take the Yellow River as the object. It is noteworthy that the Yellow River is a typical sediment-laden river, and its problems such as water shortage, uncoordinated water-sediment relationship, and fragile ecological background increase the difficulty of ecological operations. Therefore, according to the characteristics of sediment-laden rivers, a reservoir ecological operation model for the wetland protection was established in this paper, and a case study related to the Xiaolangdi Reservoir (XLDR) of the Yellow River (This reservoir is a key project to control the water supply downstream, to regulate the water-sediment relationship, and to provide ecological water replenishment for the wetland of the Yellow River Delta.) was carried out.

2 Reservoir ecological operation modelling

The key objective of reservoir operation is to maximize comprehensive regional benefits by shaping the flow process in the reservoir area downstream. Sediment transport is an important goal for sediment-laden rivers. The reservoir operation model in this paper not only involves water supply, flood control, power generation and other objectives, but also considers the ecological protection and sediment-transport objectives. It is an operation optimization model that integrates multiple objectives. The average daily process was taken as the simulation scale of the model, and the diversion gate dam project involved in this model was generalized according to the diversion site.

2.1 Model objective functions

(1) Minimum comprehensive water shortage. Water supply efficiency is improved during the operation period to reduce water shortage and provide stable water resource guarantee for

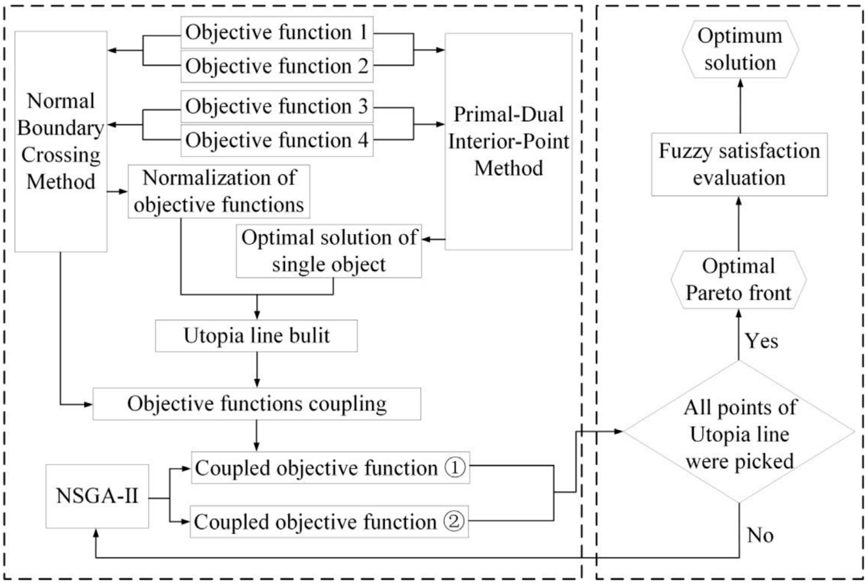

FIGURE 1
Optimization calculation process of the integrated algorithm.

the domestic and production water demand of the water service area.

$$Min\,F_1 = \sum_{t=1}^{T} \theta(t)\,[Q_d(t) - Q_s(t)]\Delta t \tag{1}$$

where $\theta(t)$ is the importance coefficient of water shortage on day t; $Q_d(t)$ and $Q_s(t)$ is the water demand and water supply on day t, m^3, respectively; Δt represents the period. $Q_s(t)$ is the decision variable.

(2) Minimum ecological water shortage. To ensure the water demand for maintaining the basic functions of the river channel downstream, simulate a reservoir discharge mode close to the natural hydrological situation, enhance the connectivity and operation of water system, meet the ecological water requirement of river channel, and maintain and improve the health of the river.

$$Min\,F_2 = \sum_{t=1}^{T} |W(t) - W_{eco}(t)| \tag{2}$$

where $W(t)$ and $W_{eco}(t)$ stand for the ecological water discharged from the reservoir and regional ecological water demand on day t, respectively, m^3. $W(t)$ is the decision variable.

(3) Maximum effective sediment transport of the river. To improve the water and sediment transport capacity of the river channel and maintain the stability of the river channel, sediment can be transported into the ocean as much as possible, and the quantity of sediments deposited in the reservoir and river channel can be reduced.

$$Max\,F_3 = \sum_{t=1}^{T} Q_{out}(t) \times \Delta t \times S_t \tag{3}$$

where $Q_{out}(t)$ is the flow rate of water discharged from the reservoir on day t, m^3/s; $Q_{out}(t) \geq [Q_s(t) + W(t)]$. S_t is the critical sediment content, and $S_t = vQ_{out}(t)^m$, kg/m^3; v and m are the parameters; S_t, as one of the key parameters to calculate the sediment transport for sediment-laden river, is expressed as the sediment content with the highest sediment transport efficiency and lowest sediment deposition risk in the reservoir operation process; and meanwhile, the sediment content in reservoir outflow cannot be higher than S_t to prevent sediment deposition and economize sediment-carrying water. $Q_{out}(t)$ is the decision variable.

(4) Maximum reservoir power generation. Maximum electricity is generated during the reservoir operation period to obtain the benefits of the reservoir.

$$Max\,F_4 = a_{ep} \sum_{t=1}^{T} KQ_{out}(t)\,[Z(t) - Z(0)]\Delta t \tag{4}$$

where $Z(t)$ stands for the water level in front of the dam on day t, m; $Z(0)$ stands for the installation elevation of the reservoir motor floor, m; K is the output coefficient of generator unit; a_{ep} is the on-grid electricity price of reservoir power generation, U.S. dollar/kW·h. $Z(t)$ is the decision variable.

2.2 Model constraint conditions

(1) Reservoir water balance constraint

$$V(t+1) = V(t) + [Q_{in}(t) + q_{in}(t) - Q_{out}(t) - Q_d(t)]\Delta t \tag{5}$$

(2) Reservoir capacity constraint

$$V_{\min} \leq V(t) \leq V_{\max} \tag{6}$$

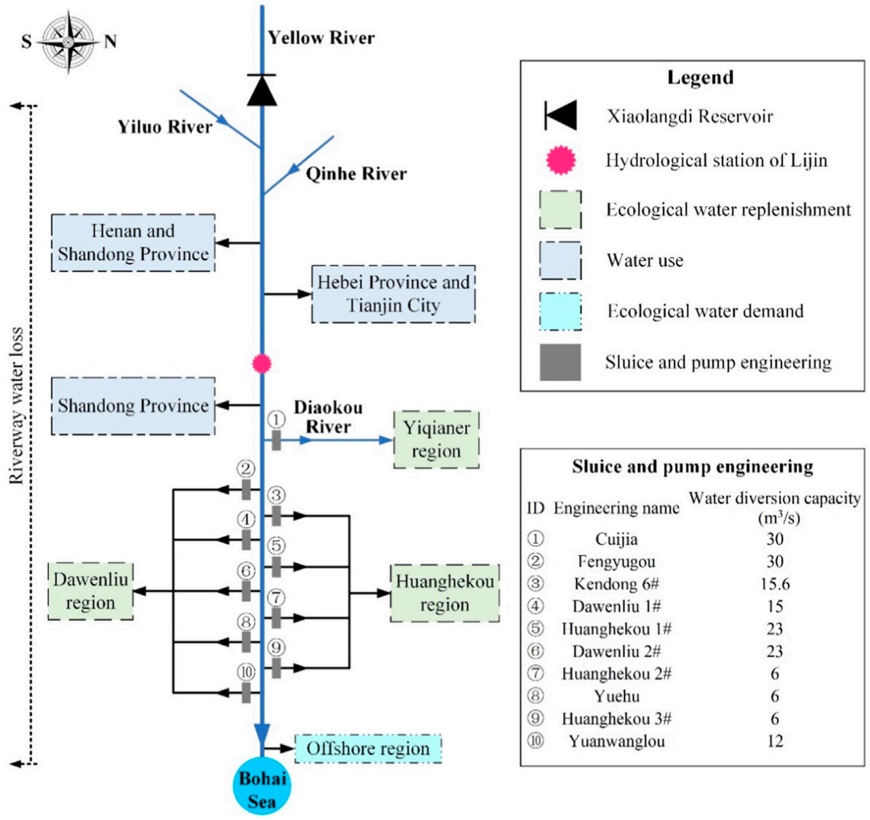

FIGURE 2
Calculation units generalization of ecological operation model.

(3) Reservoir discharge constraint

$$Q_{\min} \le Q_{out}(t) \le Q_{\max} \tag{7}$$

(4) Ecological flow constraints at key sections

$$Q_c(t) \ge EF(t) \tag{8}$$

(5) Constraint of water quantity discharged into the ocean

Considering that certain rivers were directly connected to the ocean, a certain quantity of water is required to maintain the offshore ecosystem, and the quantity was calculated as follows:

$$IS(\min) \le IS \tag{9}$$

(6) Reservoir power output constraint

$$N_{\min} \le N(t) \le N_{\max} \tag{10}$$

(7) Non-negative constraints: all the variables are non-negative values

Where $V(t+1)$ and $V(t)$ represent the storage capacity of the water reservoir on day t+1 and day t, respectively, m^3; $Q_{in}(t)$, $q_{in}(t)$, $Q_{out}(t)$ and $Q_d(t)$ represent the inflow rate on day t, inter-section catchment flow rate, reservoir discharge flow rate, and reservoir diversion flow rate (including reservoir water loss), m^3/s. $V_{\min}$ and $V_{\max}$ are the lower and upper limits of reservoir capacity, m^3. $Q_{\min}$ and $Q_{\max}$ stand for the lower and upper limits of flow rate discharged from the reservoir, respectively, m^3/s. $Q_c(t)$ is the flow rate at the section on day t, and $EF(t)$ is the ecological flow rate required in the section on day t, m^3/s. IS the flow rate discharged into the ocean, m^3, and $IS(min)$ is the minimum value of IS. $N_{\min}$ and $N_{\max}$ represent the lower and upper limits of output of the reservoir generator units on day t, kW.

2.3 Model solution

The reservoir ecological operation model proposed in the paper has four objective functions, the calculation process of multi-objective reservoir operation model has the characteristics of high dimension and multi-stage dynamics, which will be restricted and affected by different stakeholders (Zhao and Cai, 2020). The Non-dominated Sorting Genetic Algorithm-II (NSGA-II) is one method to solve optimization problems. However, the optimization efficiency and convergence speed of the NSGA-II algorithm would be reduced by the model with three or more objective functions (Liu et al., 2021). The existing study has found that an integrated algorithm that includes the normal boundary crossing method, primal-dual interior-point method, and NSGA-II can be used for lake or reservoir optimization, which is an effective way to

TABLE 1 Ecological water demand calculated by ecological operation model.

Ecological water demand (10^4 m^3)	Wet year (in 2020)	Normal year (in 2007)	Dry year (in 2016)
Qingshuigou region	18,093	15,336	8030
Diaokouhe1region	5,492	4,952	2379
Total	23,585	20,288	10,409

reduce calculation time and enhance global convergence (Liu et al., 2021). Four objective functions of the proposed model can, in this study, be converted into two coupled objective functions using the normal boundary crossing method and the primal-dual interior-point method. Subsequently, the NSGA-II is employed to solve the model with two objective functions and using the fuzzy satisfaction evaluation to filter the optimal solution in the end (Calculation process can be seen in Figure 1).

3 Case study

3.1 Study area

The XLDR is a large comprehensive water control project located at the outlet of the last gorge in the middle reaches of the Yellow River. The area of the basin upstream from the dam site is 694,200 km^2, accounting for 92.2% of the total basin (excluding the noncontributing area). The annual average runoff was measured to be 37.75 billion m^3, and the average annual sediment transport is 1.265 billion tons. Approximately 92.3% of the total area of the Yellow River basin, 87% of the natural runoff of the Yellow River, and 100% of sediment transport are controlled by the reservoir. The primary objective of the XLDR was flood (including ice) prevention and siltation reduction, with subsidiary objectives of water supply, irrigation, power generation, storing clear water and releasing muddy water, elimination of hazards and promotion of benefits, and comprehensive resource utilization (Shang et al., 2022). The normal impounded level, normal dead storage level, flood control level, and abnormal dead storage level of the reservoir are 275, 230, 254, and 220 m, respectively. Currently, the XLDR provides water for the wetland in the Yellow River Delta through large-scale discharge during the flood season.

3.2 Model input data

The inflow of the XLDR from 2000 to 2020 was arranged according to the frequency of runoff values, and the inflow runoff in the wet year (2020), normal year (2007) and dry year (2016) was selected in the model. The local inflow in the model included the Yiluo River and Qinhe River, and the local inflow was arranged according to the frequency of characteristics in the wet, normal, and dry seasons; The quantities of water required for regional living, production, and urban ecology were calculated according to the quantities of water consumed (excluding water withdrawal from the river). The monthly average water loss due to evaporation and leakage in the river was estimated to be 25 m^3/s in the wet and normal years and 20 m^3/s in the dry year. The generalized calculation units in this model are shown in Figure 2.

The wetland of the Yellow River Delta in the lower reaches of the XLDR is an important stopover, wintering, and breeding site for migratory birds around the Western Pacific and East Asia-Australia. This delta is the largest breeding place for the oriental white stork, which is the flagship species of wetland ecosystem, the second largest breeding place for the endangered species of black-headed gull, and the largest migration and stopover place for the eastern population of curly pelican, which is a first-class protected animal in China. Wetland, rare and protected birds and their habitats, and estuarine and offshore aquatic organisms and their habitats are the main ecological protection objects in this region. According to the studies undertaken by the Yellow River Engineering Consulting Co., Ltd., the ecological water demand for maintaining the stability of the ecosystem of the Yellow River Delta under different inflow conditions is listed in Table 1; Water is required from March to September; the period of April to June is critical for fish spawning in the Yellow River estuary, and the minimum amount of water discharged into the ocean from April to June in a year reaches 30×10^8 m^3. Moreover, based on the existing study from the Yellow River Engineering Consulting Co., Ltd., the critical sediment concentration of the XLDR with the best sediment transport performance is as follows: $S_t = 0.00294{Q_{out}}^{0.804}$, where Q_{out} is the amount of water discharged from the XLDR. According to the Ministry of Water Resources of China, the minimum ecological flow rate at the Lijin section is 50 m^3/s. In addition, based on the relevant research results (Xia et al., 2021), the installation elevation $Z(0)$ of the generator floor of XLDR is 129 m, and the output coefficient K of the generator units is 8.5. The on-grid electricity price a of the XLDR is 0.04562 U.S. dollar/kW·h.

3.3 Results

Due to space constraints, this paper directly presents the optimal ecological operation scheme under different reservoir inflow conditions. During a wet year (2020), the monthly average flow rate discharged from the reservoir reached a maximum of 2927.58 m^3/s in July and a minimum of 214.13 m^3/s in January. The monthly average flow rates discharged from March to September exceeded 1,000 m^3/s, and those in July to August exceeded 2000 m^3/s (see Table 2). The abundant water resource was regulated and stored by the reservoir, so the requirements of flood control and sediment transport in the flood period were met, and the flood could effectively support the ecological replenishment of the wetland in the Yellow River Delta. The utilization rate of flood was improved, and the higher requirements of regional ecological protection and restoration were met.

TABLE 2 Ecological operation optimization scheme of the XLDR in 2020.

Month	Reservoir outflow [$Q_{out}(t)$] (m^3/s)	Water consumption process (m^3/s)				
		Domestic, industrial, agricultural and environmental water [$Q_s(t)$]	Ecological water replenishment [$W(t)$]		Local inflow	Riverway water loss
			Yiqianer region	Huanghekou and dawenliu regions		
11	600.32	143.03	0.00	0.00	70.05	25.00
12	401.64	331.30	0.00	0.00	54.43	25.00
1	214.13	106.36	0.00	0.00	45.16	25.00
2	570.05	484.11	0.00	0.00	42.18	25.00
3	1384.74	1005.79	2.28	7.51	59.46	25.00
4	1285.81	898.87	2.35	7.76	34.86	25.00
5	1516.24	703.31	2.28	7.51	38.97	25.00
6	1998.27	627.76	5.65	18.61	47.26	25.00
7	2927.58	456.84	2.73	9.01	57.71	25.00
8	2225.84	409.39	2.73	9.01	191.26	25.00
9	1535.73	402.08	2.83	9.31	60.17	25.00
10	907.89	379.10	0.00	0.00	49.27	25.00

TABLE 3 Ecological operation optimization scheme of the XLDR in 2007.

Month	Reservoir outflow [$Q_{out}(t)$] (m^3/s)	Water consumption process (m^3/s)				
		Domestic, industrial, agricultural and environmental water [$Q_s(t)$]	Ecological water replenishment [$W(t)$]		Local inflow	Riverway water loss
			Yiqianer region	Huanghekou and dawenliu regions		
11	465.56	108.81	0.00	0.00	27.82	25.00
12	326.56	251.79	0.00	0.00	24.12	25.00
1	211.91	86.05	0.00	0.00	25.06	25.00
2	458.20	376.77	0.00	0.00	19.45	25.00
3	1212.01	739.60	2.05	6.36	30.89	25.00
4	1178.99	688.87	2.12	6.57	29.30	25.00
5	1199.99	417.03	2.05	6.36	13.99	25.00
6	1543.08	448.08	5.09	15.78	17.31	25.00
7	1344.11	336.59	2.47	7.63	86.51	25.00
8	922.73	302.97	2.47	7.63	169.98	25.00
9	429.08	281.53	2.55	7.89	90.41	25.00
10	615.99	282.17	0.00	0.00	53.04	25.00

In a normal year (2007), the monthly average flow rate discharged from the reservoir reached a maximum of 1,543.08 m^3/s in June and a minimum of 211.91 m^3/s in January. The monthly average flow rates discharged in March to July 1,212.01, 1,178.99, 1,199.99, 1,543.08, and 1,344.11 m^3/s, exceeded 1,000 m^3/s (see Table 3). Through the optimization of operation, the

TABLE 4 Ecological operation optimization scheme of the XLDR in 2016.

Month	Reservoir outflow [$Q_{out}(t)$] (m³/s)	Water consumption process (m³/s)				
		Domestic, industrial, agricultural and environmental water [$Q_s(t)$]	Ecological water replenishment [$W(t)$]		Local inflow	Riverway water loss
			Yiqianer region	Huanghekou and dawenliu regions		
11	263.29	101.50	0.00	0.00	31.75	20.00
12	289.58	235.10	0.00	0.00	20.30	20.00
1	131.61	79.90	0.00	0.00	18.59	20.00
2	438.36	365.09	0.00	0.00	21.19	20.00
3	1151.86	650.43	0.99	3.33	10.41	20.00
4	851.79	565.44	1.02	3.44	14.11	20.00
5	774.13	375.56	0.99	3.33	28.25	20.00
6	1021.71	446.30	2.45	8.26	38.80	20.00
7	818.27	289.37	1.18	4.00	94.36	20.00
8	466.71	263.05	1.18	4.00	62.10	20.00
9	366.13	264.49	1.22	4.13	19.88	20.00
10	340.79	238.76	0.00	0.00	24.47	20.00

requirements of day-to-day living, industry, agriculture, ecological water supply, ecological flow of Lijin section, and coastal ecological water supply in the reservoir area downstream could be met. Considering the smaller water inflow in the normal year compared to the wet year, the monthly average flow rates discharged in August to September were less than 1,000 m³/s. The storage rate of the reservoir was improved to guarantee water supply in non-flood seasons.

In another dry year (2016), the monthly average flow rate discharged from the reservoir reached a maximum of 1,151.86 m³/s in March and a minimum of 131.61 m³/s in January. The monthly average flow rates discharged in March and June 1,151.86 and 1,021.71 m³/s, exceeded 1,000 m³/s (see Table 4). This is the river-channel high-flow-rate pulse shaped by the water demand process. Due to the small inflow quantity in the dry year, the reservoir discharge was conservative. Therefore, the monthly average flow rates discharged from the reservoir in January to February, August to October, and November to December were less than 500 m³/s, and the water discharged aimed to meet the requirements of living and industrial water in the reservoir area downstream; the flow rates exceeded 500 m³/s in March to May to meet the requirement of agricultural irrigation in the reservoir area downstream.

The flow rates of the Lijin section reached or exceeded 50 m³/s under different inflow conditions, and the quantity of water discharged into the ocean from April to June of the year reached or exceeded 30×10^8 m³. But the flow rates in the Lijin section in December and January in the dry year were 54.78 and 50.3 m³/s, respectively, approaching the minimum-flow-rate requirement of the section. Therefore, operation in dry years is still an important concern. The optimized discharge processes of the reservoir in wet, normal, and dry years are shown in Figure 3. The maximum and minimum daily average flow rates discharged from the XLDR in the flood season of the wet year were 3843.25 and 315.51 m³/s. In the non-flood period, the maximum and minimum values were 3106.18 and 336.6 m³/s. The flood season in the middle and lower reaches of the Yellow River was distributed in July to August, and the peak of daily average flow rate took place on July 28. During the periods from June 29 to July 6 and from July 24 to August 1, the daily average flow rates discharged exceeded 3,000 m³/s. The maximum and minimum daily average flow rates discharged from the XLDR in the flood season of the normal year were 3,124.6 and 331.5 m³/s, respectively. In the non-flood period, the maximum and minimum values were 3,001.1 and 2,29.8 m³/s; the peak of daily average flow rate occurred on July 3. During the period from June 30 to July 5, the daily average flow rates discharged exceeded 3,000 m³/s. In the flood period of the dry year, the maximum and minimum daily average flow rates discharged were 2,862.84 and 126.59 m³/. In the non-flood period, the maximum and minimum values were 1,499.58 and 136.32 m³/s. The maximum was observed on July 7. During the period from July 5 to 9, the daily average flow rates discharged exceeded 2,000 m³/s to shape a limited high-flow-rate pulse process in the case of small quantity of inflow, to maintain the stability of the regional ecosystem. Irrigation, breeding of aquatic organisms in the river, and ecological water replenishment in the wetland are urgent in the lower reaches of the Yellow River in the period from March to May. By optimizing the reservoir operation process, the daily annual pulsed flow rate exceeding 1,000 m³/s could be successively shaped from March to May, regardless of the wet, normal, and dry years. This effect obviously mitigated the contradiction between irrigation and ecological water demand.

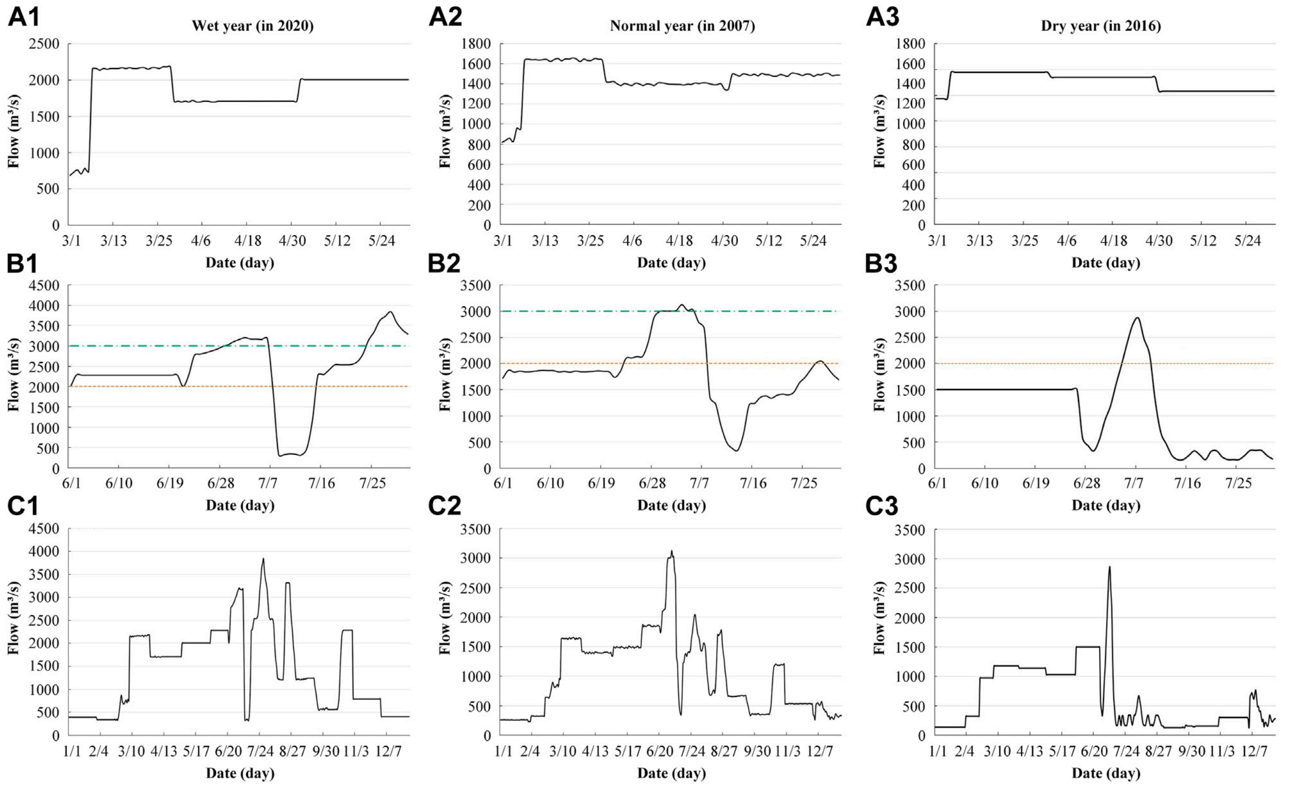

FIGURE 3
Reservoir outflow process in 2020, 2007 and 2016, respectively (a. March 1st ~ May 31st; b. June 1st ~ July 31st; c. Entire year).

4 Discussion

The optimized results from the model were compared with the actual operation processes of the reservoir. In 2020, 170 million tons of annual sediment transport and power generation of 9.067 billion kW·h with economic benefit of 0.399 billion U.S. dollar could be realized by the XLDR as per the model. In contrast, the actual annual sediment transport, power generation, and economic benefit in 2020 were 141 million tons, 9.011 billion kW·h, and 0.396 billion U.S. dollar, respectively. The power generation and economic benefits increased by 56 million kW·h and 300 thousand U.S. dollar. In 2007, 143 million tons of annual sediment transport and power generation of 6.707 billion kW·h with economic benefit of 0.295 billion U.S. dollar could be obtained as per the model. In contrast, the actual annual sediment transport, power generation, and economic benefit in 2007 were 141 million tons, 6.633 billion kW·h, and 0.291 billion U.S. dollar. The power generation and benefit were increased by 74 million kW·h and 400 thousand U.S. dollar. In 2016, the annual sediment transport, power generation, and benefit reached 26 million tons, 4.316 billion kW·h, and 0.190 billion U.S. dollar in the model. However, the actual values in 2016 were 0 ton, 4.133 billion kW·h, and 0.182 billion U.S. dollar. Power generation and benefit were increased by 183 million kW·h and 800 thousand U.S. dollar. Although the ecological operation scheme considered the objectives of ecological protection and restoration, reservoir flood control, sediment transport and power generation were not affected, and the sediment transport and power generation benefit were even improved, proving that the proposed model is reasonable and reliable.

According to the study, flood control is a key issue for the reservoir in the flood season. The water level should be decreased before the flood season, and the problem that a large quantity of water was discharged in a short time in the actual operation scheme could be addressed via the optimization of the model. Therefore, the discharge process of the reservoir in the flood season could be more stable. The damage to the river channel due to the high peak flow rate could be prevented, and the utilization rate of flood resources in the flood season could be improved. Especially, the ecological recovery and environmental improvement in the reservoir area downstream could be promoted with the abundant water resources in the wet year after the optimization of operation and storage of the reservoir. The inflow in the normal year was stable, and the normal operation met the requirements of reservoir operation. To improve the efficiency of power generation and sediment transport, the optimization scheme can be adopted. In the dry year, the shortage of inflow water had a negative impact on the supply and demand of water resources and ecological protection in the lower reaches of the Yellow River. In particular, the Yellow River began to run dry in the lower reaches in the 1970s, and this situation became serious after the 1990s. Especially in 1997, the Yellow River ran dry in the lower reaches for a total of 226 days, resulting in the shortage of domestic water, degradation of wetland in the Yellow River estuary delta, loss of biodiversity, and deterioration of ecological situation. The XLDR has become the last barrier to ensure the continuous flow in the lower reaches of the Yellow River. As per our results, the flood peak flow in the flood season of the dry year that had not been well utilized in the actual operation process was optimized, and the demand for irrigation, living and ecological water supply in the lower reaches of the Yellow River in the dry year were realized. Meanwhile, the quantity of sediment deposited in the reservoir was reduced, and the service life of the reservoir was increased in the optimized scheme. Nevertheless, the water shortage in the Yellow River is still an important issue that can be addressed through consistent water saving and inter-basin water transfer in the future.

The reservoir operation of sediment-laden river is complex, and the reservoir discharge not only aims to water supply and power generation, but also focuses on the flushing, carrying and transport of sand through the flow process. Meanwhile, as an effective ecological protection and restoration measure, reservoir operation of sediment-laden river becomes more complex with those ecological objectives involved (Huang et al., 2020). In this paper, a reserve economic operation model was built, and the case study of the XLDR revealed that the optimization and constructive collaboration of multiple objectives such as water supply, flood control, sediment transport, ecology, and power generation with interactions can be realized by the good operation and storage capacity of a large reservoir. The results showed that the model was applicable to large reservoirs. For the medium or small reservoirs, the limited storage capacity will be a major constraint during operation. In detail, the deposition of sediment will affect the storage capacity and the operation effect of the reservoir will be limited during the multi-objective optimization process, resulting in the situation that only a proportion of objectives are optimized while the benefits of remaining objective are reduced. This situation was beyond the scope of this paper. In the future, the applicability of the proposed model to medium and small reservoirs in sediment-laden rivers will be estimated, and the possibility of model evolution will be evaluated to provide improved techniques for the multi-objective optimization and operation of reservoirs in sediment-laden rivers.

5 Conclusion

Aiming at the core topic of multi-objective optimization and operation of reservoir of sediment-laden river with the consideration of ecological demand, the following conclusions are drawn.

(1) The most evident feature of sediment-laden river is the sediment content in the water, and its reservoir operation is very complex. With the consideration of ecological protection objectives, the multi-scale, multi-objective, and multi-level degrees of reservoir operation have become larger. For the multi-objective requirements of reservoir water supply, ecology, flood control, sediment transport and power generation, the minimum comprehensive water shortage, minimum ecological water shortage, maximum effective sediment transport of river, and maximum reservoir power generation were taken as the objective functions to establish an ecological operation model of reservoir of sediment-laden river for the wetland protection.

(2) The results related to the XLDR showed that a pulsed flow process with daily average flow rate continuously exceeding 1,000 m^3/s was shaped in this model to meet the requirements of the river channel in the lower reaches of the Yellow River by correcting the sudden and violent discharge process of the reservoir, enhancing the operation and storage of flood peak water in the flood season, and weakening the contradiction between irrigation and wetland ecological water replenishment, ensuring the water supply for living, agriculture, industry and ecology under different inflow conditions of the reservoir, improving the efficiency of power generation and sediment transport of the reservoir, and controlling the flood in flood seasons.

(3) The operations of reservoirs in years with a small amount of inflow water should be studied in detail. For large reservoirs, the domestic water consumption and production should be of priority, and the water required should be appropriately allocated to ensure the stability of the river ecosystem and to maintain the biodiversity of wetland. For the medium and small reservoirs, the operations may jeopardize the agricultural and ecological water demand to a certain extent, and the water shortage problem can be addressed through water transfer and water saving.

(4) Reservoir ecological operation model is reasonable and reliable and can provide a reference for the study of reservoir operation with multiple objectives such as water supply, sediment transport, ecological conservation, flood prevention and power generation in China and other countries.

Data availability statement

The original contributions presented in the study are included in the article/Supplementary Material, further inquiries can be directed to the corresponding author.

Author contributions

Conceptualization, YY and BL, Methodology, YY and BL, Resources, BL, Writing-Original draft preparation, YY, Validation, YY and BL, Writing-Reviewing and Editing, YY and BL, Funding acquisition, BL. All authors have read and agreed to the published version of the manuscript. All authors listed have made a substantial, direct, and intellectual contribution to the work and approved it for publication. All authors contributed to the article and approved the submitted version.

Funding

This work was supported by the National Key R&D Program of China (2022YFC3202405-04), and the Development Funding Project by Water Youth Talent from Beijing Jianghe Water Development Foundation.

Acknowledgments

The research would not have been possible without the interest and cooperation of Yellow River Conservancy Commission of the Ministry of Water Resources.

Conflict of interest

Author BL was employed by the company Yellow River Engineering Consulting Co., Ltd.

The remaining author declares that the research was conducted in the absence of any commercial or financial relationships that could be construed as a potential conflict of interest.

Publisher's note

References

Acreman, M., Arthington, A. H., Colloff, M. J., Couch, C., Crossman, N. D., Dyer, F., et al. (2014). Environmental flows for natural, hybrid, and novel riverine ecosystems in a changing world. *Front. Ecol. Environ.* 12 (8), 466–473. doi:10.1890/130134

Ai, Y., Ma, Z., Xie, X., Huang, T., and Cheng, H. (2022). Optimization of ecological reservoir operation rules for a northern river in China: Balancing ecological and socio-economic water use. *Ecol. Indic.* 138, 108822. doi:10.1016/j.ecolind.2022.108822

Babel, M. S., Gupta, A. D., and Nayak, D. K. (2005). A model for optimal allocation of water to competing demands. *Water Resour. Manag.* 19 (6), 693–712. doi:10.1007/s11269-005-3282-4

Baumgartner, M. T., Pitágoras, A. P., Baumgartner, G., and Gomes, L. C. (2020). Storage or run-of-river reservoirs: Exploring the ecological effects of dam operation on stability and species interactions of fish assemblages. *Environ. Manage.* 65 (2), 220–231. doi:10.1007/s00267-019-01243-x

Castellitti, A., Pianosi, F., and Palmer, R. (2008). Water reservoir control under economic, social and environmental constraints. *Automatic* 44 (6), 1595–1607. doi:10.1016/j.automatica.2008.03.003

Chen, Z., Huang, P., and Zhang, Z. (2019). Interaction between carbon dioxide emissions and eutrophication in a drinking water reservoir: A three-dimensional ecological modeling approach. *Sci. Total. Environ.* 663 (1), 369–379. doi:10.1016/j.scitotenv.2019.01.336

Deng, M. J., Huang, Q., Chang, J. X., and Huang, S. Z. (2020). Large-scale ecological operation research and practice. *J. Hydraul. Eng.* 51 (7), 757–773. (in Chinese). doi:10.13243/j.cnki.slxb.20200326

Dobson, B., Wagener, T., and Pianosi, F. (2019). An argument-driven classification and comparison of reservoir operation optimization methods. *Adv. Water. Resour.* 128 (6), 74–86. doi:10.1016/j.advwatres.2019.04.012

Gillespie, B. R., Desmet, S., Kay, P., Tillotson, M. R., and Brown, L. E. (2015). A critical analysis of regulated river ecosystem responses to managed environmental flows from reservoirs. *Freshw. Biol.* 60 (2), 410–425. doi:10.1111/fwb.12506

Grill, G., Lehner, B., Thieme, M., Geenen, B., Tickner, D., Antonelli, F., et al. (2019). Author Correction: Mapping the world's free-flowing rivers. *Nature* 569 (7755), E9–E221. doi:10.1038/s41586-019-1379-9

Hu, H. P., Liu, D. F., Tian, F. Q., and Ni, G. H. (2008). A method of ecological reservoir reoperation based-on ecological flow regime. *Adv. Sci.* 19 (3), 325–332. (in Chinese).

Huang, X. D., Wang, L., Han, P. P., and Wang, W. C. (2018). Spatial and temporal patterns in nonstationary flood frequency across a forest watershed: Linkage with rainfall and land use types. *Forests* 9 (6), 339. doi:10.3390/f9060339

Huang, L., Li, X., Fang, H. W., Yin, D., Si, Y., Wei, J., et al. (2019). Balancing social, economic and ecological benefits of reservoir operation during the flood season: A case study of the three gorges project, China. *J. Hydrol.* 572, 422–434. doi:10.1016/j.jhydrol.2019.03.009

Huang, X. D., Wang, D., Han, P. P., Wang, W. C., Li, Q. J., Zhang, X. L., et al. (2020). Spatial patterns in baseflow mean response time across a watershed in the loess plateau: Linkage with land-use types. *For. Sci.* 66 (3), 382–391. doi:10.1093/forsci/fxz084

Jiang, Z., Liu, P., Ji, C., Zhang, H., and Chen, Y. (2019). Ecological flow considered multi-objective storage energy operation chart optimization of large-scale mixed reservoirs. *J. Hydrol.* 577, 123949. doi:10.1016/j.jhydrol.2019.123949

Katrien, V. B., Patrick, M., Tim, S., Bram, D., Dries, B., Thomas, V., et al. (2020). Aligning biodiversity conservation and ecosystem ser-vices in spatial planning: Focus on ecosystem processes. *Sci. Total. Environ.* 712, 136350. doi:10.1016/j.scitotenv.2019.136350

Lan, L., Xu, Y. S., Mei, Y. D., Ren, Y. F., Tian, Y. F., and Zhang, X. (2022). Optimized flood control for the three gorges reservoir considering evolving flood propagation trends in the jingjiang reach of the Yangtze River. *Front. Env. Sci-Switz.* 10, 1013583. doi:10.3389/fenvs.2022.1013583

Li, Y. K., Lin, J. Q., Liu, Y., Yao, W., Zhang, D., Peng, Q., et al. (2022). Refined operation of cascade reservoirs considering fish ecological demand. *J. Hydrol.* 607, 127559. doi:10.1016/j.jhydrol.2022.127559

Li, G. Y. (2006). Regulation of water and sediment for the Yellow River based on joint operation of reservoirs and artificial intervention. *J. Hydraul. Eng.* 37 (12), 1439–1446. (in Chinese). doi:10.1061/(ASCE)0887-381X(2006)20:1(20)

Liu, B. J., Wang, Y., Xia, J., Quan, J., and Wang, J. (2021). Optimal water resources operation for rivers-connected lake under uncertainty. *J. Hydrol.* 595, 125863. doi:10.1016/j.jhydrol.2020.125863

Maavara, T., Chen, Q., Meter, K. V., Brown, L. E., Zarfl, C., Ni, J., et al. (2020). River dam impacts on biogeochemical cycling. *Nat. Rev. Earth. Environ.* 1, 103–116. doi:10.1038/s43017-019-0019-0

Margaret, P., and Albert, R. (2019). Linkages between flow regime, biota, and ecosystem processes: Implications for river restoration. *Science* 365 (6459), eaaw2087. doi:10.1126/science.aaw2087

Maskey, M. L., Dourado, G. F., Rallings, A. M., Rheinheimer, D. E., Medellin-Azuara, J., and Viers, J. H. (2022). Assessing hydrological alteration caused by climate change and reservoir operations in the San Joaquin River Basin, California. *Front. Env. Sci-Switz.* 10, 765426. doi:10.3389/fenvs.2022.765426

Ngor, P. B., Legendre, P., Oberdorff, T., and Lek, S. (2018). Flow alterations by dams shaped fish assemblage dynamics in the complex Me-kong-3S river system. *Ecol. Indic.* 88, 103–114. doi:10.1016/j.ecolind.2018.01.023

Niu, W. J., Feng, Z. K., Jiang, Z. Q., Wang, S., Liu, S., Guo, W., et al. (2021). Enhanced harmony search algorithm for sustainable ecological operation of cascade hydropower reservoirs in river ecosystem. *Environ. Res. Lett.* 16 (5), 055013. doi:10.1088/1748-9326/abf60c

Nyatsanza, F. F., Graas, S., and Zaag, P. (2015). The impact of dynamic environmental flow releases on hydropower production in the zambezi River basin. *J. Am. Water. Resour. As.* 51 (4), 1029–1042. doi:10.1111/jawr.12280

Poff, N. L., and Schmidt, J. C. (2016). How dams can go with the flow. *Science* 353 (6304), 1099–1100. doi:10.1126/science.aah4926

Poff, L. R. (2018). Beyond the natural flow regime? Broadening the hydro-ecological foundation to meet environmental flows challenges in a non-stationary world. *Freshw. Biol.* 63 (8), 1011–1021. doi:10.1111/fwb.13038

Sabo, J. L., Ruhi, A., Holtgrieve, G. W., Elliott, V., Arias, M. E., Ngor, P. B., et al. (2017). Designing river flows to improve food security futures in the lower Mekong Basin. *Science* 358 (6368), eaao1053. eaao1053. doi:10.1126/science.aao1053

Sale, M. J., Brill, E. D., and Herricks, E. E. (1982). An approach to optimizing reservoir operation for downstream aquatic resources. *Water Resour. Res.* 18 (4), 705–712. doi:10.1029/wr018i004p00705

Sawakuchi, H. O., Bastviken, D., Enrich-Prast, A., Ward, N. D., Camargo, P. B., and Richey, J. E. (2021). Low diffusive methane emissions from the main channel of a large Amazonian run-of-the-river reservoir attributed to high methane oxidation. *Front. Env. Sci-Switz.* 9, 655455. doi:10.3389/fenvs.2021.655455

Shang, W. X., Yan, D. M., Peng, S. M., Wang, Y., Ge, L., and Shang, Y. (2022). Analysis on the ecological impact of the Xiaolangdi reservoir on the Yellow River Delta wetland and coastal areas. *Front. Env. Sci-Switz.* 10, 953318. doi:10.3389/feart.2022.953318

Shiau, J., and Wu, F. (2007). Pareto-optimal solutions for environmental flow schemes incorporating the intra-annual and interannual variability of the natural flow regime. *Water Resour. Res.* 43 (6), 1–12. doi:10.1029/2006WR005523

Steinschneider, S., Bernstein, A., Palmer, R., and Polebitski, A. (2014). Reservoir management optimization for basin-wide ecological restoration in the Connecticut River. *J. Water Res. Plan. Man.* 140 (9), 04014023. doi:10.1061/(ASCE)WR.1943-5452.0000399

Suwal, N., Huang, X., Kuriqi, A., Chen, Y., Pandey, K. P., and Bhattarai, K. P. (2020). Optimisation of cascade reservoir operation considering environmental flows for different environmental management classes. *Renew. Energ.* 158, 453–464. doi:10.1016/j.renene.2020.05.161

Tsai, W. P., Chang, F. F., Chang, L. C., and Herricks, E. E. (2015). AI techniques for optimizing multi-objective reservoir operation upon human and riverine ecosystem demands. *J. Hydrol.* 530, 634–644. doi:10.1016/j.jhydrol.2015.10.024

Valeria, R., and Alberto, D. L. F. (2015). Assessing the link between environmental flow, hydropeaking operation and water quality of reservoirs. *Ecol. Eng.* 85, 26–38. doi:10.1016/j.ecoleng.2015.09.074

Wang, H., Brill, E. D., Ranjithan, R. S., and Sankarasubramanian, A. (2015). A framework for incorporating ecological releases in single reservoir operation. *Adv. Water Resour.* 78 (4), 9–21. doi:10.1016/j.advwatres.2015.01.006

Xia, J. Q., Chen, Y. J., Deng, S. S., Zhou, M. R., and Wang, Z. H. (2021). Coupled modeling of flow? Sediment transport and power generation in the Xiaolangdi reservoir. *Adv. Eng. Sci.* 53 (6), 113–121. (in Chinese). doi:10.15961/j.jsuese.202001085

Yan, M., Fang, G. H., Dai, L. H., Tan, Q. F., and Huang, X. F. (2021). Optimizing reservoir operation considering downstream ecological de-mands of water quantity and fluctuation based on IHA parameters. *J. Hydrol.* 600, 126647. doi:10.1016/j.jhydrol.2021.126647

You, J. J., Xue, Z. C., Lin, P. F., Jiang, Y. Z., and Wei, N. (2021). Study on the integrated river basin ecological operation based on Two-layer structure I: Methodology and Model. *J. Hydraul. Eng.* 52 (12), 1449–1457. (in Chinese). doi:10.13243/j.cnki.slxb.20210259

Zeng, C. F., Qi, W. Y., Mao, Y. Q., Liu, R., Yu, B. Y., and Dong, X. N. (2022). Water conservation ecological service function and its value response mechanism in a nested water conservancy project area. *Front. Env. Sci-Switz.* 10, 887040. doi:10.3389/fenvs.2022.887040

Zhao, Q. K., and Cai, X. M. (2020). Deriving representative reservoir operation rules using a hidden Markov-decision tree model. *Adv. Water Resour.* 146, 103753. doi:10.1016/j.advwatres.2020.103753

Zhou, Y., and Guo, S. (2013). Incorporating ecological requirement into multipurpose reservoir operating rule curves for adaptation to climate change. *J. Hydrol.* 498, 153–164. doi:10.1016/j.jhydrol.2013.06.028

frontiers | Frontiers in Environmental Science

TYPE Original Research
PUBLISHED 24 August 2023
DOI 10.3389/fenvs.2023.1221571

OPEN ACCESS

EDITED BY
Jing Zhang,
North China University of Water Conservancy and Electric Power, China

REVIEWED BY
Halil Ibrahim Burgan,
Akdeniz University, Türkiye
Mohammad Zakwan,
Maulana Azad National Urdu University, India
Chuanqi Li,
Shandong University, China

*CORRESPONDENCE
Chaochao Li,
✉ lichaochao@nxu.edu.cn

RECEIVED 12 May 2023
ACCEPTED 27 July 2023
PUBLISHED 24 August 2023

CITATION
Li C, Li C, Bao S and Li M (2023), Influence of different rainfall patterns and soil water content on hydrological processes in small watersheds.
Front. Environ. Sci. 11:1221571.
doi: 10.3389/fenvs.2023.1221571

Influence of different rainfall patterns and soil water content on hydrological processes in small watersheds

Chaochao Li[1,2,3]*, Chenglu Li[1,4], Shuping Bao[4] and Mingyang Li[1]

[1]School of Civil and Hydraulic Engineering, Ningxia University, Yinchuan, China, [2]Ningxia Research Center of Technology on Water-Saving Irrigation and Water Resources Regulation, Yinchuan, Ningxia, China, [3]Engineering Research Center for Efficient Utilization of Water Resources in Modern Agriculture in Arid Regions, Yinchuan, Ningxia, China, [4]Hydrology and Water Resources Monitoring and Warning Center of Ningxia Hui Autonomous Region, Yinchuan, Ningxia, China

Introduction: Due to climate and underlying surface changes, flash floods occur frequently in northwest China, and the extreme rainstorm weather and flash floods along the eastern foot of Helan Mountain are increasing.

Method: By constructing a hydrological model to simulate ten historical mountain flood events in the Suyukou watershed of the eastern foot of Helan Mountain, this study explores the constitutive relationship between rainfall and flood, evaluates accuracy, and analyzes errors. Six characteristic rain patterns were designed based on three parameters representing the position of rainfall peaks and the trend characteristics of rainfall, using 63 actual rainfall processes with a duration of 6 h selected from the rainfall stations of Suyukou watershed. Early warning indicators under different conditions were carried out based on the set of rain patterns.

Results: The research results indicate that eight out of the ten simulated floods have passed the qualification test and the simulation results are good. The HEC-HMS hydrological model is suitable for simulating mountain floods in small watersheds and can provide good support for the simulation and early warning of mountain flood disasters.

Discussion: Designing a rain pattern set based on actual data has put forward higher requirements for mountain flood warning and forecasting, making the warning more in line with the local actual situation and greatly improving the effectiveness of warning and forecasting.

KEYWORDS

HEC-HMS hydrological model, hydrological processes, different rainfall patterns, soil water content, Suyukou watershed

1 Introduction

For Flash flood refers to the phenomenon of natural disasters such as floods, landslides, and mudslides caused by sustained and high-intensity precipitation in hilly areas, influenced by natural conditions such as climate, river basins, and human activities (Cui et al., 2011). Flash flood poses a huge threat to social economy and people's safety, often causing serious consequences such as ecological environment damage and building damage. While causing serious economic losses to the disaster area, they also pose a huge threat to the safety of mountain people (Zhang et al., 2022). The distribution of flash flood in China is relatively widespread, and the occurrence of flood season is also relatively frequent. In recent years, due to climate and underlying surface changes, the degree of global meteorological change has intensified, with frequent occurrence of heavy rainfall in mountainous areas. The frequency of flash flood has significantly increased, and the impact on economic and social development has gradually increased.

At present, flood prevention and control in China are mainly divided into two different types of work: engineering measures and non-engineering measures (Al-Suhili et al., 2019). Engineering measures usually involve measures such as regulating river channels, constructing embankments and reservoirs, and preventing flood disasters through operations such as drainage and storage; non-engineering measures mainly include early warning and forecasting systems developed by meteorological or technical departments for monitoring floods, as well as existing policies for flood control and disaster reduction. Nowadays, the engineering system for flood control and prevention in China is still constantly improving, but the situation of flood control in China is still very severe and cannot be ignored. For the frequent occurrence of complex and highly hazardous flood disasters, water conservancy experts from various regions believe that relying solely on engineering construction measures is difficult to completely solve the flood problem. If only engineering construction measures are used to cope with flood disasters, not only will the workload of engineering construction work increase, but also cause damage to the ecological environment. Moreover, the construction cost of engineering construction work is too high, and each county, district, and country cannot afford it. Therefore, early warning and forecasting systems are an important component of the flood control system and an important means to effectively reduce the number of victims and material losses related to flood control. In recent years, a large number of scholars have conducted relevant research (Mosey et al., 2019; Yoo et al., 2019; Li et al., 2023; Wang et al., 2023). Georgios et al. (2022) combined one-dimensional modeling with two-dimensional modeling using the HEC-RAS model to simulate a disastrous flash flood in the town of Mandra, in Attica, Greece, in November 2017. The study proposed an acceptable error level for calculating the predicted water depth and flood inundation range, providing a basis for modeling flood simulation and prediction. Tu et al. (2020) used eight heavy rainfall events for model calibration and validation, indicating the effectiveness of HEC-HMS in simulating small watersheds in Sichuan Province, China. And using the Pearson III formula widely used in China, the design rainfall at different frequencies was analyzed, and flood hydrographs at different frequencies were calculated to determine two key warning indicators: the flood stage for immediate evacuation and the rate of rise. This research has shown that the early issuance of warning signals is correct and can provide reference for the early warning of flash floods in the study area and other small watersheds in mountainous areas. Huang et al. (2019) proposed a flash flood warning scheme based on hydrodynamics and critical rainfall, which uses designed rainfall, considers different rainfall and initial soil conditions, and establishes a critical rainfall database for flash flood warning, demonstrating a new flash flood warning scheme. Nguyen et al. (2019) developed a flash flood warning system based on geomorphological and hydrological methods to address the frequent occurrence of flash floods during the rainy season in Hoang Su Phi, a mountainous district in Ha Giang province, Vietnam. The system classifies rainfall thresholds and provides early flash flood warnings for the area 1–6 days in advance based on different rainfall values, allowing local governments sufficient time to prevent and mitigate losses caused by flash flood. Hu (2019) proposed a flood calculation method design based on HEC-HMS distributed model in combination with the actual situation of Miaoxia basin and the calculation of rainstorm time distribution by using the short duration rainstorm formula in Zhejiang Province, and determined the flash flood warning indicators by using the water level backward flow method. This study can provide reference for the selection of flash flood warning indicators. The existing research on early warning and forecasting is mostly based on the existing rainstorm intensity formula or a single design rainfall pattern to calculate the time distribution of rainstorm, which cannot fully express the actual meteorological characteristics. The calculation results of early warning indicators are slightly single, and the early warning and forecasting results may have some deviation. This article takes the Suyukou watershed, a typical watershed in the eastern foot of Helan Mountain, as the research object. Based on the investigation of the mechanism of flash flood in the research area, a digital watershed model is constructed and historical floods are simulated. Combined with the measured rainfall in the watershed, a characteristic rainfall pattern set based on three parameters is designed to propose a design rainfall time distribution that is more in line with the local actual situation, and the flash flood warning indicators in the research area are calculated, thus providing theoretical support for the early warning and prediction of mountain flood disasters.

2 Materials and methods

2.1 Study area

Located between the alluvial plain of the Yellow River in Ningxia and the alluvial fan of Helan Mountain, between 37° and 39° north latitude, the eastern foot of Helan Mountain is recognized as one of the most suitable areas for grape planting, wine brewing and high-end wine production in the world. In recent years, due to climate and underlying surface changes, extreme rainstorm weather and flood disasters along the Helan Mountain and at the eastern foot of Helan Mountain have increased (Yang et al., 2020a). For example, on 21 August 2016, a extremely heavy rainstorm exceeding the historical maximum occurred along the Helan Mountain, 239.5 mm precipitation occurred at Suyukou Ski Resort, Helan Mountain, followed by 219.1 mm precipitation in Ruqi gully, both exceeding the historical maximum since the meteorological records, and inducing a flood with a return period of more than 50 years. On 22 July 2018, extremely heavy rainstorm exceeded the historical maximum again along the Helan Mountain. The precipitation of Suyukou Ski Resort was 277.6 mm, the

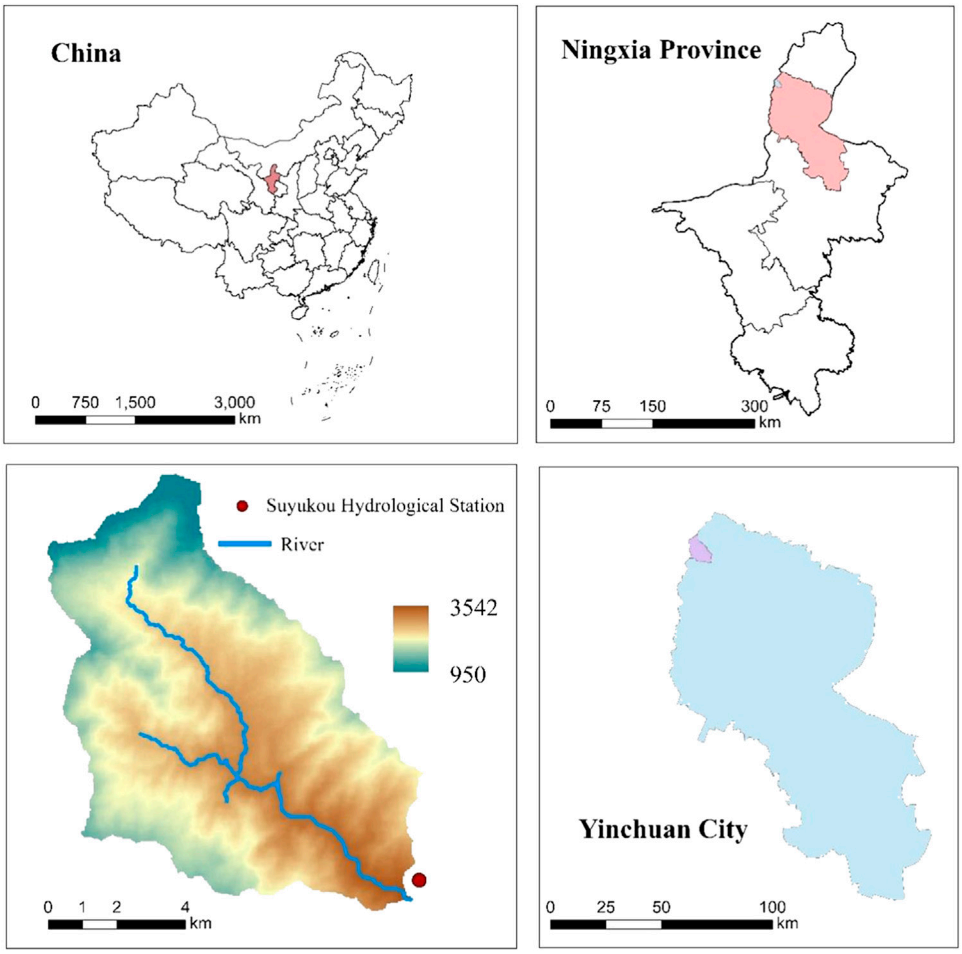

FIGURE 1
Location of Suyukou watershed.

precipitation of Ruqi gully was 247.5 mm, and the precipitation of Helan Mountain Rock Painting was 219.6 mm. This again broke the maximum daily precipitation since the meteorological observation records were available in Ningxia, resulting in 50–200 years floods in several mountain torrents and gullies in Helan Mountain, including Dawukou gully, Ruqi gully, and Suyukou gully (Yang et al., 2020b). Frequent heavy rainfall is one of the main reasons for the occurrence of flash flood in Helan Mountain (Zhou et al., 2022).

The main mountain of the eastern foot of Helan Mountain is steep, with sparse vegetation and low coverage, gradually increasing with increasing altitude. The development of gullies is mostly elongated and parallel to the ridges. There are more than 50 large and small gullies along the eastern foot of the middle section, most of which are V-shaped. The mouth of the gullies is usually a sedimentary fan formed by early debris flows or mountain floods, and later formed by runoff erosion to form a sedimentary rock sea landform. The catchment areas of various gullies on the eastern foot of Helan Mountain range from 3–5 square kilometers to several hundred square kilometers, with 13 gullies having a catchment area greater than 50 km^2 and 21 gullies having a catchment area greater than 30 km^2. A few mountain flood gullies have regular running water, while other gullies are mostly dry gullies except for floods. The surface runoff occurs in the form of rainstorm flood, which is difficult to use. The three mountain torrents in the north directly flow into the Yellow River. The small floods in other channels are lost in the form of overflow on the diluvial slopes, while the large floods wash into the lower flood detention reservoirs, drainage ditches, mountain side channels, etc.

This study is aimed at Suyukou watershed, which is 13.7 km long, 50.5 km^2 watershed area, 73.9‰ channel average gradient, 292.4 mm multi-year average precipitation, 1,230 mm multi-year average evaporation, and 1.534 million m^3 multi-year average runoff. The watershed is prone to frequent floods and poses serious harm. There is a Suyukou Hydrological Station located in gully, which was founded in February 1971 as a central flood reporting station. There are four series of fixed rainfall stations upstream, including Linkuang, Shihuiyao, Suyukou, and Dianjiangtai. On 20 May 1998, the peak flow was 560 m^3/s with a return period of over a hundred years. On 22 August 2016, the peak flow was 435 m^3/s with a 50-year return period. On 22 July 2018, the peak flow was 570 m^3/s with a return period of over two hundred years. Figure 1 shows the schematic diagram of the location information of the Suyukou watershed. The map was downloaded from the national standard map website with the map approval number GS (2019) 1822, then was digitized using ArcGIS.

2.2 Data collection

This hydrological simulation used runoff data from Suyukou Hydrological Station from 1971 to 2018 and rainfall data from two rainfall stations in the Suyukou watershed, namely, the Linkuang and Suyukou, to process abnormal and missing data. Ten complete rainfall flood sequences and 63 typical rainfall events lasting for 6 h were sorted out, providing data support for model simulation and early warning and forecasting research.

2.3 Analysis of the mechanism of flash floods

(1) Unique landforms and geographical location

The water system in the research area runs in a northwest-southeast direction, with low vegetation coverage and very sparse vegetation, mostly shrubs, with a coverage rate of about 47%. The rock mass has been exposed for a long time, with intense tectonic activity, broken mountains, and a large amount of loose material accumulated in the channels and slopes on both sides. Most of the gullies are V-shaped, with vertical and horizontal gullies and large terrain height difference (2.08 km), which is easy to form rainstorm and flash flood, and often accompanied by landslides, debris flows and other secondary disasters.

(2) Concentrated rainstorm and heavy rainfall

The research area is located in the transitional zone between arid and semi-arid regions, deep inland, with an average annual precipitation of 200–400 mm. The distribution of rainfall within and between years is extremely uneven. The precipitation mostly occurs from May to September, accounting for more than 80% of the total precipitation of the whole year, and the precipitation from July to August accounts for more than 40%, and mostly occurs in the form of rainstorm. In each rainstorm process, the precipitation in the rainstorm center is greatly different from that in the edge area. Meanwhile, there are significant interannual differences in rainfall in the study area, the rainfall is very unstable. The uneven spatiotemporal distribution of annual and interannual precipitation not only leads to significant differences in annual runoff in the study area, but also leads to sudden floods with sudden fluctuations, resulting in serious flood disasters. Taking two major floods in recent years as examples, the runoff characteristics are analyzed: the overall flood flow in the study area is large, the flood duration is not long, but the runoff is fast, and the runoff occurs quickly after rainfall, with a fast trend of flood fluctuations.

2.4 Construction of hydrological model

HEC-HMS is a computer program for the hydrological modeling system developed by the Hydrological Engineering Center of the United States Army Corps of Engineers. It can simulate the rainfall runoff and flood routing processes of a watershed under natural or artificial conditions, and it is a distributed hydrological model with physical concepts. This model divides the target research watershed into several sub watersheds, calculates the runoff generation and concentration of each sub watershed separately, and then calculates it to the outlet section of the watershed.

The HEC-GeoHMS module can automatically extract parameters such as terrain and hydrological features from digital basic data, reducing manual workload (Wang and Sun, 2019; Castro and Maidment, 2020; Cheng et al., 2021; Mehlath and Lone, 2022). Extract the river network of the study area through processing such as filling in depressions, flow direction, and confluence, and draw sub watersheds. Through the calculation and analysis of the HEC-GeoHMS module, create a watershed structure map for the HEC-HMS model to use. Import the watershed model module generated by HEC-GeoHMS into the HEC-HMS model, and then generate a watershed model for the Suyukou watershed study area based on the calculation results of the module (Aksoy et al., 2016). The sub watershed and river channel attributes of the Suyukou watershed model are shown in Table 1 and Figure 2.

The analysis and rate determination of some parameters in the HEC-HMS model need to be supported by the land use type, for example, in the initial loss stabilization infiltration method in the flow production calculation stage, the model simulation needs to pass the land use type data and calculate the impervious area parameters and soil infiltration rate of the study area. The land use data were transformed and projected, cropped and classified using ArcGIS to obtain the land use type map of the Suyukou watershed as shown in Figure 2. The land use uses the coverage data downloaded from GlobeLand30 with 30 m spatial resolution, which currently supports downloading data for 2000, 2010 and 2020. In view of the low human activities in the eastern Helan Mountains and the little change in land use types, the land use of 2020 is uniformly used in this study.

2.5 Rain type design method

The typical design for this rain patterns adopts hourly measured rainfall from the two rainfall stations, Linkuang and Suyukou, in the Suyukou watershed. The starting time is selected as the time when the rainfall during the rainfall process is more than or equal to 3 mm, and the ending time is selected as the time when the rainfall is less than 3 mm in a continuous 3-h period. Due to the small area of the sub watershed in the Suyukou watershed and the short duration and high intensity of rainfall during flash floods on the eastern foot of Helan Mountain, only 6-h short duration rainfall processes were selected as the research data in this study. Divide existing rainfall data based on the classification criteria for short-term rainfall events. This study screened 63 typical 6-h rainfall processes from hourly scale measured rainfall data from 4 rainfall stations.

This article will combine the two characteristic factors of rainfall peak position and rainfall process shape to construct a diverse rainfall pattern that represents the characteristics of rainfall peak position and rainfall shape. The parameter “rainfall peak location coefficient *r*” indicates the time of rainfall intensity peak, and the parameters “concentrated Trend Index *CTI*” and “deformation distance *d*” quantify the shape characteristics of rainfall intensity to jointly build a diversified characteristic rainfall model.

TABLE 1 Attribute table of Suyukou basin model. (A) Suyukou watershed Model, **(B)** Landuse Type.

Sub watershed name	Sub watershed area (km^2)	River name	Channel length(m)
W80	20.23	R10	3,159.01
W90	10.18	R20	7,026.42
W100	3.71	R30	78.14
W110	0.06	R40	1,255.79
W120	3.68	R50	518.78
W130	0.86	R60	807.47
W140	11.79	R70	4735.86

2.5.1 Rain peak position coefficient *r*

Rain peak position coefficient r refers to the ratio of the time period during which the maximum rainfall occurs per unit time during a rainfall process to the total duration of that rainfall, which is used to determine the time when the rainfall peak appears in that rainfall event. The calculation method is as follows:

$$r = \frac{T_{\max}}{T} \tag{1}$$

In the formula: $T_{\max}$ is the time/h at which the maximum rainfall occurs within a unit time period; T is the total duration of rainfall per hour.

2.5.2 Concentrated Trend Index (*CTI*)

CTI is a parameter used to describe the distribution of rainfall peaks and their adjacent time periods during rainfall events. The values of the boundary conditions α、β $(\alpha < \beta)$ are generally selected for the most uniform, concentrated and dispersed typical rainfall processes in the watershed. Based on the measured rainfall data of the research watershed, the *CTI* calculated from the selected typical rainfall processes is used as a reference value for determining boundary conditions. *CTI* can be used to determine the concentration of rainfall. The *CTI* principle indicates that the larger the value of *CTI*, the more precipitation is concentrated before and after the peak precipitation. On the contrary, the smaller the value of *CTI*, the more uniform the distribution of precipitation in each time period, and the total precipitation is mainly evenly distributed in each time period.

The *CTI* calculation formula is as follows:

$$CTI = \begin{cases} B \times \dfrac{P_{tr-1}^2 + P_{tr}^2 + P_{tr+1}^2}{\left(\sum_{t=1}^{T} P_t\right)^2} \times 100\%, 3 \le T \le 6; \\ B \times \dfrac{P_{tr-2}^2 + P_{tr-1}^2 + P_{tr}^2 + P_{tr+1}^2 + P_{tr+2}^2}{\left(\sum_{t=1}^{T} P_t\right)^2} \times 100\%, 7 \le T \le 12; \\ B \times \dfrac{\sum_{i=1}^{i=4} \left(P_{tr-1}^2 + P_{tr}^2\right) + P_{tr}^2}{\left(\sum_{t=1}^{T} P_t\right)^2} \times 100\%, 13 \le T \le 24. \end{cases} \tag{2}$$

In the formula: P_{tr} is the unit time period rainfall/mm at the peak of rain; P_t is the rainfall during the period/mm; T_r is the period during which the rain peak occurs; I is the number of adjacent time periods during peak rain periods; B is the normalized index per unit time period, i.e., $B = 60/\Delta T$.

2.5.3 Deformation distance (*d*)

Deformation distance d can further study the trend of increasing and decreasing precipitation intensity. This parameter refers to the jump between the cumulative precipitation at the peak and the cumulative precipitation at adjacent time points before and after the peak.

Due to the changes in the position of the rain peak during the rainfall process, it can be summarized into three situations: (a) the rain peak is located at the beginning of the rainfall; (b) the rain peak appears in the middle of the rainfall; (c) the rain peak appears at the end of the rainfall. The deformation distance d can be expressed as a piecewise function, as follows:

$$d = \begin{cases} B \times \dfrac{H_{tr+1} - H_{tr}}{H_{tr}}, r = \dfrac{1}{T}; \\ B \times \dfrac{H_{tr+1} - 2H_{tr} + H_{tr-1}}{\sqrt{\left(H_{tr+1} - H_{tr-1}\right)^2 + 4H_{tr+1}}}, \dfrac{1}{T} < r < 1; \\ B \times \dfrac{H_{tr} - H_{tr-1}}{H_{tr-1}}, r = 1. \end{cases} \tag{3}$$

In the formula: H_{tr} is the cumulative rainfall at the time of the rain peak/mm; H_{tr-1}、 H_{tr+1} are the cumulative rainfall/mm before and after the adjacent rain peaks; t_{r-1}、 t_{r+1} represent the pre and post rain peak periods/h.

2.6 Basic flow chart

Three This study analyzes the mechanism of flash floods in the Suyukou watershed by collecting historical flash flood-related data survey, collection, collation and site investigation, combining actual measured precipitation and runoff data, meteorological station distribution, digital elevation model, land use and soil type and remote sensing images in the study area. A digital watershed model based on HEC-GeoHMS is constructed to establish the relevant database, determine the rainfall weights of sub-basins and the base parameter conditions. The HEC-GeoHMS model is used to adjust the parameter rates in conjunction with historical flash flood runoff relationships, to determine the water level and flow relationships in the study area in conjunction with measured rainfall and runoff data, and to design a diverse set of rainfall types. The HEC-HMS

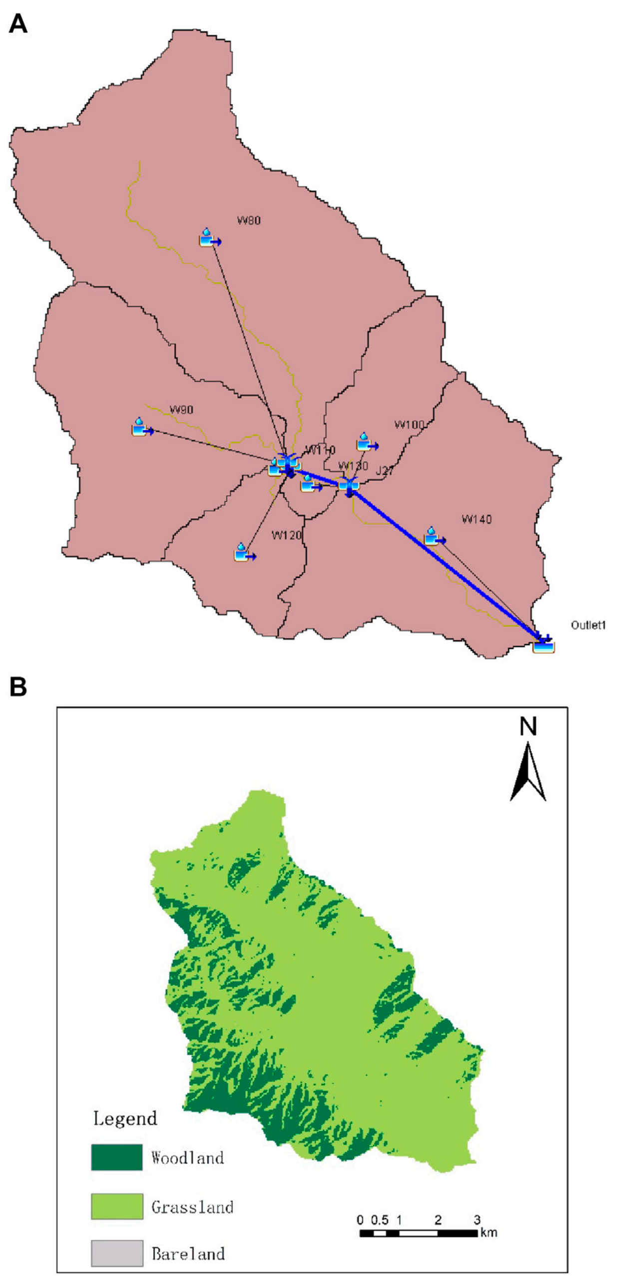

FIGURE 2
(A) Suyukou watershed Model, **(B)** Landuse type.

model, the water level and flow relationship, and the design of rainfall patterns are used to determine the early warning index calculation for flash floods in the study area. The specific basic flow of the study is shown in Figure 3.

3 Results and analysis

Due to incomplete data and other reasons, this study only used two rainfall stations in the Suyukou watershed, Suyukou and Linkuang, for flood simulation. The location of rainfall stations is shown in Figure 4A.

Seven sub watersheds use two rainfall stations, namely, Linkuang and Suyukou, and the contribution weights of the rainfall stations to each sub watershed are generalized using the Thiessen polygon, as shown in Figure 4B. The weights of rainfall data used in each sub-basin are calculated from the images and entered into the basin model.

3.1 Analysis of flood processes

Five typical flood events with detailed data from 2016 to 2018 were selected for simulation. Due to the relatively new year and relatively complete measurement of rainfall data, the time scale of rainfall and flow data during the flood period is 10 min. Using five floods with relatively complete data from 1984 to 2012 for parameter validation, the time scale of rainfall and flow data during the validation period is 1 h. Obtain the basic situation and simulation results of five typical floods on a regular basis (Table 2; Figure 5):

Based on the simulation results of five regular flood processes, the parameters were calibrated and validated using floods with relatively complete data from 1984 to 2012 to obtain flood frequency information and validation results (Table 2; Figure 5).

3.2 Accuracy assessment of flood simulation

This study selected the peak to peak time difference Δt, Relative error of flood peak RE_p and Nash efficiency coefficient (NSE) are three evaluation criteria to distinguish the simulation results of the model (Zhang and Tang, 2021). According to the relevant provisions of the *Standard for Hydrological Information and Hydrological Forecasting of the People's Republic of China* (GB22482-2008T) and international hydrological model evaluation standards, the error of flood peak occurrence time is within 3 h, the relative error of flood peak is within 20%, which is qualified, and the Nash efficiency coefficient is greater than 0.9, which is Class A accuracy; the Nash efficiency coefficient between 0.7 and 0.9 is of second order accuracy; the Nash efficiency coefficient is of Class C accuracy between 0.5 and 0.7. The calculation expressions are (Majid and Mohammad, 2021a; Majid et al., 2021b):

$$\Delta t = |t_0 - t_s| \tag{4}$$

In the formula: t_s is the simulated flood peak time; t_0 is the measured flood peak time; Δt is the time difference between peak and current.

$$RE_p = \left|\frac{Q_0 - Q_s}{Q_0}\right| \times 100\% \tag{5}$$

In the formula: Q_s is the simulated peak flow rate; Q_0 is the measured peak flow rate; Re_p is the relative error of flood peak.

$$NSE = 1 - \frac{\sum_{t=1}^{T}\left(Q_s^t - Q_0^t\right)^2}{\sum_{t=1}^{T}\left(Q_0^t - \overline{Q_0}\right)^2} \tag{6}$$

In the formula: Q_s^t is the simulated traffic at time t; Q_0^t is the measured flow rate at time t; $\overline{Q_0}$ is the average observed flow rate. If the peak time difference, relative error of flood peak, and Nash

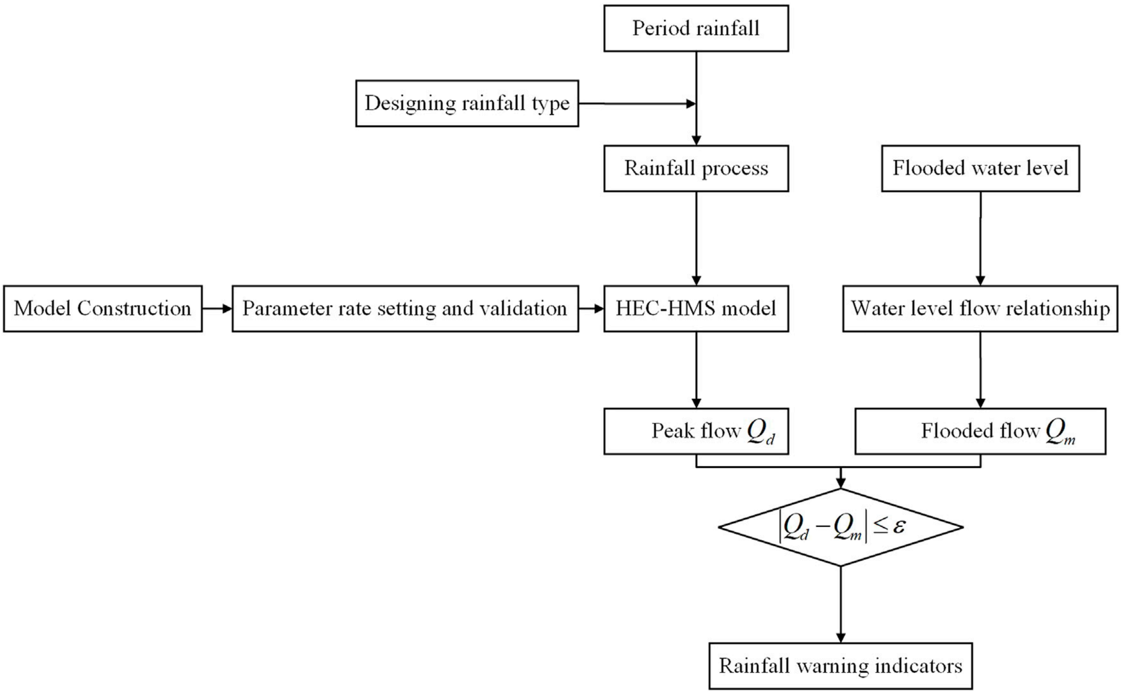

FIGURE 3
Basic flow chart.

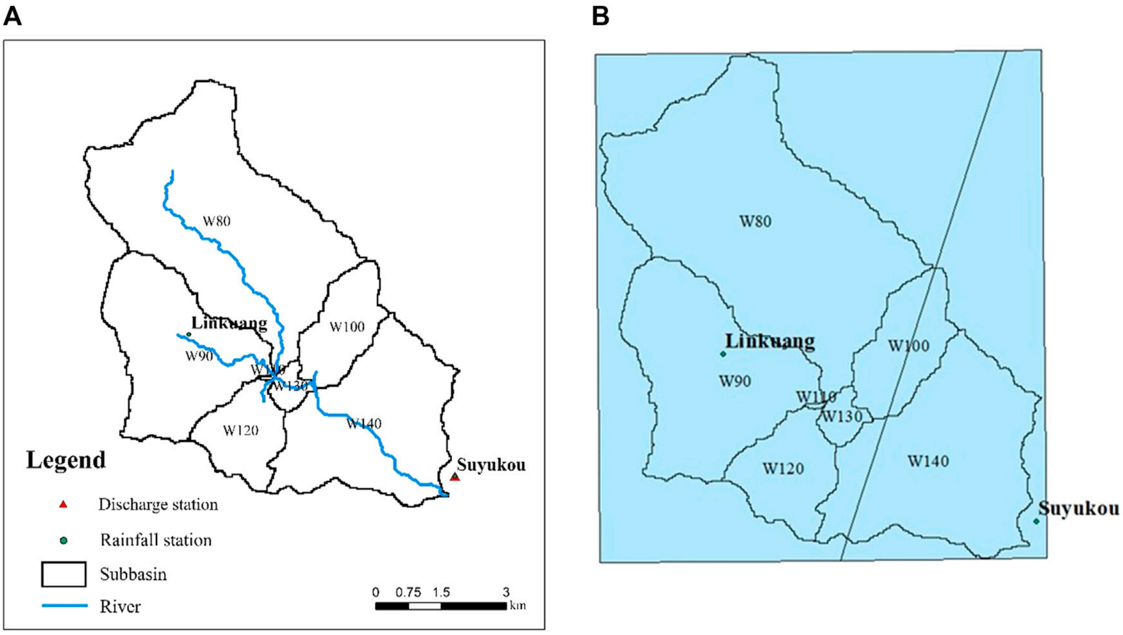

FIGURE 4
Distribution of Rainfall Stations in the Suyukou watershed. **(A)** Location of rainfall stations, **(B)** Thiessen polygon distribution.

coefficient are all qualified, it is considered qualified. The simulation results are shown in Table 3.

Table 3 reflects the basic situation and effectiveness of using HEC-HMS model to simulate five floods in the Suyukou watershed during the validation period and at regular intervals. It can be seen that within the designated period, a total of four out of five floods were simulated as qualified, with a qualification rate of 80%. From the perspective of peak occurrence time, the simulated peak

TABLE 2 Basic flood conditions.

Serial number	Flood frequency	Starting time	End time	Last(h)	Peak hour	Peak discharge (m^3/s)
1	20160821	0821 19:00	0822 6:00	11	0822 1:10	434
2	20170705	0705 11:30	0705 16:00	4.5	0705 12:40	72.4
3	20170725	0725 21:30	0726 0:00	2.5	0725 11:10	118
4	20180719	0719 6:30	0719 10:00	3.5	0719 7:20	70.7
5	20180722	0722 19:00	0723 7:00	12	0722 23:30	580
1	19840801	0801 16:00	0802 0:00	8	0801 21:00	125
2	19890803	0803 16:00	0803 23:00	7	0803 19:00	39.8
3	20060714	0714 19:00	0715 8:00	13	0714 22:00	37.2
4	20070714	0714 17:00	0714 22:00	5	0714 20:00	38
5	20120729	0729 19:00	0730 4:00	9	0729 22:00	28.9

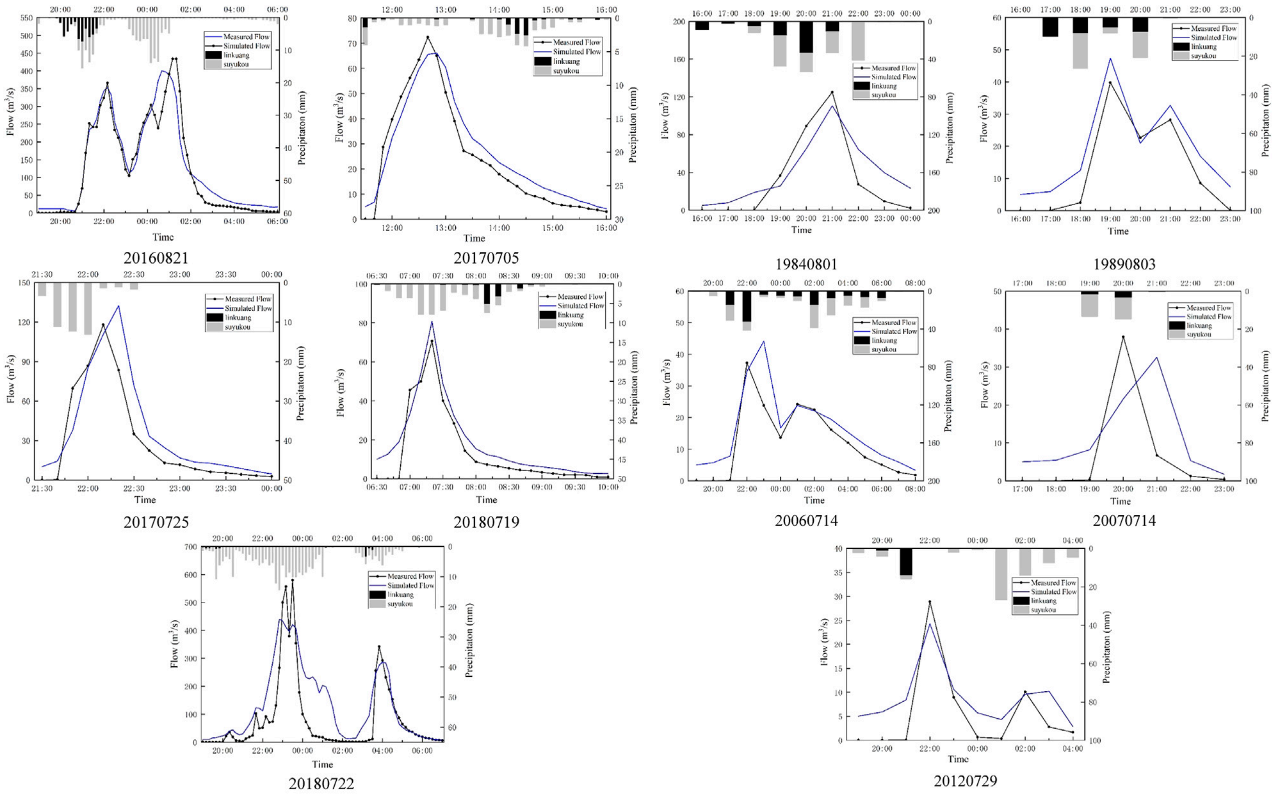

Setting period flood simulation results

Verification period flood simulation results

FIGURE 5
Flood simulation results.

occurrence time of the five floods is within 3 h of the measured value. The peak flow error of the 20180722 flood simulation reached 24.2%, which has a certain error compared to the qualified standard. The Nash efficiency coefficient is only 0.520, which is of Class C accuracy. Overall, it is evaluated as an unqualified flood simulation, and the reasons for the error are shown in Section 3.3. Among the other four flood events, the Nash efficiency coefficient of the 20160821 flood reached 0.919, overall achieving Class A accuracy, while the Nash efficiency coefficients of the remaining three floods were 0.835, 0.744, and 0.858, all of which were Class B accuracy. During the validation period, all five floods except for the 20070714 flood were simulated as qualified, with a qualification rate of 80%. Among them, the Nash efficiency coefficients of the 19840801 floods and the 19890803 floods reached 0.753 and

TABLE 3 Flood simulation results.

	Flood frequency	Simulated peak time	Measured peak time	Peak to peak time difference(h)	Simulated flood peak (m^3/s)	Measured flood peak (m^3/s)	Peak flow error (%)	Nash efficiency coefficient	Qualified or not
Setting period	20160821	0822 0:40	0822 1:10	−0.5	400.4	434	7.7	0.919	Yes
	20170705	0705 12:50	0705 12:40	0.17	66.1	72.4	8.7	0.835	Yes
	20170725	0725 22:20	0725 22:10	0.17	132.5	118	12.3	0.744	Yes
	20180719	0719 7:20	0719 7:20	0	76.9	80.9	4.9	0.858	Yes
	20180722	0722 22:50	0722 23:30	−0.67	439.7	580	24.2	0.520	No
Validation period	19840801	0801 21:00	0801 21:00	0	112.6	125	9.9	0.753	Yes
	19890803	0803 19:00	0803 19:00	0	46.4	39.8	16.6	0.783	Yes
	20060714	0714 23:00	0714 22:00	1	44.1	37.2	18.5	0.652	Yes
	20070714	0714 21:00	0714 20:00	1	32.6	38	14.2	0.090	No
	20120729	0729 22:00	0729 22:00	0	24.3	28.9	15.9	0.662	Yes

The positive value of the peak time difference in the table represents the simulated peak time lag; A negative value represents an earlier simulation peak time.

0.783, respectively, achieving Class B accuracy. The Nash efficiency coefficients for the floods of 20060714 and 20120729 were 0.652 and 0.662, respectively, achieving Class C accuracy. The peak flow rate and occurrence time error of the five floods were within a reasonable range, but the Nash efficiency coefficient of the 20070712 flood was only 0.090, indicating that the simulation results were unqualified.

3.3 Analysis of the causes of the difference in flood simulation

As shown in Section 3.2, the simulation results have achieved a good correspondence with the measured results, but there are still some errors, which may be caused by.

(1) Insufficient data monitoring accuracy

The total area of the Suyukou watershed is 50.5 km^2, and this simulation only used two rainfall stations, Linkuang and Suyukou, in the study area. Due to the remote geographical location and economic factors of the Suyukou research area, the distribution of survey stations is relatively scattered, and the distribution of survey stations is also uneven. Measurements may also have deviations (Qiu et al., 2019), which may differ from the actual flood hydrograph. In addition, due to the imperfect early monitoring system and relatively backward measuring equipment, data measurement and recording often require manual operation, and in case of a major rainstorm, there may be errors in the measurement due to the inability to obtain data in time, resulting in errors in the simulation results.

(2) The underlying surface has changed

During this study, there was a significant difference in the maximum years of simulated floods, with a maximum span of 34 years. Due to factors such as hydrological and meteorological changes in space and time, as well as human activities (Hu and Shrestha, 2020), the underlying surface conditions and specific situations at the time of each flood occurrence were actually different (Azizi et al., 2021). However, this study only used fixed and unchanged underlying surfaces to calibrate parameters, which is also the reason for the error (Mohammad, 2018).

(3) The generalized impact of rainfall data

The areal rainfall in Suyukou watershed is obtained by generalizing the rainfall weight according to the Thiessen polygon method based on the geographical location of rainfall stations, while ignoring the influence of rainstorm center on the whole rainstorm flood hydrograph. However, the rainstorm center actually has a very obvious peaking effect on the flood hydrograph, affecting the peak value and peak time in the flood simulation results, which is also the reason for the error between the measured value and the peak value.

Taking the analysis of flood simulation results from 20180722 flood as an example: It can be seen that the precipitation and flood processes in the Suyukou watershed cannot be completely matched, and the latter half of the rainfall did not produce a significant flow process. However, from 23:30 on July 22 to 1:00 on July 23, the precipitation reached 68 mm, accounting for about 1/4 of this precipitation, but the flood flow decreased rapidly. Through analysis, it was found that the possible cause of this phenomenon was the movement of the rainstorm center. The rainfall range of the rainstorm center after the movement was located at the downstream of the catchment area of the hydrological station, close to the location of the hydrological station, and had little impact on the flood process of the hydrological station, but in reality, the rainfall in the watershed is still rising. Therefore, increasing the layout of rainfall stations and improving the monitoring capacity will help to better capture the central position of rainstorm and get more accurate rain and flood forecast.

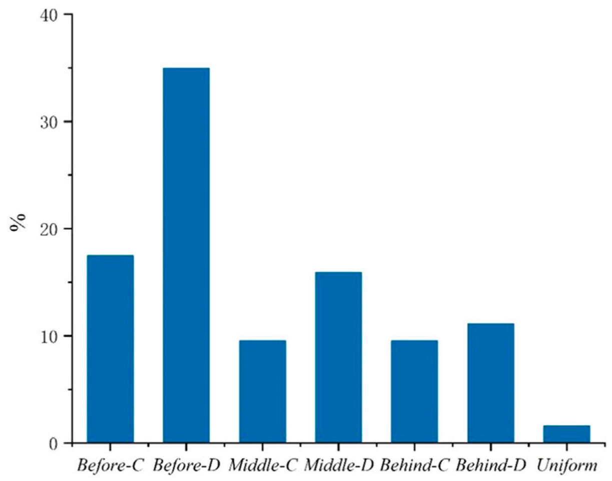

FIGURE 6
Diversity characteristics rainfall field statistics results.

3.4 Characteristic rain pattern design

The rainfall patterns in a region are not limited to a single form. Rainfall patterns always have diversity and randomness. If only one rainfall pattern is used to predict flood occurrence in early warning and forecasting research, the characteristics of other rainfall patterns in the study area are not taken into account, and the results will be greatly different from the actual situation. Therefore, this study uses different precipitation types with different characteristics for early warning and prediction. Based on the measured precipitation data in the study area, a cumulative precipitation time history distribution function with precipitation type characteristics is constructed. The distribution curve of precipitation over time is obtained through a first-order differential distribution function to determine different precipitation types corresponding to the actual precipitation situation (Yuan et al., 2019b).

Based on the actual rainfall process of the rainfall station, 63 rainfall processes with a duration of 6 h were selected to calculate the location coefficients of each rainfall peak, and the distribution pattern of typical rainfall peak positions was analyzed. Formula (2) is used to calculate the central tendency of each rainfall, where $\alpha = 0.06$, $\beta = 0.20$ is calculated by selecting the typical uniform rainfall and typical concentrated rainfall utilization Eq. 2 from the measured rainfall data in the Suyukou watershed. Calculating the deformation distance of each rainfall event with equation, which can help to analyze the shape characteristics reflected in the temporal distribution of rainfall in the Suyukou watershed, and to represent the characteristics of rainfall intensity changing over time throughout the entire rainfall event.

Based on the diversity characteristics of rainfall processes, this article proposes six representative feature rain patterns, namely, Before-Concentrated, Before-Dispersive, Middle-Concentrated, Middle-Dispersive, Behind-Concentrated and Behind-Dispersive. Due to the existence of *uniform* rainfall during the actual rainfall process, this is a type of rainfall where the variation of rainfall intensity over time is relatively small, and the difference in rainfall between different periods of the entire rainfall is not significant.

Through the statistics of 63 historical measured rainfall data, the frequency of different characteristic rainfall patterns in the Suyukou watershed is shown in Figure 6. The statistical results demonstrate the diversity of rainfall types in the Suyukou watershed. Among them, the rainfall events with the highest peak position occur the most, with a probability of 52.4%, with concentrated rainfall accounting for 17.5% and scattered rainfall accounting for 34.9%. The types of rainfall with a peak position in the middle and behind are slightly fewer, but their proportion in overall statistics is still relatively large. The proportion of rainfall with a peak position in the middle reaches 25.4%, while the proportion of rainfall with a peak position behind is 20.6%. Due to the relatively small occurrence of uniform rainfall, it can be ignored, and future research will no longer consider uniform rainfall patterns.

Due to differences in different regions, the construction and selection of cumulative precipitation distribution function and probability density function of typical precipitation in the study area should be determined in combination with the specific catchment characteristics and soil conditions in the study area to find the distribution function that conforms to the characteristics of the actual situation in the study area. In order to better fit the cumulative distribution function and the probability density function, when adjusting the cumulative rainfall distribution over time according to rainfall patterns with different characteristics, it is usually necessary to evaluate the adjustment results through evaluation. Select four indicators Adj. R-Square, RSS, Prob > F, and DFit Status for fitting evaluation.

Nonlinear fitting was performed on the short-term cumulative rainfall duration distribution curve under six diverse rainfall characteristics in the Suyukou watershed to determine the cumulative distribution function. The results are shown in Figure 7 and Table 4.

By performing first-order differentiation on the fitting functions of different characteristic rainfall patterns in Table 4, the distribution of descending rain time history for different characteristic rain patterns can be obtained as shown in Figure 8. The subsequent rainfall input sequence is designed according to the following allocation.

In summary, when determining the relationship between rainfall and runoff, the randomness and diversity of rainfall itself cannot be ignored. The specific time distribution process of rainfall should be used to describe the rainfall process in the region. Extracting the diversity characteristics of rainfall distribution characteristics in different periods of the Suyukou watershed and classifying them, analyzing and calculating the diversity of rainfall patterns that can represent their rainfall characteristics, can improve the accuracy of the rainfall runoff relationship, and provide more accurate input conditions for determining early warning indicators in mountain flood analysis research.

3.5 Calculation of warning indicators

3.5.1 Determination of warning period

In order to calculate the warning index in this study, the warning period is defined as the typical rainfall duration of the target basin. The required rainfall warning index in this study is obtained based on experimental modeling and calculation of critical rainfall at

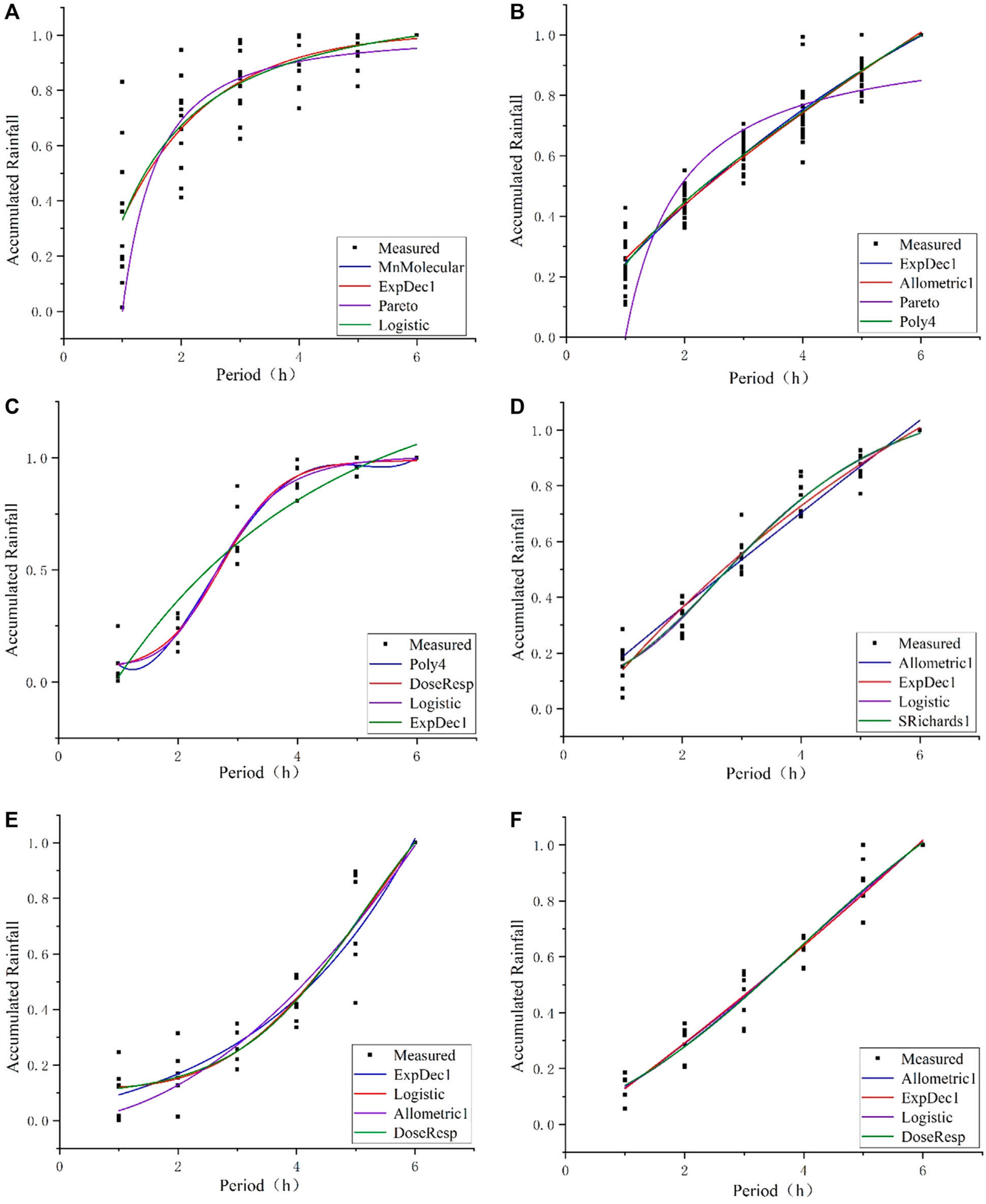

FIGURE 7
Fitting results of cumulative rainfall distribution of characteristic rainfall patterns. **(A)** Before-C, **(B)** Before-D, **(C)** Middle-C, **(D)** Middle-D, **(E)** Behind-C, **(F)** Behind-D.

different warning periods. The critical rainfall is also related to the disaster water level of the research object, which is the minimum rainfall and rainfall intensity that can be reached or exceeded when the river section water level coincides with the disaster water level. Therefore, the warning period of the watershed should be estimated in advance. Taking the Suyukou watershed as an example, the calculation method is as follows.

(1) Determine the longest catchment period: Check the hydrological basin model, where the watershed with the

TABLE 4 Optimal fitting function equation for each rain pattern.

Rainfall pattern	Fit the optimal function type	Function formula	Fit correlation
Before-C	MnMolecular	$y = 1.0126 \times (1 - \exp(-0.6615(x - 0.3968)))$	0.739
Before-D	ExpDec1	$y = 1.8246 - 1.7983e^{\frac{-x}{7.7301}}$	0.941
Middle-C	Logistic	$y = 1.0119 - \frac{0.0652}{(1+(\frac{x}{2.7550})^{5.4395})}$	0.957
Middle-D	Logistic	$y = 1.2173 - \frac{1.1012}{(1+(\frac{x}{3.5334})^{2.5366})}$	0.967
Behind-C	DoseResp	$y = 0.0883 + \frac{0.5135}{1+10^{(5.1028-x)\times p}}$	0.909
Behind-D	Allometric1	$y = 0.1308 \times x^{1.1453}$	0.958

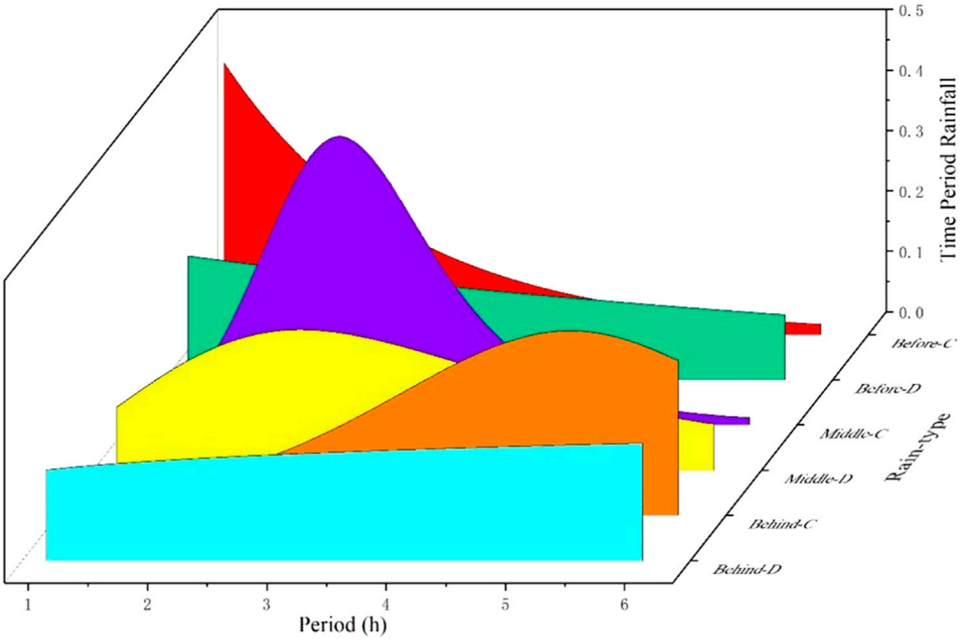

FIGURE 8
Characteristic rainfall patterns time allocation process.

farthest distance from the outlet is W80 (Figure 4A), and the catchment time to the outlet is about 6 h. Therefore, the longest catchment time for this study is determined to be 6 h.

(2) Determine the typical time period: Typically, typical time periods are determined based on various comprehensive situations in the study area. In this study, the Suyukou watershed belongs to a small watershed, so the minimum warning period is selected as 0.5 h, and other typical warning periods are selected as 1 h and 3 h, respectively. The subsequent design rainfall duration for the designated flood control section of the Suyukou wayershed is divided into four time periods: 0.5 h, 1 h, 3 h, and 6 h.

3.5.2 Soil moisture content analysis

The analysis of early warning indicators requires analyzing the degree of moisture in the soil before precipitation. Before the occurrence of rainfall events, the degree of soil moisture in the watershed has a significant impact on the generation of flow. If the soil is initially very humid, it is more likely to generate flow than if a rainfall event occurs in a dry soil state. The Suyukou watershed, which was simulated in this study, is located in the arid northwest region, with floods typically occurring during the hotter seasons of July, August, and September. This article divides the soil moisture in the early stages into three types: extremely dry, relatively dry, and average. The soil moisture content is set to: $0.2W_m$, $0.5W_m$, $0.8W_m$.

3.5.3 Calculation of water level and discharge relationship at crosssection

The calculation of critical flow rate generally involves analyzing the relationship between water level and flow rate. The critical flow rate, also known as the flow rate corresponding to the flood level, is very important for analyzing flood control capacity and warning indicators. It can be determined based on the water level flow relationship, that is, the critical flow rate can be derived based on the disaster water level of the research object.

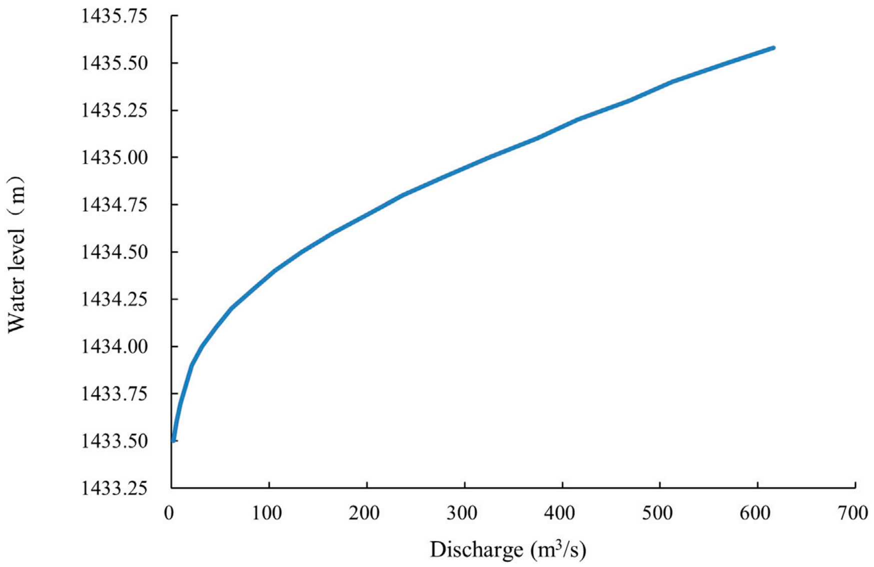

FIGURE 9
Water level discharge relationship curve.

Based on the disaster water level obtained from on-site survey and search, the water level flow relationship of the river is calculated, as shown in Figure 9. The catastrophic water level is 1,434.3 m, and the critical flow rate can be calculated to be 83.26 m^3/s based on the water level flow curve in Figure 9.

3.5.4 Calculation of early warning indicators

This article uses critical flow as a warning indicator for mountain flood warning. Based on the analysis of measurement data, the critical flow rate value of the study area was calculated. On the basis of the HEC-HMS model, with initial rainfall as the model input, based on the calculated critical flow rate, a series of design rainfall based on measured data and modeling results are assumed to simulate and analyze the flood process in the study area. The flood flow simulated by the above model were compared and analyzed with the calculated critical flow of the study area If these two flows are equal, it is assumed that the rainfall is the critical rainfall in the study area.

By distributing precipitation to various characteristic precipitation types (Yuan et al., 2019a), the precipitation distribution at different time periods within different confluence times in the Suyukou watershed was calculated, which is the rainfall sequence used to input the model. Based on the debugged parameters, the HEC-HMS model was used to calculate and compare the calculated peak flow with the disaster flow, forming a flood simulation hydrograph (Shen et al., 2021), so this assumption is that the rainfall is the critical rainfall for this research object (Table 5).

4 Dicussion

This study used HEC-HMS to simulate the flood hydrograph of small watersheds in the northwest mountainous areas of China, and the simulation effect was good. It has great application value in the analysis of early warning indicators in hilly watersheds, but there are shortcomings in the work. The simulation accuracy can be further improved from the following aspects.

The input rainfall and runoff data of the model has a significant impact on the calculation performance of the model. Currently, only two representative stations in the Suyukou watershed have been selected for flood simulation, which poses a problem of poor representativeness of rainfall data from rainfall stations. In the future, simulation should be conducted on the premise of obtaining more rainfall station data, in terms of monitoring, the accuracy of monitoring can be improved by adding monitoring points, rainfall stations, etc.

The HEC-HMS hydrological model integrates many different hydrological models and algorithms, and only by selecting and using these methods reasonably can the model maximize its benefits. In this study, due to the limitation of data and time, the selection of hydrological model simulation method is relatively hasty, and the parameters are not determined completely through the physical properties of the study area, which cannot give full play to the maximum benefit of the hydrological model. The hydrological model with physical distribution significance should be further studied in the next study to better simulate the rainstorm and flood process.

(3) This study temporarily only used HEC-HMS hydrological model for flood process simulation. Although good simulation results were achieved, the actual physical significance of some parameters was still ignored in the calibration of some parameters. At present, although there are few mature models in China that can be used for flood simulation, there are also some that can be used in practical work. In the future, further research can be strengthened on the basis of this study, using more hydrological models to simulate the region’s hydrology, comparing the simulation results, selecting the most suitable model that can use

TABLE 5 Critical rainfall results under different conditions in the study area. Unit: mm.

Early soil moisture content	Warning period(h)	Before-C	Before-D	Middle-C	Middle-D	Behind-C	Behind-D
$0.2W_m$	0.5	31.1	36.7	29.3	33.7	28.8	32.9
	1	48.3	52.8	46.4	49.6	44.3	46.4
	3	97.9	82.7	89.5	79.7	86.5	70.4
	6	143.8	123.7	132.4	121.6	129.8	115.4
$0.5W_m$	0.5	26.7	32.7	25.3	30.7	24.6	28.7
	1	42.8	49.7	37.6	47.5	35.4	43.7
	3	86.5	77.6	82.1	73.5	78.5	71.6
	6	118.5	113.8	116.3	107.7	109.8	101.6
$0.8W_m$	0.5	23.2	30.7	22.8	28.7	20.7	26.5
	1	38.5	43.6	35.3	41.4	33.2	39.7
	3	78.7	73.9	73.4	69.7	71.7	65.4
	6	121.3	108.5	117.6	105.5	114.4	102.5

multiple different hydrological models for the same area for modeling and simulation, and selecting the model with the best simulation results to achieve more comprehensive warning and forecasting indicators.

In this study, the innovation lies mainly in the design of the three-parameter rainfall set based on the actual conditions of the study area. In the research process of early warning indicators, different from the previous rainstorm intensity formula and the single design of rainstorm rainfall pattern, this study designed a characteristic rainfall pattern set that conforms to the actual situation of the study area based on the three parameters representing the peak rainfall and rainfall distribution, and designed rainfall time distribution based on the rainfall pattern set, providing support for accurate early warning of mountain torrents in the study area. In the design of rain pattern, the rain pattern describes the distribution process of rainstorm intensity on the time scale, which requires that both intensity variation and time variation be considered. Since the 1950s, many scholars have adopted different methods to study rainfall patterns, and have successively proposed the Chicago Rainfall Model (Keifer and Chu, 1957), Huff Rainfall Model (Huff, 1967), and P&C Rainfall Model (Pilgrim and Cordery, 1975), which have been used for the calculation of urban floods. Chen et al. (2023) used a hydrological and hydrodynamic model to simulate design rainfall based on the Chicago rain pattern at different return periods and rainfall peaks, analyzing the total amount of water accumulation and inundation range. With the deepening of research, rainfall patterns are gradually being applied to flash flood warning. At present, the traditional rain fall pattern (TRP) is often used to calculate the critical rainfall of a watershed. TRP is a simplified single rainfall model, which is usually determined according to the typical rainfall process in the rainstorm manual in the region. For example, the TRP in Henan Province rainstorm handbook is the typical 24 h rainfall process of "75.8" food (i.e., a terrible flood occurred in August 1975). However, due to the randomness of rainfall, a single rainfall pattern during the flood season may lead to inaccurate design floods or hydrological simulations, affecting the accuracy of critical rainfall. Therefore, in disaster warning, it is necessary to determine the appropriate rainfall pattern by considering the rainfall characteristics of small watersheds. After collecting rainfall data from Ukraine, former Soviet scholars such as Bao Gaomazova roughly divided rain patterns into seven types. By calculating the proportional relationship between rainfall at each time period and total rainfall and comparing the similarity of the seven typical rain patterns, they determined the type of rain pattern. This method is called fuzzy recognition method. Sun et al. (2019) used the fuzzy recognition method to analyze the short duration rainstorm in Nanjing in recent 25 years, identify the rain pattern of each rainstorm sample, analyze the composition structure of the rain pattern of each rainstorm sample, and explore the distribution law of the rain peak from the number and coefficient of the rain peak. Based on the distribution characteristics of actual rainfall, this study uses three characteristic parameters to describe the time distribution of rainfall process under different rainfall peak locations and rainfall trends, selects an appropriate cumulative distribution function, and uses probability density function to characterize the characteristic rainfall model. Compared to single design rain patterns and fixed rain patterns, using characteristic parameters to classify rain patterns is more flexible, and the determined set of rain patterns is more in line with local actual conditions, which has good applicability and is worth promoting.

5 Conclusion

In this paper, Suyukou watershed, a typical watershed in the eastern foot of Helan Mountain, is taken as the main research object. HEC-HMS model is used to simulate the flood process in the watershed. The model parameters are optimized and calibrated through five floods with newer years and more complete data. The rationality of model parameters is verified with five data validation of floods with longer years, and good simulation results are obtained. The main conclusions are as follows.

(1) The HEC-GeoHMS extension module of ArcGIS is used to generate a digital water system map of the Suyukou watershed through a digital elevation model and establish a watershed model. Using the constructed hydrological model, using rainfall data from two rainfall stations, Linkuang and Suyukou, and runoff data from Suyukou hydrological station, five floods were selected for parameter calibration analysis. The model simulation results were validated using five floods. The results showed that 8 out of 10 typical floods passed the qualification test, with a qualification rate of 80%. The simulation results are good. This indicates that HEC-HMS has good applicability in small watersheds in mountainous areas, and has guiding significance for model simulation of small watersheds in mountainous areas. It can provide a foundation for flood warning and prediction in mountainous areas and can be widely used.

(2) A characteristic rain pattern set is designed based on three parameters that represent the position of rain peaks and the trend of rainfall, and a cumulative precipitation time history distribution function with precipitation type characteristics was constructed by conbining with the actual measured rainfall data in the research area. Through first-order differentiation, obtain the distribution curve of precipitation over time, and determine the rainfall set corresponding to the actual rainfall situation. Based on the characteristic parameter design, the characteristic rain pattern set adapted to the measured rainstorm in the Suyukou wateshed found that the rainfall frequency in front of the peak position appeared most, accounting for 52.4% of the total rainfall frequency, of which the concentrated rainfall accounted for 17.5% and the dispersed rainfall accounted for 34.9%. Rainfall with a peak at the center and a peak at the back account for 25.4% and 20.6%, respectively. The frequency of scattered rainfall in different peak positions is higher than that of centralized rainfall. Compared with a single designed rain pattern, rain patterns based on actual rainfall characteristics can more fully represent the actual situation of the research area and provide more accurate input conditions for the determination of early warning and forecasting.

(3) The measured cross-sectional map of the research area was obtained through on-site investigation and establish a water level discharge relationship curve. Then, based on on-site investigation and relevant staff experience, obtain water level warning indicators and calculate the critical flow rate. Design rainfall time history allocation under different characteristic rainfall patterns as input conditions for the model, determine different warning periods based on the study area's convergence time, and combine three soil moisture content models. Apply model trial calculation method to continuously calculate the critical rainfall of the research object under different soil states, rainfall duration, and characteristic rainfall patterns as warning indicators. It can be seen that there are significant differences in the warning indicators under different rain patterns; the longer the warning time, the higher the warning indicators; the lower the soil moisture content, the higher the warning indicators. The results provide theoretical support for the Suyukou watershed flash flood warning and forecasting system.

Data availability statement

The original contributions presented in the study are included in the article/supplementary material, further inquiries can be directed to the corresponding author.

Author contributions

CcL: Project administration, conceptualization, methodology. CgL: Software, formal analysis, writing—original draft. SB: Investigation, supervision. ML: Writing—review and editing. All authors contributed to the article and approved the submitted version.

Funding

The work described in this publication was supported by 1) The National Key Research and Development Program of China (No. 2022YFC3002902). 2) Natural science foundation of Ningxia Hui Autonomous Region (No. 2023AAC03034). 3) The National Natural Science Foundation of China Yellow River Water Science Research Joint Fund Project (No. U2243601-02). 4) The University First Class Discipline Construction Project of Ningxia, China (NXYLXK 2021A03).

Acknowledgments

This is a short text to acknowledge the contributions of specific colleagues, institutions, or agencies that aided the efforts of the authors.

Conflict of interest

The authors declare that the research was conducted in the absence of any commercial or financial relationships that could be construed as a potential conflict of interest.

Publisher's note

References

Aksoy, H., Kirca, V. S. O., Burgan, H. I., and Kellecioglu, D. (2016). Hydrological and hydraulic models for determination of flood-prone and flood inundation areas. *Proc. IAHS.* 373, 137–141. doi:10.5194/piahs-373-137-2016

Al-Suhili, R., Cullen, C., and Khanbilvardi, R. (2019). An urban flash flood alert tool for megacities—application for manhattan, New York city, USA. *Hydrology* 6 (2), 56. doi:10.3390/hydrology6020056

Azizi, S., Ilderomi, A. R., and Noori, H. (2021). Investigating the effects of land use change on flood hydrograph using HEC-HMS hydrologic model (case study: Ekbatan Dam). *Nat. Hazards* 109 (1), 145–160. doi:10.1007/s11069-021-04830-6

Castro, C. V., and Maidment, D. R. (2020). GIS preprocessing for rapid initialization of HEC-HMS hydrological basin models using web-based data services. *Environ. Model. Softw.* 130, 104732. doi:10.1016/j.envsoft.2020.104732

Chen, J., Li, Y., and Zhang, C. (2023). The effect of design rainfall patterns on urban flooding based on the Chicago method. *Int. J. Environ. Res. Public Health* 20, 4245. doi:10.3390/ijerph20054245

Cheng, X., Ma, X., Wang, W., Xiao, Y., Wang, Q., and Liu, X. (2021). Application of HEC-HMS parameter regionalization in small watershed of hilly area. *Water Resour. Manag.* 35, 1961–1976. doi:10.1007/s11269-021-02823-5

Cui, Y., Kong, J., and Tian, S. (2011). The critical role for heavy rainfall in the evolution of the mountain hazards chains. *Mt. Res.* 29, 87–94+8. doi:10.1007/s12182-011-0118-0

Georgios, M., Elpida, P., Vasiliki, S., Evangelos, B., Michalis, D., Efthymios, L., et al. (2022). Optimizing the performance of coupled 1D/2D hydrodynamic models for early warning of flash floods. *Water* 14, 2356. doi:10.3390/w14152356

Hu, S., and Shrestha, P. (2020). Examine the impact of land use and land cover changes on peak discharges of a watershed in the midwestern United States using the HEC-HMS model. *Pap. Appl. Geogr.* 6, 101–118. doi:10.1080/23754931.2020.1732447

Hu, Y. B. (2019). Determination of mountain flood warning index based on distributed hydrological model. *IOP Conf. Ser. Earth Environ. Sci.* 267, 032050. doi:10.1088/1755-1315/267/3/032050

Huang, W., Cao, Z., Huang, M., Duan, W., Ni, Y., and Yang, W. (2019). A new flash flood warning scheme based on hydrodynamic modelling. *Water* 11, 1221. doi:10.3390/w11061221

Huff, F. A. (1967). Time distribution of rainfall in heavy storms. *Water Resour. Res.* 3, 1007–1019. doi:10.1029/wr003i004p01007

Keifer, C. J., and Chu, H. H. (1957). Synthetic storm pattern for drainage design. *J. Hydraulics Div.* 83, 104. doi:10.1061/jyceaj.0000104

Li, C., Wang, M., Chen, F., Coulthard, T. J., and Wang, L. (2023). Integrating the SLIDE model within CAESAR-Lisflood: Modeling the ‘rainfall-landslide-flash flood’ disaster chain mechanism under landscape evolution in a mountainous area. *Catena* 227, 107124. doi:10.1016/j.catena.2023.107124

Majid, N., and Mohammad, Z. (2021a). Application of MGGP, ANN, MHBMO, GRG, and linear regression for developing daily sediment rating curves. *Math. Problems Eng.* 2021, 13. doi:10.1155/2021/8574063

Majid, N., and Mohammad, Z. (2021b). Assessment of artificial intelligence models for developing single-value and loop rating curves. *Complexity* 2021, 21. doi:10.1155/2021/6627011

Mehlath, S., and Lone, L. M. (2022). Flood modeling and simulation using HEC-HMS/HEC-GeoHMS and GIS tools for river sindh-NW himalayas. *KN - J. Cartogr. Geogr. Inf.* 72, 325–333. doi:10.1007/s42489-022-00116-4

Mohammad, Z. (2018). Comparative analysis of the novel infiltration model with other infiltration models. *Water Environ. J.* 33 (4), 620–631. doi:10.1111/wej.12435

Mosey, H. I. R., Pandara, D. P., Bobanto, M. D., and Sangian, H. S. (2019). A simple low-cost video-based surveillance system for a flash flood warning system. *IOP Conf. Ser. Mater. Sci. Eng.* 567, 012043. doi:10.1088/1757-899x/567/1/012043

Nguyen, T. N., Pham, C. X., Nguyen, H. Q., and Dang, T. N. B. (2019). Establishing an early warning system for flash floods in Hoang Su Phi district, ha Giang province, vietnam. *Singap. J. Trop. Geogr.* 40, 312–333. doi:10.1111/sjtg.12276

Pilgrim, D. H., and Cordery, I. (1975). Rainfall temporal patterns for design floods. *J. Hydraulics Div.* 101, 81–95. doi:10.1061/jyceaj.0004197

Qiu, Z., Su, E., Yao, C., and Wang, L. (2019). Impact of rain gauge network intensity on flood simulation and model parameters. *Water Power* 45, 20–24.

Shen, Z., Ding, Y., and Kong, Q. (2021). Application study of coupling rainfall-runoff modeling and floodplain inundation mapping. *J. Geo-information Sci.* 23, 1473–1483. doi:10.12082/dqxxkx.2021.200621

Sun, Z., Bao, Z., Shu, Z., Liu, Y., Liu, Y., and Wang, G. (2019). Patterns characteristics of short duration rainstorms in nanjing city over recent 25 years. *J. China Hydrology* 39, 78–83. doi:10.19797/j.cnki.1000-0852.20180191

Tu, H., Wang, X., Zhang, W., Peng, H., Ke, Q., and Chen, X. (2020). Flash flood early warning coupled with hydrological simulation and the rising rate of the flood stage in a mountainous small watershed in sichuan province, China. *Water* 12, 255. doi:10.3390/w12010255

Wang, L., and Sun, W. (2019). Research on HEC-HMS and vflo rainfall characteristics simulation and comparative based on dem data: A case of miyun district, beijing. *Acta Sci. Circumstantiae* 39, 3559–3564. doi:10.13671/j.hjkxxb.2019.0275

Wang, X., Chen, R., Li, K., Yang, Y., Liu, J., Liu, Z., et al. (2023). Trends and variability in flood magnitude: A case study of the floods in the qilian mountains, northwest China. *Atmosphere* 14, 557. doi:10.3390/atmos14030557

Yang, K., Ji, X., Mao, L., Zhang, C., Yang, J., and Zhang, S. (2020a). Cell polarity: Regulators and mechanisms in plants. *J. Nat. Disasters* 29, 132–147. doi:10.13577/j.jnd.2020.0114

Yang, K., Ji, X., Mao, L., and Zhang, S. (2020b). Numerical simulation and comparative analysis of topographic effects on two extraordinary severe flood rainstirms in Helan Mountain. *J. Arid Meteorology* 38, 581–590. doi:10.11755/j.issn.1006-7639(2020)-04-0581

Yoo, C., Lee, J., Chang, K., and Yang, D. (2019). Sensitivity evaluation of the flash flood warning system introduced to ungauged small mountainous basins in Korea. *J. Mt. Sci.* 16, 971–990. doi:10.1007/s11629-018-4984-4

Yuan, W., Song, H., and Liu, M. (2019a). An early warning model for flash floods based on random rainfall patterns. *Adv. Water Sci.* 30, 515–527. doi:10.14042/j.cnki.32.1309.2019.04.007

Yuan, W., Song, H., and Liu, M. (2019b). Study on critical rainfall threshold space of flash flood based on rainfall population. *Water Resour. Hydropower Eng.* 50, 70–79. doi:10.13928/j.cnki.wrahe.2019.07.009

Zhang, W., Liu, Y., Zhang, X., Tang, W., and Song, S. (2022). Flood routing simulation and analysis of lian’anwei flood protection zone. *Water Resour. Prot.* 38, 1–6. doi:10.3880/j.issn.1004-6933.2022.02.001

Zhang, Z., and Tang, Y. (2021). Simulation accuracy analysis of HEC-HMS distributed hydrological model under different objective functions. *World Sci. Res. J.* 7, 13. doi:10.6911/WSRJ.202105_7(5).0017

Zhou, C., Chen, Y., and Jia, H. (2022). Study on meteorological warning indexes of mountain torrent disasters in shizuishan section of eastern helan moutains. *J. Ningxia Univ. Sci. Ed.* 43, 425–428.

frontiers | Frontiers in Environmental Science

TYPE Original Research
PUBLISHED 18 October 2023
DOI 10.3389/fenvs.2023.1261239

OPEN ACCESS

EDITED BY
Buddhi Wijesiri,
Queensland University of Technology, Australia

REVIEWED BY
Ali Danandeh Mehr,
Antalya Bilim University, Türkiye
Anoop Kumar Shukla,
Manipal Academy of Higher Education, India

*CORRESPONDENCE
Chuanqi Li,
✉ lichuanqi@sdu.edu.cn

RECEIVED 20 July 2023
ACCEPTED 06 October 2023
PUBLISHED 18 October 2023

CITATION
Wang W, Gao J, Liu Z and Li C (2023), A hybrid rainfall-runoff model: integrating initial loss and LSTM for improved forecasting.
Front. Environ. Sci. 11:1261239.
doi: 10.3389/fenvs.2023.1261239

A hybrid rainfall-runoff model: integrating initial loss and LSTM for improved forecasting

Wei Wang[1], Jie Gao[1], Zheng Liu[2] and Chuanqi Li[1]*

[1]School of Civil Engineering, Shandong University, Jinan, China, [2]Jinan Water Resources Engineering Service Center, Jinan, China

Accurate rainfall-runoff modeling is crucial for disaster prevention, mitigation, and water resource management. This study aims to enhance precision and reliability in predicting runoff patterns by integrating physical-based models like HEC-HMS with data-driven models, such as LSTM. We present a novel hybrid model, Ia-LSTM, which combines the strengths of HEC-HMS and LSTM to improve hydrological modeling. By optimizing the “initial loss” (Ia) with HEC-HMS and utilizing LSTM to capture the effective rainfall-runoff relationship, the model achieves a substantial improvement in precision. Tested in the Yufuhe basin in Jinan City, Shandong province, the Ia-LSTM consistently outperforms individual HEC-HMS and LSTM models, achieving notable average Nash-Sutcliffe Efficiency (*NSE*) values of 0.873 and 0.829, and average R^2 values of 0.916 and 0.870 for calibration and validation, respectively. The study shows the potential of integrating physical mechanisms to enhance the efficiency of data-driven rainfall-runoff modeling. The Ia-LSTM model holds promise for more accurate runoff estimation, with wide applications in flood forecasting, water resource management, and infrastructure planning.

KEYWORDS

rainfall-runoff modeling, hybrid model, initial loss (Ia), HEC-HMS, LSTM

1 Introduction

Rainfall-runoff modeling is essential in hydrology, especially for tasks like reservoir management, flood forecasting, and water resource planning (Chen and Adams, 2006; Young and Liu, 2015). Despite significant progress, accurately predicting runoff remains a big challenging due to the complex, nonlinear, and dynamic nature of the rainfall-runoff process (Wang et al., 2006; Xie et al., 2019). This complexity is further compounded by various influencing factors, including rainfall patterns, initial soil moisture, terrain, land cover, and infiltration (Wang and Ding, 2003; Perera et al., 2019). Sudden rainstorms further emphasize the need for a comprehensive understanding of primary rainfall patterns (Xie et al., 2023a; Xie et al., 2023b). The impact of urban imperviousness on runoff and flooding dynamics has also emerged as a crucial factor in recent studies (Shukla et al., 2020; Mehr and Akdegirmen, 2021).

Vegetation and soil properties play a significant role in regulating the hydrological cycle, impacting various processes such as interception, infiltration, evaporation, and surface depression storage (Shukla et al., 2018). Notably, initial loss or initial abstraction (Ia) represents the rainfall occurring before the initiation of surface runoff. Ia is influenced by factors like vegetation cover, soil infiltration capacity, and antecedent moisture condition in the soil. Its magnitude is closely tied to both climatic conditions and moisture level in the watershed, making accurate estimation Ia for runoff determination and flood management (Zheng et al., 2020).

Rainfall-runoff models are broadly classified into physically-based models and data-driven models (Devia et al., 2015; Bartoletti et al., 2018; Mohammadi et al., 2022). Physically-based models, such as the Hydrologic Engineering Center-Hydrologic Modeling System (HEC-HMS) (Feldman, 2000), Xinanjiang (XAJ) model (Zhao, 1992), soil and water assessment tool (SWAT) (Arnold et al., 1998), MIKE-SHE (Jaber and Shukla, 2012), and HSPF (Bicknell et al., 1997), employ mathematical equations to represent hydrological processes. While these models provide valuable insights, their development demands a deep understanding of hydrological processes and extensive basin parameters, leading to a complex and time-consuming development process (Fenicia et al., 2008; Chen et al., 2022). The Hydrologic Modeling System (HMS), designed by the Hydrologic Engineering Center (HEC) of the United States Army Corps of Engineers, is a widely adopted rainfall-runoff analysis tool worldwide. The physical processes are so complex in hydrological models that it is difficult to discover the information from the available inputs.

Data-driven models offer a compelling alternative, establishing relationships between input and output data without the need for detailed understanding of underlying physical processes (Noori and Kalin, 2016; Yaseen et al., 2016; Lees et al., 2021). These models rely on historical rainfall and runoff data, making them suitable for handling non-linear and stochastic systems (Hu et al., 2018; Kratzert et al., 2018; Gao et al., 2020). Prominent data-driven methods for rainfall-runoff modeling include artificial neural networks (ANN) (Haykin and Network, 2004), support vector machines (SVM) (Cortes and Vapnik, 1995), genetic programming (Savic et al., 1999; Danandeh and Nourani, 2018), random forests (Breiman, 2001), fuzzy logic (Hundecha et., 2001) and regression in the reproducing kernel hilbert space (RRKHS) (Safari et al., 2020). These models use historical data to identify patterns and associations, enabling them to make precise predictions or estimates based on observed data patterns.

In recent years, deep learning, as a type of data-driven modeling, has gained substantial attention in hydrology due to its adaptability and minimal data requirements (Beven, 2020; Gu et al., 2020; Zhou et al., 2023). Among various deep learning approaches, Long Short-Term Memory (Hochreiter and Schmidhuber, 1997) networks have proven their effectiveness in various hydrological applications, including rainfall prediction (Barrera-Animas et al., 2022), flood forecasting (Hu et al., 2018; Rahimzad et al., 2021), and river water table prediction (Kim et al., 2022). As emphasized by Kratzert et al. (2018), the strength of the LSTM models lies in their capacity to capture long-term dependencies between the input and output.

The integration of physically-based and data-driven models in rainfall-runoff modeling has received considerable interest, driven by their complementary strengths (Tian et al., 2018; Sun et al., 2019; Zhou et al., 2022). Several hybrid models have exhibited promise in this domain. For instance, the XAJ-LSTM model, proposed by Cui et al. (2021), combines the Xinanjiang (XAJ) conceptual model with LSTM neural networks for multistep-ahead flood forecasting. This hybrid model utilizes the model forecast results of XAJ as input variables for LSTM, thus enhancing the physical mechanisms of hydrological simulation. By incorporating discharge forecasts from the XAJ model, the XAJ-LSTM hybrid model overcomes the limitations of LSTM's input variables, resulting in notably improved performance. Similarly, Gholami & Khaleghi (2021) conducted a comparative analysis of ANN and HEC-HMS models in rainfall-runoff simulation. Narayana Reddy and Pramada, (2022) integrated HEC-HMS with ANN to enhance daily discharge simulation and yearly peak discharge prediction. Farfan et al. (2020) used streamflow series forecasts from a conceptual model as input for back-propagation neural networks, leading to markedly improved streamflow predictions. Hitokoto and Sakuraba (2020) successfully integrated a rainfall-runoff model with a feed-forward artificial neural network to predict real-time water level processes. These instances highlight the effectiveness of hybrid models in enhancing predictive accuracy.

While previous research has made significant progress in rainfall-runoff modeling, there remains a critical need for innovative approaches to address the limitations of current models. Notably, the absence of physical mechanism poses a substantial obstacle in applying machine learning methods, which typically rely on labeled observations (Xie et al., 2021). The consideration of initial loss (Ia) within a deep learning network for rainfall-runoff simulation has received limited attention. Ia represents a crucial stage in the rainfall-runoff process. To address these challenges, this study proposes the hybrid rainfall-runoff model, integrating initial loss and LSTM. This integration harnesses the strengths of both physically-based and data-driven approaches, offering the potential for substantial advancements in accurately predicting and managing rainfall-induced runoff events.

The main objectives of this study are: 1) to develop the Ia-LSTM hybrid model, combining the advantages of the widely used hydrologic model, HEC-HMS, with the predictive capabilities of LSTM; 2) to conduct a comprehensive evaluation of the performance of the proposed hybrid model against the individual HEC-HMS and LSTM models. To assess the model's effectiveness, a case study is undertaken in the Yufuhe Basin, located in Jinan City, Shandong Province. The integration of the HEC-HMS model with LSTM enables a more comprehensive representation of the rainfall-runoff process, considering both the physical processes and historical data patterns. The incorporation of initial loss estimation and LSTM aims to improve the accuracy and reliability of runoff forecasting.

The contributions of this paper can be summarized as follows. First, it introduces the Ia-LSTM model, a novel rainfall-runoff model based on the integration of initial loss and LSTM. Second, the model is applied to the tasks of individual rainfall-runoff modeling in the Yufuhe basin, demonstrating its effectiveness.

The paper is organized as follows: Section 2 provides an overview of the study area and the data utilized. It also briefly describes the HEC-HMS model, LSTM network, and Ia-LSTM hybrid model. Section 3 presents the research results and discussions. Finally, Section 4 concludes the paper by summarizing the key findings.

2 Materials and methods

This section provides an overview of the study area and data (Section 2.1), introduces the HEC-HMS model (Section 2.2), explains the LSTM model structure (Section 2.3), presents the

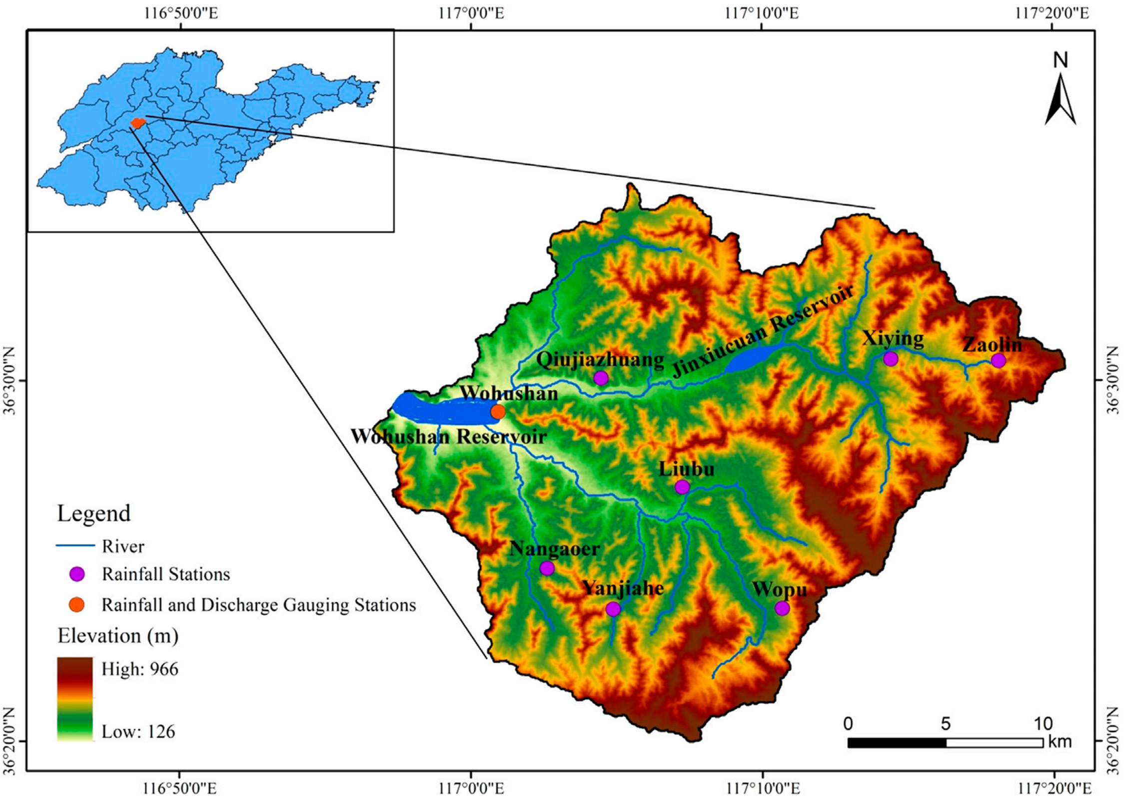

FIGURE 1
Elevation and distribution of rainfall stations in the study area.

proposed framework based on the LSTM (Section 2.4), and outlines the evaluation metrics of model performance (Section 2.5).

2.1 Study area and data

This study focuses on the Yufuhe basin, located upstream of the Wohushan Reservoir in Jinan city, Shandong Province, China. Encompassing an area of 557km^2, the basin exhibits vulnerability to floods and droughts due to its unique natural and geographical conditions. Notably, both 2007 and 2013 witnessed large-scale floods resulting in significant economic losses in Jinan (Zhang et al., 2016). The basin plays a critical role in flood control and water management, featuring diverse topography including mountains, hills, and a complex river network.

The study area is characterized by a sub-humid continental monsoon climate, with an annual average temperature of 14.3°C and an average annual precipitation of 670.0 mm. Rainfall is concentrated within the flood season from June to September, marked by intense, short-duration rainfall events. The flood season accounts for approximately 70% of the annual precipitation, posing flood risks in the basin.

Within the Yufuhe basin, there are seven rain-gauge stations and one Wohushan stream flow gauge station located at the basin outlet. Figure 1 illustrates the location of the watershed, elevation, distribution of rainfall and flow gauging stations, as well as the streams. The land use and land cover (LULC) map for the Yufuhe basin in 2020 was sourced from the Institute of Geographic Sciences and Resources of the Chinese Academy of Sciences (http://www.resdc.cn/), offering a detailed representation at a 30-m resolution. The basin is characterized by abundant vegetation, with agricultural land accounting for approximately 38% and forests covering 35% of the total area (Figure 2).

Hourly flow runoff data from the Wohushan hydrological station and hourly precipitation data from seven gauges were collected from 1973 to 2020. After data preprocessing, 30 rainfall and runoff events, including 6136 one-hourly rainfall and runoff records, were selected for this study. Among these flood events, 20 were used for model calibration, and the remaining 10 were used for model validation.

2.2 HEC-HMS model

The HEC-HMS model, developed by the U.S. Army Corps of Engineers (USACE), can accurately predict streamflow, runoff volume, and other hydrologic parameters. It incorporates inputs such as land use, soil types, channel networks, and rainfall data. HEC-HMS offers variood, unit hydrograph method, Snyder unit hydrograph method, and others [(USACE 2000us hydrologic modeling methods, including the Soil Conservation Service (SCS) curve number meth]. These methods are selected based on the specific characteristics of the modeled watershed.

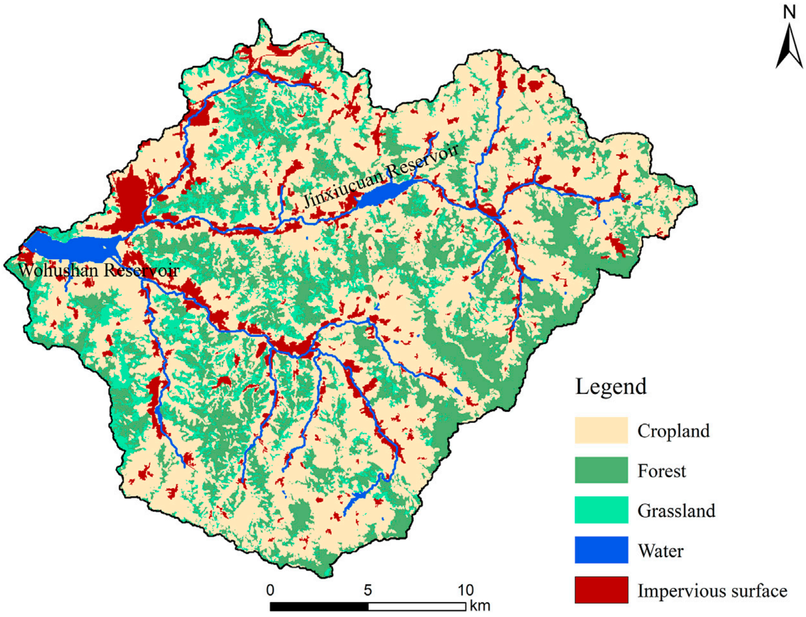

FIGURE 2
Land use map in the study area.

The HEC-HMS model comprises four main components: the basin model, meteorological model, control specifications, and time series model. The rainfall runoff process is delineated through four modules: loss, transformation, routing, and baseflow. Detailed information on the model's structure and processes can be found in the Technical Reference Manual (USACE-HEC, 2000) and the User's Manual of HEC-HMS.

2.2.1 Initial and constant loss method

The initial and constant loss method estimates surface losses in rainfall runoff modeling and is suitable for watersheds with limited soil data. This method requires two parameters: initial loss and constant rate. Initially, all rainfall is absorbed until the specified initial loss volume is attained, after which rainfall is lost at a constant rate. It considers antecedent moisture conditions and losses prior to reaching ultimate infiltration capacity. This method assumes a single soil layer for estimating moisture content changes, making it ideal for event simulation, particularly in data-scarce watersheds. The initial loss is influenced by antecedent moisture conditions and losses before reaching the ultimate infiltration capacity. It is worth noting that the initial loss parameter should be calibrated using observed data, although it is often estimated based on the soil moisture state at the beginning of the simulation and an assumed active layer depth. Throughout the simulation, a constant maximum potential rate of precipitation loss, f_c, is assumed.

The net rainfall, $P_{et,}$ at time t, is calculated using the following equation (USACE, 2000b):

$$P_{et} = \begin{cases} 0 & if \sum P_i < I_a \\ P_i - f_c \Delta t & if \sum P_i > I_a \, and \, P_i > f_c \\ 0 & if \sum P_i > I_a \, and \, P_t < f_c \end{cases} \tag{1}$$

where P_{et} represents the net rainfall (mm), I_a denotes the initial loss (mm), P_i represents cumulative rainfall from time t to $t+\Delta t$ (mm), and f_c represents the average infiltration rate (mm/h).

Optimal values of the initial loss and the constant loss rate are determined during the calibration of HEC-HMS model, primarily to match the depths of effective precipitation and direct runoff.

2.2.2 Direct runoff calculation

The Snyder unit hydrograph method is used to estimate surface direct runoff resulting from excess precipitation. It utilizes a standardized unit hydrograph incorporating parameters like peak lag time, peak flow, and total duration. These parameters play a crucial role in understanding the hydrological response of a watershed to rainfall events.

The standard unit hydrograph relates rainfall duration (t_r) to basin lag time (t_p) as follows:

$$t_p = 5.5 t_r \tag{2}$$

The Snyder Unit hydrograph method requires specifying input parameters such as the basin lag time (t_p) and peak coefficient (C_p). Peak lag time is calculated using the following formula:

$$t_p = C C_t (L L_C)^{0.3} \tag{3}$$

in which L is the length of the main stream from outlet to the divide (km); Lc is the length along the main stream to the nearest point of the watershed centroid; Ct is a coefficient (usually 1.8–2.2); C is a conversion constant (0.75 for SI units).

2.2.3 Baseflow calculation

Baseflow calculation involves accounting for the flow through a channel or the influence of groundwater in a hydrological system. HEC-HMS offers two methods for baseflow

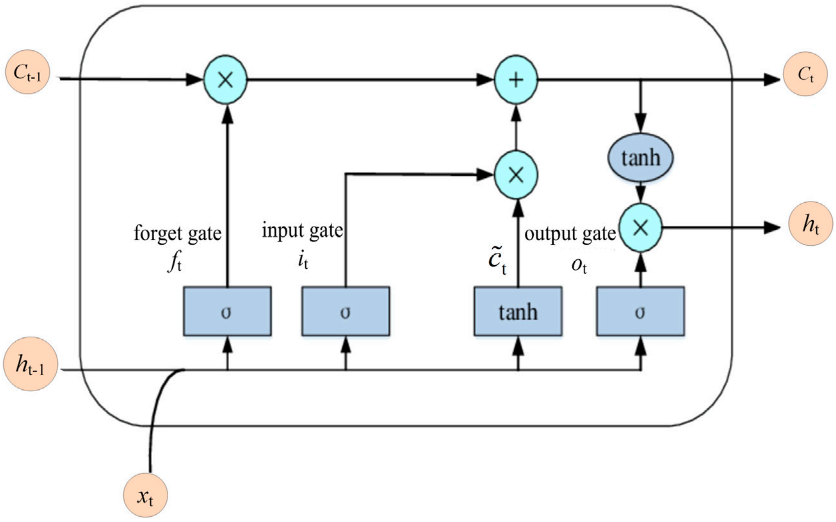

FIGURE 3
The structure of a LSTM cell.

calculation: recession and constant monthly. The recession method, utilized in this study, represents the drainage process from natural storage within a watershed. It employs an exponential decay function (Knebl et al., 2005) to relate the baseflow (Q_t) at a specific time (t) to an initial value (Q_0). The equation is defined as:

$$Q_t = Q_0 K^t \tag{4}$$

where K represents the exponential decay constant.

2.2.4 Flood routing

Flood routing in HEC-HMS provides various options for routing flood hydrographs through different reaches. The Muskingum method is commonly used for general flood routing.

In this study, the Muskingum method is adopted to compute the outflow from each reach during flood routing. This method is based on the following equation:

$$Q_{j+1} = C_1 I_{j+1} + C_2 I_j + C_3 Q_j \tag{5a}$$

where

$$C_1 = \frac{\Delta t - 2KX}{2K(1-X) + \Delta t} \tag{5b}$$

$$C_2 = \frac{\Delta t + 2KX}{2K(1-X) + \Delta t} \tag{5c}$$

$$C_3 = \frac{2K(1-X) - \Delta t}{2K(1-X) + \Delta t} \tag{5d}$$

where C_1, C_2 and C_3 are the routing coefficients for the concerned reach; I_j, I_{j+1} are the inflows to the reach at the beginning and end of the computation interval $\triangle t$, respectively, Q_j and Q_{j+1} correspond to the outflows from the reach at the beginning and end of computation interval, respectively. K denotes the travel time through the reach, and X is the Muskingum weighting factor ($0 \le X \le 0.5$). The coefficients C_1, C_2, and C_3 must satisfy the condition that their sum equals 1.0.

2.2.5 Parameter optimization methods

Calibrating the parameters of HEC-HMS model is a crucial step for improving the agreement between model results and observed data. The primary objective is to determine the most appropriate parameter values that yield the closest match between computed and observed hydrographs. This involves quantifying the match using an objective function, which compares the simulated and observed flow data. The objective function serves to assess the accuracy of the model's performance.

To execute parameter calibration, HEC-HMS provides two search methods: the Univariate Gradient algorithm (UG) and the Nelder-Mead algorithm (NM). These algorithms assist in minimizing the objective functions and determining the parameter values that provide the best fit.

In this study, the Peak-Weighted Root Mean Square Error (PWRMSE) function is chosen as the objective function for parameter calibration. The Nelder-Mead algorithm is employed to optimize the model parameters and obtain the most suitable values, ensuring accurate simulation results.

2.3 Long short-term memory (LSTM) network

The Long Short-Term Memory (LSTM) network was selected due to its exceptional ability to handle extended data sequences, a challenge commonly faced by conventional Recurrent Neural Networks (RNNs) (Hochreiter and Schmidhuber, 1997). In hydrological modeling, where processes like rainfall-runoff relationships exhibit complex temporal patterns, LSTM' capability to capture long-term dependencies is crucial.

Specifically, LSTM excels in preserving vital information over extended periods, allowing it to accurately model complex water-related processes. This type of deep learning model is designed to address challenges encountered by traditional RNNs, such as gradient exploding or vanishing problems. It achieves this through specialized gate mechanisms that control information flow, proving highly effective in processing sequential data.

The basic unit of the LSTM network includes a memory and three types of gates: input gate, forget gate, and output gate. These gates play a crucial role in managing memory and capturing relevant features by controlling information flow within the LSTM unit. Figure 3 provides a visual representation of the structure of an LSTM cell.

The forget gate, represented by f_t, determines how much of the previous memory to discard, based on the current input x_t and the previous cell state c_{t-1}. The input gate, represented by i_t, controls the information to be stored in the cell state c_t. The output gate, represented by o_t, filters the output variable h_t. The equations for the gates are given as follows (Kratzert et al., 2018):

$$f_t = \sigma\left(W_{hf}h_{t-1} + W_{xf}x_t + b_f\right) \tag{6}$$

$$i_t = \sigma\left(W_{hi}h_{t-1} + W_{xi}x_t + b_i\right) \tag{7}$$

$$o_t = \sigma\left(W_{ho}h_{t-1} + W_{xo}x_t + b_o\right) \tag{8}$$

$$\tilde{c}_t = \tanh\left(W_{hc}h_{t-1} + W_{xc}x_t + b_c\right) \tag{9}$$

$$c_t = f_t \odot c_{t-1} + i_t \odot \tilde{c}_t \tag{10}$$

$$h_t = o_t \odot \tanh\left(c_t\right) \tag{11}$$

where xt denotes the input, f_t is a forget gate, i_t is an input gate, o_t is an output gate, c_t is the cell state at time t; σ is Sigmoid function, ⊙denotes the element-wise multiplication of two vectors, bf, bi, bo, and bc are the corresponding bias; W_{hf}, W_{xf}, W_{hi}, W_{xi}, W_{ho}, W_{xo}, W_{hc} and W_{xc} are the network weights matrices; *tanh* is hyperbolic tangent function; h_{t-1} is the output of hidden state of previous step; and x_t is the input.

To train the LSTM model, it is crucial to configure the hyperparameters that govern the training process (Tian et al., 2018). Several hyperparameters, including learning rate, loss function, optimizer, dropout rate, batch size, and number of epochs, were tested and evaluated to determine the optimal values that give the best evaluation metrics. The final selected hyperparameters were as follows: a time step of 10, 256 neurons in the hidden layer, dropout rate of 0.20, and a batch size of 32. The Root Mean Square prop (RMSprop) optimizer with a decay coefficient of 0.8 and a learning rate of 0.0001 was utilized for model training. The training process involved 1000 iterations. The mean squared error (MSE) served as the loss function, measuring the average squared difference between the predicted values and the actual values.

To ensure accurate data analysis and enhance the efficiency and performance of the model, it is essential to preprocess the input data and map their attribute values to the range [0, 1]. Normalizing the input variables eliminates the influence of magnitude, thereby improving the accuracy and efficiency of network learning.

In this study, the rainfall and runoff data were preprocessed using min-max normalization method, which can be defined by Eq 1:

$$x_{norm} = \frac{x_i - x_{\min}}{x_{\max} - x_{\min}} \tag{12}$$

where x_{norm}, x_i, $x_{\min}$, $x_{\max}$ represents the normalized, observed, minimum and maximum values of rainfall or runoff, respectively. This normalization process ensures that the input variables are scaled appropriately and enables effective analysis and learning by the network.

2.4 Ia-LSTM hybrid model

This study proposes an Ia–LSTM model to improve the accuracy of hourly runoff discharge predictions using LSTM. The model incorporates HEC-HMS model for dataset generation, using the effective rainfall data series obtained by subtracting the initial loss (Ia) from the total rainfall data. By considering the influence of Ia, the LSTM model is trained to predict flow discharge sequences, resulting in improved precision in rainfall-runoff predictions. Figure 4 illustrates the overall workflow of the Ia-LSTM the hybrid model. The Ia-LSTM hybrid model optimizes the determination of Ia using HEC-HMS and considers factors such as infiltration, vegetation interception, and evaporation that impact rainfall-runoff dynamics.

The development of the Ia-LSTM hybrid model involves the following steps:

(1) Data preparation: Historical rainfall-runoff data for the study area are collected and organized into rainfall-runoff data sequences.
(2) Dataset generation: The HEC-HMS model is used to optimize and accurately estimate the initial loss (Ia) by considering factors such as rainfall-runoff, land use, soil type, and DEM data. The effective rainfall data is derived by subtracting Ia from the total rainfall. This step involves generating a dataset comprising effective rainfall-runoff pairs.
(3) LSTM model construction and training: The LSTM model is constructed, with effective rainfall data serving as the input variable and the corresponding runoff data as the output. The model is trained to capture the hidden mapping relationship between the inputs and outputs. Throughout the training process, various parameter combinations are explored to identify the optimal settings that enhance performance and efficiency.
(4) LSTM model forecasting: The trained LSTM model is used to predict runoff by inputting the effective rainfall data sequence. As a reference, the LSTM model is also trained on the original rainfall-runoff sequence. The performance of the LSTM rainfall-runoff prediction model, accounting for Ia, is evaluated and compared.

2.5 Evaluation metrics of model performance

The performance of the developed models is assessed using four widely used metrics in other hydrological studies: Nash-Sutcliffe efficiency (*NSE*), root mean square error (*RMSE*), relative error of peak discharge (*REP*), and coefficient of determination (R^2).

NSE is extensively used for evaluating rainfall-runoff simulation (Kumar et al., 2016). It quantifies the agreement between simulated and observed data by comparing their variances. *NSE* is calculated using the following formula:

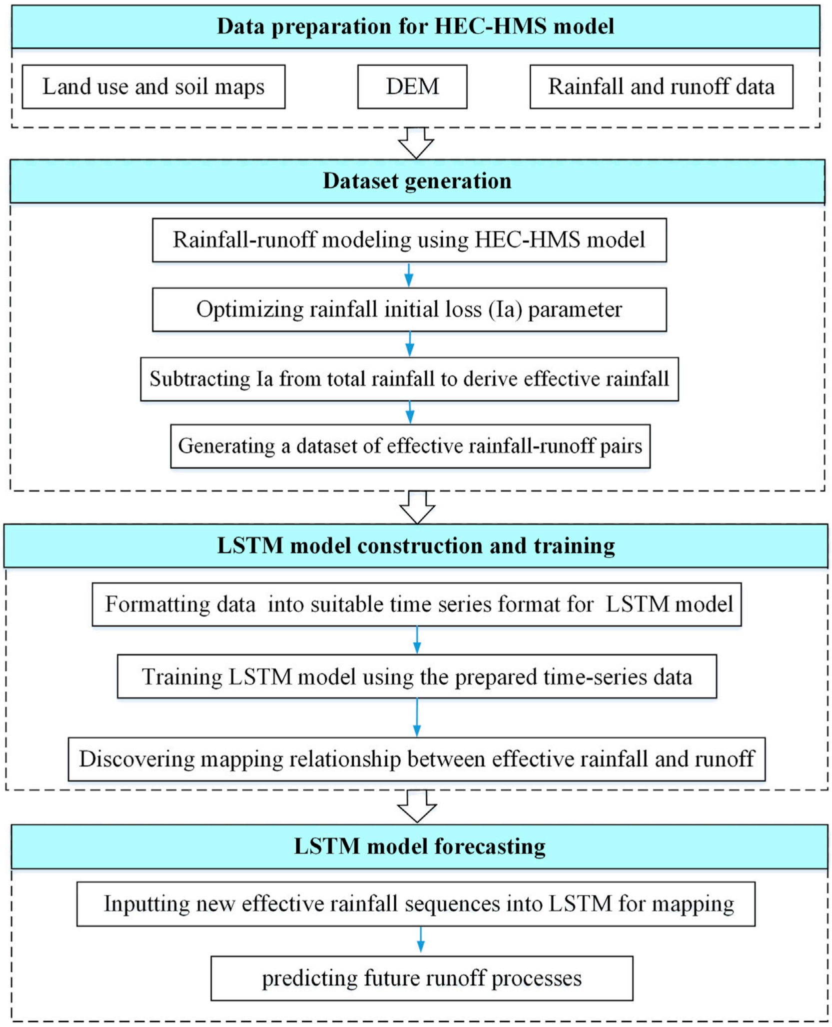

FIGURE 4
The flowchart of Ia-LSTM Hybrid Model.

$$NSE = 1 - \frac{\sum_{i=1}^{N} (O_i - P_i)^2}{\sum_{i=1}^{N} (O_i - \bar{O})^2} \tag{13}$$

where O_i and P_i represent the observed and predicted runoff at the time step i, respectively; $\bar{O}$ is the average observed runoff, and N is the total number of observations. *NSE* ranges from - ∞ to 1, with 1 indicating a perfect match between the predictions and observations.

Root mean square error (*RMSE*) measures the effectiveness of the model and is the average of the squared difference between model simulated and observed values. *RMSE* is used to represent the model's ability to predict flood events. *RMSE* can be calculated by:

$$RMSE = \sqrt{\frac{1}{N} \sum_{i=1}^{N} (O_i - P_i)^2} \tag{14}$$

A lower *RMSE* indicates better model simulation performance, with an *RMSE* of 0 indicating an exact match simulated and observed values.

REP assesses the accuracy and uncertainty associated with peak discharge estimation. It is calculated as:

$$REP = \frac{|O_p - P_p|}{O_p} \times 100\% \tag{15}$$

where O_p and P_p represent the observed and predicted peak river flow discharge, respectively. A lower *REP* value indicates better performance, indicating that the model's predictions are closer to the actual observed results.

The coefficient of determination (R^2) quantifies the degree of correlation between the simulated and observed runoff (Kumarasamy and Belmont, 2018). It is calculated using the formula:

$$R^2 = \left(\frac{\sum_{i=1}^{N} (O_i - \bar{O})(P_i - \bar{P})}{\sqrt{\sum_{i=1}^{N} (O_i - \bar{O})^2} \sqrt{\sum_{i=1}^{n} (P_i - \bar{P})^2}} \right)^2 \tag{16}$$

where $\bar{O}$ and $\bar{P}$ represent the average value of observed and predicted runoff, O_p and P_p are the observed and predicted runoff, respectively. R^2 values range from 0 to 1, with higher values indicating a better fit between the model outputs and the target outputs. Higher R^2 values suggest greater predictive power. An R^2 equal to 1 denotes an ideal

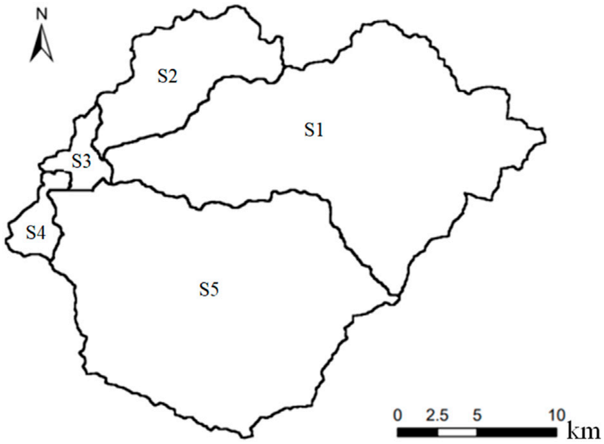

FIGURE 5
Divisions of the Yufuhe basin.

TABLE 1 Key characteristics of sub-basins in the Yufuhe basin.

Sub-basin	Area (km^2)	Average slope	Stream length (km)
S1	227.5	0.023	20.4
S2	58.6	0.020	7.9
S3	16.4	0.020	34.1
S4	11.9	0.095	5.6
S5	242.6	0.021	32.4

fit. Model performance is categorized as very good ($0.7 < R^2 < 1$), good ($0.6 < R^2 < 0.7$), satisfactory ($0.5 < R^2 < 0.6$), or unsatisfactory ($R^2 < 0.5$) (Ayele et al., 2017).

These metrics collectively provide a comprehensive assessment of the model's performance, encompassing simulation quality, accuracy of peak discharge predictions, and the correlation with observed data.

3 Results and discussion

3.1 Estimation of initial loss

To accurately estimate initial losses, the Yufuhe basin was divided into sub-basins (S1, S2, S3, S4, S5) as shown in Figure 5. Table 1 provides key characteristics of these sub-basins, including their areas, average slopes, and stream lengths. This subdivision allowed for a precise assessment of initial losses. The initial and constant loss method requires the specification of parameters including the percent impervious area, initial loss (Ia), and constant loss rate. The Thiessen polygon method was employed to estimate the average rainfall for the entire watershed, and specific runoff parameters for each sub-basin were determined.

The value of initial loss (Ia) depends on the topography and land use conditions within the watershed. Typically, it is set at 10%–20% of the total rainfall for forested areas. In this study, based on the soil and land use characteristics, the Ia value was determined as 30 mm, while the constant loss rate ranged from 0.30 mm/h to 1.16 mm/h.

TABLE 2 Optimization of initial loss (Ia) values for different flood events.

Flood No.	Precipitation (mm)	S1	S2	S3	S4	S5
19730715	101.0	19.1	21.5	18.5	21.3	18.3
19740801	105.1	18.8	19.4	19.8	17.2	19.4
19740812	47.3	9.8	12.6	11.3	15.0	13.5
19770716	38.5	15.8	13.5	16.1	12.9	16.1
19780701	97.4	14.4	17.3	14.7	16.6	14.0
19780713	51.5	8.8	9.7	9.4	10.6	8.0
19800629	169.2	24.1	22.9	22.7	19.3	19.3
19850729	240.8	12.3	12.7	11.9	11.8	12.7
19900709	31.8	14.3	17.0	16.3	15.1	14.3
19900720	58.2	7.0	6.5	10.8	8.1	96
19900814	73.4	12.5	14.0	14.7	11.5	10.2
19910727	65.2	17.1	19.4	16.5	17.5	18.6
19940702	90.9	18.1	17.5	20.6	19.0	17.3
19940712	53.8	8.3	9.8	9.6	8.7	7.8
19950815	18.2	12.4	13.3	11.4	12.2	12.6
19950902	65.5	10.2	8.9	9.5	10.4	10.8
19960803	94.2	12.4	13.3	11.4	12.2	12.6
19980702	37.9	10.9	11.2	9.3	9.9	9.9
19980802	113.1	21.3	17.9	20.7	20.7	21.1
20000809	162.8	13.0	16.3	14.2	13.7	14.7
20030828	58.0	8.3	9.8	9.6	8.7	7.8
20040729	65.1	12.1	14.9	15.6	17.2	18.0
20050918	156.5	18.1	15.6	16.3	16.7	17.9
20110811	50.4	19.2	15.4	17.3	19.9	14.6
20110831	42.3	10.9	11.2	9.3	9.9	11.9
20120714	82.7	17.0	16.2	16.6	20.7	17.1
20130723	124.5	10.8	13.5	11.6	13.5	12.2
20160715	24.0	12.0	16.5	14.2	13.3	11.4
20190815	123.0	9.5	11.4	10.2	9.3	12.0
20200807	56.0	13.9	15.6	13.3	12.5	12.2

The optimization procedure involved using a search method to minimize an objective function and find optimal parameters. To determine the optimal values of Ia for different flood events, the parameters were optimized using the Nelder-Mead optimization algorithm, with the peak-weighted root mean square as the objective function. The resulting optimized values are presented in Table 2. The analysis of Table 2 reveals the following conclusions regarding the relationship between rainfall and initial loss values:

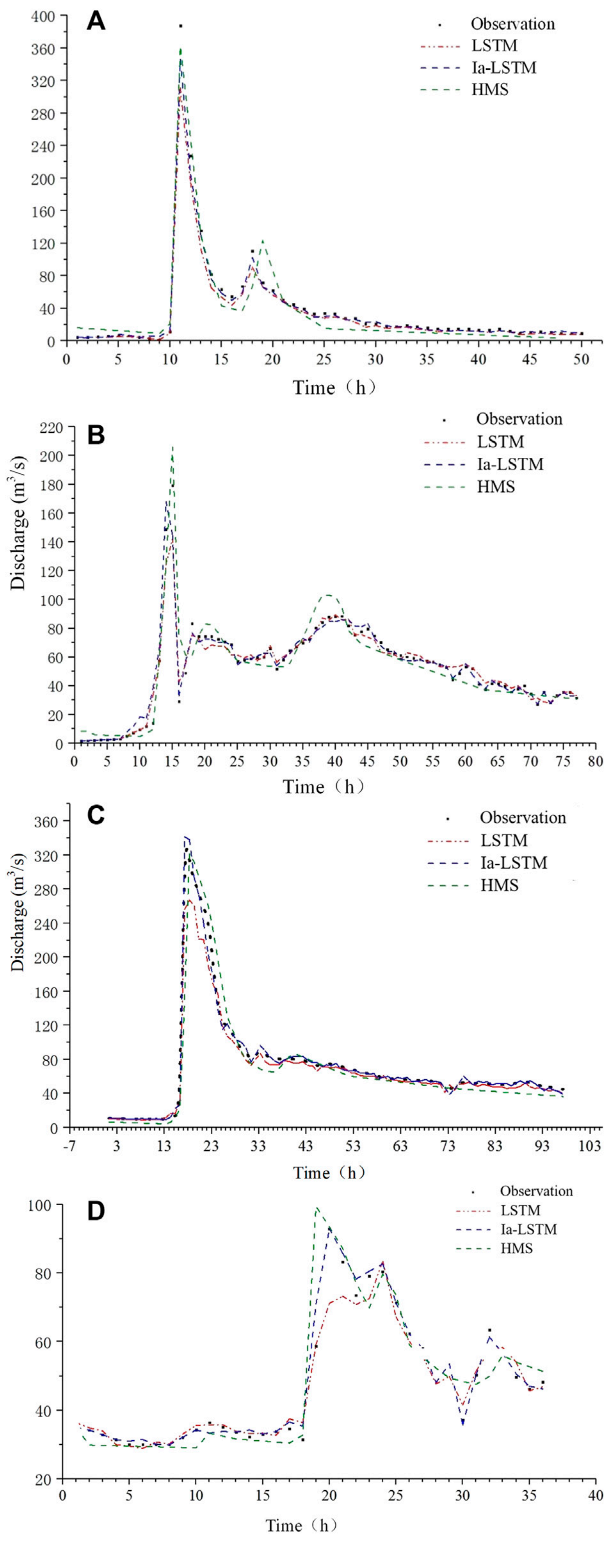

FIGURE 6
Comparison of observed and simulated discharge using three models: **(A)** flood No. 20000809, **(B)** flood No. 20050918, **(C)** flood No.20130723, **(D)** flood No.20190815.

Different sub-basins exhibit varying initial loss values for the same flood event. For example, in the flood event on 19730715 with a rainfall of 101 mm, the corresponding initial loss values for the sub-basins are as follows: S1-19.1 mm, S2-21.5 mm, S3-18.5 mm, S4-21.3 mm, and S5-18.3 mm.

The magnitude of initial loss values is not solely determined by the amount of rainfall. Other factors, such as the surface condition, rainfall characteristics, topography and slope, soil type and moisture content, and antecedent rainfall, play a significant role in determining initial loss values. These factors interact and collectively influence the extent of initial rainfall loss.

There is no clear linear relationship between rainfall and initial loss values in Table 2. This suggests that the estimation of initial loss values cannot solely rely on the amount of rainfall. Instead, a comprehensive understanding and consideration of the various factors influencing initial loss is necessary for accurate estimation.

3.2 Performance comparison

Flood events No. 20000809 and 20050918 were selected for model calibration, while flood events 20130918 and 20190815 were used for model validation. Figure 6 presents a comparison of simulated and observed discharges for four flood events in the Yufuhe basin using three models: HEC-HMS, LSTM, and Ia-LSTM. The figure shows that these models can generally capture the overall runoff process during the rainfall-runoff forecasting. However, some discrepancies exist in accurately simulating localized peak values. Despite this, the predicted values exhibit consistent trends with the observed values.

Regarding the comparison of relative error of peak discharge (*REP*) for the three models, Table 3 shows that different models exhibit varying performance in simulating peak discharge for each flood event. The LSTM model exhibits relatively large relative errors, particularly exceeding 20% for the flood event on 20130918. In contrast, both the Ia-LSTM and HEC-HMS models demonstrate significantly smaller relative errors, with all four flood events falling within the acceptable range. Notably, the Ia-LSTM model outperforms the other models, with a mere 1.3% error for the peak discharge during the flood event on 20190815. On average, the HEC-HMS model has a relative error of 9.8%, while the Ia-LSTM model has 8.1% for the peak discharge across all four flood events. These findings highlight the superior performance of the Ia-LSTM model in simulating peak discharge.

Table 4 presents the errors in peak time for different flood events predicted by the HEC-HMS, LSTM, and Ia-LSTM models. For the flood event on 20190815, the LSTM model exhibited a peak time error of 2 h. Conversely, for the flood event on 20130918, both HEC-HMS model and LSTM had a peak time error of 1 h. In contrast, the Ia-LSTM model achieved accurate peak time predictions for three out of the four flood events, with a maximum peak time error of 1 h. Notably, the Ia-LSTM model outperformed the other models by accurately simulating the temporal pattern of peak discharge propagation.

Table 5 presents a comprehensive comparison of three models (HEC-HMS, LSTM, and Ia-LSTM) based on key performance metrics: Nash-Sutcliffe Efficiency (*NSE*), Root Mean Square Error (*RMSE*), and Coefficient of Determination (R^2). Notably, during the flood event on 20000809, all models demonstrated exceptional performance with *NSE* coefficients above 0.86, *RMSE* values ranging from 7.234 to 14.503, and R^2 coefficients

TABLE 3 Comparison of relative error of peak discharge (*REP*) for three models.

Flood No.	Observed flow (m^3/s)	HEC-HMS		LSTM		Ia-LSTM	
		Predicted flow (m^3/s)	Relative error %	Predicted flow (m^3/s)	Relative error %	Predicted flow (m^3/s)	Relative error %
20000809	387.22	362.62	−6.4	310.94	−19.7	345.86	−10.7
20050918	179.37	205.92	14.8	142.23	−20.7	164.65	−8.2
20130918	360.00	321.77	11.1	274.18	−23.8	314.46	−12.1
20190815	92.92	99.39	7.0	78.42	−15.6	94.13	1.3

exceeding 0.90. The HMS model showed heightened accuracy in predicting the flood event on 20190815, potentially due to its detailed consideration of the rainfall process. Additionally, the Ia-LSTM model consistently displayed commendable performance across various flood events, with *NSE* coefficients ranging from 0.755 to 0.923, *RMSE* values between 2.314 and 7.234, and R^2 coefficients from 0.798 to 0.941. Importantly, the Ia-LSTM model consistently outperformed the LSTM model, highlighting its effectiveness in flood prediction and modeling.

The Ia-LSTM model consistently outperforms in various flood events, showing lower *RMSE*, and higher *NSE* and R^2 values. This highlights its effectiveness in flood prediction, especially compared to the LSTM model, emphasizing the importance of initial loss incorporation for accurate simulations.

3.3 Impact of initial loss

The analysis of initial loss in the proposed hybrid model provides valuable insights for improving rainfall-runoff predictions. By integrating initial loss estimation with LSTM neural networks, the Ia-LSTM model captures the complex interactions among various hydrological components, including rainfall, vegetation, soil, and runoff. This integration allows for a more comprehensive representation of the rainfall-runoff process, leveraging the strengths of physically-based and data-driven modeling approaches.

Consistent results demonstrate the superiority of the Ia-LSTM hybrid model over the individual HEC-HMS and LSTM models in estimating peak discharge, predicting peak time, and achieving higher *NSE*, lower *RMSE*, and greater R^2 values. The incorporation of initial loss estimation enhances the model's ability to simulate runoff dynamics. This leads to improved accuracy and reliability. In the Yufuhe basin case study, the Ia-LSTM model demonstrates an average improvement of 6.05% and 13.7% in peak discharge estimation compared to the HEC-HMS model and LSTM, respectively.

These findings emphasize the importance of accurate initial loss estimation in rainfall-runoff modeling, particularly for flood management and forecasting. Accurate initial loss estimation provides a clearer understanding of the initial loss processes and their impact on runoff generation. Through the optimization of initial loss values obtained from the HEC-HMS model, the Ia-LSTM model achieves heightened accuracy and reliability in simulating rainfall-runoff dynamics.

3.4 Comparison with previous studies

The Ia-LSTM hybrid model represents a significant advancement in rainfall-runoff modeling. Previous studies in the Yufuhe basin have employed various methodologies and models. For instance, Zhang et al. (2016) developed a distributed flood forecasting model based on sub-basins, river reaches, and reservoirs, achieving high performance with a Nash-Sutcliffe Efficiency (*NSE*) exceeding 0.70 and a Relative Error of Peak Discharge (*REP*) below 10%. Similarly, Yang et al. (2013) focused on the application of the SWAT distributed hydrological model, yielding satisfactory results with *NSE* and R^2 exceeding 0.70, and a relative error in peak flow below 15%. Their work highlights the effectiveness of their model in capturing key influencing factors of floods within the Yufuhe basin.

In recent years, machine learning models, particularly those based on LSTM, have exhibited promise in runoff forecasting. For instance, Xiang and YanDemir, (2020) proposed an LSTM-sequence-to-sequence rainfall-runoff model, demonstrating notable predictive power for short-term flood predictions. The LSTM model produced *NSE* values of 0.72, 0.80, and 0.93 for the Tripoli, Independence, and Anamosa stations, respectively. Additionally, an LSTM network was applied to build a data-driven model for streamflow prediction in an urban watershed.

While deep learning algorithms may not fully capture the rainfall-runoff process, they can be used to discern streamflow patterns and to identify effective variables, making them the preferred choice for modeling in data-poor catchments.

In our study, the Ia-LSTM model outperforms previous models, exhibiting *NSE* coefficients ranging from 0.755 to 0.923, *RMSE* values between 2.314 and 7.234 m^3/s, and R^2 coefficients from 0.798 to 0.941. These results signify substantial advancements in rainfall-runoff modeling.

This research builds upon earlier works by incorporating initial loss estimation and utilizing the powerful Ia-LSTM hybrid model. This approach significantly enhances accuracy and reliability in simulating rainfall-runoff dynamics, particularly in terms of estimating peak discharge and predicting peak time.

The findings of this study have important implications for flood forecasting and water resource management. The Ia-LSTM hybrid model demonstrates superior performance in simulating peak discharge and predicting peak time compared to individual HEC-HMS and LSTM models. This suggests its potential for accurate and reliable rainfall-runoff modeling, which is crucial for disaster prevention, mitigation, and water resource management.

TABLE 4 Comparison of errors in peak time.

Calibration and Validation	Flood No.	Observed peak time	HEC-HMS		LSTM		Ia-LSTM	
			Predicted peak time	Period time error	Predicted peak time	Period time error	Predicted peak time	Period time error
Calibration	20000809	24	23	−1	24	0	24	0
Validation	20050918	15	15	0	15	0	14	−1
	20130918	17	18	1	18	1	17	0
	20190815	20	19	−1	22	2	20	0

Additionally, the integration of initial loss estimation with LSTM neural networks represents a significant advancement in rainfall-runoff modeling. This approach captures complex interactions among various hydrological components, providing a more comprehensive representation of the rainfall-runoff process.

The Ia-LSTM hybrid model shows promise for a wide range of applications, including flood forecasting, water resource management, and infrastructure planning. Its effectiveness in data-driven rainfall-runoff modeling with integrated physical mechanisms can significantly enhance the efficiency of flood prediction and management.

4 Conclusion

This study presents a hybrid rainfall-runoff model combining initial loss estimation with LSTM networks, significantly enhancing runoff forecasting accuracy. Effective runoff, obtained by subtracting initial loss from total rainfall through HEC-HMS simulations, was used as the input for the LSTM network. The Ia-LSTM hybrid model, integrating physically-based and data-driven modeling approaches, outperforms both individual HEC-HMS and LSTM models, as evidenced by case studies in the Yufuhe basin.

The integration of physically-based and data-driven modeling techniques in the Ia-LSTM hybrid model offers a comprehensive representation of the rainfall-runoff process. This integration significantly improves the model's ability to capture the complex dynamics of rainfall-runoff, resulting in enhanced peak discharge estimation. The optimized initial loss values derived from the HEC-HMS model contribute to the increased accuracy of the Ia-LSTM model.

The case studies conducted in the Yufuhe basin demonstrate the effectiveness of the Ia-LSTM model in simulating peak discharge and accurately predicting peak time for the flood events. The performance of Ia-LSTM model was evaluated with Nash-Sutcliffe Efficiency (*NSE*), root mean square error (*RMSE*), relative error of peak discharge (*REP*) and coefficient of determination (R^2). The Ia-LSTM model, in particular, shows an average improvement of 6.05% and 13.7% in peak discharge estimation compared to the HEC-HMS model and LSTM, respectively. The model achieves *NSE* values ranging from 0.755 to 0.923, *RMSE* values between 2.314 and 7.234 m^3/s, and R^2 coefficients from 0.798 to 0.941. This demonstrates the consistent outperformance of the Ia-LSTM model across various flood events, as indicated by lower *RMSE*, and higher *NSE* and R^2 values.

These findings highlight the importance of accurate initial loss estimation and the potential of hybrid modeling approaches in improving rainfall-runoff predictions. Accurate estimation of initial loss enables a better understanding of the runoff generation process and its influence on peak discharge. The integration of initial loss estimation with LSTM in the hybrid model contributes to its superior performance in simulating peak discharge and capturing the temporal pattern of peak flow propagation. These findings offer promise for enhancing the accuracy and reliability of hydrological forecasting models.

While LSTM has been effective in rainfall-runoff forecasting, there's room for improvement. Extending the output sequence length using historical rainfall-runoff data will significantly enhance long-term predictions.

Simplifying the complex process of initial loss estimation, which currently relies on HEC-HMS, is crucial. Future research can explore efficient techniques like the SCS curve method, considering factors

TABLE 5 Comparison of *NSE, RMSE* and R^2.

Flood No.	*NSE*			*RMSE* (m^3/s)			R^2		
	HMS	LSTM	Ia-LSTM	HMS	LSTM	Ia-LSTM	HMS	LSTM	Ia-LSTM
20000809	0.890	0.861	0.923	14.503	13.088	7.234	0.923	0.909	0.956
20050918	0.784	0.786	0.823	7.635	6.614	6.050	0.822	0.725	0.875
20130918	0.862	0.820	0.902	10.202	15.657	6.783	0.916	0.875	0.941
20190815	0.741	0.552	0.755	4.120	8.800	2.314	0.805	0.626	0.798

such as soil type, pre-rainfall soil moisture, and the CN parameter. This streamlined approach makes initial loss estimation practical and applicable in real-world scenarios.

Data availability statement

The raw data supporting the conclusion of this article will be made available by the authors, without undue reservation.

Author contributions

WW: Writing–original draft. JG: Data curation, Formal Analysis, Writing–review and editing. ZL: Investigation, Writing–review and editing. CL: Funding acquisition, Methodology, Writing–review and editing.

Funding

The author(s) declare financial support was received for the research, authorship, and/or publication of this article. Natural Science Foundation of Shandong Province, China (ZR2021ME030), Special Project for Sustainable Development of Shenzhen Science and Technology Innovation Committee (KCXFZ20201221173407021), and Jinan Water Science and Technology Project (JNSWKJ202105) provided support for this study.

Conflict of interest

The authors declare that the research was conducted in the absence of any commercial or financial relationships that could be construed as a potential conflict of interest.

Publisher's note

References

Arnold, J. G., Srinivasan, R., Muttiah, R. S., and Williams, J. R. (1998). Large area hydrologic modeling and assessment part I: model development 1. *JAWRA J. Am. Water Resour. Assoc.* 34 (1), 73–89. doi:10.1111/j.1752-1688.1998.tb05961.x

Barrera-Animas, A. Y., Oyedele, L. O., Bilal, M., Akinosho, T. D., Delgado, J. M. D., and Akanbi, L. A. (2022). Rainfall prediction: a comparative analysis of modern machine learning algorithms for time-series forecasting. *Mach. Learn. Appl.* 7, 100204. doi:10.1016/j.mlwa.2021.100204

Bartoletti, N., Casagli, F., Marsili-Libelli, S., Nardi, A., and Palandri, L. (2018). Data-driven rainfall/runoff modelling based on a neuro-fuzzy inference system. *Environ. Model. Softw.* 106, 35–47. doi:10.1016/j.envsoft.2017.11.026

Beven, K. (2020). Deep learning, hydrological processes and the uniqueness of place. *Hydrol. Process.* 34 (16), 3608–3613. doi:10.1002/hyp.13805

Bicknell, B. R., Imhoff, J. C., Kittle, J. L., Jr, Donigian, A. S., Jr, and Johanson, R. C. (1997). *Hydrological simulation program—FORTRAN user's manual for version 11.* Report No. EPA/600/R-97/080. Athens, GA, USA: US Environmental Protection Agency.

Breiman, L. (2001). Random forests. *Mach. Learn.* 45, 5–32. doi:10.1023/a:1010933404324

Chen, C., Jiang, J., Liao, Z., Zhou, Y., Wang, H., and Pei, Q. (2022). A short-term flood prediction based on spatial deep learning network: a case study for Xi County, China. *J. Hydrology* 607, 127535. doi:10.1016/j.jhydrol.2022.127535

Chen, J., and Adams, B. J. (2006). Integration of artificial neural networks with conceptual models in rainfall-runoff modeling. *J. Hydrology* 318 (1-4), 232–249. doi:10.1016/j.jhydrol.2005.06.017

Cortes, C., and Vapnik, V. (1995). Support-vector networks. *Mach. Learn.* 20, 273–297. doi:10.1007/bf00994018

Cui, Z., Zhou, Y., Guo, S., Wang, J., Ba, H., and He, S. (2021). A novel hybrid XAJ-LSTM model for multi-step-ahead flood forecasting. *Hydrology Res.* 52 (6), 1436–1454. doi:10.2166/nh.2021.016

Danandeh Mehr, A., and Nourani, V. (2018). Season algorithm-multigene genetic programming: a new approach for rainfall-runoff modelling. *Water Resour. Manag.* 32, 2665–2679. doi:10.1007/s11269-018-1951-3

Devia, G. K., Ganasri, B. P., and Dwarakish, G. S. (2015). A review on hydrological models. *Aquat. procedia* 4, 1001–1007. doi:10.1016/j.aqpro.2015.02.126

Farfán, J. F., Palacios, K., Ulloa, J., and Avilés, A. (2020). A hybrid neural network-based technique to improve the flow forecasting of physical and data-driven models: methodology and case studies in Andean watersheds. *J. Hydrology Regional Stud.* 27, 100652. doi:10.1016/j.ejrh.2019.100652

Feldman, A. D. (2000). *Hydrologic modeling system HEC-HMS: technical reference manual.* Washington, D.C, USA: US Army Corps of Engineers, Hydrologic Engineering Center.

Fenicia, F., Savenije, H. H., Matgen, P., and Pfister, L. (2008). Understanding catchment behavior through stepwise model concept improvement. *Water Resour. Res.* 44 (1), 1–13. doi:10.1029/2006wr005563

Gholami, V., and Khaleghi, M. R. (2021). A simulation of the rainfall-runoff process using artificial neural network and HEC-HMS model in forest lands. *J. For. Sci.* 67 (4), 165–174. doi:10.17221/90/2020-jfs

Gu, H., Xu, Y. P., Ma, D., Xie, J., Liu, L., and Bai, Z. (2020). A surrogate model for the Variable Infiltration Capacity model using deep learning artificial neural network. *J. Hydrology* 588, 125019. doi:10.1016/j.jhydrol.2020.125019

Haykin, S., and Network, N. (2004). A comprehensive foundation. *Neural Netw.* 2, 41.

Hitokoto, M., and Sakuraba, M. (2020). Hybrid deep neural network and distributed rainfall-runoff model for real-time river-stage prediction. *J. JSCE* 8 (1), 46–58. doi:10.2208/journalofjsce.8.1_46

Hochreiter, S., and Schmidhuber, J. (1997). Long short-term memory. *Neural Comput.* 9 (8), 1735–1780. doi:10.1162/neco.1997.9.8.1735

Hu, C., Wu, Q., Li, H., Jian, S., Li, N., and Lou, Z. (2018). Deep learning with a long short-term memory networks approach for rainfall-runoff simulation. *Water* 10 (11), 1543. doi:10.3390/w10111543

Hundecha, Y., Bardossy, A., and Werner, H. W. (2001). Development of a fuzzy logic-based rainfall-runoff model. *Hydrological Sci. J.* 46 (3), 363–376. doi:10.1080/02626660109492832

Jaber, F. H., and Shukla, S. (2012). MIKE SHE: model use, calibration, and validation. *Trans. ASABE* 55 (4), 1479–1489. doi:10.13031/2013.42255

Kim, D., Lee, J., Kim, J., Lee, M., Wang, W., and Kim, H. S. (2022). Comparative analysis of long short-term memory and storage function model for flood water level forecasting of Bokha stream in NamHan River, Korea. *J. Hydrology* 606, 127415. doi:10.1016/j.jhydrol.2021.127415

Knebl, M. R., Yang, Z. L., Hutchison, K., and Maidment, D. R. (2005). Regional scale flood modeling using NEXRAD rainfall, GIS, and HEC-HMS/RAS: a case study for the San Antonio River Basin Summer 2002 storm event. *J. Environ. Manag.* 75 (4), 325–336. doi:10.1016/j.jenvman.2004.11.024

Kratzert, F., Klotz, D., Brenner, C., Schulz, K., and Herrnegger, M. (2018). Rainfall–runoff modelling using long short-term memory (LSTM) networks. *Hydrology Earth Syst. Sci.* 22 (11), 6005–6022. doi:10.5194/hess-22-6005-2018

Kumar, P. S., Praveen, T. V., and Prasad, M. A. (2016). Artificial neural network model for rainfall-runoff-A case study. *Int. J. Hybrid Inf. Technol.* 9 (3), 263–272. doi:10.14257/ijhit.2016.9.3.24

Kumarasamy, K., and Belmont, P. (2018). Calibration parameter selection and watershed hydrology model evaluation in time and frequency domains. *Water* 10 (6), 710. doi:10.3390/w10060710

Lees, T., Buechel, M., Anderson, B., Slater, L., Reece, S., Coxon, G., et al. (2021). Benchmarking data-driven rainfall–runoff models in Great Britain: a comparison of long short-term memory (LSTM)-based models with four lumped conceptual models. *Hydrology Earth Syst. Sci.* 25 (10), 5517–5534. doi:10.5194/hess-25-5517-2021

Mehr, A. D., and Akdegirmen, O. (2021). Estimation of urban imperviousness and its impacts on flashfloods in Gazipaşa, Turkey. *Knowledge-Based Eng. Sci.* 2 (1), 9–17. doi:10.51526/kbes.2021.2.1.9-17

Mohammadi, B., Safari, M. J. S., and Vazifehkhah, S. (2022). IHACRES, GR4J and MISD-based multi conceptual-machine learning approach for rainfall-runoff modeling. *Sci. Rep.* 12 (1), 12096. doi:10.1038/s41598-022-16215-1

Narayana Reddy, B. S., and Pramada, S. K. (2022). A hybrid artificial intelligence and semi-distributed model for runoff prediction. *Water Supply* 22 (7), 6181–6194. doi:10.2166/ws.2022.239

Noori, N., and Kalin, L. (2016). Coupling SWAT and ANN models for enhanced daily streamflow prediction. *J. Hydrology* 533, 141–151. doi:10.1016/j.jhydrol.2015.11.050

Perera, T., McGree, J., Egodawatta, P., Jinadasa, K. B. S. N., and Goonetilleke, A. (2019). Taxonomy of influential factors for predicting pollutant first flush in urban stormwater runoff. *Water Res.* 166, 115075. doi:10.1016/j.watres.2019.115075

Rahimzad, M., Moghaddam Nia, A., Zolfonoon, H., Soltani, J., Danandeh Mehr, A., and Kwon, H. H. (2021). Performance comparison of an LSTM-based deep learning model versus conventional machine learning algorithms for streamflow forecasting. *Water Resour. Manag.* 35 (12), 4167–4187. doi:10.1007/s11269-021-02937-w

Safari, M. J. S., Arashloo, S. R., and Mehr, A. D. (2020). Rainfall-runoff modeling through regression in the reproducing kernel Hilbert space algorithm. *J. Hydrology* 587, 125014. doi:10.1016/j.jhydrol.2020.125014

Savic, D. A., Walters, G. A., and Davidson, J. W. (1999). A genetic programming approach to rainfall-runoff modelling. *Water Resour. Manag.* 13, 219–231. doi:10.1023/a:1008132509589

Shukla, A. K., Ojha, C. S. P., Garg, R. D., Shukla, S., and Pal, L. (2020). Influence of spatial urbanization on hydrological components of the upper ganga river basin, India. *J. Hazard. Toxic, Radioact. Waste* 24 (4), 04020028. doi:10.1061/(asce)hz.2153-5515.0000508

Shukla, A. K., Pathak, S., Pal, L., Ojha, C. S. P., Mijic, A., and Garg, R. D. (2018). Spatio-temporal assessment of annual water balance models for upper Ganga Basin. *Hydrology Earth Syst. Sci.* 22 (10), 5357–5371. doi:10.5194/hess-22-5357-2018

Sun, A. Y., Scanlon, B. R., Zhang, Z., Walling, D., Bhanja, S. N., Mukherjee, A., et al. (2019). Combining physically based modeling and deep learning for fusing GRACE satellite data: can we learn from mismatch? *Water Resour. Res.* 55 (2), 1179–1195. doi:10.1029/2018wr023333

Tian, Y., Xu, Y. P., Yang, Z., Wang, G., and Zhu, Q. (2018). Integration of a parsimonious hydrological model with recurrent neural networks for improved streamflow forecasting. *Water* 10 (11), 1655. doi:10.3390/w10111655

Wang, W., and Ding, J. (2003). Purification of boiling-soluble antifreeze protein from the legume Ammopiptanthus mongolicus. *Nat. Sci.* 1 (1), 67–80. doi:10.1081/PB-120018370

Wang, W., Vrijling, J. K., Van Gelder, P. H., and Ma, J. (2006). Testing for nonlinearity of streamflow processes at different timescales. *J. Hydrology* 322 (1-4), 247–268. doi:10.1016/j.jhydrol.2005.02.045

XiangYan, Z. J., and Demir, I. (2020). A rainfall-runoff model with LSTM-based sequence-to-sequence learning. *Water Resour. Res.* 56 (1). doi:10.1029/2019wr025326

Xie, K., Liu, P., Zhang, J., Han, D., Wang, G., and Shen, C. (2021). Physics-guided deep learning for rainfall-runoff modeling by considering extreme events and monotonic relationships. *J. Hydrology* 603, 127043. doi:10.1016/j.jhydrol.2021.127043

Xie, T., Zhang, G., Hou, J., Xie, J., Lv, M., and Liu, F. (2019). Hybrid forecasting model for non-stationary daily runoff series: a case study in the Han River Basin, China. *J. Hydrology* 577, 123915. doi:10.1016/j.jhydrol.2019.123915

Xie, X., Huang, L., Marson, S. M., and Wei, G. (2023b). Emergency response process for sudden rainstorm and flooding: scenario deduction and Bayesian network analysis using evidence theory and knowledge meta-theory. *Nat. Hazards* 117 (3), 3307–3329. doi:10.1007/s11069-023-05988-x

Xie, X., Tian, Y., and Wei, G. (2023a). Deduction of sudden rainstorm scenarios: integrating decision makers' emotions, dynamic Bayesian network and DS evidence theory. *Nat. Hazards* 116 (3), 2935–2955. doi:10.1007/s11069-022-05792-z

Yang, S., Xu, Z., Kong, Ke., Miao, S., and Zhang, S. (2013). A flow simulation based on SWAT model in Wohushan reservoir basin. *China Rural Water and Hydropower* (5), 11–18. doi:10.3969/j.issn.1007-2284.2013.05.003

Yaseen, Z. M., Jaafar, O., Deo, R. C., Kisi, O., Adamowski, J., Quilty, J., et al. (2016). Stream-flow forecasting using extreme learning machines: a case study in a semi-arid region in Iraq. *J. Hydrology* 542, 603–614. doi:10.1016/j.jhydrol.2016.09.035

Young, C. C., and Liu, W. C. (2015). Prediction and modelling of rainfall–runoff during typhoon events using a physically-based and artificial neural network hybrid model. *Hydrological Sci. J.* 60 (12), 2102–2116. doi:10.1080/02626667.2014.959446

Zheng, Y., Li, J., Dong, L., Rong, Y., Kang, A., and Feng, P. (2020). Estimation of initial abstraction for hydrological modeling based on global land data assimilation system–simulated datasets. *J. Hydrometeorol.* 21 (5), 1051–1072. doi:10.1175/jhm-d-19-0202.1

Zhang, L., Yang, Z., and Liu, G. (2016). A forecast model of distributed flood in Yufuhe basin and its application. *J. Water Resour. Water Eng.* 27 (3), 66–72. doi:10.11705/j.issn.1672-643X.2016.03.13

Zhao, R. J. (1992). The Xinanjiang model applied in China. *J. Hydrology* 135, 371–381. doi:10.1016/0022-1694(92)90096-e

Zhou, Q., Teng, S., Situ, Z., Liao, X., Feng, J., Chen, G., et al. (2023). A deep-learning-technique-based data-driven model for accurate and rapid flood predictions in temporal and spatial dimensions. *Hydrology Earth Syst. Sci.* 27 (9), 1791–1808. doi:10.5194/hess-27-1791-2023

Zhou, Y., Cui, Z., Lin, K., Sheng, S., Chen, H., Guo, S., et al. (2022). Short-term flood probability density forecasting using a conceptual hydrological model with machine learning techniques. *J. Hydrology* 604, 127255. doi:10.1016/j.jhydrol.2021.127255

Frontiers in Environmental Science

TYPE Original Research
PUBLISHED 01 December 2023
DOI 10.3389/fenvs.2023.1286929

OPEN ACCESS

EDITED BY
Jing Liu,
University of Birmingham,
United Kingdom

REVIEWED BY
Holger Rupp,
Helmholtz Association of German
Research Centres (HZ), Germany
Kang Liang,
University of Maryland, College Park,
United States
Samuel Pelacani,
University of Florence, Italy

*CORRESPONDENCE
Dimaghi Schwamback,
✉ dimaghis@gmail.com

RECEIVED 31 August 2023
ACCEPTED 14 November 2023
PUBLISHED 01 December 2023

CITATION
Schwamback D, Persson M,
Berndtsson R, Anache JAA and
Wendland EC (2023), Adaptive design of
tipping bucket flow meters for
continuous runoff measurement.
Front. Environ. Sci. 11:1286929.
doi: 10.3389/fenvs.2023.1286929

Adaptive design of tipping bucket flow meters for continuous runoff measurement

Dimaghi Schwamback[1,2]*, Magnus Persson[1], Ronny Berndtsson[1], Jamil A. A. Anache[2] and Edson Cezar Wendland[2]

[1]Division of Water Resources Engineering, Department of Building and Environmental Technology, Lund University, Lund, Sweden, [2]Department of Hydraulic Engineering and Sanitary, São Carlos School of Engineering (EESC), University of São Paulo (USP), São Carlos, Brazil

Introduction: Runoff measurement and monitoring is a laborious, time-consuming, and costly task. Additionally, common runoff monitoring usually primarily provide water level, requiring information on the stage-discharge relation. Automatic equipment such as flow meter tipping bucket (TB) is a potential option to simplify and provide continuous runoff monitoring in small catchments. However, a proper description of how to size and adapt the design under different flow conditions is still lacking.

Methodology: In this paper we present a novel standardized framework for the design of TB that can be used for low-cost and real-time runoff monitoring under many different conditions. The framework consists of an estimation of the runoff peak rate using the rational equation and a volumetric capacity estimate of the cavity based on runoff rate, operation speed, and inclination angle of TB when at resting position. The proposed framework was implemented in a case study where four TBs were designed for continuous runoff monitoring from experimental plots (100 m^2) with different land use (sugarcane, soybean, and bare soil).

Results: During field tests (five months), the designed TBs had a recovery rate of actual runoff ranging from 61% to 81% and were able to capture features poorly studied (starting/ending time and peak flow) that have potential importance in hydrological models.

Discussion: The proposed framework is flexible and can be used for different environmental conditions to provide continuous runoff data records.

KEYWORDS

overland flow, *in-situ* monitoring, hillslope hydrology, land use and land cover, device

1 Introduction

Changes in Land Use and Land Cover (LULC) are important sources of increasing sediment discharge and surface flow, which may have strong impact on downstream areas (Ebabu et al., 2023). In this context, in-situ studies are important to, e.g., reduce nutrient losses (Zhang et al., 2020), improve the efficiency of agricultural production (Benedetti et al., 2019), and promote sustainable development (Tarolli and Straffelini, 2020). However, experimental studies are scarce due to local heterogeneities and uncertainties in hydrological and pedological measurements (Beven and Germann, 2013; Anache et al., 2017), but mainly due to cost and laborious processes involved in erosion monitoring. From the list of 23 unsolved problems that aim to orient hydrological research worldwide, Blöschl et al. (2019) highlight the importance of developing and using innovative technologies to measure surface and subsurface flow properties in a range of spatial and temporal scales under affordable investment.

The runoff volume for a given area can be quantified using different technologies, such as mass and pressure sensors, volumetric boxes, spillways, and tipping bucket flow meter (TBs). Using TBs is an option for automatic and direct monitoring of surface flow in small study areas, such as bounded experimental plots and hillslopes (Wang et al., 2020) and small hydrographic basins (Peyrard et al., 2016), due to its low construction cost, durability, easy installation, and high mobility (Bashagakule et al., 2018; Shimizu et al., 2018). It is based on a simple principle, consisting of two symmetrical cavities. The collected flow is directed to one of the cavities that fills until it reaches its maximum capacity (nominal volume), shifting the gravity center towards the rotating axis, releasing the water, and allowing the second cavity to fill. Coupling TBs with a reed switch and datalogger allows automation and continuous readings with a high temporal resolution (usually 10 min but also as detailed as per minute), aiding in identifying the start, end, and peak of the flow (Corona et al., 2013; Zabret et al., 2018).

The first tipping bucket flow meter record used for measuring runoff in experimental plots (hillslope for runoff measurement) dates back to 1928 (Nebol'sin, 1928). Since then, TBs have been used as a hydrological monitoring tool with different monitoring applications: quantification of runoff in plots (Johnston, 1942; Whipkey, 1965; Calder and Kidd, 1978; Hollis and Ovenden, 1987; Khan and Ong, 1997; Klik et al., 2004; Nehls et al., 2011; Corona et al., 2013; Elder et al., 2014; Langhans et al., 2019; Wang et al., 2020), experimental basins (Chow, 1976; Kim et al., 2005; Peyrard et al., 2016) and green roofs (Perales-Momparler et al., 2017); quantification of subsurface runoff (Peyrard et al., 2016; Lamb et al., 2019; Wang et al., 2020); and quantification of internal precipitation or stemflow (Takahashi et al., 2010; Iida et al., 2012; Shimizu et al., 2018; Zabret et al., 2018). The volumetric capacity of a TB varies greatly from 15 mL (Somavilla et al., 2019) up to 12 L (Edwards et al., 1974), based on the flow expected to be measured. There are many different constructing designs of TBs that differ based on the cavity shape (rectangular, circular, or triangular), rotating angle (180° or 360°), and number of cavities (two or multiple ones).

Errors in TBs can be categorized as systematic or random (Shimizu et al., 2018; Iida et al., 2020). Systematic errors refer to design flaws and operation practices. These can be predicted and minimized through proper design framework and maintenance practices, e.g., regular lubrication. Random errors occur in unexpected situations, such entry of animals and flow inlet clogging. Following this definition, the under or oversizing of TBs is one example of a systematic error source that can be minimized. TBs with a too-low storage capacity under high runoff events will have a high error due to the kinetic effect of the increased flow through the water inlet (Shimizu et al., 2018). Similarly, TBs with a too-high storage capacity under runoff events with low intensity may not tip, also resulting in large measurement errors. The ideal design of TB will increase the accuracy of such monitoring equipment.

As highlighted by the vast number of studies, TBs are well-tested and established monitoring techniques. However, to the best of our knowledge, no previous studies have presented a standard or given detailed description of the sizing and construction of TBs that allows replicability under different environmental conditions. Previous research described TBs as a unique art craft, instead of trying to adapt it into a broader potential monitoring technique. Thus, this paper aims to present a novel standardized framework for the design of flow meter TBs, allowing the replication and implementation of TBs for low-cost and real-time runoff monitoring under any environmental condition. The proposed methodology was validated in the design of four TBs for the runoff monitoring in experimental plots in contrasting LULC commonly found in the Southeast region of Brazil (sugarcane, soybean, and bare soil). The designed TBs for the case study were calibrated and employed in the runoff monitoring during the rainy season.

2 Methodology

2.1 TB design framework

The TB gauge consists of two connected cavities (Figure 1). When one of the cavities reaches a critical volume (nominal volume), the center of mass of the structure is shifted by gravity towards the side of the filled cavity, directing the water volume downwards, discarding it, and the other cavity starts to fill.

The proposed design framework for TBs is meant to quantify runoff and reduce errors arising from improper design. The framework consists of the following steps: calculation of design flow, calculation of the nominal volume, choice of the structural design, and calibration and validation. In Figure 2 we summarize the proposed framework, and a more detailed description of each step is given below.

2.1.1 Design flow and cavity size

The TB design flow, Q_d, is the peak runoff discharge to be measured. To calculate it, in-situ measurements or estimations are required. In case of no in-situ measurements, we suggest the use of the rational metho d (Eq. 1):

$$Q_d = C*I*A/1000 \tag{1}$$

where: Q_d $_d$ is the design flow ($m^3\ h^{-1}$); C is the runoff coefficient (dimensionless); I is the rainfall intensity ($mm\ h^{-1}$); and A is the runoff contributing area (m^2).

The runoff coefficient is the ratio between runoff and rainfall, varying between 0 (completely permeable) and 1 (completely impermeable), depending on many complex factors, such as soil composition and compaction, antecedent moisture, ground slope, infiltration, root system, surface land cover, etc. Compared to the other input variables, this is the most difficult to estimate from in-situ data and therefore, it is common to use average values based on land cover and ground slope. When the study area is composed of sections with different characteristics (land cover or soil type), it is necessary to create a composite runoff coefficient weighted on the area of each respective land use (Eq. 2). Supplementary

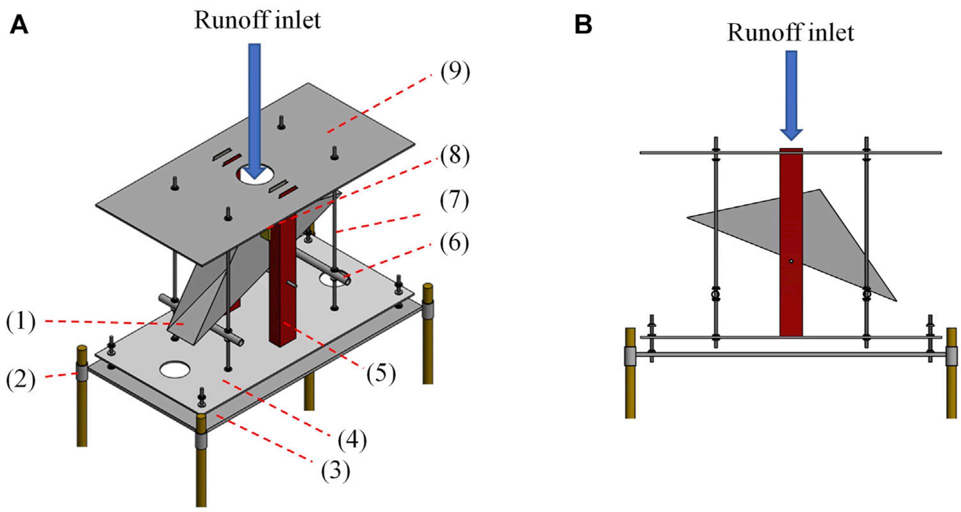

FIGURE 1
Illustration of the tipping bucket used to quantify runoff in perspective **(A)** and side **(B)** view where: (1) cavity; (2) anchoring rod on the ground; (3) fixed supporting plate; (4) mobile supporting plate; (5) vertical bar to support the reed switch and the upper plate; (6) height control bar; (7) support rod of the height control bar; (8) reed switch and cable connecting to the datalogger; and (9) upper plate.

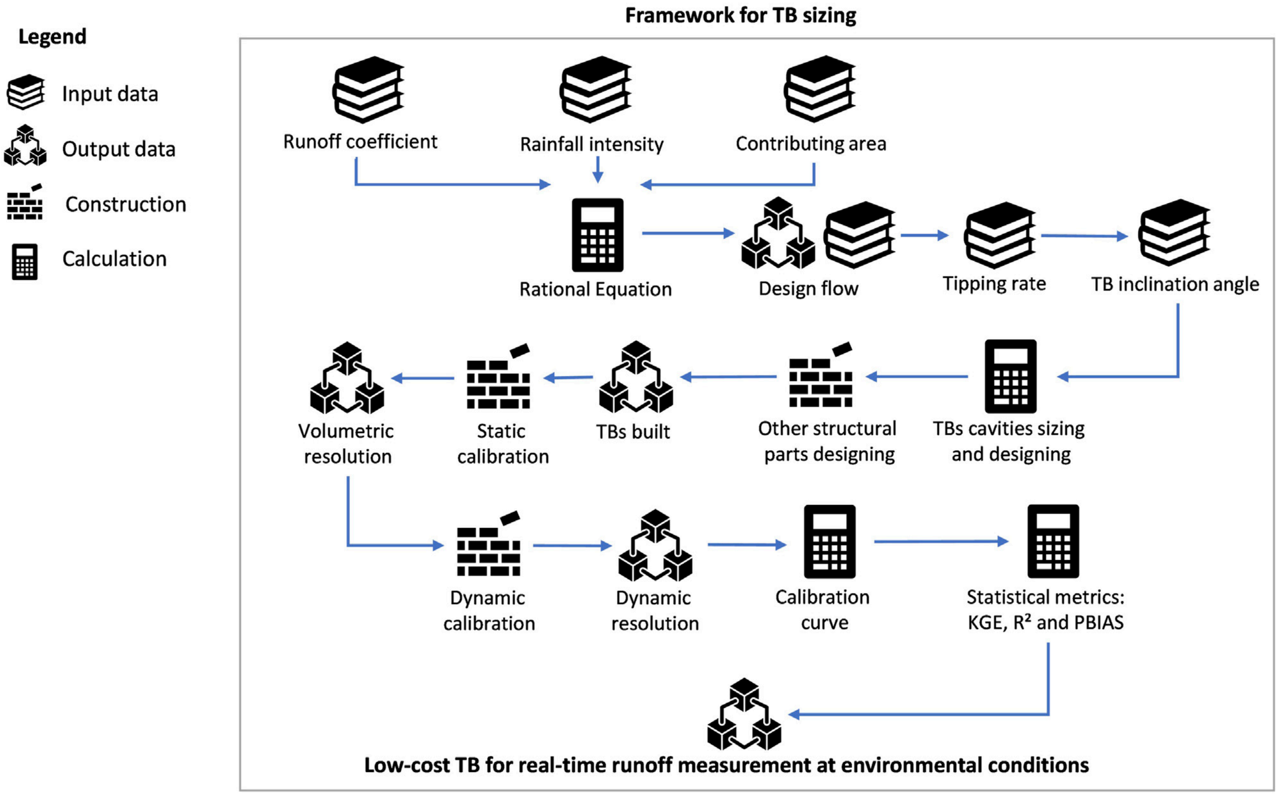

FIGURE 2
Schematic of proposed methodology for TB design.

Material A gives a list of C factors for urban and rural watersheds. Further information is given by Chin (2012) and Chow et al. (1988):

$$C_w = \frac{\sum_{j=1}^{n} C_j A_j}{\sum_{j=1}^{n} A_j} \tag{2}$$

where: C_w is the weighted runoff coefficient; C_j is the runoff coefficient for area j; A_j is the runoff area for land cover j; and n is the number of distinct land uses.

The second variable, rainfall intensity, is ideally found using data from a nearby rain gauge. However, if not possible, rainfall intensity data through third-party sources (environmental or national databases) can be used and later interpolated to where the study case is located. Once having a reliable dataset, we suggest the creation of a histogram to enable the visualization of the rainfall intensity. It is important to define an ideal range of performance because using a bucket with too low storage capacity during an intense runoff rate can lead to significant measurement errors caused by the kinetic effect of increased water flow through the inlet. Conversely, a too-large bucket during low-intensity runoff events may not even tip, resulting in inaccurate measurements. In order to have an optimum storage capacity, we suggest adopting rainfall intensities in Eq. 1 that correspond to between 70% and 90% of the accumulated occurrences recorded in the rainfall histogram, depending on how uniform the rainfall is.

The last variable is the runoff area. There is no limitation regarding the size of the area where the TB will be employed. However, we recommend that the estimated design flow should be less than 10 L per min. A higher flow rate will require a bigger TB cavity and/or higher tipping velocity, resulting in higher monitoring errors. Flow portioning devices before the TB can be used, see Pinson et al. (2004) or Supplementary Material B.

The nominal volume is estimated by Eq. 3, which considers the design flow (estimated previously by Eq. 1), operation speed (number of tippings per time unit), and inclination angle of TB at resting position. Based on previous operation tests investigating the relationship between errors and operation speed, the optimum operating speed should be between three and four tippings per minute (Schwamback et al., 2022).

$$V = \frac{2.5Q\theta}{n} \tag{3}$$

where Q is the runoff rate (mL/min); V is the cavity volumetric capacity (mL); θ is the inclination angle of the cavity (radians); and n is the tipping rate (tippings per minute).

Lastly, we suggest an inclination angle between 25% and 35%. The higher the inclination angle, the higher the storage capacity, and thus, higher runoff rate can be covered by raising the inclination angle. Once the volume of the TB cavity is defined, it is possible to define the dimensions, shape (cylindrical or rectangular, Figure 3), and construction material (Table 1). We recommend the use of PVC tubes in projects that require cavities with storage capacity below 270 mL since it is an easy working material and inexpensive material. In projects with larger cavity volume, galvanized steel sheet is recommended since it has a greater resistance to high impact during tipping.

2.1.2 TB construction

The equipment structure consists of two parts connected by threaded rods. The first part (fixed structure) is a rectangular base

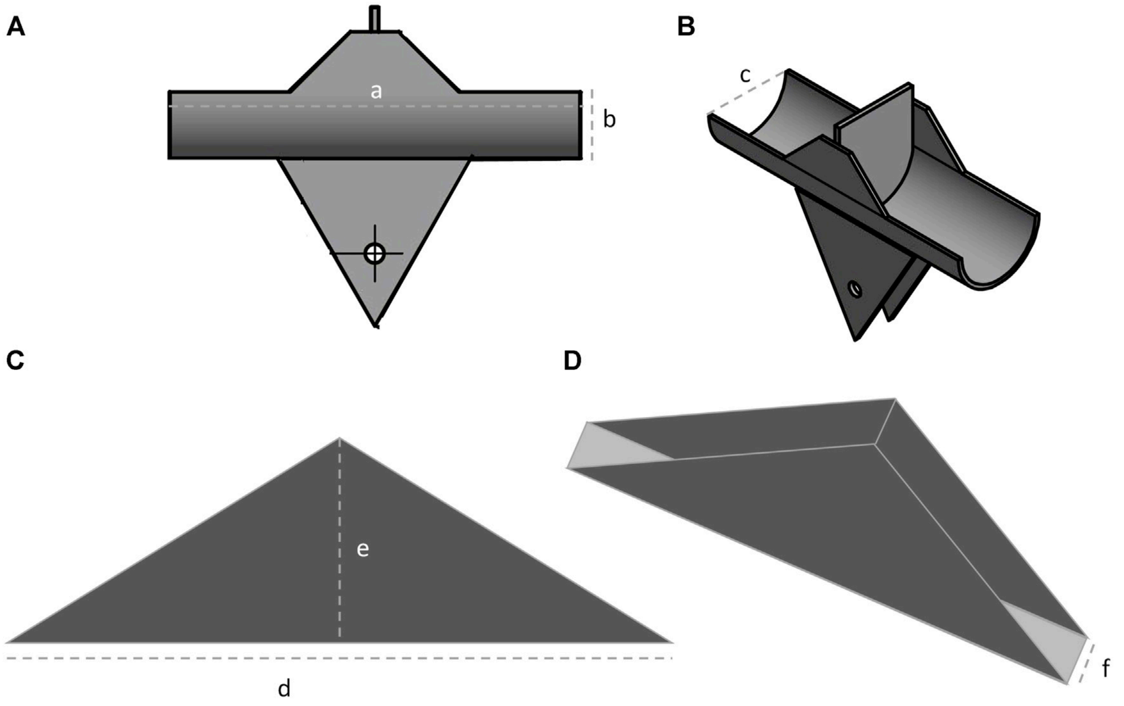

FIGURE 3
Sizing cylindrical (A, B) and rectangular (C, D) tipping bucket cavity.

TABLE 1 Indication of sizing equations, construction material, and shape for cavity construction based on the cavity volumetric capacity. The dimensions are given in mm and the letters in the equations show design presented in Figure 3.

Volumetric capacity	Equations for cavity sizing	Construction material	Shape
Up to 250 mL	$a = V/1.8$	PVC tube	Cylindrical
	$b = 2/3c$		
	$c = V/1.5$		
	Adjust the c value to the closest commercial tube diameter		
Between 250 and 4000 mL	$d = V/1.5$	Steel	Rectangular
	$e = V/5$		
	$f = V/10$		

built-in metallic profile, in which the corners are fixed to the ground by steel bars (see Figure 1). The bars placed in the ground serve as a foundation for the equipment, inhibiting unevenness due to the tipping kinetic action. The second part of the structure (movable structure) is a steel plate, on which the vertical support bars of the upper plate are welded and the height control bars are threaded. The mobile plate makes it easy to remove the equipment to carry out maintenance and calibration tests in the laboratory.

Two pairs of threaded rods are installed at each corner, connecting the lower and upper plates. A metallic cylinder linking each pair of rods allows the adjustment of the height of each bucket when in operation. The smaller the height between the plate and the bucket, the greater the nominal capacity in the opposite cavity. Thus, the purpose of the bars is to adjust the nominal volume and, consequently, tipping speed, as necessary. The equipment has then a useable capacity of 30% higher volume, enabling possible adjustments, if necessary, by lifting or lowering the height control bar.

We suggest the automatization of tipping counting using a reed switch, a low-cost electronic device. The reed switch is proposed to be attached to one of the supporting bars of the TB structure while the magnet will be fixed to the central portion of the bucket. Each time the tipping bucket device releases water, the fixed magnet will pass close to the reed switch, creating a magnetic field and joining its two internal metallic filaments, allowing the passage of current and registering the tipping time as a pulse signal. The electrical signal (pulse) can be recorded and stored by any commercial or low-cost (Arduino or Raspberry) datalogger.

2.1.3 Laboratory tests and calibration

Calibration should be performed in two steps: static (volumetric) and dynamic. Static calibration consists of determining the volume of water necessary for the center of mass to be shifted towards the filling cavity, leading to its tipping. The volume determined in this step corresponds to the volumetric resolution or nominal volume (NV) of the equipment used during the dynamic calibration. The dynamic calibration consists of creating adjustment curves to correct errors between the flow rates estimated by the equipment through a constant flow input (Shedekar et al., 2016).

During the construction of the calibration curve, it is important to mimic real field conditions. Among these conditions, a high concentration of sediments can change the density of the water, as well as accumulate in the cavities of the equipment, in both cases resulting in malfunctions and measurement errors. This point was already brought forward by Barfield and Hirschi (1986) while indicating that the effect of sediments is significant, but can be neglected when the concentration is lower than 20 g/L. We suggest investigating the expected soil loss rate of the monitored area where the TB will be employed to come up with the best approach for runoff monitoring, such as: disregarding soil presence, construction of calibration curve using water rich in soil particles, or correcting factor of water density.

To determine the volumetric resolution, a graduated pipette, and a suction pear can be used. The water must drip slowly so that the kinetic effect does not interfere with the process until one of the cavities tips and the volume is identified. The procedure must be performed several times (we suggest 10) in each cavity and then the average between the replicates is applied to determine the equipment's volumetric resolution. Once the volumetric capacity is determined, dynamic calibration during equipment motion with continuous water entry is required. Connect the TB to a constant flow water outlet, like a public water supply system's refilled column, to generate motion. The test should include varied flow intensities associated with return periods using local IDF curves, up to a maximum level set by the designer. Adjust the inflow rate to reach the desired sampling point and measure it using simple methods like gravimetry. The reed switch on the TB, coupled with a datalogger, automatically counts and records tip numbers. Simulated flow is calculated as the product of tips and volumetric cavity resolution. Correlation between simulated and reference flow rates can be determined using standard mathematical models such as linear, polynomial, potential, inverse flow rates over time, and quadratic. More information regarding calibration process, and errors sources is given by Schwamback et al. (2022).

2.2 Case study location

Surface runoff monitoring took place in experimental plots of 100 m^2 (20 m long and 5 m wide), implemented in 2011 at the São José farm in Itirapina county, Central region of the State of São Paulo, Brazil (Figure 4). The area was chosen once it has been continuously monitored since 2011, but only containing information of runoff after rainfall events and the use the TB would provide a continuous detailed characterization of surface

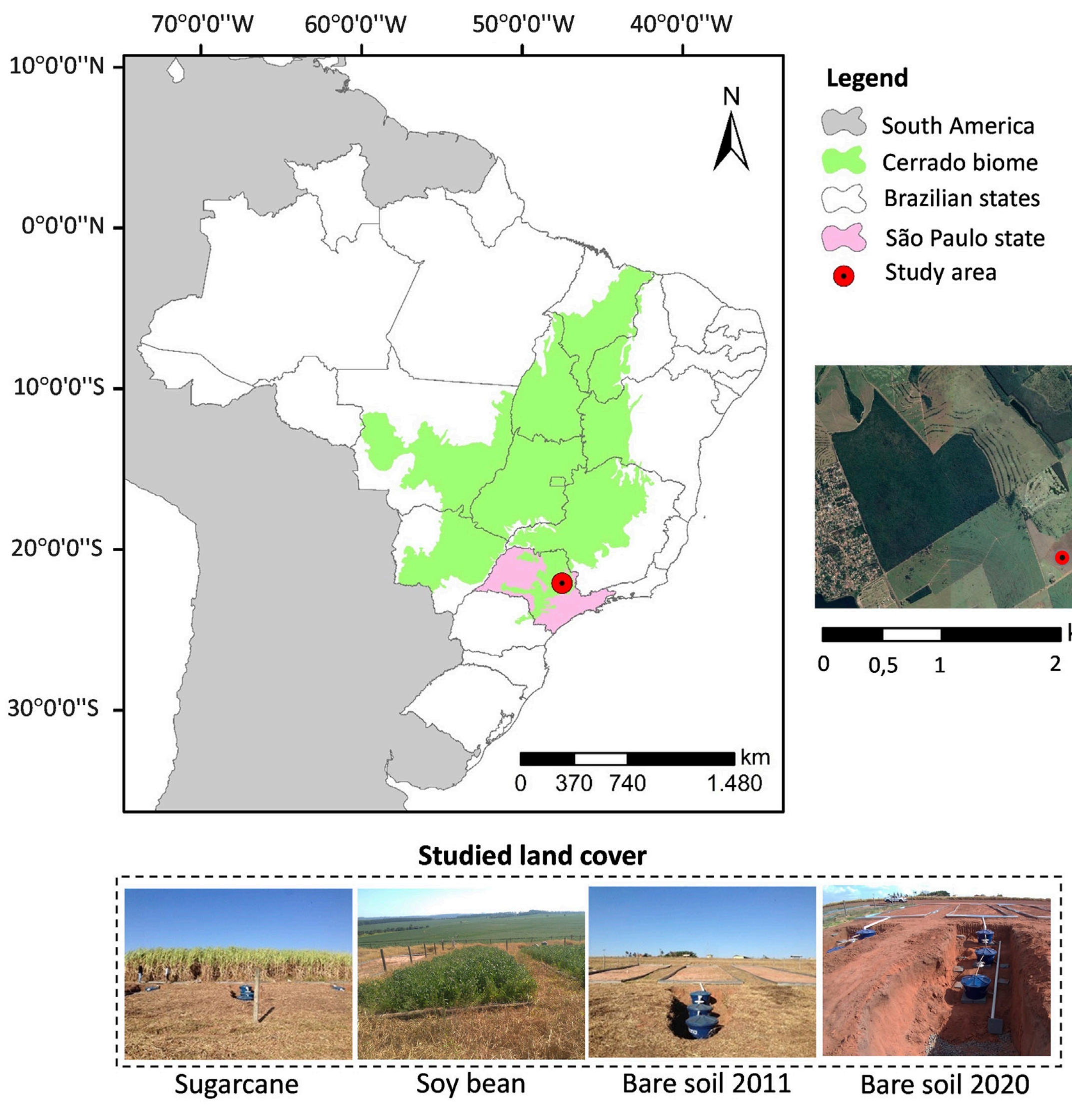

FIGURE 4
Location of experimental study areas covered with sugarcane (TB1), soy bean (TB2), and bare soil constructed in 2011 (TB3) and 2020 (TB4), where tipping buckets (TB) were installed.

processes. Based on the above-described TB design criteria, four TBs were built and installed at experimental plots on four LULC: sugarcane (TB1), soybean (TB2), and bare soil built in 2011 (TB3) and 2020 to study the long-term environmental exposure effects on soil loss (TB4). The expected flow rate influenced on the designed TB that varied on volumetric capacity and construction material, while more details are given on session 3.1.1. Even though the plots were built in triplicates, only one TB was installed at the outlet of each LULC. The TB field test occurred during the rainy season (779 mm) between November 15th, 2021 and April 19th, 2022. Once runoff starts, the flow is orientated through metallic boards to a PVC tube connected to the tipping bucket flow meters, similar to the field monitoring process used by Bashagaluke et al. (2018) and Sun et al. (2014). The reed switches previously installed on the TBs (Figure 1), coupled to a datalogger (Campbell Scientific Inc CR1000 and measuring at 10 min interval) used on the nearby weather station and a 12 V battery powered by a solar panel, allowed the counting and automatic recording of the number of tips. After measurements, the water was stored in 310 L boxes to compute the equipment recovery rate (PBIAS) used for the measurement validation.

3 Results and discussion

3.1 Case study

3.1.1 TB design

Runoff peak flows at the experimental plots were estimated by Eq. 1 based on local information of rainfall intensity, runoff coefficient, and contributing area, while the volumetric capacity of the TB cavity was estimated by Eq. 3 employing the runoff peak, cavity inclination angle, and tipping rate (see Table 2).

Rainfall intensity was determined using field data collected between November 2011 and October 2018 at an automatic station located in the study area. Data were divided into independent precipitation events with a minimum interval between events of 60 min (Molina-Sanchis et al., 2016), resulting in 1845 independent events. Using histograms made it possible to understand the intensity variation for the study area, in which a higher occurrence of low (less than 1.8 mm/h) and medium (1.8–7.8 mm/h) intensity events was observed. Based on this, the TBs were designed to collect runoff resulting from these rainfall-intensity events. The intensity of 3 mm/10 min (18 mm/h) was adopted as the standard intensity for sizing the tipping bucket cavities, which represented approximately 85% of the accumulated occurrences recorded in the period. Under this flow intensity, we expected a tipping rate of about three tippings per minute. The second variable required to estimate runoff was the coefficient that relates rainfall to runoff generation considering the LULC and soil class. We adopted the surface flow coefficients estimated by Anache et al. (2019) derived from a previous study where we intended to employ the TBs. Finally, the last variable was the contribution area, here 100 m^2. After estimating TB4 volumetric cavity, it was increased by 20% (V = 756 mL) based on the preliminary field observations that runoff was higher in that plot than in its neighboring one where C value was estimated (TB3).

The cavities of the TB1 and TB2 were constructed using PVC tubes, 50 and 75 mm in diameter, respectively, cut in half. Due to the high storage capacity needed, the cavities of the TB3 and TB4 were made from galvanized steel sheets, a material resistant to the high impact during water disposal.

Supplementary Material C presents the technical drawings, sizing, and materials used in the construction of TB1, TB2, and TB3. Most parts were constructed using metal (stainless steel) since we were balancing durability, versatility, and cost. Different materials can also be used in the construction, such as plastic and wood (Shiraki et al., 2019), and future studies may be addressed to asses if the material influence on the equipment performance. It is estimated that about $500.00 was spent to purchase materials and build the four tipping bucket flow meters presented. In Supplementary Material D we give some considerations regarding the sizing, installation, operation, and maintenance. Figure 5 shows photographs of the tipping buckets after construction. After taking the photographs, the TBs were painted to prevent corrosion.

By constructing a histogram of the sediment concentration from data collected in the study area from 2011 to 2017, it was noted that the highest concentration recorded in the period was 10.2 g/L, while most of the monitored events (95%) had a concentration of below 3.0 g/L (Youlton et al., 2016). Since the concentrations of sediments previous monitored were below 20 g/L (Anache et al., 2019), the presence of sediments was neglected (Barfield and Hirschi, 1986) and, thus, water from the public supply system was used for calibration and testing instead of a mixture of water and soil.

3.1.2 Volumetric and dynamic calibration

After performing the procedure related to static calibration of TBs designed for the case study, it was found that the nominal volume was 64.16 mL, 139.86 mL, 660.95 mL, and 792.33 for TB1, TB2, TB3, and TB4, respectively. In Supplementary Material E is given the mean and standard deviation of observations for each cavity and global analysis (both cavities) of TBs designed. During the dynamic calibration process, positive errors were registered indicating an underestimation of reference flows. The highest mean PBIAS (21.4%) observed in TB4, followed by TB3 (13.6%) TB2 (9.3%), and TB1 (5.7%) indicated a positive correlation (Pearson's correlation of 0.78), but statistically insignificant (p-value of 0.22), between the TBs nominal volumes and the PBIAS index after curve implementation. It means that as it expands the cavity size, the greater the residual flow underestimation. The inverse correlation between size and accuracy is expressed through the decline of different statistical metrics used available in Supplementary Material F. Besides cavity size, operating speed also plays an important contributing factor in errors (Figure 6), with high errors under extremely low and intense flow rates, as observed by Sun et al. (2014) who sized and calibrated TBs for runoff measurements with a nominal resolution of 2.5 L. It is believed that under low flow rates, the surface tension of the

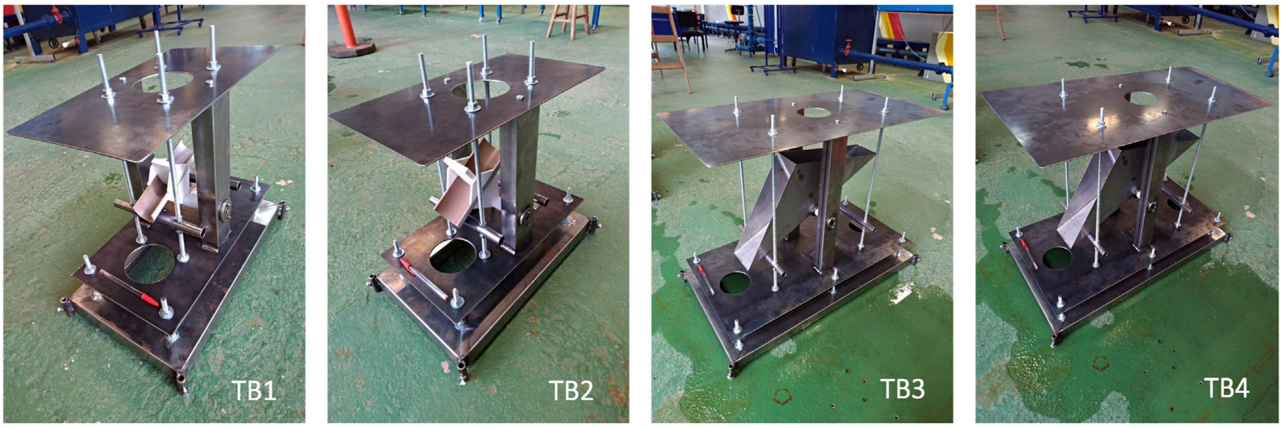

FIGURE 5
Photographs of the designed TBs.

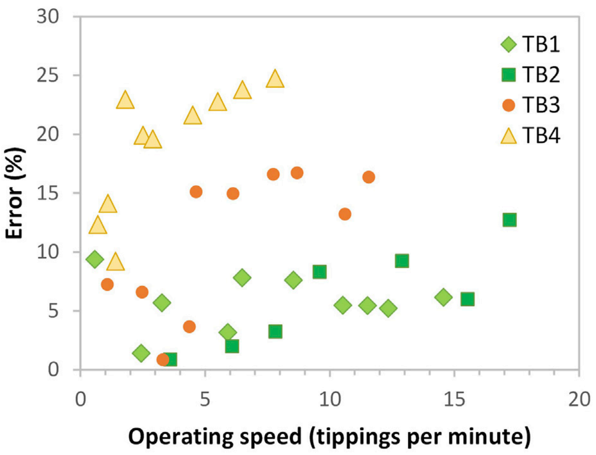

FIGURE 6
Percent error at different operating speed during dynamic calibration of TBs.

water influences the displacement along the surface of the cavity (Sun et al., 2014), while at high flow rates, the slow and subtle shift, ideal in the gravity center, is affected by the rapid entry of water under turbulent flow (Iida et al., 2012). Another error source that contributes to the registered discrepancies between reference and measured flow comes from the water left in the cavities after one replicate ends and that is not sufficient to tip, as also already highlighted by Nehls et al. (2011).

After implementing the calibrationcurves (Supplementary Material G), we observed an underestimation ranging from 0.079% (TB1) to 1.612% (TB4). The calibration performance obtained here (Supplementary Material H) are similar to those obtained by Somavilla et al. (2019), Yahaya et al. (2009), and Sun et al. (2014) when applying linear curves to reduce error during the calibration of TBSs of different size. Khan and Ong (1997) carried out the calibration process of a tipping bucket with a volumetric capacity of approximately 3 L and obtained a coefficient of determination of 0.99 with a residual overestimation error of 2%. Similarly, Sun et al. (2014) calibrated a TB with a capacity of 2.5 L, finding a good linear correlation (R^2 equal to 0.99) between reference and measured flows and a low mean error (2.1%). It is important to note that the nominal volume of TB4 (660.95 mL) is smaller than those studies mentioned, which would then be expected to have a lower error, as it happened (1.4%), proving its efficiency.

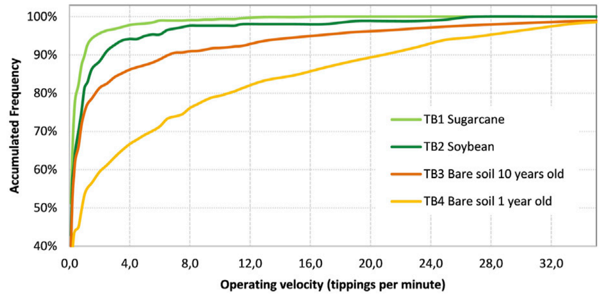

FIGURE 7
Accumulated frequency of TBs' operating velocity during annual field test.

3.1.3 Field test

The main purpose of the performed field tests was to evaluate the applicability of the proposed design methodology in runoff monitoring. During the sizing of the TBs constructed for this study case, we designed them considering an operating rate of three tippings per minute (Table 2) to cover 85% of the accumulated runoff intensity. Figure 7 shows the accumulated frequency of operating velocity during the field test. Schwamback et al. (2022) investigated sources of errors in TBs and identified that operating velocity is not linearly correlated to TB errors, but that there is an optional operating zone between two and four tippings per minute. The field test showed that considering the designed operating velocity, most TBs were within the criteria of covering 85% of the accumulated runoff: TB1 (97%), TB2 (93%), TB3 (86%), and TB4 (67%), demonstrating that TBs are operating within a good velocity range and were well sized. During the field test, TB4 operated under a mean velocity higher than expected. TB4 was designed using a runoff coefficient from a similar area (C factor = 0.063) to which we added a 20% increase in volumetric capacity as a safety factor based on initial field monitoring. After runoff data collection, the area where TB4 was installed proved to actually have a runoff coefficient of 0.098. The underestimation of C was the main source of flow underestimation that led to the high operating velocity shown in Figure 8, highlighting the importance of having reliable input data. Considering this new C factor, the TB4 volumetric capacity needs to be increased from 792 mL to 1225 mL (54% higher) and it can be easily reach by lowering the height control bar (Figure 1), which will raise the inclination angle of the cavity at rested position (θ) from the actual 23° (0.4 radians) to 29° (0.5 radians).

TABLE 2 Input information used to estimate runoff peak (Q) and volumetric capacity of the TB cavity (V) based on Eq. 1 and Eq. 3 for each of the four investigated TBs designed for the case study.

TB	C	I	A	Q	θ	n	V
TB1	0.007	18	100	210	0.4	3	70
TB2	0.029	18	100	870	0.3	3	163
TB3	0.063	18	100	1890	0.4	3	630
TB4	0.063	18	100	1890	0.4	3	630

Where: C is the Runoff coefficient (dimensionless); I is the rainfall intensity (mm/h); A is the runoff area (m^2); Q is the runoff peak (mL/min); θ is the cavity inclination angle (radians); n is the tipping rate (tippings per min); and V is the volumetric capacity of the TB cavity (mL).

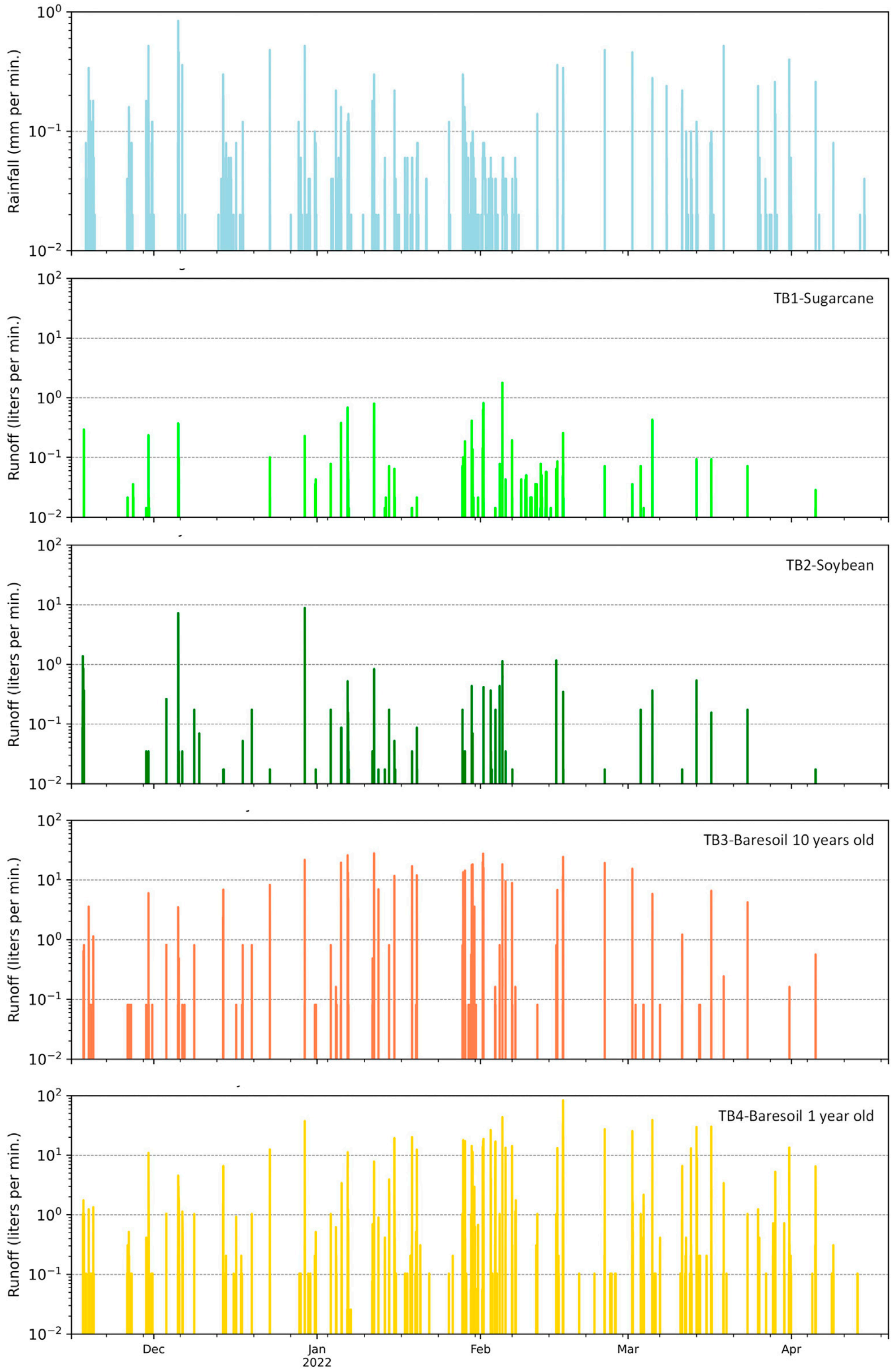

FIGURE 8
Real-time runoff observed by large TBs during rainy season.

The use of TBs for surface runoff monitoring aims to create runoff hydrographs providing information regarding the peak, volume, and duration of runoff events. Figure 8 presents the real-time runoff by the TBs while Figure 9 provides the same information downscaled to selected events, enabling a clearer view of the peak flow rate and the starting and ending periods. Besides single event analysis, the long-term monitoring of runoff at different land covers employing TBs enable the study of vegetation on hydrological

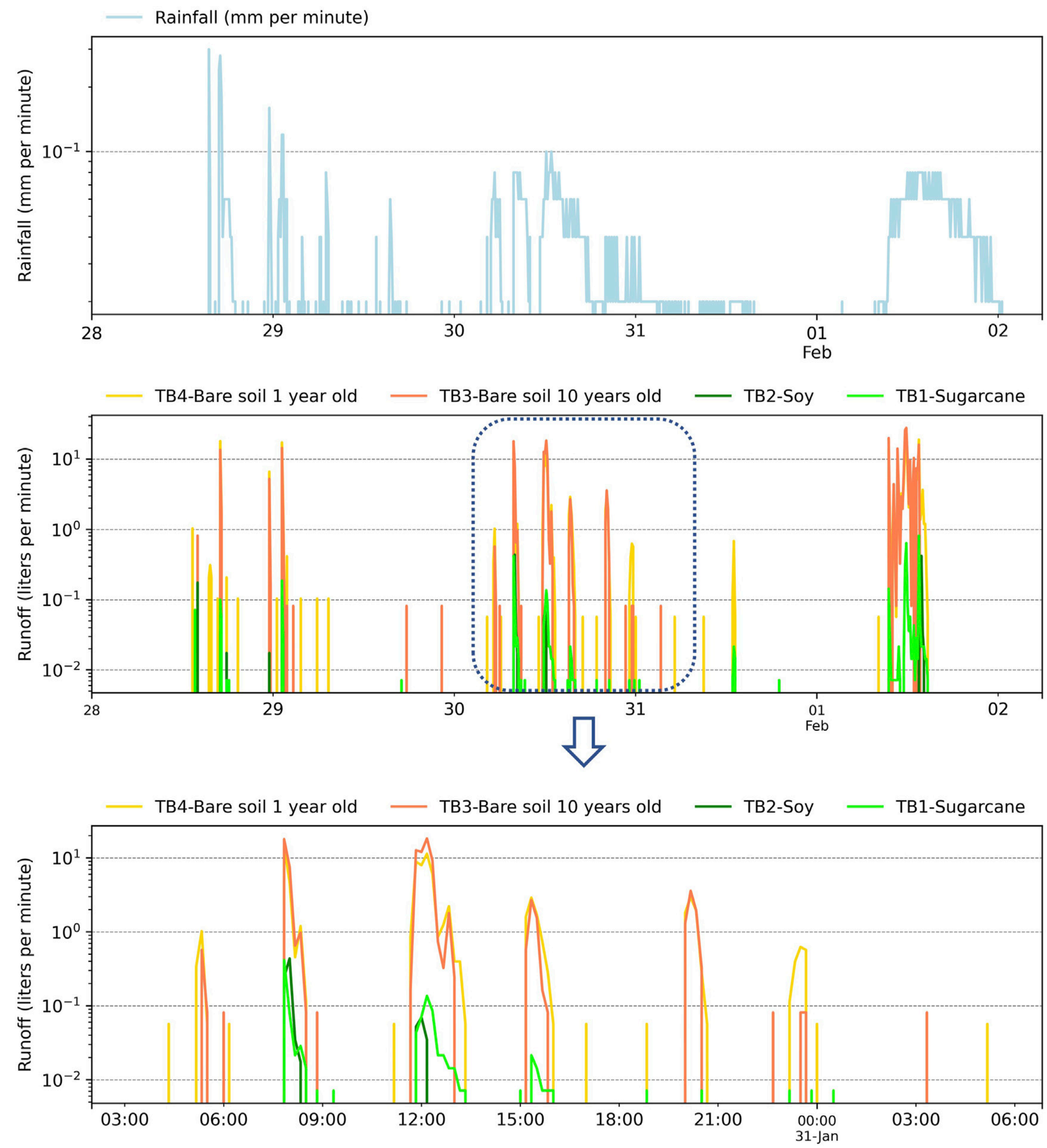

FIGURE 9
Real-time runoff observed by large TBs at event scale.

features at a longer scale (Figure 10; Supplementary Material J). Based on 84 runoff curves assembled, the experimental plot planted with soybean has a three times higher mean runoff volume, shorter runoff duration, and peak time compared to sugarcane-covered plots. This can be explained by that the soybean plot has a superficial root system, has short life span and went through yearly harvesting and replanting, disturbing the soil. On the other hand, sugarcane has a deeper root system, slow vegetative development, and besides being harvested yearly, is replanted in contour lines every 4 years. Comparing the hydrological behavior of unvegetated plots, TB3 is monitoring runoff in a plot kept exposed to the environment since 2011 while TB4 monitored a plot recently exposed (installed in 2020). Runoff duration and peak time are longer in TB4 than TB3, while peak volume and total volume are higher in TB3, indicating flush runoff characteristics in TB3 even under the same design and slope. Bare soil exposed to precipitation and constant solar radiation over 10 years modified the pedological characteristics of the area, causing: pore clogging, dragging of the surface layers of the soil, and particle breakdown. Such alterations have a direct impact on the infiltration capacity of the soil and, consequently, on the total drained volume (Table 3) and runoff duration (Figure 8; Figure 10).

Despite our application in experimental plots, the monitoring of peak time, duration, and intensity of runoff hydrographs describe the environmental influence (land cover, slope, climate, infiltration capacity, soil proprieties, among others) on water flow dynamics in a certain studied area providing broader insights. Flow peak time, for instance,

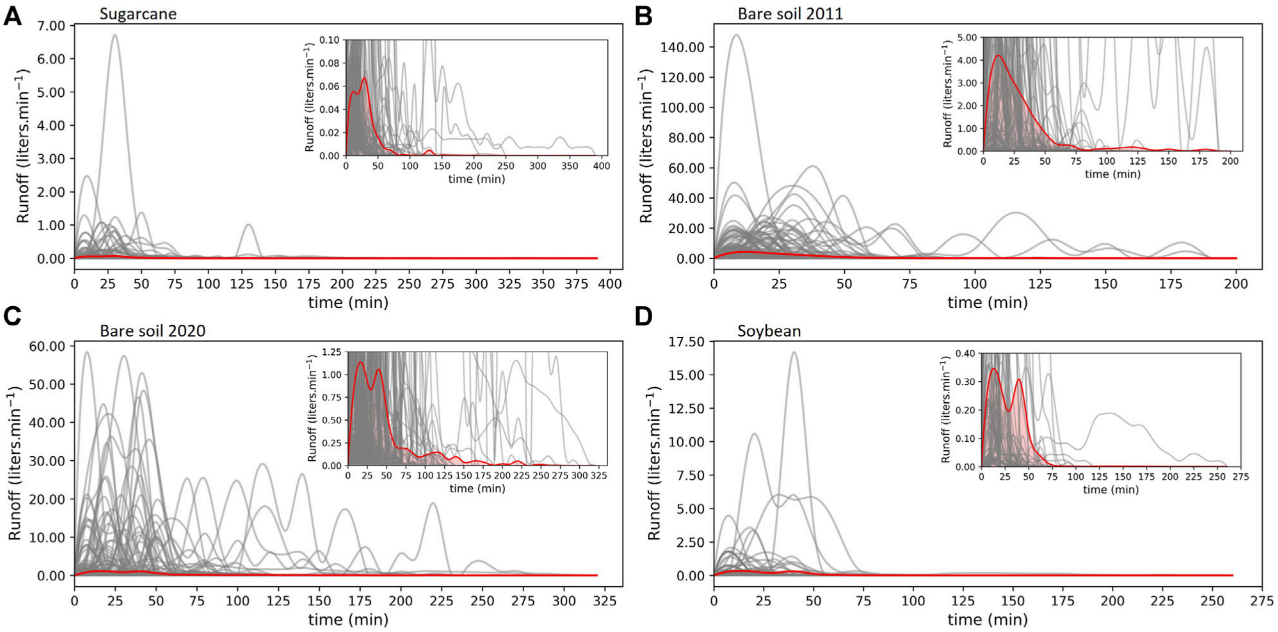

FIGURE 10
Runoff ensemble curves (grey color) monitored at experimental plots covered with sugarcane **(A)**, bare soil since 2011 **(B)** and 2020 **(C)**, and soybean **(D)**. Inside each plot, we zoomed in for a better visualization of the mean runoff distribution (red color).

reveals when the highest water flow occurs, enabling calibration of flood prediction models in large basins (Zhai et al., 2021) and identification of shifts in overland flow due to changes in land cover (Guzha et al., 2018; Procházka et al., 2019) or climate change (Saraswat et al., 2016). The duration of hydrographs provides insight into the persistence of runoff, essential for assessing the risk of soil erosion and the design of effective erosion control strategies (Bettoni et al., 2023). Meanwhile, intensity data helps in gauging the erosive power of rainfall and, consequently, informs the development of soil conservation policies aimed at mitigating the impacts of erosion (Bettoni et al., 2023). In essence, a comprehensive understanding of flow peak time, duration, and intensity is the linchpin for informed decision-making in hydrology studies and the formulation of effective soil conservation measures under current or future conditions of changes in land cover and climate.

From the comparison between the volumes measured by the TBs and those stored in the boxes, it was possible to estimate the TBs recovery rate during the field test period (Table 3), which varied between 69% and 98%. As already expected, the accuracy is directly related to the volumetric capacity of the TB. There are many different possible errors source that might explain the mismatch between runoff data, such as: kinetic effect during water entry, continuous entry of water into the TB cavity when it is already in motion, loss of lubrication, entry of animals and leaves, flow inlet clogging, etc. Despite the TBs being a robust and low-cost equipment, there are still limitations and difficulties in carrying out data collection in the field, e.g., there was a need for constant checking of the equipment operation at the monitoring site, to ensure that they were working properly.

3.2 Other examples of TB sizing and applications

The proposed TB framework can be easily applied to other land uses, slopes, soil types, and hillslopes of other sizes, once it is possible to collect and drive the runoff to pass through the TB (Table 4; Table 5). Table 4 shows the volumetric capacity of the tipping cavity when designed for different common land uses under the same standardization characteristics (rainfall and drainage area) found in the case study. Table 5 gives the estimated TB volumetric capacity for bare soil under common rainfall intensity rates when applied to different plot sizes, demonstrating the adaptability of the TB solution for multiple-scale rainfall simulations. Nonetheless, the use of smaller plots would prevent high sediment mass under intense rainfall, which may affect the accuracy of the equipment.

TABLE 3 TBs recovery rate at measuring annual runoff during field test.

	TB1	TB2	TB3	TB4
Runoff measured in the storage boxes (m^3)	2.44	8.35	130.42	114.09
Runoff measured by the TBs (m^3)	1.98	6.62	90.94	158.26
Recovery rate	80.98%	79.19%	69.72%	61,29%

TABLE 4 Estimated TBs volumetric capacity for other land uses under an average rainfall intensity of 18 mm h^{-1} and drainage area of 100 m^2.

Land use	Runoff coefficient	Reference	Estimated TB volumetric capacity (mL)
Orchard	0.080	Tu et al. (2018)	800
Tobacco	0.083	Antoneli et al. (2018)	830
Eucalyptus	0.189	Jaleta et al. (2017)	1890
Coffee	0.200	Ramos-Scharrón and Thomaz (2017)	2000
Vineyard	0.248	Cerdà and Rodrigo-Comino (2020)	2480

TABLE 5 Estimated TBs volumetric capacity (mL) for bare soil (C = 0.063) (Anache et al., 2019) under different simulated rainfall intensities and drainage areas.

	Plot area		
Rainfall intensity	1 m^2	10 m^2	100 m^2
20 mm h^{-1}	7.0 mL	70.0 mL	700.0 mL
40 mm h^{-1}	14.0 mL	140.0 mL	1400.0 mL
60 mm h^{-1}	21.0 mL	210.0 mL	2100.0 mL
80 mm h^{-1}	28.0 mL	280.0 mL	2800.0 mL
100 mm h^{-1}	35.0 mL	350.0 mL	3500.0 mL

4 Conclusion

Although using empirical methods provides satisfactory estimations regarding water resources, *in situ* monitoring is indispensable for calibration and validation. Among the existing alternatives, such as Parshall flumes, level, and mass sensors, spillway, and storage boxes, tipping bucket flow meters (TBs) are considered a low-cost construction and installation alternative, easy to operate, which allow measurements with high temporal resolution and data accuracy. Nonetheless, those who intend to use this monitoring equipment have so far not had a detailed methodology to design and calibrate the TBs.

Our main contribution was to provide a novel standardized framework for the design of TB that can be easily performed for TBs under any land cover, rainfall, and contributing area. The methodology consists in first estimating the runoff peak rate by the rational equation and later estimating the nominal volume of the cavity based on runoff rate, operation speed, and inclination angle of TB when at resting position. Based on the standardized framework we provided, hydrologists can design a low-cost TB specific for the environmental conditions they face and collect real-time runoff data.

The proposed methodology was implemented in a case study where four TBs were designed for continuous runoff monitoring in experimental plots under commonly found and contrasting LULC in the southeast region of Brazil (soy, sugarcane, and bare soil). Due to the different runoff coefficients, each TB had a specific volumetric resolution for each LULC: 64.16 mL (TB1—sugarcane), 139.86 mL (TB2—soy), 660.95 mL (TB3—bare soil) and 792.33 mL (TB4—bare soil). Besides the case study, we also provided extensive examples of the applicability for sizing the TB other LULC, runoff contributing, and rainfall intensity.

The proposed equipment consists of instruments for continuous monitoring of runoff in remote areas without access to high-voltage electricity. They were tested in the field over 5 months and enabled the capture of runoff features (starting/ending time and flow rate) poorly studied. During the field test the designed TBs demonstrated excellent capacity to represent occurring runoff hydrographs, with a recovery rate between 81% and 61% of total occurring runoff. The continuous monitoring of the runoff in contrasting environments (natural and agricultural LULCs) will provide information about runoff behavior and human disturbance along a detailed timescale. Lastly, the methodology proposed can be easily reproduced to construct tipping buckets consistent with other surface or subsurface flow conditions, such as stem, green roof, and paved surfaces.

Data availability statement

The original contributions presented in the study are included in the article/Supplementary Material, further inquiries can be directed to the corresponding author.

Author contributions

DS: Conceptualization, Data curation, Formal Analysis, Investigation, Methodology, Project administration, Visualization, Writing–original draft. MP: Formal Analysis, Funding acquisition, Investigation, Supervision, Writing–review and editing. RB: Supervision, Writing–review and editing. JA: Conceptualization, Methodology, Writing–review and editing. EW: Funding acquisition, Resources, Supervision, Writing–review and editing.

Funding

The author(s) declare financial support was received for the research, authorship, and/or publication of this article. This study was funded in part by the São Paulo Research Support Foundation (FAPESP, grants 2015/03806-1, 2019/24292-7 and 2021/14016-2), the Brazilian National Council for Scientific and Technological Development (CNPq, grant numbers 165101/2018-0), and lastly by the Coordination for the Improvement of Higher Education Personnel (CAPES, Finance Code 001).

Acknowledgments

The authors acknowledge the Graduate Program in Hydraulic Engineering and Sanitation-PPGSHS at the University of São Paulo (EESC-USP) and Department of Building and Environmental Technology at Lund University for the scientific support and the Arruda Botelho Institute (IAB) for allowing the development of this study on its private land.

Conflict of interest

The authors declare that the research was conducted in the absence of any commercial or financial relationships that could be construed as a potential conflict of interest.

Publisher's note

Supplementary material

The Supplementary Material for this article can be found online at: https://www.frontiersin.org/articles/10.3389/fenvs.2023.1286929/full#supplementary-material

References

Anache, J. A. A., Wendland, E., Rosalem, L. M. P., Youlton, C., and Oliveira, P. T. S. (2019). Hydrological trade-offs due to different land covers and land uses in the Brazilian Cerrado. *Hydrol. Earth Syst. Sci.* 23, 1263–1279. doi:10.5194/hess-23-1263-2019

Anache, J. A. A., Wendland, E. C., Oliveira, P. T. S., Flanagan, D. C., and Nearing, M. A. (2017). Runoff and soil erosion plot-scale studies under natural rainfall: a meta-analysis of the Brazilian experience. *Catena* 152, 29–39. doi:10.1016/j.catena.2017.01.003

Antoneli, V., Lenatorvicz, H. H., Bednarz, J. A., Pulido-Fernández, M., Brevik, E. C., Cerdà, A., et al. (2018). Rainfall and land management effects on erosion and soil properties in traditional Brazilian tobacco plantations. *Hydrol. Sci. J.* 63, 1008–1019. doi:10.1080/02626667.2018.1472379

Barfield, B. J., and Hirschi, M. C. (1986). Tipping bucket flow measurements on erosion plots. *Trans. ASAE* 29, 1600–1604. doi:10.13031/2013.30360

Bashagakule, J. B., Logah, V., Opoku, A., Tuffour, O., Sarkodie-Addo, J., Quansah, C., et al. (2018). New method for runoff estimation under different soil management practices. *Biorxiv. Org.* 86, 1–23. doi:10.1101/424069

Bashagaluke, J. B., Logah, V., Opoku, A., Sarkodie-Addo, J., and Quansah, C. (2018). Soil nutrient loss through erosion: impact of different cropping systems and soil amendments in Ghana. *PLoS One* 13, e0208250. doi:10.1371/journal.pone.0208250

Benedetti, I., Branca, G., and Zucaro, R. (2019). Evaluating input use efficiency in agriculture through a stochastic frontier production: an application on a case study in Apulia (Italy). *J. Clean. Prod.* 236, 117609. doi:10.1016/J.JCLEPRO.2019.117609

Bettoni, M., Maerker, M., Bosino, A., Conedera, M., Simoncelli, L., and Vogel, S. (2023). Land use effects on surface runoff and soil erosion in a southern Alpine valley. *Geoderma* 435, 116505. doi:10.1016/j.geoderma.2023.116505

Beven, K., and Germann, P. (2013). Macropores and water flow in soils revisited. *Water Resour. Res.* 49, 3071–3092. doi:10.1002/wrcr.20156

Blöschl, G., Bierkens, M. F. P., Chambel, A., Cudennec, C., Destouni, G., Fiori, A., et al. (2019). Twenty-three unsolved problems in hydrology (UPH) – a community perspective. *Hydrol. Sci. J.* 64, 1141–1158. doi:10.1080/02626667.2019.1620507

Calder, I. R., and Kidd, C. H. R. (1978). A note on the dynamic calibration of tipping-bucket gauges. *J. Hydrol.* 89, 383–386. doi:10.1016/0022-1694(78)90013-6

Cerdà, A., and Rodrigo-Comino, J. (2020). Is the hillslope position relevant for runoff and soil loss activation under high rainfall conditions in vineyards? *Ecohydrol. Hydrobiol.* 20, 59–72. doi:10.1016/j.ecohyd.2019.05.006

Chin, D. (2012). *Water-resources engineering*. Michigan: Pearson. Third.

Chow, T. L. (1976). Overland flow and subsurface stormflow studies. *Can. J. Soil Sci.* 56, 197–202. doi:10.4141/cjss76-028

Chow, V.Te, Maidment, D. R., and Mays, L. W. (1988). *Applied hydrology.* McGraw-Hill.

Corona, R., Wilson, T., D'Adderio, L. P., Porcù, F., Montaldo, N., and Albertson, J. (2013). On the estimation of surface runoff through a new plot scale rainfall simulator in sardinia, Italy. *Procedia Environ. Sci.* 19, 875–884. doi:10.1016/J.PROENV.2013.06.097

Ebabu, K., Taye, G., Tsunekawa, A., Haregeweyn, N., Adgo, E., Tsubo, M., et al. (2023). Land use, management and climate effects on runoff and soil loss responses in the highlands of Ethiopia. *J. Environ. Manage.* 326, 116707. doi:10.1016/j.jenvman.2022.116707

Edwards, I. J., Jackon, W. D., and Fleming, P. M. (1974). Tipping bucket gauges for measuring run-off from experimental plots. *Agric. Meteorol.* 13, 189–201. doi:10.1016/0002-1571(74)90046-6

Elder, K., Marshall, H. P., Elder, L., Starr, B., Karlson, A., Robertson, J., et al. (2014). "Design and installation of a tipping bucket snow lysimeter," in International Snow Science Workshop 2014 Proceedings, Banff, Canada (Montana State University Libraryskip navigation), 817–824. Available at: http://arc.lib.montana.edu/snow-science/item/2157.

Guzha, A. C., Rufino, M. C., Okoth, S., Jacobs, S., and Nóbrega, R. L. B. (2018). Impacts of land use and land cover change on surface runoff, discharge and low flows: evidence from East Africa. *J. Hydrol. Reg. Stud.* 15, 49–67. doi:10.1016/j.ejrh.2017.11.005

Hollis, G. E., and Ovenden, J. C. (1987). A tipping bucket flowmeter for roadside gully runoff. *Hydrol. Process.* 1, 391–396. doi:10.1002/hyp.3360010407

Iida, S., Shimizu, T., Kabeya, N., Nobuhiro, T., Tamai, K., Shimizu, A., et al. (2012). Calibration of tipping-bucket flow meters and rain gauges to measure gross rainfall, throughfall, and stemflow applied to data from a Japanese temperate coniferous forest and a Cambodian tropical deciduous forest. *Hydrol. Process.* 26, 2445–2454. doi:10.1002/hyp.9462

Iida, S., Shimizu, T., Shinohara, Y., Takeuchi, S., and Kumagai, T. (2020). *The necessity of sensor calibration for the precise measurement of water fluxes in forest ecosystems*. Cham: Springer, 29–54. doi:10.1007/978-3-030-26086-6_2

Jaleta, D., Mbilinyi, B. P., Mahoo, H. F., and Lemenih, M. (2017). Effect of Eucalyptus expansion on surface runoff in the central highlands of Ethiopia. *Ecol. Process.* 6, 1–8. doi:10.1186/s13717-017-0071-y

Johnston, C. N. (1942). Tilt buckets for measuring runoff and erosion. *Agric. Eng.* 23, 161–162.

Khan, A. A. H., and Ong, C. K. (1997). Design and calibration of tipping bucket system for field runoff and sediment quantification. *J. Soil Water Conserv.* 52, 437–443.

Kim, H. J., Sidle, R. C., and Moore, R. D. (2005). Shallow lateral flow from a forested hillslope: influence of antecedent wetness. *CATENA* 60, 293–306. doi:10.1016/J.CATENA.2004.12.005

Klik, A., Sokol, W., and Steindl, F. (2004). Automated erosion wheel: a new measuring device for field erosion plots. *J. Soil Water Conserv.* 59, 116–121.

Lamb, K. J., MacQuarrie, K. T. B., Butler, K. E., Danielescu, S., Mott, E., Grimmet, M., et al. (2019). Hydrogeophysical monitoring reveals primarily vertical movement of an applied tracer across a shallow, sloping low-permeability till interface: implications for agricultural nitrate transport. *J. Hydrol.* 573, 616–630. doi:10.1016/J.JHYDROL.2019.03.075

Langhans, C., Diels, J., Clymans, W., Van den Putte, A., and Govers, G. (2019). Scale effects of runoff generation under reduced and conventional tillage. *Catena* 176, 1–13. doi:10.1016/j.catena.2018.12.031

Molina-Sanchis, I., Lázaro, R., Arnau-Rosalén, E., and Calvo-Cases, A. (2016). Rainfall timing and runoff: the influence of the criterion for rain event separation. *J. Hydrol. Hydromechanics* 64, 226–236. doi:10.1515/johh-2016-0024

Nebol'sin, S. I. (1928). *Elementary surface runoff.* Moscow.

Nehls, T., Rim, Y. N., and Wessolek, G. (2011). Technical note on measuring run-off dynamics from pavements using a new device: the weighable tipping bucket. *Hydrol. Earth Syst. Sci.* 15, 1379–1386. doi:10.5194/hess-15-1379-2011

Perales-Momparler, S., Andrés-Doménech, I., Hernández-Crespo, C., Vallés-Morán, F., Martín, M., Escuder-Bueno, I., et al. (2017). The role of monitoring sustainable drainage systems for promoting transition towards regenerative urban built environments: a case study in the Valencian region, Spain. *J. Clean. Prod.* 163, S113–S124. doi:10.1016/J.JCLEPRO.2016.05.153

Peyrard, X., Liger, L., Guillemain, C., and Gouy, V. (2016). A trench study to assess transfer of pesticides in subsurface lateral flow for a soil with contrasting texture on a sloping vineyard in Beaujolais. *Environ. Sci. Pollut. Res.* 23, 14–22. doi:10.1007/s11356-015-4917-5

Pinson, W. T., Yoder, D. C., Buchanan, J. R., Wright, W. C., and Wilkerson, J. B. (2004). Design and evaluation of an improved flow divider for sampling runoff plots. *Appl. Eng. Agric.* 20, 433–438. doi:10.13031/2013.16489

Procházka, J., Pokorný, J., Vácha, A., Novotná, K., and Kobesová, M. (2019). Land cover effect on water discharge, matter losses and surface temperature: results of 20 years monitoring in the Šumava Mts. *Ecol. Eng.* 127, 220–234. doi:10.1016/j.ecoleng.2018.11.030

Ramos-Scharrón, C. E., and Thomaz, E. L. (2017). Runoff development and soil erosion in a wet tropical montane setting under coffee cultivation. *L. Degrad. Dev.* 28, 936–945. doi:10.1002/ldr.2567

Saraswat, C., Kumar, P., and Mishra, B. K. (2016). Assessment of stormwater runoff management practices and governance under climate change and urbanization: an analysis of Bangkok, Hanoi and Tokyo. *Environ. Sci. Policy* 64, 101–117. doi:10.1016/j.envsci.2016.06.018

Schwamback, D., Anache, J. A. A., and Wendland, E. C. (2022). Calibration and error investigation of large tipping bucket flow meters. *CATENA* 209, 105834. doi:10.1016/J.CATENA.2021.105834

Shedekar, V. S., King, K. W., Fausey, N. R., Soboyejo, A. B. O., Harmel, R. D., and Brown, L. C. (2016). Assessment of measurement errors and dynamic calibration methods for three different tipping bucket rain gauges. *Atmos. Res.* 178–179, 445–458. doi:10.1016/j.atmosres.2016.04.016

Shimizu, T., Kobayashi, M., Iida, S., and Levia, D. F. (2018). A generalized correction equation for large tipping-bucket flow meters for use in hydrological applications. *J. Hydrol.* 563, 1051–1056. doi:10.1016/j.jhydrol.2018.06.036

Shiraki, K., Dulnakij, K., Kunita, K., Negi, K., and Sun, J. (2019). Specification of modified handmade tipping buckets flow meters and their calibration system. *J. F. Sci.* 17, 23–32.

Somavilla, A., Gubiani, P. I., and Zwirtz, A. L. (2019). Tipping bucket prototype for automatic quantification of surface runoff rate in plots. *Rev. Bras. Cienc. do Solo* 43, 1–7. doi:10.1590/18069657rbcs20180096

Sun, T., Cruse, R. M., Chen, Q., Li, H., Song, C., and Zhang, X. (2014). Design and initial evaluation of a portable *in situ* runoff and sediment monitoring device. *J. Hydrol.* 519, 1141–1148. doi:10.1016/j.jhydrol.2014.08.048

Takahashi, M., Giambelluca, T. W., Mudd, R. G., DeLay, J. K., Nullet, M. A., and Asner, G. P. (2010). Rainfall partitioning and cloud water interception in native forest and invaded forest in Hawai'i Volcanoes National Park. *Hydrol. Process.* 25, 448–464. doi:10.1002/hyp.7797

Tarolli, P., and Straffelini, E. (2020). Agriculture in hilly and mountainous landscapes: threats, monitoring and sustainable management. *Geogr. Sustain* 1, 70–76. doi:10.1016/J.GEOSUS.2020.03.003

Tu, A., Xie, S., Yu, Z., Li, Y., and Nie, X. (2018). Long-term effect of soil and water conservation measures on runoff, sediment and their relationship in an orchard on sloping red soil of southern China. *PLoS One* 13, e0203669. doi:10.1371/journal.pone.0203669

Wang, S., Fu, Z., Chen, H., Nie, Y., and Xu, Q. (2020). Mechanisms of surface and subsurface runoff generation in subtropical soil-epikarst systems: implications of rainfall simulation experiments on karst slope. *J. Hydrol.* 580, 124370. doi:10.1016/J.JHYDROL.2019.124370

Whipkey, R. Z. (1965). Subsurface stormflow from forest slopes. *Hydrol. Sci. J.* 10, 74–85. doi:10.1080/02626666509493392

Yahaya, O., Olufayo, A. A., Akinro, A. O., and Mogaji Kehinde, O. (2009). Development and calibration of an automatic Runoff-meter. *J. Eng. Appl. Sci.* 4, 8–16.

Youlton, C., Wendland, E., Anache, J. A. A., Poblete-Echeverría, C., and Dabney, S. (2016). Changes in erosion and runoff due to replacement of pasture land with sugarcane crops. *Sustain* 8, 685–712. doi:10.3390/su8070685

Zabret, K., Rakovec, J., and Šraj, M. (2018). Influence of meteorological variables on rainfall partitioning for deciduous and coniferous tree species in urban area. *J. Hydrol.* 558, 29–41. doi:10.1016/J.JHYDROL.2018.01.025

Zhai, X., Zhang, Y., Zhang, Y., Guo, L., and Liu, R. (2021). Simulating flash flood hydrographs and behavior metrics across China: implications for flash flood management. *Sci. Total Environ.* 763, 142977. doi:10.1016/j.scitotenv.2020.142977

Zhang, W., Li, H., Pueppke, S. G., Diao, Y., Nie, X., Geng, J., et al. (2020). Nutrient loss is sensitive to land cover changes and slope gradients of agricultural hillsides: evidence from four contrasting pond systems in a hilly catchment. *Agric. Water Manag.* 237, 106165. doi:10.1016/J.AGWAT.2020.106165

frontiers | Frontiers in Environmental Science

TYPE Original Research
PUBLISHED 07 December 2023
DOI 10.3389/fenvs.2023.1324690

OPEN ACCESS

EDITED BY
Jing Liu,
University of Birmingham,
United Kingdom

REVIEWED BY
Xungui Li,
Guangxi University, China
Dongyong Sun,
Chang'an University, China

*CORRESPONDENCE
Fang Wan,
✉ wanxf1023@163.com

RECEIVED 20 October 2023
ACCEPTED 22 November 2023
PUBLISHED 07 December 2023

CITATION
Chai Q, Wan F, Zhang F, Wu F, Han W, Ding Z and Yang S (2023), Early warning analysis of mountain flood disaster based on Copula function risk combination. *Front. Environ. Sci.* 11:1324690.
doi: 10.3389/fenvs.2023.1324690

Early warning analysis of mountain flood disaster based on Copula function risk combination

Qihui Chai, Fang Wan*, Fei Zhang, Feng Wu, Wenhao Han,
Zelin Ding and Shifeng Yang

North China University of Water Resources and Electric Power, ZhengZhou, China

Mountain torrent disaster prevention is the focus of flood control and disaster reduction in China. Critical rainfall is an important indicator to determine the success or failure of mountain torrent disaster early warning. In this paper, the M-Copula function is introduced, the multi-dimensional joint distribution of critical rainfall is constructed, and the joint distribution of rainfall and peak rainfall intensity is analyzed. Taking A village in Xinxian County as an example. The critical rainfall of the combined probability is calculated, and the critical rainfall of the flash flood disaster water level, the pre-shift warning and the sharp-shift warning is warned and analyzed. The results show that the flood peak modulus calculated by Yishangfan group is 8.89, which has certain rules for the flood peak modulus of rivers in hilly areas. The larger the basin area is, the smaller the flood peak modulus is, the smaller the area is, and the larger the flood peak modulus is. The calculation result of the design flow of 533 m^3/s is reasonable. It is reasonable and reliable to select the M-Copula function as the connection function to fit the joint distribution of rainfall and peak rainfall intensity, which can provide theoretical support for flash flood disaster warning in other regions.

KEYWORDS

mountain flood disaster warning, critical rainfall, mixed Copula function, joint distribution, Xinxian county

Introduction

In recent years, due to the increasing impact of climate change and human activities, mountain flood disasters have become more and more frequent. Mountain flood disasters have become one of the main natural disasters in the world, causing a large number of casualties and social and economic losses (He et al., 2021; Ren Z. H. et al, 2023). In order to prevent mountain flood disasters and reduce disaster losses, timely and effective disaster warning is the key factor to determine the success or failure of mountain flood disaster prevention and control. Therefore, many experts and scholars have studied the early warning of mountain flood disasters. Europe has developed a flood warning system by coupling climate model and hydrological model, which can be combined with fine weather forecast to realize early flood warning (Park et al., 2019). Japan established the relationship between rainfall and surface runoff, and proposed a mountain flood warning method based on watershed rainfall index to achieve high-precision mountain flood warning (He, 2020). The underlying surface conditions and the mechanism of mountain flood disasters in China are complex, and the critical rainfall is the main influencing factor of mountain flood disasters. At present, the calculation methods of critical rainfall mainly include data-driven method and hydrological hydraulics method (Wang, 2021; Shen and Hao, 2022; Zhao, 2022). Han, J. T. et al. (2022) constructed a mountain flood disaster warning method based on the dynamic critical rainfall method, and obtained the critical flow and critical rainfall corresponding to the risk level. Wang, W. L. et al. (2022b) introduced the pattern recognition algorithm into the calculation of critical rainfall, and proposed a calculation method of critical rainfall based on Fisher discriminant algorithm. Based on the HEC-HMS model, Zhang, S. S. et al. (2019) selected the rainfall warning index, and comprehensively considered the factors such as soil water content and confluence time to reverse the critical rainfall.

Copula function has become the main means of probabilistic risk research (Li, 2020). Domestic and foreign scholars research on Copula function mainly focuses on univariate and bivariate perspectives. For example, Yang, et al. (2018) used the Palmer dry early index and Copula function to evaluate the risk of dry early in Northwest China, and identified the frequency of extreme drought and extreme wetness; Hui-Mean, et al. (2019) introduced the joint distribution of multivariate Copula functions to study the correlation and dependence between drought risk variables in the Malaysian Peninsula; Menna, et al. (2022) constructed the joint probability distribution of SPI and SSI based on Copula function to study the dry and early risk analysis of the basin. In the above research, the spatial scale of the research is mainly concentrated in large areas, but there is a lack of research on the local regional scale, and the joint distribution function is rarely related to its respective edge distribution function.

In general, the research results of critical rainfall are fruitful, but the critical rainfall and corresponding early warning analysis of several risk combinations are not considered. The random variables in the field of hydrological science often show various complex linear and nonlinear correlations. Therefore, the Copula function is introduced to describe the correlation between rainfall and peak rainfall intensity variables in this paper. The Copula function can connect the joint distribution function with its respective marginal distribution function, and can describe the nonlinear, asymmetric and symmetric correlation between variables, and it is widely used in hydrological science (Chen, 2022; Wan, 2022; Wang, 2022; Zheng, 2022).

Study area

Xinxian County is located in the Dabie Mountains in the southeastern part of Henan Province. It is located on the ridge line of the Yangtze River and Huaihe River basins and on the boundary between the northern subtropical and the northern warm temperate zones. It is a transitional zone between the summer monsoon and the subtropical high moving north and south. Frequent rainstorms, complex geological landforms, and the impact of human activities have led to frequent flash flood disasters. Mountain torrent disasters are widely distributed in the county and are characterised by fierce, fast flowing, destructive and sudden, and are difficult to forecast, predict and prevent. It not only causes devastating damage to the infrastructure of the hilly area, but also poses a great threat to the life safety of the people, and has become a prominent problem in the current disaster prevention and mitigation work. It is one of the important constraints on the sustainable economic and social development of the hilly area.

Xinxian County is a subtropical continental monsoon climate, a north-south climate transition zone, four distinct seasons, water and heat at the same time, ravines, rivers, rivers in the county can be summarised as “two major watersheds, six major water systems”. Among them, the Huaihe River Basin has four water systems: Huanghe River, Bailu River, Zhugan River, and Zhaihe River; there are two water systems in the Yangtze River Basin: Daoshui River and Jushui River. The average drop of the main rivers is 320 m, and the river gradient is generally above 0.3%, and the maximum is 3.3%. Large slope, short flow, fast confluence and narrow riverbed form the characteristics of fierce water potential and large difference in water volume change in Xinxian River.

The disaster-causing factors of mountain torrent disaster in Xinxian County have the dual attributes of natural geography and economic society. The general trend of the terrain in Xinxian County is high in the middle and low in the north and south. The mountains in the territory are towering, the mountains are stacked, and the streams are crisscrossed. Rainfall factor is the direct factor and excitation condition of mountain flood disaster. Rainfall is large, and high-intensity rainfall is one of the most important causes of flash flood disasters. Under the same conditions, the longer the rainfall duration, the greater the rainfall, the greater the runoff generated, and the more serious the loss of flash flood disasters. The law of mountain torrent disasters in Xinxian County has the following characteristics: the occurrence time is relatively concentrated, generally in June to September; affected by factors such as uneven spatial and temporal distribution of rainfall, high mountains and steep slopes, the rainstorm produces fast runoff, short confluence time, fierce water potential and great destructiveness. Mountain torrent geological disasters are prone to a wide range, sudden and difficult to monitor.

Data were collected from Resource and Environment Science and Data Center (https://www.resdc.cn/Default.aspx) and the National Meteorological Science and Data Center (http://data.cma.cn/).

Determination of critical rainfall of risk combination probability of mixed Copula function

Copula function distribution model

The Copula function can be used to describe the correlation between variables, which can connect the function of the joint distribution with its respective marginal distribution function (Song, 2023).The relationship between the variables in the hydrological system is complex and changeable, not confined to a specific relationship (Li, 2021). The commonly used Copula function can only reflect a certain aspect of the correlation between hydrological variables, so it is difficult to use a simple Copula function to fully describe the correlation between hydrological variables. Therefore, this paper selects the mixed Copula

(M-Copula) function to describe the correlation between variables in the hydrological system (Li, 2022).

The expression is:

$$\begin{cases} MC_3 = w_G C_G + w_F C_F + w_{Cl} C_{Cl} \\ w_G + w_F + w_{Cl} \geq 0 \\ w_G + w_F + w_{Cl} = 1 \end{cases} \tag{1}$$

where C_G, C_F, C_{cl} are Gumbel Copula, Frank Copula, Clayton Copula functions respectively; w_G, w_F, w_{cl} are the weight coefficients of the corresponding Copula functions.

Parameter estimation, test and evaluation of Copula model

In this paper, the maximum likelihood estimation is used to estimate the parameters. The density function of its joint distribution function is:

$$\begin{aligned} f(x_1, x_2, ..., x_N; \theta) &= c(F_1(x_1; \theta_1), F_2(x_2; \theta_2), ..., F_N(x_N; \theta_N); \theta_c)\prod_{n=1}^{N} f_n(x_n; \theta_n) \\ &= c(u_1, u_2, ..., u_N; \theta_c)\prod_{n=1}^{N} f_n(x_n; \theta_n) \end{aligned} \tag{2}$$

where θ_c is the $1 \times m_c$ dimensional parameter vector of the Copula function; $F_n(x_n; \theta_n)$ is the edge distribution function; θ_n is a $1 \times m_n$-dimension parameter vector of edge distribution function $F_n(x_n; \theta_n)$; $\theta = (\theta_1, \theta_2, ..., \theta_N, \theta_c)'$; $n = 1, 2, ..., N$.

The fitness evaluation of Copula function is calculated by using the minimum criterion of root mean square error RSME, its definition is as formula (3):

$$RSME = \sqrt{\frac{1}{N}\sum_{i=1}^{N}\left(p_c(i) - p_0(i)\right)^2} \tag{3}$$

where N is sample size; i is the sample serial number; p_c is the theoretical frequency calculated by the model; p_0 is the empirical frequency of joint distribution.

Critical rainfall determination for risk portfolio probabilities

Suppose that random variables X and Y obey the marginal distribution $FX(\mathrm{x})$ and $FY(\mathrm{y})$, respectively, and the joint distribution function is $F(x, y)$, where X is the total rainfall, and Y is the peak rainfall intensity, then there exists a Copula function:

$$P(\mathrm{x}, y) = P(X \leq \mathrm{x}, Y \leq y) = C(FX(x), FY(y)) \tag{4}$$

There are many coupling situations between the total rainfall and the peak rainfall intensity in the critical rainfall. The above joint probability distribution model can be used to calculate their joint distribution probability. This paper mainly considers the exceedance probability and conditional probability, that is, when the total rainfall exceeds a certain value, the conditional probability of the occurrence of the rainfall pattern when the peak rainfall intensity exceeds a certain value, as shown in Eq. 5.

$$\begin{aligned} FY|XA(\mathrm{X}, Y) &= P(Y \geq \mathrm{y} \mid X \geq XA) \\ &= \frac{1 - FY(y) - FX(xA) + F(XA, Y)}{1 - FX(xA)} \end{aligned} \tag{5}$$

In the formula, XA represents the total rainfall value with probability A; y represents a certain peak rainfall intensity value.

Therefore, the combination probability (A, B) of rain risk is defined as:

$$(A, B) = \left(P(X \geq XA), P(Y \geq \mathrm{y} \mid X \geq XA)\right) \tag{6}$$

In the early warning and forecast of mountain torrent disasters, the return period is usually used to describe the magnitude of rainstorm. For the exceeding probability, the calculation formula of return period is as follows.

$$T = \frac{1}{P(X \geq x)} = \frac{1}{1 - FX(x)} \tag{7}$$

Early warning analysis of mountain flood disaster based on critical rainfall in Xinxian County

Risk warning calculation of critical rainfall with combined probability

Considering the river valley shape, flood rise rate, early warning response time and site location of the disaster prevention object, the early warning indicators of ready transfer and immediate transfer are determined on the basis of critical rainfall. The early warning index is used to check and correct the rainstorm flood, so as to avoid the large difference between the disaster water level and the corresponding rainstorm flood frequency.

Under normal circumstances, since the critical rainfall is calculated from the flood corresponding to the water level, the critical rainfall is numerically considered to be the immediate transfer index. For the preparation transfer index, it is ’ reduced ’ according to the preparation transfer time and flood hydrograph on the basis of critical rainfall.

This paper takes a village in Xinxian County as an example. Under the condition of different soil moisture content, the critical rainfall of 1h, 3h, 6h and 24 h is calculated by using the risk probability rainfall pattern, and the critical rainfall warning threshold is shown in Table 1. Threshold map of water level warning is shown in Figure 1. Threshold maps for the preparation and immediate diversion of early warning rainfall is shown in Figure 2.

Rationality analysis of results

The flood peak modulus of rivers in hilly areas has certain rules. The larger the basin area, the smaller the flood peak modulus, the smaller the area, and the larger the flood peak modulus. Therefore, the rationality of the design flood peak flow can be indirectly evaluated according to the statistical data of the flood peak modulus of the hydrological section in the hilly

TABLE 1 Table of critical rainfall warning thresholds.

Soil water content	Time period (h)	Critical rainfall	
		Preparing transfer index (mm)	Immediate transfer index (mm)
0.2Wm	1	74	103
	3	112	154
	6	153	218
	24	251	367
	convergence time (5)	135	186
0.5Wm	1	58	86
	3	86	129
	6	115	179
	24	184	297
	convergence time (5)	104	155
0.8Wm	1	42	70
	3	63	105
	6	80	143
	24	124	234
	convergence time (5)	76	127

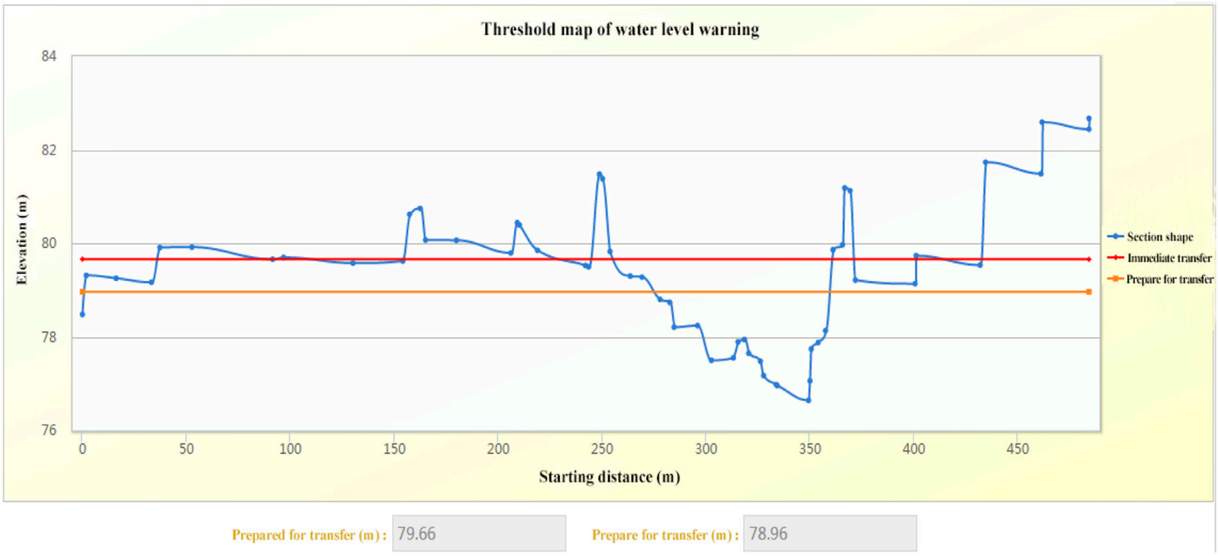

FIGURE 1
Threshold map of water level warning.

area of Henan Province. According to previous empirical data (Fan and Bao, 2022; Ren Z. H. et al, 2023), the flood peak modulus corresponding to the design flood peak flow of the small and medium-sized river section once in 50 years is generally about 10.0, and the majority is below 10.0. It can be seen from Table 2; Figure 3, the flood peak modulus calculated by Yishangfan group is 8.89, so the design flow calculation results are considered to be basically reasonable.

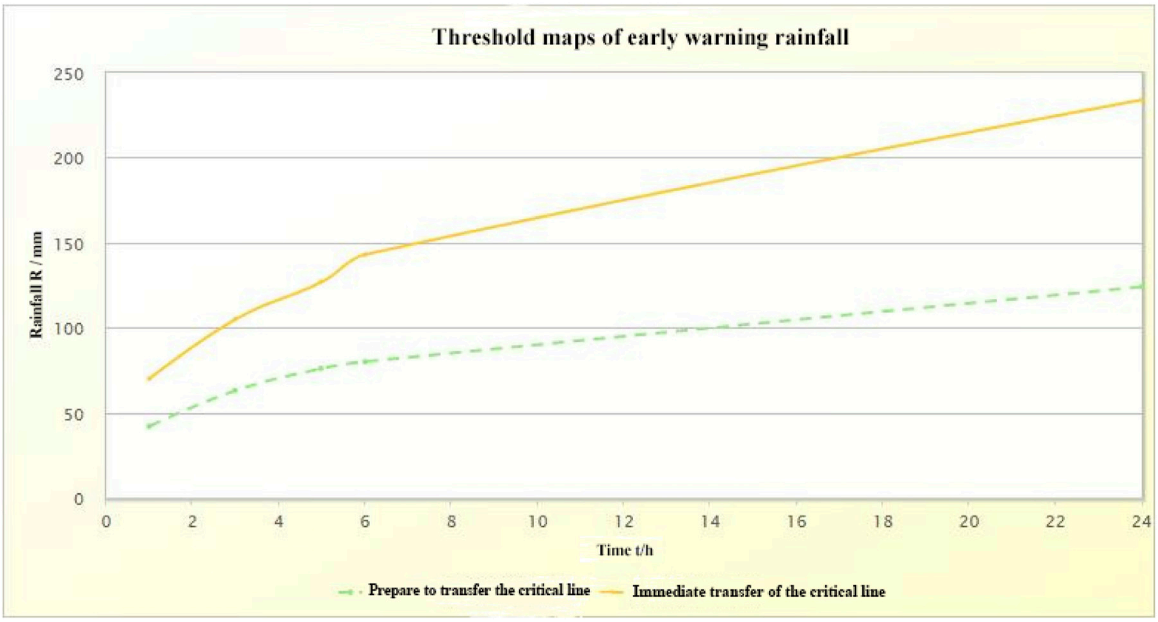

FIGURE 2
Threshold maps for the preparation and immediate diversion of early warning rainfall.

TABLE 2 Analysis on rationality of calculation results.

Name of administrative village	Control section coding	Watershed area (km^2)	Roughness factor	Q (m^3/s) p = 0.02 Pa = 0.5Wm	V (m/s)	Flood peak modulus
Yishangfan group	411523202223000X0002	137.093	0.024	533.00	2.96	8.89

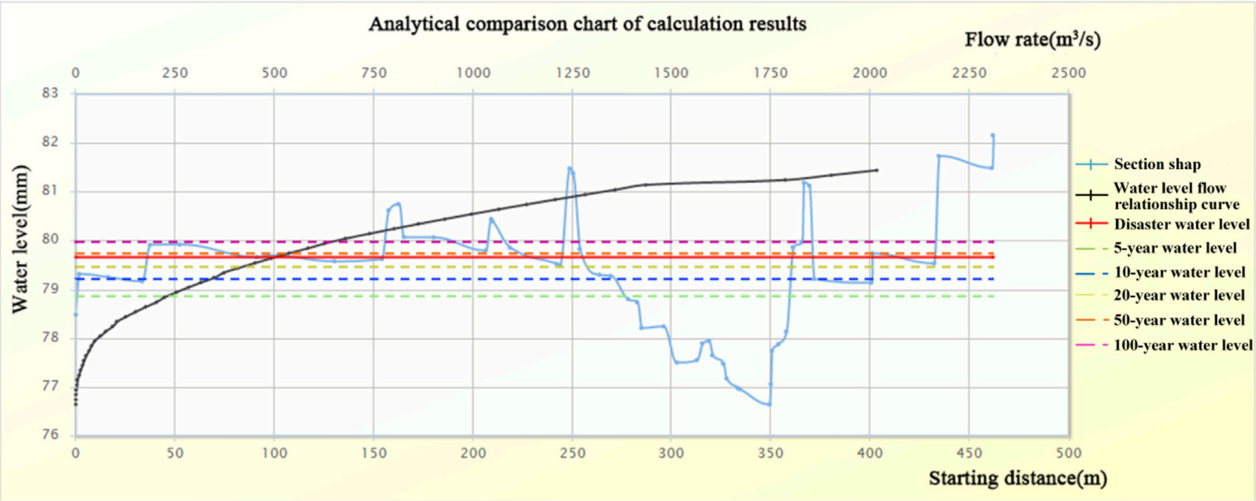

FIGURE 3
Comparison chart of water level at different stages.

Conclusion

The analysis of mountain flood warnings in the Xinxian County shows that the mixed Copula function can describe the correlation between variables in the hydrological system more flexibly. The Copula distribution function can well fit the correlation structure and distribution between the two-dimensional joint distribution function variables of total rainfall and peak rainfall intensity. According to the minimum criterion of root mean square error RSME, the M-Copula function is selected as the connection function to fit the joint distribution of critical rainfall. Based on the calculation and analysis of a village in Xinxian County, the critical rainfall of combined probability is calculated, and the critical rainfall of water level, preparation transfer warning and immediate transfer warning of mountain flood disaster is warned and analyzed. The results show that the flood peak modulus of rivers in hilly areas has certain rules. The larger the basin area is, the smaller the flood peak modulus is. The smaller the area is, the larger the flood peak modulus is. The calculation result of 533 m^3/s is reasonable. Therefore, the early warning analysis of mountain torrent disaster should ensure the safety of the people to the maximum extent. In the analysis and evaluation, the flood duration of villages along the river is taken as the basis, the response time and distribution of rainstorm flood warning in villages along the river are analyzed, which plays an important role in the preparation and early warning of mountain torrent disaster prevention and control plan.

Data availability statement

The data analyzed in this study is subject to the following licenses/restrictions: The data is confidential. Requests to access these datasets should be directed to https://www.resdc.cn/NewsInfo.aspx?NewsID=9.

Author contributions

QC: Writing–original draft. FaW: Writing–review and editing. FZ: Writing–review and editing. FeW: Writing–review and editing. WH: Writing–review and editing. ZD: Writing–review and editing. SY: Writing–review and editing.

Funding

The author(s) declare financial support was received for the research, authorship, and/or publication of this article. The research was supported by the National Key Research and Development Program of China (2022YFC3202300), Open Fund of Key Laboratory of Flood and Drought Disaster Defense, the Ministry of Water Resources (KYFB202307260036), Open Research Fund of Science and Technology Innovation Platform of Engineering Technology Research Center of Dongting Lake Flood Control and Water Resources Protection of Hunan Province, Hunan Water Resources and Hydropower Survey, Design, Planning and Research Co., Ltd. (HHPDI-KFKT-202304), Major Science and Technology Special Projects in Henan Province (201300311400), General Science Foundation Program of Henan Province (222300420491).

Conflict of interest

The authors declare that the research was conducted in the absence of any commercial or financial relationships that could be construed as a potential conflict of interest.

Publisher's note

References

Chen, Q., Li, G. F., and Bao, J. (2022). Analysis of encounter probability of rainstorm in jingdezhen city and flood of changjiang river based on copula function. *Water Resour. Power* 40 (12), 125–128+151. doi:10.20040/j.cnki.1000-7709

Fan, H. L., and Bao, S. (2022). Study on key hydrological problems in early warning of Mountain Flood disaster. *Haihe Water Resour.* (02), 93–96+111.

Han, J. T., Wang, Z. R., and Yang, Y. T. (2022). Flash flood grading and warning based on dynamic rainfall thresholds. *J. Hydroelectr. Eng.* 41 (09), 67–76.

He, B. S. (2020). Overview of flash flood early warning methods of Japan Meteorological Agency. *China Flood Drought Manag.* 30 (Z1), 149–152. doi:10.15961/j.jsuese.202000981

He, B. S., Ma, M. H., Li, Q., Liu, L., and Wang, X. H. (2021). Current situation and characteristics of flash flood prevention in China. *China Rural Water Hydropower* (5), 133–138.

Hui-Mean, F., Yusof, F., Yusop, Z., and Suhaila, J., Trivariate copula in drought analysis: acase study in peninsular Malaysia. *Theor. Appl. Climatol.*, 2019.138(1): 657–671. doi:10.1007/s00704-019-02847-3

Li, H. S. (2021). *Precipitation monitoring network optimization based on spatial information balancing model and integrated entropy-copula model*. Nanjing, China: Nanjing University. doi:10.27235/d.cnki.gnjiu.2021.000356

Li, H. W. (2022). *Assessment of meteorological drought risk in Xinjiang and its impact on agriculture and vegetation based on Copula method*. Beijing, China: North China Electric Power University. doi:10.27140/d.cnki.ghbbu.2022.000090

Menna, B. Y., Mesfin, H. S., Gebrekidan, A. G., Siyum, Z. G., and Tegene, M. T. (2022). Meteorological drought analysis using copula theory for the case of upper Tekeze river basin, Northern Ethiopia. *Theor. Appl. Climatol.* 149, 621–638. doi:10.1007/s00704-022-04061-0

Park, S., Berenguer, M., and Sempere-Torres, D. (2019). Long-term analysis of gauge-adjusted radar rainfall accumulations at European scale. *J. Hydrology* 573, 768–777. doi:10.1016/j.jhydrol.2019.03.093

Ren, Z. H., Sang, Y. F., Yang, M. Y., Wang, Y., and Shang, L. (2023a). Progress of research on the methods for the early warning of mountain flash flood disasters. *Prog. Geogr.* 42 (01), 185–196. doi:10.18306/dlkxjz.2023.01.015

Ren, Z. H., Sang, Y. F., Yang, M. Y., Wang, Y. L., and Shang, L. (2023b). Progress of research on the methods for the early warning of mountain flash flood disasters. *Prog. Geogr.* 42 (01), 185–196. doi:10.18306/dlkxjz.2023.01.015

Shen, W. B., and Hao, P. (2022). Calculation of critical rainfall of flash flood in small watershed based on rainfall pattern analysis. *Yellow River* 44 (01), 52–57.

Song, Y. X., Suo, M. Q., and Liu, L. P., Application of Copula function in the analysis of joint drought characteristics in the upper reaches of Zhanghe River. *Water Resour. Power*, 2023,41(10): doi:10.20040/j.cnki.1000-7709.2023.2022

Wan, F., Xiao, L. F., Chai, Q. H., and Li, L. (2022). Study on the streamflow compensation characteristics of reservoirs in Luanhe River Basin based on Copula function. *Water Supply* 22 (2), 2311–2321. doi:10.2166/ws.2021.380

Wang, F. Y., Zhang, Y., Wang, S., Ying, Q. L., and Yu, F. L. (2022b). Using copula model to analyze consecutive wetting-drying occurrence in rainfall-runoff in hanjiang basin. *J. Irrigation Drainage* 41 (08), 95–105. doi:10.13522/j.cnki.ggps.2021546

Wang, W. L., Sang, G. Q., Cao, F. J., and Liu, C. J. (2022a). Critical rainfall indicator calculation for Mountain Flood disasters based on Fisher discrimination algorithm. *J. China Hydrology* 42 (02), 1–6. doi:10.19797/j.cnki.1000-0852.20200219

Wang, X. K., Yang, P., Sun, T., and Xu, Z. X. (2021). Study on division early warning of flash flood disaster caused by rainstorm in mountainous small watersheds. *Adv. Eng. Sci.* 53 (1), 29–38.

Yang, P., Xia, J., Zhang, Y., Zhan, C., and Qiao, Y. (2018). Comprehensive assessment of drought risk inthe arid region of Northwest China based on the global palmer drought severityindex gridded data. *Sci. Total Environ.* 627, 951–962. doi:10.1016/j.scitotenv.2018.01.234

Zhang, S. S., Wang, J. T., and Xu, Z. H. (2019). Mountain flood rainfall early warning based on HEC-HMS model in small watershed. *China Rural Water Hydropower* (7), 40–44.

Zhao, L., Sang, G. Q., Wu, W., Liu, C. J., and Wang, J. N. (2022). Critical rainfall prediction model for Mountain Torrent disaster based on random forest regression algorithm. *J. Univ. Jinan* 36 (04), 404–411+423. doi:10.13349/j.cnki.jdxbn.20220325.001

Zheng, J., Liu, D. X., Lan, Y. J., and Liao, J. (2022). Research on the ecological flow of the qujiang river using the monthly frequency calculation method lmproved by the copula. *China Rural Water Hydropower* (08), 29–34.

frontiers | Frontiers in Environmental Science

TYPE Original Research
PUBLISHED 07 December 2023
DOI 10.3389/fenvs.2023.1310181

OPEN ACCESS

EDITED BY
Xudong Huang,
North China University of Water Conservancy and Electric Power, China

REVIEWED BY
Sheng Li,
Xinjiang University, China
Xue Yanye,
Jilin University, China
Guirong Hou,
Sichuan Agricultural University, China

*CORRESPONDENCE
Jianhua Ping,
✉ pingjianhua@zzu.edu.cn

RECEIVED 09 October 2023
ACCEPTED 23 November 2023
PUBLISHED 07 December 2023

CITATION
Zhang M, Ping J, Mei X, Leng W, Li H, Zhao J and Liu J (2023), The trend of groundwater recharge in the secondary perched reaches of the Yellow River in the past 50 years.
Front. Environ. Sci. 11:1310181.
doi: 10.3389/fenvs.2023.1310181

The trend of groundwater recharge in the secondary perched reaches of the Yellow River in the past 50 years

Min Zhang[1,2], Jianhua Ping[2,3]*, Xuemei Mei[2,3], Wei Leng[2,3], He Li[1,2], Jichang Zhao[4] and Jiaqi Liu[2,3]

[1]School of Water Conservancy and Transportation, Zhengzhou University, Zhengzhou, China, [2]Geothermal and Ecological Geology Research Center, Zhengzhou University, Zhengzhou, China, [3]College of Ecology and Environment, Zhengzhou University, Zhengzhou, China, [4]China Institute of Geo-Environmental Monitoring, Beijing, China

Precipitation infiltrates into the soil or river and then percolates downward through the deeper mineral soil to the groundwater. Understanding the interactions between surface water and groundwater in the river ecosystem is crucial for supporting decision-making in eco-construction and the efficient use of water resources. In our study, the secondary perched reach of the lower Yellow River was taken as the research area. The trend analysis and correlation relationship were evaluated using the M−K significance test and gray correlation; furthermore, the groundwater recharge was quantified by Darcy's law and the water balance method based on 50 years of hydrological data. The results showed that 1) from 1972 to 2020, the runoff and water level of the Huayuankou hydrological station and the Jiahetan hydrological station showed a significant downward trend. 2) The calculation of the gray correlation degree method shows that the groundwater level is mainly affected by the Yellow River. The river water and groundwater levels show a significant downward trend using the M−K significance test. 3) The unit width recharge values of the secondary perched river to the groundwater in the dry year were calculated to be 566.79 and 374.13 $m^3/m{\cdot}d$, using Darcy's law and the water balance method, respectively, indicating that the results of the two methods are basically the same. Our findings highlight the storage capacity of groundwater and can provide support for regulation and sustainable management of water resources in the ecosystem.

KEYWORDS

hydrological response, ecohydrological processes, ecosystem, hydrology, sustainable management practices

1 Introduction

As the second longest river in China, the Yellow River is known as the "mother river" of China because of its contribution to Chinese civilization. It is an important water supply source in arid and semi-arid areas of Northwest and North China (Yang et al., 2004). The Yellow River is crucial to the survival of the local residents and for sustainable economic development (Zhang et al., 2009; Xu et al., 2022). Since 1986, due to climate change and the intensification of human activities, especially due to the increase of agricultural irrigation along the Yellow River (Zhang et al., 2014), the runoff in the lower reaches of the Yellow River has decreased significantly, which has greatly affected the production, life, and ecological environment of the people along the riverbank.

In recent years, scholars have carried out a series of studies on the river runoff, water level, infiltration, sediment, topography, river morphology, and groundwater in the typical secondary perched reach of the lower Yellow River. Using meteorological data, combined with irrigation data, the long-term changes in the runoff of the Yellow River were studied in order to find out the causes of the Yellow River cutoff (Yang et al., 2004). The sustainability of the Yellow River water resources was analyzed by using the system dynamics method (Xu et al., 2002). The *in situ* measurement of the hydraulic conductivity of riverbed sediments was carried out by using the groundwater dynamics method, and the leakage of groundwater recharged by river water in the lower reaches of the Yellow River was calculated. Based on the principles of hydrogeology and environmental isotopes, the interaction between Yellow River water and groundwater in the secondary perched reach and its hydrochemical evolution law were studied (Acero et al., 2015; Li et al., 2022; Li et al., 2014; Wang et al., 2021). At the same time, the risk assessment and regulation of groundwater development in the secondary perched reach of the lower Yellow River were studied (Yan et al., 2023). The three-dimensional numerical simulation model was used to study the relationship between the secondary perched reach of the Yellow River (Henan section) and the regional groundwater recharge and discharge, and the average annual recharge resources of groundwater and the evaluation of exploitable resources were determined (Gu et al., 2013; Fu et al., 2020; Li et al., 2022).

In summary, most of the current studies focus on the evolution of the water–sediment relationship and analysis of water chemical characteristics of the Yellow River Basin, and the qualitative analysis of the Yellow River and the groundwater along the river. However, the quantitative research on the long-time series of the Yellow River water and the groundwater needs further study. Therefore, the recharge relationship between the secondary perched reach of the Yellow River and the groundwater is an urgent problem to be solved at present. This study mainly focuses on these problems for in-depth research and discussion.

2 Study area

The lower reaches of the Yellow River have formed the world-famous "The secondary perched reach of the Yellow River" due to its large amount of sediment deposition, and the Huayuankou–Jiahetan section is the most typical section of the Yellow River (Figure 1).

This research paper takes the secondary perched reach river of the Huayuankou–Jiahetan section of the Yellow River as the study area and studies the evolution characteristics of the secondary perched reach river water and groundwater dynamic field of the Yellow River in the past 50 years. The latitude and longitude of the study area are between 113°35′17″–114°48′29″N and 34°26′11″– 35°13′42″E, respectively. The length of the secondary perched reach river is 105 km, which is the largest area of groundwater recharge in the lower Yellow River (Figure 2).

The study area belongs to the alluvial plain in the lower reaches of the Yellow River. The terrain is flat, and the river runoff rate is slow. Moreover, 25% of the sediment carried by the river runoff is deposited here leading to the Yellow River riverbed being 3–10 m higher than the plain ground outside the river embankment. The highest riverbed is located in Liuyuankou, 8 km north of Kaifeng City, which is 7–8 m higher than the ground of Kaifeng City. The width of the river is 1,000 m, and the embankment is approximately 15 m high. The bottom of the riverbed is the fine sand and medium coarse sand layer of the Yellow River alluvial and is directly connected with the shallow aquifer group of the beach. The water level of the Yellow River (82–92 m (Huayuankou) and 71–75 m (Jiahetan)) is higher than the groundwater level on both sides (82–76 m; 92–77 m). It can be seen that the water level difference between them is 6–15 m, and the secondary perched reach river has become an important source of recharge for shallow groundwater along the riverbank. The aquifer has become the main mining layer supplying water for cities, industry, and agriculture along the Yellow River.

The study area belongs to the groundwater system of the alluvial plain in the lower reaches of the Yellow River. The landform belongs to the alluvial plain of the Yellow River. The groundwater mainly occurs in the Quaternary loose rock, with a total thickness of more than 300 m. The aquifers composed of Holocene (Q_4) and Late Pleistocene (Q_3) strata can be classified as shallow aquifer groups. The lithology is mostly sand, fine sand, and clay interbedded, and the bottom depth varies from 60 to 120 m. The deep aquifer group is composed of various types of sand layers and gravel layers in the early Pleistocene (Q_1) and middle Pleistocene (Q_2). The aquifer is up to 6–7 layers, forming a multi-structural micro-confined aquifer, with hydraulic connections in local areas. Between the shallow and deep aquifer groups, there is a weak permeable layer composed of a layer of more stable clay with a thickness of 20–30 m. The weak permeable layer makes the hydraulic connection between shallow

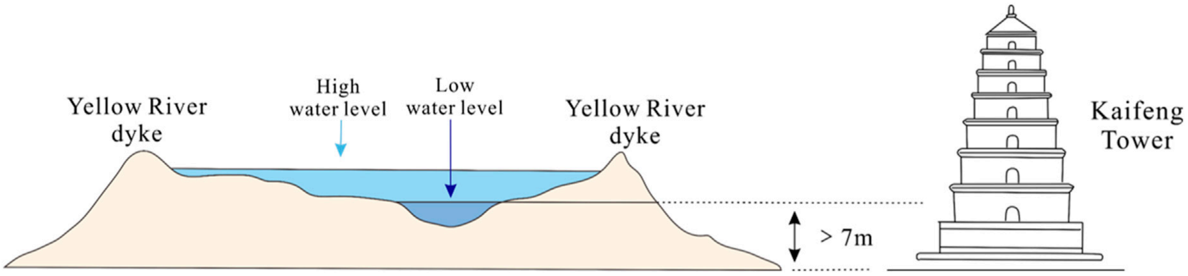

FIGURE 1
Schematic drawing of the secondary perched reach of the Yellow River.

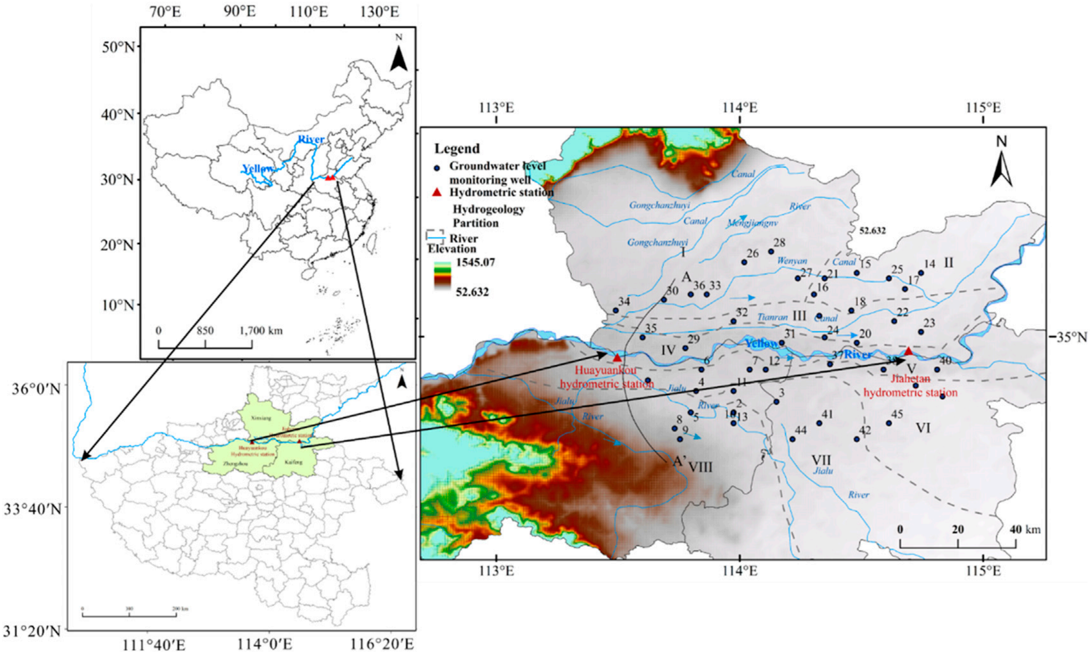

FIGURE 2
Geographical location of the Huayuankou–Jiahetan study area.

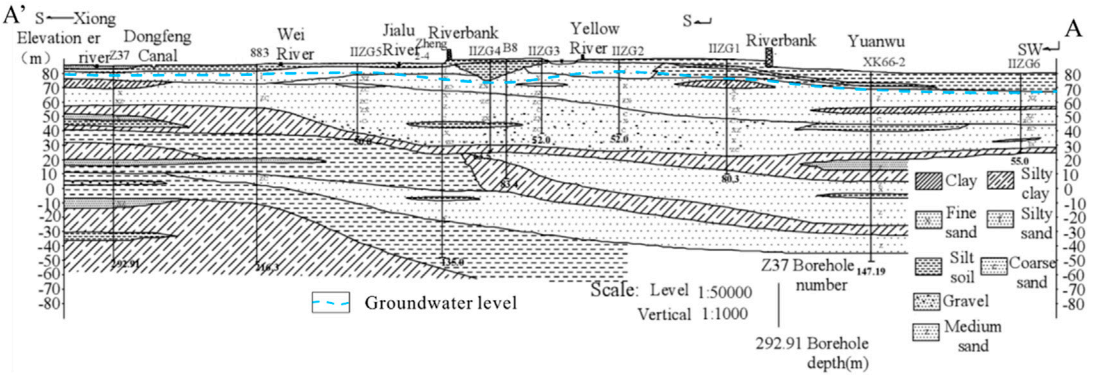

FIGURE 3
Hydrogeological profile of the study area.

and deep groundwater weak. According to the hydrogeological conditions of the study area, the study area is divided into eight hydrogeological zones. The study area is mainly to study the relationship between the secondary perched reach river and shallow groundwater (Figure 3).

3 Materials and methods

3.1 Materials

The water level and discharge data on the Huayuankou and Jiahetan hydrological stations in the lower reaches of the Yellow River from 1972 to 2020 were provided by the Yellow River website (http://www.yrcc.gov.cn/). The groundwater level data on groundwater monitoring wells in the study area from 1972 to 2020 are from the compilation of "Groundwater Data of Henan Province" by the Henan Provincial Hydrology and Water Resources Bureau (Table 1).

3.2 Methods

3.2.1 Hydrology statistics

The frequency analysis method in hydrological statistics was used to determine the wet years, normal years, and dry years of the

TABLE 1 Typical monitoring well water level elevation (m).

Monitoring well Time (year)	#6	#12	#20	#29	#31	#35	#37	#38
1972	83.51	78.19	72.06	85.02	78.92	87.21	76.38	72.26
1975	83.09	78.28	71.93	85.97	78.82	86.43	76.12	72.37
1980	81.94	77.54	72.03	85.46	78.87	87.04	76.18	71.86
1985	82.69	79.18	72.55	85.82	78.91	87.74	75.93	72.41
1990	82.65	78.00	71.81	86.08	78.48	87.30	76.73	71.19
1995	80.63	77.92	71.80	84.91	79.09	85.69	76.58	72.42
2000	81.46	77.23	71.39	84.92	78.62	86.05	76.30	70.71
2005	81.5	78.27	71.56	84.85	77.62	85.45	75.81	70.19
2010	80.43	77.62	71.12	80.01	76.36	84.12	75.40	70.83
2015	78.33	74.65	69.42	79.23	76.03	80.49	74.82	69.59
2020	76.27	72.91	68.09	78.23	75.5	78.90	74.87	67.38

secondary perched reach river of the Yellow River. When judging the significance of the secondary perched reach river and groundwater, the Pearson correlation coefficient was used for significance statistics.

3.2.2 Mann–Kendall trend test

In the series analysis of discharge and water level data, the Mann–Kendall trend test method was selected. The Mann–Kendall method is not affected by outliers and is more suitable for trend analysis of time series with outliers (Yue et al., 2002). The M–K non-linear statistical method can perform non-linear detection on time series variables. It has a powerful detection function and can eliminate the influence of non-linear changes in variables. It has been widely used in hydrological series trend and mutation analysis; compared with other methods, the M–K non-linear statistical method is more accurate in precipitation trend and mutation analysis (Cheng et al., 2019).

This method assumes that the time data sequence $(x_1, x_2, \ldots, x_n)$ is an independent and random sample sequence of the same variable distribution. The test statistical variable *S* and the standardized test statistics Z_{MK} are calculated as follows:

$$S = \sum_{i=1}^{n-1} \sum_{j=i+1}^{n} \operatorname{sgn}(X_j - X_i), \tag{1}$$

$$\operatorname{sgn}(X_j - X_i) = \begin{cases} +1 \text{ if } (X_j - X_i) > 0, \\ 0 \text{ if } (X_j - X_i) = 0, \\ -1 \text{ if } (X_j - X_i) < 0, \end{cases} \tag{2}$$

$$Var(S) = \frac{1}{18}\left[n(n-1)(2n+5) - \sum_{p=1}^{q} t_p (t_p - 1)(2t_p + 5) \right], \tag{3}$$

$$Z_{MK} = \begin{cases} \dfrac{S-1}{\sqrt{Var(S)}} & \text{if } S > 0, \\ 0 & S = 0, \\ \dfrac{S-1}{\sqrt{Var(S)}} & \text{if } S < 0. \end{cases} \tag{4}$$

In the formula, sgn is the sign function, n is the number of data in the sequence, q is the number of knots (repeated datasets) in the sequence, t_p is the width of the knot (the number of repeated data in the repeated dataset of group p), and Z_{MK} is the test statistic. The Z_{MK} statistic conforms to the normal distribution. At a given confidence level α, if it is the absolute value of *Z*, it means that the null hypothesis (no trend) is rejected. When the Z_{MK} statistic is greater than 1.65, 1.96, and 2.32, then the confidence level is 90%, 95%, and 99%, respectively, of the significance test, meaning that it becomes more significant the greater the trend.

3.2.3 Gray relational analysis

When analyzing the influencing factors of the groundwater level change along the river, the gray correlation method was used. Gray correlation analysis is a method of multi-factor statistical analysis (Deng et al., 1989). This paper calculated the correlation degree between the five influencing factors and the groundwater level of observation wells in the study area in order to determine the key factors affecting the change of groundwater level along the river. The five influencing factors are the river water level, runoff, precipitation, evaporation, and groundwater exploitation.

Gray correlation analysis calculation: first, select the reference sequence X_0 and the comparison sequence X_i. Second, perform dimensionless processing of the original data:

$$X_i(t) = x_i(t) / X_1(t). \tag{5}$$

In Eq. 5, $X_i(t)$ is the *i*th indicator dimensionless value in year t, $x_i(t)$ is the original data on the *i*th indicator in year t, and $X_i(1)$ is the *i*th indicator data in year 1. Third, calculate the absolute difference, the minimum difference, and the maximum difference between the reference sequence X_0 and the comparison sequence X_i:

$$\Delta i(t) = |X_0(t) - X_i(t)|. \tag{6}$$

In Eq. 6, $X_0(t)$ is the dimensionless value of the reference sequence in year t, $X_i(t)$ is the *i*th index data of the comparison sequence in year t. $\min\min|X_0(t) - X_i(t)|$ is a two-level minimum difference, where $\min|X_0(t) - X_i(t)|$ is the first-level minimum difference, which represents the minimum difference between X_i and X_0; $\min\min|X_0(t)-X_i(t)|$ is the second-level minimum difference, indicating that on the basis of the first-level minimum difference, the minimum difference of all factor sequences is found. $\max\max|X_0(t)-X_i(t)|$ is a two-level maximum difference, $\max|X_0(t)-X_i(t)|$ is the first-level maximum difference, which represents the maximum difference between X_i and X_0; $\max\max|X_0(t)-X_i(t)|$ is the second-level maximum difference, indicating that on the basis of the first-level maximum difference, the maximum difference of all factor sequences is found.

Fourth, find the gray correlation coefficient:

$$\varepsilon_i = \frac{\min\min|X_0(t)-X_i(t)| + \rho\max\max|X_0(t)-X_i(t)|}{|X_0(t)-X_i(t)| + \rho\max\max|X_0(t)-X_i(t)|}. \qquad (7)$$

In Equation 7, ρ is the coefficient of resolution, $\rho = [0, 1]$, according to the experience in general $\rho = 0.5$.

Fifth, calculate the correlation degree. The correlation r_i is obtained by adding and averaging the correlation coefficients of the comparison sequence X_i and the reference sequence X_0. n represents the number of influencing factors. The calculation formula is as follows:

$$r_i = \frac{1}{n}\sum_{i=1}^{n}\varepsilon_i(t). \qquad (8)$$

3.2.4 Darcy's law

Darcy's law is the theoretical basis of groundwater seepage calculation (Vincent et al., 2014). The formula for calculating the single-width infiltration volume of groundwater recharged by the infiltration of the secondary perched reach river is as follows:

$$q = K \cdot h \cdot J \qquad (9)$$

$$J = \Delta H/L. \qquad (10)$$

In the formula, q is the unit width exchange capacity of groundwater and surface water, $m^3/(d\cdot m)$, K is the comprehensive permeability coefficient of the riverbed sediment and aquifer, m/d; h is the average thickness of the phreatic aquifer, m; J is the hydraulic gradient between surface water and groundwater, dimensionless; ΔH is the water level difference between surface water and groundwater, m; and L is the distance between the river and the groundwater monitoring well, m.

3.2.5 Water balance method

When the water level of the studied river (canal) section is higher than the groundwater level on both sides of the river, the recharge effect of the leakage of river (canal) water on the underground aquifer can be obtained by this method. The following formula is used to calculate the infiltration recharge amount of the river using the water balance method:

$$S_{infiltration} = S_{upstream} + S_{precipitation} - S_{downstream} - S_{diversion} - S_{evaporation}. \qquad (11)$$

In the formula, $S_{infiltration}$ is the river water infiltration ($m^3/m\cdot d$); $S_{upstream}$ is the upstream river water ($m^3/m\cdot d$); $S_{precipitation}$ is atmospheric precipitation ($m^3/m\cdot d$); $S_{downstream}$ is the downstream river water ($m^3/m\cdot d$); $S_{diversion}$ is the amount of water from the Yellow River ($m^3/m\cdot d$); and $S_{evaporation}$ is the evaporation of river water ($m^3/m\cdot d$).

4 Results

4.1 Variation characteristics of the river discharge and level

4.1.1 Variation characteristics of the river discharge

The discharge of the Huayuankou and Jiahetan hydrological stations showed a downward trend in the past 50 years, and the trend was significant (Figure 4A). The M–K statistical values of the discharge at the Huayuankou and Jiahetan hydrological stations are −2.656 and −2.433, respectively. They passed the significance test with an M–K confidence of 95% (Table 2).

From 1974 to 1976, the discharge showed an increasing trend. During this period, the increase in discharge of the Huayuankou hydrological station was 93.14%, and the increase in that of the Jiahetan hydrological station was 83.82%. These increases were due to the "75·8 Flood" in Henan in 1975, which led to a significant increase in the discharge. From 1976 to 2001, the increase and decrease of river discharge fluctuated greatly. In the 25 years from 1972 to 1996, there were 19 years of river stem cutoff, with an average of three times in 4 years. From 2002 to 2020, the overall discharge showed a significant upward trend, and the change tended to be stable. The Xiaolangdi Reservoir officially operated water and sediment regulation so that the discharge of the Yellow River channel tended to be stable.

4.1.2 Variation characteristics of the water level

The annual water level data on hydrological stations from 1972 to 2020 were statistically analyzed, and the M–K trend change analysis and mutation characteristics were analyzed (Table 3). The water level of the Huayuankou and Jiahetan hydrological stations showed a significant downward trend in the past 50 years (Figure 4B). The M–K statistical values of the water level of the Huayuankou and Jiahetan hydrological stations are −4.065 and −2.879, respectively. They passed the significance test of the M–K confidence level of 95%.

From 1972 to 1989, the water level of the Yellow River at the Huayuankou hydrological station had a certain downward trend. From 1990 to 1999, the water level showed an upward trend, and it was significant. The water level showed a significant downward trend from 2000 to 2020 (Table 3).

4.2 Change in the groundwater level and its influencing factors

4.2.1 Changes in the groundwater level along the Yellow River

For nearly 50 years from 1972 to 2020, the groundwater level in the lower reaches of the Yellow River formed a flow field with the Yellow River as the watershed, which gradually decreased to the north and south, and the groundwater level gradually decreased from the west to the east along the Yellow River. The groundwater level of the monitoring wells along the secondary perched reach river was mostly in the range of −10 ~ 0 m, and the groundwater levels of only a few monitoring wells were in the range of −5 ~ 0 m. The groundwater level of wells far away from the riverbank gradually dropped, by up to −20~−10 m. With the increase in distance, the

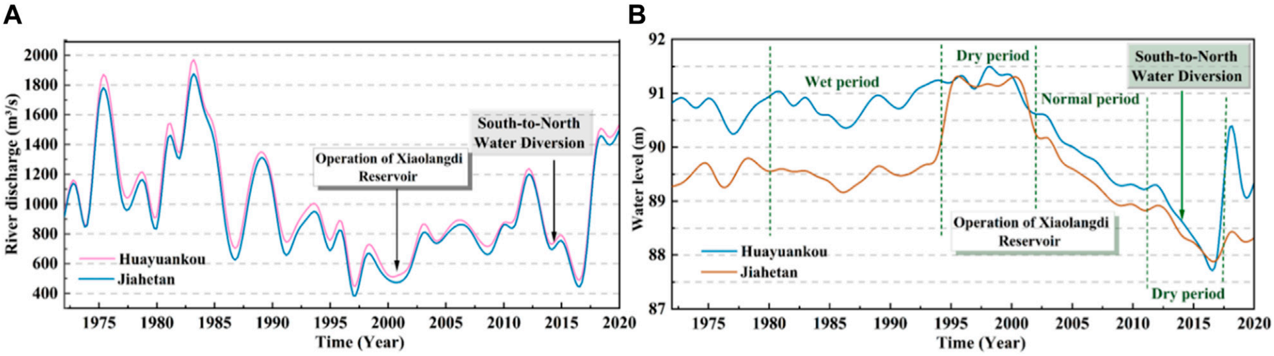

FIGURE 4
Years of discharge and water level changes at the Huayuankou and Jiahetan hydrological stations. **(A)** River discharge changes and **(B)** water-level changes.

TABLE 2 M–K trend analysis Z_{MK} statistical value of the river runoff from 1972 to 2020.

Hydrologic station	Annual variation (year)	Interdecadal variation (year)				
	1972–2020	1972–1979	1980–1989	1990–1999	2000–2009	2010–2020
Huayuankou	−2.656	0.495	−0.805	−2.057	1.34	1.01
Jiahetan	−2.433	0.741	−0.982	−1.88	1.34	0.856

TABLE 3 Z_{MK} statistical value of the river water level from 1972 to 2020.

Hydrologic station	Annual variation (year)	Interdecadal variation (year)				
	1972–2020	1972–1979	1980–1989	1990–1999	2000–2009	2010–2020
Huayuankou	−4.065	−1.237	−1.34	2.773	−4.025	0.39
Jiahetan	−2.879	1.978	−1.163	3.131	−4.025	−2.415

recharge of the Yellow River to groundwater gradually weakened and the groundwater level decreased greatly (Figure 5). Affected by the riverside water source, the groundwater level in some areas dropped deeper. For example, the shallow groundwater level in the water source area of Zhengzhou City on the south bank of the secondary perched reach river was 15 m deep, and its total funnel area was 358 km^2. The shallow groundwater level was 8 m deep in the riverside water source area of Yuanyang County on the north bank of the secondary perched reach river. The shallow groundwater depth in Kaifeng City, located on the south bank of the secondary perched reach river, was 10 m.

On both sides of the Yellow River, eight monitoring wells with a uniform distance and close to the river were selected as typical monitoring wells. Based on the annual groundwater level data on typical monitoring wells (# 35, # 29, # 31, # 20, # 6, # 12, # 37, and # 38) along the secondary perched reach river in 1972–2020, the trend of M–K change was analyzed. This information can be seen in Table 3. The Z_{MK} values of the M–K trend test results of each typical monitoring well were negative, indicating that the groundwater level of each monitoring well showed a downward trend, and it was significant (Table 4).

The groundwater levels of typical monitoring wells along the riverbank from 1972 to 2020 were statistically analyzed. The monitoring wells #35, #29, and #20 tended to be stable before 2010 and showed a significant downward trend after 2010. The changing trend in the water level of the #31 monitoring well was not obvious. The changes in wells #6, #12, and #38 tended to be stable before 2010 and showed a significant downward trend after 2010. The changing trend of the water level of the #37 monitoring well was not obvious (Figure 6).

4.2.2 Influencing factors of the groundwater level change

According to the recharge, runoff, and excretion characteristics of the groundwater flow field in the study area, the groundwater level of the observation well was taken as the reference sequence. The river discharge, river level, precipitation, evaporation, and groundwater exploitation were taken as the comparison sequence. The gray correlation degree between each factor and the groundwater level was calculated (Figure 7). Based on the correlation degree of each influencing factor, each

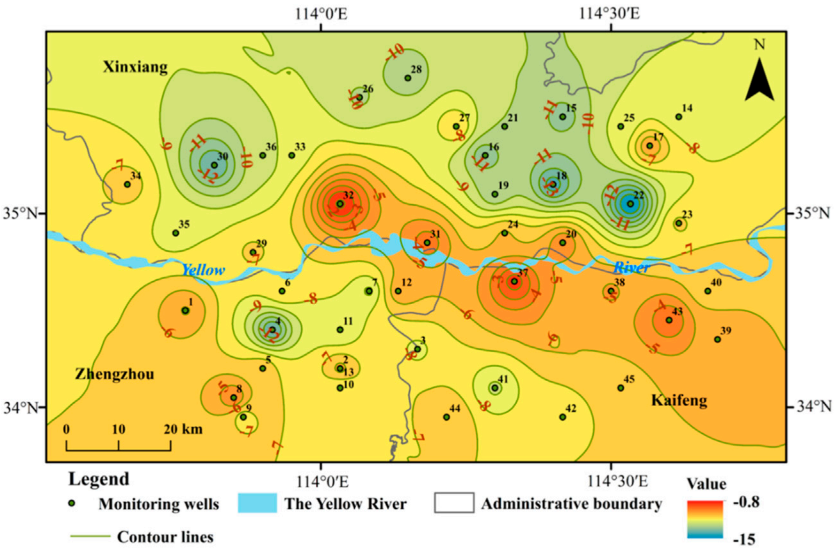

FIGURE 5
Spatial distribution of the groundwater level change.

TABLE 4 Z_{MK} statistical value of the groundwater level in typical monitoring wells from 1972 to 2020.

Monitoring well Statistic value	#35	#29	#31	#20	#6	#12	#37	#38
Z_{MK}	−7.238	−6.194	−5.272	−6.792	−7.745	−4.968	−4.603	−5.616
Trend	Decrease	Decrease	Decrease	Decrease	Decrease	Decrease	Decrease	Decrease
Significance	Obvious	Obvious	Obvious	Obvious	Obvious	Obvious	Obvious	Obvious

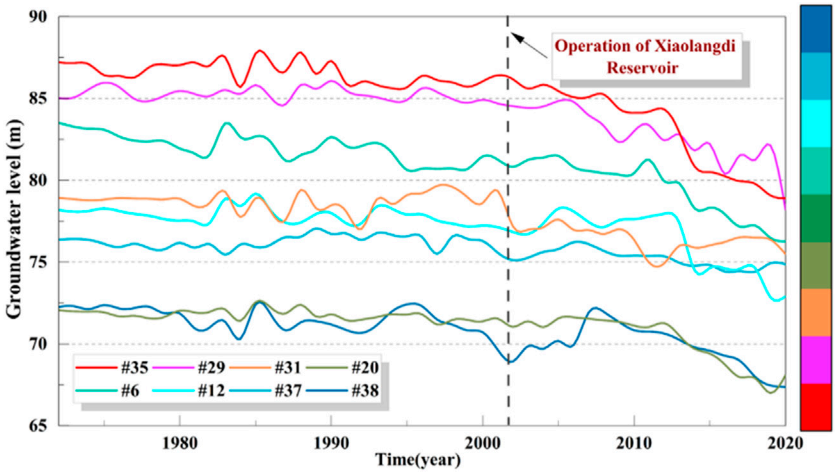

FIGURE 6
Groundwater level changes year by year of a typical monitoring well.

observation well was divided into five categories, namely, affected by the secondary perched reach river discharge, water level, precipitation, evaporation, and groundwater exploitation. The groundwater level of the monitoring well was greatly affected by the water level and discharge of the secondary perched reach river (the influence factor was greater than 0.65).

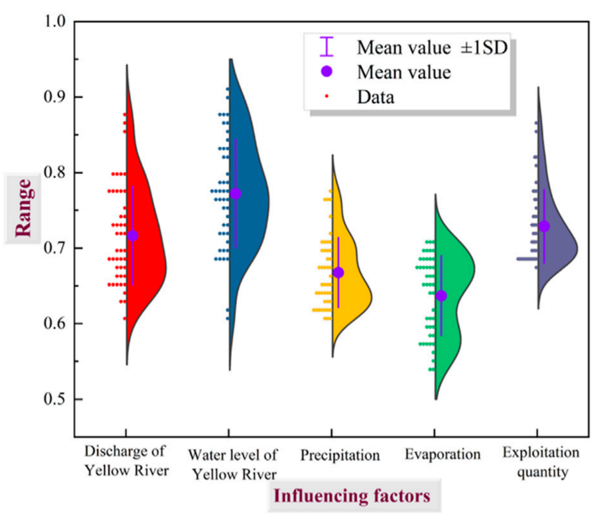

FIGURE 7
Statistics of influencing factors of the groundwater level.

4.3 Recharge of the secondary perched reach of the Yellow River to groundwater in different hydrological years

4.3.1 Characteristics of the Yellow River water runoff and groundwater level along the river

The linear correlation significance test was carried out on the Yellow River water runoff and the groundwater level at the Huayuankou and Jiahetan hydrological stations. When the significance test coefficient $p < 0.05$, it indicated that the significance test of 0.05 was passed. Most of the Yellow River water runoff and groundwater level at the Huayuankou and Jiahetan hydrological stations passed the 0.05 significance test, indicating that the Yellow River water runoff was significantly correlated with the groundwater level along the riverbank (Table 5).

Pearson's correlation coefficient (Pearson), commonly used to determine the linear correlation, was used to measure the correlation between two variables. Through the long sequence of the groundwater and river levels, the Pearson correlation coefficient between them could be calculated, and the correlation between them could be quantitatively analyzed. The correlation coefficient had the following relationship: $|r| < 0.3$, weak correlation; $0.3 < |r| < 0.5$, low correlation; $0.5 < |r| < 0.8$, significant correlation; and $0.8 < |r| < 1$, highly correlated.

The secondary perched reach river has a lag in the recharge of groundwater along the river. The river water discharge groundwater was divided into the current month, 1-month lag, 2-month lag, and 3-month lag. The correlation and lag between the river runoff and groundwater level are discussed.

The results of correlation and hysteresis between the river runoff and groundwater at the Huayuankou hydrological station indicated that the river runoff has a lag effect on the recharge of groundwater. Because the runoff in January, September, October, November, and December is significantly correlated with groundwater lagging in 1, 2, and 3 months (Table 7).

The correlation and lag between the river runoff and groundwater in the Jiahetan hydrological station were calculated. The results showed that the runoff in June and August is significantly correlated with groundwater lagging for 1, 2, and 3 months (Table 6), indicating that the river runoff has a lag effect on the recharge of groundwater.

4.3.2 Influence of the secondary perched reach of the Yellow River water level on the groundwater level

The significant test of the river water and groundwater levels at the Huayuankou and Jiahetan hydrological stations showed that most of the river water level and groundwater at the two hydrological stations passed the 0.05 significant test, indicating that the river water level is related to the groundwater level (Table 7).

The river water level at the Huayuankou hydrological station is significantly correlated with the groundwater level at the lag of 1, 2, and 3 months, indicating that the river water level has a lag in the replenishment of the groundwater level (Table 8).

The calculation results of the correlation and hysteresis between the river water level and groundwater at the Jiahetan hydrological station showed that the lag of the river water level to the discharge of groundwater is not strong.

TABLE 5 Significant test of the Yellow River water discharge and groundwater level at the two hydrological stations.

Hydrological station	Month Lag month	1	2	3	4	5	6	7	8	9	10	11	12
Huayuankou	Current month	0.01	0.46	0.34	0.29	0.70	0.01	0.43	0.01	0.00	0.00	0.00	0.00
	Lag 1 month	0.00	0.79	0.65	0.21	0.43	0.00	0.61	0.01	0.00	0.01	0.00	0.03
	Lag 2 months	0.01	0.54	0.65	0.47	0.39	0.01	0.67	0.02	0.00	0.00	0.01	0.11
	Lag 3 months	0.02	0.66	0.48	0.53	0.36	0.01	0.88	0.02	0.00	0.01	0.04	0.00
Jiahetan	Current month	0.09	0.96	0.83	0.11	0.28	0.00	0.87	0.01	0.00	0.04	0.00	0.05
	Lag 1 month	0.05	0.77	0.89	0.17	0.47	0.01	0.91	0.00	0.00	0.03	0.01	0.30
	Lag 2 months	0.04	0.86	0.98	0.22	0.40	0.00	0.84	0.00	0.00	0.09	0.02	0.31
	Lag 3 months	0.14	0.96	0.86	0.18	0.38	0.00	0.57	0.00	0.00	0.11	0.01	0.24

TABLE 6 Yellow River discharge and groundwater level lag at the two hydrological stations.

Hydrological station	Month Lag month	1	2	3	4	5	6	7	8	9	10	11	12
Huayuankou	Current month	0.35	0.11	0.14	−0.16	0.06	−0.38	0.12	0.38	0.52	0.47	0.41	0.43
	Lag 1 month	0.44	0.04	0.07	−0.18	0.12	−0.43	0.08	0.38	0.49	0.37	0.49	0.31
	Lag 2 months	0.36	0.09	0.07	−0.11	0.13	−0.39	0.06	0.34	0.43	0.43	0.38	0.23
	Lag 3 months	0.33	0.06	0.10	−0.09	0.13	−0.36	0.02	0.33	0.43	0.39	0.30	0.40
Jiahetan	Current month	0.24	−0.01	−0.03	−0.23	−0.16	−0.43	−0.02	0.38	0.42	0.29	0.45	0.28
	Lag 1 month	0.29	0.04	−0.02	−0.20	−0.10	−0.39	0.02	0.41	0.50	0.30	0.39	0.15
	Lag 2 months	0.30	0.03	0.00	−0.18	−0.12	−0.40	−0.03	0.48	0.48	0.24	0.32	0.15
	Lag 3 months	0.21	0.01	0.03	−0.19	−0.13	−0.40	0.08	0.46	0.44	0.23	0.36	0.17

TABLE 7 Significant test of the Yellow River water and groundwater levels at the two hydrological stations.

Hydrological station	Month Lag month	1	2	3	4	5	6	7	8	9	10	11	12
Huayuankou	Current month	0.00	0.00	0.00	0.02	0.01	0.01	0.00	0.00	0.00	0.00	0.00	0.00
	Lag 1 month	0.00	0.00	0.01	0.00	0.00	0.02	0.00	0.00	0.00	0.00	0.00	0.00
	Lag 2 months	0.00	0.01	0.00	0.00	0.00	0.01	0.00	0.00	0.00	0.00	0.00	0.00
	Lag 3 months	0.00	0.00	0.00	0.00	0.00	0.02	0.00	0.00	0.00	0.00	0.00	0.00
Jiahetan	Current month	0.03	0.04	0.11	0.17	0.26	0.39	0.25	0.04	0.01	0.01	0.01	0.05
	Lag 1 month	0.03	0.03	0.11	0.28	0.23	0.52	0.13	0.03	0.01	0.01	0.01	0.04
	Lag 2 months	0.02	0.03	0.18	0.24	0.28	0.35	0.14	0.02	0.01	0.02	0.01	0.06
	Lag 3 months	0.03	0.07	0.16	0.30	0.18	0.27	0.07	0.04	0.01	0.01	0.02	0.05

TABLE 8 River water level and the groundwater level lag of the two hydrological stations.

Hydrological station	Month Lag month	1	2	3	4	5	6	7	8	9	10	11	12
Huayuankou	Current month	0.46	0.45	0.46	0.35	0.39	0.36	0.51	0.49	0.51	0.58	0.51	0.46
	Lag 1 month	0.50	0.46	0.37	0.41	0.48	0.35	0.51	0.50	0.46	0.58	0.50	0.42
	Lag 2 months	0.51	0.38	0.43	0.48	0.49	0.35	0.49	0.46	0.58	0.58	0.41	0.41
	Lag 3 months	0.41	0.45	0.49	0.51	0.49	0.34	0.42	0.48	0.44	0.49	0.42	0.51
Jiahetan	Current month	0.31	0.29	0.23	0.20	0.17	0.13	0.17	0.30	0.37	0.37	0.36	0.29
	Lag 1 month	0.32	0.31	0.23	0.16	0.18	0.09	0.22	0.31	0.38	0.35	0.35	0.29
	Lag 2 months	0.33	0.30	0.20	0.17	0.16	0.14	0.21	0.34	0.35	0.34	0.35	0.28
	Lag 3 months	0.31	0.26	0.20	0.15	0.20	0.16	0.26	0.30	0.35	0.36	0.34	0.28

The correlation between the discharge and water level of the Yellow River at the Huayuankou hydrological station and the water level of the groundwater observation well is higher than that of the Yellow River at the Jiahetan hydrological station. The discharge and water level of the Yellow River at the Huayuankou hydrological station has a greater impact on the water level of the groundwater observation well in the secondary perched reach of the lower Yellow River.

4.3.3 Secondary perched reach of Yellow River recharges groundwater in different hydrological years

The wet year, normal year, and dry year were divided by the guarantee rate. The discharge series generally obeys the probability distribution of P_III (Pearson type III). The frequency analysis method was used to determine the

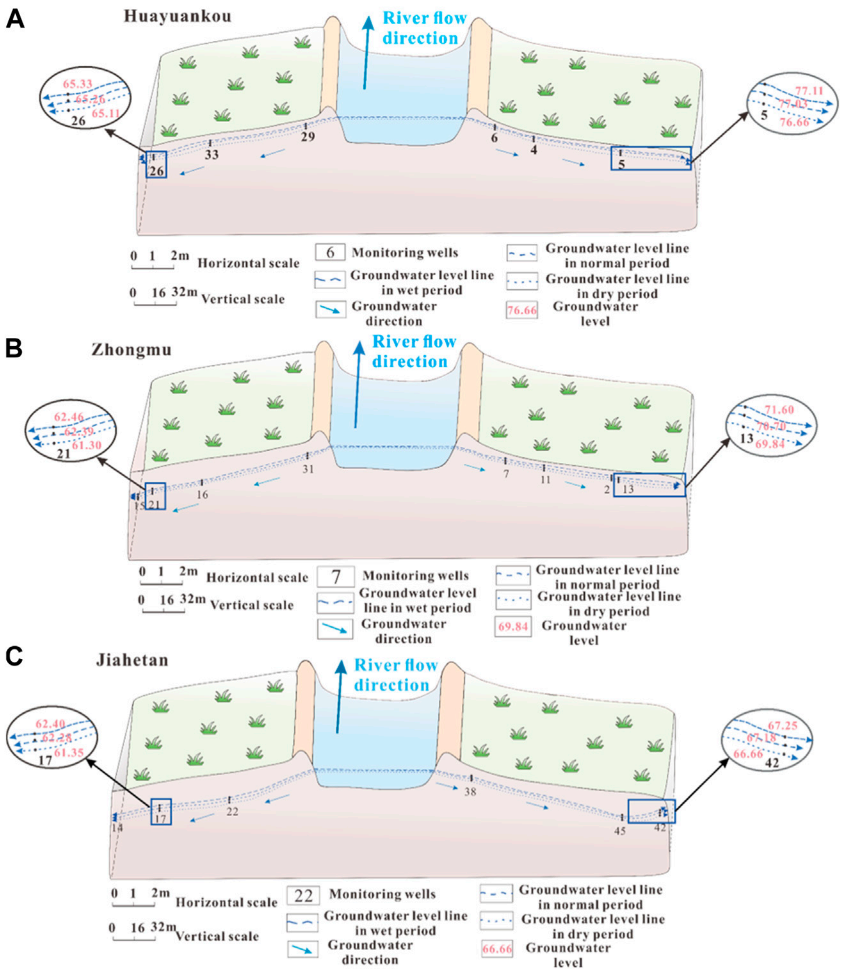

FIGURE 8
Groundwater recharge along the river in different hydrological years. **(A)** Huayuankou section, **(B)** Zhongmu section, **(C)** and Jiahetan section.

statistical parameters and the design values of each frequency, which was used as the standard for dividing the water level runoff series. When the guarantee rate $p \leq 37.5\%$, it was considered a wet year; when $37.5\% < p \leq 62.5\%$, it was deemed a normal year; and when $p>62.5\%$, it was considered a dry year.

The number of occurrences in the wet year accounted for 36.7% of the total series, the number of occurrences in the normal year accounted for 26.6% of the total series, and the number of occurrences in the dry year accounted for 36.7%. The percentage of the three periods was mainly balanced throughout the three periods. It was considered that the representativeness of the series, namely, the division of wet, normal, and dry years, was appropriate and able to reflect the objective law. According to the classification criteria of wet, normal, and dry years, the runoff was divided into four distinct periods: 1980–1994 was categorized as the wet year period, 1995–2002 was the dry year period, 2003–2011 was the normal year period, and 2012–2020 was another dry year period. According to the different wet, normal, and dry years of the secondary perched reach river and the different periods of the three sections of Huayuankou, Zhongmu, and Jiahetan, the recharge of the secondary perched reach river to the groundwater showed that when the river recharged the groundwater in the wet year of the Huayuankou section, Zhongmu section, and Jiahetan section, the groundwater level was higher than that in the normal year and the dry year. The water level of the Huayuankou hydrological station was 91.07 m in the wet year, 90.63 m in the normal year, and 89.30 m in the dry year. The water level of the Jiahetan hydrological station was 74.48 m in the wet year, 73.60 m in the normal year, and 72.53 m in the dry year. The groundwater level of the Zhongmu section was 72.35 m in the wet year, 71.86 m in the normal year, and 70.68 m in the dry year (Figure 8).

4.3.4 Seepage of the secondary perched reach river was calculated by the analytical method

By using the analytical method, the amount of groundwater recharged by the secondary perched reach river infiltration was calculated by formula (9) and formula (10). From 1972 to 2020, the annual average unit width recharge of groundwater along the secondary perched reach river recharge (south bank) was 462.18 $m^3/m{\cdot}d$. The annual recharge in wet years was 566.79 $m^3/m{\cdot}d$, in normal years it was 439.25 $m^3/m{\cdot}d$, and in dry years it was 374.13 $m^3/m{\cdot}d$ (Figure 9).

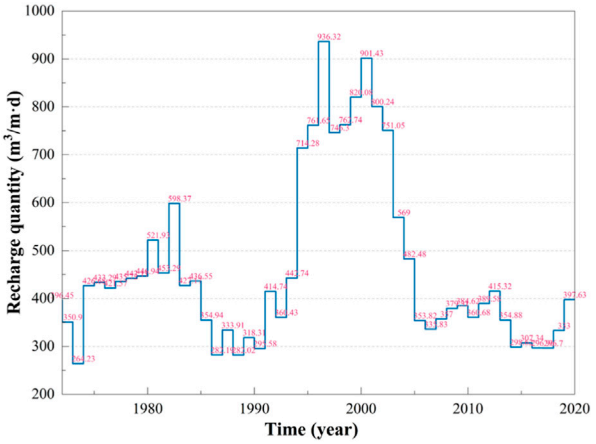

FIGURE 9
Amount of groundwater recharge by infiltration of the secondary perched reach.

4.3.5 Water balance method to calculate the amount of groundwater recharge by the secondary perched reach of the Yellow River

The Huayuankou hydrological station of the Yellow River is 105 km away from the Jiahetan hydrological station. The water consumption balance method was calculated by Eq. 11. The interval loss was 240 million m^3, and the unit length loss was 649.65 m^3/m d. Due to the differences in lithology, thickness, and permeability of the aquifers on both sides, the lateral infiltration ratio was different and the lateral infiltration on the north bank was larger than that on the south bank. It was calculated that the lateral infiltration of the south bank was only 70% of that of the north bank, that is, 454.75 m^3/m·d. This showed that the calculation results were consistent with the analytical method Darcy formula.

4.4 Impact of Xiaolangdi Reservoir operation on the ecological environment on both sides of the river

Due to the “sediment and water regulation” of the reservoir, the river channel has been affected in many aspects. In addition to the regulation of runoff in the river, the natural fluctuation process is weakened, and the change of the sediment concentration and the discharge of low-temperature water affect the reproduction of aquatic organisms. The main channel is scoured, and the river bottom is cut down. Under the same flow condition, the river water level decreases, which reduces the probability of an overbank flood. Overbank floods reduced, riparian beaches and wetlands shrank and degenerated, and the wetland area in the river channel decreased from 724 km^2 in 1997 (before the operation of the reservoir) to 651 km^2 in 2003 (after the operation) (Zhu et al., 2018). In the wetland ecosystem outside the river, part of the surface water in the marshland dried up and the vegetation decreased, which affected the habitat of a large number of birds (Liu et al., 2008).

The Huayuankou–Jiahetan section is located on the axis of the alluvial fan and alluvial plain of the Yellow River. It is the largest area of groundwater recharge by river water infiltration in the lower reaches of the Yellow River. The Yellow River Wetland Bird National Nature Reserve in Xinxiang, Henan Province; the Yellow River in Zhengzhou; and the Liuyuankou Wetland Provincial Nature Reserve in Kaifeng are distributed on both sides of the river from 5 to 20 km away from the embankment. They are important inland wetland ecosystems in China. Affected by the operation of the Xiaolangdi Reservoir, the recharge base level is reduced, and the shallow groundwater level in the Yellow River influence zone continues to decline. In 2019, compared with 2003, the area with groundwater depth greater than 8 m gradually expanded, from 4 km^2 to 268 km^2 in the north bank embankment and from 1 km^2 to 1,257 km^2 outside the embankment. On the south bank, it expanded from 58 km^2 to 247 km^2, and outside the embankment, it expanded from 66 km^2 to 697 km^2. The area with a buried depth of less than 2 m gradually shrunk, from 124 km^2, the area disappeared outside the north bank, and it decreased from 55 to 26 km^2 outside the south bank.

5 Discussion

5.1 Change in the secondary perched reach of the Yellow River discharge and water level

From 1972 to 2002, due to the increase in the irrigation amount of the Yellow River, the annual average runoff of the Huayuankou and Jiahetan hydrological stations decreased by 39.36% and 38.97%, respectively. Since the Xiaolangdi Reservoir was officially regulated by water and sediment in 2002, the operation of the dam has reduced the flood peak runoff, and the change of the river runoff tends to be stable. The amount of irrigation from the Yellow River has been reduced, resulting in an increase in the Yellow River water runoff compared with 1990–2000 (Figure 3A).

From 1972 to 2002, the river water level of the Huayuankou and Jiahetan hydrological stations did not decrease significantly. After the construction of the Xiaolangdi Reservoir (2002), the water level of the same discharge at the Huayuankou and Jiahetan hydrological stations is lower than that before the construction of the Xiaolangdi Reservoir (1990). The water level of the same runoff shows a downward trend year by year. The water level of the Huayuankou hydrological station decreased by 2.13, 3.13, and 3.85 m, respectively, in the initial stage (2005) and stable stage (2010 and 2020) of reservoir operation compared with that before reservoir construction (1990), and the water level of the Jiahetan hydrological station decreased by 2.11, 3.04, and 3.91 m, respectively. Since 2002, the Xiaolangdi Reservoir has carried out water and sediment regulation once a year and four times in a row. The sediment in the reservoir has been reduced by 310 million m^3, the downstream channel has been scoured by 340 million m^3, and the runoff capacity of the downstream channel has been increased from 1,800 m^3/s to 3,000 m^3/s. The trend of sedimentation deterioration in the downstream channel has been effectively controlled (Kong et al., 2015). The downstream river channel is continuously scoured, which alleviates the siltation of the river channel, and the river channel is cut down. The water level of the Huayuankou and Jiahetan rivers shows a significant downward trend (Figure 3B).

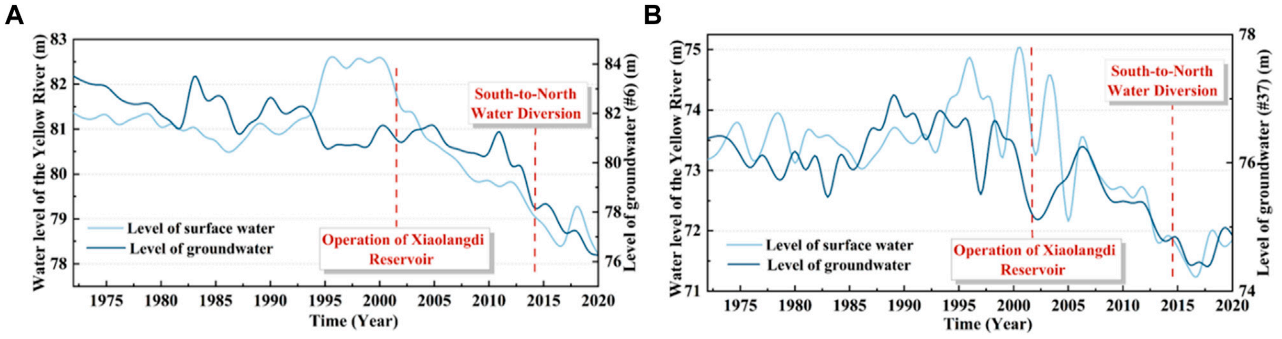

FIGURE 10
Relationship between surface water and groundwater. **(A)** #6 well water level and the middle Yellow River water level; **(B)** #38 well water level and the Jiahetan Yellow River water level.

5.2 Variation in the groundwater level along the river

In the past 50 years, the groundwater level along the secondary perched reach river has generally shown a downward trend. The groundwater levels of typical monitoring wells #35, #29, #31, #20, #6, #12, #37, and #38 along the secondary perched reach river of the Yellow River have decreased by 8.31, 6.79, 3.42, 3.97, 7.24, 5.28, 1.51, and 4.88 m, respectively. Before 2002, the downward trend of the groundwater level was relatively gentle, with an average decline of 1.32 m. After 2002, the downward trend of the water level became more significant, with an average decline of 3.53 m (Figure 10). After the stable operation of water and sediment regulation of the Xiaolangdi Reservoir, the secondary perched reach riverbed was scoured, and the sediment particles in the riverbed were coarsened, which was conducive to the recharge of the secondary perched reach river to the groundwater. The scouring of the riverbed by the Xiaolangdi Reservoir will make the river channel cut down, making the hydraulic gradient smaller (Sun et al., 2016). Compared with this, the riverbed coarsening has less impact on groundwater recharge and the groundwater level along the riverbank still shows a downward trend.

5.3 Characteristics of river recharge along the riverbank in the secondary perched reach

According to the calculation in Section 4.3, the quantity of groundwater recharge by the secondary perched reach river in different hydrological years is different. In the wet season, the secondary perched reach river level is higher, the hydraulic gradient is larger, and the groundwater recharge is stronger. As the difference between the Yellow River water level and the monitoring well water level increases, the single-width infiltration flow of the Yellow River increases, that is, the infiltration recharge increases (Li et al., 2022). The lower reaches of the Yellow River were interrupted by many factors from 1992 to 1998. In order to ensure water supply for the local industrial and agricultural sectors, the Huayuankou station transferred water from the middle reaches and other places for many years during this period, reaching 800 m^3/s in spring. During this period, the width of this section of the river decreased from 1.7 km in 1990 to 0.8 km in 1999, and the depth of the river increased from 1.2 to 1.8 m. The river discharge decreased from 1,135 m^3/s to 663.5 m^3/s, but the sediment discharge increased from 5.5×10^8t to 11×10^8t, and 25% of the average sediment discharge was deposited in this reach, causing the river level to rise. As a result, the river flow decreases and the river level rises. After the operation of the Xiaolangdi Reservoir, from 1999 to 2004, as the median particle size of D_{50} of bed sand at each section of Huayuankou increased to 0.15 mm, the riverbed profile developed in the direction of narrowness and depth, forming a higher river level. After 2003, except for the Huayuankou section, D_{50} of other sections increased slightly or remained unchanged. Therefore, the sediment coarsening of the downstream riverbed was the most significant in the first 4 years after the operation of the Xiaolangdi Reservoir, and the changes in the riverbed led to an increase in river water infiltration. From the two factors mentioned above, the Yellow River infiltration was higher from 1994–2004 (Ma et al., 2022). Since then, with the decrease in the river flow, the weakening of bed sand coarsening and the reduction of river level, the infiltration recharge of the Yellow River has gradually decreased. The reduction intensity was the largest in 2006 (Figure 4), and the infiltration reduction rate in the following years was between 2.47% and 0.5%. With the operation of the "South-to-North Water Diversion Project," the river volume and water level of the secondary perched reach tend to rise, and the infiltration of the Yellow River has been increasing.

6 Conclusion

(1) In the past 50 years, the river discharge and water level of the secondary perched reach of the Yellow River in the Huayuankou–Jiahetan section, and the groundwater level on both sides of the river have shown a significant downward trend. Since 2002, affected by the operation of the Xiaolangdi Reservoir, the river water runoff has stabilized and the river water has scoured the riverbed. The average depth of the riverbed undercutting is 2.44–3.77 m, resulting in a decrease in the river water level (Huayuankou decreased by 0.68 m and Jiahetan decreased by 2.7 m). The hydraulic gradient of groundwater decreases, the groundwater recharge weakens, and the groundwater level decreases significantly.

(2) It was observed, by using the gray correlation method, that the main factors affecting the groundwater level were the river discharge and the river water level. The hydraulic connection between the secondary perched river and the aquifer is strong. The Pearson correlation coefficient of the secondary perched river and the aquifer was calculated, indicating that the river discharge and water level of the river have a lag in the recharge of groundwater along the river. In the wet year, the water level of the secondary perched river is higher, the hydraulic gradient is larger, the recharge to the groundwater is stronger, and the unit width recharge is larger (566.79 $m^3/m\cdot d$). In the dry year, the recharge is less and the unit width recharge is 374.13 $m^3/m\cdot d$.

(3) Since the operation of the South-to-North Water Diversion Project in 2014, the irrigation amount of the Yellow River has been reduced. In 2020, the water discharge of the Yellow River in the Huayuankou and Jiahetan hydrologic stations increased from 735 m^3/s to 1,536.9 m^3/s and from 701 m^3/s to 1,500.8 m^3/s, respectively. The groundwater level (<2 km) showed a downward trend except for the rise of the water level of the Zheng 9 well. This reflects that Zhengzhou city receives water supply from the South-to-North Water Diversion Canal every year, approximately 580 million m^3/a, reducing groundwater exploitation by 488×10^4 m^3/a and making the groundwater level rise. In other areas, the water supply of canals is small, and the groundwater level shows a downward trend.

(4) This study focuses on the interannual mean variation characteristics of the water volume, water level and groundwater level of the Yellow River. The monthly mean value is used in the study of the lag of the water level of the groundwater and the secondary perched reach of the Yellow River, we will further carry out a multidisciplinary comprehensive study of river and groundwater dynamics on the monthly and daily data on river and groundwater.

Data availability statement

The original contributions presented in the study are included in the article/Supplementary Material; further inquiries can be directed to the corresponding author.

Author contributions

MZ: writing–original draft. JP: writing–original draft. XM: writing–original draft. WL: writing–review and editing. HL: writing–review and editing. JZ: writing–review and editing. JL: writing–review and editing.

Funding

The author(s) declare that financial support was received for the research, authorship, and/or publication of this article. This research was funded by the Research Startup Fund for Academician Team of Zhengzhou University (grant no. 13432340370), High-level talents of Zhengzhou University (grant nos. 134-32340364 and 135-32340122), the National Natural Science Foundation of China–Henan Talent Training Joint Foundation (grant no. U1504404) and Dual-source groundwater ecological environment quality monitoring network in Henan Province and groundwater environment monitoring Early warning platform construction (Phase II) project B package (grant no. SJCAQ-HT-2023-036).

Acknowledgments

The authors specially thank the Yellow River Water Conservancy Commission for providing the water level and runoff data on the Huayuankou and Jiahetan hydrological stations in the lower reaches of the Yellow River from 1972 to 2020. They also specially thank the Henan Provincial Bureau of Hydrology and Water Resources for providing “Henan groundwater data”.

Conflict of interest

The authors declare that the research was conducted in the absence of any commercial or financial relationships that could be construed as a potential conflict of interest.

Publisher’s note

References

Acero, P., Auque, L. F., Galve, J. P., Gutierrez, F., Carbonel, D., Gimeno, M. J., et al.(2015). Evaluation of geochemical and hydrogeological processes by geochemical modeling in an area affected by evaporite karstification. *J. Hydrol.* 529, 1874–1889. doi:10.1016/j.jhydrol.2015.07.028

Chen, J. Y., Tang, C. Y., Sakura, Y., Kondoh, A., and Shen, Y. J. (2002). Groundwater flow and geochemistry in the lower reaches of the Yellow River: a case study in Shandong Province, China. *Hydrogeol. J.* 10 (6), 674. doi:10.1007/s10040-002-0231-7

Cheng, Q., Gao, L., Zuo, X., and Zhong, F. (2019). Statistical analyses of spatial and temporal variabilities in total, daytime, and nighttime precipitation indices and of extreme dry/wet association with large-scale circulations of Southwest China. *Atmos. Res.* 219, 166–182. doi:10.1016/j.atmosres.2018.12.033

Deng, J. (1989). Introduction to grey system theory. *J. Grey Syst.* 1 (1), 1–24.

Fu, Y., Dong, Y., Xie, Y., Xu, Z., and Wang, L. (2020). Impacts of regional groundwater flow and river fluctuation on floodplain wetlands in the middle reach of the Yellow River. *Water-Sui* 12 (7), 1922. doi:10.3390/w12071922

Gao, P., Xie, Y., Song, C., Cheng, C., and Ye, S. (2023). Exploring detailed urban-rural development under intersecting population growth and food production scenarios: trajectories for China’s most populous agricultural province to 2030. *J. Geogr. Sci.* 33 (2), 222–244. doi:10.1007/s11442-023-2080-3

Gu, L., Shao, J., Sun, Y., and Zhao, Y. (2013). Groundwater flow simulation and resource evaluation of the affected zone along the Yellow River (henan section). *Prog. Environ. Sci. Eng.* 610-613, 2713–2718. doi:10.4028/www.scientific.net/AMR.610-613.2713

Kong, D., Miao, C., Wu, J., Duan, Q., Sun, Q., Ye, A., et al.(2015). The hydro-environmental response on the lower Yellow River to the water-sediment regulation scheme. Ecol. Eng. 79, 69–79. doi:10.1016/j.ecoleng.2015.03.009

Li, J., Li, F., Liu, Q., and Zhang, Y. (2014a). Trace metal in surface water and groundwater and its transfer in a Yellow River alluvial fan: evidence from isotopes and hydrochemistry. *Sci. Total Environ.* 472, 979–988. doi:10.1016/j.scitotenv.2013.11.120

Li, P., Wu, J., and Qian, H. (2014b). Hydrogeochemistry and quality assessment of shallow groundwater in the southern part of the Yellow River alluvial plain (zhongwei section), northwest China. *Earth Sci. Res. J.* 18 (1), 27–38. doi:10.15446/esrj.v18n1.34048

Li, X., Yan, B., Wang, Y., Wang, X., Li, Y., and Gai, J. (2022). Study of the interaction between Yellow River Water and groundwater in henan province, China. *Sustainability-Basel* 14 (14), 8301. doi:10.3390/su14148301

Liu, Q., Yang, Z., and Cui, B. (2008). Spatial and temporal variability of annual precipitation during 1961-2006 in Yellow River Basin, China. *J. Hydrol.* 361 (3-4), 330–338. doi:10.1016/j.jhydrol.2008.08.002

Ma, H., Nittrouer, J. A., Fu, X., Parker, G., Zhang, Y., Wang, Y., et al.(2022). Amplification of downstream flood stage due to damming of fine-grained rivers. *Nat. Commun.* 13 (1), 3054. doi:10.1038/s41467-022-30730-9

Qu, L., Li, Y., Wang, Y., Dong, S., and Wen, Q. (2022). Dynamic evolution and the mechanism of modern gully agriculture regional function in the Loess Plateau. *J. Geogr. Sci.* 32 (11), 2229–2250. doi:10.1007/s11442-022-2045-y

Sun, Z., Wang, W., Li, Y., Zhang, M., Shang, H., and Zhang, F. (2016). Can the narrowing of the Lower Yellow River by regulation result in non-siltation and even channel scouring? *J. Geogr. Sci.* 26 (9), 1337–1348. doi:10.1007/s11442-016-1330-z

Vincent, K. K., Muthama, M. N., and Muoki, S. N. (2014). Darcy's law equation with application to underground seepage in earth dams in calculation of the amount of seepage. *Am. J. Appl. Math. Statistics* 2 (3), 143–149. doi:10.12691/ajams-2-3-8

Wang, Z., Jin, J., Liu, W., Deng, T., Zhao, Y., and Du, X. (2021). Chemical characteristics and factors affecting groundwater chemistry from the Yellow River irrigation area in tumochuan plain in the middle and upper reaches of the Yellow River basin. *Res. Square*. doi:10.21203/rs.3.rs-584081/v1

Xu, H., Li, Y., Huang, Z., Bai, Y., and Zhang, J. (2022). Energy dissipation caused by boundary resistance in a typical reach of the lower Yellow River and the implications for riverbed stability. *J. Geogr. Sci.* 32 (11), 2311–2327. doi:10.1007/s11442-022-2049-7

Xu, Z. X., Takeuchi, K., Ishidaira, H., and Zhang, X. W. (2002). Sustainability analysis for Yellow River water resources using the system dynamics approach. *Water Resour. Manag.* 16 (3), 239–261. doi:10.1023/A:1020206826669

Yan, J., Xu, H., Xu, L., Gurkalo, F., and Gao, X. (2023). Evolution characteristics of long time series of secondary perched River in typical reaches of the lower Yellow River. *Water-Sui* 15 (20), 3674. doi:10.3390/w15203674

Yang, D. W., Li, C., Hu, H. P., Lei, Z. D., Yang, S. X., Kusuda, T., et al.(2004). Analysis of water resources variability in the Yellow River of China during the last half century using historical data. *Water Resour. Res.* 40 (6). doi:10.1029/2003WR002763

Yue, S., Pilon, P., and Cavadias, G. (2002). Power of the Mann-Kendall and Spearman's rho tests for detecting monotonic trends in hydrological series. *J. Hydrol.* 259 (1-4), 254–271. doi:10.1016/S0022-1694(01)00594-7

Zhang, Q., Peng, J., Singh, V. P., Li, J., and Chen, Y. D. (2014). Spatio-temporal variations of precipitation in arid and semiarid regions of China: the Yellow River basin as a case study. *Glob. Planet Change* 114, 38–49. doi:10.1016/j.gloplacha.2014.01.005

Zhang, Q., Xu, C. Y., and Yang, T. (2009). Variability of water resource in the Yellow River Basin of past 50 Years, China. *Water Resour. Manag.* 23 (6), 1157–1170. doi:10.1007/s11269-008-9320-2

Zhou, P., Li, M., and Lu, Y. (2017). Hydrochemistry and isotope hydrology for groundwater sustainability of the coastal multilayered aquifer system (zhanjiang, China). *Geofluids* 2017, 1–19. doi:10.1155/2017/7080346

Zhu, C., Zhang, X., and Huang, Q. (2018). Four decades of estuarine wetland changes in the Yellow River delta based on landsat observations between 1973 and 2013. *Water-Sui* 10 (7), 933. doi:10.3390/w10070933

frontiers | Frontiers in Environmental Science

TYPE Original Research
PUBLISHED 20 December 2023
DOI 10.3389/fenvs.2023.1327622

OPEN ACCESS

EDITED BY
Jing Liu,
University of Birmingham,
United Kingdom

REVIEWED BY
Dongyong Sun,
Chang'an University, China
Bai Tao,
Xi'an University of Technology, China

*CORRESPONDENCE
Qiubo Long,
✉ longqiubo17@126.com

RECEIVED 25 October 2023
ACCEPTED 30 November 2023
PUBLISHED 20 December 2023

CITATION
Wan F, Han W, Long Q, Wang W, Wang G and Zhang F (2023), Study on the evolution law and stage response relationship between meteorological elements and hydrological drought in Xiangtan area.
Front. Environ. Sci. 11:1327622.
doi: 10.3389/fenvs.2023.1327622

Study on the evolution law and stage response relationship between meteorological elements and hydrological drought in Xiangtan area

Fang Wan[1,2], Wenhao Han[1], Qiubo Long[2]*, Weijun Wang[2], Guoqing Wang[2,3,4,5] and Fei Zhang[1]

[1]North China University of Water Resources and Electric Power, Zhengzhou, China, [2]Engineering Technology Research Center of Dongting Lake Flood Control and Water Resources Protection of Hunan Province, Changsha, China, [3]The National Key Laboratory of Water Disaster Prevention, Nanjing Hydraulic Research Institute, Nanjing, China, [4]Cooperative Innovation Center for Water Safety and Hydro Science, Hohai University, Nanjing, China, [5]Yangtze Institute for Conservation and Development, Nanjing, China

Studying the propagation law and response relationship between meteorological elements and hydrological drought is conducive to exploring the propagation mechanism and transmission time of drought, and providing a basis for reasonable and efficient drought relief work. In this paper, the area above Xiangtan station is taken as the research area, and the temperature and precipitation are selected as the meteorological elements. The standardized flow index (SDI) is used to characterize the hydrological drought. The linear regression method and Mann-Kendall trend test are used to analyze the evolution sequence of meteorological elements and hydrological drought at different scales. The characteristics and laws of drought propagation are revealed, and the hydrological drought is divided into stages by combining the ordered cluster analysis method and the sliding t-test method. The Pearson correlation analysis method is used to analyze the stage correlation degree between meteorological elements and hydrological drought, reflecting the response relationship between meteorological elements and hydrological drought under different types and different scales, and the response period of hydrological drought to meteorological elements at different time scales is obtained. Studying the development trend and evolution law of meteorological elements and hydrological drought, and deeply exploring the phased response relationship are conducive to improving the drought resistance ability and drought disaster reduction management ability of Xiangtan area.

KEYWORDS

evolution law, response relationship, meteorological element, hydrological drought, Xiangtan area

1 Introduction

In the past century, with the rapid development of human civilization and the intensification of global warming, the impact of drought on human survival and development has become more and more obvious (Zhang et al., 2020). In general, the development of drought is characterized by frequent, continuous and concurrent, and there is obvious differentiation in time series and spatial distribution (Dai and Zhao, 2017). At present, the global losses caused by drought account for about 55% of the total losses of natural disasters, making 30% of the world‘s land and 20% of the population threatened by drought (Xu, 2014). This paper takes the area above Xiangtan Station as the research area. Xiangjiang River Basin is an important commodity grain and industrial raw material producing area. In recent years, with the influence of climate change and human activities (population density increase, urbanization level increase, etc.), drought has a deepening impact on economic and social development, making water shortage, desertification, ecological and environmental deterioration and other negative effects (Ling et al., 2023). Therefore, it is necessary to study the evolution trend of hydrological and meteorological factors in Xiangtan area and their phased response relationship, which is of great value in drought risk assessment and drought prevention and disaster reduction planning measures.

Drought evolution is a hot topic in current academic research. It mainly explores the characteristics and laws of multi-type drought evolution by optimizing methods and constructing more scientific and effective drought indicators. For example, Wang et al. (2023) constructed the joint distribution of hydrological drought variables based on Copula function to explore the evolution law of return period and drought; Jiang et al. (2023) standardized the precipitation evapotranspiration index, and optimized the combination of run theory, wavelet theory, Copula function and other methods to analyze the spatial and temporal evolution and periodic characteristics of drought. Zheng et al. (2023) combined the distributed hydrological model with the attribution analysis method, and used the binary water cycle optimization model to explore the impact of human society on the evolution of hydrological drought. Tian et al. (2023) established a multivariate drought index to characterize drought. At the same time, combined with meteorological factors and hydrological factors, a standardized drought index capable of characterizing meteorology and hydrology was constructed to evaluate and study the spatial and temporal evolution of drought in the Xijiang River Basin. The results show that the drought index can fully reflect the drought situation. Gu et al. (2023) selected the standardized precipitation index, combined with a linear regression method, Mann-Kendall rank test and other methods to analyze the evolution direction and persistence of meteorological drought; Liang et al. (2023) analyzed and compared the calculation results of Pearson correlation method and cross wavelet method, and obtained the strongest correlation factor among many climatic factors, revealing the main reasons for the intensification of regional drought; Ribeiro Neto et al., 2022 developed a new method of drought cycle analysis to predict and evaluate the occurrence and evolution of drought events; By improving the spatial hierarchical clustering method, Li et al. (2020a) comprehensively divided the characteristics of drought evolution from the perspective of time and space. Most of the above studies studied the evolution of drought from the perspective of optimizing drought indicators, improving methods and theories, and rarely analyzed the evolution of hydrological and meteorological factors from a multi-scale perspective, and there were few studies on the stage of multi-type drought response.

In this paper, the area above Xiangtan station is taken as the research area. The linear regression method and Mann-Kendall trend test method are used to analyze the evolution characteristics of hydrological drought and meteorological elements in the area above Xiangtan station. The standardized flow index (SDI) is used to study the evolution trend of hydrological drought. The orderly cluster analysis method and the sliding t-test method are used to divide the hydrological drought into stages (Li et al, 2020b; Lu and Li, 2020). The Pearson correlation analysis method is used to study the response relationship between multi-type meteorological elements and multi-scale hydrological drought in different stages. It provides a new direction and idea for the study of drought propagation law and drought control in this area.

1.1 Overview of the study area

Xiangjiang River is an important tributary of the Yangtze River and the largest river in the Dongting Lake system. It spans four provinces: Hunan, Guangxi, Jiangxi and Guangdong (Figure 1). The basin area of each province accounts for 90.22%, 8.17%, 1.51% and 0.10% (Luo, 2020) of the total basin area, respectively. The Xiangjiang River Basin has a subtropical monsoon humid climate. The climate is mild and the rainwater is relatively concentrated. The summer and autumn seasons are dry and the high temperature period is long. The average annual temperature of the basin is 17.4°C, the average annual evaporation is 1275.5 mm, and the average annual precipitation is 1,441 mm (Comprehensive Planning of Xiangjiang River Basin, 2015). Since 2000, the frequency of hydrological drought in Xiangtan area has increased significantly, and hydrological drought occurred every 2 years on average from 2003 to 2013 (Wu et al., 2023). Xiangtan area is the region with the strongest intensity of hydrological drought in Xiangjiang River Basin. The longest duration of hydrological drought is 10 months, and the main occurrence periods are summer, autumn and winter (Wen et al., 2021; Luo, 2020). The total length of the mainstream of the Xiangjiang River Basin is about 850 km, and the runoff is unevenly distributed during the year, and the interannual variation is small (Development Planning Office of Hunan Development and Reform Commission, 2013). Due to the influence of monsoon, the spatial and temporal distribution of rainfall is not balanced. April to June is the Meiyu season, and the precipitation in 3 months accounts for more than 40% of the annual precipitation. The unbalanced distribution of precipitation makes drought events occur frequently (Comprehensive Planning of Xiangjiang River Basin, 2015). Xiangjiang River is an important water source in Hunan Province. More than 60% of the water used by industrial enterprises in Hunan Province comes from Xiangjiang River. In the past 50 years, the urbanization rate has increased by about 45%, and the continuous improvement of social and economic needs has aggravated the degree of drought (Liu, 2020).

The hydrometeorological data in this paper are derived from the Hydrological Yearbook and the geospatial data cloud website. The meteorological element data are monthly series data (January 1959~December 2010), and the hydrological data are monthly series data (January 1959~December 2013). The time range of the final drought stage is unified from January 1959 to December 2010.

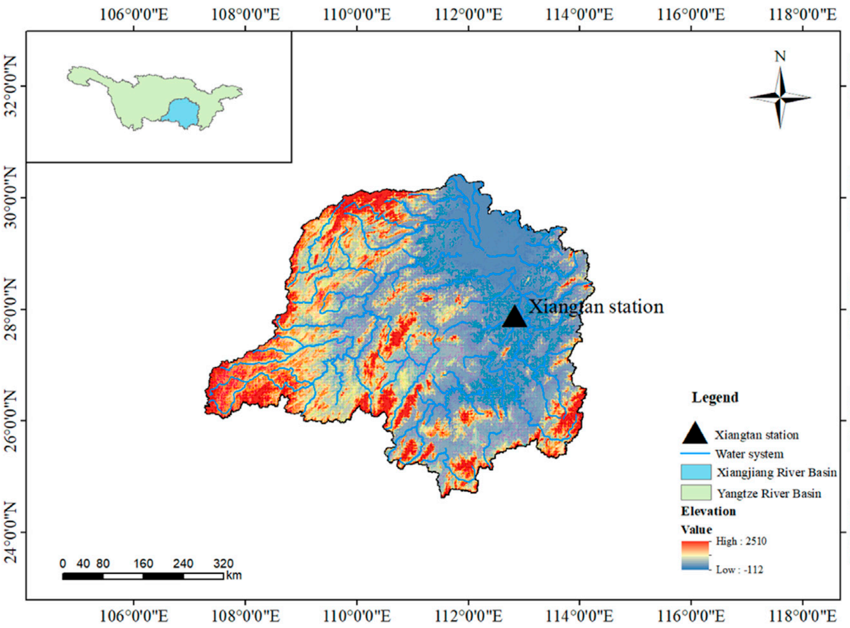

FIGURE 1
Xiangjiang river basin Zoning map.

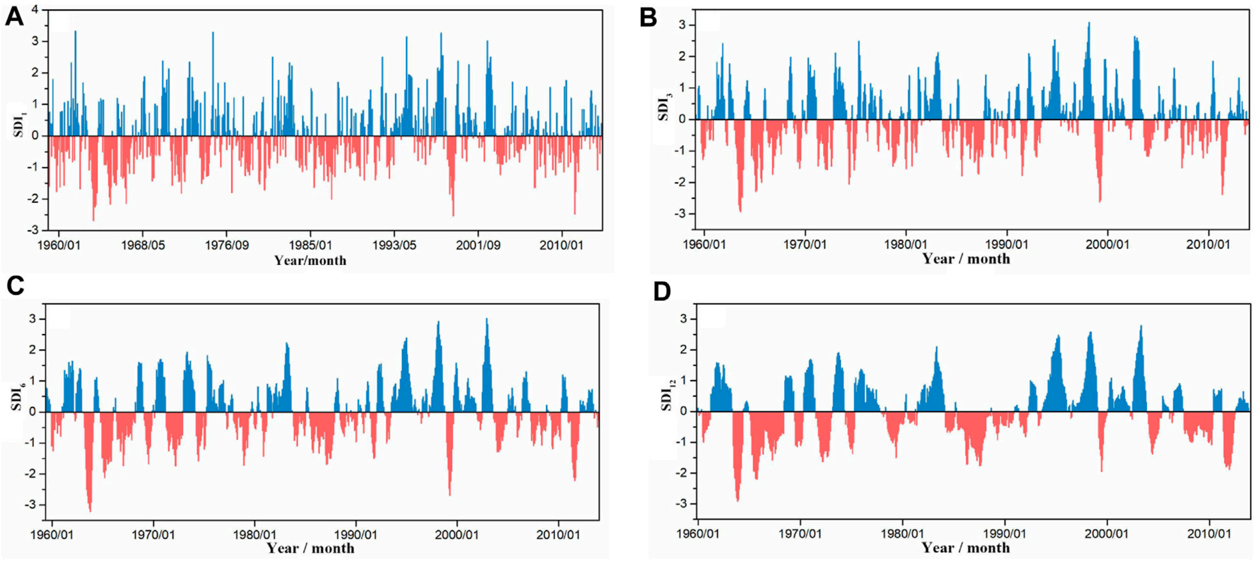

FIGURE 2
Evolution of SDI sequence at four scales.

2 Research methods

2.1 Hydrological and meteorological evolution characteristics

Based on the monthly data of temperature, precipitation and flow in the study area from 1959 to 2010, combined with the linear regression method and Mann-Kendall trend test method, the inter-annual and annual evolution characteristics of meteorological elements in the area above Xiangtan station were analyzed. At the same time, the evolution law of multi-scale sequence of hydrological drought index was analyzed, which provided a basis for the study of the relationship between meteorology and hydrological response. The linear regression method is widely used and not specifically introduced. The calculation steps of the Mann-Kendall trend test method are as follows:

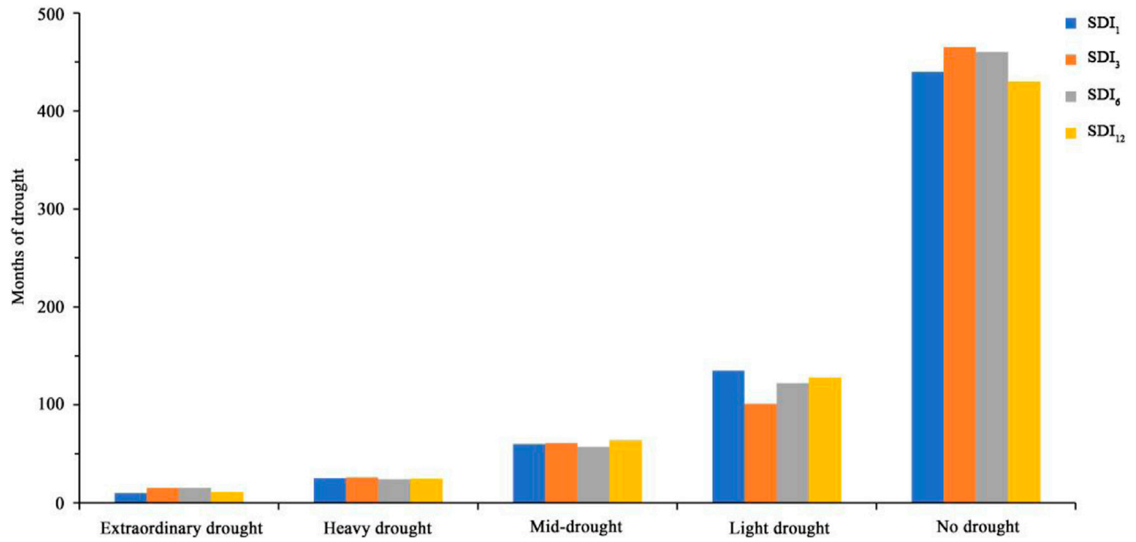

FIGURE 3
Cumulative months of different drought levels in SDI series at four scales.

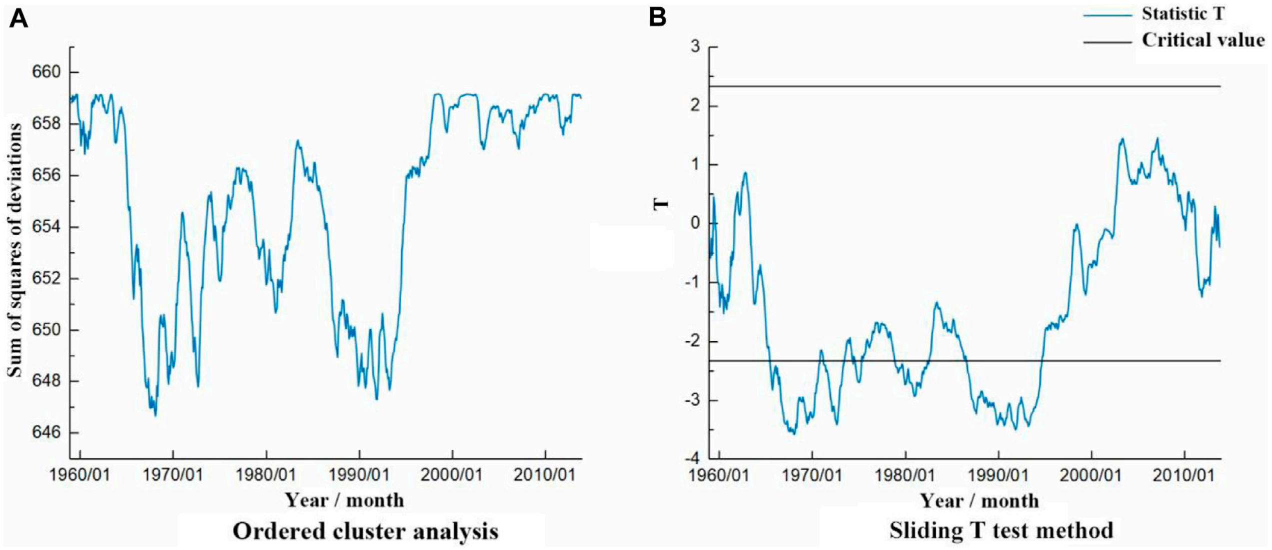

FIGURE 4
Ordered clustering and sliding *t*-test analysis chart.

TABLE 1 Hydrological drought stage division.

Hydrological drought stage	Time horizon	Duration (months)
1	January 1959~February 1968	110
2	March 1968~September 1972	55
3	October 1972~January 1980	88
4	February 1980~September 1987	92
5	October 1987~December 1991	51
6	January 1992~December 2010	228

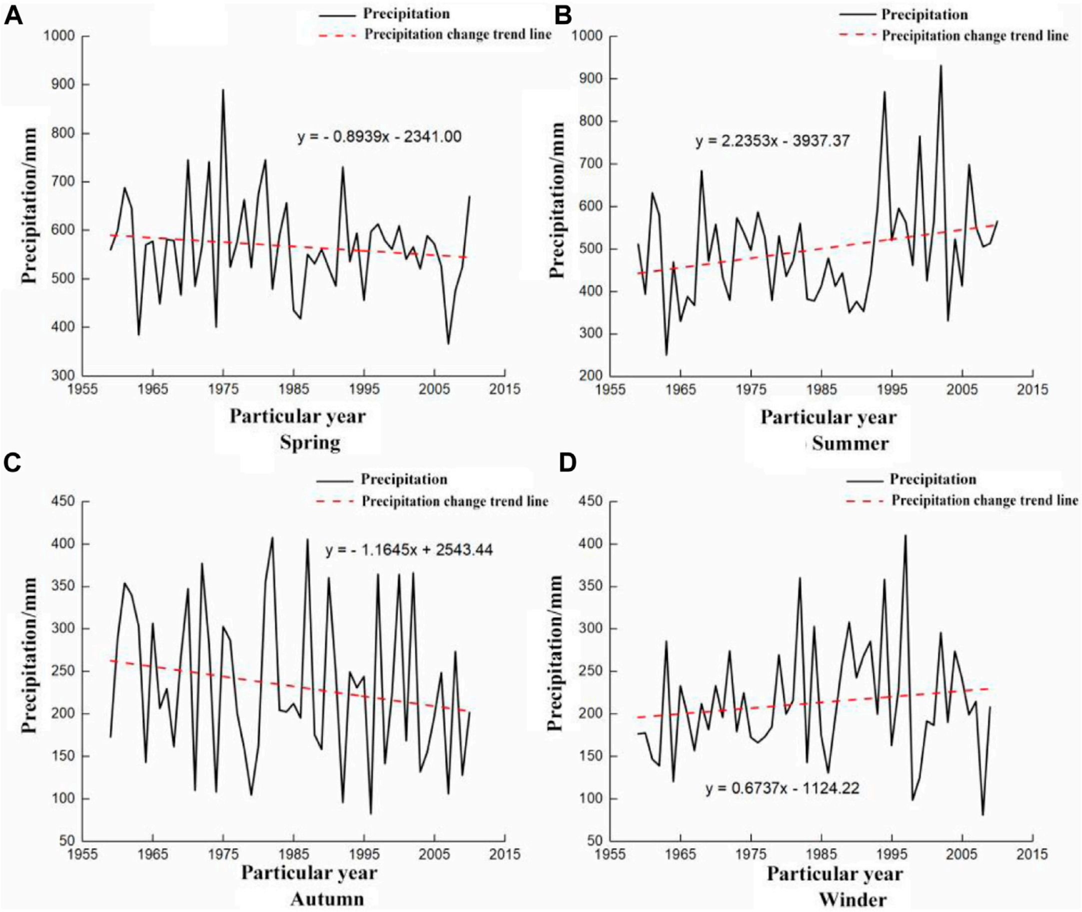

FIGURE 5
The trend of precipitation changes in the four seasons of the year.

Let a data sequence $zi\,(i = 1, 2, 3 \ldots n)$, n is the length of the sequence, and the statistic S is defined as:

$$S = \sum_{k=1}^{n-1}\sum_{j=k+1}^{n} sgn\left(X_j\text{-}X_k\right) \tag{1}$$

Among them, X_j and X_k are the year data corresponding to the time series, and $X_j - X_k$ is the symbol function. When $X_j > X_k$, $sgn = 1$; when $X_j < X_k$, $sgn = -1$; when $X_j = X_k$, $sgn = 0$.

When $n \geq 10$, the statistic S obeys the normal distribution, the expected value $E(S) = 0$, and the variance is:

$$Var(S) = n(n\text{-}1)(2n\text{+}5)/18 \tag{2}$$

The following standardized test statistic Z can be constructed:

$$Z = \begin{cases} \dfrac{S-1}{\sqrt{Var(S)}}\ (S > 0) \\ 0\,(S = 0) \\ \dfrac{S-1}{\sqrt{Var(S)}}\ (S < 0) \end{cases} \tag{3}$$

When $Z > 0$, the sequence shows an upward trend; When $Z < 0$, the sequence shows a downward trend; $|Z| \geq Z_{1-\lambda/2}$, the sequence has a significant upward or downward trend. Among them, $Z_{1-\lambda/2}$ is the standard normal variance, and λ is the significant level (0.01).

2.2 Stage division and response relationship

Combined with the ordered cluster analysis method and the sliding t-test method, the mutation points of the hydrological drought index sequence were analyzed, and the hydrological drought was divided into stages. The correlation analysis method was used to analyze the response relationship between hydrological drought and multi-type meteorological factors in different stages. The correlation analysis method is widely used, and the specific principle is not described.

(1) Ordered cluster analysis. The ordered cluster analysis method is to estimate the mutation point and find the optimal segmentation point. For the sample sequence x, the main points of the optimal bipartition method are as follows:

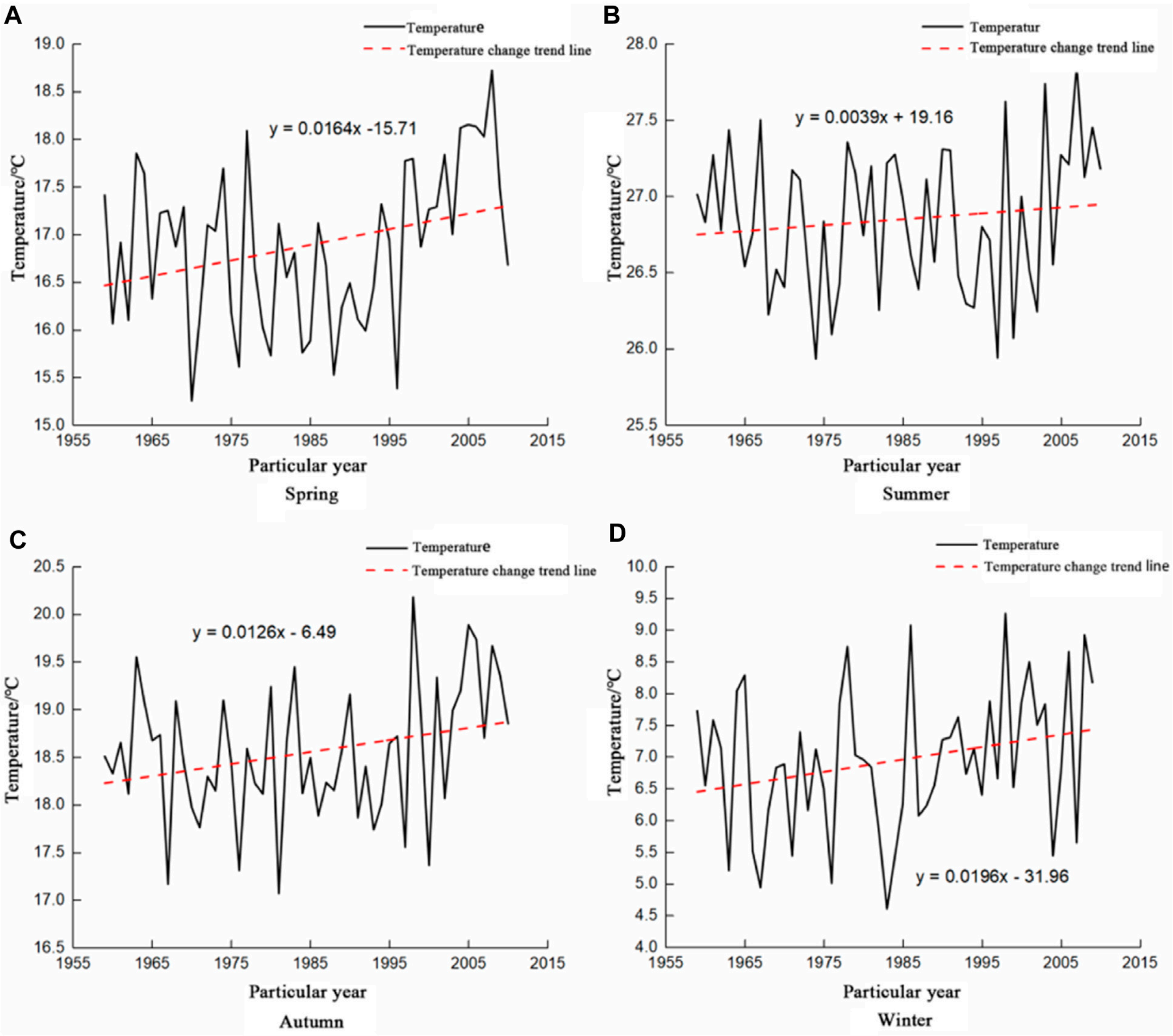

FIGURE 6
The trend of temperature change in the four seasons of the year.

Assuming that the possible mutation point is t, then the sum of squares of deviations before and after the mutation point is:

$$V_\tau = \sum_{i=1}^{\tau} (x_i - \bar{x}_\tau)^2 \tag{4}$$

$$V_{n-\tau} = \sum_{i=\tau+1}^{n} (x_i - \bar{x}_{n-\tau})^2 \tag{5}$$

In the formula: $\bar{x}_\tau$ and $\bar{x}_{n-\tau}$ are the mean values of the two parts, respectively. The objective function is defined as:

$$S = \min_{2\le\tau\le n-1} S_n(\tau) = \min_{2\le\tau\le n-1} (V_\tau + V_{n-\tau}) \tag{6}$$

The τ corresponding to the minimum value of S is the optimal two-segmentation point, which can be used as the mutation point.

(2) Sliding t-test. The sliding t-test method is to identify the mutation point by testing whether the difference between the mean values of the two random sample sequences before and after the sliding point is significant. A random sample sequence $x_1, x_2, \cdots, x_n$ is divided into two sub-sequences with capacity of n_1 and n_2 at the sliding point, and the statistics are constructed:

$$T = \frac{\bar{u}_1 - \bar{u}_2}{S\sqrt{\frac{1}{n_1} + \frac{1}{n_2}}} \tag{7}$$

$$S = \sqrt{\frac{n_1 s_1^2 + n_2 s_2^2}{n_1 + n_2 - 2}} \tag{8}$$

In the formula: $\bar{u}_1, \bar{u}_2$ are the mean value of two subsequences respectively; s_1, s_2 are the variances of the two subsequences; The statistic obeys the t distribution with degree of freedom $n_1 + n_2 - 2$. Given a significant level α, if a sliding point t satisfies $|T| > T_\alpha (n-2)$, then there is a significant difference in the mean value of the subsequence before and after the sliding point, that is, it is considered that there may be a mutation near the point, and the

TABLE 2 Trend characteristics and significance of annual and inter-annual precipitation and temperature.

Time interval		Types of elements	b	a	Trend	U values	$\alpha = 0.05$ $U_{\alpha/2} = 1.96$	$\alpha = 0.10$ $U_{\alpha/2} = 1.645$	$\alpha = 0.20$ $U_{\alpha/2} = 1.282$
Annual	Spring	Precipitation	2341.00	−0.8939	Decrease	−0.852	—	—	—
		Air temperature	−15.71	0.0164	Elevation	2.068	√	√	—
	Summer	Precipitation	−3937.37	2.2353	Increase	1.357	—	—	√
		Air temperature	19.16	0.0039	Elevation	0.584	—	—	—
	Autumn	Precipitation	2543.44	−1.1645	Decrease	−1.405	—	—	√
		Air temperature	−6.49	0.0126	Elevation	1.673	—	√	—
	Winter	Precipitation	−1124.22	0.6737	Increase	1.308	—	—	√
		Air temperature	−31.96	0.0196	Elevation	1.746	—	√	—
Inter-annual	Precipitation		−89.08	0.8081	Increase	0.126	—	—	—
	Air temperature		−9.36	0.0134	Elevation	2.967	√	√	√

sliding point can be preliminarily identified as the mutation point. On the contrary, it shows that there is no significant difference in the mean value of the subsequence before and after the sliding point, that is, there is no mutation near the sliding point.

3 Evolution analysis of hydrological drought and meteorological factors

The meteorological elements (temperature and precipitation) are divided into two scales: annual and inter-annual. The linear regression method and Mann-Kendall trend test method are used to analyze the time-history evolution characteristics. At the same time, the evolution law of multi-scale hydrological drought index (SDI) is studied. The sequential cluster analysis method and the sliding t-test method are used to calculate the mutation point of SDI_1 sequence, and the stage division of hydrological drought evolution is carried out.

3.1 Hydrological drought evolution law and stage division

3.1.1 Evolution law of hydrological drought

Based on the data and evolution characteristics of the flow series, the standardized flow index (SDI) was standardized to characterize the hydrological index series, and the hydrological drought conditions in the study area were evaluated based on different time scales. Four scales of SDI_1, SDI_3, SDI_6 and SDI_{12} were selected to study the evolution of hydrological drought. Figure 2 is the evolution of SDI sequence at four scales. Figure 3 is the cumulative months of different drought levels in SDI series at four scales.

It can be seen from Figures 2, 3 that the cumulative months of no drought, light drought, moderate drought, severe drought and extreme drought in SDI_1, SDI_3, SDI_6 and SDI_{12} scale sequences were relatively close, and the average frequencies of five drought grades in four scales were 68.55%, 16.32%, 9.33%, 3.67% and 1.83%, respectively. The 2-month drought events occurred more frequently in SDI_1, with a total of 42 drought events. The 4-month drought events occurred more frequently in SDI_3, with a total of 41 drought events. SDI_6 had the highest number of 6-month drought events, with a total of 29 drought events. SDI_{12} had the highest number of drought events in 3, 9, and 12 months, with a total of 18 drought events.

3.1.2 Division of evolution stages

According to the mutation point of SDI_1 drought index sequence, SDI_1 is divided into stages, and the stage characteristics of hydrological drought are analyzed, which provides a basis for further study on the stage characteristics of multi-type response relationship. Figure 4 is the ordered clustering and sliding t-test analysis chart.

In this paper, the segmentation point is judged according to the diagnostic results of the ordered cluster analysis method and the square of the sequence deviation. If the square of the sequence deviation has a minimum value and the absolute value of the T value is greater than the critical value, it passes the *t*-test and is the optimal two-segmentation point. It can be seen from Figure 4A that the sum of squared deviations of SDI drought index sequence reached the minimum value in February 1968, that is, the optimal two-segmentation point. December 1991, September 1972, July 1969, September 1987 and January 1980 correspond to the minimum values, respectively, which are the mutation points. After the mutation point is tested by sliding t-test, the absolute value of T value at all mutation points in Figure 4B is greater than the critical value $T_{0.05}$ $(n-2)$ (n is the sequence length), that is, all mutation points pass the significance test of $\alpha = 0.05$. It is divided into six stages: January 1959 to February 1968, March 1968 to September 1972, October 1972 to January 1980, February 1980 to September 1987, October 1987 to December 1991, January 1992 to December 2010.

Table 1 divides the period from 1959 to 2010 into six stages on a monthly scale. The longest duration (228 months) was stage 6 (January 1992~December 2010), and the shortest duration (51 months) was stage 5 (October 1987~December 1991). The average duration was 104 months, and the duration of stage range was 177 months. The characteristics of hydrological

TABLE 3 The correlation between annual and inter-annual temperature and standardized flow index (SDI) at different time scales.

Time interval	The correlation coefficient/ significance of annual temperature-SDI$_1$	The correlation coefficient/ significance of annual temperature-SDI$_3$	The correlation coefficient/ significance of annual temperature-SDI$_6$	The correlation coefficient/ significance of annual temperature-SDI$_{12}$	The correlation coefficient/ significance of inter-annual temperature-SDI$_1$	The correlation coefficient/ significance of inter-annual temperature-SDI$_3$	The correlation coefficient/ significance of inter-annual temperature-SDI$_6$	The correlation coefficient/ significance of inter-annual temperature-SDI$_{12}$
1	0.41/significant	0.78/significant	0.28/significant	−0.12/significant	0.21/non-significant	0.41/significant	0.63/significant	−0.11/non-significant
2	0.47/significant	0.86/significant	0.36/significant	0.11/non-significant	0.16/significant	0.47/significant	0.71/significant	0.19/significant
3	0.53/non-significant	0.88/significant	0.31/significant	−0.18/significant	0.25/significant	0.56/non-significant	0.67/significant	−0.10/significant
4	0.58/significant	0.79/significant	0.18/non-significant	0.06/significant	0.36/significant	0.49/significant	0.87/significant	0.05/significant
5	0.46/significant	0.90/significant	0.21/non-significant	−0.01/significant	0.13/non-significant	0.51/significant	0.75/significant	−0.06/non-significant
6	0.56/significant	0.85/significant	0.29/significant	0.17/non-significant	0.35/significant	0.37/significant	0.82/significant	0.13/significant

TABLE 4 The correlation between annual and inter-annual precipitation and standardized flow index (SDI) at different time scales.

Time interval	The correlation coefficient/ significance of annual precipitation-SDI$_1$	The correlation coefficient/ significance of annual precipitation-SDI$_3$	The correlation coefficient/ significance of annual precipitation-SDI$_6$	The correlation coefficient/ significance of annual precipitation-SDI$_{12}$	The correlation coefficient/ significance of inter-annual precipitation-SDI$_1$	The correlation coefficient/ significance of inter-annual precipitation-SDI$_3$	The correlation coefficient/ significance of inter-annual precipitation-SDI$_6$	The correlation coefficient/ significance of inter-annual precipitation-SDI$_{12}$
1	0.61/significant	0.29/significant	0.18/non-significant	−0.42/non-significant	0.68/significant	0.21/significant	−0.43/significant	−0.41/significant
2	0.77/significant	0.36/non-significant	0.16/significant	0.51/significant	0.76/significant	0.37/significant	−0.31/significant	0.59/significant
3	0.83/significant	0.48/significant	−0.31/significant	−0.68/significant	0.85/significant	0.36/non-significant	−0.37/significant	−0.50/significant
4	0.68/significant	0.39/significant	−0.18/significant	0.46/significant	0.86/significant	0.39 significant	−0.47/significant	0.55/non-significant
5	0.86/significant	0.30/significant	0.19/significant	−0.51/non-significant	0.83/significant	0.21/non-significant	−0.25/significant	−0.66/significant
6	0.76/significant	0.55/non-significant	0.18/non-significant	−0.57/significant	0.75/significant	0.27/significant	−0.22/significant	0.63/significant

drought are staged, which provides a basis for further research on the stage characteristics of multi-type response relationships.

3.2 Evolution characteristics of meteorological elements

Taking temperature and precipitation as meteorological elements, the evolution characteristics of annual and inter-annual are studied by linear regression method and Mann-Kendall trend test method. Figure 5 is the trend of precipitation change in the four seasons of the year. Figure 6 is the trend of temperature change in the four seasons of the year. Table 2 is the trend characteristics and significance of annual and inter-annual precipitation and temperature.

It can be seen from Figure 5 that the linear change rate of precipitation during the year is the largest in summer, 2.2 mm/a, −1.2 mm/a in autumn and 0.7 mm/a in winter. Due to the influence of the monsoon, the summer precipitation changes dramatically. The maximum precipitation (931.4 mm) is 3.7 times of the minimum precipitation (249.3 mm). The precipitation in spring also changes greatly. The maximum precipitation (890.0 mm, 1975) is 2.4 times of the minimum precipitation (365.9 mm, 2007). The variation of seasonal precipitation in autumn and winter is small, ranging from 50 to 400 mm. It can be seen from Figure 6 that the average temperature difference in the four seasons is small. The average temperature in spring and autumn is close to 17°C, the average temperature in summer is 26.9°C, and the average temperature in winter is 6.9°C. The overall temperature of the four seasons shows an upward trend, and the upward trend of winter temperature is the most obvious, with a linear change rate of 0.20°C/10a.

It can be seen from Table 2 that except for summer, the annual temperature in other seasons has passed the significance test of 0.10, and the rising trend of temperature in spring and winter is more obvious. The precipitation during the year showed a decreasing trend in spring and autumn, and an increasing trend in summer and winter. Except for spring, the other seasons passed the significance test of 0.20. The average annual temperature was 17.3°C, and the average annual maximum temperature (18.4°C) and the average annual minimum temperature (16.2°C) appeared in 2007 and 1984, respectively. The overall annual average temperature showed an upward trend, with a linear change rate of 0.13°C/10a, and the upward trend passed the significance test of 0.05. The annual average annual precipitation was 1515 mm. The annual maximum precipitation (2121.9 mm) and the annual minimum precipitation (1118.3 mm) appeared in 2002 and 1963, respectively. The range multiple was 1.9 times, and there was no significant change trend in general.

4 Response relationship between hydrological drought and meteorological factors

4.1 Multi-type response relationship analysis

Pearson correlation coefficient is used to represent the correlation between annual and inter-annual climatic factors (temperature, precipitation) and multi-time scale Standardized flow index (SDI), and the correlation between the two is verified by significance test. Table 3 is the correlation status of annual and inter-annual temperatures with Standardized flow index (SDI) at different time scales, and Table 4 is the correlation status of annual and inter-annual precipitation with Standardized flow index (SDI) at different time scales.

It can be seen from Tables 3, 4 that on the whole, the correlation intensity of all periods in each type is basically the same, and most of them conform to the significant test. The following analysis will regard the six periods as a whole. It can be seen from Table 3 that the correlation between annual temperature and SDI_1, SDI_3, SDI_6 and SDI_{12} is moderate positive correlation, strong positive correlation, weak positive correlation and moderate negative correlation, respectively. Among them, the correlation between annual temperature and SDI at 3-month scale is the strongest, and it passes the significance level test. It shows that with the increase of time scale, the annual temperature is the most sensitive to SDI at 3-month scale, and the response period of hydrological drought to annual temperature is 3 months. At the same time, the correlation between annual temperature and SDI_1, SDI_3, SDI_6, SDI_{12} was weak or irrelevant, moderate positive correlation, strong positive correlation, extremely weak or irrelevant, respectively. Among them, the correlation between annual temperature and SDI at 6-month scale was the strongest, which passed the significance test, indicating that the annual temperature was most sensitive to SDI at 6-month scale, and the response period of hydrological drought to annual temperature was 6 months.

It can be seen from Table 4 that the correlation between annual precipitation and SDI_1, SDI_3, SDI_6 and SDI_{12} is strong positive correlation, weak or moderate positive correlation, weak negative or irrelevant, moderate negative correlation, respectively. Among them, the correlation between annual precipitation and SDI at 1-month scale is the strongest, which has passed the significance level test. The annual precipitation is most sensitive to SDI at 1-month scale, that is, the response period of annual precipitation to SDI at 1-month scale is 1 month, and the response duration is short and the influence is strong. The correlation between annual precipitation and SDI_1, SDI_3, SDI_6, SDI_{12} were strong positive correlation, weak positive correlation, weak or moderate negative correlation, moderate or strong negative correlation, respectively. The correlation between annual precipitation and SDI at 1-month scale was the strongest, which passed the significance test. Inter-annual precipitation was also most sensitive to SDI at 1-month scale. The response period of annual precipitation to SDI at 1-month scale was 1 month. Precipitation has a great influence on hydrological drought, and the response period is short.

4.2 Discussion

Based on the monthly temperature, precipitation and flow data from 1959 to 2010, this paper divides six periods to study the response of hydrological drought to meteorological factors. The correlation strength of each period is consistent, and the significance in each type is significant as a whole. It shows that the correlation between meteorological element data sequence (temperature, precipitation) and hydrological drought index sequence (SDI) is strong. Therefore, it can accurately verify the correlation degree of multi-type response relationship and scientifically evaluate the response characteristics of hydrological drought to meteorological factors.

The response periods of annual temperature and inter-annual temperature to hydrological drought were 3 months and 6 months, respectively, which passed the significance test. From the annual scale to the inter-annual scale, the sensitivity of drought response weakened, so the response period also became longer. The response period of annual precipitation and inter-annual precipitation to hydrological drought is 1 month. Precipitation has a direct and main influence on hydrological drought, and the response of hydrological drought is affected by multi-level and multi-directional complex effects (such as underlying surface changes, accelerated urbanization, etc.). At the same time, there are differences in spatial and temporal characteristics in different regions, so the response period of annual precipitation and inter-annual precipitation to hydrological drought is short.

Among the data studied in this paper, the years with higher temperature are 1963 (17.99°C), 1998 (18.24°C) and 2007 (18.38°C), and the years with less precipitation are 1963 (1118.3 mm), 1971 (1204.4 mm), 1986 (1237.0 mm) and 2003 (1171.9 mm). According to the records of "China Meteorological Disaster Canon · Hunan Volume," "China Water Disaster Prevention: Strategy, Theory and Practice · Drought Disaster Prevention" and "Yearbook of Meteorological Disasters in China," serious drought events occurred in the above mentioned years. Therefore, based on the results of series of data calculation, this paper can scientifically reflect the rationality of the evolution characteristics of meteorological elements and the evolution law of hydrological drought, and then can accurately obtain the response relationship between hydrological drought and meteorological elements, and provide scientific value for the study of drought evolution and transmission in the region.

5 Conclusion

Based on the evolution characteristics and laws of meteorological elements and hydrological drought, this paper analyzes and studies the response of hydrological drought to meteorological elements in the area above Xiangtan station. The correlation of six periods in each type is basically the same. The response periods of annual temperature and inter-annual temperature to hydrological drought were 3 and 6 months, respectively. The response periods of annual precipitation and inter-annual precipitation to hydrological drought were both 1 month. The correlation coefficients reached the strongest positive correlation and passed the significance test. By scaling meteorological elements and hydrological drought indicators, the response characteristics of hydrological drought to climate factors can be fully reflected through the analysis of multi-type response relationships. The area above Xiangtan station needs to plan drought response measures and drought forecast plan in 1, 3, and 6 months of drought response period. With global warming, the drought response period will be shortened, and the trend of shortening will increase the frequency of drought. The decision-making departments of drought prevention and disaster reduction need to adjust the drought relief plan in time to improve the efficiency and level of drought control. The results of this paper provide a favorable value for the study of drought response and drought remediation in the region. However, in practice, the propagation and response of drought are affected by multiple factors and multi-level interference and influence, and the driving factors of drought response can be further studied in the future.

Data availability statement

The datasets presented in this article are not readily available because Data is confidential. Requests to access the datasets should be directed to https://www.resdc.cn/NewsInfo.aspx?NewsID=9; http://www.dsac.cn/DataProduct/Detail/200800; http://data.cma.cn/.

Author contributions

FW: Writing–original draft, Conceptualization. WH: Conceptualization, Writing–original draft. QL: Writing–original draft, Investigation, Supervision. WW: Writing–original draft, Supervision. GW: Writing–original draft, Formal Analysis, Investigation. FZ: Writing–original draft, Methodology.

Funding

The authors declare financial support was received for the research, authorship, and/or publication of this article. The Research was Supported by the Open Research Fund of Science and Technology Innovation Platform of Engineering Technology Research Center of Dongting Lake Flood Control and Water Resources Protection of Hunan Province, Hunan Water Resources and Hydropower Survey, Design, Planning and Research Co., Ltd (HHPDI-KFKT-202304); Water Resources Science and Technology Program of Hunan Province (XSKJ2021000-05); Water Resources Science and Technology Program of Hunan Province (XSKJ2023059-06); Open Fund of Key Laboratory of Flood & Drought Disaster Defense, the Ministry of Water Resources (KYFB202307260036); Major Science and Technology Special Projects in Henan Province (201300311400).

Conflict of interest

The authors declare that the research was conducted in the absence of any commercial or financial relationships that could be construed as a potential conflict of interest.

Publisher's note

References

Comprehensive Planning of Xiangjiang River Basin (2015). *Changsha: hunan water resources and hydropower Survey, Design*. Planning and Research CO., LTD. Available at: http://www.hunan.gov.cn/hnszf/xxgk/fzgh/201403/t20140304_4902771.html.

Dai, A., and Zhao, T. (2017). Uncertainties in historical changes and future projections of drought. Part I: estimates of historical drought changes. *Clim. Change* 144 (3), 519–533. doi:10.1007/s10584-016-1705-2

Development Planning Office of Hunan Development and Reform Commission (2013). *Overall plan for scientific development of Xiangjiang River Basin*. http://www.hnfgw.gov.cn/hgzh/qygh/37668.html.

Gu, G., Li, H., and Huo, S. (2023). Analysis of evolution characteristics of meteorological drought in fuxian lake basin from 1964 to 2021. *Pearl River* 44 (S1), 27–32. doi:10.3969/j.issn.1001-9235.2023.S1.006

Jiang, Z., Xu, G., and Zhang, K. (2023). Spatiotemporal variation and bivariate regional frequency analysis of meteorological droughts inGuizhou Province based on SPEI. *J. Water Resour. Water Eng.* 34 (05), 20–31. doi:10.11705/j.issn.1672-643X.2023.05.03

Li, L., Lu, T., Liu, M., Hu, L., and Wang, S. (2020b). Characteristics of hydrological drought based on standardized flow index in Shiyang River Basin of China. *J. Desert Res.* 40 (04), 24–33. doi:10.7522/j.issn.1000-694X.2020.00010

Li, M., Cao, F., Wang, G., Chai, X., and Zhang, L. (2020a). Evolutional characteristics of regional meteorological drought and their linkages with southern oscillation index across the loess plateau of China during 1962–2017. *Sustainability* 12 (18), 7237. doi:10.3390/su12187237

Liang, X., Yuan, S., and Wang, J. (2023). Progress and prospects of research on causes of meteorological drought in different regions in China. *J. Arid Meteorology* 41 (01), 1–13. doi:10.11755/j.issn.1006-7639

Ling, M., Guo, X., Zhang, Y., Yu, L., and Xia, Q. (2023). Drought evolution in the Haihe River basin during 1960–2020 and the correlation with global warming, sunspots, and atmospheric circulation indices. *J. Water Clim. Change* 14 (1), 369–386. doi:10.2166/WCC.2022.510

Liu, Q. (2020). *Study on the impact of climate variability and human activities on the shortage of blue/green water resources in the Xiangjiang River Basin based on SWAT model*. Changsha, China: Hunan University. doi:10.27135/d.cnki.ghudu.2020.004009

Lu, T., and Li, L. (2020). Study on hydrological drought characteristics in the middle reaches of Shiyang River Basin based on SDI. *Agric. Science-Technology Inf.* (06), 41–43. doi:10.15979/j.cnki.cn62-1057/s.2020.06.019

Luo, Y. (2020). *Satellite-based soil moisture and precipitation for drought monitoring and prediction in Xiang River Basin*. Dhaka, Bangladesh: Southeast University. doi:10.27014/d.cnki.gdnau.2020.002509

Luo, Y. (2022). *Drought monitoring in Xiangjiang River Basin based on remote sensing soil moisture and remote sensing precipitation*. Southeast University. doi:10.27014/d.cnki.gdnau.2020.002509

Ribeiro Neto, G. G., Melsen, L. A., Martins, E. S. P. R., Walker, D. W., and van Oel, P. R. (2022). Drought cycle analysis to evaluate the influence of a dense network of small reservoirs on drought evolution. *Water Resour. Res.* 58 (1). doi:10.1029/2021WR030799

Tian, Q., Fei, W., Yu, T., Yunzhong, J., Peiyao, W., and Jinbei, L. (2023). Copula-based comprehensive drought identification and evaluation over the Xijiang River Basin in south China. *Ecol. Indic.*, 154. doi:10.1016/j.ecolind.2023.110503

Wang, X., Tao, P., Ying, B. X., Bojuan, L., Xiaohua, D., Jiali, G., et al. (2023). Evolution characteristics of hydrological drought in the middle reaches of the Han River before and after Danjiangkou reservoir. *Resour. Environ. Yangtze Basin* 32 (07), 1479–1490. doi:10.11870/cjlyzyyhj202307011

Wen, X., Zhou, J., Liu, S., Ma, Y., Xu, Z., and Ma, J. (2021). Spatio-temporal characteristics of surface evapotranspiration in source region of rivers in Southwest China based on multi-source products. *Water Resour. Prot.* 37 (03), 32–42. doi:10.3880/j.issn.1004-6933.2021.03.006

Wu, Z., Zhang, J., Cheng, D., Fan, S. Q., He, H., and Li, Y. (2023). Study of comprehensive drought in dex based on water deficits of surface, soil, and crop. *Water Resour. Prot.* 39 (03), 55–64. doi:10.3880/j.issn.1004-6933.2023.03.007

Xu, C. (2014). *The spatial and temporal features of drought in the five provinces of southwest China from 1961 to 2012*. Nanjing, China: Nanjing Agricultural University. doi:10.7666/d.Y2974372

Zhang, Q., Yao, Y., Li, Y., Huang, J., Ma, Z., Wang, Z., et al. (2020). Causes and changes of drought in China: research progress and prospects. *J. Meteorological Res.* 34 (3), 460–481. doi:10.1007/s13351-020-9829-8

Zheng, J., Zuhao, Z., Jiajia, L., Ziqi, Y., ChongYu, X., Yunzhong, J., et al. (2023). A novel framework for investigating the mechanisms of climate change and anthropogenic activities on the evolution of hydrological drought. *Sci. total Environ.*, 900. doi:10.1016/j.scitotenv.2023.165685

TYPE Original Research
PUBLISHED 04 April 2024
DOI 10.3389/fenvs.2024.1392768

OPEN ACCESS

EDITED BY
Xudong Huang,
North China University of Water Conservancy and Electric Power, China

REVIEWED BY
Yuzhuang Chen,
China Institute of Water Resources and Hydropower Research, China
Lixia Niu,
Sun Yat-sen University, China

*CORRESPONDENCE
Libin Yang,
✉ slqnbjrc@126.com

RECEIVED 28 February 2024
ACCEPTED 21 March 2024
PUBLISHED 04 April 2024

CITATION
Liu B, Yang L, Cui C, Wan W and Liang S (2024), Is water replenishment an effective way to improve lake water quality? Case study in Lake Ulansuhai, China.
Front. Environ. Sci. 12:1392768.
doi: 10.3389/fenvs.2024.1392768

Is water replenishment an effective way to improve lake water quality? Case study in Lake Ulansuhai, China

Bojun Liu[1,2], Libin Yang[1,2]*, Changyong Cui[1], Weifeng Wan[1,2] and Shuntian Liang[1]

[1]Yellow River Engineering Consulting Co., Ltd., Zhengzhou, China, [2]Key Laboratory of Water Management and Water Security for Yellow River Basin, Ministry of Water Resources, Zhengzhou, China

Lakes are an important component of the global water cycle and aquatic ecosystem. Lake water quality improvement have always been a hot topic of concern both domestically and internationally. Noncompliant outflow water quality frequently occurs, especially for lakes that rely mainly on irrigation return flow as their water source. External water replenishment to improve the water quality of lakes is gradually being recognized as a promising method, which however, is also a controversial method. Lake managers, in the case of constant controversy, hesitate about the appropriateness of lake water replenishing. Thus, taking Lake Ulansuhai in China as an example, this study aimed to construct a lake hydrodynamic and water quality model, under the constraint of multiple boundary conditions, that has sufficient simulation accuracy, and to simulate and analyze the changes in COD (Chemical Oxygen Demand) and TN (Total Nitrogen) concentrations in the lake area before and after water replenishment, and explore whether water replenishment was an effective method for improving lake water quality. The results showed that when the roughness value of Lake Ulansuhai was 0.02, the TN degradation coefficient K was 0.005/d, and the COD degradation coefficient K was 0.01/d; the simulation and measured values had the best fit, and the built model is reasonable and reliable can be used to simulate lake water quality changes. By external water replenishment lasting 140 days in the water volume of 4.925 × 108 m^3, the COD and TN concentrations in Lake Ulansuhai could be stabilized at the Class V water quality requirement, which helped improve the self-purification ability of the lake area. Water replenishment was proved to be an effective method for improving the water quality of the lake, but water replenishment is only an emergency measure. Lake water replenishment is more applicable to areas with abundant water resources. External source control and internal source reduction of lake pollution and protection of lake water ecology are the main ways to improve lake water quality for water-deficient areas under the rigid constraints of water resources. In the future, key technologies for reducing and controlling pollution in irrigation areas, construction of lake digital twin platforms, and active promotion of lake legislation work should be the main research direction for managing the lake water environment.

KEYWORDS

water replenishing, modeling, water quality simulation, effect evaluation, lake management, Lake Ulansuhai

1 Introduction

Lakes are an important component of the ecosystem, playing an irreplaceable role in flood control, water resource regulation, water quality purification, wetland protection, maintenance of biodiversity, local climate regulation, and ecological landscape. They have become a key link in maintaining the health of the regional ecological environment and providing a foundation for human survival and socioeconomic development (Karlsson et al., 2009; Vitense et al., 2019; Liu et al., 2021a). Lakes worldwide are experiencing water shortage, water quality deterioration, and algal blooms under the combined influence of climate change and human activities. Most water pollution in lakes is related to the input of substances such as nitrogen, phosphorus, and salt under human activities (Ho et al., 2019; Geng et al., 2021). Problems such as less precipitation, high evaporation, and insufficient inflow often occur due to the limitation of climatic conditions, especially in lakes located in arid and semi-arid areas (Wu et al., 2017; Fu et al., 2021). Some lakes lack stable and high-quality water sources due to poor water system connectivity, resulting in insufficient water dynamics and low self-purification ability (Huser et al., 2016; Rosińska et al., 2018; Liu et al., 2021b). Meanwhile, with the continuous increase in population, the inflow of agricultural drainage, domestic sewage, and industrial wastewater into lakes has exacerbated eutrophication, caused the degradation of water ecological functions, and created a poor lake water environment (Lürling and Oosterhout, 2013; Schindler et al., 2016; Vinçon-Leite and Casenave, 2019). Currently, lakes globally are encountering significant environmental issues related to water such as declining water quality, worsening eutrophication, decreasing biodiversity, and coastal environmental damage. Improving the quality of lake water and preventing and controlling the damage to lake water ecosystems are urgent issues that have attracted the attention of scholars at home and abroad (Song et al., 2014; Hu et al., 2020; Li et al., 2022).

For large lakes, the real-time monitoring of hydrodynamic conditions and pollutant concentrations in the lake area is difficult to achieve. Numerical simulations of hydrodynamic processes and pollutant concentrations in lakes are an important strategy for exploration (Shen et al., 1995; Parinet et al., 2004; Lai et al., 2013; Munar et al., 2018). Hydrodynamic processes are an essential basis for the transport and transformation of pollutants in lakes and are closely related to the water inflow. Different inflow rates can change the movement trajectory of lake water, thereby affecting the circulation morphology, structure, and flow velocity distribution in the lake area, ultimately affecting the water quality of the lake (Na and Park, 2006). Steinman et al. (2002) found that low flow rates positively affected the process of algal enrichment. Therefore lake water replenishment has become a way to alleviate water quality deterioration. For example, Green Lake in the United States has reduced the nutrient concentration in the lake area and balanced the content of planktonic algae by introducing water into the lake, thus improving the eutrophication level of the lake (Oglesby, 1969). In The Netherlands, the water quality of the Veluwemeer Lake has significantly improved after implementing a water system connection project that regulates the inflow of water into the lake area (Hosper, 1998). In the United States, the hydrodynamic processes in the lake area were strengthened, the self-purification capacity of the lake area was improved, and the degradation trend of the wetlands around the lake area was curbed by introducing Mississippi River water into Lake Pontchartrain (Lane et al., 2001). The hydrodynamic ecological model analysis of Lake Manzala in Egypt found that the significant changes in the water quality of the lake over the past 30 years were closely related to the changes in the inflow of fresh water and land use (Rasmussen et al., 2009). After introducing other water sources, the high-quality population of algae in the Tega Lake in Japan has undergone significant changes, which has played a positive role in improving the water quality of the lake area (Amano et al., 2010). The North-South Water Transfer Project in the United States and the West-East Water Transfer Project in Pakistan have both improved the water quality of the lakes in the receiving areas by introducing a large amount of clean water through dilution and hydrodynamic strengthening (Manghi et al., 2012). Some studies have shown that water transfer has a significant impact on the quality of lake water and can be simulated and calculated using models (Feng et al., 2017; Peng et al., 2020)]. Research on Lake Arrowhead in California, USA, revealed that the changes in precipitation processes could affect the water quality of the lake by changing the water level of the lake (Saber et al., 2020). In China, the Yangtze River-Taihu Lake Water Transfer Project (supplementing Taihu Lake with water from the Yangtze River through the Wangyu River), the Yellow River-Jide Water Transfer Project (introducing water from the Yellow River to supplement Baiyangdian), and the Niulanjiang-Dianchi Lake Water Replenishment Project (introducing water from the Niulanjiang River to supplement Dianchi Lake) have all improved the self-purification capacity of the water body and achieved the comprehensive management goal of the water environment in the lake area (Huang et al., 2015; Wu et al., 2018; He et al., 2020).

Although the lake water quality has been improved successfully through water replenishment both domestically and internationally, the situation of each lake is different. Lakes with low pollution levels or strong water dynamics or with sufficient water volume and high self-purification ability may achieve the goal of improving water quality through short-term water replenishment (Zhang et al., 2012). However, the response of the aquatic ecosystems to the changes in water volume is very sensitive for large shallow lakes or lakes with water resources exceeding the water quality standard, especially shallow lakes with shallow water, weak water dynamics, and complex patterns (Qing et al., 2020). The migration process of pollutants in the lake has a certain time lag effect on the changes in water volume (Liu et al., 2021b), which increases the difficulty of predicting the effect of water replenishment on improving the water quality. Whether water replenishment can really improve the water quality of the lake is a key issue worthy of further research and has practical application value for the protection and restoration of lake ecosystems. Lake Ulansuhai in China is a typical agricultural water retreat lake and closely connected with the Yellow River, in which the hydrodynamic and water quality conditions are complicated. Lake water replenishing has potential effects on pollutant diffusion process and then may causes the polluted water flowing into the Yellow River. It has always been a controversial issue, in recent years, how well does the ecological water replenishment for Lake Ulansuhai works? Is this a temporary measure or a long-term measure to improve lake water quality? The above questions make water resources and water environment management of Lake Ulansuhai more difficult. Thus, Taking the large shallow Lake Ulansuhaias an example, this study aimed to construct a lake hydrodynamic and water quality model, under the constraint of multiple boundary conditions, that has sufficient

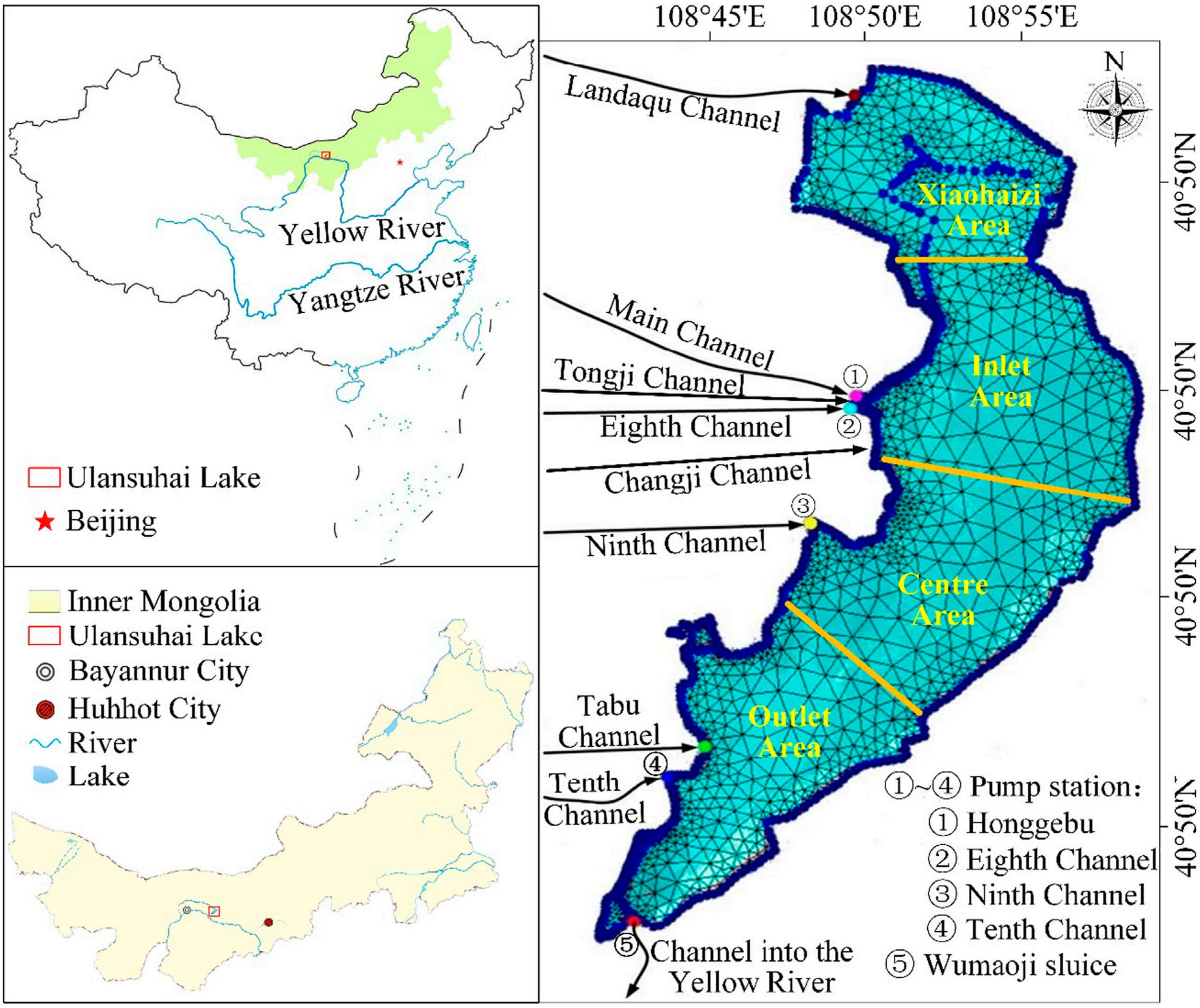

FIGURE 1
The location of Lake Ulansuhai and its key water network.

simulation accuracy, and to simulate and evaluate the effect of different water replenishment schemes on improving lake water quality, and explore the effectiveness and timeliness of water replenishment, so as to provide a reference for comprehensive lake management.

2 Study area

Lake Ulansuhai is one of the eight major freshwater lakes in China, located in Bayannur City, Inner Mongolia (seen in Figure 1). It is situated in a cold and arid region of China, and is a river trace lake formed by the diversion of the Yellow River. It has multiple ecological functions such as water storage for flood control, agricultural irrigation, tourism, and aquaculture. It mainly receives drainage, precipitation, and mountain floodwater from the Hetao Irrigation District and is a typical large shallow lake (Mao et al., 2015). It is also a rare large multifunctional lake in the arid grasslands and desert areas of the world. The geographical coordinates of Lake Ulansuhai are 40°36′–41°03′N, 108°43′–108°57′E, with a storage capacity of 250–350 million m^3 and a total water area of approximately 293 km^2. The measured average water depth is about 1.53 m.

Lake Ulansuhai is long and narrow in shape, resembling a crescent moon, with a length of 35–40 km from north to south and 5–10 km from east to west. More than 90% of the water supply for Lake Ulansuhai comes from agricultural drainage, followed by industrial wastewater, domestic sewage, rainfall, and surface runoff. All of the water sources are collected through various channels, which then flow into the main channel, second channel, third channel, fourth channel, fifth channel, sixth channel, seventh channel, Zhaosha channel, and Yitong channel before entering the main drainage channel. From there, the water flows through the eighth channel, ninth channel, tenth channel, Tongji channel, and Tabu channel before entering Lake Ulansuhai. Finally, the water flows through the Wumaoji sluice and enters the Yellow River (Figure 1).

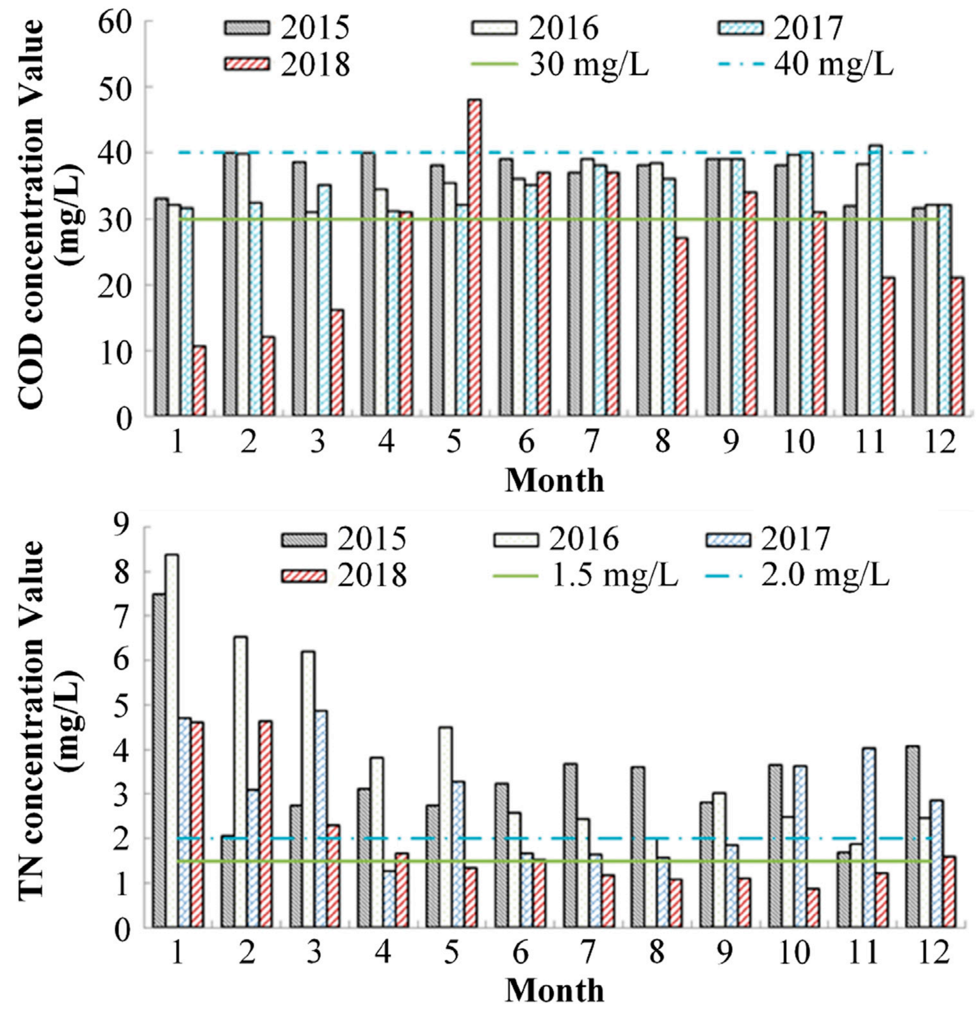

FIGURE 2
Variation characteristics of COD and TN concentration at the Wumaoji sluice.

It can be found that, through the analysis of COD (Chemical Oxygen Demand) and TN (Total Nitrogen) concentration changes at the Wumaoji sluice, in 2015~2018, the average concentration value of COD and TN is 33.90 mg/L and 3.01 mg/L, respectively, the water quality of lake water into the Yellow River in 2018 was worse than that in 2016~2017 (seen in Figure 2), and TN pollution was such a serious problem that it has aroused concerns from the whole society. Meanwhile, the monthly average values of COD and TN concentration showed an unstable state. The high-quality water in the Yellow River has been affected by polluted water from Lake Ulansuhai.

3 Method and data

3.1 Hydrodynamic and water quality model

Considering the unclear hydrodynamic characteristics of Lake Ulansuhai, a two-dimensional hydrodynamic and water quality model was used to simulate the dynamic changes in pollutant transport, diffusion, and degradation under different inflow conditions in the lake area. Based on the topographical features of Lake Ulansuhai, the vertical variation of the lake was ignored, and it was assumed that the hydrodynamic pressure along the water depth followed the distribution of fluid static pressure (Liu et al., 2021b). The two-dimensional depth-averaged hydrodynamic equation of Lake Ulansuhai could be expressed as follows:

$$\frac{\partial \zeta}{\partial t} + \frac{\partial (Hu)}{\partial x} + \frac{\partial (uv)}{\partial y} = 0 \tag{1}$$

$$\frac{\partial u}{\partial t} + g\frac{\partial \zeta}{\partial x} + \frac{\partial u^2}{\partial x} + \frac{\partial uv}{\partial y} + \frac{gu\left(u^2+v^2\right)^{1/2}}{HC^2} - \frac{A_x}{p}\left(\frac{\partial^2 u}{\partial x^2} + \frac{\partial^2 u}{\partial y^2}\right) - fv - f_W|W|W_x = 0 \tag{2}$$

$$\frac{\partial v}{\partial t} + g\frac{\partial \zeta}{\partial y} + \frac{\partial v^2}{\partial x} + \frac{\partial uv}{\partial x} + \frac{gu\left(u^2+v^2\right)^{1/2}}{HC^2} - \frac{A_y}{p}\left(\frac{\partial^2 v}{\partial x^2} + \frac{\partial^2 v}{\partial y^2}\right) - fu - f_W|W|W_y = 0 \tag{3}$$

$$H = \zeta + h \tag{4}$$

Where ζ is the lake water level, m; f is the Coriolis force coefficient, and $f = 2\omega\sin\varphi$; h denotes the lake water depth, m; u and v represent mean flow velocity component in the x and y direction, respectively,

m^3/s; C is the Chezy coefficient, $C = 1/n(\zeta+h)^{1/6}$, in which n is the roughness coefficient; f_W represents the wind resistance coefficient; A_x and A_y are the eddy viscosity coefficient in the x and y direction; p is the static pressure, Pa; t is the time, s; W is the wind speed 10 m above the water surface; W_x and W_y are the wind speed component in the x and y direction, m/s; C_d is the wind drag stress coefficient, g is the acceleration of gravity; τ_{xx}, τ_{yx} and τ_{xy} represent the shear stress corresponding to 0°, 45°, 90° of the x-y coordinate axis (Liu et al., 2021b; Liu et al., 2021c).

The lake water quality equation is expressed as follows:

$$\frac{\partial Hp}{\partial t} + \frac{\partial Hup}{\partial x} + \frac{\partial Hvp}{\partial y} = \frac{\partial}{\partial x}\left(HD_x\frac{\partial p}{\partial x}\right) + \frac{\partial}{\partial y}\left(HD_y\frac{\partial p}{\partial y}\right) + kHF(p) + S \tag{5}$$

Where p denotes the concentration of a pollutant, mg/L; k represents the lake degradation coefficient, s^{-1}. The left side of the equal sign of Eq. 5 is the time-varying term, the advection terms in the x and y directions, respectively. The right side of Eq. 5 indicates the diffusion term, biochemical reaction term in the x and y directions, respectively. S represents the lake pollution load, $g/(m^2 \cdot s)$ (Liu et al., 2021b; Liu et al., 2021c).

Detailed solving procedures for the above models can be seen in our published articles (Liu et al., 2021b; Liu et al., 2021c).

3.2 Used data

Daily water level data of the Honggebu station and Wumaoji sluice in 1985~2019; Daily inflow data of the Eighth, Ninth, Tenth channels in 1985~2019; And daily pollutant concentration data of COD and TN in the Inlet area, Centre area, Outlet area from 2014 to 2019 are all collected from the Water Conservancy Development Center of the Hetao Irrigation District and the Water Resources Bureau of Bayannur City in Inner Mongolia.

4 Modelling

4.1 Boundary condition

The boundary of Lake Ulansuhai included the Honggebu station, the Eighth, Ninth, and Tenth channels, the Xin'an branch channel, and the Wumaoji sluice. A new Landaqu pumping station was planned to be built. The drainage of the Honggebu station entered the lake, while the drainage of the Tenth channel flowed into the main lake area after 8 km northward through the southwest side of the lake. The lake boundary was set to 0 in the model calculation due to its non-sliding condition. The daily water-level data of the Honggebu station and the daily inflow data of the Eighth, Ninth, and Tenth channels from 1985 to 2019 were selected as the outflow boundary of the two-dimensional hydrodynamic model of Lake Ulansuhai, while the other rivers and channels were ignored. The COD and TN were chosen as the characteristic pollutants of the lake, and the COD and TN monitoring concentrations in the inlet and outlet areas of Lake Ulansuhai from 2014 to 2019 were used as the upper and lower boundaries of the water quality model. The diversion dike and grid waterway constructed in the lake area were generalized as hydraulic structures in the model, and the water loss of Lake Ulansuhai was set to 2.73 mm/d.

4.2 Initial condition

Lake Ulansuhai has a large surface area, shallow average depth, and a winding shoreline with many tributaries flowing into it. Moreover, many water conservancy projects, such as dams, bridges, and channels, are also found in the lake area. The model used nonstructured mesh coupling triangles and rectangles to achieve better simulation results. A simulation area of 329.4 km^2 was chosen for Lake Ulansuhai, with a grid spacing of 300–500 m for the water catchment and lakeshore areas, and 100–200 m for the grid spacing. The simulation grid accuracy was controlled within 1 km^2, and Lake Ulansuhai was divided into 3276 calculation grids (Figure 1). The stability and accuracy of the model was ensured by setting the calculation time to $\triangle t = 60$ s, the simulation step to 21,600 s, and the water-level starting condition to 1,019.48 m.

The initial water level of Lake Ulansuhai was set at the mean water level of 1,018.79 m (Yellow Sea elevation), and the average water depth was set at the mean water depth of 1.0 m. The initial values of COD and TN were set at the concentration mean values of 33.90 mg/L and 3.01 mg/L, respectively, and the initial flow rate was 0. We set the dry water depth (h_{dry}) at 0.005 m, the flooded water depth(h_{flood}) at 0.05 m, and the wet water depth (h_{wet}) at 0.1 m to avoid instability in the model calculation because Lake Ulansuhai was located at the boundary between wet and dry areas in the model. The eddy viscosity coefficient was estimated using the Smagorinsky formula, and the corresponding Smagorinsky coefficient was set at 0.28 m^2/s. The initial roughness values for the clear water area and the reed area in the lake were set at 32 $m^{1/3}/s$ and 3.7 $m^{1/3}/s$, respectively. The water depth of Lake Ulansuhai was shallow, ranging from 0.7 m to 4.0 m, and was influenced by wind-induced currents (Wang et al., 2021). Based on previous research, the wind speed in the lake area was set at 2.6 m/s, with a southwesterly wind direction. In the water quality model, the pollution sources entering the lake were generalized as point sources.

4.3 Model calibration and validation

The relative error (RE), certainty coefficient (R^2), and Nash coefficient (E_{NS}) were used to evaluate the simulation effect of the Lake Ulansuhai hydrodynamic and water quality model (Liu et al., 2021b; Liu et al., 2021c). Generally, when the RE was ±20%, the simulation results of the model were acceptable. The closer the R^2 was to 1, the higher the degree of agreement between the measured and simulated values. The closer the E_{NS} was to 1, the higher the credibility of the model. The hydrodynamic model was calibrated and validated using daily flow data from the Honggebu station and daily water-level data from the Wumaoji sluice. The water quality model was calibrated and validated using COD and TN concentration data from the inlet, central, and outlet areas. Table 1 shows that when the roughness value of Lake Ulansuhai was 0.02, the TN degradation coefficient K was 0.005/d, and the COD degradation coefficient K was 0.01/d; the simulation and

TABLE 1 Results of model calibration and validation.

Index		Location	Calibration period			Validation period		
			RE(%)	R^2	E_{NS}	*RE*(%)	R^2	E_{NS}
Hydrodynamic	Flow	Honggebu station	0.03	0.90	0.86	−4.63	0.70	0.69
	Water level	Wumaoji sluice	−5.48	0.89	0.78	6.74	0.81	0.69
Water quality	COD	Inlet area	−6.83	0.76	0.84	−6.91	0.71	0.70
		Center area	−6.22	0.80	0.85	7.78	0.69	0.77
		Outlet area	5.48	0.80	0.73	8.62	0.73	0.80
	TN	Inlet area	−5.05	0.75	0.70	6.19	0.76	0.71
		Center area	−0.04	0.74	0.87	12.99	0.80	0.77
		Outlet area	2.05	0.80	0.86	15.07	0.74	0.73

measured values had the best fit. The *RE*s between the simulated and measured values of the Honggebu station flow, Wumaoji sluice water level, and pollutant concentration were all within 10%, and the R^2 and E_{NS} values were both greater than 0.78, indicating that the model parameters were reasonable. In addition, the *RE*s of the model's flow, water level, and pollutant concentration simulations were within ±20%, with a maximum value of 15.07%. The R^2 and E_{NS} values were greater than 0.69, and the errors were within an acceptable range, indicating that the Lake Ulansuhai hydrodynamic and water quality model was reliable and could be used to simulate the water quality changes in the lake area.

5 Results and discussion

5.1 Results

Two lake water replenishment schemes were set up: Scheme 1 did not replenish water throughout the year; Scheme 2 replenished 4.925×10^8 m^3 of water into the lake through the Main Channel and Landaqu Channel (according to the research results of the Yellow River Engineering Consulting Co., Ltd, the lake needed to be replenished with a net water volume of 4.925×10^8 m^3 to meet the requirements of lake pollution purification and salt dilution), with 3.740×10^8 m^3 of water replenished through the Main Channel and 1.185×10^8 m^3 of water replenished through the Landaqu Channel. COD and TN were used as pollution indicators employing a simulated duration of 365 days/year, and the constructed model was used for simulation analysis. According to the lake management requirements, the water quality is considered to meet the requirements when the COD and TN concentrations at the outlet of Lake Ulansuhai reach Class V standards in China's Environmental quality standards for surface water (GB 3838-2002) (Table 2).

5.1.1 Scheme 1

Of the 365 days, Lake Ulansuhai met the surface water Class IV standard for COD concentration for 104 days, met the surface water Class V standard for COD concentration for 24 days, and was in the inferior Class V for COD concentration for the remaining days. Using Lake Ulansuhai's water discharge as the evaluation standard for surface water Class V, the annual COD exceedance rate was 64.93%, making it difficult to meet the requirements for entering the Yellow River. The COD concentration change process of Wumaoji sluice is depicted in Figure 3.

Of the 365 days, the TN concentration was in the fifth category of inferior quality for 295 days in Lake Ulansuhai. The annual TN exceedance rate for Lake Ulansuhai's effluent was 80.82% based on the standard of surface water category V. The current purification capacity of the lake could not meet the degradation requirements of TN concentration. The TN concentration change process of the Wumaoji sluice is shown in Figure 4.

5.1.2 Scheme 2

Figures 5, 6 show that the overall trend of COD and TN concentrations in Lake Ulansuhai demonstrated an increase–decrease stabilization pattern. This was because the pollution concentration in the lake area was higher in the north and lower in the south before water replenishment. The pollutants were pushed toward the Wumaoji sluice with the influx of water, causing poor water quality conditions in that area. Subsequently, the newly added water resources enhanced the self-purification ability of the lake area, and the pollutant concentration at the Wumaoji sluice began to decrease. Finally, water replenishment allowed the water quality in the lake area to reach a stable state. The simulation results showed that when the water replenishment period reached 137 days, the COD concentration at the outlet of Lake Ulansuhai met the stable surface water Class V standard. When the water replenishment period reached 140 days, the TN concentration at the outlet of Lake Ulansuhai could stably meet the surface water Class V standard. In other words, by external water replenishment for 140 days, the COD and TN concentrations in the lake could be stabilized at the Class V water quality requirement, which helped improve the self-purification ability and water quality of the lake area. Water replenishment is an effective way to improve the water environment quality of the lake area for lakes requiring irrigation return water and having poor water quality background or weak lake system connectivity, but this method is not sustainable.

TABLE 2 Results of model calibration and validation.

Pollutant	Standard (mg/L) (≤)				
	Class I	Class II	Class III	Class IV	Class V
COD	15.0	15.0	20.0	30.0	40.0
TN	0.2	0.5	1.0	1.5	2.0

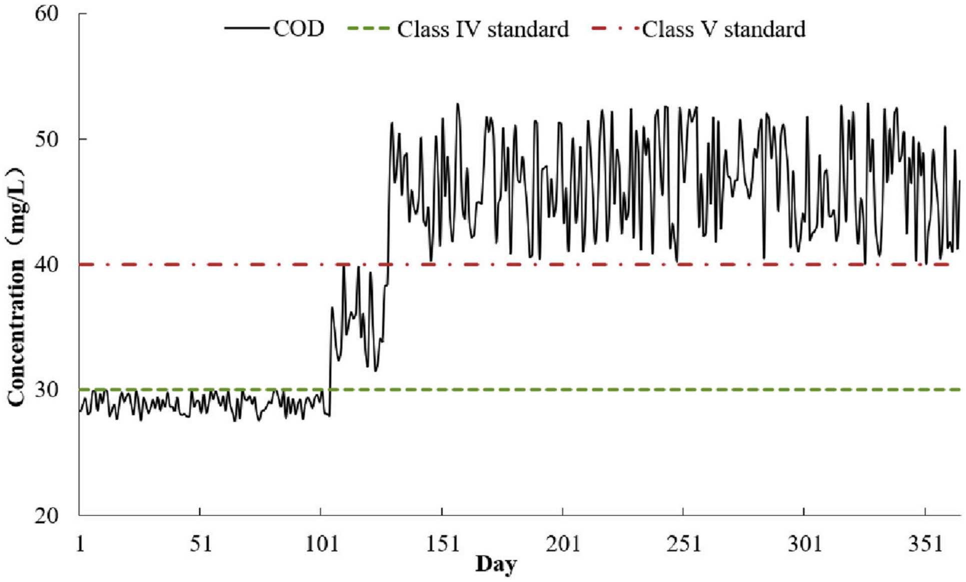

FIGURE 3
COD concentration change process of Wumaoji sluice in Scheme 1.

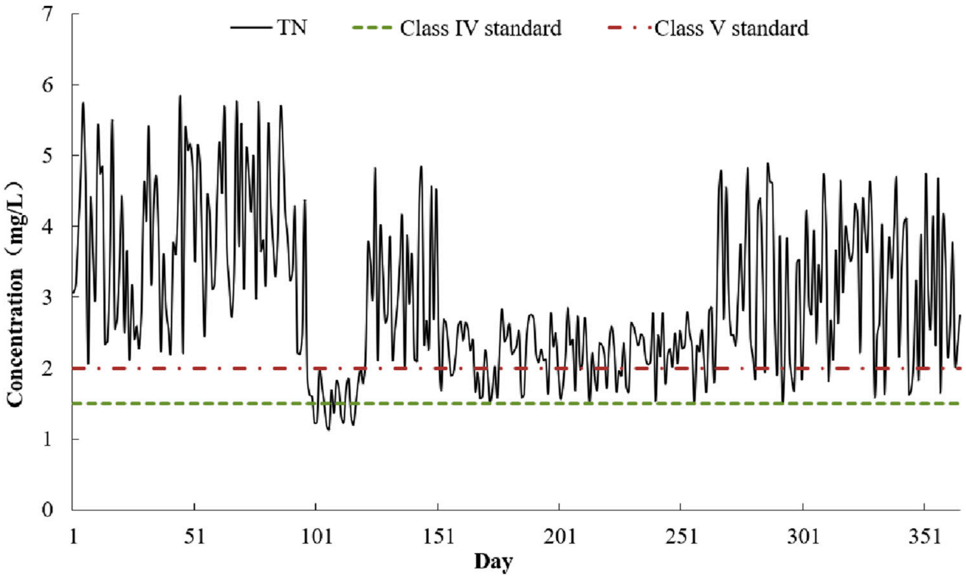

FIGURE 4
TN concentration change process of Wumaoji sluice in Scheme 1.

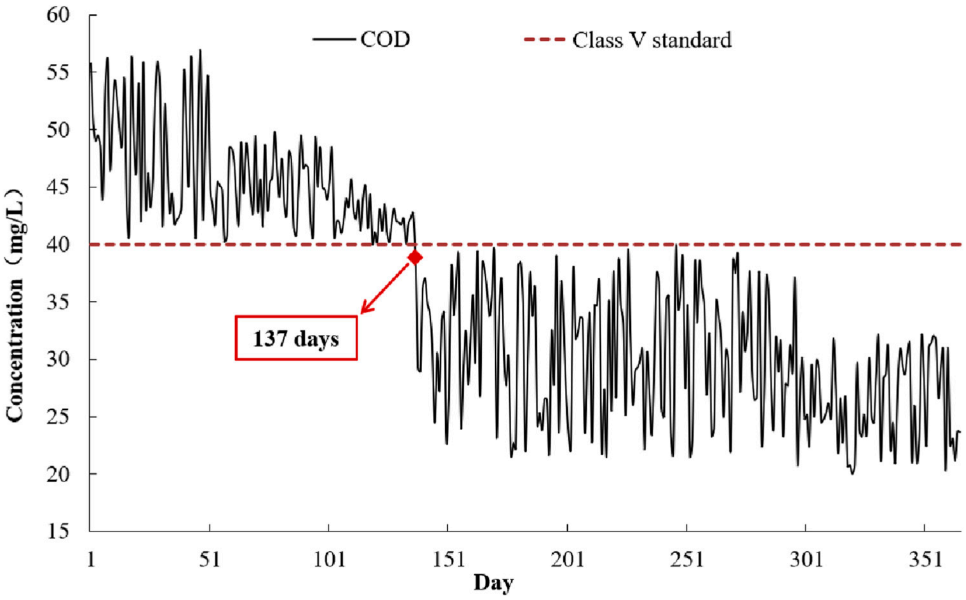

FIGURE 5
COD concentration change process of Wumaoji sluice in Scheme 2.

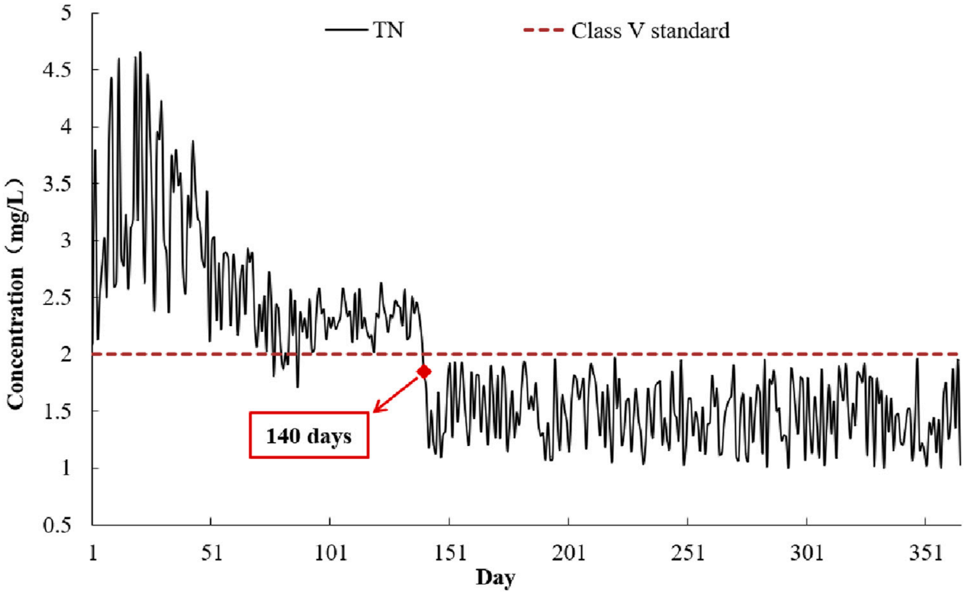

FIGURE 6
TN concentration change process of Wumaoji sluice in Scheme 2.

5.2 Discussion

Lake Ulansuhai is located in the cold and arid region of China, where water scarcity is severe and the supply-demand contradiction of water resources is prominent. The summer irrigation period of the Hetao Irrigation District in Inner Mongolia (the main irrigation period, accounting for about 60% of the total irrigation water) is especially from April to June. In addition, the autumn irrigation period is from July to mid-September, and from late September to October, large-scale flooding is used to reduce land salinization. At the same time, the winter anti-icing task of the Yellow River in Inner Mongolia is heavy. The upstream river channel is prone to form a peak flow especially after the ice is thawed, while the downstream river channel is still frozen, which can easily form ice dams and silt up the river channel, endangering the lives and property of people on both sides of the Yellow River. The Main Channel and Landaqu Channel should be used to replenish water during the irrigation interval in the Hetao Irrigation District to improve the water quality of the lake area so as to minimize the conflict between irrigation water and replenishment water and reduce the risk of ice flood. However, it should be noted that improving the water quality of lakes through water replenishment requires a large amount of freshwater resources. The temporary introduction of excess water resources into the lake to improve the water environment of the lake area is feasible for areas with abundant water resources, both technically and in terms of public opinion. However, it may be challenging to achieve this in water-deficient areas, not because of technical limitations but due to public perception. In areas with limited freshwater resources, using them to control water environmental problems may be considered as a luxury behavior by the public. The simulation results imply that lake water replenishment can reduce the concentration of pollutants in the lake area and ensure the water quality of the lake outflow, but a clear threshold exists for the number of replenishment days, and longer is not necessarily better. This is closely related to factors such as pollutant concentration, replenishable water volume, and lake system connectivity. In other words, water replenishment is effective in accelerating the renewal of lake water and controlling the concentration of pollutants in the lake area. However, water replenishment should have emergency and opportunistic characteristics and should not be implemented as a long-term measure. The real-time evaluation of the ecological water replenishment effect is necessary to reduce unnecessary water replenishment times and for the intensive and efficient use of water resources.

For Lake Ulansuhai, controlling external pollution sources and reducing internal sources, as well as protecting the aquatic ecology of the lake, are important measures for water environmental management. In particular, controlling the discharge of pollutants into the lake is the most direct and effective method. Based on the systematic management concept of “source control-process interruption-end interception-water ecological restoration,” pollution control and interception in the Hetao Irrigation District are emphasized. For example, a water ecological protection zone (consisting of retention ponds, vegetation buffer zones, and so forth) with a width of 20–150 m can be constructed in the area connecting the irrigation area and the lakeshore to intercept agricultural nonpoint source pollution and rainwater with poor water quality in the early rainy season. The heavily polluted inflow channels into the lake should be dredged. The government can adopt market regulation measures to provide tax incentives or funding subsidies for enterprises or individuals who actively reduce pollutant emissions by actively guiding social forces to participate in lake water environmental management. In addition, building an integrated water environmental monitoring and early warning system is also a good method. Digital twin technology has been used to develop a lake environment similar to the actual lake on the computer. Data analysis algorithms and hydrological, hydrodynamic, water quality, and water resource simulation models were integrated into it. The visual effects and intelligent decision-making capabilities of the lake information platform were used to provide technical support for solving practical problems such as “what pollution,” “where pollution,” “how much pollution,” “how to regulate,” “how much water replenishment is needed,” and “how to manage.” In addition, certain explorations have been made at home and abroad for managing lake water resource development and protection; however, no effective measures have been proposed for lake water environment and aquatic ecology protection. It is necessary to organize legislation work for lakes as soon as possible and further improve the legal system for lake protection and management.

Against the backdrop of global warming and intensified human activities, lake water quality has always been a major challenge in the field of global water environment, especially for lakes relying primarily on irrigation return water as their main water source. At present, the research results are still insufficient to support managers in carrying out high-level water environment protection and comprehensively managing them. This study focused on exploring whether supplementary water was an effective means for improving lake water quality; many mechanism issues have not been addressed yet. In the future, dynamic regulation mode research on emergency water replenishment in lakes can be carried out by coupling field observation and model simulation, with real-time rolling updates to optimize water replenishment time, amount, and route. Meanwhile, the mechanism of winter lake water environment evolution can be studied, and the corresponding relationship between lake water environment factors and changing environments can be explored to support the organic updating of the environment management technology for the irrigation area water.

6 Conclusion

Aiming at the core topic of lake water quality improvement using water replenishment, the following conclusions are drawn:

(1) This study took Lake Ulansuhai in China as an example to construct a two-dimensional hydrodynamic and water quality model for cold and arid lake areas. The model simulated the changes in pollutant concentrations of COD and TN in the lake area, and the simulation error was within an acceptable range, indicating that the model constructed in this study was reliable.

(2) The simulation results showed that water replenishment could enhance the self-purification ability of lakes by accelerating the renewal of lake water, thereby achieving the goal of improving lake water quality. However, water replenishment consumes a large amount of freshwater resources. For areas with abundant water resources, water replenishment is an effective measure to improve lake water quality. For water-deficient areas, external source control and internal source reduction of pollutants and protection of lake water ecology are the main ways to manage the lake water environment. Moreover, water replenishment should be used as an emergency and opportunistic measure, and not as a long-term solution, to ensure the sustainable maintenance of the lake water environment.

(3) In the future, for the lakes relying on irrigation area drainage as their main water source, the focus of water quality improvement research should be on key technologies for reducing and controlling pollution in irrigation areas, the

construction of digital twin platforms for lakes, and actively promoting legislation for lakes.

Data availability statement

The raw data supporting the conclusion of this article will be made available by the authors, without undue reservation.

Author contributions

BL: Conceptualization, Funding acquisition, Methodology, Validation, Writing–original draft, Writing–review and editing. LY: Methodology, Resources, Supervision, Writing–original draft. CC: Funding acquisition, Methodology, Software, Writing–review and editing. WW: Validation, Writing–review and editing, Validation, Writing–review and editing. SL: Validation, Writing–review and editing.

Funding

The author(s) declare that financial support was received for the research, authorship, and/or publication of this article. This work was supported by the National Key R&D Program of China (2022YFC3202405; 2023YFC3206703), the MWR Major Science & Technology Program (SKS-2022007), the Natural Science Foundation of Henan (222300420422), and the Development Funding Project by Water Youth Talent from Beijing Jianghe Water Development Foundation (2022-05).

Acknowledgments

The research would not have been possible without the interest and cooperation of the Water Conservancy Development Center of the Hetao Irrigation District and the Water Resources Bureau of Bayannur City in Inner Mongolia.

Conflict of interest

Authors BL, LY, CC, WW, and SL were employed by Yellow River Engineering Consulting Co., Ltd.

Publisher's note

References

Amano, Y., Sakai, Y., Sekiya, T., Takeya, K., Taki, K., and Machida, M. (2010). Effect of phosphorus fluctuation caused by river water dilution in eutrophic lake on competition between blue-green alga Microcystis aeruginosa and diatom Cyclotella sp. *J. Environ. Sci.* 22 (11), 1666–1673. doi:10.1016/s1001-0742(09)60304-1

Feng, T., Wang, C., Hou, J., Wang, P., Liu, Y., Dai, Q., et al. (2017). Effect of inter-basin water transfer on water quality in an urban lake: a combined water quality index algorithm and biophysical modelling approach. *Ecol. Indic.* 92, 61–71. doi:10.1016/j.ecolind.2017.06.044

Fu, C., Wu, H., Zhu, Z., Song, C., Xue, B., Wu, H., et al. (2021). Exploring the potential factors on the striking water level variation of the two largest semi-arid-region lakes in northeastern Asia. *Catena* 198, 105037. doi:10.1016/j.catena.2020.105037

Geng, M., Wang, K., Yang, N., Li, F., Zou, Y., Chen, X., et al. (2021). Evaluation and variation trends analysis of water quality in response to water regime changes in a typical river-connected lake (Dongting Lake), China. *Environ. Pollut.* 268 (Pt A), 115761. doi:10.1016/j.envpol.2020.115761

He, J., Wu, X., Zhang, Y., Zheng, B., Meng, D., Zhou, H., et al. (2020). Management of water quality targets based on river-lake water quality response relationships for lake basins – a case study of Dianchi Lake. *Environ. Res.* 186, 109479. doi:10.1016/j.envres.2020.109479

Ho, J. C., Michalak, A. M., and Pahlevan, N. (2019). Widespread global increase in intense lake phytoplankton blooms since the 1980s. *Nature* 574 (7780), 667–670. doi:10.1038/s41586-019-1648-7

Hosper, S. H. (1998). Stable states, buffers and switches: an ecosystem approach to the restoration and management of shallow lakes in The Netherlands. *Water Sci. Technol.* 37 (3), 151–164. doi:10.2166/wst.1998.0196

Hu, K., Wang, Y., Feng, B., Wu, D., Tong, Y., and Zhang, X. (2020). Calculation of water environmental capacity of large shallow lakes – a case study of Taihu Lake. *Water Policy* 22 (2), 223–236. doi:10.2166/wp.2020.076

Huang, J., Gao, J., Zhang, Y., and Xu, Y. (2015). Modeling impacts of water transfers on alleviation of phytoplankton aggregation in Lake Taihu. *J. Hydroinform.* 17 (1), 149–162. doi:10.2166/hydro.2014.023

Huser, B. J., Egemose, S., Harper, H., Hupfer, M., Jensen, H., Pilgrim, K. M., et al. (2016). Longevity and effectiveness of aluminum addition to reduce sediment phosphorus release and restore lake water quality. *Water Res.* 97 (Jun), 122–132. doi:10.1016/j.watres.2015.06.051

Karlsson, J., Byström, P., Ask, J., Ask, P., Persson, L., and Jansson, M. (2009). Light limitation of nutrient-poor lake ecosystems. *Nature* 460 (7254), 506–509. doi:10.1038/nature08179

Lai, X., Jiang, J., Liang, Q., and Huang, Q. (2013). Large-scale hydrodynamic modeling of the middle Yangtze River Basin with complex river–lake interactions. *J. Hydrol.* 492, 228–243. doi:10.1016/j.jhydrol.2013.03.049

Lane, R. R., Day, J. W., Kemp, G. P., and Demcheck, D. K. (2001). The 1994 experimental opening of the bonnet carre spillway to divert Mississippi River water into Lake Pontchartrain, Louisiana. *Ecol. Eng.* 17 (4), 411–422. doi:10.1016/s0925-8574(00)00170-1

Li, B., Yang, G., Wan, R., Lai, X., and Wagner, P. D. (2022). Impacts of hydrological alteration on ecosystem services changes of a large river-connected lake (Poyang Lake), China. *J. Environ. Manage.* 310, 114750. doi:10.1016/j.jenvman.2022.114750

Liu, B., Cai, S., Wang, H., Cui, C., and Cao, X. (2021c). Hydrodynamics and water quality of the Hongze Lake in response to human activities. *Environ. Sci. Pollut. R.* 28 (34), 46215–46232. doi:10.1007/s11356-021-12960-4

Liu, B., Wang, Y., Xia, J., Quan, J., and Wang, J. (2021a). Optimal water resources operation for rivers-connected lake under uncertainty. *J. Hydrol.* 595, 125863. doi:10.1016/j.jhydrol.2020.125863

Liu, B., Xia, J., Zhu, F., Quan, J., and Wang, H. (2021b). Response of hydrodynamics and water-quality conditions to climate change in a shallow lake. *Water Resour. Manag.* 35 (14), 4961–4976. doi:10.1007/s11269-021-02982-5

Lürling, M., and Oosterhout, F. V. (2013). Case study on the efficacy of a lanthanum-enriched clay (Phoslock®) in controlling eutrophication in Lake Het Groene Eiland (The Netherlands). *Hydrobiologia* 710 (1), 253–263. doi:10.1007/s10750-012-1141-x

Manghi, F., Williams, D., Safely, J., and Hamdi, M. R. (2012). Groundwater flow modeling of the arlington basin to evaluate management strategies for expansion of the arlington desalter water production. *Water Resour. Manag.* 26 (1), 21–41. doi:10.1007/s11269-011-9899-6

Mao, X., Yuan, D., Huang, X., Wei, X., and Chen, Q. (2015). Purification-efficient-based hydroecoregion in a lake of irrigation return water, China. Fresen. *Environ. Bull.* 24 (3b), 1142–1149.

Munar, A. M., Cavalcanti, J. R., Bravo, J. M., Fan, F. M., Motta-Marques, D., and Fragoso, C. R. (2018). Coupling large-scale hydrological and hydrodynamic modeling:

toward a better comprehension of watershed-shallow lake processes. *J. Hydrol.* 564, 424–441. doi:10.1016/j.jhydrol.2018.07.045

Na, E. H., and Park, S. S. (2006). A hydrodynamic and water quality modeling study of spatial and temporal patterns of phytoplankton growth in a stratified lake with buoyant incoming flow. *Ecol. Model.* 199 (3), 298–314. doi:10.1016/j.ecolmodel.2006.05.008

Oglesby, R. T. (1969). Effects of controlled nutrient dilution on a eutrophic lake. *Adv. Water Pollut. Res.*, 747–757. doi:10.1016/B978-0-08-012999-0.50087-3

Parinet, B., Lhote, A., and Legube, B. (2004). Principal component analysis: an appropriate tool for water quality evaluation and management—application to a tropical lake system. *Ecol. Model.* 178 (3-4), 295–311. doi:10.1016/j.ecolmodel.2004.03.007

Peng, Z., Hu, W., Zhang, Y., Liu, G., Zhang, H., and Gao, R. (2020). Modelling the effects of joint operations of water transfer project and lake sluice on circulation and water quality of a large shallow lake. *J. Hydrol.* 593 (10), 125881. doi:10.1016/j.jhydrol.2020.125881

Qing, S., A, R., Shun, B., Zhao, W., Bao, Y., and Hao, Y. (2020). Distinguishing and mapping of aquatic vegetations and yellow algae bloom with Landsat satellite data in a complex shallow Lake, China during 1986–2018. *Ecol. Indic.* 112, 106073. doi:10.1016/j.ecolind.2020.106073

Rasmussen, E. K., Petersen, O. S., Thompson, J. R., Flower, R. J., and Ahmed, M. H. (2009). Hydrodynamic-ecological model analyses of the water quality of Lake Manzala (nile delta, northern Egypt). *Hydrobiologia* 622, 195–220. doi:10.1007/s10750-008-9683-7

Rosińska, J., Kozak, A., Dondajewska, R., Kowalczewska-Madura, K., and Gołdyn, R. (2018). Water quality response to sustainable restoration measures – case study of urban Swarzędzkie Lake. *Ecol. Indic.* 84 (Jan), 437–449. doi:10.1016/j.ecolind.2017.09.009

Saber, A., James, D. E., and Hannoun, I. A. (2020). Effects of lake water level fluctuation due to drought and extreme winter precipitation on mixing and water quality of an alpine lake, Case Study: lake Arrowhead, California. *Sci. Total Environ.* 714, 136762. doi:10.1016/j.scitotenv.2020.136762

Schindler, D. W., Carpenter, S. R., Chapra, S. C., Hecky, R. E., and Orihel, D. M. (2016). Reducing phosphorus to curb lake eutrophication is a success. *Environ. Sci. Technol.* 50 (17), 8923–8929. doi:10.1021/acs.est.6b02204

Shen, H., Tsanis, I. K., and D'Andrea, M. (1995). A three-dimensional nested hydrodynamic/pollutant transport simulation model for the nearshore areas of Lake ontario. *J. Gt. Lakes. Res.* 21 (2), 161–177. doi:10.1016/s0380-1330(95)71029-2

Song, C., Huang, B., Ke, L., and Richards, K. S. (2014). Remote sensing of alpine lake water environment changes on the Tibetan Plateau and surroundings: a review. *ISPRS J. Photogramm.* 92, 26–37. doi:10.1016/j.isprsjprs.2014.03.001

Steinman, A., Havens, K. E., and Hornung, L. (2002). The managed recession of Lake okeechobee, Florida: integrating science and natural resource management. *Ecol. Soc.* 6 (2), art17–1663. doi:10.5751/es-00417-060217

Vinçon-Leite, B., and Casenave, C. (2019). Modelling eutrophication in lake ecosystems: a review. *Sci. Total Environ.* 651, 2985–3001. doi:10.1016/j.scitotenv.2018.09.320

Vitense, K., Hanson, M. A., Herwig, B. R., Kyle, D., Zimmer, K. D., and Fieberg, J. (2019). Predicting total phosphorus levels as indicators for shallow lake management. *Ecol. Indic.* 96, 278–287. doi:10.1016/j.ecolind.2018.09.002

Wang, Z., Shi, Q., Li, X., Li, W., Yang, W., and Yu, L. (2021). The influences of uniform wind and throughput flow on the flow field of Wuliangsu lake. *Oceanol. Limnologia Sinica* 52 (3), 614–623. (in Chinese). doi:10.11693/hyhz20201000279

Wu, J., Xue, C., Tian, R., and Wang, S. (2017). Lake water quality assessment: a case study of Shahu Lake in the semiarid loess area of northwest China. *Environ. Earth Sci.* 76 (5), 232. doi:10.1007/s12665-017-6516-x

Wu, S., Dai, J., and Shi, S. (2018). Progress in assessment of hydro-ecological effects in lakes induced by water diversion. *J. N. Inst. Techno.* 37 (6), 14–26. (in Chinese). doi:10.3969/j.issn.1006-4869.2018.06.003

Zhang, R., Qian, X., Li, H., Yuan, X., and Ye, R. (2012). Selection of optimal river water quality improvement programs using QUAL2K: a case study of Taihu Lake Basin, China. *China. Sci. Total Environ.* 431, 278–285. doi:10.1016/j.scitotenv.2012.05.063

frontiers | Frontiers in Environmental Science

TYPE Original Research
PUBLISHED 02 May 2024
DOI 10.3389/fenvs.2024.1380979

OPEN ACCESS

EDITED BY
Xudong Huang,
North China University of Water Conservancy and Electric Power, China

REVIEWED BY
Elizabeth Graham,
University College London, United Kingdom
Zhuoran Wang,
Shandong Agricultural University, China
Zhong-Xiu Sun,
Shenyang Agricultural University, China

*CORRESPONDENCE
Wenjing Wang,
✉ wangwenjing_2012@163.com

RECEIVED 02 February 2024
ACCEPTED 10 April 2024
PUBLISHED 02 May 2024

CITATION
Zha L, Wang W, Zhong J, Su Y and Chang D (2024), How did ancient human activities influence the properties and development of soil?—a case study of the Yangshao Village cultural relic site, Henan Province.
Front. Environ. Sci. 12:1380979.
doi: 10.3389/fenvs.2024.1380979

How did ancient human activities influence the properties and development of soil?—a case study of the Yangshao Village cultural relic site, Henan Province

Lisi Zha[1], Wenjing Wang[2,3]*, Junhong Zhong[4], Yiqi Su[5] and Dandan Chang[1]

[1]School of Public Administration, Guangdong University of Finance and Economics, Guangzhou, Guangdong Province, China, [2]School of Resource and Environmental Sciences, Hebei Normal University for Nationalities, Chengde, Hebei, China, [3]Centre for Human Sciences, Universiti Malaysia Pahang AL-Sultan Abdullah, Kuantan, Malaysia, [4]Guangdong University of Technology, Guangzhou, Guangdong Province, China, [5]Jinan University, Guangzhou, Guangdong Province, China

Introduction: What were the effects of paleoanthropogenic activities on the physicochemical properties and degree of the development of soil? To search for this answer, we can not only understand the different types of ancient human activities but also explore the intensity and characteristics of the activities.

Methods: In this study, soil samples from different soil layers and two profiles in the Yangshao Village cultural site in Henan Province were collected. Their physicochemical properties and the sporophyte phyllosilicates they contain were analyzed and compared.

Results: We found that the paleoanthropogenic activities started in the relatively low-lying area, in which the slash-and-burn activities resulted in the soil being filled with intrusions such as charcoal debris and ceramic shards. At the same time, the coarse-grained matter was affected by the plowing activities and mostly decomposed into fine particles, and the content of clay particles reached an extreme value. The total nitrogen, phosphorus, and calcium carbonate content exceeded the average value of the natural profile, indicating that ancient humans had used human and animal feces to a certain extent to restore the fertility of arable land.

Discussion: Overall, ancient human activities hindered the development of the soil, especially the ground created due to habitation activities. From the type and content of clay minerals, it could be seen that the soil in this layer has been transported from other places, has a high content of clay particles, and has experienced fire baking. It was assumed that the ground was used to cover the grain or bury the garbage and lay with clay in order to achieve the effect of sealing. As a result, the soil voids and structure had been damaged to some extent, which prevented the downward leaching or precipitation of soil particles and minerals to a certain extent, thus affecting soil development.

KEYWORDS

Yangshao Village site, archaeological soil, soil properties, soil development, paleoenvironment

1 Introduction

In 1883, Vasily Vasilievich Dokuchaev published "Russian Chernozem," which first formally put forward the five major factors of soil formation (climate, topography, soil parent matter, biological factors, and time). This was a great achievement in the history of soil science, which had long been known to soil scientists. The impact of human activities on the soil was not taken seriously at that time. However, in the last century, human beings have been recognized as an important component of biological factors, and increasing attention has been paid to the influence of human activities on soil. In the study of archaeological soil, in 2004, a critical review of the current methods of sampling and analyzing soils for the determination of metals in archaeological prospection was presented (R. Haslam and Tibbett, 2004). During the same period, the plant physiological investigation of starch grains found as residues on artifacts and in archaeological sediments was reviewed (M. Haslam, 2004).

In 2008, soil analyses in archeology as a subject developed during the 1950s and 1960s, and the effects of human activities on soils were first investigated (Macphail, 2008). Furthermore, how soil research can reveal the impact of human activities on landscapes and spaces was described (Walkington, 2010). Soil analysis was a very useful tool to investigate the effects of human activities on soil development and burying bodies on soil contamination, raw material provenance, paleoenvironmental reconstruction, and the environmental impact of cultural heritage (Pastor et al., 2016). The types and intensities of ancient human activities can be recognized by analyzing the physical and chemical properties of soil and inclusions. A multi-element analysis of soils has been used to understand the former space use. Results from these studies indicated that activity areas can often be chemically detected and interpreted (Knudson et al., 2004; Sullivan and Kealhofer, 2004; Terry et al., 2004; Wells, 2004; Wilson et al., 2008). Specifically, in the study of ancient agricultural production and ancient human activity areas, phosphorus, carbon, and nitrogen were frequently taken into account. This method had been used for a long time and is well-developed (Schlezinger and Howes, 2000; Fernández et al., 2002; Suleimanov and Obydennova, 2006; Lu et al., 2009; Homburg and Sandor, 2011; Gerlach et al., 2012; Migliavacca et al., 2013; Salisbury, 2013; Ferro-Vázquez et al., 2014; Nielsen and Kristiansen, 2014; Adam et al., 2016). Other elements can also provide effective clues for different land use patterns and intensities of ancient humans, especially some metal elements and trace elements, through which much more detailed areas of different ancient human activities can be distinguished (Parnell et al., 2002; Wilson et al., 2008; Kamenov et al., 2009; Dirix et al., 2013; Gallello et al., 2013; Vittori Antisari et al., 2013; Zgłobicki, 2013; Cook et al., 2014; Nielsen and Kristiansen, 2014; Stinchcomb et al., 2014; Fleisher and Sulas, 2015; Turner et al., 2021). Analyzing the magnetic susceptibility of soil can help archaeologists find evidence of ancient humans using fire (Linford and Canti, 2001; Church et al., 2007; Shi et al., 2007; Brown et al., 2009; Carrancho and Villalaín, 2011; Zhang et al., 2014). In contrast, the physical properties of soil were less analyzed, such as chroma and particle composition. However, in paleoenvironmental studies, soil physical property analysis was often used (Arnaud-fassetta et al., 2000; Tsatskin and Nadel, 2003; Kidder et al., 2012; Kim et al., 2012; Sitzia et al., 2012; Blasi et al., 2013; Solís-Castillo et al., 2013; Cruz-y-Cruz et al., 2015). In addition, clay minerals were often used in the paleoenvironment as well (Dou et al., 2010; El Ouahabi et al., 2017; Manalt et al., 2001; Oonk et al., 2009; J. Wang et al., 2015; Wilson et al., 2008), while they were less used in the study of archaeological research. Ancient human activities could change the local environment, and soil physical properties and clay minerals can also reflect the influence of ancient human activities on soil.

Yangshao Village was a Neolithic site in the Yellow River Basin of China and is the namesake of the Yangshao culture. In October 1921, the Swedish geologist Antsen and the Chinese geologist Yuan Fuli carried out the first archaeological investigation and excavation and obtained a large amount of cultural relics, which confirmed that this site was a Neolithic cultural relic. According to many archaeological excavations and research, it was found that the stratigraphy of two cultures, Yangshao and Zhongyuan Longshan, with four different stages of development, was superimposed on each other, with the late Yangshao culture being the main one (Yan, 1989). The existence of a large number of ash pits and relics within the site indicated that the ancient human activities on the site were diverse and intense, and they must have left a lot of information of ancient human activities in the soil. Combined with the results of existing paleoclimatic studies, the ancient humans at this site experienced a sudden cooling event and a great flood (SHI et al., 1992; Marcott et al., 2013; Chen et al., 2015), and the culture was in the transition to the Longshan culture of the Central Plains, so the study of the soil characteristics of the site will help us understand the production and living conditions of ancient humans in the context of paleoenvironmental changes and cultural evolution.

2 Materials and methods

2.1 Experimental framework

The Yangshao Village site is located on a terrace approximately 7.5 km north of Yangshao Village, Mianchi County, Henan Province, Eastern China (Figure 1C). The site is approximately 900 m long and 300 m wide. According to the book Soil Series of China (Henan), the zonal soil is loess, which belongs to the general development of dry and semi-arid cambisols (Wu et al., 2019). The sampling area is situated on a gentle slope to the east of Antesheng Road in Yangshao Village (34°48′51″N, 111°46′36″E), with an elevation of 621 m and a slope gradient of 5°–8°. The area spans approximately 160 m north to south and 80 m east to west. The current land use is pepper plantations. Due to site protection management requirements, there is no excessive artificial maintenance; pepper trees rely on natural precipitation, and from the scene full of weeds, it can be judged that there is minimal modern human interference. Based on the field conditions, the area can be divided into three regions from south to north: sparse pepper forest (I), dense pepper forest (II), and grassland (III). Soil samples were collected from one to two locations in the center of each region and at the boundaries between the regions. Additionally, sampling points were established along the north–south axis at 20 m intervals to the east and west of the central axis. In regions II and III, the sampling was mainly conducted to the east due to modern disturbances

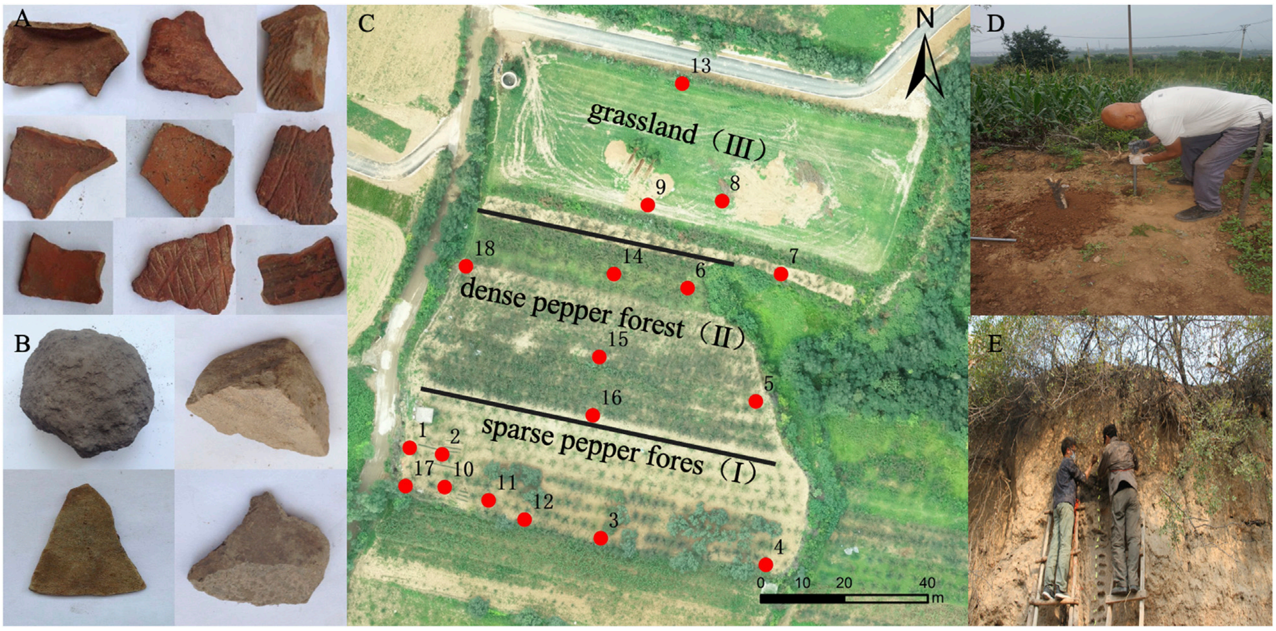

FIGURE 1
Sampling area and method.

caused by burial activities in the western region, which was identified as a burial area by the Henan Provincial Institute of Cultural Relics Research in 1981. Within region I, location Nos 1, 2, 10, 11, and 17 were previously excavated, particularly at location No. 17, where a large number of pottery shards (Figure 1A) and stone tools (Figure 1B) were found in the cultural layer. Therefore, this region was densely sampled to obtain more information of ancient cultivation activities. Location No. 18 is a natural soil profile, which was taken for comparative analysis. Soil samples were collected using soil augers at locations Nos 1 to 16, reaching the paleosol layer from the surface. Based on the soil texture and color, combined with stratigraphic dating, the soil was divided into several layers, and intact samples were collected from each layer (Figure 1D). A total of 49 samples were obtained for N, P, and CaO analysis and field observations. At location Nos 17 and 18, samples were taken directly from the profile by scraping the surface to obtain samples at a 10 cm interval, and 80 samples were taken (Figure 1E), including samples of spore pollen, phytolith, and conventional physical and chemical analysis samples.

2.2 Dating and analytical methods

The dating samples were taken according to the occurrence layer, and soil samples were collected from the bottom of each layer. However, for the cultural profile, due to human interference, although the soil layer is spatially continuous, the age would be broken, so samples were also collected from the top of some occurrence layers. In addition, some special soil layers formed by ancient human interference were also sampled and analyzed to have a clear understanding of the age sequence of the profile. Four samples were collected from the natural profile, and eight samples were collected from the cultural profile, totaling 12 samples, all of which were valid for analysis. The dating of the soil samples was carried out using the carbon-14 accelerated mass spectrometer (AMS) method, which was completed in the Laboratory of Archaeological Chronology, School of Archeology and Letters and Museums, Peking University. The 14C half-life used was 5,568 years, and B.P. is dated to 1950. The measured ages were corrected to calendar ages using the tree-wheel correction method provided by Reimer et al. (Paula et al., 2004), the curve used for the correction was IntCal04, and the program used was OxCal v3.10. Soil samples from the natural profile at 40, 220, 300, and 400 cm were measured. The results were 4,055, 5,583, 6,898 and 10,248 a B.P., respectively. Soil samples from the cultural profile at 20, 70, 100, 145, 160, 210, 230, and 400 cm were measured. The results were 3,641, 4,891, 5,531, 27,789, 6,400, 7,524, 8,241, and 12,800 a B.P., respectively. Based on the dating results, it was roughly known that culture layer 1 was formed during the Central Longshan Culture, the ash layer was formed in the late Yangshao period, culture layer 2 was formed during the middle Yangshao culture, and culture layer 3 was formed during the early Yangshao culture. According to the dating results of the two profiles, it can be roughly known from the chronological point of view that the two paleosoil layers corresponded well, the transition layer of the natural profile roughly corresponded to culture layer 3 of the culture profile, and the loess layer of the natural profile roughly corresponded to culture layers 2 and 1.

Clay minerals were identified by X-ray diffractograms. Particle size analysis was carried out using the Mastersizer 2000 laser particle sizer, magnetic susceptibility analysis was carried out using the Bartington MS-2 dual-frequency magnetic susceptibility meter, and total mineral content analysis was carried out based on ICP-AES. The spore powder was extracted via acid–base treatment,

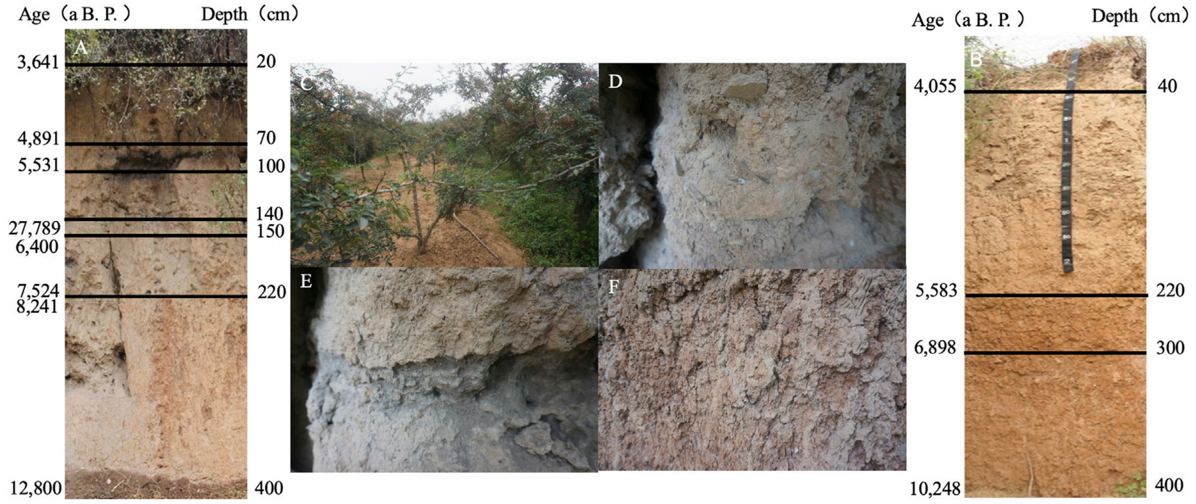

FIGURE 2
Soil profile and stratification.

heavy liquid flotation, and sieving, and the identification and counting were carried out under a Leica biomicroscope (magnification of ×400). Charcoal debris were identified and counted under a Nissan Olympus BX-51 optical microscope (magnification ×400), and charcoal debris with a diameter greater than 50 μm were counted. In addition, phyllosilicate analysis was carried out on the soil layers disturbed by paleoanthropogenic activities in the cultural profile. The phyllosilicate was separated and extracted with reference to the wet gray image method, and the extracted phyllosilicate was made into a fixation slice using neutral gum and observed, counted, and micrographically photographed under a Leica biomicroscope (magnification of × 400); its identification and classification were referred to in the relevant literature (Peninsula, 1983; Fredlund and Tieszen, 1994; Kelly et al., 1998), and the nomenclature was based on international rules (Neumann et al., 2019).

3 Result

3.1 Basic physical and chemical characteristics of soil profiles and soil columns

The soil profile at locations No. 17 (Figure 2A) and 18 (Figure 2B) exhibited distinct macroscopic differences in each layer. In order to reflect the soil characteristics of the site, combined with the classification of archaeological soil layers according to color, structure, tightness, and inter-layer contact relationship, the cultural profile can be divided from top to bottom into seven layers (Table 1). Among them, the ash layer was the remains of ancient human fire, and the cultural layer was the remains of ancient human habitation; both of them are horizontally distributed, the boundary shape was flat and regular, and in both of them, the Yangshao period red and gray ceramic tablets of the Longshan culture period of the Central Plains were found. The conical ash pits next to them are the pits dug for ancient human life garbage or food reserves, which can prove that the ash and cultural layers are the remains of ancient human activities. The topsoil layer was mostly brown, and the texture was loamy soil (Figure 2C); the cultural layer was mostly gray-brown, and the texture was powdery loam, which contained many kinds of intruders such as pottery shards and bones (Figure 2D) or special materials such as charcoal chips (Figure 2E). The paleosoil layer was turbid orange, and the texture was clay loam (Figure 2F). The entire profile was clearly layered. The natural profile is untouched by traces of disturbance, and it is divided into four layers according to the color, structure, tightness, and interlayer contact relationship. The specific descriptions of the various layers are detailed in Table 1. The average total nitrogen, phosphorus, and calcium carbonate content of the cultural profile were 0.98, 2.83, and 108.43 g kg^{-1}, respectively, while those of the natural profile were 0.57, 1.94, and 85.5 g kg^{-1}, respectively.

From locations No. 1 to 16, the soil column sampling points can also be divided into topsoil, cultural layer, and paleosol layer. Overall, the average thickness of the topsoil was 72 cm, with a dry color, mainly brown. The cultural layer had an average thickness of 112 cm, and no traces of modern human activity interference or modern intrusions were found during on-site excavation. Its dry color was mainly grayish-brown. The paleosol layer had a dry color, mainly turbid orange, which was noticeably different from the previous two layers. The soil structure of each layer was granular, while the structures at locations No. 5 and 10 were plate-like, suggesting human or fluvial deposition. Intrusions mainly consist of pottery shards and stone tools, indicating the cultural characteristics of that period. Additionally, the presence of charcoal fragments indicated the use of fire by the ancient people. The average total nitrogen content at location No. 16 is 0.87 g kg^{-1} in the topsoil, 0.85 g kg^{-1} in the cultural layer, and 0.56 g kg^{-1} in the paleosol layer. The average total phosphorus content is 1.62 g kg^{-1} in the topsoil, 2.93 g kg^{-1} in the cultural layer, and 1.31 g kg^{-1} in the paleosol layer. The average carbonate

TABLE 1 Field description and chemical analysis of each soil layer.

Sampling	Layer and depth (cm)	Dry color	Texture	Intruder	N (g·kg^{-1})	P (g·kg^{-1})	$CaCO_3$ (g·kg^{-1})
1	Topsoil layer (0–80 cm)	Brown (7.5 YR 4/3)	Loam		0.91	1.71	80
	Topsoil layer (80–100 cm)	White (7.5 YR 8/1)	Silt loam		0.53	1.46	75
	Culture layer (100–250 cm)	Grayish brown (7.5 YR 4/2)	Silt loam	Black potsherd	0.46	4.52	129
	Culture layer (250–285 cm)	Cloudy yellow (10 YR 7/2.5)	Silt loam	Charcoal crumbs	0.52	1.67	128
	Culture layer (285–290 cm)	Cloudy orange (10 YR 7/3)	Silt loam		0.53	3.38	122
	Culture layer (290–320 cm)	White (7.5 YR 8/1)	Silt loam		0.51	1.66	112
	Paleosoil layer (320 cm~)	Cloudy orange (7.5 YR 6/4)	Clay loam		0.52	1.51	55
2	Culture 9 (0–80 cm)	Brown (7.5 YR 4/3)	Loam	Red and gray potsherd and charcoal crumbs	0.62	1.62	81
	Culture layer (80–230 cm)	Light brown (7.5 YR 7/2)	Silt loam		0.58	3.76	105
	Culture layer (230–280 cm)	Grayish brown (7.5 YR 4/2)	Silt loam	Bone and black and red potsherd	0.58	2.95	122
	Paleosoil layer (280 cm~)	Cloudy orange (7.5 YR 6/4)	Clay loam		0.47	1.85	53
3	Topsoil layer (0–50 cm)	Brown (7.5 YR 4/3)	Loam		1.12	1.01	52
	Paleosoil layer (50 cm~)	Cloudy orange (7.5 YR 6/4)	Clay loam		0.42	1.53	88
4	Topsoil layer (0–120 cm)	Brown (7.5 YR 4/3)	Loam		0.94	1.64	80
	Paleosoil layer (120 cm~)	Cloudy orange (7.5 YR 6/4)	Clay loam		0.44	1.85	90
5	Topsoil layer (0–60 cm)	Brown (7.5 YR 4/3)	Loam		0.87	1.55	80
	Culture layer (60–170 cm)	Cloudy yellow (10 YR 6.5/3)	Silt loam	Red potsherd	0.56	2.33	115
	Paleosoil layer (170 cm~)	Cloudy orange (7.5 YR 6/4)	Clay loam		0.52	1.46	48
6	Topsoil layer (0–100 cm)	Brown (7.5 YR 4/3)	Loam		0.71	1.51	91
	Culture layer (100–120 cm)	Light brown (7.5 YR 7/2)	Silt loam	Gray potsherd	0.56	2.17	105
	Paleosoil layer (120 cm~)	Cloudy orange (7.5 YR 6/ 4 (	Clay loam		0.66	0.84	64
7	Topsoil layer (0–55 cm)	Brown (7.5 YR 4/3)	Loam		0.54	1.61	88
	Culture layer (55–80 cm)	Cloudy yellow–orange (10 Y 7/2.5)	Silt loam	Gravel	0.5	2.44	129
	Culture layer (80–210 cm)	Grayish brown (7.5YR 4/2)	Silt loam		0.53	2.93	121
	Paleosoil layer (210 cm~)	Cloudy orange (7.5 YR 6/4	Clay loam		0.75	0.96	62
8	Topsoil layer (0–30 cm)	Brown (7.5 YR 4/3)	Loam		0.82	1.53	96

(Continued on following page)

TABLE 1 (*Continued*) Field description and chemical analysis of each soil layer.

Sampling	Layer and depth (cm)	Dry color	Texture	Intruder	N ($g \cdot kg^{-1}$)	P ($g \cdot kg^{-1}$)	$CaCO_3$ ($g \cdot kg^{-1}$)
	Paleosoil layer (30 cm~)	Cloudy orange (7.5 YR 6/4)	Clay loam		0.74	1.13	61
9	Topsoil layer (0–100 cm)	Brown (7.5 YR 4/3)	Loam		1.02	1.47	84
	Paleosoil layer (100 cm~)	Cloudy orange (7.5 YR 6/4)	Clay loam		0.69	0.96	70
10	Topsoil layer (0–80 cm)	Brown (7.5 YR 4/3)	Loam		1.19	1.57	75
	Culture layer (80–100 cm)	Cloudy yellow (10 YR 6.5/3)	Silt loam		0.59	1.64	73
	Culture layer (100–220 cm)	Grayish brown (7.5 YR 4/2)	Silt loam	Gravel and red and gray potsherd	0.53	3.52	134
	Culture layer (220–300 cm)	Grayish brown (7.5 YR 4/2)	Silt loam		0.52	3.59	122
	Paleosoil layer (300 cm~)	Cloudy orange (7.5 YR 6/4)	Clay loam		0.53	0.68	114
11	Topsoil layer (0–120 cm)	Brown (7.5 YR 4/3)	Loam		1.21	2.65	95
	Culture layer (120–180 cm)	Grayish brown (7.5 YR 4/2)	Silt loam	Ash	0.53	3.01	143
	Paleosoil layer (180 cm~)	Cloudy yellow–orange (10 Y 7/2.5)	Clay loam		0.81	2.64	671
12	Topsoil layer (0–60 cm)	Cloudy yellow (10 YR 6.5/3)	Loam		0.59	1.61	75
	Paleosoil layer (60 cm~)	Cloudy orange (7.5 YR 6/4)	Clay loam		0.52	1.55	55
13	Topsoil layer (0–70 cm)	Cloudy yellow (10 YR 6.5/3)	Loam		1.12	1.61	75
	Culture layer (70–120 cm)	Light brown (97.5 YR 7/2)	Silt loam	Black potsherd and red soil residue	0.55	3.99	138
	Paleosoil layer (120 cm~)	Cloudy orange (7.5 YR 6/4)	Clay loam		0.48	0.74	65
14	Topsoil layer (0–60 cm)	Brown (7.5 YR 4/3)	Loam		0.88	1.77	77
	Paleosoil layer (60 cm~)	Cloudy orange (7.5 YR 6/4)	Clay loam		0.53	1.63	62
15	Topsoil layer (0–50 cm)	Brown (7.5 YR 4/3)	Loam		0.83	1.36	76
	Paleosoil layer (50 cm~)	Cloudy orange (7.5 YR 6/4)	Clay loam		0.52	1.52	55
16	Topsoil layer (0–20 cm)	Cloudy yellow (10 YR 6.5/3)	Loam		0.53	2.64	104
	Culture layer (20–100 cm)	Cloudy orange (7.5 YR 7/3)	Silt loam	Red soil residue	0.71	2.71	109
	Paleosoil layer (100 cm~)	Cloudy orange (7.5 YR 6/4)	Clay loam		0.47	1.67	55
17	Topsoil layer (0–20)	Cloudy orange (7.5 YR 6/4)	Loam		1.11	1.51	72
	Culture layer 1 (20–70 cm)	Light brown (7.5 YR 7/2)	Silt loam	Gray potsherd	1.22	3.38	135

(Continued on following page)

TABLE 1 (*Continued*) Field description and chemical analysis of each soil layer.

Sampling	Layer and depth (cm)	Dry color	Texture	Intruder	N (g·kg^{-1})	P (g·kg^{-1})	$CaCO_3$ (g·kg^{-1})
	Ash layer (70–100 cm)	Grayish brown (7.5 YR 4/2)	Silt loam	Jade rings, stoneware, and charcoal crumbs	0.71	1.15	49
	Culture layer 2 (100–140 cm)	Cloudy orange (7.5 YR 7/3)	Silt loam	Red potsherd and bone	1.01	4.76	161
	Viscosity layer (140–150 cm)	Cloudy orange (7.5 YR 6/4)	Clay loam		0.68	4.04	113
	Culture layer 3 (150–220 cm)	Cloudy orange (7.5 YR 6/4)	Silt loam	Red potsherd	1.61	4.51	166
	Paleosoil layer (220–400 cm)	Cloudy orange (7.5 YR 6/4)	Clay loam		0.56	0.47	63
18	Topsoil layer (0–20 cm)	Brown (7.5 YR 4/3)	Loam		0.75	1.65	91
	Loess layer (20–170 cm)	Light brown (7.5 YR 7/2)	Silt loam		0.51	2.10	111
	Transition layer (170–320 cm)	Grayish brown (7.5 YR 4/2)	Silt loam		0.57	2.34	78
	Paleosoil layer (255–410 cm)	Cloudy orange (7.5 YR 6/4)	Clay loam		0.43	1.66	62

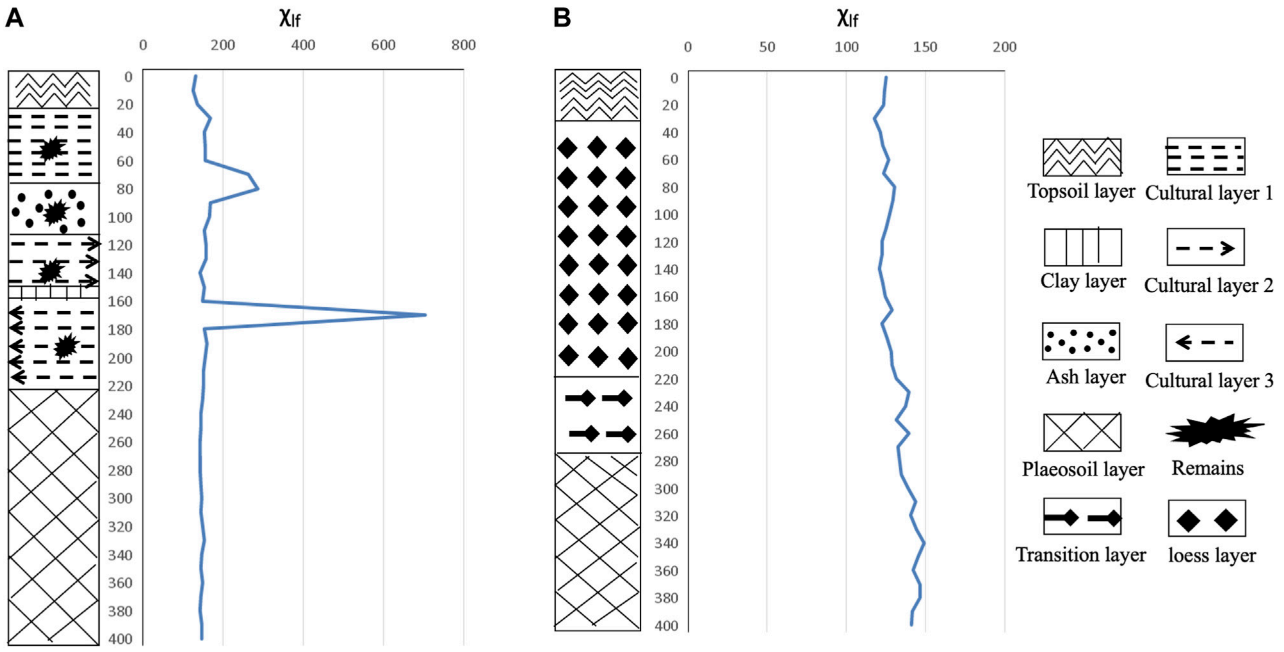

FIGURE 3
Change in the magnetic susceptibility of the natural profile.

content is 81.81 g kg^{-1} in the topsoil, 116.59 g kg^{-1} in the cultural layer, and 64.25 g kg^{-1} in the paleosol layer. Overall, the total nitrogen content is the highest in the topsoil and decreases with depth, but there are peak values in certain cultural layers. The total phosphorus and carbonate contents increase with depth, reaching the highest values in the cultural layer and decreasing to the lowest values in the paleosol layer. For more detailed information, refer to Table 1.

3.2 Magnetic susceptibility

The magnetic susceptibility data χ_{lf} in the cultural profile generally ranged from 131.67 to 705.51*10^{-8} m^3 kg^{-1}, with an average of 174.13*10^{-8} m^3 kg^{-1}. Figure 3A shows the change in magnetic susceptibility in the cultural profile. χ_{lf} showed extreme values in both the ash and cultural layers, especially reaching the maximum at 170 cm, well above the maximum of the natural profile.

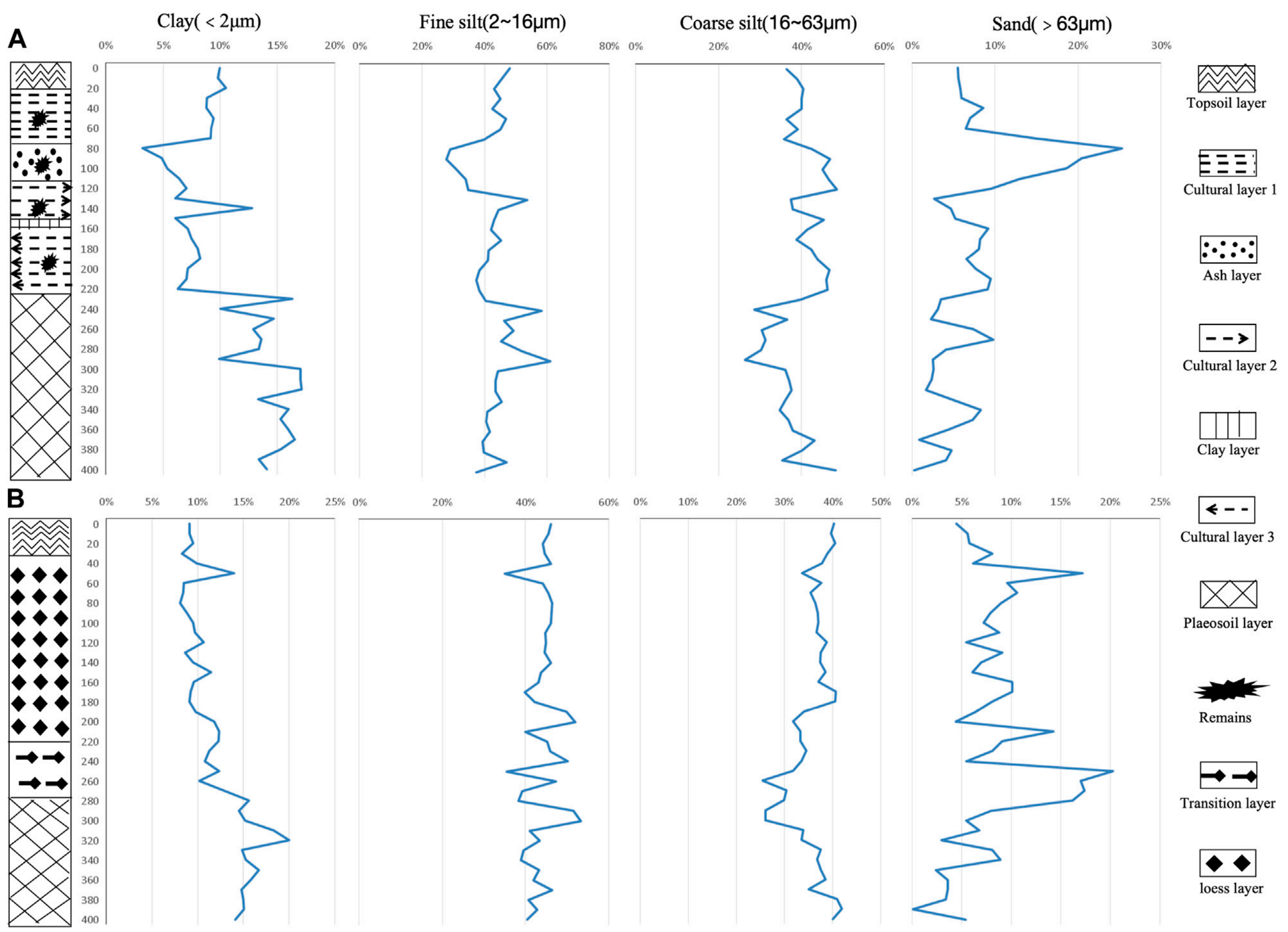

FIGURE 4
Change in the particle size of cultural and natural profiles.

The magnetic susceptibility data χ_{lf} in the natural profile generally ranged from 120.67 to 149.09 $*10^{-8}\,m^3\,kg^{-1}$, with an average of $132.11*10^{-8}\,m^3\,kg^{-1}$. Figure 3B shows the change in magnetic susceptibility in the natural profile, where the value of χ_{lf} generally decreased with depth.

3.3 Particle size

Particle size data in the cultural profile generally averaged 10.74% for clay, 39.59% for fines, 36.30% for coarser sands, and 14.13% for sands. Figure 4A shows the change in particle size in the cultural profile, where the content of clay and fine silt increased with depth, while coarse silt and sand decreased.

The grain size data for the natural profiles averaged 11.97% for clay, 44.09% for fine chalky sand, 35.79% for coarse chalky sand, and 8.15% for sand. Figure 4B shows the change in particle size in the natural profile, where the content of clay increased with depth, while sand decreased, and fine silt and coarse sand fluctuated greatly.

In the ash layer, the sand content reached the highest value, which was much higher than the maximum value of the natural profile, while the clay content reached the lowest value, which was lower than the minimum value of the natural profile. In the culture layer, the clay content reached an extreme value.

3.4 Clay mineral

In the natural profile, characteristic peaks of kaolinite and illite were detected in the paleosoil layer. The kaolinite characteristic peaks were observed at 0.72 nm and 0.36 nm, with intensities of 89.3% and 61.7%, respectively. For illite, the characteristic peaks were found at 0.50 nm and 0.34 nm, with intensities of 37.8% and 100%, respectively (Figure 5A). In the transition layer, a variety of clay mineral characteristic peaks were detected. These included kaolinite at 0.72 nm (50.5% intensity), montmorillonite at 0.50 nm (24.0% intensity), chlorite at 0.46 nm and 0.36 nm (8.8% and 41.8% intensities, respectively), and ilmenite at 0.33 nm (73.1% intensity) (Figure 5B). In the loess layer, characteristic peaks of illite and montmorillonite were identified. Illite peaks were observed at 0.50 nm and 0.34 nm, with intensities of 12.9% and 36.0%, respectively, while montmorillonite exhibited a peak at 1.48 nm, with an intensity of 36.1% (Figure 5C). In the topsoil layer, characteristic peaks of ilmenite and chlorite were detected. Ilmenite peaks were found at 1.01 nm and 0.50 nm, with intensities of 100% and

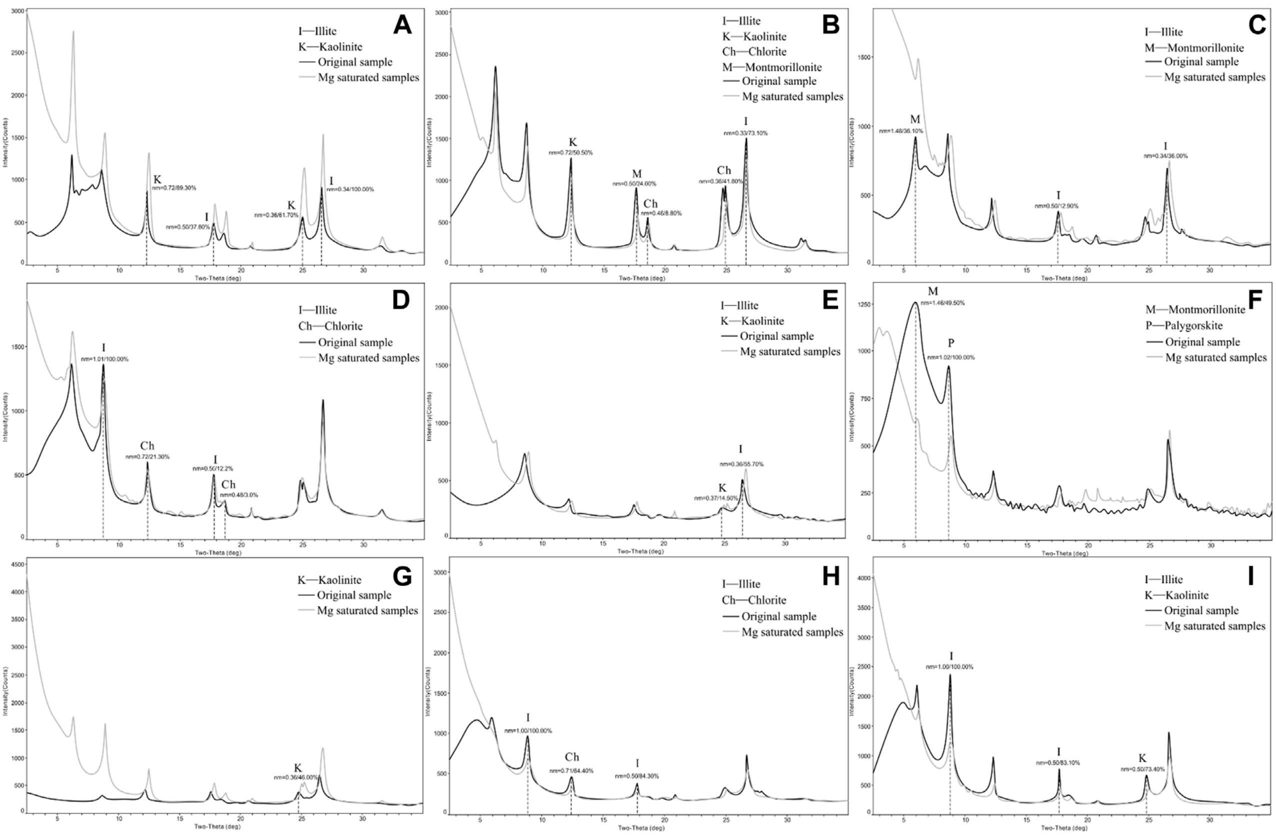

FIGURE 5
Directional map of clay minerals.

12.2%, respectively, while chlorite exhibited peaks at 0.72 nm and 0.48 nm, with intensities of 21.3% and 3.0%, respectively (Figure 5D).

In the cultural profile, characteristic peaks of kaolinite and illite were detected in the paleosoil layer, with kaolinite at 0.37 nm (intensity 14.5%) and illite at 0.36 nm (intensity 55.7%) (Figure 5E). In culture layer 3, peaks of montmorillonite and pozzolanite were identified. Montmorillonite exhibited a peak at 1.46 nm with an intensity of 49.5%, while pozzolanite showed a peak at 1.02 nm with an intensity of 100% (Figure 5F). In culture layer 2, a kaolinite peak was observed at 0.46 nm with an intensity of 46%, and it exhibited an un-sharp peak shape (Figure 5G). In culture layer 1, characteristic peaks of illite and chlorite were detected. Illite peaks were found at 1.00 and 0.50 nm, with intensities of 100% and 84.3%, respectively, while chlorite exhibited a peak at 0.71 nm, with an intensity of 64.4% (Figure 5H). In the topsoil layer, characteristic peaks of illite and kaolinite were observed. Illite peaks were detected at 1.00 and 0.50 nm, with intensities of 100% and 83.1%, respectively, while kaolinite exhibited a peak at 0.50 nm, with an intensity of 73.4% (Figure 5I).

3.5 Soil development indexes

The cultural profile development indexes Sa, Saf, and ba ranged from 7.63 to 10.94, 14.19 to 20.35, and 0.18 to 0.29, respectively, and the change rule of the three values was the same (Figure 6A). In the topsoil layer, there was almost no change in the three, with mean values of 8.73, 16.30, and 0.22, respectively. In culture layer 1, the values of the three increased slightly with depth, with mean values of 8.82, 16.46, and 0.23, respectively. Since the ash layer is no longer a general soil material due to the foreign materials added by ancient humans, its development indicator values are not significant. In culture layer 2, the values of the three increased significantly with depth, and the average values of the three were 8.80, 16.48, and 0.23, respectively. In culture layer 3, the three values have no change, and the average values of the three are 8.78, 16.38, and 0.22, respectively. In the paleosol, the three values increased slightly with depth, reached a peak at 350 cm, and an anomalous peak appeared at 270 cm, indicating that the soil development experienced strong anomalous environmental effects, and then began to decrease slightly, with the three average values of 8.02, 15.01, and 0.19, respectively.

The natural profile development indexes Sa, Saf, and ba ranged from 6.98 to 8.64, 12.96 to 16.25, and 0.15 to 0.23, respectively, and the change pattern of the three values was the same (Figure 6B). In the loess layer, the three values increased with depth while slightly fluctuating, and they reached the maximum value at the bottom; however, at 130 cm, there was an abnormal trough, and the average values of the three values were 8.26, 15.71, and 0.21, respectively. In the transition layer, the three values decreased with depth, in which the changes in Sa and Saf values fluctuated slightly, and the average values of the three were 8.18, 15.45, and 0.20, respectively. In the paleosol layer, the three values increased with depth, and at 270 cm,

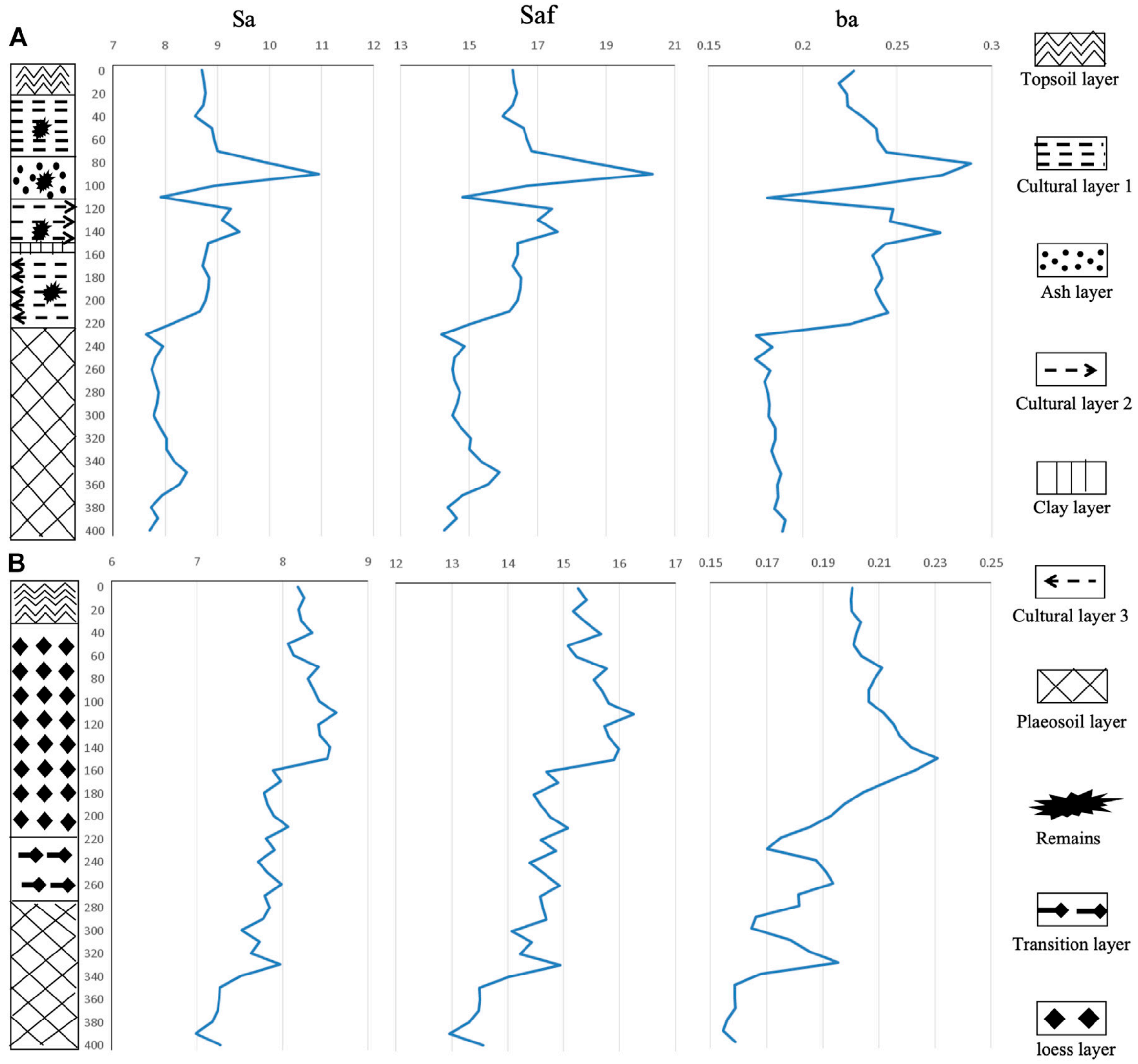

FIGURE 6
Change in the soil development indexes of cultural and natural profiles.

there was an anomalous peak, and the average values of the three values were 8.01, 14.97, and 0.19, respectively.

It can be seen that the degree of development of the cultural and natural profiles increases with depth, reaching a maximum in the paleosols, and at this point, both the developmental indicators have similar values, suggesting that both have similar environmental contexts.

3.6 Spore pollen and charcoal

The typical spore and pollen images identified are shown in Figure 7. The percentage content of pollen in the cultural profile samples was mainly composed of herbaceous plant pollen, indicating a temperate grassland vegetation landscape at that time. The identified herbaceous plant pollen was mainly composed of Gramineae, Chenopodiaceae, and Artemisia, with content changes ranging from 3.50% to 72.64%, 1.49% to 32.81%, and 4.37% to 61.39%, and the average values were 24.81%, 9.43%, and 37.85%, respectively. In addition, it was found that pollen from woody plants appeared in most layers, with Castanea, Juglans, Carpinus, Betula, Quercus, and Pinus being the main pollen species, with the content of 0%–2.70%, 0%–2.13%, 0%–4.90%, 0%–4.35%, 0%–1.50%, and 0%–10.53%, and the average values were 0.58%, 0.57%, 0.91%, 1.50%, 4.39%, and 3.09%, respectively. *Fern* pollen mainly appeared in the upper part of the cultural profile and rarely in other layers. The content changes from 0% to 20.56%, with an average value of 2.69%. The concentration value of carbon chips identified and counted ranged from 548 to 438,152 particles/g, with an average value of 57,931 particles/g.

The percentage of the pollen content in the natural profile samples was also mainly composed of herbaceous plant pollen. The identified grass pollen was mainly composed of Gramineae, Chenopodiaceae, and Artemisia pollen, whose content ranged from 1.46% to 24.41%, 2.50% to 20.28%, and 3.47% to 78.00%, and the

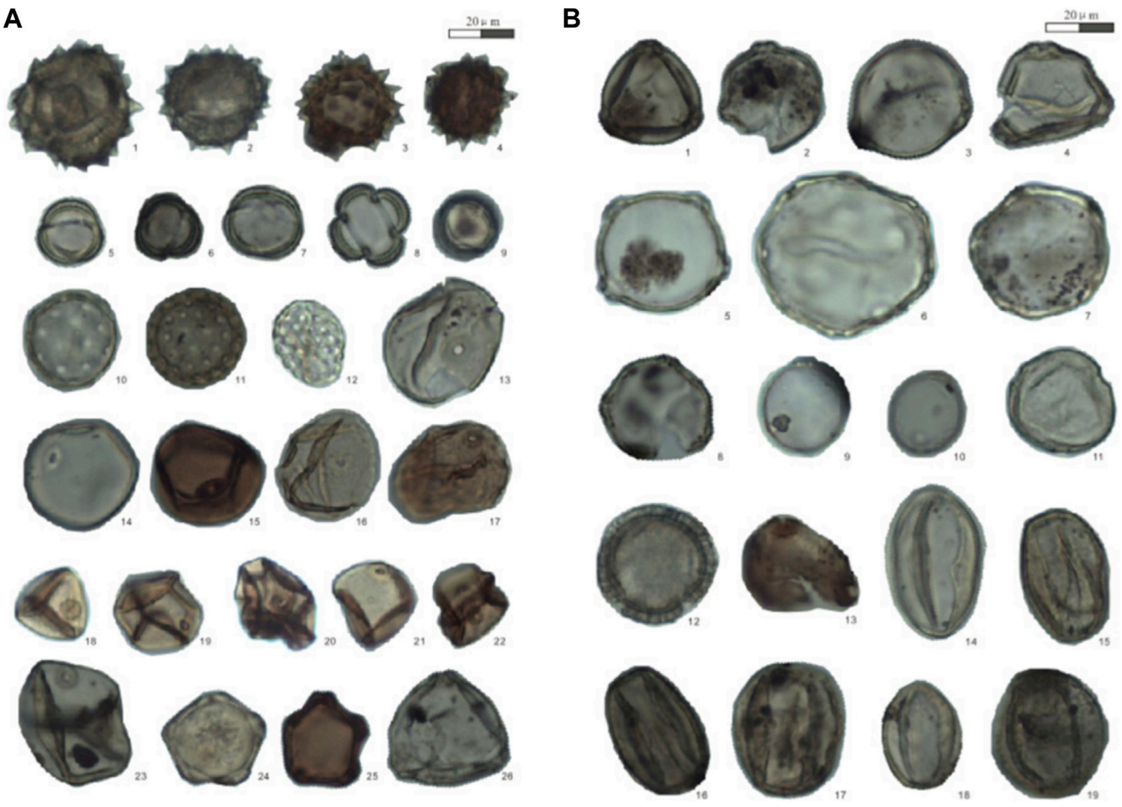

FIGURE 7
Pollen plate 1 **(A)** and plate 2 **(B)** (A: 1–4. Compositae; 5–9. Artemisia; 10–12. Chenopodiaceae; 13–23. Gramineae; 24–25. Alnus; and 26. Corylus; **(B)** 1–4. Betula; 5. Carpinus; 6. Juglans; 7. Pterocarya; 8. Carpinus; 9–10. Humulus; 11. Carya; 12. Polygonum; 13. Tilia; and 14–19. Quercus).

average values were 9.69%, 7.45%, and 41.02%, respectively. In addition, it was found that woody plant pollen appeared in most layers, with the main pollen being Castanea, Juglans, Carpinus, Betula, Quercus, and Pinus, whose content varied from 0% to 1.03%, 0% to 1.74%, 0% to 20.45%, 0% to 5.58%, 0% to 8.02%, and 0.94% to 6.90%, with an average of 0.38%, 0.43%, 2.25%, 1.13%, 3.35%, and 2.74%, respectively. The pollen of ferns mainly appears in the upper part of the natural section, and it rarely appears in the other layers. The variation range was 0%–46.50%, with an average value of 12.63%. The concentration value of carbon chips identified and counted ranges from 829 to 106,376 particles/g, with an average value of 14,394 particles/g.

3.7 Phytolith

More than 20 typical types of phytoliths were found in the cultural profile, with the main ones being rod type, dumbbell type, cross type, duct type, fan type, and square type. Among these types, crop phytoliths such as millet and rice were also found (Figure 8). Among them, the identified millet and millet-type phytoliths all came from the lemma shell of the seeds, while the identified rice phytoliths mainly came from the fan-shaped and side-by-side dumbbell-shaped stem and leaf tissues. The vast majority of the phytolith types identified in all samples were Gramineae, with dumbbell- and rod-shaped ones being the main types.

4 Discussion

4.1 Impact of soil physical and chemical properties

From the analysis of the surface data of the whole study area and based on the thickness data of paleosoil, cultural, and topsoil layers at 18 locations, the kriging interpolation method and ContextCapture software were used to generate the three-dimensional model of each soil layer. Combined with the results of paleoclimate research at the site (ZHA et al., 2020), the climate warmed and turned stable, warm, and humid after entering the Holocene, corresponding to the paleosoil layer (Figure 9A). Ancient humans started their activities in the relatively low-lying areas I and III, and the soil layer began to accumulate to form a cultural layer (Figure 9B), which contained a cultivation layer, especially in area I, where the low-lying area was convenient for irrigation and was super-southern, with sufficient light, making it easy to carry out agricultural activities. Most researchers believed that agriculture in the Yangshao culture in the Central Plains was practiced in the form of shifting cultivation, which was cultivating a plot of land for a period of time and then transferring it to a new plot of land to cultivate crops when the fertility of the land was depleted. The expansion of new plots of land was generally believed to be through the "slash-and-burn" method (Chang, 1967; Li, 1980; An, 1988). Slash-and-burn cultivation led the soil to be filled with charcoal

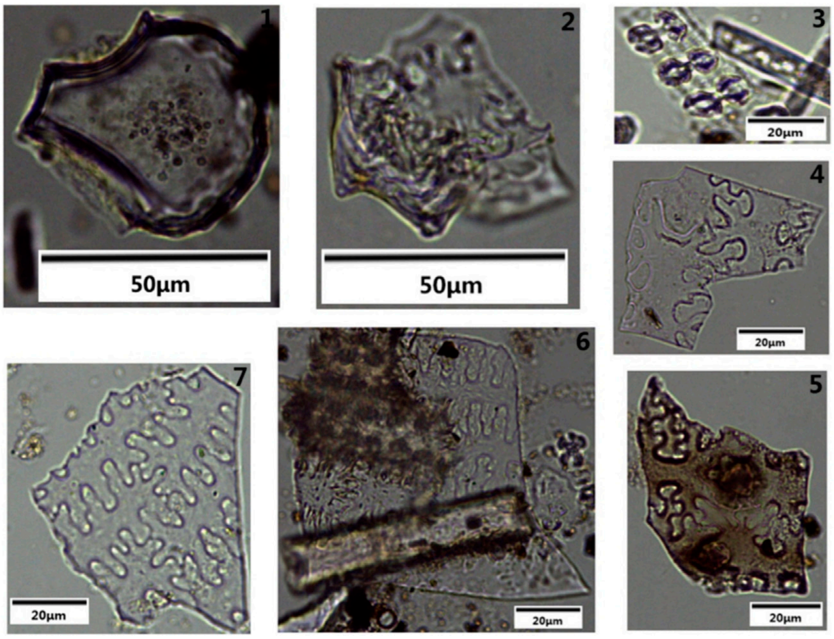

FIGURE 8
Main types of agricultural phytolith in the cultural site (1. rice fan-shaped; 2. rice bimodal; 3. rice side-by-side dumbbell-shaped; 4–5. corn husk Ω-type; 6–7. millet glume η-type).

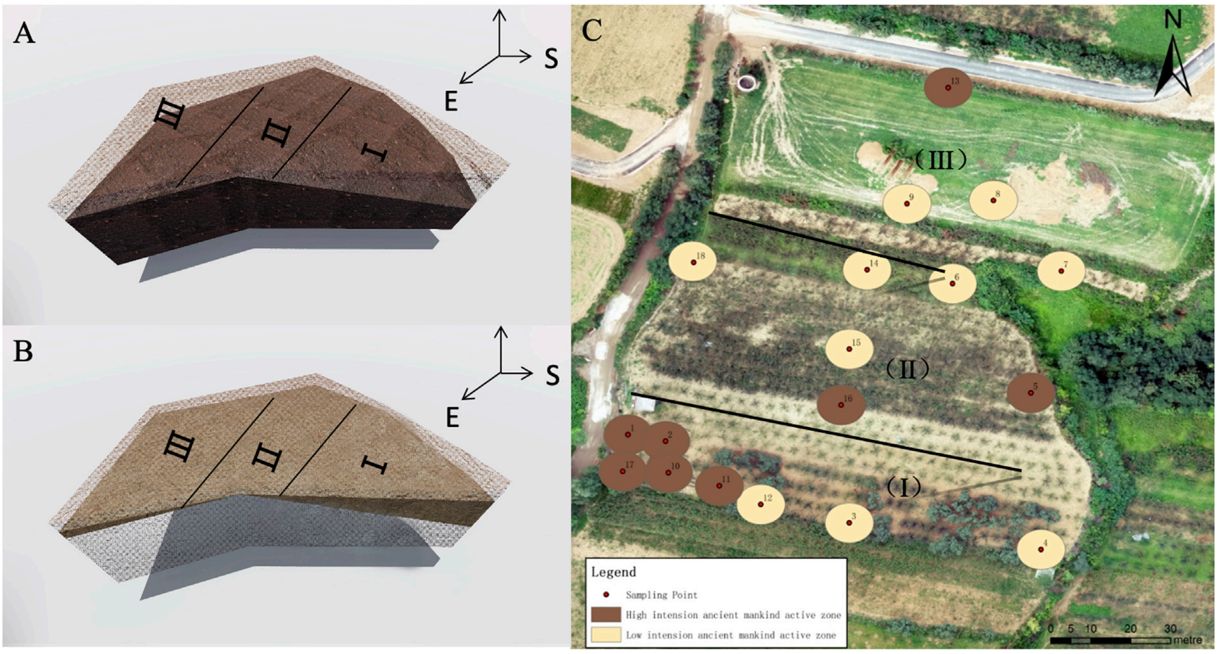

FIGURE 9
Probability area of ancient farming.

debris and other intruders, and therefore, the magnetization value was outside the extreme range. At the same time, the coarse-grained matter was affected by the plowing activities and decomposed into fine particles with a high content of sticky particles.

Combining the results of the macro-observation and basic physicochemical analysis of soil at each sampling point, there was a good correspondence between them, and the probability of ancient farming activities can be divided into two categories: high

TABLE 2 Main soil characteristics and ancient tillage probability at various locations.

Sample point	Macroscopic observation	Basic physical and chemical analysis	Ancient probability of tillage
1	Black pottery flakes and charcoal	$T(N) < \overline{X(N)}$,$T(P) > \overline{X(P)}$, and $T(Ca) > \overline{X(Ca)}$	High
2	Calcium carbonate nodules, red-black gray pottery, charcoal, and bones	$T(N) < \overline{X(N)}$, $T(P) > \overline{X(P)}$, and $T(Ca) > \overline{X(Ca)}$	High
3	No traces of artificial disturbance	$T(N) > \overline{X(N)}$ $T(P) < \overline{X(P)}$, and $T(Ca) < \overline{X(Ca)}$	Low
4	No traces of artificial disturbance	$T(N) > \overline{X(N)}$,$T(P) < \overline{X(P)}$, and $T(Ca) < \overline{X(Ca)}$	Low
5	Soil structure sheet and red pottery	$T(N) > \overline{X(N)}$,$T(P) < \overline{X(P)}$, and $T(Ca) < \overline{X(Ca)}$	Low
6	Gray pottery	$T(N)> \overline{X(N)}$,$T(P) < \overline{X(P)}$, and $T(Ca) > \overline{X(Ca)}$	Low
7	No traces of artificial disturbance	$T(N) > \overline{X(N)}$, $T(P) \approx \overline{X(P)}$, and $T(Ca) > \overline{X(Ca)}$	Low
8	No traces of artificial disturbance	$T(N) > \overline{X(N)}$, $T(P) < \overline{X(P)}$, and $T(Ca) < \overline{X(Ca)}$	Low
9	No traces of artificial disturbance	$T(N) > \overline{X(N)}$, $T(P) < \overline{X(P)}$, and $T(Ca) < \overline{X(Ca)}$	Low
10	Flaky calcium carbonate nodules, red ash pottery, and gravel	$T(N) > \overline{X(N)}$, $T(P) > \overline{X(P)}$, and $T(Ca) > \overline{X(Ca)}$	High
11	Carbon chips	$T(N) > \overline{X(N)}$,$T(P) > \overline{X(P)}$, and $T(Ca) > \overline{X(Ca)}$	High
12	No traces of artificial disturbance	$T(N) < \overline{X(N)}$, $T(P) < \overline{X(P)}$, and $T(Ca) < \overline{X(Ca)}$	Low
13	Black pottery and red soil slag	$T(N) > \overline{X(N)}$,$T(P) > \overline{X(P)}$, and $T(Ca) > \overline{X(Ca)}$	High
14	No traces of artificial disturbance	$T(N) > \overline{X(N)}$, $T(P) < \overline{X(P)}$, and $T(Ca) < \overline{X(Ca)}$	Low
15	No traces of artificial disturbance	$T(N) > \overline{X(N)}$ $T(P) < \overline{X(P)}$, and $T(Ca) < \overline{X(Ca)}$	Low
16	Red soil slag	$T(N) \approx \overline{X(N)}$, $T(P) > \overline{X(P)}$, and $T(Ca) > \overline{X(Ca)}$	High
17	Crumb granular, red ash pottery, jade ring, stone, bone, and charcoal	$T(N) > \overline{X(N)}$ $T(P) > \overline{X(P)}$, and $T(Ca) > \overline{X(Ca)}$	High
18	No traces of artificial disturbance	$T(N) < \overline{X(N)}$, $T(P) < \overline{X(P)}$, and $T(Ca) < \overline{X(Ca)}$	low

and low, as shown in Table 2. The high-probability sample points mostly showed the presence of artifact intrusions, such as pottery shards and charcoal chips, and the total nitrogen, phosphorus, and calcium carbonate content exceeded the average value of the natural profile. This is not only consistent with the study of agriculture in the Central Plains of the Yangshao culture but also with the study of prehistoric rice soils in the south, as well as the results of the international study of ancient dryland soils, which indicated that ancient humans used human and animal feces to a certain extent to restore the fertility of arable land (Cao et al., 2007; Dahms, 1998; X; Wang et al., 2018; Zhong and Zhao, 2023). The probability space distribution is shown in Figure 9C.

In addition, the speculation about farming activities was also confirmed by comparing the sporoderm content and the species of the cultural and natural profiles (Table 3). It was found that the concentration of pollen in the dense samples of the cultural profile was significantly higher than that of the natural profile, and it was observed that the content of Gramineae varied most obviously, the average content of the cultural profile was about three times that of the natural profile, and the crop phytosilicates of maize, millet, and rice that were identified belonged to the Gramineae group of plants. In addition to Gramineae, the content of *Quinoa* in the cultural profile is also significantly higher than that in the natural profile, and spinach, thick-skinned lettuce, sugar beet, and pigweed in the *Quinoa* family were all available for human consumption. Other major species and genera identified, such as Artemisia, Artocarpus, Selaginella, and other non-food crops, were found in large quantities in the natural profiles, and their contents were much higher than those in the cultural profiles. This indicated that when ancient human activities began to enhance, the ancient humans

TABLE 3 Comparison of sporopollen and charcoal between the cultural and natural profiles.

	Cultural profile			Natural profile		
	Maximum value	Minimum value	Mean value	Maximum value	Minimum value	Mean value
Concentration of spore powder (grain/g)	1,570.55	7.83	247.99	902.07	1.65	160.86
Concentration of charcoal dust (grains/g)	438,152.87	548.23	57,931.44	106,376.29	828.80	14,394.43
A/C	10.33	0.50	4.55	31.20	0.58	6.82
Herbaceous proportion (%)	96.02	67.29	84.43	95.69	38.00	71.98
Woody proportion (%)	23.76	3.98	12.04	30.30	4.31	12.09
Proportion of ferns (%)	21.96	0.00	3.53	46.50	0.00	15.94
Broad-leaved woody pollen content (%)	18.32	2.91	9.46	25.00	2.44	8.96
Warm-loving pollen content (%)	4.74	0.00	1.41	4.78	0.00	1.40
Cyclophyllum concentration (grains/g)	125.64	0.00	10.03	319.79	0.00	45.44
Cyclophyllum/spore pollen	3.39	0.00	0.22	8.30	0.00	0.73
AP/NAP	0.29	0.04	0.15	0.73	0.05	0.20
Artemisia (%)	61.39	4.37	37.85	78.00	3.47	41.02
Compositae (%)	9.00	0.00	2.70	21.05	0.47	4.68
Chenopodiaceae (%)	32.81	1.49	9.43	20.28	2.50	7.45
Carpinus (%)	4.90	0.00	0.95	20.45	0.00	2.25
Gramineae (%)	72.64	3.50	24.81	24.41	1.46	9.69
Quercus (%)	10.50	0.00	4.39	8.02	0.00	3.35
Selaginella (%)	5.14	0.00	0.50	43.00	0.00	4.37

selectively planted and harvested the plants needed for survival and living, resulting in an obvious increase in the content of Gramineae and *Quinoa*, while the plants with little utilization value were cut down and burned due to the needs of habitation and cultivation, which led to a decrease in the content of woody and fern-like plants.

From the point data analysis of the two typical profiles, the ratio of the average contents of clay, fine silt, coarse silt, and sand between the cultural and natural profiles is 0.91, 0.95, 1.01, and 1.38, respectively, and the ratio of the coefficient of variation is 1.50, 1.59, 0.98, and 1.25, respectively, which shows that the degree of change in the particle size of the cultural profile is greater than that of the natural profile, and the change in the clay particle is especially obvious. In addition, the particle size composition is coarser than that of the natural profile, especially in the ash layer, where a large number of sand grains were produced by ancient humans using fire, and its content reached the highest value of 293.99 g kg^{-1}, much higher than the maximum value of the natural profile. However, in the cultural layer, the content of clay grains reaches a great value, and it is hypothesized that ancient human habitation activities increased the content of clay grains. The ratio of the mean value of χlf between the cultural and natural profiles is 1.15, and the ratio of the coefficient of variation is 1.96. It can be seen that the degree of variation of χlf in the cultural profile is greater than that in the natural profile, and the value is larger than that in the natural profile, especially in the ash and cultural layers, which reached $300.72 \times 10^{-8}\,m^3\,kg^{-1}$ and $231.06 \times 10^{-8}\,m^3\,kg^{-1}$, respectively, and an anomalous maximum value of $705.51 \times 10^{-8}\,m^3\,kg^{-1}$ appeared in cultural layer 3. It is hypothesized that the increase in the content of soil magnetic material was caused by the activities of ancient human beings, such as using fire and living. Comparing the clay mineral types of the two profiles, the more obvious difference is in the transition layer of the natural profile, where the clay mineral type is a mixture of illite, montmorillonite, kaolinite, and chlorite, while the clay mineral types of the corresponding cultural layer 3 in the same period are illite and kaolinite, which indicated that the clay mineral types had become relatively homogeneous due to the disturbance of paleoanthropogenic activities.

4.2 Impact of soil development

Although farming activities promoted the decomposition of coarse soil particles into fine particles, the primitive farming technique of slash-and-burn cultivation produced a large amount

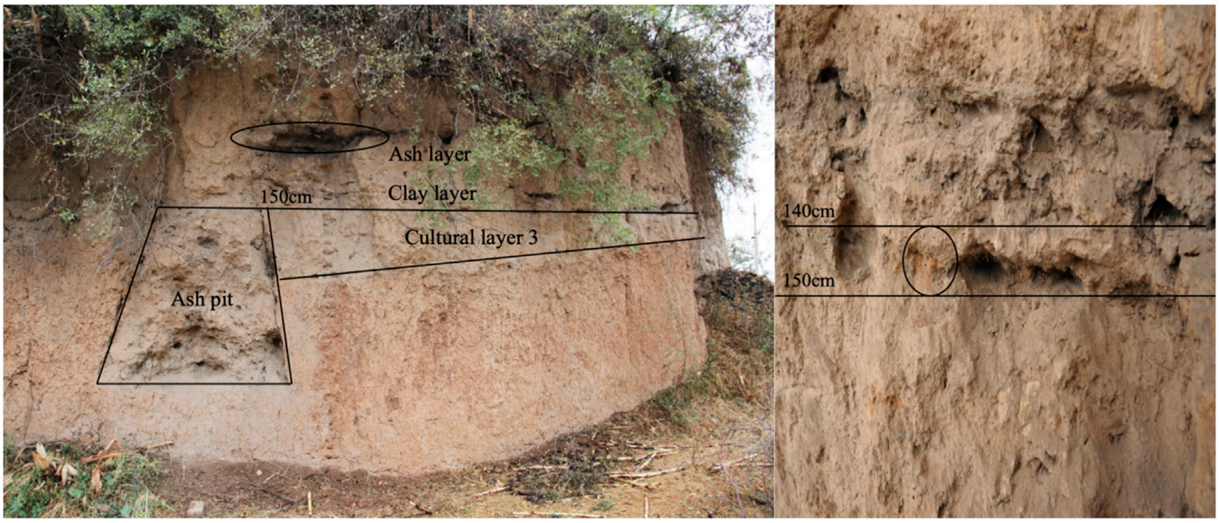

FIGURE 10
Clay layer in the cultural profile.

of ash and formed an ash layer with a very high sand content, which had a limited effect on promoting the development of the overall soil profile. Moreover, slash-and-burn farming mainly involves cutting down and burning forest trees without turning over the soil and practicing a farming system that leaves the land fallow after sowing seeds, which lacks turning, disturbing, and artificial ripening. Based on the soil development indicators, the inference is also further justified. By comparing the values of the developmental indicators in the cultural and natural profiles, the impact of paleoanthropogenic activities on soil development was investigated from a holistic perspective. In the cultural profile, the average values of Sa, Saf, and ba were 8.53, 15.94, and 0.22, respectively. On the other hand, in the natural profile, the average values were 7.94, 14.82, and 0.19, respectively. It can be found that the development indexes of the cultural profiles were all higher than those of the natural profiles, the degree of development of the natural profiles was higher than that of the cultural profiles, and the paleoanthropogenic activities in general hindered soil development. In addition, by comparing the values of the development indexes of the cultural layer with those of the topsoil and paleosoil layers within the cultural profile to explore the influence of paleo-human activities on soil development from a localized perspective, the average values of the development indexes of the cultural layer were 8.80, 16.44, and 0.23, respectively, while in the natural layer, they were 8.38, 15.66, and 0.21, respectively. It can be found that the development indexes of the cultural layer in the cultural profile were higher than those of the natural layer, the development of the cultural layer was weaker than that of the natural layer, and ancient human activities hindered the development of the soil layer.

One of the most obvious activities that hindered soil development was the hardening of the ground by ancient humans as a result of their habitation activities. In culture layer 2, kaolinite was found. According to the dating results, the climate was relatively dry and cold during this period, making it difficult for kaolinite to appear under natural conditions. Combined with field observations, a turbid orange clay layer (Figure 10) was found at the bottom of the layer (140–150 cm), with properties similar to those of the paleosoil. Combined with the soil particle size analysis, the clay content is high, and the dating data are abnormal, which is older than the paleosoil at the bottom. It is hypothesized that ancient humans carried the soil from other periods for covering grain or burying garbage and laid down the clay to achieve the effect of sealing. The magnetization value of this layer reaches an anomalous maximum, indicating that it has experienced fire baking and is presumed to have been hardened by fire. The soil layer that has been artificially compacted and baked, soil voids, and structure had suffered some damage, which had prevented the downward leaching or precipitation of soil particles and minerals to a certain extent, thus affecting soil development.

5 Conclusion

Ancient humans began their activities in the relatively low-lying area, in which farming activities led to an increase in the content of Gramineae and Quinoa in the soil, especially the appearance of phytosilicon bodies such as millet, corn, and rice, which confirms that ancient humans carried out primitive agricultural activities in this area. Slash-and-burn activities led to the filling of the soil with intruders such as charcoal chips and pottery shards, while at the same time, the coarse-grained texture was affected by the farming activities, which mostly decomposed into fine particles, and the content of sticky particles reached an extreme value. The total nitrogen, phosphorus, and calcium carbonate content exceeded the average value of the natural profile, indicating that ancient humans used human and animal excreta to fertilize the farmland.

The comparison of two typical profiles of the soil, under the influence of ancient human activities, macroscopically showed that the intruders in the soil body and morphological characteristics of the profile had obvious differences with the natural profile, and the macroscopically indicative features were mainly manifested in the presence of abundant relic remains. The microscopic indicative features were mainly characterized by a sandy grain size composition, high χlf, and a relatively single clay mineral type.

Slash-and-burn cultivation not only produced a large amount of sand particles but also lacked soil tilling and artificial ripening, which had a limited effect on promoting the development of the soil. Through the analysis and comparison of the development indices of the cultural and natural profiles, it was found that ancient human activities hindered the development of the soil. In particular, the soil voids and structure of the ground created as a result of habitation activities were damaged to some extent, which prevented soil particles and minerals from leaching or precipitating downward to a certain extent, thus affecting soil development.

Data availability statement

The datasets presented in this study can be found in online repositories. The names of the repository/repositories and accession number(s) can be found in the article/Supplementary material.

Author contributions

LZ: methodology, project administration, supervision, validation, writing–review and editing, funding acquisition, and conceptualization. WW: methodology, project administration, validation, writing–review and editing, and conceptualization. JZ: formal analysis, software, validation, visualization, and writing–original draft. YS: formal analysis, validation, and writing–original draft. DC: validation and writing–original draft.

Funding

The author(s) declare that financial support was received for the research, authorship, and/or publication of this article. This research was funded by the National Natural Science Foundation of China (grant no. 41907001) and The Third Batch of Huizhi Leader Creative Space Project in Chengde Hi-Tech Zone (grant no. HZLC2024023).

Acknowledgments

This work was supported by the National Natural Science Foundation of China.

Conflict of interest

The authors declare that the research was conducted in the absence of any commercial or financial relationships that could be construed as a potential conflict of interest.

Publisher's note

References

Adam, P., Schaeffer, P., Schmitt, G., Bailly, L., Courel, B., Fresnais, M., et al. (2016). Identification and mode of formation of hopanoid nitriles in archaeological soils. *Org. Geochem.* 91, 100–108. doi:10.1016/j.orggeochem.2015.10.013

An, Z. (1988). Prehistoric agriculture in China. *Archaeol. J.* 4, 369–381.

Arnaud-fassetta, G., De Beaulieu, J. L., Suc, J. P., Provansal, M., Williamson, D., Leveau, P., et al. (2000). Evidence for an early land use in the rhone delta (mediterranean France) as recorded by late holocene fluvial paleoenvironments (1640–100 bc). *Geodin. Acta* 13 (6), 377–389. doi:10.1080/09853111.2000.11105381

Blasi, A., Politis, G., and Bayón, C. (2013). Palaeoenvironmental reconstruction of La Olla, a Holocene archaeological site in the Pampean coast (Argentina). *J. Archaeol. Sci.* 40 (3), 1554–1567. doi:10.1016/j.jas.2012.09.016

Brown, K. S., Marean, C. W., Herries, A. I. R., Jacobs, Z., Tribolo, C., Braun, D., et al. (2009). Fire as an engineering tool of early modern humans. *Science* 325 (5942), 859–862. doi:10.1126/science.1175028

Cao, Z., Yang, L., and Lin, X. (2007). Morphological characteristics of paddy fields, paddy soil profile, phytolith and fossil rice grain of the Neolithic Age in Yangtze River Delta. *Acta Pedol. Sin.* 44 (5), 838–847.

Carrancho, Á., and Villalaín, J. J. (2011). Different mechanisms of magnetisation recorded in experimental fires: archaeomagnetic implications. *Earth Planet. Sci. Lett.* 312 (1–2), 176–187. doi:10.1016/j.epsl.2011.10.006

Chang, K. C. (1967). The yale expedition to taiwan and southeast asian horticulture evolution. *Discovery* 11 (2), 3.

Chen, F., Xu, Q., Chen, J., Birks, H. J. B., Liu, J., Zhang, S., et al. (2015). East Asian summer monsoon precipitation variability since the last deglaciation. *Sci. Rep.* 5, 11186–11211. doi:10.1038/srep11186

Church, M. J., Peters, C., and Batt, C. M. (2007). Sourcing fire ash on archaeological sites in the Western and Northern Isles of Scotland, using mineral magnetism. *Geoarchaeology* 22 (7), 747–774. doi:10.1002/gea.20185

Cook, S. R., Clarke, A. S., Fulford, M. G., and Voss, J. (2014). Characterising the use of urban space: a geochemical case study from Calleva Atrebatum (Silchester, Hampshire, UK) Insula IX during the late first/early second century AD. *J. Archaeol. Sci.* 50 (1), 108–116. doi:10.1016/j.jas.2014.07.003

Cruz-y-Cruz, T., Sánchez, G., Sedov, S., Terrazas-Mata, A., Solleiro-Rebolledo, E., Tovar-Liceaga, R. E., et al. (2015). Spatial variability of Late Pleistocene-Early Holocene soil formation and its relation to early human paleoecology in Northwest Mexico. *Quat. Int.* 365, 135–149. doi:10.1016/j.quaint.2014.11.042

Dahms, D. E. (1998). Reconstructing paleoenvironments from ancient soils: a critical review. *Quat. Int.* 51, 58–60. doi:10.1016/s1040-6182(98)90222-1

Dirix, K., Muchez, P., Degryse, P., Kaptijn, E., MuŠič, B., Vassilieva, E., et al. (2013). Multi-element soil prospection aiding geophysical and archaeological survey on an archaeological site in suburban Sagalassos (SW-Turkey). *J. Archaeol. Sci.* 40 (7), 2961–2970. doi:10.1016/j.jas.2013.02.033

Dou, Y., Yang, S., Liu, Z., Clift, P. D., Yu, H., Berne, S., et al. (2010). Clay mineral evolution in the central Okinawa Trough since 28 ka: implications for sediment provenance and paleoenvironmental change. *Palaeogeogr. Palaeoclimatol. Palaeoecol.* 288 (1–4), 108–117. doi:10.1016/j.palaeo.2010.01.040

El Ouahabi, M., Hubert-Ferrari, A., and Fagel, N. (2017). Lacustrine clay mineral assemblages as a proxy for land-use and climate changes over the last 4 kyr: the Amik Lake case study, Southern Turkey. *Quat. Int.* 438, 15–29. doi:10.1016/j.quaint.2016.11.032

Fernández, F. G., Terry, R. E., Inomata, T., and Eberl, M. (2002). An ethnoarchaeological study of chemical residues in the floors and soils of Q'eqchi' maya houses at las pozas, Guatemala. *Geoarchaeology - An Int. J.* 17 (6), 487–519. doi:10.1002/gea.10026

Ferro-Vázquez, C., Martínez-Cortizas, A., Nóvoa-Muñoz, J. C., Ballesteros-Arias, P., and Criado-Boado, F. (2014). 1500 Years of soil use reconstructed from the chemical properties of a terraced soil sequence. *Quat. Int.* 346, 28–40. doi:10.1016/j.quaint.2014.03.023

Fleisher, J., and Sulas, F. (2015). Deciphering public spaces in urban contexts: geophysical survey, multi-element soil analysis, and artifact distributions at the 15th-16th-century AD Swahili settlement of Songo Mnara, Tanzania. *J. Archaeol. Sci.* 55, 55–70. doi:10.1016/j.jas.2014.12.020

Fredlund, G. G., and Tieszen, L. T. (1994). Modern phytolith assemblages from the north American great plains. *J. Biogeogr.*, 21(3), 321–335. doi:10.2307/2845533

Gallello, G., Pastor, A., Diez, A., La Roca, N., and Bernabeu, J. (2013). Anthropogenic units fingerprinted by REE in archaeological stratigraphy: mas d'Is (Spain) case. *J. Archaeol. Sci.* 40 (2), 799–809. doi:10.1016/j.jas.2012.10.005

Gerlach, R., Fischer, P., Eckmeier, E., and Hilgers, A. (2012). Buried dark soil horizons and archaeological features in the Neolithic settlement region of the Lower Rhine area, NW Germany: formation, geochemistry and chronostratigraphy. *Quat. Int.* 265, 191–204. doi:10.1016/j.quaint.2011.10.007

Haslam, M. (2004). The decomposition of starch grains in soils: implications for archaeological residue analyses. *J. Archaeol. Sci.* 31 (12), 1715–1734. doi:10.1016/j.jas.2004.05.006

Haslam, R., and Tibbett, M. (2004). Sampling and analyzing metals in soils for archaeological prospection: a critique. *Geoarchaeology An Int. J.* 19 (8), 731–751. doi:10.1002/gea.20022

Homburg, J. A., and Sandor, J. A. (2011). Anthropogenic effects on soil quality of ancient agricultural systems of the American Southwest. *Catena* 85 (2), 144–154. doi:10.1016/j.catena.2010.08.005

Kamenov, G. D., Brenner, M., and Tucker, J. L. (2009). Anthropogenic versus natural control on trace element and Sr-Nd-Pb isotope stratigraphy in peat sediments of southeast Florida (USA), ~1500 AD to present. *Geochimica Cosmochimica Acta* 73 (12), 3549–3567. doi:10.1016/j.gca.2009.03.017

Kelly, E. F., Chadwick, O. A., and Helinski, T. E. (1998). Kelly1998_Article_TheEffectOfPlantsOnMineralWeat.pdf. *Biogeochemistry* 42, 21–53. doi:10.1023/a:1005919306687

Kidder, T., Liu, H., Xu, Q., and Li, M. (2012). The alluvial geoarchaeology of the sanyangzhuang site on the Yellow River floodplain, henan Province, China. *Geoarchaeology* 27 (4), 324–343. doi:10.1002/gea.21411

Kim, J. C., Lee, Y.Il, Lim, H. S., and Yi, S. (2012). Geochemistry of quaternary sediments of the jeongokri archaeological site, korea: implications for provenance and palaeoenvironments during the late pleistocene. *J. Quat. Sci.* 27 (3), 260–268. doi:10.1002/jqs.1540

Knudson, K. J., Frink, L., Hoffman, B. W., and Price, T. D. (2004). Chemical characterization of Arctic soils: activity area analysis in contemporary Yup'Ik fish camps using ICP-AES. *J. Archaeol. Sci.* 31 (4), 443–456. doi:10.1016/j.jas.2003.09.011

Li, Y. (1980). An experimental exploration of the tools of production in primitive Chinese society. *Archaeology* 6, 515–520.

Linford, N. T., and Canti, M. G. (2001). Geophysical evidence for fires in antiquity: preliminary results from an experimental study. Paper given at the EGS XXIV General Assembly in The Hague, April 1999. *Archaeol. Prospect.* 8 (4), 211–225. doi:10.1002/arp.170

Lu, J., Hu, Z., Xu, Z., Cao, Z., Zhuang, S., Yang, L., et al. (2009). Effects of rice cropping intensity on soil nitrogen mineralization rate and potential in buried ancient paddy soils from the Neolithic age in China's Yangtze River delta. *J. Soils Sediments* 9 (6), 526–536. doi:10.1007/s11368-009-0138-1

Macphail, R. I. (2008). Soils and archaeology - science direct. *Encycl. Archaeol.*, 2064–2072.

Manalt, F., Beck, C., Disnar, J. R., Deconinck, J. F., and Recourt, P. (2001). Evolution of clay mineral assemblages and organic matte in the Late glacial-Holocene sedimentary infill of Lake Annecy (northwestern alps): paleoenvironmental implications. *J. Paleolimnol.* 25 (2), 179–192. doi:10.1023/A:1008140114714

Marcott, S. A., Marcott, S. A., Shakun, J. D., Clark, P. U., and Mix, A. C. (2013). A reconstruction of regional. 1198. doi:10.1126/science.1228026

Migliavacca, M., Pizzeghello, D., Ertani, A., and Nardi, S. (2013). Chemical analyses of archaeological sediments identified the ancient activity areas of an Iron age building at Rotzo (Vicenza, Italy). *Quat. Int.* 289, 101–112. doi:10.1016/j.quaint.2012.07.016

Neumann, K., Strömberg, C. A. E., Ball, T., Albert, R. M., Vrydaghs, L., and Cummings, L. S. (2019). International code for phytolith nomenclature (ICPN) 2.0. *Ann. Bot.* 124 (2), 189–199. doi:10.1093/aob/mcz064

Nielsen, N. H., and Kristiansen, S. M. (2014). Identifying ancient manuring: traditional phosphate vs. multi-element analysis of archaeological soil. *J. Archaeol. Sci.* 42 (1), 390–398. doi:10.1016/j.jas.2013.11.013

Oonk, S., Slomp, C. P., Huisman, D. J., and Vriend, S. P. (2009). Geochemical and mineralogical investigation of domestic archaeological soil features at the Tiel-Passewaaij site, The Netherlands. *J. Geochem. Explor.* 101 (2), 155–165. doi:10.1016/j.gexplo.2008.06.004

Parnell, J. J., Terry, R. E., and Nelson, Z. (2002). Soil chemical analysis applied as an interpretive tool for ancient human activities in Piedras Negras, Guatemala. *J. Archaeol. Sci.* 29 (4), 379–404. doi:10.1006/jasc.2002.0735

Pastor, A., Gallello, G., Cervera, M. L., and Guardia, M.De. (2016). Mineral soil composition interfacing archaeology and chemistry. *Trends Anal. Chem.* 78, 48–59. doi:10.1016/j.trac.2015.07.019

Paula, J., Mike, G. L., Warren, J., Chanda, J. H., Paul, G., Caitlin, E., et al. (2004). *IntCal04 terrestrial radiocarbon age calibration, 0-26 cal kyr BP Radiocarbon Publisher ' s PDF, also known as Version of record Publication date: 0–26.*

Peninsula, P. R. (1983). *Division s-5-soil genesis, morphology, and classification*, 1–7.

Salisbury, R. B. (2013). Interpolating geochemical patterning of activity zones at late neolithic and early copper age settlements in eastern Hungary. *J. Archaeol. Sci.* 40 (2), 926–934. doi:10.1016/j.jas.2012.10.009

Schlezinger, D. R., and Howes, B. L. (2000). Organic phosphorus and elemental ratios as indicators of prehistoric human occupation. *J. Archaeol. Sci.* 27 (6), 479–492. doi:10.1006/jasc.1999.0464

Shi, W., Zhu, C., and Xu, W. (2007). Relationship between abnormal phenomena of magnetic susceptibility curves of profiles and human activities at Zhongba Site in Chongqing. *ACTA Geogr. SINICA-CHINESE EDITION-* 62 (3), 267.

Shi, Y. F., Kong, Z. C., and Wang, S. M. (1992). Climate fluctuation and important events in Holocene warm period in China. *Sci. China Chem.* 22, 1300–1308.

Sitzia, L., Bertran, P., Boulogne, S., Brenet, M., Crassard, R., Delagnes, A., et al. (2012). The paleoenvironment and lithic taphonomy of Shi'Bat dihya 1, a middle paleolithic site in wadi surdud, Yemen. *Geoarchaeology* 27 (6), 471–491. doi:10.1002/gea.21419

Solís-Castillo, B., Solleiro-Rebolledo, E., Sedov, S., Liendo, R., Ortiz-Pérez, M., and López-Rivera, S. (2013). Paleoenvironment and human occupation in the maya lowlands of the usumacinta river, southern Mexico. *Geoarchaeology* 28 (3), 268–288. doi:10.1002/gea.21438

Stinchcomb, G. E., Messner, T. C., Stewart, R. M., and Driese, S. G. (2014). Estimating fluxes in anthropogenic lead using alluvial soil mass-balance geochemistry, geochronology and archaeology in eastern USA. *Anthropocene* 8 (2014), 25–38. doi:10.1016/j.ancene.2015.03.001

Suleimanov, R. R., and Obydennova, G. T. (2006). Soil-archaeological studies of the bronze-age settlement on the Urshak River floodplain, Bashkortostan. *Eurasian Soil Sci.* 39, 820–825. doi:10.1134/s1064229306080035

Sullivan, K. A., and Kealhofer, L. (2004). Identifying activity areas in archaeological soils from a colonial Virginia house lot using phytolith analysis and soil chemistry. *J. Archaeol. Sci.* 31 (12), 1659–1673. doi:10.1016/j.jas.2004.04.007

Terry, R. E., Fernández, F. G., Parnell, J. J., and Inomata, T. (2004). The story in the floors: chemical signatures of ancient and modern Maya activities at Aguateca, Guatemala. *J. Archaeol. Sci.* 31 (9), 1237–1250. doi:10.1016/j.jas.2004.03.017

Tsatskin, A., and Nadel, D. (2003). Formation processes at the Ohalo II submerged prehistoric campsite, Israel, inferred from soil micromorphology and magnetic susceptibility studies. *Geoarchaeology* 18 (4), 409–432. doi:10.1002/gea.10069

Turner, S., Graham, E., Macphail, R., Duncan, L., Rose, N. L., Yang, H., et al. (2021). Mercury enrichment in anthrosols and adjacent coastal sediments at a Classic Maya site, Marco Gonzalez, Belize. *Geoarchaeology* 36 (6), 875–896. doi:10.1002/gea.21868

Vittori Antisari, L., Cremonini, S., Desantis, P., Calastri, C., and Vianello, G. (2013). Chemical characterisation of anthro-technosols from bronze to middle age in bologna (Italy). *J. Archaeol. Sci.* 40 (10), 3660–3671. doi:10.1016/j.jas.2013.04.023

Walkington, H. (2010). Soil science applications in archaeological contexts: a review of key challenges. *Earth-Science Rev.* 103 (3–4), 122–134. doi:10.1016/j.earscirev.2010.09.002

Wang, J., Li, A., Xu, K., Zheng, X., and Huang, J. (2015). Clay mineral and grain size studies of sediment provenances and paleoenvironment evolution in the middle Okinawa trough since 17ka. *Mar. Geol.* 366, 49–61. doi:10.1016/j.margeo.2015.04.007

Wang, X., Fuller, B. T., Zhang, P., Hu, S., Hu, Y., and Shang, X. (2018). Millet manuring as a driving force for the Late Neolithic agricultural expansion of north China. *Sci. Rep.* 8 (1), 5552–5610. doi:10.1038/s41598-018-23315-4

Wells, E. C. (2004). Investigating activity patterns in Prehispanic plazas: weak acid-extraction ICP–AES analysis of anthrosols at classic period El Coyote, Northwestern Honduras. *Archaeometry* 46 (1), 67–84. doi:10.1111/j.1475-4754.2004.00144.x

Wilson, C. A., Davidson, D. A., and Cresser, M. S. (2008). Multi-element soil analysis: an assessment of its potential as an aid to archaeological interpretation. *J. Archaeol. Sci.* 35 (2), 412–424. doi:10.1016/j.jas.2007.04.006

Wu, K., Li, L., Ju, B., and Chen, J. (2019). Soil Series of China (He nan). *China Sci. Publ.*

Yan, W. (1989). *Yangshao culture research*. Beijing: Cultural Relics Publishing House.

Zgłobicki, W. (2013). Impact of microtopography on the geochemistry of soils within archaeological sites in SE Poland. *Environ. Earth Sci.* 70 (7), 3085–3092. doi:10.1007/s12665-013-2368-1

Zha, L., Wu, K., Liang, S., and Zhuang, D. (2020). Study on physical and chemical characteristics of soil and reconstructing the paleoenvironment of an archaeological site at the Yangshao, village. *Ecol. Environ. Sci.* 29 (6), 1268–1276. doi:10.16258/j.cnki.1674-5906.2020.06.024

Zhang, Y., Guo, Z., Deng, C., Zhang, S., Wu, H., Zhang, C., et al. (2014). The use of fire at Zhoukoudian: evidence from magnetic susceptibility and color measurements. *Chin. Sci. Bull.* 59 (10), 1013–1020. doi:10.1007/s11434-013-0111-7

Zhong, H., and Zhao, Z. (2023). A preliminary study of agricultural production patterns in the central plains during the late Yangshao culture period. *Agric. Hist. China* 02, 52–61.

frontiers | Frontiers in Environmental Science

TYPE Original Research
PUBLISHED 19 July 2024
DOI 10.3389/fenvs.2024.1425044

EDITED BY
Jing Liu,
University of Birmingham, United Kingdom

REVIEWED BY
Niu Yu hua,
Henan University, China
Xuemei Mei,
Zhengzhou University, China
Xiaodie Hu,
Huazhong Agricultural University, China

*CORRESPONDENCE
Xu-Dong Huang,
✉ huangxudong269@163.com

RECEIVED 29 April 2024
ACCEPTED 25 June 2024
PUBLISHED 19 July 2024

CITATION
Huang X-D, Li Y-J, Han P-P, Zheng R, Yan H-J, Zhao P-P, Zhang X-L, Feng L-L, Wang D and Zeng F-J (2024), Research on spatial patterns of soil erosion in wind erosion region based on the revised wind erosion equation and partial least squares regression.
Front. Environ. Sci. 12:1425044.
doi: 10.3389/fenvs.2024.1425044

Research on spatial patterns of soil erosion in wind erosion region based on the revised wind erosion equation and partial least squares regression

Xu-Dong Huang[1,2]*, Yue-Jia Li[1], Pei-Pei Han[3], Ran Zheng[3], Hua-Jie Yan[1], Pan-Pan Zhao[1,2], Xiao-Li Zhang[1,2], Li-Li Feng[1,2], Dong Wang[4] and Feng-Juan Zeng[5]

[1]College of Water Resources, North China University of Water Resources and Electric Power, Zhengzhou, China, [2]Henan Key Laboratory of Water Resources Conservation and Intensive Utilization in the Yellow River Basin, Zhengzhou, China, [3]Henan Yellow River Hydrological Survey and Design Institute, Zhengzhou, China, [4]International Joint Research Laboratory of Global Change Ecology, School of Life Sciences, Henan University, Kaifeng, Henan, China, [5]China Construction Seventh Engineering Division Corp., Ltd., Zhengzhou, China

Understanding the complex influencing factors of soil erosion is critical for maintaining regional ecological security. The revised wind erosion equation (RWEQ) and partial least squares regression (PLSR) model were used to reveal the primary factors affecting soil erosion. Based on the results of the RWEQ model, the wind erosion area was 8,439.3 km^2 in 2018, accounting for 54.3% of the total planning area, and mild erosion, moderate erosion, intense erosion, very intense erosion, and fierce erosion accounted for 18.22%, 11.43%, 11.78%, 10.16%, and 2.74% of the total planning area, respectively. Based on the results of the PLSR model, the results indicate that the proportion of mining land, meteorological indicators, and mean square deviation of slope difference were positively correlated with the soil erosion area, intensity, and severity, respectively. The proportion of grassland and forest land was negatively correlated with the soil erosion area, intensity, and severity. The mean square deviation of slope difference, the mean square deviation of difference in elevation, and the proportion of urban land use contributed the most to the soil erosion severity index, with variable importance in projection (VIP) scores of 1.55, 1.44 and 1.43, respectively. The mean square deviation of slope difference, the proportion of urban land, and the mean square deviation of difference in elevation contributed the most to the soil erosion area, with VIP scores of 1.53, 1.26 and 1.24, respectively. The results provide new insights into wind erosion and the influences of weather conditions and human influences, which can guide regional soil and water conservation planning in wind erosion regions.

KEYWORDS

soil erosion, wind erosion, vegetation, partial least squares regression, ecological protection

1 Introduction

Topography, precipitation, wind speed, and the soil type affect soil erosion in wind erosion regions (Luo et al., 2023). The slope degree and length are considered to be the direct factors affecting the intensity of soil erosion, and the relief height is considered to be a necessary condition (Peng and Quan, 2023). A positive correlation exists between the threshold of the slope gradient and steepness, which decreases or stays constant as the value increases to the critical threshold (Zhao et al., 2015). As the proportion of meteorological factors affecting soil erosion has increased, the spatial and temporal heterogeneity of rainfall erosion has also increased, and rainfall has become an important indicator of erosion risk (Ma et al., 2012). The soil type, parent material, and vegetation cover influence soil erodibility, which is commonly assessed using the K-factor (Battista et al., 2022). Vegetation reduces the soil erosion level because the roots anchor the soil (Wang, 2023).

The topography, land ownership, non-agricultural activities, and inefficient water conservation measures can negatively affect soil and water conservation. The education level of farmers and soil and water conservation extension personnel positively influences soil and water conservation (Huang X. et al., 2020). Farmers use soil and water conservation measures to protect cultivated land and increase food production. As a result, the rate of soil erosion has decreased in cultivated land areas (Udayakumara et al., 2012). A significant positive correlation exists between population density and soil and water erosion intensity (Istanbuly et al., 2022). Many studies have shown that population density and economic density are indicators of soil erosion (Yang and Tian, 2024).

Most studies focused on the temporal and spatial variations in soil erosion in water erosion areas and their influencing factors. However, soil erosion is more complex in wind erosion than in water erosion regions. Traditional methods for evaluating soil erosion and its influencing factors include models, such as the Markov model, statistical methods, and the gray system theory. These methods have been used to clarify the influences of various factors on soil erosion. However, they did not consider the multicollinearity of the influencing factors, and it is difficult to identify the main controlling factors of soil erosion in the areas where wind erosion are intertwined (Lin et al., 2022). Partial least squares regression (PLSR) is an advanced method for solving multivariate linear problems. It minimizes the error between the true and predicted values and is used in many fields of academic research. This method is suitable for assessing the factors influencing soil erosion (Huang et al., 2016; Huang X. D. et al., 2020).

In order to study the wind erosion area more accurately, the study area is chosen to be a part of the Xinjiang Zhundong Economic and Technological Development Region, where extensive wind erosion occurs, and many industrial and mining enterprises are located (ZDR). The ZDR pertains to typical areas of wind erosion, and the areas resulting in soil erosion are characterized by their diversity and greatly affected by human activities, which brings great difficulties to soil and water conservation programs and ecological environmental protection (Yang et al., 2016). Taking ZDR as an example, the PLSR model is used to analyze the spatial heterogeneity and influencing factors of soil erosion in a wind erosion region affected by anthropogenic and natural factors. The results can guide soil and water conservation projects in wind erosion regions to ensure normal human life in the face of variable weather factors and better ecological restoration of eroded areas.

2 Study area and date collection

2.1 Study area

The ZDR extends from the western border of Jimusaer County, the eastern border of the Kalamaili Mountain Ungulate Nature Reserve, the northern border of Changji Prefecture, and the southern border of the Kalamaili Mountain Ungulate Nature Reserve. The geographical center coordinates are 90°15′19″E and 44°42′46″N. The east–west length is 220 km, and the average north–south width is 60 km. It covers an area of 15,500 km^2. The schematic diagram of the planning scope of the ZDR is shown in Figure 1.

It has a semi-arid climate with extensive wind in spring and summer. The mean annual temperature is 3°C, the average annual precipitation is 106 mm, most of which falls from June to July, and the total annual solar radiation is 565 kJ/cm^2.

In the delineated area of interest, the dominant soil type is calcareous brown soil (Figure 2). The area has sparse vegetation and a thin topsoil. The dry, windy conditions coupled with scarce precipitation have resulted in few surface water sources. The vegetation status in the ZDR is shown in Figure 3. The average wind speed is 3.4 m/s, the maximum wind speed is 28.4 m/s, and the number of windy days annually is 28 days. These conditions have resulted in extensive wind erosion and soil degradation. Various climatic factors contribute to soil erosion, including wind velocity, temperature, rainfall intensity, solar exposure, and snowfall.

2.2 Data collection

A 1:50,000 digital elevation model (DEM) with a Xi'an 80 coordinate system, 1985 National Elevation Datum (NED), and Gauss–Krüger projection was used to assess the topography of the region. The elevation contour distance was 5 m in flat areas and 10 m in mountainous areas.

The ZDR has no meteorological stations. Thus, meteorological data from 1990 to 2018 were obtained from eight surrounding meteorological stations (Fuhai, Fuyun, Changji, Miquan, Fukang, Jimusaer, Dabancheng, and Mulei). The data included wind direction, daily precipitation, snowfall amount, monthly average temperature, and monthly average relative humidity. Other meteorological data were obtained from the China Meteorological Data Network.

Landsat series images data from 1990, 2000, 2015, and 2018 were downloaded from the Geospatial Data Cloud. The resolution was 30 m for Landsat 5 TM and 15 m for Landsat 8 OLI data.

This study selected 42 sampling points to investigate and analyze the elevation, slope, land use types and proportions, soil types, soil texture, vegetation types, and vegetation coverage. The distribution of sampling points is shown in Figure 1.

3 Method

3.1 Evaluation indicators of driving factors of soil erosion

The Soil Erosion Classification and Grading Standard (SL190-2007) defines the soil erosion areas as the sum of the water erosion areas with

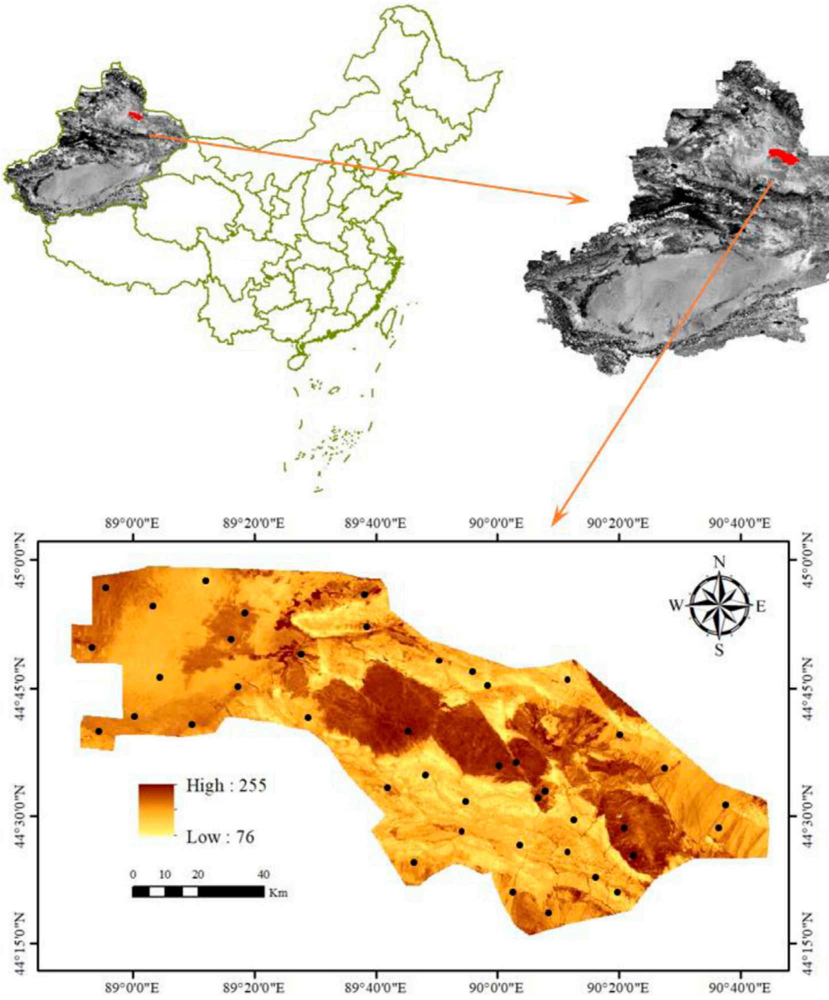

FIGURE 1
Schematic diagram of the planning scope of the ZDR.

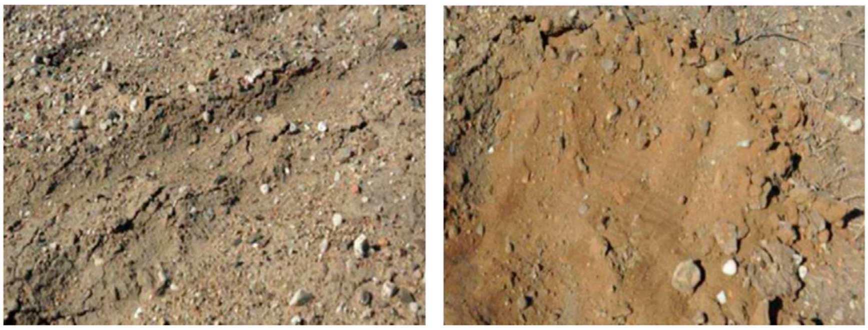

FIGURE 2
Soil and surface constituents of ZDR.

levels above low erosion. We used the soil erosion severity index to quantify soil erosion at the county level administrative district.

In order to reflect the contribution of a certain level of erosion intensity to the soil erosion severity index, the median value of the erosion modulus for different intensity levels in the Soil Erosion Classification and Grading Standard (SL190-2007) was used to determine the weight of Mi. To expand the difference and highlight the severity of erosion of different intensities, the proportional series was used to determine the Mi of the corresponding erosion intensity grade. Since the erosion modulus

FIGURE 3
Status of vegetation in the ZDR.

TABLE 1 Classification of degrees of soil erosion, modulus mid-value, and weight.

	Average erosion modulus [t/(km^2·a)]	Median modulus [t/(km^2·a)]	Weight metrics M_i
Minority	<200, <500, <1,000	250	0
Mild	200, 500, 1,000–2,500	1,250	1.5
Moderate	2,500–5,000	3,750	3
Intense	5,000–8,000	6,500	6
Very intense	8,000–15,000	11,500	12
Fierce	>15,000	22,500	24

of micro-erosion areas is relatively small and the effect on soil degradation is minimal, the weight was set to 0 for these areas. The weights of erosion intensity grades at each level are determined, as shown in Table 1.

Three dependent variables were used:

Soil erosion severity index (SECI, Y1)—It is a comprehensive indicator of soil erosion, which comprehensively measures the severity of soil erosion.

Soil erosion area (SEArea, Y2)—It represents the rate of the sum of wind erosion areas above the mild erosion level to the total area.

Average soil erosion modulus (SEIndens, Y3)—It represents the area of the median value of the erosion modulus above the low erosion level. It was summed to obtain the soil erosion modulus in the region, use the total soil erosion modulus to divide it by the total area of the mild or above level of soil erosion, and get the average soil erosion modulus for the eroded area in the region.

$$\mathrm{Mavg} = \frac{\sum_{i=2}^{n} M_i \times A_i}{A} \quad (2 \le i \le 6), \tag{1}$$

where A_i is the area of class i, M_i is the median soil erosion intensity for class i, and $M_i \times A_i$ is the total erosion area for class i (i ranges from 2 to 6). The total erosion area for five classes was obtained by summing; $A = \sum_{i=2}^{6}$, where A is the total erosion area with levels above low erosion.

3.2 Determination of explanatory variables of the soil erosion evaluation index

The standard deviation of the elevation and slope differences in the counties (districts) was calculated to reflect the complexity of topography and geomorphology in the study areas. The daily rainfall

TABLE 2 Index implication and calculation method.

Number	Code		Factor		Unit	Calculation method	Description
X1	Slope		Mean square deviation of slope difference			Slope mean square difference	Indicators of geomorphological complexity of geographical environments
X2	DEM		Mean square deviation of difference in elevation			Relative mean square deviation of difference in elevation	Indicators of topographic elevation differences in the geographical environment
X3	WF		Weather indicators		mm		Indicators of annual rainfall in the climate
X4	PGA		Proportion of the grassland area (48.47%)		Percentage		Degree of grass cover
X5	PFLA		Proportion of the forested land area (48.37%)		Percentage		Degree of afforestation
X6	PUL		Proportion of urban land (1.24%)		Percentage		Degree of development of urban land
X7	ML	CE	Mining land (1.92%)	Coal and electricity	Percentage		Extent of mining land development
X8		CCI		Coal chemical industry	Percentage		
X9		NEI		New energy industry	Percentage		
X10		NMI		New material Industry	Percentage		

and average wind speed of the ZDR from 2022 to 2023 were selected as natural factors. The soil erodibility K-factor was assumed to be stable because it does not change significantly over time.

Due to great complexity, there are a large number of variables, and there are even problems such as repeated selection of variables in terms of human factors, but land use factors, including cultivated land, forest land, mining land, and urban land, are the most active factors affecting soil erosion in the short term (Tilahun et al., 2022). Therefore, only land use was used as the social drivers affecting soil erosion. The index implication and calculation method was shown in Table 2.

3.3 Research on wind erosion methods

The revised wind erosion equation (RWEQ) was used to quantify wind erosion in the ZDR, and the RWEQ model is the soil transfer caused by a combination of multiple factors such as weather factors, soil crust factor, vegetation cover factor, surface roughness, and other factors. The maximum transfer capacity is defined in Eq. 2. The amount of the transferred volume reaching 63.2% of transfer capacity is called the key plot length (S) in Eq. 3, and the total amount of all soil transfers in the study area is the amount of soil loss (SL) in Eq. 4. The calculations were performed in the ArcGIS map algebra module.

$$Q_{max} = \left[WF \cdot EF \cdot SCF \cdot K' \cdot C \right], \tag{2}$$

$$S = 150.17\left(WF \cdot EF \cdot SCF \cdot K' \cdot C \right)^{-0.3711}, \tag{3}$$

$$S_L = \frac{2z}{S^2} Q\text{-}\,(z/s)^2{}_{max}, \tag{4}$$

where Q_{max} is the maximum transfer capacity (kg/m); *S* is the length of the key plots (m); S_L is the amount of soil loss (kg/m^2); *z* is the downwind distance, which is 50 m in this calculation; *EF* is the soil erodibility factor [(t·hm^2·h)/(hm^2·MJ·mm)]; *WF* is the meteorological factor; *SCF* is the soil crust factor; *K*′ is the soil roughness; and *C* is the vegetation cover.

(1) Weather factor (WF)

The weather factor (WF), i.e., the response of various types of meteorological factors to the combined effects of wind erosion, is expressed in Eq. 5.

$$WF = W_f . \frac{\rho}{g} . SW.SD, \tag{5}$$

$$\rho = 348.0\left(\frac{1.013\text{-}0.1183EL + 0.0048EL^2}{T} \right), \tag{6}$$

$$SW = \frac{ET_p\text{-}\,(R + I)\frac{R_d}{N_d}}{ET_p}, \tag{7}$$

$$ET_p = 0.0162 \times \left(\frac{SR}{58.5} \right) \times (DT + 17.8), \tag{8}$$

$$SD = 1\text{-}P, \tag{9}$$

where *WF* is the weather factor (kg/m); W_f is the wind speed (m/s) ^{3}; ρ is the air density (kg/m^3), which is derived from the elevation (EL) (km) and absolute temperature T (degrees Kelvin); *g* is the gravity acceleration (m/s^2); *SW* is the soil moisture factor, dimensionless; *R* is the rainfall amount (mm); *I* is the irrigation volume (mm); R_d is the number of rainfall events; N_d is the number of observation days; *SR* is the total solar radiation (cal/cm^2); *DT* is the mean temperature (°C); *P* is the probability of snow depth greater than 25.4 mm; and *SD* is the snow cover factor, dimensionless.

(2) Soil erodibility factor (EF)

Soil erodibility refers to the soil's vulnerability and the resistance of the surface soil to wind erosion. The RWEQ model was used to establish a relationship between the physicochemical properties of soil samples by analyzing their physical and chemical properties and the soil erodibility factors:

$$EF = \frac{29.09 + 0.31sa + 0.17si + 0.33\left(\frac{sa}{cl}\right)\text{-}2.59OM\text{-}0.95CaCo_3}{100}, \quad (10)$$

where *Sa* is the sand content (%), *Si* is the silt content (%), *Cl* is the clay content (%), *OM* is the organic matter content (%), and *$CaCO_3$* is the calcium carbonate content (%).

(3) Soil crust factor (SCF)

A soil crust can reduce soil erosion due to fewer erodible particles on the surface. It can reduce the abrasive effect of soil particles, which is conducive to the fixation of sand dunes and significantly impacts the soil's physical and chemical characteristics, wind erosion resistance, and soil stability (Nosrati, 2013). We established an equation to quantity the soil crust factor using wind tunnel tests on soils with different clay and organic matter contents:

$$SCF = \frac{1}{\left(1 + 0.0066cl^2 + 0.021OM^2\right)}, \quad (11)$$

where *cl* is the soil clay content (%) and *OM* is the organic matter content (%).

(4) Vegetation cover factor (C)

The amount of vegetation has a significant effect on wind erosion. It increases surface roughness, reduces wind speed, and slows the movement of particles (Li and Bo, 2019). The vegetation cover, denoted as C, is defined as follows:

$$C = e^{-0.0438SC}, \quad (12)$$

where *SC* is the vegetation cover (%).

(5) Surface roughness factor (K′)

The RWEQ model describes the effect of surface roughness on wind erosion. In agricultural settings, roughness refers to soil ridges due to plowing (Li et al., 2019). It distinguishes between random roughness, C_{rr}, and ridge roughness, K_r. The surface roughness factor K′ is defined as

$$K' = e^{\left(1.86K_r - 2.41K_r^{0.934} - 0.127C_{rr}\right)}. \quad (13)$$

It is difficult to determine the random roughness C_{rr} in the cultivated areas at the regional scale, and no cultivated areas occur in the study area. Thus, the ridge roughness K_r is replaced by calculating the topographic roughness as

$$K_r = 0.2 \times \frac{\Delta(H)^2}{L}, \quad (14)$$

where K_r is the topographic roughness (cm); C_{rr} is a random roughness factor (cm), which is 0 here; K' is the topographic roughness factor (cm); *L* is the topographic relief parameter; and $\triangle H$ is the difference in elevation within the distance L (cm). The ArcGIS neighborhood tool was used to calculate the terrain relief in adjacent DEM pixels within the distance L.

(6) Wind erosion modulus

Using the database management function and raster spatial analysis function of ArcGIS, a total of five factor thematic maps of WF, EF, SCF, K′, and C of the generated model (Figure 4) were used to generate wind erosion class distribution maps through Eqs. 1–3 based on the same projection method and accuracy in the ArcGIS platform. According to the Soil Erosion Classification Standard (Ministry of Water Resources, SL190-2007) (Table 3), the erosion raster map was classified into six categories, namely, minor, mild, moderate, intense, very intense, and fierce, and the soil erosion class map was obtained.

3.4 Partial least squares regression modeling

We used PLSR to analyze the influence of the factors on soil erosion. The predictive variables included topographical and meteorological factors and land use (grassland, forest land, urban land, and mining areas). PLSR is not significantly affected by multicollinearity. We created a data matrix X with n samples and p features and an outcome matrix Y with the same number of samples and q outcomes. PLSR can handle multiple responses and predict outcomes beyond the range of Y. The model coefficients describe the degree of influence and directionality between predictors and responses. The variable importance in projection (VIP) score reflects the relative importance of the effect of the variables on the outcome, providing insights into the influence of various factors on soil erosion in this study.

4 Results

4.1 Wind erosion results

4.1.1 Wind erosion impact factors

The meteorological factors (wind speed, air density, soil moisture, and other factors) had a high impact of 523.07 in the northeastern part of the ZDR, with a decreasing trend in the southeastern lower mountainous areas and a minimum of 206.3 in the southeastern part of the region (Figure 4A). The soil erodibility factors had higher scores in the southwestern to southeastern regions and lower values in the northern than in the southern part of the eastern region. The oil crust factor had higher values in the southeastern to southwestern regions and lower values in the northwest and northeast regions. The vegetation cover was high in the ZDR, with higher values in the northwest and northeast and lower values in the southcentral part of the ZDR (Figure 4B). The roughness coefficients were low, with higher values in the central part and the highest value of 0.68 in the northwestern part of the region (Figure 4C).

The erosion raster map was categorized into six categories of erosion, and Table 3 shows a large proportion of low-erosion areas. The northcentral zone has low vegetation cover and a large proportion of areas with moderate and severe wind erosion (Figure 4D).

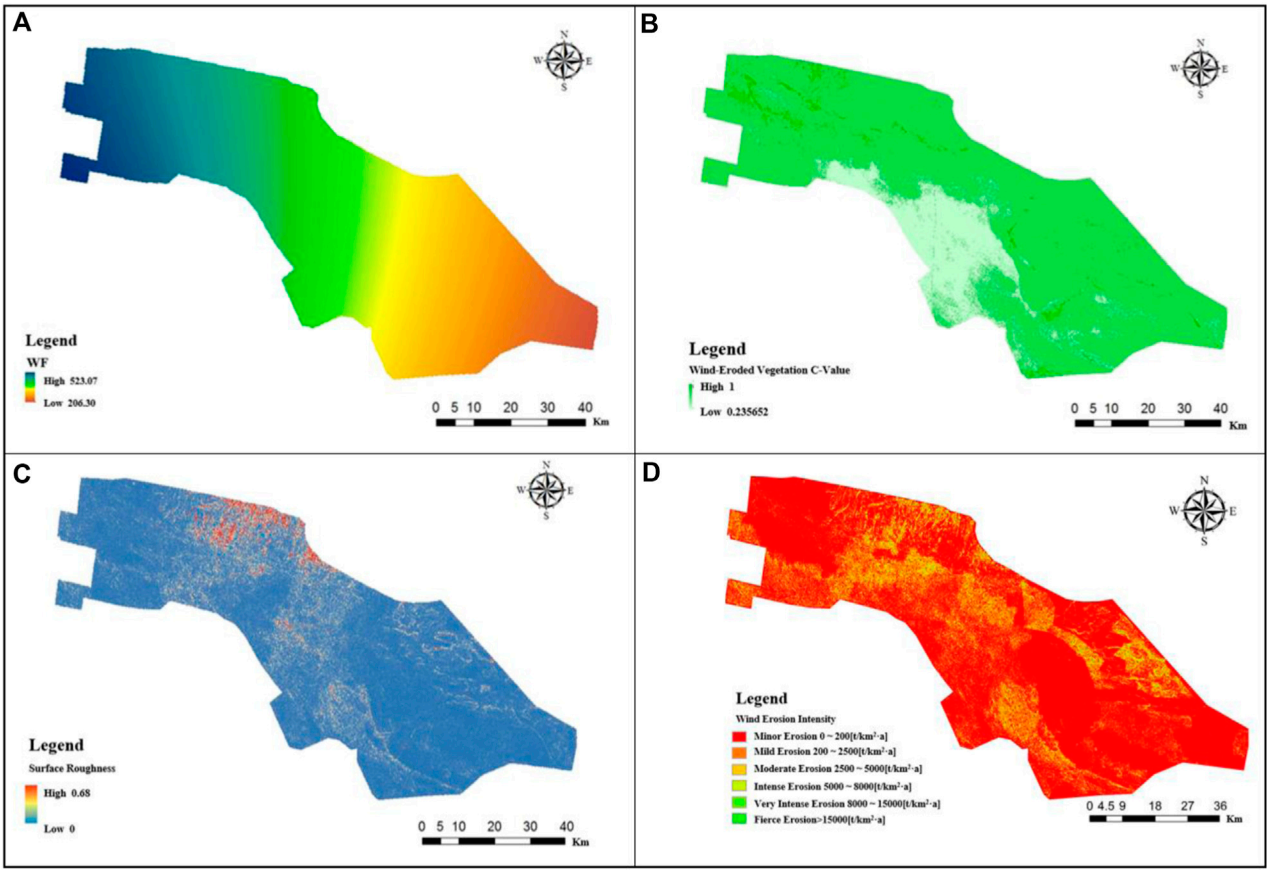

FIGURE 4
Wind erosion impact factors. **(A)** weather factor **(B)** Vegetation cover factor **(C)** Surface roughness factor **(D)** Wind erosion intensity.

TABLE 3 Wind erosion intensity classification.

Erosion classification	Modulus of erosion ($t{\cdot}km^{-2}{\cdot}a^{-1}$)
Minor erosion	<500
Mild erosion	500–2,500
Moderate erosion	2,500–5,000
Intense erosion	5,000–8,000
Very intense erosion	8,000–15,000
Fierce erosion	>15,000

4.1.2 Soil erosion areas and intensity

In the RWEQ model calculations, meteorological elements include daily average wind speed, wind direction data, daily precipitation, snow accumulation, monthly average temperature, and monthly average relative humidity, and all meteorological data are from the China Meteorological Data Network. Soil texture spatial distribution data were obtained from the Chinese Academy of Sciences Resources and Environment Data Cloud Platform, and soil organic matter content data were obtained from the National Science and Technology Basic Condition Platform. The final formula from the RWEQ model yields the following data.

The wind erosion area of the ZDR was 8,439.3 km^2 in 2018, accounting for 54.3% of the total area of the planning area; the area of mild erosion was 2,830.0 km^2, accounting for 33.5% of the total wind erosion area; the moderate erosion area was 1776.3 km^2, accounting for 21.0% of the total wind erosion area; the intense erosion area was 1829.7 km^2, accounting for 21.7% of the wind erosion area; the very intense erosion area was 1,578.2 km^2, accounting for 18.7% of the wind erosion area; and the area of fierce erosion was 425.1 km^2, and the percentage of the wind erosion area is 5.0%. The erosion area in the planning area is shown in Table 4, and the percentage of the total erosion area caused by wind erosion of different intensities is shown in Figure 5.

4.2 Soil erosion drivers

The symbol R2X in Table 5 indicates the explanatory power of component th to X, R2 (X; th), h = 1, 2. R2Y indicates the explanatory power of the component th to Y, R2(Y; th), h = 1, 2. Q2 indicates the cross-validated residuals. Q2Y (cum) of all PLS principal components was extracted, i.e., the precision with which the dependent variable can be explained. The results are listed in Table 5.

The regression coefficients and variables important in projection importance values of the three dependent variables of the main

TABLE 4 Basic information on the area and intensity of soil erosion in the planning area.

Project	Area without obvious erosion (km^2)	Soil and water erosion area (km^2)					Total area (km^2)
		Mild erosion	Moderate erosion	Intense erosion	Very intense erosion	Fierce erosion	
Area	7,094.7	2,830.0	1776.3	1829.7	1,578.2	425.1	15,534
Total planning area (%)	45.67	18.22	11.43	11.78	10.16	2.74	
Wind erosion area (%)	—	33.5	21.0	21.7	18.7	5.0	

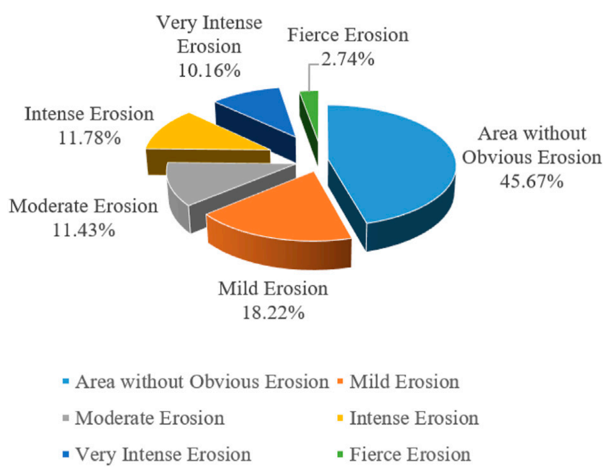

FIGURE 5
Proportion of erosion areas of different intensities in the planning area.

correlation factors and soil erosion are shown in Figure 6. For the three variables, the proportion of the soil erosion area (SEArea) had the greatest amount of explanation for Y, and with two components extracted, it was more stable for modeling the soil erosion composite index (SECI). Therefore, VIP1 and VIP2 refer to the amount of explanation of SEArea and SECI by the dependent variable, respectively. The mean square deviation of the slope difference, the mean square deviation of difference in elevation, and the proportion of the urban land contributed the most to the first component, with variables important in projection values of 1.55, 1.44 and 1.43, respectively. The mean square deviation of slope difference, the proportion of urban land, and the mean square deviation of differences in elevation contributed the most to the second component, with variables important in projection values of 1.53, 1.26 and 1.24, respectively. The coefficient of variation indicated the high importance of these variables. Although variables important in projection values of the proportion of Energy Industry and new Material Industry did not exceed 1, the values of R2Y (cum) and Q2 (cum) were reduced after removing these factors. The regression coefficients of the explanatory variables and the dependent variables are both large, as shown in Figure 7, indicating a high correlation between these factors and the dependent variables.

Figure 7 shows that the mean square deviation of slope difference, weather indicators, and the proportions of the urban land and mining land were positively correlated with the amount of soil erosion. In contrast, the proportion of the grassland and forest land was negatively correlated. The area of soil erosion in each county (district), which shows a stronger correlation between its mining land and urban land, shows a positive correlation. The correlation between the topographical factors and the second component was relatively high, indicating that the topographic has a certain correlation with the distribution of soil erosion. The third dependent variable, soil erosion intensity, describes the distribution of the average degree of soil erosion across counties (districts) and is more highly and positively correlated with the proportion of mining land.

Figure 8 shows that the explanatory variable of the mean square deviation of the slope differenced error was positively correlated with both the soil erosion area and soil erosion intensity, i.e., as the slope difference decreased from mountains to hills to plains, the soil erosion area and intensity also decreased.

The mining areas were positively correlated with the degree of soil erosion. The same was observed for the urban population density, which reflects urbanization in 2018. The severity of soil erosion in these regions was not as high as in the northwestern part of the ZDR and the southeastern part, where the proportion of urban population is lower.

5 Discussion

In addition to climatic factors (wind, rainfall, air temperature, etc.,) and subsurface factors (vegetation cover, soil texture, topography, etc.,), there are also unscientific and irrational production and construction, indiscriminate logging, and anthropogenic factors, which are specifically manifested in the following two aspects.

5.1 Natural factors

(1) Wind factor: The study area is located in the Gobi Desert, which is extremely windy. The average number of windy days is 25, and there are few mountains acting as barriers. The wind speed is typically at a level of 4 to 5, and northwesterly winds prevail, resulting in extensive wind erosion.

TABLE 5 Accuracy comparison of PLS models.

Dependent variable	Principal component	R2Y	R2Y (cum)	Q2Y	Q2 limit	Q2Y (cum)
SECI	Comp 1	0.421	0.421	0.371	0.05	0.371
	Comp 2	0.019	0.440	0.001	0.05	0.377
SEArea	Comp 1	0.299	0.299	0.269	0.05	0.269
	Comp 2	0.175	0.474	0.090	0.05	0.365
SEIndens	Comp 1	0.220	0.220	0.201	0.05	0.201
	Comp 2	0.084	0.284	0.041	0.05	0.239

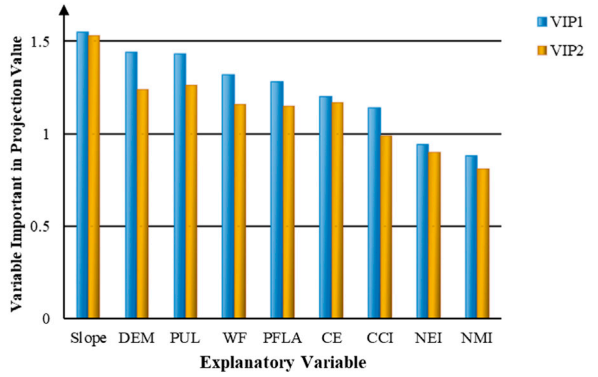

FIGURE 6
Variables important in the projection value of the PLS model of the ZDR.

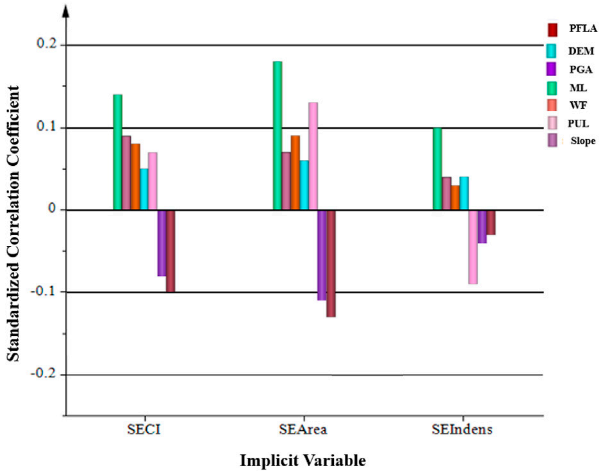

FIGURE 7
Coefficient values of the PLS model of the ZDR.

(2) Vegetation factor: Soil and water conservation in this area has focused on increasing vegetation cover and creating a hierarchical vegetation structure. The vegetation cover in the study area is relatively low, the vegetation height is uniform, and exposed soil is common, resulting in moderate or higher soil erosion.

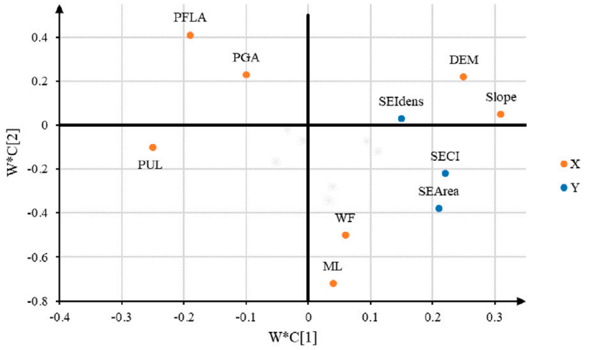

FIGURE 8
Loading plots of the PLS of the ZDR.

5.2 Anthropogenic factors

Soil erosion is closely related to human socioeconomic activities. With the development of society and the continuous increase in population, the intensity of human utilization of natural resources has strengthened, leading to increased awareness of resource environmental protection. Inappropriate land use has caused soil and water erosion.

(1) Resource exploitation is the main reason for soil erosion and environmental degradation. In September 2012, the State Council approved the establishment of the state-level ZDR. In December 2012, the People's Republic approved the "ZDR (2012–2030)". The ZDR is a national-level energy construction demonstration. The construction of coal power plants and coal-based chemical plants, coupled with the population increase, has resulted in environmental degradation, reducing the carrying capacity of the land and increasing soil erosion.

(2) Significant construction has occurred in the ZDR due to extensive development. Highway, oil, hydropower, thermal power, natural gas, coal and coal chemical industries, and other construction projects have been started. These activities have increased the areas of disturbance due to slag piles, breaking the region's original soil erosion law, resulting in original soil erosion which is not too serious areas but produced intense soil erosion. Soil erosion has also increased in sandy soil. Thus, construction activities have exacerbated soil erosion.

(3) The awareness of soil and water conservation is not strong in this area. The focus has been on development and construction but not on protection and conservation. Thus, soil and water erosion and environmental damage due to human activities are crucial problems. Therefore, the focus should be changed to consider ecological protection to reduce soil erosion and create a sustainable, virtuous cycle.

6 Conclusion

The area of the ZDR without erosion was 7,094.7 km^2, accounting for 45.67% of the total area. The area of wind erosion was 8,439.3 km^2, accounting for 54.33% of the total area of the planning area, and the area of mild erosion was 18.22%. These results indicate that the ZDR is dominated by areas with mild erosion, showing a step in the right direction. The proportions of areas with moderate and higher soil erosion levels indicate that the risk of soil erosion in this area is high.

We used the RWEQ and PLSR model to determine factors affecting soil erosion. The mean square deviation of slope difference, the mean square deviation of difference in elevation, and the proportion of urban land use contributed the most to the soil erosion severity index, with VIP scores of 1.55, 1.44 and 1.43, respectively. The mean square deviation of slope difference, the proportion of urban land, and the mean square deviation of difference in elevation contributed the most to the soil erosion area, with VIP scores of 1.53, 1.26 and 1.24, respectively. Mining land, weather indicators, the mean square deviation of difference in elevation, and the mean square deviation of slope difference were positively correlated with the soil erosion area, soil erosion intensity, and soil erosion severity index. Areas with the elevation exceeding 1,000 m or a slope greater than 20° had the highest soil erosion risk.

Data availability statement

The original contributions presented in the study are included in the article/Supplementary Material; further inquiries can be directed to the corresponding author.

Author contributions

X-DH: funding acquisition, writing–original draft, and Writing–review and editing. Y-JL: writing–original draft. P-PH: data curation, methodology, and writing–review and editing. RZ: data curation and writing–review and editing. H-JY: writing–review and editing. P-PZ: funding acquisition and writing–review and editing. X-LZ: funding acquisition and writing–review and editing. L-LF: funding acquisition and writing–review and editing. DW: writing–review and editing. F-JZ: writing—review and editing.

Funding

The authors declare that financial support was received for the research, authorship, and/or publication of this article. This work was supported by the National Natural Science Foundation of China (42207100, 51979106, and 42007158), the Key Science and Technology Program of Henan Province, China (222102320083 and 232102320019), the Science and Technology Major Project of Henan Province (21100320200), and the National Key Research and Development Program of China (2023YFC3006602).

Acknowledgments

The research would not have been possible without the interest and cooperation of the North China University of Water Resources and Electric Power.

Conflict of interest

Author F-JZ was employed by China Construction Seventh Engineering Division Corp., Ltd.

The remaining authors declare that the research was conducted in the absence of any commercial or financial relationships that could be construed as a potential conflict of interest.

Publisher's note

References

Battista, G., Molnar, P., and Burlando, P. (2022). Modelling impacts of spatially variable erosion drivers on suspended sediment dynamics. *Earth Surf. Dyn.* 8 (3), 619–635. doi:10.5194/esurf-8-619-2020

Huang, X., Lu, Q., and Yang, F. (2020a). The effects of farmers' adoption behavior of soil and water conservation measures on agricultural output. *Int. J. Clim. Change Strategies Manag.* 12, 599–615. doi:10.1108/IJCCSM-02-2020-0014

Huang, X. D., Shi, Z. H., Fang, N. F., and Li, X. (2016). Influences of land use change on baseflow in mountainous watersheds. *Forests* 7 (1), 16. doi:10.3390/f7010016

Huang, X. D., Wang, D., Han, P. P., Wang, W. C., Li, Q. J., Zhang, X. L., et al. (2020b). Spatial patterns in baseflow mean response time across a watershed in the loess plateau: linkage with land-use types. *For. Sci.* 66 (4), 382–391. doi:10.1093/forsci/fxz084

Istanbuly, M. N., Josef, K., and Amiri, B. J. (2022). How socio-economic drivers explain landscape soil erosion regulation services in polish catchments. *Int. J. Environ. Res. Public Health* 19 (4), 2372. doi:10.3390/ijerph19042372

Li, X., and Bo, T. (2019). Statistics and spectra of turbulence under different roughness in the near-neutral atmospheric surface layer. *Earth Surf. Process. Landforms* 44 (5), 1460–1470. doi:10.1002/esp.4588

Lin, D., Shi, P., Meadows, M., Yang, H., Wang, J., Zhang, G., et al. (2022). Measuring compound soil erosion by wind and water in the eastern agro–pastoral ecotone of northern China. *Sustainability* 14 (10), 6272. doi:10.3390/su14106272

Luo, B., Li, J., Gong, C. M., Zhong, S. q., and Wei, C. f. (2023). Driving forces and their interactions of soil erosion in soil and water conservation regionalization at the county scale with a high cultivation rate. *J. Mt. Sci.* 20 (9), 2502–2518. (in Chinese). doi:10.1007/s11629-023-8033-6

Ma, Q., Yu, X., Lü, G., and Liu, Q. (2012). The changing relationship between spatial pattern of soil erosion risk and its influencing factors in Yimeng mountainous area, China 1986–2005. *Environ. Earth Sci.* 66 (5), 1535–1546. doi:10.1007/s12665-011-1393-1

Miao, C. Y., Yang, L., Chen, X. H., and Gao, Y. (2012). The vegetation cover dynamics (1982–2006) in different erosion regions of the Yellow River Basin, China. *Land Degrad. Dev.* 23 (1), 62–71. doi:10.1002/ldr.1050

Nosrati, K. (2013). Assessing soil quality indicator under different land use and soil erosion using multivariate statistical techniques. *Environ. Monit. Assess.* 185 (4), 2895–2907. doi:10.1007/s10661-012-2758-y

Pei, L., Wang, C., Sun, L., and Wang, L. (2022). Temporal and spatial variation (2001–2020) characteristics of wind speed in the water erosion area of the typical black soil region, northeast China. *Int. J. Environ. Res. Public Health* 19 (17), 10473. doi:10.3390/ijerph191710473

Peng, X., and Quan, H. D. (2023). Drivers of soil erosion and subsurface loss by soil leakage during karst rocky desertification in SW China. *Int. Soil Water Conservation Res.* 10 (2), 217–227. (in Chinese). doi:10.1016/j.iswcr.2021.10.001

Tang, Q., Li, H., Cao, Y. F., Jiang, L., and Cai, C. F. (2023). Human activities are the key driver of water erosion changes in northeastern China. *Land Degrad. Dev.* 35 (9), 62–75. doi:10.1002/ldr.4897

Tilahun, D., Gashu, K., and Shiferaw, G. T. (2022). Effects of agricultural land and urban expansion on peri-urban forest degradation and implications on sustainable environmental management in southern Ethiopia. *Sustainability* 14, 16527. doi:10.3390/su142416527

Udayakumara, E. P. N., Shrestha, R. P., Samarakoon, L., and Schmidt-Vogt, D. (2012). Mitigating soil erosion through farm-level adoption of soil and water conservation measures in Samanalawewa Watershed, Sri Lanka. *Acta Agric. Scand. B* 62, 273–285. doi:10.1080/09064710.2011.608708

Wang, K. L., Zhou, J., Tan, M. L., Lu, P. D., Xue, Z., Liu, M., et al. (2024). Impacts of vegetation restoration on soil erosion in the Yellow River Basin, China. *CATENA* 234 (11), 107547. doi:10.1016/j.catena.2023.107547

Wang, T. (2023). Analysis of the effects of vegetation on improving soil erosion and water loss. *Haihe River Water Resour.* (07), 8–10. (in Chinese).

Wei, W., Chen, L., Yang, L., Fu, B., and Sun, R. (2012). Spatial scale effects of water erosion dynamics: complexities, variabilities, and uncertainties. *Chin. Geogr. Sci.* 340 (s1-2), 127–143. CNKI: SUN: ZDKX.0.2012-02-002. doi:10.1007/s11769-012-0524-2

Yang, Y., and Tian, P. (2024). Vulnerability assessment of soil erosion in Southwest Hubei based on RUSLE model and geodetector. *J. Soil Water Conservation* 38 (01), 91–103. doi:10.13870/j.cnki.stbcxb.2024.01.015

Yang, Z., Gao, J., Yang, M., and Sun, Z. (2016). Effects of freezing intensity on soil solution nitrogen and microbial biomass nitrogen in an alpine grassland ecosystem on the Tibetan Plateau, China. *J. Arid Land* 8 (5), 749–759. doi:10.1007/s40333-016-0012-0

Zhao, Q., Li, D., Zhuo, M., Guo, T., Liao, Y., and Xie, Z. (2015). Effects of rainfall intensity and slope gradient on erosion characteristics of the red soil slope. *Stoch. Environ. Res. Risk Assess.* 29, 609–621. doi:10.1007/s00477-014-0896-1

frontiers | Frontiers in Environmental Science

TYPE Brief Research Report
PUBLISHED 30 August 2024
DOI 10.3389/fenvs.2024.1400569

OPEN ACCESS

EDITED BY
Jing Liu,
University of Birmingham, United Kingdom

REVIEWED BY
Xudong Huang,
North China University of Water Conservancy and Electric Power, China
Zang Chao,
Zhengzhou University, China

*CORRESPONDENCE
Han Xiao,
hxiao0716@163.com

RECEIVED 14 March 2024
ACCEPTED 14 August 2024
PUBLISHED 30 August 2024

CITATION
Xiao H, Yang Y, Liu Q, Zang Y, Lian X, Xia F and Jiang Y (2024) Numerical modeling the impacts of increasing groundwater pumping upon discharge decline of the BL Spring located in Xilin Gol League in east inner Mongolia, China. *Front. Environ. Sci.* 12:1400569.
doi: 10.3389/fenvs.2024.1400569

Numerical modeling the impacts of increasing groundwater pumping upon discharge decline of the BL Spring located in Xilin Gol League in east inner Mongolia, China

Han Xiao[1,2]*, Yu Yang[1,2], Qiyuan Liu[1,2], Yongge Zang[1,2], Xinying Lian[1,2], Fu Xia[1,2] and Yonghai Jiang[1,2]

[1]State Key Laboratory of Environmental Criteria and Risk Assessment, Chinese Research Academy of Environmental Sciences, Beijing, China, [2]State Environmental Protection Key Laboratory of Simulation and Control of Groundwater Pollution, Chinese Research Academy of Environmental Sciences, Beijing, China

Spring discharge decline induced by increasing groundwater pumping under the background of increasing water demand for agricultural, industrial, and domestic utilizations has been recognized as a significant geo-environmental issue which poses a great threat to springshed eco-environmental safety. In this study, numerical approach was utilized and a series of 3D groundwater flow models based on the MODFLOW module were developed to simulate current-stage and future trends of spring discharges under the impacts of increasing groundwater pumping due to the rapid development of tourism in the BL spring located in Xilin Gol League in east Inner Mongolia (China), for the purpose of understanding the responses of spring discharges to various groundwater pumping scenarios in future. Simulation results indicated that: (1) spring discharge has reduced from 201.4 m^3/d to 193.7 m^3/d (reduction ratio of 3.80%) under current-stage pumping scheme; (2) the spring-discharge-affected zone is 2.025 km^2 under current-stage pumping scheme and groundwater pumping within this zone contributes to spring discharge decline; (3) impact of the pumping well located nearest to the BL spring is the most significant while impact of the pumping well located farthest to the BL spring is negligible; and (4) spring discharge would reduce 25%, 50%, 75%, and 100% if total pumping rate of the seven abstraction wells would increase from 45.8 m^3/d (current-stage pumping scheme) to 297.7, 586.2, 888.5, and 1,176 m^3/d, respectively. The outcome of this study can provide useful references for advising sustainable groundwater exploitation strategies to meet the requirement of groundwater supply under the premise of spring discharge management and eco-environmental protection.

KEYWORDS

spring discharge decline, increasing groundwater pumping, spring-discharge-affected zone, numerical modeling, east inner Mongolia (China)

Highlight

- This paper describes numerical modeling of the impacts of increasing groundwater pumping rates on spring discharge decline.
- A linear relationship between spring discharge and groundwater pumping rate is demonstrated.
- Reaching an equilibrium between increasing groundwater pumping rate and spring discharge decline is important to maintain springshed eco-environmental safety.

1 Introduction

Spring which provides a natural drainage pathway for groundwater discharge is considered as an obvious observable indicator inferring the status of groundwater systems, and is recognized as one of the important components in hydrological cycle (Batelaan et al., 2003; Mechal et al., 2017). From hydrological and hydrogeological perspectives, spring discharge can be affected by climate change (e.g., changing precipitation/evaporation/temperature regimes) and anthropogenic activities (e.g., groundwater pumping, coals/mines dewatering) (Frisbee et al., 2013; Work, 2020; Meyers et al., 2022; Gai et al., 2023). Due to population growth and economic development, groundwater supply for agricultural, industrial, and domestic utilizations increased in many populated areas worldwide, while groundwater over-exploitation and/or coals/mines dewatering resulted in declining or even diminishing of spring discharge in those areas (Musgrove et al., 2010; Filippini et al., 2024). For long-term management and protection of spring discharge, the fundamental task is to quantitatively investigate historical and current-stage as well as predict future trends of spring discharge for deeper understanding the impacts of climate change and anthropogenic activities upon spring discharge (Nolin et al., 2023).

To date, two approaches have been seen frequently used to quantitively evaluate climate change and anthropogenic activities impacts upon spring discharge, that is, physical-based method and data-driven method (Li et al., 2023). Physical-based method based on numerical modeling approach has been demonstrated to be the most important and effective predictive tool available for simulating hydrological and hydrogeological processes and predicting how spring discharge might respond to climate change and anthropogenic activities (Rooij et al., 2013; Aamery et al., 2021). In recent years, fruitful research upon changing trends of spring discharge were conducted based on numerical modeling approach. For example, Scanlon et al. (2003) conducted a case study regarding modeling regional groundwater flow and spring discharge of the Barton Springs (Texas, United States), and comparisons between simulation results and field investigations indicated that numerical modeling tool can fairly accurately simulate the temporal variation of spring discharge; Duran and Gill (2021) developed a MODFLOW-USG model to assess the dynamics of groundwater flow field in a small-scale watershed feeding the Manorhamilton Spring (located in county Leitrim, Ireland), and the developed model turned out that a good agreement between the monitored and simulated spring discharge with high simulation accuracy had been achieved; Xu and Hu (2021) developed numerical models based on field investigated data to quantify the understanding of hydrogeological processes in the Woodville Karst Plain in northern Florida, United States; Li et al. (2022) developed a MODFLOW-CFP model to evaluate the maximum groundwater pumping rate of those extraction wells closed to the BL Sping, and found that groundwater extraction rate cannot exceed 0.69 m^3/s for ensuring continuous flow of the Jinan Spring (Jinan, China); Other similar modeling studies included, but were not limited to, Doummar et al. (2012), Doummar et al. (2018), Chang et al. (2019), Chen (2021). Unlike the physical-based method, data-driven method based on machine learning approach was emerged with the development of artificial intelligence recently by predicting spring discharge through historical discharge data (capturing the relationship between input and target variables and identifying the inherent patterns concealed in the time-series data) without understanding the underlying physical properties used in physical-based method (Cerqueira et al., 2019; Bai and Tahmasebi, 2023). Data-driven method utilizes water balance elements as model input (e.g., precipitation, infiltration, seepage, pumping, etc.), and modeling methods include, but are not limited to, multiple linear regression (Shi et al., 2015), support vector machine (Barzegar et al., 2018), K-Nearest Neighbor (Rahmati et al., 2019), random forest (Rahmati et al., 2019; Sezen et al., 2019; Wang et al., 2018), etc. However, data-driven method as a novel approach still has many deficiencies, such as its disadvantages of focusing on the relationships between time series while ignoring spatial dependence (Frederik et al., 2018), requiring large amounts of historical monitoring data for searching for inherent patterns, and incapability of predicting hydrological dynamics in those watersheds with stable hydrological conditions (Zhou and Zhang, 2023).

For effective management of spring discharge and better protection of springshed eco-environment, it is very important and necessary to understand the impacts of climate change and anthropogenic activities upon spring discharge (Dass et al., 2021). In this study, a baseline model (based on the MODFLOW module) was developed and calibrated to simulate current-stage groundwater flow and spring discharge, and a series of predictive models (based on the MODFLOW module) were developed to predict future trends of spring discharge on a basis of the baseline model as well as multiple scenarios regarding various groundwater pumping schemes, aiming at quantitatively evaluating the negative effects of increasing groundwater pumping on spring discharge decline. To the best knowledge of the authors, this research is the first effort to unravel the relationships between spring discharge and pumping rate for determination of the "equilibrium" between tourism development and eco-environment protection of the BL spring located in Xilin Gol League in east Inner Mongolia (China), and simulation results can be used to analyze the maximum groundwater withdrawal rate to meet the requirement of groundwater supply under the premise of maintaining a certain level of spring discharge.

2 Overview of study area

The study area is the BL spring located in Xilin Gol League in east Inner Mongolia, China (shown in Figure 1A). The study area used to be a sparsely-populated area far away from cities, agricultural lands and industrial areas while spring discharge remained stable under its natural conditions (approximately

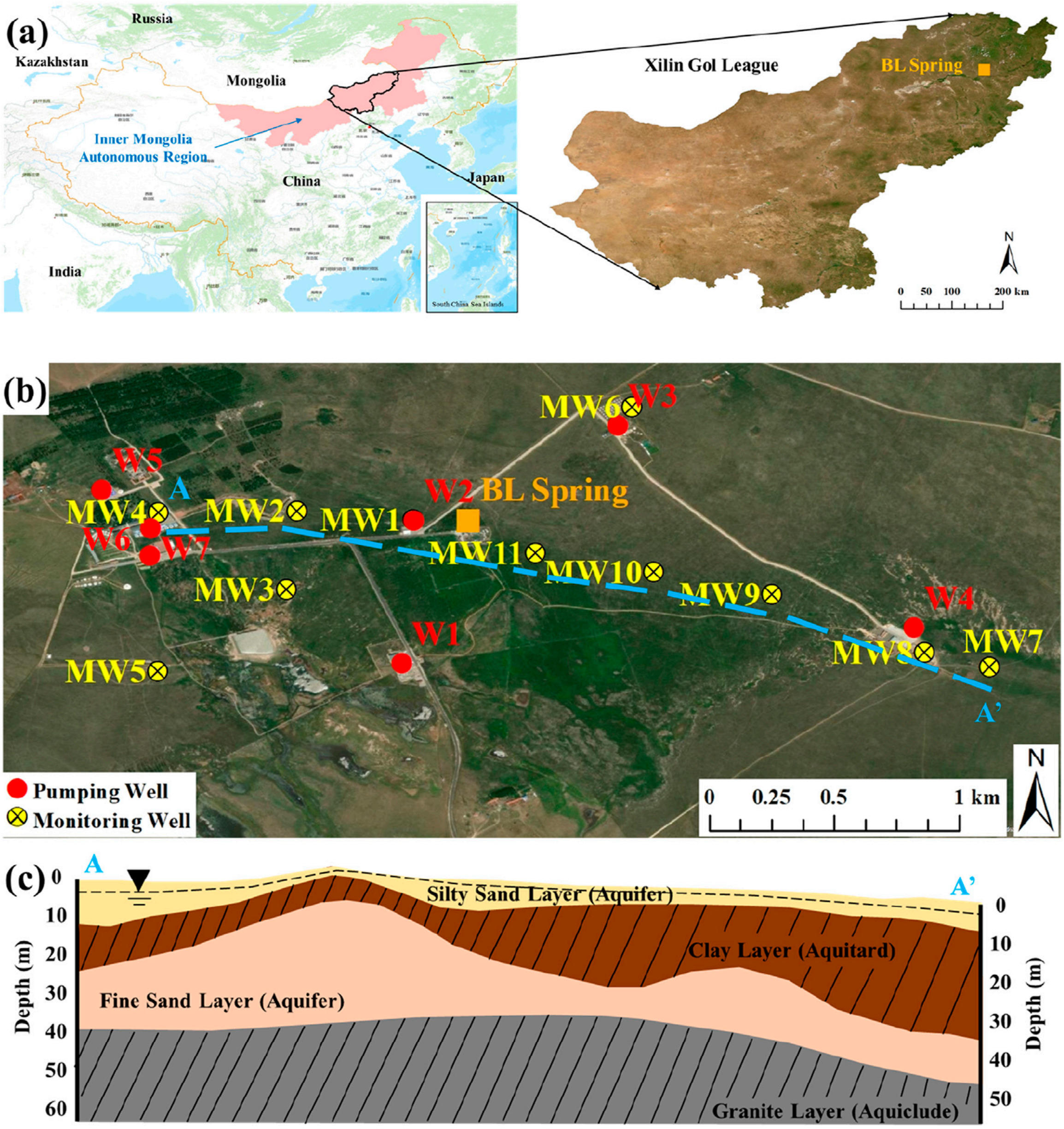

FIGURE 1
(A) Location of the BL Spring; **(B)** Locations of the pumping wells and monitoring wells adjacent to the BL Spring; **(C)** Hydrogeological formations of the cross-section A-A′.

200 m^3/d all over 1 year). With the rapid development of tourism since 2017, several hotels and restaurants were implemented to host visitors and seven groundwater pumping wells were installed to ensure water supply for domestic utilizations (see Figure 1A of these pumping wells' locations), while a slow decline of spring discharge has been seen based on monitoring data since 2019.

2.1 Hydro-climatic conditions

The study area is in the temperate continental climate region featuring with short and windy springs, short and wet summers, short and moderate falls, and long and dry winters: annual-average temperature ranges from −7.4°C to 8.6°C with the highest temperature in July (average temperature 19.9°C) and the lowest temperature in January (average temperature −22.3°C); annual-average rainfall is 320.9 mm (>70% rainfall occurs in the wet season from June to August) and annual-average evaporation is 1,542.7 mm. The Wulagai River (endorheic river with its depth 0.2–0.8 m and maximum flowrate 17.6 m^3/d) and its main tributary the Seyeleji River are located approximately 25 km far away from the study area (Xilin Gol League's Water Resources Bulletin, http://www.xilinhaote.gov.cn/xilinhaote/2023-08/04/article_20230804104607500025.html).

2.2 Hydrogeological conditions

Based on borehole data, the sedimentary deposits of the hydrogeological formations can be classified into four layers including, from top to bottom, the silty sand layer, the clay layer, the fine sand layer, and the granite layer. The silty sand layer's (Holocene series) thickness is varied from 3.4 to 15.2 m, and groundwater stored within this layer is unconfined with water table depth ranging from 0 to 4.5 m (water table elevation ranging from 903.0 to 908.7 m); the clay layer's (Pleistocene series) thickness is varied from 8.9 to 27.1 m, and this layer is considered as an aquitard with relatively low hydraulic conductivity; The fine sand layer's (Pliocene series) thickness is varied from 10.4 to 31.6 m, and groundwater stored within this layer is confined or semi-confined; The granite layer's (Miocene series) thickness is greater than 120 m (upper bound elevation ranging from 854.1 to 867.5 m), and this layer is considered as an aquiclude which limits groundwater downward migration to deeper zones. Hydrogeological parameters such as hydraulic conductivity, porosity, specific yield, and specific storage of the silty sand layer, clay layer, and fine sand layer (see Supplementary Table S1) were determined by hydrogeological experiments such as pumping tests. The hydrogeological formations of cross-section A-A' (see Figure 1A for its location within the study area) were visualized in Figure 1B.

2.3 Spring water source

Based on historical data before 2017, spring discharge was under "steady-state" condition since it remained unchanged in monthly-scale and annual-scale, and spring water temperature always stayed around 5°C throughout the year, indicating that spring water should be yielded from the confined aquifer (fine sand layer). For the sake of determination of whether spring water is yielded from the unconfined aquifer (silty sand layer) or the confined aquifer (fine sand layer), water quality of the spring discharge, the silty sand layer, and the fine sand layer were analyzed, and the Piper diagram and the Gibbs diagram were plotted for comparison of water quality between spring discharge and the silty sand layer, as well as water quality between spring discharge and the fine sand layer. Note that groundwater samples from spring outlet and the monitoring wells of MW2 (fine sand layer), MW4 (silty sand layer), MW5 (silty sand layer), MW6 (fine sand layer), MW8 (fine sand layer), and MW11 (fine sand layer) were collected twice in 2023 (April and October), and the mean values were shown in Supplementary Table S2.

Based on water quality data in Supplementary Table S2, the piper diagram and the Gibbs diagram were plotted as shown in Supplementary Figures S1A, B, respectively. From Supplementary Figure S1A, it can be observed that water quality of spring discharge (dark grey square symbol located within the purple eclipse) and the monitoring wells of MW2, MW6, MW8, and MW11 in the fine sand layer were similar (Cl—Ca), while water quality of spring discharge and the monitoring wells of MW4 and MW5 in the silty sand layer were different (HCO_3—Ca), indicating that spring water is primarily yielded from the fine sand layer; From Supplementary Figure S1B, it can be observed that water quality of spring discharge (red star symbol located within the red eclipse) and the monitoring wells of MW2, MW6, MW8, and MW11 in the fine sand layer were attributed to water-rock interactions, while water quality of the monitoring wells of MW4 and MW5 in the silty sand layer were different, which further demonstrated that spring water is yielded from the fine sand layer.

2.4 Data sources

Discrete groundwater levels were gained from monitoring wells located adjacent to the BL Spring, and were interpolated to delineate groundwater level contours for representing regional-scale groundwater flow fields. Precipitation and evapotranspiration data were gained from weather station, and groundwater pumping rate as well as the amount of groundwater consumption were gained from water resources bulletin promulgated by the local government.

The top elevations of the upmost layer were assigned land surface elevations gained from the Shuttle Radar Topography Mission (SRTM) data which were used to generate digital elevation data with a resolution of 3 arc-seconds (https://www.usgs.gov/centers/eros/science/usgs-eros-archive-digital-elevation-shuttle-radar-topography-mission-srtm-non), and the bottom elevations of each layer were assigned based on the thickness of each hydrogeological formation.

Hydrogeological parameters including hydraulic conductivity, specific yield, and specific storage of various layers were yielded from *in-situ* pumping tests.

3 Numerical modeling

A 3D numerical groundwater flow model (the baseline model) was developed based on hydro-climatical and hydrogeological data and calibrated against observed groundwater levels to simulate current-stage spring discharge. Based on the developed/calibrated baseline model, a series of 3D numerical groundwater flow models (the predictive models) were developed to simulate future trends of spring discharge under various groundwater pumping scenarios, and the simulated spring discharges of the baseline model and predictive models were compared for the purpose of quantitatively evaluating pumping effects on spring discharge.

3.1 Simulation code

The MODFLOW module which was one of the most frequently-used numerical simulation tool that has been successfully applied to many cases studies worldwide was selected, and the Groundwater Vistas software which has been demonstrated to be one of the most useful graphical-user-interface and data pre- and post-processor was utilized for implementing and calibrating numerical models. The governing equation of the MODFLOW module which was used to simulate groundwater flow is:

$$\frac{\partial}{\partial x}\left(K_x\frac{\partial H}{\partial x}\right)+\frac{\partial}{\partial y}\left(K_y\frac{\partial H}{\partial y}\right)+\frac{\partial}{\partial z}\left(K_z\frac{\partial H}{\partial z}\right)+W=S_s\frac{\partial H}{\partial t}$$

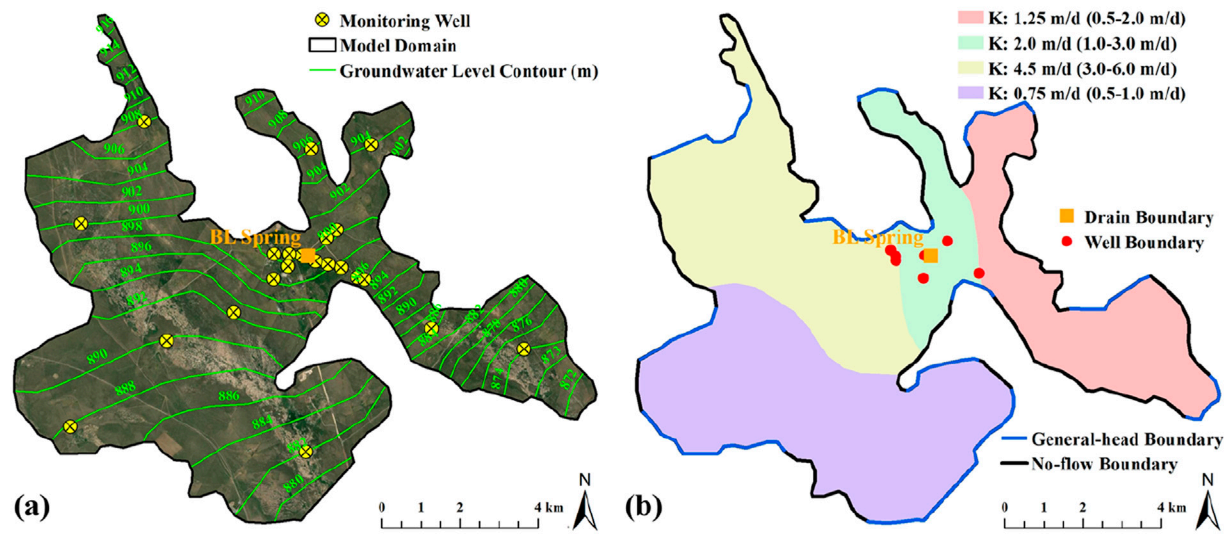

FIGURE 2
(A) Model domain; **(B)** Spatial variation of general-head boundary and no-flow boundary as well as horizontal hydraulic conductivity zones in the fine sand layer.

where: H is groundwater level elevation [L]; K_x, K_y, K_z are hydraulic conductivity in the x-, y-, and z- directions [LT^{-1}]; W is source/sink [T^{-1}]; S_s is specific storage [L^{-1}]; and t is time [T].

3.2 Model domain

The model domain (see Figure 2A) of the baseline model and the predictive models was determined based on current-stage regional-scale groundwater flow field (Xilin Gol League's Water Resources Bulletin, http://www.xilinhaote.gov.cn/xilinhaote/2023-08/04/article_20230804104607500025.html) that model boundaries were either parallel or perpendicular to the groundwater level contours (the fine sand layer). The model domain covers an area approximately 106 km^2, and the silty sand layer, the clay layer, and the fine sand layer were included.

3.3 Hydrogeological parameters

Hydrogeological parameters of the baseline model and the predictive models included, but were not limited to, hydraulic conductivity, porosity, specific yield and specific storage. Based on the results from pumping tests (see Supplementary Table S1), horizontal hydraulic conductivity of the silty sand layer and the clay layer were assigned constant values of 5 m/d and 0.0005 m/d, while spatial variation of horizontal hydraulic conductivity of the fine sand layer were interpolated and switched to zoned values as shown in Figure 2B. Vertical anisotropy (the ratio of vertical/horizontal hydraulic conductivity) was assumed to be 0.1. Porosity, specific yield, and specific storage of the silty sand layer and the fine sand layer were designated based on the values in Supplementary Table S1. Note that the values of these hydrogeological parameters were slightly adjusted during model calibration processes for better model performance.

3.4 Boundary and initial conditions

Boundary conditions of the baseline model and the predictive models were implemented based on hydrological and hydrogeological conditions of each hydrostratigraphic unit. General-head boundary and no-flow boundary were assigned to lateral boundaries (referred to the eastern, western, southern, and northern boundaries), while recharge/evaporation boundary and no-flow boundary were assigned to vertical boundaries (referred to the top and bottom boundaries). The general-head boundary was assigned to the lateral boundaries that are parallel to groundwater level contours to represent groundwater inflow/outflow at model boundary (see Figure 2B), while the no-flow boundary was assigned to the lateral boundaries that are perpendicular to groundwater level contours to represent zero groundwater flux into/out of model boundary (see Figure 2B); the recharge boundary and evaporation boundary were assigned to the top boundary of the top layer, while the no-flow boundary was assigned to the bottom boundary of the bottom layer. The spatial variation of recharge rate (representing infiltration from precipitation) was estimated based on the spatial variation of precipitation (recharge rate specified as a net flux of 5% of precipitation), while the spatial variation of evaporation was estimated based on the spatial variation of potential evaporation with extinction depth limit of 4 m.

Current-stage groundwater level contours (see Figure 2A) were utilized to represent initial heads of the baseline model, and spatial variation of groundwater levels simulated by the baseline model were utilized to represent initial heads of the predictive models.

3.5 Sources and sinks

Sources and sinks of the baseline model and the predictive models mainly include infiltrated rainwater (annual rainfall

320.9 mm with infiltration/rainfall ratio assumed to be 0.1), evaporation (annual evaporation 1,542.7 mm), groundwater pumping (seven wells 45.8 m^3/d in total with single well 6.54 m^3/d) and spring discharge (calculated by the developed model). The recharge boundary and the evaporation boundary were assigned to the upper bound of the top layer to represent infiltrated rainwater and evaporation. The well boundary was assigned to the fine sand layer to represent groundwater pumping (see Figure 2B). The drain boundary was assigned to the fine sand layer to represent spring discharge (see Figure 2B). The spring discharge was affected by the differences between potentiometric level and land surface elevation, and was calculated automatically during MODFLOW simulation period by multiplying the differences between potentiometric level and land surface elevation by conductance coefficient. Note that the conductance coefficient was used to represent head loss of spring discharge from subsurface conduits to land surface, and its value was assigned to be 100 m^2/d based on empirical value.

3.6 Spatial-temporal discretization

Spatially, the model domain of the baseline model and the predictive models was horizontally divided into 260 rows and 299 columns (with a cell size of 50 m × 50 m) and vertically divided into 3 layers with Layers 1, 2, and 3 representing the silty sand layer, the clay layer, and the fine sand layer, respectively. Land surface elevations were assigned to the top elevations of Layer 1, while the bottom elevations of Layers 1, 2, and 3 were assigned based on the thickness of each hydrogeological formation (see Figure 1B). Temporally, the baseline model was steady-state which simulated current-stage spring discharge, the predictive models were transient and the simulation periods were set 10 years with 10 stress periods (1 year per stress period) and 120 time steps (1 month per time step).

4 Results and discussion

4.1 Model calibration

The baseline model was calibrated using the trial-and-error method by gradually adjusting the values of horizontal hydraulic conductivity and vertical anisotropy within a reasonable range, aiming at matching the simulated groundwater levels with the observed groundwater levels from the 22 monitoring wells (see Figure 2A) to a satisfactory degree.

The scatter diagram showing the goodness of fit between the simulated and observed groundwater levels was shown in Supplementary Figure S2. After calibration, the Nash-Sutcliffe efficiency coefficient reaches 0.95, and the simulated spring discharge (193.7 m^3/d) was very closed to the monitored value (192.6 m^3/d), indicating that the implementation of the baseline model (e.g., boundary and initial conditions, hydrogeological parameters, spatial and temporal discretization, etc.) was appropriate and the predictive models developed based on the baseline model were reliable.

4.2 Simulation results of the baseline model

4.2.1 Spring discharge

The simulated water table of the silty sand layer and potentiometric level of the fine sand layer were shown in Figures 3A,B, respectively. It can be observed from Figure 3A that water table in the northwest was highest while in the southeast was lowest, indicating that groundwater flow in the silty sand layer is from northwest to southeast. It can also be observed from Figure 3B that potentiometric level in the northwest was highest while in the southeast was lowest, indicating that groundwater flow in the fine sand layer is from northwest to southeast. In addition, it can be observed from Figures 3A,B that the silty sand layer's groundwater flow at the spring location was diverged whereas the fine sand layer's groundwater flow at the spring location was converged, which further demonstrated that spring water source is yielded from the fine sand layer. Note that potentiometric level is higher than water table, revealing that the overlying silty sand layer may receive upward recharge from the fine sand layer.

The simulated spring discharge was 193.7 m^3/d, which was very closed to the monitored value (192.6 m^3/d). To quantitatively assess the impacts of current-stage pumping scheme upon spring discharge, nine pumping scenarios (Scenarios 0–8) were implemented as described in Supplementary Table S3. Scenario 0 represented the "natural stage" without groundwater pumping; Scenarios 1, 2, 3, 4, 5, 6, and 7 represented single-well pumping scheme (only one well was active (pumping rate 6.54 m^3/d) while the other six wells were inactive (pumping rate 0 m^3/d)); and Scenario 8 represented the current-stage pumping scheme (same with the baseline model that pumping rate 45.8 m^3/d in total with single well 6.54 m^3/d).

With respect to Scenarios 0, 1, 2, 3, 4, 5, 6, 7, and 8, the spring discharge was simulated to be 201.4, 200.0, 198.4, 200.4, 201.4, 200.9, 200.7, 200.6, and 193.7 m^3/d, indicating a reduction of 1.4, 3.0, 1.0, 0, 0.5, 0.7, and 0.8 m^3/d when only Well #1, #2, #3, #4, #5, #6, and #7 is active and a reduction of 7.7 m^3/d when all wells are active in comparison to the "natural stage" spring discharge of 201.4 m^3/d. It can be seen that: 1) current-stage pumping scheme can affect spring discharge with a reduction ratio of 3.80%; 2) single pumping of Well #1, #2, #3, #5, #6, and #7 can affect spring discharge with a reduction ratio of 0.70%, 1.49%, 0.50%, 0.25%, 0.35%, 0.40%, respectively; 3) the impact of Well #2 pumping on spring discharge decline is the most significant in that the distance of Well #2 to spring is the nearest; and 4) the impact of Well #4 pumping on spring discharge decline is negligible in that the distance of Well #4 to spring is the farthest.

4.2.2 Spring-discharge-affected zone

Based on the simulated groundwater flowlines of the fine sand layer, the spring-discharge-affected zone where groundwater flow directions headed to the BL spring was visualized in Figure 3C. It can be seen that Wells #1, #2, #3, #5, #6, and #7 are located within the spring-discharge-affected zone, whereas Well #4 is located outside the spring-discharge-affected zone. Under current-stage pumping scheme, the area of the spring-discharge-affected zone was calculated to be 2.025 km^2, and the farthest distance from the BL spring to the boundary of this zone was measured to be 1.12 km.

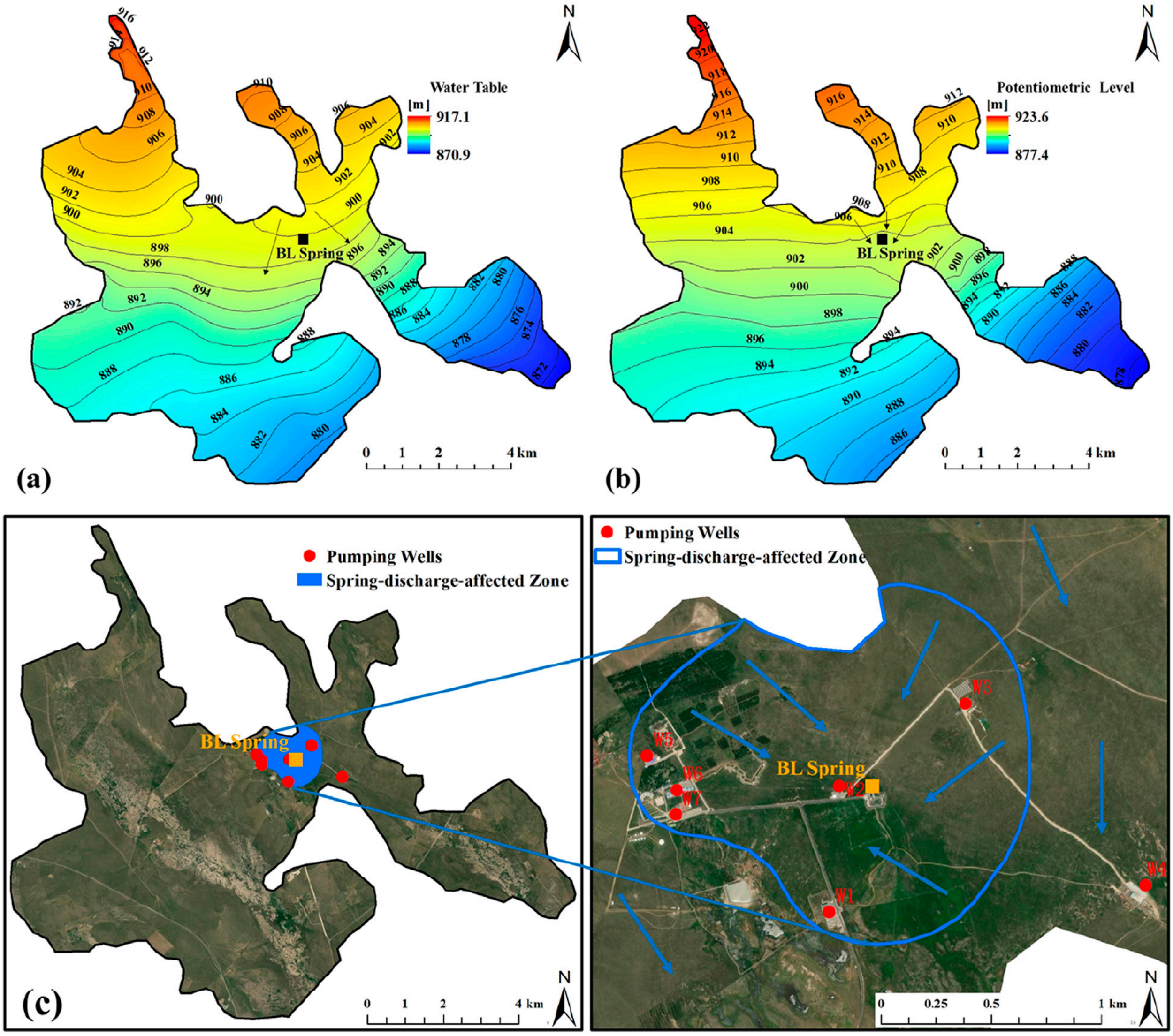

FIGURE 3
(A) Spatial variation of water table of the silty sand layer; **(B)** Spatial variation of potentiometric level of the fine sand layer; **(C)** Location of the spring-discharge-affected zone under current-stage pumping scheme.

Since Well #4 is located outside the spring-discharge-affected zone, groundwater abstraction from Well #4 may not affect spring discharge. Since Well #1, Well #3, Well #5, Well #6, and Well #7 were located adjacent to the boundary of the spring-discharge-affected zone, the impacts of groundwater pumping from these five abstraction wells were relatively small. Since Well #2 is located adjacent to the BL Spring, the impacts of groundwater abstraction at Well #2 were significant.

4.3 Simulation results of the predictive models

To assess the impacts of increasing groundwater pumping due to the rapid development of tourism on spring discharge, a series of predictive models were implemented by adjusting the values of pumping rates of the Well boundary condition of the developed and calibrated baseline model. Twelve groundwater pumping scenarios (Scenarios 9–20) regarding twelve pumping rates which represented various pumping schemes in future were applied to the twelve predictive models (see Supplementary Table S4). Note that: 1) Scenario 0 represented the "natural stage" without groundwater pumping; 2) Scenario 8 represented the current-stage pumping scheme (same with the baseline model); and 3) Scenarios 9–20 represented the situations of groundwater pumping rates being 2, 4, 6, 7.5, 8, 10, 12, 15, 19.4, 20, 25, and 25.7 times of the current-stage pumping rate (45.8 m^3/d). Note that the length of the stress period of each predicted model was set 10 years. The simulated potentiometric levels of the fine sand layer with respect to Scenarios 9–20 were visualized in Figures 4A–L, respectively. It can be observed from Figures 4A–L that local-scale groundwater flow field and potentiometric level contours began to change and

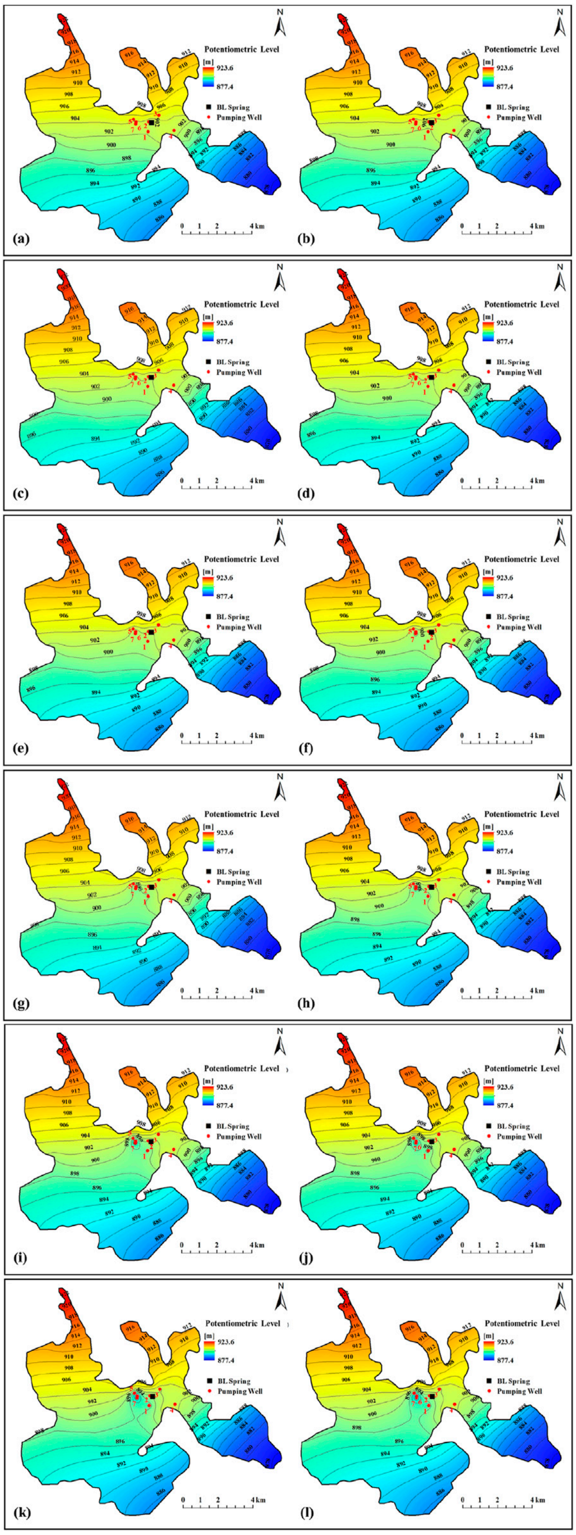

FIGURE 4
Groundwater flow field and potentiometric level contours of the fine sand layer: **(A)** Scenario 9; **(B)** Scenario 10; **(C)** Scenario 11; **(D)** Scenario 12; **(E)** Scenario 13; **(F)** Scenario 14; **(G)** Scenario 15; **(H)** Scenario 16; **(I)** Scenario 17; **(J)** Scenario 18; **(K)** Scenario 19; **(L)** Scenario 20.

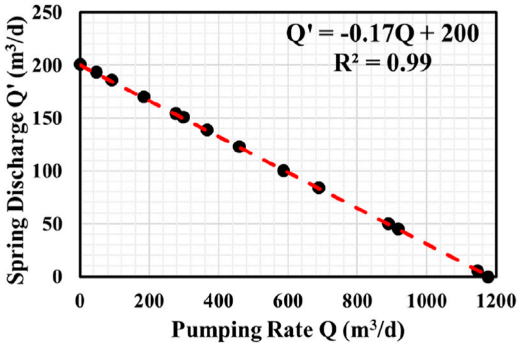

FIGURE 5
Relationship between spring discharge Q' and pumping rate Q.

groundwater depression zones started to form with an increasing groundwater pumping rate.

With respect to Scenarios 9–20, the spring discharge was simulated to be 185.9, 170.2, 154.5, 151.1, 138.9, 123.2, 100.7, 84.0, 50.4, 45.0, 5.8, and 0 m^3/d, indicating a reduction of 15.5, 31.2, 46.9, 50.3, 62.5, 78.2, 100.7, 117.4, 151.0, 156.4, 195.6, and 201.4 m^3/d in comparison to the "natural stage" spring discharge of 201.4 m^3/d. It can be seen that: 1) a 1, 3, 5, 7, 9, 14, 19, and 24 times increase of pumping rate in future comparison to the current-stage pumping rate would result in a spring discharge decline of 7.7%, 15.5%, 23.3%, 31.0%, 38.8%, 58.3%, 77.1%, and 97.1%, respectively; and 2) the spring discharge would reduce 25%, 50%, 75%, and 100% if future pumping rate would increase from 45.8 m^3/d (current-stage pumping scheme) to 297.7, 586.2, 888.5, and 1,176 m^3/d, respectively.

Based on the simulation results of various spring discharges (Q') with respect to different pumping rates (Q), a linear relationship between Q' and Q was yielded (shown in Figure 5). Note that the fitting coefficient R^2 was calculated to be 0.99, indicating that the linear relationship between Q' and Q was reasonable. The fitting equation can be used to estimate spring discharge if groundwater pumping rate is decided. As mentioned above, several hotels and restaurants were implemented to host visitors and groundwater pumping rate increased significantly with the rapid development of tourism since 2017, because groundwater served as the sole source of water supply in this region. Although the recent rapid development of tourism has raised local tax and boosted local GDP, degradation of local eco-environment such as reduction of spring discharge has paid the price. Hence, it is very important and necessary to reach an "equilibrium" between economic growth and eco-environment degradation. In other words, it is imperative to determine the maximum groundwater withdrawal rate under the premise of protecting spring discharge to a certain degree. The yielded fitting equation can serve as a useful tool for water resources managers to make reasonable plans of groundwater exploitation to meet the requirements of increasing groundwater supply due to rapid development of tourism while maintaining spring discharge at a reasonable level in the meanwhile.

4.4 Uncertainty analysis

Uncertainties mainly included, but were not limited to: uncertainties of model parameters, uncertainties of simulation models, uncertainties of values assigned to boundary conditions, and uncertainties of monitoring data.

Under the circumstances of the complexity of groundwater systems (e.g., heterogeneity), hydrogeological parameters such as hydraulic conductivity, specific yield, and specific storage determined from the limited borehole pumping tests might not be representative of regional-scale hydrogeological conditions. Besides, empirical values were assigned to the hydrological parameters of recharge coefficient (infiltration/rainfall ratio) and evaporation extinction depth. Unrealistic expectations and inappropriate implementation of hydrogeological and hydrological parameters may result in uncertainties of model parameters.

Real groundwater systems are complicated while limited borehole data may not be able to unravel the complex variation of hydrogeological conditions precisely, resulting in uncertainties of conceptual model. Numerical model solvers are usually optimized and adjusted for achievements of reasonable computation time and cost, causing computation error especially in local-scale groundwater levels and flowrates, resulting in uncertainties of numerical model.

Uncertainty of model results from boundary conditions was largely yielded from uncertainties of head values assigned to the GHB boundary. The head values assigned to the GHB boundary were determined by groundwater level contours interpolated from the monitoring wells, whereas inaccurate head values assigned to the GHB boundary may sacrifice the accuracy of model output.

Systematic errors and random errors exist unavoidably during data collection and management procedures (e.g., sampling, measurement, recording, digitization, archiving, etc.), resulting in uncertainties of monitoring data.

4.5 Future work

The performance of the baseline model and the predictive models require improvements. The most effective and efficient approach is to gather more groundwater level measurements for increasing the accuracy of conceptual model design and parameterization. It is highly expected that a real-time monitoring network of groundwater levels and spring discharges would be implemented in future for more comprehensive simulation of the long-term variation of spring discharges under the impacts of climate change and anthropogenic activities.

5 Conclusion

Recently, spring discharge decline due to groundwater exploitation has been recognized as a significant issue posing a great threat to eco-environmental safety. In this study, numerical approach was utilized and 3D groundwater flow models based on the MODFLOW module were developed to simulate current-stage and future spring discharges under the impacts of increasing groundwater pumping due to the rapid development of tourism in the BL spring located in Xilin Gol League in east Inner Mongolia (China).

Simulation results indicated that: 1) spring discharge has reduced from 201.4 m^3/d to 193.7 m^3/d (reduction ratio of 3.80%) under current-stage pumping scheme; 2) the area of the spring-discharge-affected zone is 2.025 km^2 and the farthest distance from the BL spring to the boundary of this zone is 1.12 km under current-stage pumping scheme; 3) the impact of Well #2 (located nearest to the BL spring) pumping on spring discharge decline is the most significant while the impact of Well #4 (located farthest to the BL spring and outside the spring-discharge-affected zone) pumping is negligible; and 4) spring discharge would reduce 25%, 50%, 75%, and 100% if future pumping rate would increase from 45.8 m^3/d (current-stage pumping scheme) to 297.7, 586.2, 888.5, and 1,176 m^3/d, respectively.

The outcome of this study can provide a useful reference for long-term planning and management of sustainable groundwater exploitation under the premise of spring discharge management and springshed eco-environmental protection in the BL spring and other springs in the vicinities in east Inner Mongolia, China.

Data availability statement

The datasets presented in this article are not readily available because Data can be provided upon request. Requests to access the datasets should be directed to hxiao0716@163.com.

Author contributions

HX: Conceptualization, Data curation, Investigation, Methodology, Software, Validation, Visualization, Writing–original draft, Writing–review and editing. YY: Conceptualization, Supervision, Writing–review and editing. QL: Data curation, Validation, Writing–review and editing. YZ: Data curation, Writing–review and editing, Funding acquisition, Investigation, Methodology. XL: Data curation, Writing–review and editing, Visualization. FX: Data curation, Writing–review and editing, Funding acquisition, Supervision. YJ: Conceptualization, Writing–review and editing, Project administration.

Funding

The author(s) declare that financial support was received for the research, authorship, and/or publication of this article. This research was supported by the Yangtze River Joint Phase II Program (No. 2022-LHYJ-02-0509-05) and Fundamental

Research Funds for the Central Public Interest Scientific Institution (2023YSKY30).

Conflict of interest

The authors declare that the research was conducted in the absence of any commercial or financial relationships that could be construed as a potential conflict of interest.

Publisher's note

Author disclaimer

The opinions, findings and conclusions expressed in this manuscript were those of the author(s) and not necessarily those of the funding agencies.

Supplementary material

The Supplementary Material for this article can be found online at: https://www.frontiersin.org/articles/10.3389/fenvs.2024.1400569/full#supplementary-material

References

Aamery, N. A., Adams, E., Fox, J., Husic, A., Zhu, J., Gerlitz, M., et al. (2021). Numerical model development for investigating hydrologic pathways in shallow fluviokarst. *J. Hydrology* 593, 125844. doi:10.1016/j.jhydrol.2020.125844

Bai, T., and Tahmasebi, P. (2023). Graph neural network for groundwater level forecasting. *J. Hydrology* 616, 128792. doi:10.1016/j.jhydrol.2022.128792

Barzegar, R., Moghaddam, A. A., Deo, R., Fijani, E., and Tziritis, E. (2018). Mapping groundwater contamination risk of multiple aquifers using multi-model ensemble of machine learning algorithms. *Sci. Total Environ.* 621, 697–712. doi:10.1016/j.scitotenv.2017.11.185

Batelaan, O., De Smedt, F., and Triest, L. (2003). Regional groundwater discharge: phreatophyte mapping, groundwater modelling and impact analysis of land-use change. *J. Hydrology* 275 (1-2), 86–108. doi:10.1016/s0022-1694(03)00018-0

Cerqueira, V., Torgo, L., and Soares, C. (2019). Machine learning vs statistical methods for time series forecasting: size matters. *Comput. Res. Repos.* doi:10.48550/arXiv.1909.13316

Chang, Y., Wu, J., Jiang, G., Liu, L., Reimann, T., and Sauter, M. (2019). Modelling spring discharge and solute transport in conduits by coupling CFPv2 to an epikarst reservoir for a karst aquifer. *J. Hydrology* 569, 587–599. doi:10.1016/j.jhydrol.2018.11.075

Chen, X. (2021). A study of effects of reduction of submarine groundwater discharge on thermal habitats for manatee in a spring-fed estuary using a laterally averaged hydrodynamic model. *Ecol. Model.* 456, 109653. doi:10.1016/j.ecolmodel.2021.109653

Dass, B., Abhishek Sen, S., Bamola, V., Sharma, A., and Sen, D. (2021). Assessment of spring flows in Indian Himalayan micro-watersheds – a hydro-geological approach. *J. Hydrology* 598, 126354. doi:10.1016/j.jhydrol.2021.126354

Doummar, J., Kassem, A. H., and Gurdak, J. J. (2018). Impact of historic and future climate on spring recharge and discharge based on an integrated numerical modelling approach: application on a snow-governed semi-arid karst catchment area. *J. Hydrology* 565, 636–649. doi:10.1016/j.jhydrol.2018.08.062

Doummar, J., Sauter, M., and Geyer, T. (2012). Simulation of flow processes in a large-scale karst system with an integrated catchment model (Mike She) – identification of relevant parameters influencing spring discharge. *J. Hydrology* 426–427, 112–123. doi:10.1016/j.jhydrol.2012.01.021

Duran, L., and Gill, L. (2021). Modeling spring flow of an Irish karst catchment using Modflow-USG with CLN. *J. Hydrology* 597, 125971. doi:10.1016/j.jhydrol.2021.125971

Filippini, M., Segadelli, S., Dinelli, E., Failoni, M., Stumpp, C., Vignaroli, G., et al. (2024). Hydrogeological assessment of a major spring discharging from a calcarenitic aquifer with implications on resilience to climate change. *Sci. Total Environ.* 913, 169770. doi:10.1016/j.scitotenv.2023.169770

Frederik, K., Daniel, K., Claire, B., Karsten, S., and Mathew, H. (2018). Rainfall-runoff modelling using long short-term memory (LSTM) networks. *Hydrology Earth Syst. Sci.* 22 (11), 6005–6022. doi:10.5194/hess-22-6005-2018

Frisbee, M. D., Phillips, F. M., White, A. F., Campbell, A. R., and Liu, F. (2013). Effect of source integration on the geochemical fluxes from springs. *Appl. Geochem.* 28, 32–54. doi:10.1016/j.apgeochem.2012.08.028

Gai, Y., Wang, M., Wu, Y., Wang, E., Deng, X., Liu, Y., et al. (2023). Simulation of spring discharge using graph neural networks at Niangziguan Springs, China. *J. Hydrology* 625, 130079. doi:10.1016/j.jhydrol.2023.130079

Li, C., Xing, L., Dong, Y., Pen, Y., Xing, X., Li, C., et al. (2022). Numerical simulation and protection of the dynamic change of Jinan karst spring based on coupling of seepage and conduit flow. *Heliyon* 8, e10428. doi:10.1016/j.heliyon.2022.e10428

Li, S., Zhou, Y., Cheng, J., and Yao, H. (2023). Delay-aware karst spring discharge prediction. *J. Hydrology* 626, 130250. doi:10.1016/j.jhydrol.2023.130250

Mechal, A., Birk, S., Dietzel, M., Leis, A., Winkler, G., Mogessie, A., et al. (2017). Groundwater flow dynamics in the complex aquifer system of Gidabo River Basin (Ethiopian Rift): a multi-proxy approach. *Hydrogeology J.* 25 (2), 519–538. doi:10.1007/s10040-016-1489-5

Meyers, Z. P., Rademacher, L. K., Frisbee, M. D., and Warix, S. R. (2022). Extending classical geochemical weathering studies through the mountain block: the effect of increasing scale on geochemical evolution in the Sierra Nevada (CA). *Chem. Geol.* 598, 120831. doi:10.1016/j.chemgeo.2022.120831

Musgrove, M., Stern, L. A., and Banner, J. L. (2010). Springwater geochemistry at Honey Creek State Natural Area, central Texas: implications for surface water and groundwater interaction in a karst aquifer. *J. Hydrology* 388, 144–156. doi:10.1016/j.jhydrol.2010.04.036

Nolin, A. F., Girardin, M. P., Adamowski, J. F., Barzegar, R., Boucher, M. A., Tardif, J. C., et al. (2023). Observed and projected trends in spring flood discharges for the Upper Harricana River, eastern boreal Canada. *J. Hydrology Regional Stud.* 48, 101462. doi:10.1016/j.ejrh.2023.101462

Rahmati, O., Choubin, B., Fathabadi, A., Coulon, F., Soltani, E., Shahabi, H., et al. (2019). Predicting uncertainty of machine learning models for modelling nitrate pollution of groundwater using quantile regression and UNEEC methods. *Sci. Total Environ.* 688, 855–866. doi:10.1016/j.scitotenv.2019.06.320

Rooij, R., Perrochet, P., and Graham, W. (2013). From rainfall to spring discharge: coupling conduit flow, subsurface matrix flow and surface flow in karst systems using a discrete–continuum model. *Adv. Water Resour.* 61, 29–41. doi:10.1016/j.advwatres.2013.08.009

Scanlon, B. R., Mace, R. E., Barrett, M. E., and Smith, B. (2003). Can we simulate regional groundwater flow in a karst system using equivalent porous media models? Case study, Barton Springs Edwards aquifer, USA. *J. Hydrology* 276, 137–158. doi:10.1016/s0022-1694(03)00064-7

Sezen, C., Bezak, N., Bai, Y., and õSraj, M. (2019). Hydrological modelling of karst catchment using lumped conceptual and data mining models. *J. Hydrology* 576, 98–110. doi:10.1016/j.jhydrol.2019.06.036

Shi, H. J., Qi, X., and Jin, H. (2015). Prediction of karst groundwater level based on R Language, taking Jinci Spring Basin as an example. *Appl. Mech. Mater.* 730, 230–234. doi:10.4028/www.scientific.net/amm.730.230

Wang, X., Liu, T., Zheng, X., Peng, H., Xin, J., and Zhang, B. (2018). Short-term prediction of groundwater level using improved random forest regression with a combination of random features. *Appl. Water Sci.* 8 (125), 1–12. doi:10.1007/s13201-018-0742-6

Work, K. (2020). Not just an arid landscape problem: springflow declines in a region with high rainfall. *Limnologica* 82, 125766. doi:10.1016/j.limno.2020.125766

Xu, Z., and Hu, B. X. (2021). Decadal exploration of karst hydrogeology in the Woodville Karst Plain (WKP): a review of field investigation and modeling development. *J. Hydrology* 594, 125937. doi:10.1016/j.jhydrol.2020.125937

Zhou, R., and Zhang, Y. (2023). Linear and nonlinear ensemble deep learning models for karst spring discharge forecasting. *J. Hydrology* 627, 130394. doi:10.1016/j.jhydrol.2023.130394

frontiers | Frontiers in Environmental Science

TYPE Original Research
PUBLISHED 20 September 2024
DOI 10.3389/fenvs.2024.1431068

Influence of different application rates of FGD gypsum and aeolian sand on CO_2 and N_2O emissions from cotton-capsicum saline-alkali soil

Yiwei Chen, Fan Luo, Yao Guan*, Xinghong He*, Jian Wang, Debao Fan and Rui Gao

College of Hydraulic and Architectural Engineering, Tarim University, Alaer, China

Check for updates

OPEN ACCESS

EDITED BY
Jing Liu,
University of Birmingham, United Kingdom

REVIEWED BY
Peiling Yang,
China Agricultural University, China
Chenchen Wei,
Changjiang River Scientific Research Institute (CRSRI), China

*CORRESPONDENCE
Yao Guan,
417512676@qq.com
Xinghong He,
hexinghong0611@163.com

RECEIVED 13 May 2024
ACCEPTED 08 August 2024
PUBLISHED 20 September 2024

CITATION
Chen Y, Luo F, Guan Y, He X, Wang J, Fan D and Gao R (2024) Influence of different application rates of FGD gypsum and aeolian sand on CO_2 and N_2O emissions from cotton-capsicum saline-alkali soil.
Front. Environ. Sci. 12:1431068.
doi: 10.3389/fenvs.2024.1431068

As two important greenhouse gases in the atmosphere, CO_2 and N_2O have been paid much attention to their environmental effects. As a large agricultural and population country in the world, agricultural soil is an important source of greenhouse gas emissions. In recent years, unreasonable agricultural measures will make the soil structure deteriorate and lead to the increase of saline-alkali cultivated land area. Therefore, the comprehensive utilization of saline-alkali land has practical significance for agricultural production and ecological environment safety in our country. In this study, the 11th Regiment of Alar City of the First Division of Xinjiang carried out field tests on saline-alkali cultivated land, and improved the saline-alkali cultivated land with desulfurized gypsum and aeolian sand. Six treatments were set up (blank treatment (CK) desulfurized gypsum 15 t/ha (LH), desulfurized gypsum 30 t/ha (LA), desulfurized gypsum 15 t/hamixed application (FL), Aeolian sand 15 t/ha (FH), and Aeolian sand 30 t/ha (FA)). The effects of different treatments on CO_2 and N_2O emission fluxes in cotton-pepper soil were observed. The results show that: (1) In the growth stage of cotton-pepper, compared with CK, soil moisture increased, and soil ammonium nitrogen decreased; The conductivity increases with the increase of desulphurized gypsum and the decrease of aeolian sand. The results showed that LA treatment had the best water retention effect and FA treatment had the best salt reduction effect. (2) Compared with CK, the cumulative CO_2 emission fluxes of cotton soil under different treatments were CK > LH > FL > FH > LA > FA treatment, and those of pepper soil were CK > FL > LH > FH > FA > LA treatment. Among them, the inhibition effect of cumulative soil CO_2 emission under LA and FA treatment reached a significant level. (3) Compared with CK, the cumulative N_2O emission fluxes of LH, LA, FL, FH and FA treated soil in cotton field were CK > LA > LH > FH > FL > FA, and that of pepper soil was CK > FA > LH > LA > FL > FH. Among them, the inhibition effect of aeolian sand (FA and FH) on soil N_2O cumulative emission reached a significant level. (4) Compared with CK, LH, LA, FL, FH and FA treatments reduced the comprehensive greenhouse effect of cotton field and pepper crops by inhibiting soil CO_2 emission fluxes, among which FA treatment had the lowest comprehensive greenhouse effect. Therefore, the effects of different treatments on physicochemical properties and gas emissions of saline-alkali soil were comprehensively analyzed, and FA treatment had the best effect on inhibiting CO_2 and N_2O emissions and improving soil physicochemical properties.

KEYWORDS

salinized soil, desulfurized gypsum, aeolian sand, soil CO_2 and N_2O emission fluxes, comprehensive greenhouse effect salinized soil, comprehensive greenhouse effect

1 Introduction

Climate change is one of the serious challenges facing mankind, and with the increase in global temperature, the issue of climate change has become the biggest risk facing the whole world at present, in which greenhouse gas emissions caused by human activities are the main cause of climate change. As two important greenhouse gases, CO_2 and N_2O in the atmosphere contribute 80% to the greenhouse effect (Kiehl and Trenbeth, 1997). As a large agricultural and population country in the world, the greenhouse gas (GHG) emissions associated with agricultural activities in China are about 828 million tons of carbon dioxide equivalent (CO_2-eq), which is about 7.9% of the total global GHG emissions, and N_2O also contributes more than 300 million tons of CO_2-eq (Zhang et al., 2023). China has about 3.6×10^7 ha of saline-alkali land, which has 4.88% of the available land area in the country (Li et al., 2014). Therefore, the study of GHG emissions from saline soils in agricultural fields is a topic that needs to be focused on.

The low nutrient content in saline soils, salinization of saline soils severely inhibits the accumulation of organic matter in saline soils, as well as poor soil structure and high soil salinity (Chen, 2023), which leads to reduced crop yields and seriously affects the development of agriculture. Among them, the application of soil conditioners can effectively improve saline and alkaline soils. As an important safeguard for agricultural production and one of the important measures to improve saline soils, different soil amendments can improve soil physical and chemical properties and soil structure while at the same time affecting GHG emissions. In agroecosystems, GHG emissions, soil physicochemical properties and crop yields can vary significantly depending on the amount and method of application (Shao et al., 2022). Zhang et al. (2019) showed that gypsum has the best effect on inhibiting greenhouse gas emissions. Li (2023); Wang (2020) and Xiang (2018) reported that soil greenhouse gas emissions were significantly suppressed with the application of FGD gypsum Jiang et al. (2023). The study indicated that as the amount of desulphurized gypsum applied increased, the rate of decrease in the percentage of sodium exchanged and the rate of increase in crop yield showed an increasing and then decreasing trend, while the rate of increase in the electrical conductivity of the soil leachate showed an increasing trend. As FGD gypsum itself is a kind of salt, long-term application or mismanagement may lead to an increase in the total salt content of the soil (Huang et al., 2011). Therefore, different alkaline soil improvement also requires strict control of FGD gypsum application. Sand mixing can improve soil structure, increase the effective porosity and permeability of soil (Zhang et al., 2019), accelerate water infiltration, increase water content and reduce soil salinity. Therefore, in this study, a field experiment was conducted to monitor the response of CO_2 and N_2O emissions from cotton-chilli soils in the extreme arid zone to different amounts of FGD and FGD gypsum applied, with the aim of selecting the most beneficial soil amendment for saline-alkaline soils by determining the CO_2 and N_2O emissions and the main influencing factors under different cropping modes, with a view to providing theoretical support for the sustainable development of agriculture in the region.

2 Materials and methods

2.1 Overview of the study area

The experiment was carried out in 2023 in the 11th regiment of Alar City, the first division of Xinjiang, the experimental field is located in the south of Tianshan Mountain, adjacent to the northern edge of the Taklamakan Desert, geographic location 40.38° N, 81.37° E. The land belongs to the extreme continental climate of the warm zone, the average temperature during the test period is 33°C, the average annual rainfall is 40.1–82.5 mm, and the basic physical and chemical properties of the soil are shown in Table 1.

2.2 Experimental design

In this study, plots without the application of amendments were used as controls, and FGD gypsum 15 t/ha (LH), FGD gypsum 30 t/ha (LA), FGD gypsum 15 t/ha and aeolian sand 15 t/ha mixed (FL), aeolian sand 15 t/ha (FH), aeolian sand 30 t/ha (FA), and the control (without the application of the amendment CK), with a total of six treatments, each with three replicates and a plot area of 18 m × 3.3 m. Before sowing the crops, the plots containing FGD gypsum (from Alar City Lantian Thermal Co., Ltd.) and aeolian sand (from the 11th Regiment of Alar City, the First Division of Xinjiang - the Gate of Taklamakan Desert) were rotofilled using agricultural machinery, so that the soil conditioner in the single- and mixed-application treatments was uniformly distributed in the 0–30 cm soil layer.

2.3 The test crops were cotton and chilli pepper

They were planted with under-mulched drip irrigation, with a film width of 200 cm, and drip irrigation tapes were laid in 6 rows of 1 film and 3 tubes, with a wide spacing of 60 cm, a narrow spacing of 30 cm, and a plant spacing of 20 cm; the seeds were sown

TABLE 1 Basic physical and chemical properties of soils.

Soil depth (cm)	Mass fraction of particles of different sizes (%)			Conductivity	pH	Organic carbon	Nitrate nitrogen	Ammonium nitrogen
	Clay grains	Silt grains	Sand grains					
	(<0.002 mm)	(0.002–0.02 mm)	(0.02–2 mm)	(Us/cm)		(g/kg)	(g/kg)	(mg/kg)
0~20	4.28	57.88	37.84	1,185	8.31	14.28	0.68	16.34

on 27th April 2023, and the harvest took place on 8th October 2023, and the planting of cotton and chilli was carried out in the same way. Diamine phosphate (220 kg/ha) and urea (60 kg/ha) were applied as the base fertilizer before sowing, and urea and compound fertilizer were added at the bud stage, bolling stage and fluffing stage of cotton. A total of 10 times of irrigation throughout the reproductive period, a single irrigation rate of 360 m^3/ha Greenhouse gas sample collection and analysis.

2.3.1 Greenhouse gas emission flux capture

Soil CO_2 and N_2O gas emissions were collected continuously everyday before and after irrigation during the cotton bolling stage, and the gases were collected *in situ* using the static dark box method. The static chamber consisted of a top box (0.5 m × 0.5 m × 0.5 m) and a base (0.5 m × 0.5 m × 1.5 m). A thermometer slot is provided in the box to observe the temperature change in the box during sampling. A foam plate with a thickness of 2 cm is arranged outside the box to prevent the temperature in the box from rising too fast during sampling. The base was buried in the soil of each test plot in the field, with the soil surface flush with the top of the base, and the top of the base was equipped with a 5-cm-thick groove for placing the top box, which was filled with water and sealed with water to prevent the exchange of air between inside and outside of the sampling box when collecting gases (Figure 1). The collection time was from 11:00 to 14:00 p.m., and the gas was collected every 15 min for 45 min after hooding the box, and the collected gas was transferred to a 100 mL gas collection bag with a 50 mL syringe (Wei et al., 2021). After gas collection, the collected samples were brought back to the laboratory on the same day for analysis, and a gas chromatograph was used to determine the gas concentration in the gas sampling bag.

2.3.2 Determination of greenhouse gas emission fluxes

(1) The GHG analyses were carried out using a gas chromatograph to determine the CO_2 and N_2O concentrations in the gas sampling bags. The gas emission formula is (Guo et al., 2022):

$$F = \rho h \times \frac{273}{273 + T} \frac{\Delta c}{\Delta t} \tag{1}$$

where F represents the emission flux of CO_2 and N_2O (mg/(m^2·h)), ρ denotes the density of the gas in the standard state (g/L), h is the height of the box (m), T is the average temperature inside the box (°C); Δc is the gas concentration difference, Δt is the time difference (h), and $\Delta c/\Delta t$ is the emission rate of CO_2 and N_2O gas concentrations during the collection time, which was calculated according to the linear regression equation.

(2) The cumulative emission fluxes of the greenhouse gases CO_2 and N_2O were calculated as follows (Guo et al., 2022):

$$M = \sum_{i=1}^{n} \frac{(F_{i+1} + F_i) \times (t_{i+1} - t_i) \times 24}{2 \times 100} \tag{2}$$

where M is the cumulative emission flux of soil CO_2 and N_2O (kg/ha), F is the emission flux of soil CO_2 and N_2O (mg/(m^2·h)), i is the number of sampling times, and t is the sampling time (d).

(3) On a 100-year scale, the warming potential effect of N_2O is 298 times greater than that of CO_2, the global warming potential (GWP) effects of the greenhouse gases CO_2 and N_2O are calculated as follows (Wang et al., 2019):

$$\mathrm{GWP} = M_{CO_2} + M_{N_2O} \tag{3}$$

where GWP is the potential effect of greenhouse gas emissions from cotton fields on global warming (kg/ha), M_{CO_2}, M_{N_2O} are the cumulative emissions of soil CO_2 and N_2O, respectively (kg/ha).

2.4 Testing of soil indicators

Soil water content: the soil was taken at 0–60 cm using a tube soil extractor at depths of 0–10 cm, 10–20 cm, 20–40 cm and 40–60 cm, respectively, and the retrieved soil samples were placed in an aluminum box in a constant temperature oven at 105°C for 24 h, and weighed to obtain the soil water content. The soil electrical conductivity was determined using a 308-type conductivity meter to determine the conductivity value (EC1:5) of the soil extract samples. Soil ammonium nitrogen and nitrate nitrogen contents were determined using a Smartchem fully automatic intermittent analyzer to determine the ammonium nitrogen and nitrate nitrogen contents.

2.5 Statistical analyses

Excel 2023 was used for experimental data processing and correlation analysis in SPSS 26.0 software was used to deal with the relationship between soil CO_2 and N_2O emission fluxes as well as soil physicochemical properties of the two crops, cotton-pepper, under different soil improvement measures. Origin 2021 software was used for graphing.

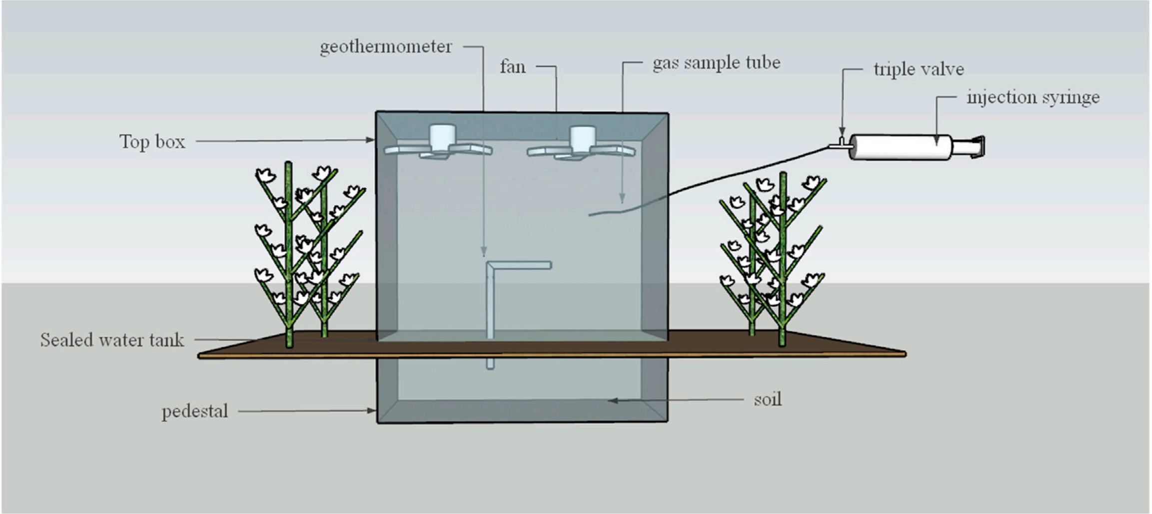

FIGURE 1
Static box device diagram.

3 Results and analyses

3.1 Effect of application of FGD gypsum and aeolian sand to different crops on soil physicochemical properties

3.1.1 Effect of application of desulphurized gypsum and aeolian sand to different crops on soil moisture

Soil moisture is an important component of soil and is the main source of water absorption for plants. Suitable soil moisture is conducive to the reproduction and metabolism of soil microorganisms, the decomposition of soil organic matter and the release of nutrients, thus promoting plant growth. The effect of growing two crops, cotton and chilli pepper, under different amounts of FGD gypsum and aeolian sand on soil moisture at the 0–40 cm soil horizon is shown in Figure 2. Under the CK treatment, the soil moisture of cotton-chilli at the 0–10 cm and 20–40 cm soil horizons was increased by 4.88% and 21.42% compared to that of chilli. In 10–20 cm soil layer cotton soil moisture decreased by 4.47% compared to chilli. Under LH treatment, cotton soil moisture increased by 5.32% and 5.84% in 0–10 cm and 20–40 cm soil layers than chilli. In 10–20 cm soil layer cotton soil moisture decreased by 9.31% compared to chilli. Under LA treatment, cotton soil moisture in 10–20 cm soil layers was same as chilli and in 0–10 cm and 20–40 cm soil layer chilli soil moisture was 1.53% and 18.77% less than cotton. Under FL, FH and FA treatments, cotton soil moisture in the 0–10 cm, 10–20 cm and 20–40 cm soil layers was reduced by 11.03%–18.09%, 20.42%–24.46% and 3.54%–6.47%, respectively, compared to chilli.

In summary, the soil moisture of cotton field-pepper increased gradually with the increase of FGD gypsum and sand application. Under FGD gypsum treatments (LH and LA), cotton field soil moisture was greater than chilli soil moisture in the 0–10 cm and 20–40 cm soil horizons, and cotton field soil moisture was less than chilli soil moisture in the 10–20 cm soil horizons. Cotton soil moisture was less than chilli soil moisture in the 0–10 cm, 10–20 cm and 20–40 cm soil horizons under aeolian sand treatments (FL, FH and FA).

3.1.2 Effect of application of desulphurized gypsum and aeolian sand to different crops on soil conductivity

The effect of growing two crops, cotton and chilli pepper, under different amounts of FGD gypsum and aeolian sand on soil conductivity at 0–40 cm soil layer is shown in Figure 3. It can be seen from the figure that soil conductivity of cotton-soil at 0–10 cm soil layer increased by 5.98% in comparison to that of chilli under CK treatment. At 10–20 cm and 20–40 cm soil layers cotton soil conductivity decreased by 6.4% and 20.83% than chilli, respectively. Under LH and LA treatments, cotton soil conductivity increased by 42.88%–47.55%, 49.21%–65.52%, and 3.37%–6.36% in 0–10 cm, 10–20 cm and 20–40 cm soil layers, respectively, compared to chilli. Under FL treatment, soil conductivity varied from 16.34% to 18.15% in cotton and 19.64%–20.5% in chilli. In 0–10 cm soil layer chilli soil conductivity was reduced by 51.96% compared to cotton. In 10–20 cm and 20–40 cm soil layers cotton soil conductivity was reduced by 37.64% and 6.86% than chilli, respectively. Similarly, under FH and FA treatments, soil conductivity of cotton increased by 24.44%–45.54% and 10.78%–34.31% in 0–10 cm, 10–20 cm and 20–40 cm soil layers, respectively, compared to that of chilli.

In summary, the soil conductivity gradually increased with the increase of FGD gypsum application, and the soil conductivity gradually decreased with the increase of sand application. It showed that the aeolian sand treatment had a salt-reducing effect, among which the aeolian sand 30 t/ha (FA) treatment had the best salt-reducing effect. In the 0–10 cm, 10–20 cm and 20–40 cm soil layers, the soil conductivity of cotton field was greater than that of chilli pepper in LH, LA, FH and FA treatments.

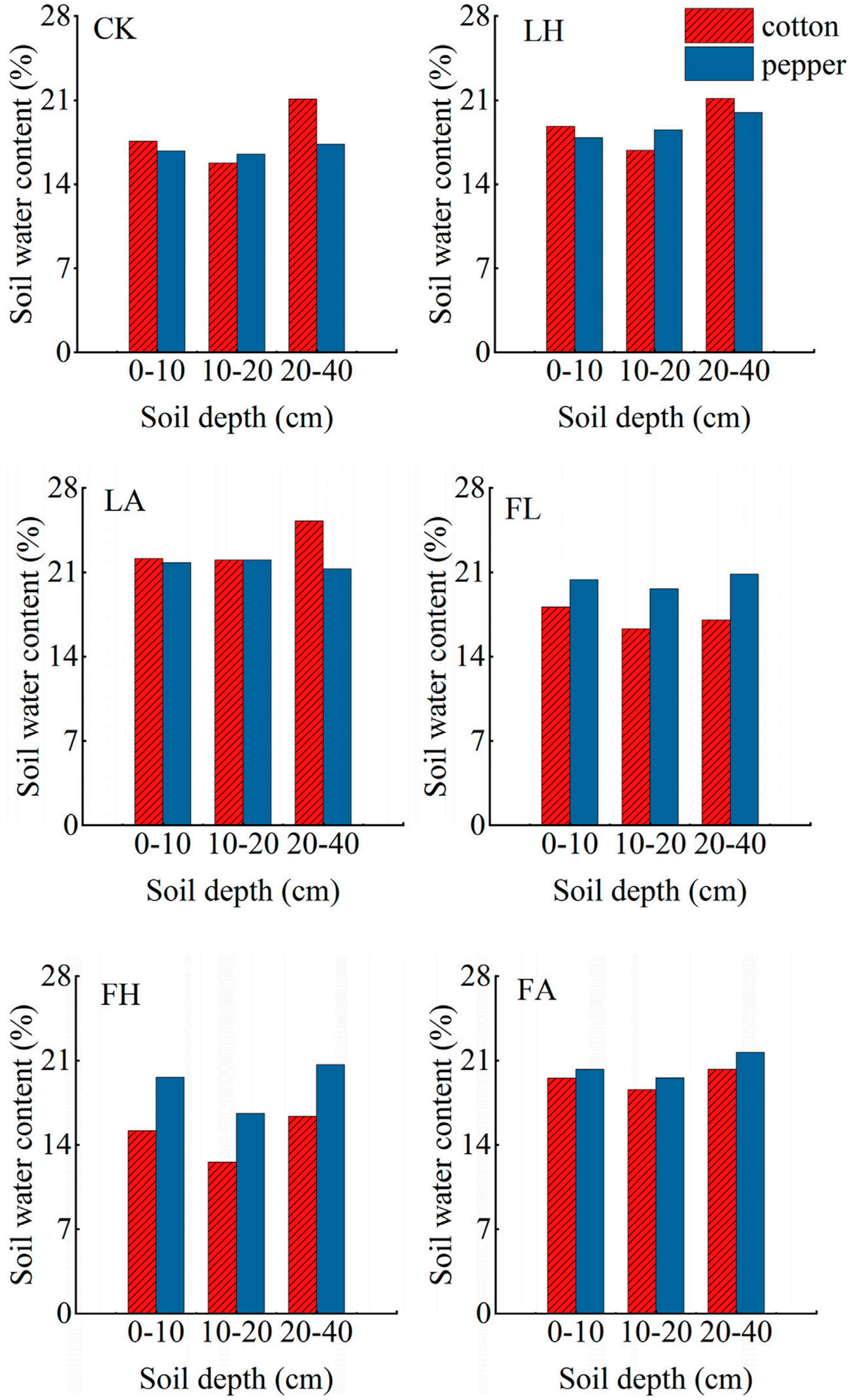

FIGURE 2
Soil moisture in different soil layers of two crops.

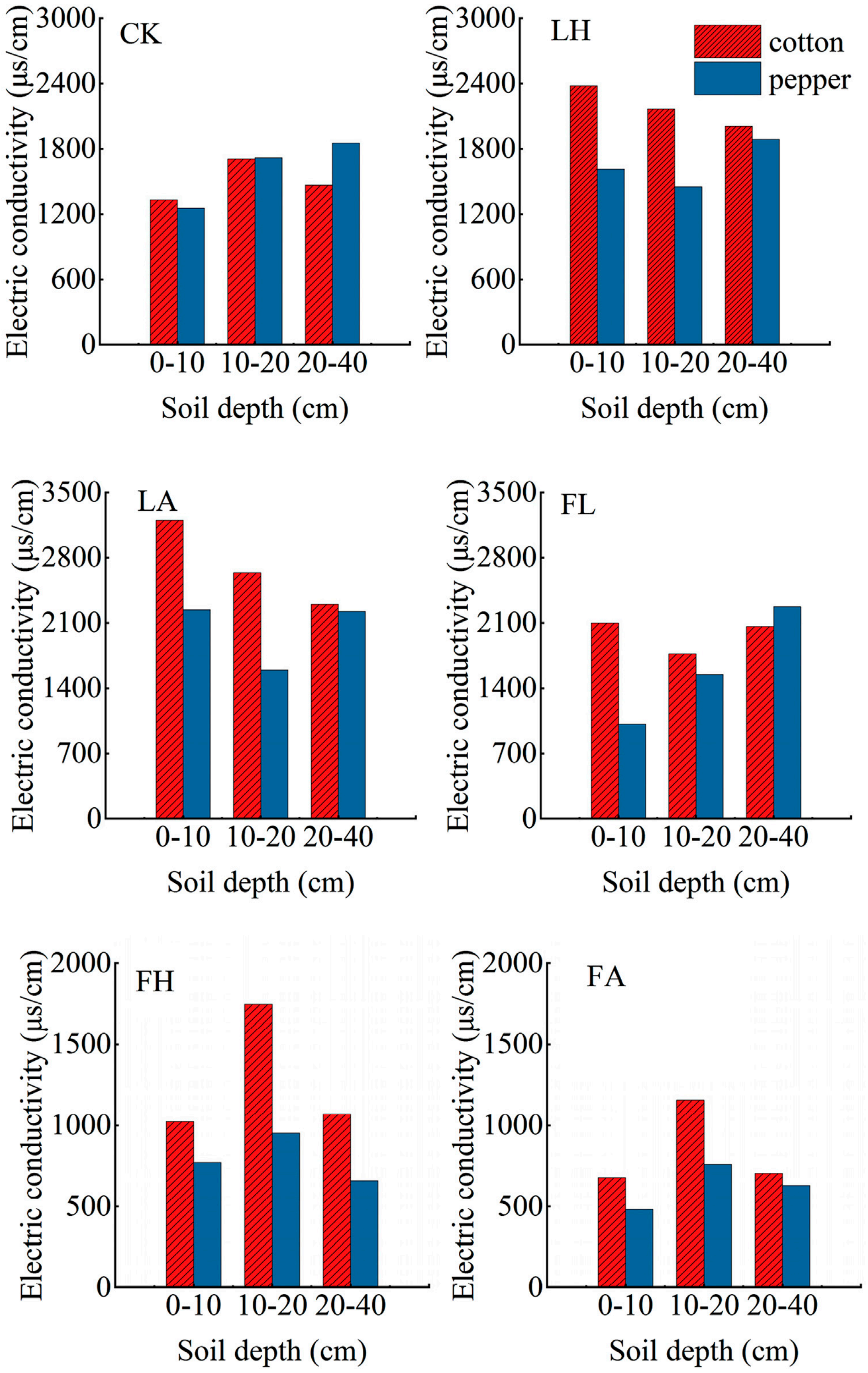

FIGURE 3
Soil conductivity of two crops in different soil layers.

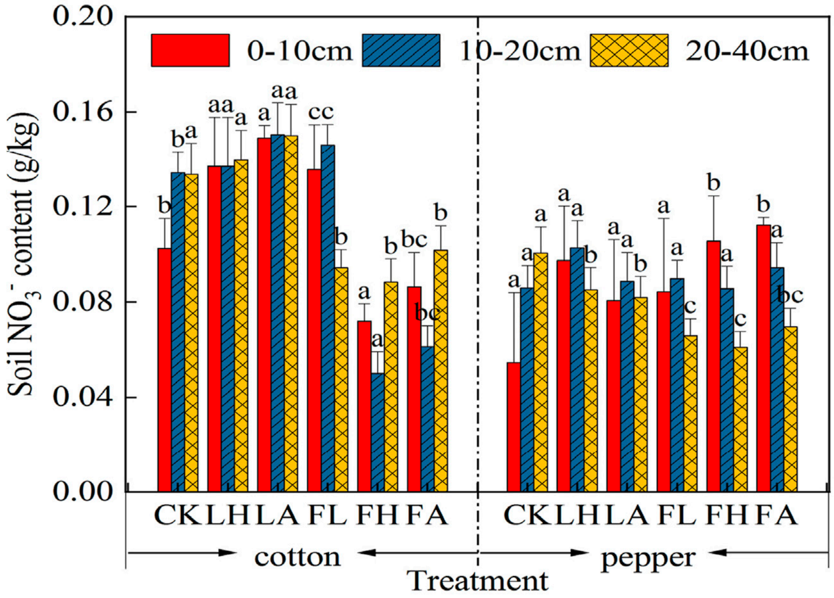

FIGURE 4
Soil nitrate nitrogen content in different soil layers of two crops.

3.1.3 Effect of application of desulphurized gypsum and aeolian sand on soil nitrate nitrogen in different crops

Soil is an important source of nutrients for plants, and nitrate nitrogen and ammonium nitrogen are the two inorganic forms of nitrogen in soil that are easily absorbed and utilized by plants (Liu et al., 2023; Tong et al., 2024). The effect of planting two crops, cotton and chilli pepper, under different amounts of FGD gypsum and sand, on soil nitrate nitrogen at 0–40 cm is shown in Figure 4. After different amounts of FGD gypsum and sand were applied to the soil, the nitrate nitrogen content of the soil under each treatment of cotton was significantly different at 0–10, 10–20 and 20–40 cm. Compared with the CK treatment, the nitrate nitrogen content in the 0–10 cm soil layer was increased in the LH, LA and FL treatments, with growth rates of 33.79%, 45.51%, 32.49%, respectively. The soil nitrate nitrogen content in the 10–20 cm soil layer showed an increasing trend with the increase in the amount of FGD gypsum and sand application, and the nitrate nitrogen content in the LH, LA and FL treatments was increased, with growth rates of 2.01%, 11.94% and 8.71%, respectively. At 20–40 cm, LA and LH treatments increased nitrate nitrogen content with growth rates of 4.54% and 12.28%.

There were significant differences in soil nitrate nitrogen content at 0–10, 10–20 and 20–40 cm under each treatment of chilli. Compared with the CK treatment, the nitrate nitrogen content at 0–10 cm and 10–20 cm soil layer showed an increasing trend with the decrease of FGD gypsum dosage and the increase of aeolian sand dosage, with the growth rate of 47.74%–93.22% and 0.35%–19.7%, respectively. At 20–40 cm, soil nitrate-nitrogen content showed an increasing trend with the decrease of FGD gypsum use and the increase of aeolian sand use, and the nitrate-nitrogen content of all treatments decreased compared with that of CK, with the rates of decrease of 15.37%, 18.65%, 34.49%, 39.26% and 30.75%, respectively.

3.1.4 Effect of application of desulphurized gypsum and aeolian sand on soil ammonium nitrogen in different crops

The effects of growing cotton and chilli crops with different amounts of FGD gypsum and sand were shown in Figure 5. Soil ammonium nitrogen content in the 0–40 cm soil layer was significantly different in the 0–10, 10–20, 20–40 and 40–60 cm soil layers in cotton treatments with different amounts of FGD gypsum and sand applied to the soil. The ammonium nitrogen content was reduced at 0–10 cm, 10–20 cm and 20–40 cm soil layers by 2.08%–30.5%, 6.94%–32.75% and 4.24%–37.31%, respectively, as compared to the CK treatment.

Soil ammonium nitrogen content of chilli peppers decreased with the increase of FGD gypsum and aeolian sand application in 0–10 cm soil layer, and showed an increasing trend with the increase of FGD gypsum and aeolian sand application at 10–20 cm and 20–40 cm soil layer. Compared with the CK treatment, all treatments increased the ammonium nitrogen content at 10–20 cm and 20–40 cm, with growth rates ranging from 11.65% to 20.03%, 4.2% to 22.17%, respectively.

3.2 Impact of FGD gypsum and aeolian sand application on soil GHG emissions for different crops

3.2.1 Effect of application of desulphurized gypsum and aeolian sand on CO_2 emission fluxes from cotton-pepper soils

Soil CO_2 emission is the process by which soil emits CO_2 due to metabolism, of which plant root respiration and soil microbial respiration are the most important components (Shi et al., 2010). The poor physicochemical properties of alkaline soils lead to a clayey texture and low water infiltration coefficient (Yin, 2011). Therefore,

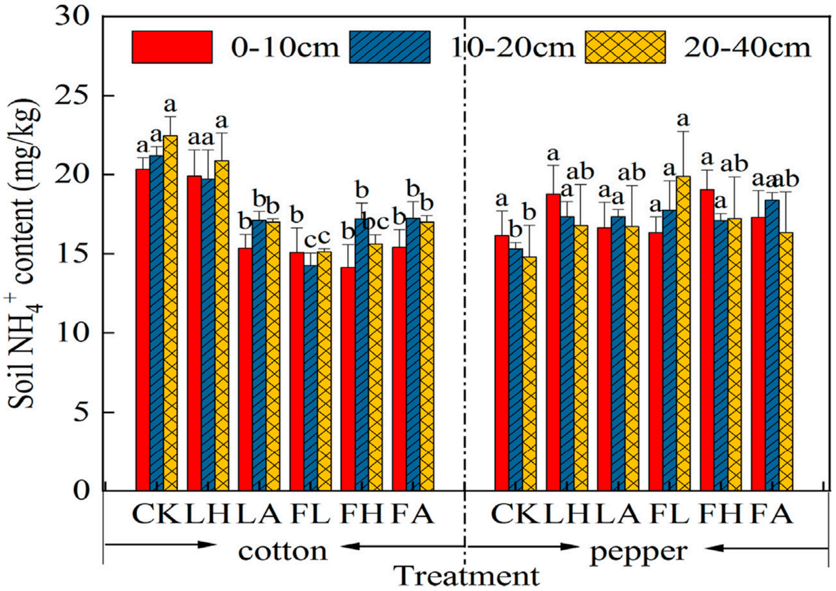

FIGURE 5
Soil ammonium nitrogen content in different soil layers of two crops.

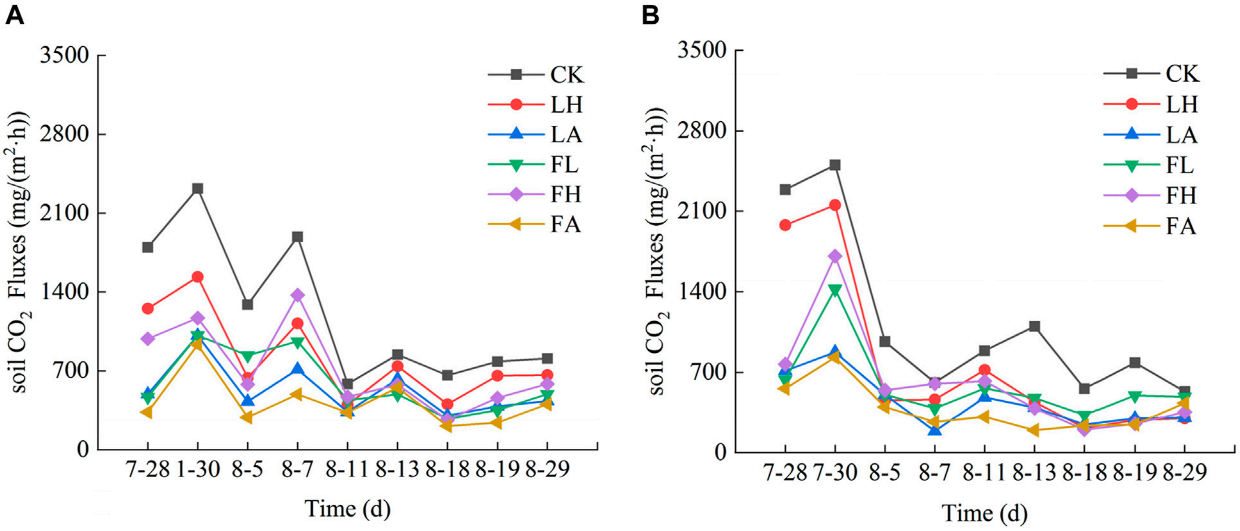

FIGURE 6
(A) Changes in soil CO_2 emission fluxes of cotton under different treatments (Note: a is soil CO_2 emission flux from cotton fields). **(B)** Changes in soil CO_2 emission fluxes of pepper under different treatments (Note: b is soil CO_2 emission flux from chilli peppers).

the application of different amendments to the soil had a positive effect on improving the soil structure and soil environment, which in turn altered the microbial activity in the soil and the physiological activity of the crop root system, thereby affecting the CO_2 emission fluxes. The effects of different application rates of FGD gypsum and aeolian sand on CO_2 emission fluxes of cotton-pepper soil are shown in Figures 6A, B. The soil CO_2 emission fluxes of the two crops showed similar trends, with peaks on the first day after irrigation and fertilizer application, followed by a gradual decline. The average daily soil CO_2 emission fluxes of LH, LA, FL, FH and FA treatments in cotton field ranged from 211.23 to 2319.79 mg/(m^2 h), and the average daily CO_2 emission fluxes of the treatments were reduced by 32.49%, 56.93%, 51.47%, 41.14%, and 65.55%, respectively, when compared with that of control CK. The average daily CO_2 emission fluxes of soil in chilli LH, LA, FL, FH and FA treatments ranged from 186.95 to 2499.71 mg/(m^2 h), respectively, and were reduced by 31.47%, 60.83%, 48.10%, 46.80%, and 66.01%, respectively, compared with the control CK.

This shows that both cotton and chilli crops significantly suppressed CO_2 emissions in all treatments under different

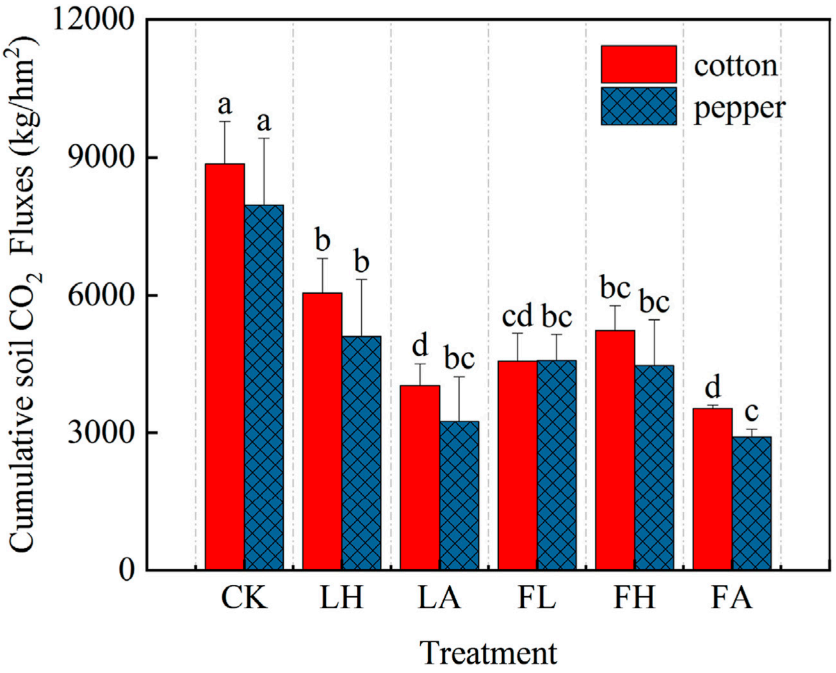

FIGURE 7
Changes in soil CO_2 emission fluxes of pepper under different treatments (Note: b is soil CO_2 emission flux from chilli peppers).

application rates of FGD and sand, indicating that both FGD and sand amendments have the property of suppressing CO_2 emissions, and soil CO_2 emission fluxes decreased with the increase of FGD and sand applications, and the overall performances of soil CO_2 emission fluxes in all treatments of cotton-chilli were all The overall performance of soil CO_2 emission fluxes of cotton field-pepper treatments was CK > LH > FH > FL > LA > FA in order.

3.2.2 Effect of application of desulphurized gypsum and aeolian sand on cumulative emission fluxes of CO_2 from cotton-pepper soils

Cumulative soil CO_2 emission fluxes were calculated for cotton-pepper at fertility stage. The following results were obtained from Figure 7. The cumulative CO_2 emission fluxes of the cotton treatments ranged from 3528.21 to 8861.06 kg/ha. Compared with the CK treatment, the LH, LA, FL, FH and FA treatments decreased by 31.69%, 54.58%, 48.56%, 41.08% and 60.18%, respectively. The cumulative CO_2 emission fluxes of chilli peppers ranged from 2909.63 to 7960.34 kg/ha. It was reduced by 36.02%, 59.2%, 42.56%, 44%, and 63.45% in LH, LA, FL, FH, and FA treatments, respectively, compared to CK treatment.

Comparison of cumulative CO_2 emission fluxes of cotton and pepper among different treatments showed that the cumulative soil emission fluxes of cotton and pepper were CK > LH > FH > FL > LA > FA, and the cumulative soil CO_2 emission fluxes of all treatments in cotton field were higher than those of pepper. Under the conditions of different amounts of FGD gypsum and sand accumulation, the cumulative soil CO_2 emission fluxes of chilli treatments were 10.16%, 15.87%, 19.31%, −0.32%, 14.61% and 17.53% lower than those of cotton field, respectively.

In summary, the cumulative soil CO_2 emission fluxes of the two crops, cotton and chilli pepper, gradually decreased with the increase of FGD gypsum and fenugreek application, which was mainly due to the fact that FGD gypsum and fenugreek were rich in trace elements and ions that inhibited the microbial activity of the soil, and affected the composition and content of organic matter in the soil, thus affecting the respiration of soil microorganisms and the decomposition of organic matter by soil microorganisms to reduce soil CO_2 emission. By improving the physical and chemical properties of the soil and activating the soil nutrients or affecting the ratio of soil carbon and nitrogen, the composition and content of organic matter in the soil directly or indirectly affects the respiration of soil microorganisms and the decomposition of organic matter by soil microorganisms to reduce the emission of soil CO_2.

3.2.3 Effect of application of desulphurized gypsum and aeolian sand on N_2O emissions from cotton-pepper soils

Soil N_2O is produced by nitrification and denitrification processes under aerobic and anaerobic conditions, and this process is closely related to crop root growth. The effects of different application rates of FGD gypsum and windblown sand on N_2O emission fluxes from cotton-pepper soils are shown in Figures 8A, B. Soil N_2O emission fluxes from the two crops followed similar trends, with peaks usually occurring on the first day after irrigation and fertilizer application, followed by a gradual decline thereafter. The average daily soil N_2O emission fluxes of LH, LA, FL, FH and FA treatments in cotton field ranged from 0.0249 to 0.1980 mg/(m^2·h), respectively, and the overall performance of soil N_2O emission fluxes of the treatments was CK > LH > LA >

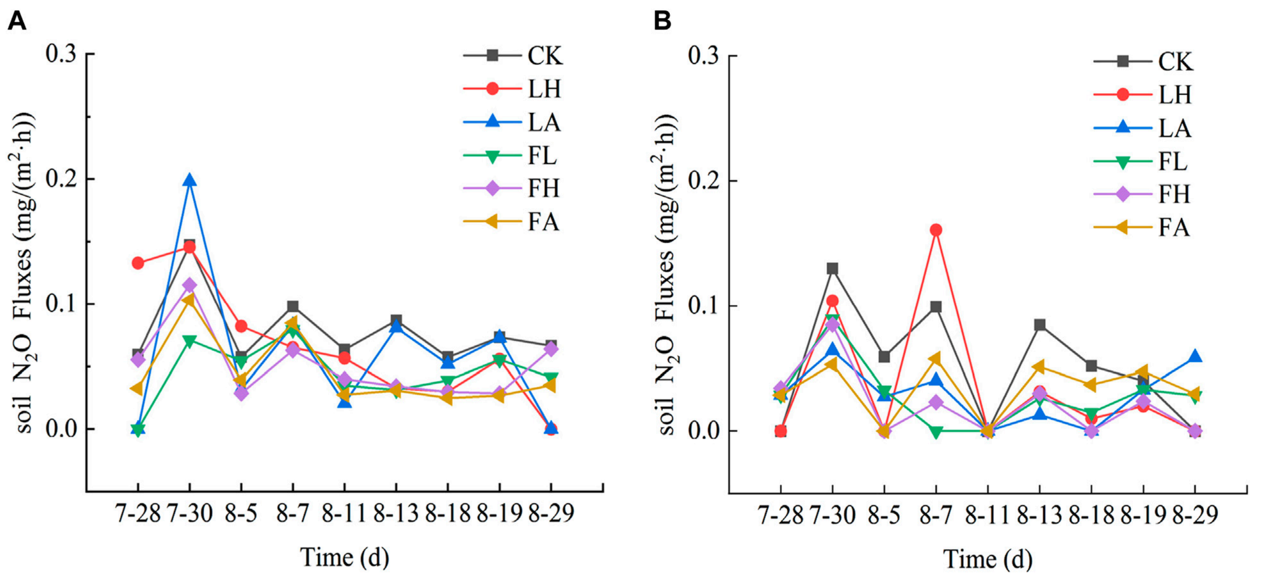

FIGURE 8
(A) Changes in soil N_2O emission fluxes of cotton under different treatments (Note: a is soil N_2O emission flux from cotton fields). **(B)** Changes in soil N_2O emission fluxes of pepper under different treatments (Note: b is soil N_2O emission flux from chilli peppers).

FH > FL > FA in the order of CK > LH > LA > FH > FL > FA. Compared with the control CK, the average daily N_2O emission fluxes of the treatments were reduced by 15.34%, 24.05%, 42.68%, 35.40%, and 42.94%, respectively. The average daily soil N_2O emission fluxes of pepper LH, LA, FL, FH and FA treatments ranged from 0.024 to 0.13 mg/(m^2 h), respectively, and the overall performance of soil N_2O emission fluxes of the treatments were in the order of CK > LH > FA > LA > FL > FH. Compared with the control CK, the average daily N_2O emission fluxes of the treatments were reduced by 29.84%, 42.98%, 45.5%, 57.79%, and 34.49%, respectively. This shows that both cotton and chilli crops significantly suppressed N_2O emissions in all treatments under different application rates of FGD gypsum and aeolian sand, suggesting that both amendments, FGD gypsum and aeolian sand, have the property of suppressing N_2O gas emissions, and that the flux of soil N_2O emissions decreases with an increase in the application rate of FGD gypsum and aeolian sand.

3.2.4 Effect of application of desulphurized gypsum and aeolian sand on cumulative emission fluxes of N_2O from cotton-pepper soils

Calculation of cumulative soil N_2O emission fluxes in cotton-pepper at fertility stage. The following results were obtained from Figure 9, the cumulative N_2O emission fluxes of the treatments in the cotton field ranged from 0.3467 to 0.6179 kg/ha. Compared with the CK treatment, the LH, LA, FL, FH and FA treatments showed a reduction of 25.42%, 19.61%, 38.5%, 36.88% and 43.89%, respectively. Therefore, the cumulative soil emission fluxes of the different amendments were as follows: CK > LA > LH > FH > FL > FA.The cumulative N_2O emission fluxes of chilli pepper treatments were in the range of 0.1633–0.4144 kg/ha. Compared with the CK treatment, the LH, LA, FL, FH, and FA treatments decreased by 33.47%, 39.96%, 43.39%, 60.59%, and 35.55%. Therefore, the cumulative soil emission fluxes of different amelioration measures were shown as CK > FA > LH > LA > FL > FH. Comparison of the cumulative emission fluxes of N_2O from cotton and chilli among different treatments showed that the cumulative emission fluxes of soil N_2O from all treatments in cotton field were higher than those from all treatments in chilli. Under the conditions of applying different amounts of desulfurization gypsum and aeolian sand, the cumulative soil CO_2 emission fluxes of pepper treatments were 32.93%, 40.17%, 49.91%, 38.26%, 58.13% and 22.96% lower than those of cotton fields, respectively.

In summary, the cumulative soil N_2O emission fluxes of both crops, cotton and chilli pepper, decreased gradually with the increase of FGD gypsum and sand application, and the cumulative soil N_2O emission fluxes of all treatments in the cotton field were higher than those of all treatments in the chilli field, and the effects of the different amelioration measures on the cumulative soil N_2O emission fluxes were significant.

3.3 Analysis of factors affecting greenhouse gas emission fluxes from FGD gypsum application and aeolian sand cotton-pepper soils

The correlation coefficients of CO_2 and N_2O cumulative emission fluxes and soil physicochemical properties of cotton-pepper soils under different treatments are shown in Table 2. Cotton field soil CO_2 cumulative emission fluxes were significantly negatively correlated with 0–10 cm and 10–20 cm soil moisture, 0–10 cm and 20–40 cm electrical conductivity. Cotton field soil N_2O cumulative emission flux was significantly positively correlated with 0–10 cm, 10–20 cm

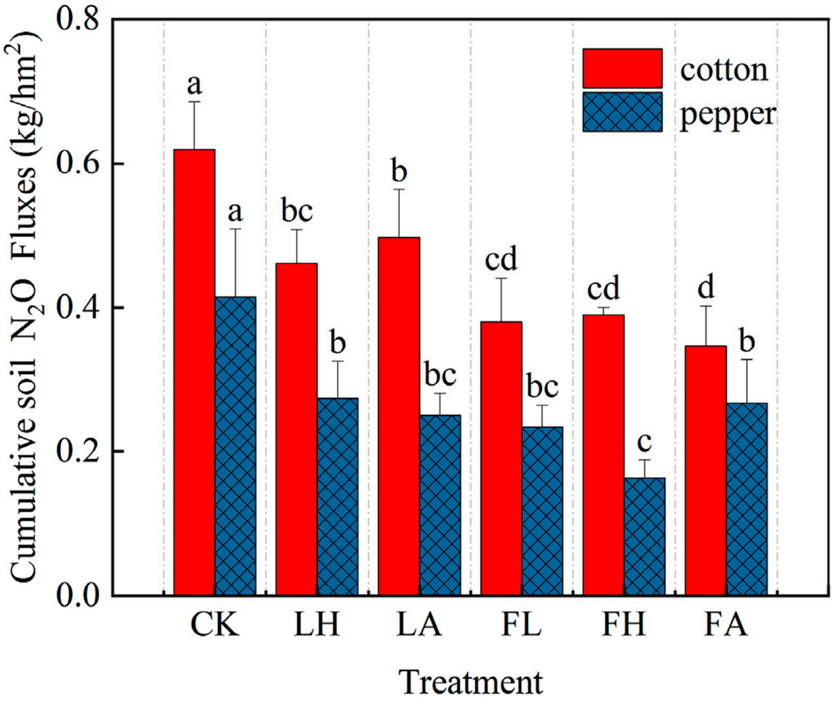

FIGURE 9
Changes in cumulative emission fluxes of N_2O from cotton field and pepper soil under different treatments.

and 20–40 cm soil moisture, soil nitrate nitrogen and ammonium nitrogen, and 0–10 cm and 10–20 cm soil conductivity. The cumulative CO_2 emission flux of chilli soil was significantly negatively correlated with soil moisture, and positively correlated with soil ammonium nitrogen. Cumulative N_2O emission flux of chilli soil was significantly negatively correlated with soil moisture, soil nitrate nitrogen and soil conductivity.

3.4 Effect of FGD gypsum and aeolian sand application on the combined greenhouse effect of cotton-pepper soils

The net warming potential and GHG emission intensity of cotton fields with different application rates of FGD gypsum and aeolian sand are shown in Table 3, and the combined warming potential (GWP) of the treatments at the centennial scale is positive, indicating a warming effect. On this basis, the data in Table 3 were evaluated, and the GWP of cotton field LH, LA, FL, FH and FA treatments varied from 3631.53 to 9045.19 kg/ha; compared with the control CK treatment, the treatments applying the improvement measures all reduced the GWP of the cotton field, with a reduction of 31.56%, 53.87%, 48.35%, 41% and 59.85%, respectively. The different treatments GWP in descending order were CK > LH > FH > FL > LA > FA. Carbon dioxide was the main contributor to the integrated warming potential of cotton fields, and its contribution to GWP ranged from 96% to 98%, while the variation of N_2O's contribution to GWP ranged from 0.0068% to 0.0119%. The GWP of chilli LH, LA, FL, FH and FA treatments varied from 2989.23 to 8083.83 kg/ha; all the treatments applying the improvement measures reduced the GWP of the cotton field by 35.98%, 58.91%, 42.57%, 44.25% and 63.02%, respectively, compared to the control CK treatment. The GWP of different treatments in descending order was CK > LH > FL > FH >> LA > FA. Carbon dioxide was the main contributor to the integrated warming potential of cotton fields, and its contribution to GWP ranged from 97% to 99%, while the variation of N_2O's contribution to GWP ranged from 0.0036% to 0.0089%.

4 Discussion

As the most active component of the carbon and nitrogen cycle in terrestrial ecosystems, greenhouse gas emissions from agricultural soils will certainly have a large impact on the carbon and nitrogen cycle at the regional and global scales (Yan, 2023). There are many factors affecting the emission of greenhouse gases from soils, and soil moisture, as one of the main factors affecting CO_2 emission from soils, mainly affects the production and emission of greenhouse gases by influencing the physicochemical properties of soils, permeability, microbial activity and the rate of greenhouse gases diffusion from soils to the atmosphere (Li et al., 2007). In this experiment, the correlation of soil moisture on CO_2 and N_2O emissions from farmland showed that soil CO_2 emission fluxes were significantly negatively correlated with soil moisture and soil N_2O emissions were significantly positively correlated with soil moisture under

TABLE 2 Correlation between cumulative soil CO_2 and N_2O emission fluxes and soil physicochemical properties under different crops.

Soil indicators		Soil depth/(cm)	Cumulative CO_2 emission flux	Cumulative emission flux of N_2O
Cotton	Soil moisture	0–10	−0.517*	0.595*
		10–20	−0.562*	0.567*
		20–40	−0.330	0.735**
	Conductivity	0–10	−0.585*	0.754**
		10–20	−0.373	0.826**
		20–40	−0.650*	0.399
	NH_4^+	0–10	0.381	0.530*
		10–20	0.316	0.514*
		20–40	0.396	0.484
	NO_3^-	0–10	0.302	0.696**
		10–20	0.393	0.680**
		20–40	0.066	0.744**
Chilli pepper	Soil moisture	0–10	−0.675*	0.323
		10–20	−0.570*	0.614*
		20–40	−0.422	0.268
	Conductivity	0–10	−0.520	0.653*
		10–20	−0.299	0.517
		20–40	−0.447	0.704*
	NH_4^+	0–10	0.547*	−0.585
		10–20	0.043	−0.109
		20–40	0.550*	−0.432
	NO_3^-	0–10	−0.287	0.159
		10–20	−0.110	0.838**
		20–40	−0.178	0.795**

Note: * Significant at the 0.05 level (two-tailed); significant at the 0.01 level (two-tailed).

the two crop cropping modes of cotton-chilli, so soil moisture was a significant factor influencing CO_2 and N_2O emission fluxes in this experiment. In addition to soil moisture, conductivity, nitrate nitrogen, ammonium nitrogen, and changes in soil structure by different amendment measures affected GHG emissions. In this experiment, the treatments suppressed greenhouse gas emissions to varying degrees under the conditions of applying different amounts of FGD gypsum and aeolian sand, as opposed to no amendment measures. The cumulative soil CO_2 emissions of cotton and pepper crops showed a decreasing trend with the increase of the amount of desulphurized gypsum and aeolian sand, which was because the application of desulphurized gypsum increased the soil Ca^{2+} content, and a large amount of Ca^{2+} reacted with the CO_2 produced by soil respiration to generate calcium carbonate precipitation, thereby reducing the soil CO_2 emissions (He et al., 2017). Researches from Li (2023) and Xu et al. (2023) also showed that the larger the FGD gypsum addition, the more obvious the CO_2 reduction effect, which is consistent with the results of this study.

Nitrification and denitrification are processes required for the conversion of N_2O (Sun, 2022). Nitrification is the conversion of ammonium to nitrate and partially to N_2O by microorganisms in the soil under soil aeration conditions. Among the main factors affecting soil GHG emissions, conductivity is one of the main factors. In this experiment, the cumulative emission fluxes of N_2O were significantly and positively correlated with the conductivity, indicating that, with the increase of the conductivity, the cumulative emission fluxes of N_2O increased with the increase of the conductivity. However, there is a critical value between salinity and N_2O cumulative emission flux, and Zeng (2015) showed that in alkaline soil, salinity in the range of 5.52 ds/m would inhibit the nitrification reaction rate. The upper limit of soil conductivity in this experiment was 2,989 μs/cm, and with the increase of FGD gypsum application and the decrease of windblown sand application, the cumulative N_2O emission

TABLE 3 Comprehensive greenhouse effect of soil CO_2 and N_2O under different treatments.

Treatment		Cumulative emission/ (kg/ha)		Integrated greenhouse effect (GWP)	Contribution to GWP/(%)	
		CO_2	N_2O	/(kg/ha)	CO_2	N_2O
Cotton	CK	8861.06^a	0.6179^a	9045.19	98	0.0068
	LH	6053.2^b	0.4608^{bc}	6190.52	98	0.0074
	LA	4024.44^d	0.4967^b	4172.46	96	0.0119
	FL	4558.34^{cd}	0.3800^{cd}	4671.58	98	0.0081
	FH	5220.84^{bc}	0.3900^{cd}	5337.06	98	0.0071
	FA	3528.21^d	0.3467^d	3631.53	97	0.0096
Chilli pepper	CK	7960.34^a	0.4144^a	8083.83	98	0.0051
	LH	5092.84^b	0.2757^b	5174.00	98	0.0053
	LA	3247.47^{bc}	0.2488^{bc}	3321.61	98	0.0075
	FL	4572.79^{bc}	0.2346^{bc}	4642.70	99	0.0051
	FH	4458.04^{bc}	0.1633^c	4506.70	99	0.0036
	FA	2909.63^c	0.2671^b	2989.23	97	0.0089

Note: lowercase letters indicate that there are significant differences in soil CO_2 and N_2O emissions under different improvement measures ($P < 0.05$).

gradually increased,but would be lower than the control treatment CK, which was in agreement with the above results, and also in agreement with the experimental results of Wang (2020); Dou (2020), and Ceng (2015) that the addition of FGD gypsum had an inhibitory effect on the emission fluxes of N_2O, but in agreement with the Zhang (2023) test results in soda alkali soils in Northeast China: the application of FGD gypsum significantly reduces CH_4 and CO_2 emission fluxes and increases N_2O emissions. The reason for the increase in soil conductivity is due to the increase in the amount of FGD gypsum applied, which is a salt as a by-product, and the newly generated salt ions are not completely eliminated due to environmental factors or insufficient irrigation water, thus leading to an increase in soil conductivity (Xu, 2023). At the same time, the level of nitrate and ammonium nitrogen in the soil, as inorganic nitrogen, can reflect the nitrogen supply of the soil (Liu et al., 2001). The addition of FGD gypsum and aeolian sand to the soil produces corresponding changes in the physical structure of the soil, and with the increase in the amount of FGD gypsum and WDS applied, the soil bulk density decreases and the porosity increases, which is conducive to the absorption of nitrogen. In this experiment, with the increase of FGD gypsum application, NH_4^+ gradually decreased and NO_3^- gradually increased in cotton field soil, indicating that soil microorganisms converted ammonium salts into nitrates and promoted the aeolian nitrification process, whereas chilli pepper crop promoted the nitrification process in the aeolian sand treatment; with the increase of aeolian sand application, NH_4^+ gradually increased and NO_3^- gradually decreased in cotton field soil, indicating that the aeolian sand treatment inhibited the nitrification process of ammonia and oxygen in the aeolian sand treatment, Nitrification process was inhibited and nitrogen uptake was promoted. The correlation between NH_4^+, NO_3^- and N_2O emissions showed that after the application of different improvement measures, the ammonium nitrogen content of cotton soil gradually increased and the nitrate nitrogen content of soil gradually decreased with the increase of the application of aeolian sand; and with the increase of FGD gypsum dosage, the ammonium nitrogen content of chilli soil gradually increased and the nitrate nitrogen content of soil gradually decreased, and the overall presentation of the cumulative emissions of soil N_2O. It was significantly positively correlated with conductivity and nitrate nitrogen, and significantly negatively correlated with ammonium nitrogen, and the results of the study were similar to those of Sun (2014).

5 Conclusion

1) During the monitoring period, cotton and pepper were planted. Compared with CK, LA had the best water retention effect and FA had the best water retention and salt reduction effect. 2) Compared with CK, FA treatment significantly inhibited soil cumulative greenhouse gas emission fluxes, and reduced the comprehensive greenhouse effect of cotton fields and pepper crops by inhibiting soil CO_2 emission fluxes. 3) Through comprehensive analysis, it is reasonable to apply FA treatment to saline-alkali soil, which can better achieve the effect of water preservation, salt reduction and emission reduction.

Data availability statement

The raw data supporting the conclusions of this article will be made available by the authors, without undue reservation.

Author contributions

YC: Conceptualization, Data curation, Formal Analysis, Investigation, Methodology, Project administration, Software, Writing–original draft, Writing–review and editing. FL: Writing–original draft, Writing–review and editing. YG: Writing–original draft, Writing–review and editing. XH: Writing–original draft, Writing–review and editing. JW: Writing–original draft, Writing–review and editing. DF: Writing–original draft, Writing–review and editing. RG: Writing–original draft, Writing–review and editing.

Funding

The author(s) declare that financial support was received for the research, authorship, and/or publication of this article. XPCC Southern Xinjiang Key Industries Innovation and Development Support Project (2021DB017); Joint Foundation of Tarim University, Agricultural University of China (2019TC157).

Acknowledgments

We are thankful to Weixiong Huang (orcid.org/0000-0002-1704-5550) for his help in English editing for the paper.

Conflict of interest

The authors declare that the research was conducted in the absence of any commercial or financial relationships that could be construed as a potential conflict of interest.

Publisher's note

References

Ceng, D. P. (2015). *The effect of exotic matters amendments on greenhouse gases emmision in Fuzhou paddy fields*. Master. Fujian Normal University. Available at: https://kns.cnki.net/kcms2/article/abstract?v=29axctaKF3wx0ojCaNf3spZnt4o-0tu5PGWrmEOUiXcrXFYK4YF1L2v3XYEPkVAuUcUnNQgV6UPQs8vw66_j1jYG9afRqEHHI21THD0Hglk1T12iMgOX0flPPNdcycSobYnObqW5N73RgPBvL_Vb1g==&uniplatform=NZKPT&language=CHS.

Chen, X. L. (2023). Effects of biochar on water and solute migration in coastal saline-alkali soil Master's Degree. *Zhejiang Univ. Sci. Technol.* doi:10.27840/d.cnki.gzjkj.2023.000064

Dou, Y. Y. (2020). *Effects of mixed application of desulfurized gypsum and biochar on N_2O emissions from paddy fields*. Master. Southwest University. doi:10.27684/d.cnki.gxndx.2020.004601

Guo, Y. F., Zhang, L. P., Wang, G. S., Shang, R. C., Zhang, H., Zhu, Z. H., et al. (2022). Effects of the tillage and combination of water and fertilizer on the greenhouse gas emissions of wheat-maize field. *Chin. J. Agric. Eng.* (13), 95–104.

He, K., Li, X. P., Zhou, C. L., Zhou, J., Dong, L. L., and Mao, Y. M. (2017). Influence of flue gas desulfurization gypsum on speciation of phosphorus in coastal cultivated soils. *Acta Ecol. Sin.* 37 (09), 2935–2942. doi:10.5846/stxb201601170111

Huang, J. Y., Yu, H. L., Zhang, J. H., Sun, Z. J., and He, W. S. (2011). Effects of flue gas desulfurization gypsum and krilium application on alkali soil amelioration. *Soil Bull.* (6), 1467–1471. doi:10.19336/j.cnki.trtb.2011.06.034

Jiang, Z. B., Ning, S. R., and Wang, Q. J. (2023). A comprehensive evaluation of the effect of desulfurized gypsum for improving saline-alkali soil. *J. Soil*, 1–18. Available at: http://kns.cnki.net/kcms/detail/32.1119.p.20231023.1618.004.html.

Kiehl, J. T., and Trenberth, K. E. (1997). Earth's annual global mean energy budget. *Bull. Amer. Meteor. Soc.* 78 (2), 197–208. doi:10.1175/1520-0477(1997)078<0197:EAGMEB>2.0.CO;2

Li, H. F., Xia, H. P., Xiong, Y. M., and Zhang, X. F. (2007). Mechanism of greenhouse gases fluxes from soil and its controlling factors: a review. *Ecol. Environ.* (6), 1781–1788. doi:10.16258/j.cnki.1674-5906.2007.06.027

Li, H. W. (2023). Effects of desulfurization gypsum and wind-bound sand in improving soil and controling CO_2 emission in saline cotton field. *Master. Tarim. Univ.* doi:10.27708/d.cnki.gtlmd.2023.000156

Li, J. G., Pu, L. J., Han, M. F., Zhu, M., Zhang, R. S., and Xiang, Y. Z. (2014). Soil salinization research in China: advances and prospects. *J. Geogr. Engl.* 24 (5), 943–960. doi:10.1007/s11442-014-1130-2

Liu, C. L., Zhou, Z. D., Wang, H. K., and Xue, J. H. (2023). Effects of microplastics on soil physicochemical properties and functional microorganisms related to nitrogen cycling. *J. Environ. Sci.* (08), 396–406. doi:10.13671/j.hjkxxb.2023.0029

Liu, X. H., Hao, M. D., and Tian, M. X. (2001). Contribution of soil mineral nitrogen and soil mineralization nitrogen to seasonal crop. *Soil Environ.* (03), 207–209.

Shao, X. H., Tang, S. R., Meng, L., Wu, Y. Z., Li, J. Q., and Gou, G. L. (2022). Effect of different fertilization treatments on methane and nitrous oxide emissions from rice-vegetable rotation in a tropical region, China. *Environ. Sci.* 43 (11), 5149–5158. doi:10.13227/j.hjkx.202112213

Shi, X. H., Zhang, X. P., Liang, A. Z., Shen, Y., Fan, R. Q., and Yang, X. M. (2010). Advance in the main factors controlling soil carbon dioxide flux. *Soil Bull.* (03), 761–768. doi:10.19336/j.cnki.trtb.2010.03.049

Sun, L. B. (2022). *Mechanism of microbially driven nitrous oxids production in agricultural soils of Northern China*. Master's Degree thesis. Jilin Jianzhu University. doi:10.27714/d.cnki.gjljs.2022.000208

Sun, X. (2014). Effect of salinity, pH、Nitrogen ferilizer on saline alkali soil N_2O emission. Master. *Inn. Mong. Norm. Univ.* Available at: https://kns.cnki.net/kcms2/article/abstract?v=29axctaKF3yPZJ6fXpnBM5Y0QsoikbwfCEQu6E85aLx-x9pF01oFTH244tRKf7MJLq-QdO77-nVZqfBVP9LucrpbwPs0rcyFpF_pKLQM0pAPzQuNEpzbp6AYrEyR57bwEAI8wTNph8QSnSo0b4swig==&uniplatform=NZKPT&language=CHS.

Tong, Y. S., Zhang, C. P., Dong, Q. M., Yu, Z. H., Yang, Z. Z., Zhang, X. F., et al. (2024). The effects of nitrogen forms on biomass allocation and leaf photosynthetic characteristics of dominant species in alpine artificial grassland plant communities. *Ecology*, 1–11. Available at: http://kns.cnki.net/kcms/detail/21.1148.q.20240318.1728.011.html.

Wang, F. (2020). *Response of greenhouse gases emissions and net greenhouse effect to nutrient management in purple soil*. PhD Dissertation. Southwest University. doi:10.27684/d.cnki.gxndx.2020.005571

Wang, X. Y., Cai, H. J., Li, L., Xu, J. T., and Chen, H. (2019). Effects of water deficit on greenhouse gas emission in wheat field in different periods. *Environ. Sci.* 40 (5), 2413–2425. doi:10.13227/j.hjkx.201808075

Wei, C. C., Ren, S. M., Xu, Z. A., Zhang, M. T., Wei, R., and Yang, P. L. (2021). Effects of irrigation water salinity and irrigation water amount on greenhouse gas emissions and spring maize growth. *Chin. J. Agric. Mach.* (07), 251–260+236.

Xiang, Q. J. (2018). *Effects of sulfur-containing industrial by-products on greenhouse gases emissions from yellow paddy fields*. Master's Degree. Southwest University. Available at: https://kns.cnki.net/kcms2/article/abstract?v=29axctaKF3xRz7GUAqqVaj4nrrTygH_iWFWfeM4u5SQuLow7knawWgbSXaCJbHcEvHsD0VjkdT5DsPwnJ9ZCRtKn_W3cTI8SkK1viJ85VVHzAaj3iCfMkSCAtkpmPPLgLHmC3u6dO-Hof5TR4p4y3w==&uniplatform=NZKPT&language=CHS.

Xu, X. (2023). *Improvement and safety evaluation of phosphogypsum-based soil amendment in mintigating soil salinity stress*. Master. Beijing University of Chemical Technology. doi:10.26939/d.cnki.gbhgu.2023.000492

Xu, Y., Luo, M. L., Mu, Z. J., Lei, Y., Shan, Q. L., Liu, S. P., et al. (2023). Effects of mixed application of biochar and desulfurized gypsum on carbon emission in paddy field. *J. Agric. Environ. Sci.* (11), 2614–2624.

Yan, Q. (2023). *Modelling greenhouse gas emissions of maize farmland under climate change using DayCent*. Master's thesis. Northwest A&F University. doi:10.27409/d.cnki.gxbnu.2023.002321

Yin, Q. R. (2011). *Effects of salinization on physical and hydrodynamics characteristics*. Master's Degree. Northwest A&F University. Available at: https://kns.cnki.net/kcms2/article/abstract?v=29axctaKF3yoV2gFkxMLtWTFxd8UfaIm7YIxkyQ6-iFbd-6pDdntx_2owJV5tbDg7mJYiLpNOaRLtCfnxK9yVliBHnVwRX1iiIViOsCuWYGNrRWLAaKiVi-LAKNSNCypUvJVcqjzbrqxuCy2-1US9w==&uniplatform=NZKPT&language=CHS.

Zeng, W. Z. (2015). *Research and simulation for the coupling effects of water, nitrogen, and salt on sunflower*. Ph.D. Dissertation. Wuhan University. Available at: https://kns.cnki.net/kcms2/article/abstract?v=29axctaKF3yqZIsUA2A3DEjJSLMpjHSpOiq9tevC46yHD2erdUIh9RL2Uk53nDVc5Y2fGjG_715tIYft7FYzoWrk_cpmao4ZCkRbWWDDmKZesf3848IRwIc27yJ-q4aeuG36jTlbPL63Yc7PNi_uhA==&uniplatform=NZKPT&language=CHS.

Zhang, F. M. (2023). *Study on the effects of different amendments on ammonia volatilization and greenhouse gas emissions from soda-saline rice paddy fields*. Master. Northeast Normal University. doi:10.27011/d.cnki.gdbsu.2023.001613

Zhang, G. B., Ma, J., Xu, H., and Yan, X. Y. (2023). *Status quo* of research and suggestions on reduction of non-CO_2 greenhouse gas emission from Chinese farmland. *Proc. Chin. Acad. Sci.* (03), 504–517. doi:10.16418/j.issn.1000-3045.20211112001

Zhang, Y. (2019). Research on the effects of Different Amendments and irrigation methods on Saline-alkali land Improvement and greenhouse gas emission. *Master's thesis. Inn. Mong. Agric. Univ.* doi:10.27229/d.cnki.gnmnu.2019.000327

Zhang, Y. H., Gao, P. L., Zhang, Q. W., Zhao, Y. D., and Yang, D. M. (2019). Effect of mixing sand with surface soil on moderately salinized soil water-salt transport and summer maize growth. *Chin. soil fertilizer* (02), 83–90.

Frontiers in Environmental Science

TYPE Original Research
PUBLISHED 06 November 2024
DOI 10.3389/fenvs.2024.1466691

OPEN ACCESS

EDITED BY
Xudong Huang,
North China University of Water Conservancy and Electric Power, China

REVIEWED BY
Chaochao Li,
Ningxia University, China
Feilong Jie,
Xinjiang University, China

*CORRESPONDENCE
Xudong Fang,
✉ fang_xd@hdec.com

RECEIVED 18 July 2024
ACCEPTED 25 October 2024
PUBLISHED 06 November 2024

CITATION
Chen K, Liu K and Fang X (2024) Study on optimization of maize irrigation scheduling in Shaanxi Province.
Front. Environ. Sci. 12:1466691.
doi: 10.3389/fenvs.2024.1466691

Study on optimization of maize irrigation scheduling in Shaanxi Province

Kaijie Chen[1,2], Kejie Liu[1,2] and Xudong Fang[1,2]*

[1]PowerChina HuaDong Engineering Corporation Limited, Hangzhou, China, [2]PowerChina ChongQing Engineering Corporation Limited, Chongqing, China

With the impact of climate change in recent years, the instability of precipitation and the increase of evaporation have made water resources in Shaanxi Province more and more stressed. How to maintain stable economic development while ensuring the sustainable development of agriculture within the limited water resources has become an important issue facing Shaanxi Province. This paper analyzes the temporal and spatial distribution characteristics of maize irrigation water requirement in Shaanxi Province based on meteorological data and obtains the ideal irrigation water requirement. However, considering the agricultural water scarcity issue in this region, this paper establishes different water scarcity scenarios, adopts the Jensen model to construct an objective function aimed at minimizing crop yield reduction, and solves it using a genetic algorithm to obtain the optimized maize irrigation scheduling under different water scarcity scenarios. The results analysis indicates the following: (1) The effective rainfall in Shaanxi Province from 1960 to 2019 shows a slight upward trend, while the maize water requirement and maize irrigation water requirement shows a downward trend. (2) The spatial distribution of maize irrigation water requirement in Shaanxi Province decreases gradually from north to south. High-value areas are mainly distributed in the northern regions of Yulin City and Yan'an City in Shanbei. Low-value areas are distributed in Ankang City in Shannan. (3) In the face of water scarcity, spring maize should ensure water use during the middle growth period, fast development period, and initial growth periods. Under the same water scarcity conditions, the yield reduction rate is the highest in Guanzhong, followed by the Shannan, and the lowest in Shanbei. This paper aims to provide a scientific and reasonable optimization plan for maize irrigation in Shaanxi Province by calculating and analyzing the maize irrigation water requirement in Shaanxi Province, combined with optimization tools such as genetic algorithms, to address the challenges brought by water resource constraints.

KEYWORDS

water resources, irrigation water requirement, Jensen model, irrigation scheduling optimization, Shaanxi province

1 Introduction

Facing the dual pressures of global climate change and population growth, water scarcity has emerged as a global challenge. As the most populous country globally, China boasts a large total water resource volume. However, its *per capita* water resource availability significantly falls below the global average, highlighting a pronounced issue of water scarcity. In 2020, China's total water resources amounted to 31,605.2 billion cubic meters, accounting for only 6% of the world's water resources, indicating a relative scarcity of water resources in the country. Meanwhile, as an agricultural powerhouse, China's agricultural water consumption has remained persistently high. Agriculture, as the foundation of the national economy, is one of the primary sectors consuming water resources. In 2020, agricultural water use in China accounted for 61.5% of total water use, a proportion significantly higher than in other countries. This high proportion of agricultural water use not only exacerbates the stress on China's water resources but also poses a serious threat to the sustainable development of agricultural production. In agricultural production, traditional irrigation methods often lead to substantial waste of water resources, exacerbating the already strained water resources. Furthermore, rapid industrialization and urbanization have led to an increasing requirement for water in industrial and urban sectors, further exacerbating the supply-demand imbalance of water resources.

As a crucial province in the northwest plains of China, Shaanxi Province serves as both a significant agricultural production base and faces the dilemma of water scarcity. With the influence of climate change in recent years, the instability of precipitation and increased evaporation have intensified the strain on water resources in Shaanxi Province. Agriculture, as the primary sector consuming water resources, requires crucial control and management of water usage. Balancing economic stability within limited water resources while ensuring the sustainability of agriculture has become a critical issue for Shaanxi Province. In recent years, with the continuous advancement of technology, significant improvements have been made in agricultural water use efficiency. Improvements in agricultural irrigation techniques, the development of water-saving agriculture, and the construction of agricultural water conservancy projects have all provided strong support for enhancing agricultural water use efficiency and reducing the proportion of agricultural water consumption. However, despite some achievements, water scarcity remains one of the crises faced by Shaanxi Province. To address this challenge, continuous improvement of irrigation schedulings and reduction of agricultural water usage have become focal points of research for many scholars.

Research progress on crop irrigation schedulings can be analyzed from multiple perspectives. In terms of water-saving irrigation technology application and development, China's agricultural water-saving irrigation technology is also constantly improving, and micro irrigation technology has been proven to be the most effective water-saving technology, saving 50%–70% of water compared to surface flood irrigation; Compared to sprinkler irrigation, it saves 15%–20% of water. (Zhang and Hu, 2021). Additionally, the impact and mechanisms of water-saving irrigation technologies such as controlled irrigation, alternate wetting and drying irrigation, and dry seeding cover on rice yield have been extensively studied (Wang et al., 2022; Gu et al., 2022). Regarding the optimization of irrigation schedulings, researchers have proposed various models and methods to optimize the allocation of crop water resources. These include multi-objective planning models considering economic and ecological benefits (Li et al., 2005), as well as single-crop models and multi-crop water resource optimization models based on SPAC theory (Wang et al., 2014). The aim of these studies is to achieve efficient utilization of water resources and maximize crop yields through scientifically designed irrigation schedulings. The selection of efficient water-saving irrigation models is also a current research focus. Studies indicate that selecting efficient water-saving irrigation models adapted to the needs of sustainable development in the region is crucial for addressing agricultural water scarcity issues (Zhang et al., 2019).

Moreover, research on non-adequate irrigation decision indicators provides a scientific basis for the rational use of limited water resources (Guo et al., 2007). The impact of changes in irrigation management practices on crop water use is also an important aspect of research. For example, the accelerated pace of irrigation management reform in the Yellow River Basin irrigation areas, where the transformation from water user associations exceeds contracted management, has become the leading mode of reform (Wang et al., 2011). This underscores the significant role of innovation and reform in irrigation management practices in improving irrigation efficiency and promoting agricultural sustainable development.

The main focus of this article is on researching the optimization of irrigation schedulings. For instance, Reta et al. (2024) considered the impact of climate change on future crop water demand and irrigation systems, and used a generalized algebraic modeling system with non negative constraints and non negative constraints based on farmer adaptation to program and optimize farmland allocation. Ashkan et al. (2022) combined the Taguchi optimization method with the HYDRUS-1D model, and its successful application provides a promising method for optimizing the triggered irrigation scheduling of walnut seedlings. Martínez-Romero et al. (2021) used AquaCrop and MOPECO models to calculate and compare the crop water yield and irrigation water productivity functions of typical irrigated crops in the region under several irrigation strategies, and evaluated the performance of the models through experiments. Gao et al. (2023) conducted field experiments to analyze cotton yield and water-salt distribution characteristics in southern Xinjiang under two irrigation modes and various irrigation quotas. Ma et al. (2024) determined the irrigation scheduling for rice in the Hohai University water-saving garden by constructing multi-objective functions. Guo et al. (2017) analyzed the irrigation scheduling for alfalfa based on the Jensen model. Wang et al. (2007) used the Jensen model and aimed to maximize relative yield to determine the optimized irrigation scheduling for rice in the semi-arid areas of western Heilongjiang Province. While Shaanxi Province serves as a significant agricultural production base in China, with maize being one of its primary crops, there is a lack of research on optimal irrigation systems for corn in Shaanxi Province.

Therefore, based on meteorological data from Shaanxi Province, this article conducts in-depth calculations and analyses to determine the water requirement and irrigation water requirement for maize, considering various water scarcity scenarios. By adopting a strategy with minimizing grain yield reduction as the objective function and utilizing genetic algorithms for optimization, different water allocation schemes for maize under different water scarcity scenarios are obtained. These schemes provide important scientific basis and guidance for Shaanxi Province to achieve stable and sustainable agricultural production under limited water resources conditions.

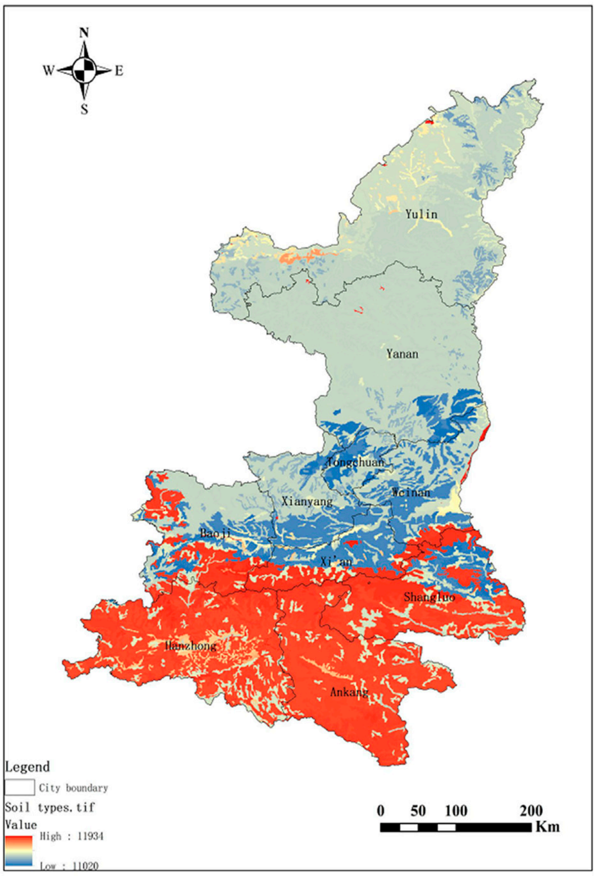

FIGURE 1
Topographical map of Shaanxi Province.

2 Materials

2.1 Geographical characteristics

Shaanxi Province, located in the inland of China and situated in the middle reaches of the Yellow River, belongs to the relatively water-scarce northwest plain region. Climatically, Shaanxi Province transitions gradually from temperate to warm-temperate and further to subtropical climates from north to south. This climatic diversity provides rich conditions for agricultural production and ecological diversity in Shaanxi Province, but it also brings about uneven distribution of water resources. During the warm and humid seasons, the southern region is susceptible to extreme weather events like heavy rainstorms, while the northern region tends to be relatively dry, exacerbating water scarcity issues. In terms of topography, Shaanxi Province generally features higher terrain in the north and south with lower elevation in the central region. The two major mountain ranges, the Beishan and Qinling Mountains, naturally divide Shaanxi Province into three main regions: the northern part is the Loess Plateau, the central part is the Guanzhong Plain, and the southern part is the Qinba Mountainous region. This topographical variation significantly impacts the distribution of water resources in Shaanxi Province. The northern Loess Plateau has relatively scarce water resources due to its higher elevation, while the Guanzhong Plain, despite its flat terrain, faces prominent water supply-demand contradictions due to dense population and frequent agricultural activities. The Qinba Mountainous region possesses relatively abundant water resources, but due to its complex terrain, the difficulty in development and utilization is higher. From the perspective of water resources, Shaanxi Province faces severe spatial and temporal disparities in water resource distribution. On one hand, influenced by climate and topography, water resources in Shaanxi Province exhibit significant differences in both time and space. On the other hand, with rapid economic development and continuous population growth, the requirement for water resources in Shaanxi Province is increasing, while the available water resources are relatively limited, leading to an increasingly prominent water supply-demand contradiction in the province.

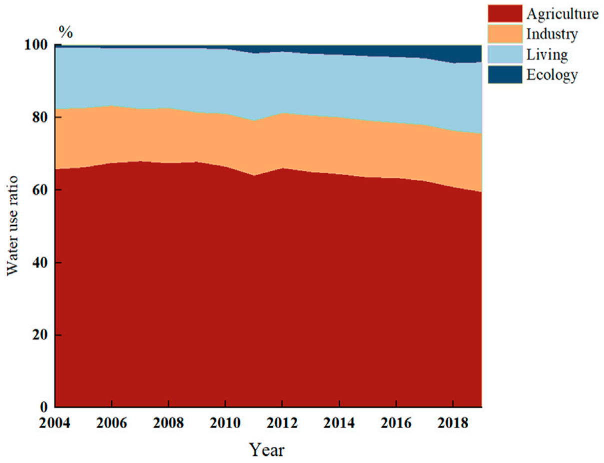

FIGURE 2
Schematic diagram of water use structure in Shaanxi Province.

The topographic map of Shaanxi Province is shown in Figure 1.

2.2 Status of water use

From the perspective of agricultural water usage, it constitutes a substantial portion of the total water consumption in Shaanxi Province. In 2004, agricultural water usage accounted for 65.83% of the total, decreasing to 59.50% by 2019. The decreasing trend in the proportion of agricultural water usage over time indicates significant improvements in farmland irrigation efficiency due to advancements in agricultural technology and the widespread adoption of water-saving irrigation measures, leading to a substantial reduction in water usage per unit of land area. Simultaneously, the optimization of agricultural structure has also contributed to reducing agricultural water requirement, with a decrease in the cultivation area of high-water-consuming crops and a gradual increase in the cultivation area of water-saving crops. These factors collectively contribute to the decline in the proportion of agricultural water usage.

Similar to agricultural water usage, industrial water usage also demonstrates a declining trend. With the upgrading of industrial technology and increasing environmental awareness, industrial enterprises in Shaanxi Province have actively implemented

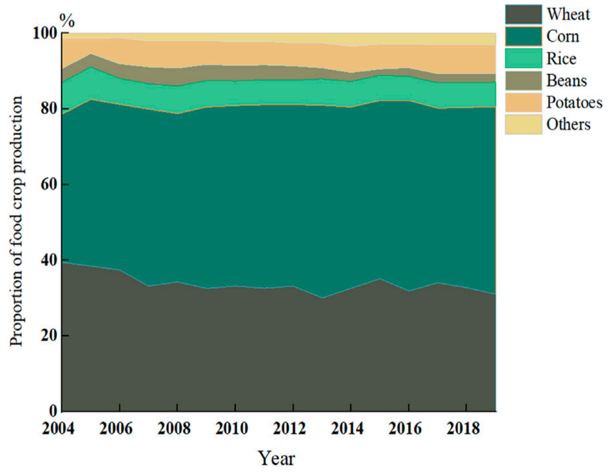

FIGURE 3
Schematic diagram of the proportion of grain crop production in Shaanxi Province.

water-saving measures to enhance water resource utilization efficiency. Additionally, some high-water-consuming and highly polluting industrial projects have been gradually phased out or relocated, thereby reducing the requirement for industrial water usage. The proportions of domestic and ecological water usage have been continuously increasing. With population growth and the accelerated urbanization process, the domestic water usage of residents has steadily increased. As people's demands for living standards continue to rise, there is also a growing requirement for ecological water usage, such as urban greening and landscape construction.

The schematic diagram of the urban water use structure in Shaanxi Province is shown in Figure 2.

2.3 Crop yields

From Figure 3, it is apparent to observe the proportion of wheat and maize as the two major staple crops in Shaanxi Province, and based on this, analyze the changing trend in the structure of grain production. Wheat, as a traditional staple crop, once held a significant position in the grain production structure of Shaanxi Province. However, over time, the proportion of wheat production has shown a noticeable decline. This change may be influenced by various factors, including a reduction in cultivation area, limitations in cultivation techniques, and changes in market demand. With its long growth cycle and high demands on soil and water resources, amidst increasingly scarce resources, the decreasing proportion of wheat production also reflects the adjustment and optimization of agricultural production structure.

The proportion of maize production, on the other hand, shows an increasing trend. Maize, as a highly adaptable crop with a short growth cycle, high yield, and strong market demand, has seen a rapid growth in production. With advancements in agricultural technology and adjustments in planting structures, more and more farmers are choosing to cultivate maize, thereby driving the rapid increase in maize production. The increase in maize production not only meets market demand but also brings new growth points to grain production in Shaanxi Province. Apart from wheat and maize, the changes in production of other crops are relatively less pronounced. These crops may exhibit relatively stable production changes due to factors such as smaller cultivation scale and relatively stable market demand. Nevertheless, they still hold a certain proportion in the grain production structure of Shaanxi Province, playing an important role in enriching grain varieties and meeting diversified demands.

FIGURE 4
Distribution map of meteorological stations in Shaanxi Province.

The changing trend in grain production structure aligns with the variation in the cultivated area of grain crops in Shaanxi Province. The fluctuation in cultivated area directly impacts the production of grain crops, while the changes in production structure reflect the adjustment and optimization of agricultural production structure. Therefore, by analyzing the changes in cultivated area and production structure, we can gain a deeper understanding of the development trends and challenges faced by grain production in Shaanxi Province.

2.4 Data sources

The water usage data for Shaanxi Province is sourced from the Shaanxi Provincial Water Resources Bulletin, while the cultivation production data are obtained from the Shaanxi Provincial Statistical

Yearbook. The meteorological station data is sourced from the National Meteorological Information Center of the China Meteorological Administration, comprising 34 meteorological stations with daily meteorological data spanning 60 years from 1960 to 2019.

Based on the changes in agricultural water usage, cultivation area, and production of grain crops in Shaanxi Province as described earlier, this study focuses on analyzing the irrigation water requirements and optimizing irrigation schedulings for maize cultivation based on meteorological station data. Shaanxi Province is divided into three climatic regions, namely Shanbei, Guanzhong Plain, and Shannan, based on geographical location and climate differences. Shanbei mainly refers to the cities of Yan'an and Yulin in Shaanxi Province, including the counties and districts under the jurisdiction of these two cities. Guanzhong is located north of the Qinling Mountains, south of the Beishan Mountains, east of the Longshan Mountains, and west of the Yellow River. It is a river valley plain basin surrounded by mountains on three sides: south, north, and west, and open to the east, extending for more than 300 km from east to west. Shannan includes three prefecture level cities, Hanzhong, Ankang, and Shangluo. Shanbei and Shannan mainly cultivate spring maize, while Guanzhong Plain, due to its geographical and climatic characteristics, practices double cropping with mainly summer maize cultivation. Therefore, this study primarily investigates spring maize in Shanbei and Shannan, and summer maize in the Guanzhong Plain region. The distribution of meteorological stations can be observed in Figure 4.

3 Methods

3.1 Effective rainfall

The effectiveness of precipitation is related to factors such as rainfall characteristics, groundwater depth, crop growth conditions, soil texture, and structure (Wang et al., 2013; Yao et al., 2018). Due to the numerous factors influencing effective rainfall, in practical agricultural production, the calculation of effective rainfall often employs the method of effective utilization coefficient, which is based on empirical formulas (Allen et al., 1998). The calculation methods of effective rainfall and effective rainfall coefficient are shown in Equations 1, 2.

$$P_e = \alpha P \tag{1}$$

$$\alpha = \begin{cases} 0 \ P \leq 5\text{mm} \\ 1.0 \ P = 5 \sim 50\text{mm} \\ 0.8 \sim 0.75 \ P = 50 \sim 150\text{mm} \\ 0.7 \ P > 150\text{mm} \end{cases} \tag{2}$$

In the formula, P_e represents effective rainfall (mm); P represents natural rainfall (mm); α represents the effective rainfall coefficient.

3.2 Maize water requirement

The water requirement of maize refers to the amount of water consumed during the growth period of maize, which is relatively stable under certain yield conditions and in specific regions (Guo et al., 2017; Xiao et al., 2008). The water requirement of maize is calculated using the single crop coefficient method recommended by the FAO, it is expressed by Equation 3 (Zhang et al., 2020).

$$ET_c = K_c \cdot ET_0 \tag{3}$$

In the equation, ET_c represents the crop water requirement (mm); K_c represents the crop coefficient; ET_0 represents the reference crop evapotranspiration is calculated by Equation 4.

$$ET_0 = \frac{0.408\Delta(R_n - G) + \gamma \frac{900}{T+273} U_2 (e_s - e_a)}{\Delta + \gamma(1 + 0.342U_2)} \tag{4}$$

In the equation, Δ represents the slope of the relationship curve between saturated water vapor pressure and air temperature, $kP_a/$°C; R_n represents the net radiation on the crop surface, $MJ/(m^2 \cdot d)$; G represents the soil heat flux, $MJ/(m^2 \cdot d)$; γ represents the dry constant of the temperature table, $kP_a/$°C; T represents the daily average air temperature, °C; U_2 represents the wind speed at a height of 2 m above the ground, m/s; e_s represents the saturated water vapor pressure, kP_a; e_a represents the actual water vapor pressure, kP_a.

The crop coefficient is calculated using the segmented single-value average method recommended by FAO-56 in 1998. When using it, it needs to be revised according to local conditions. According to the growth and development characteristics of crops, the crop growth stages are divided into the initial growth stage, rapid development stage, mid-growth stage, and maturity stage. In this study, the entire growth stages of maize are divided into four stages: initial growth period, fast development period, middle growth period, and maturity stage. The division of time nodes for each growth stage is shown in Table 1 (Qin et al., 2016; Li and Fan, 2015).

*In the following paragraphs, ① is used to represent the Initial growth period; ② is used to represent the Fast development period; ③ is used to represent the Middle growth period; ④ is used to represent the Maturity.

The values of crop coefficients need to consider local conditions, and the revised values of crop coefficients refer to research by Liang et al. (2011) and Kang et al. (1990) as shown in Table 2.

3.3 Maize irrigation water requirement

The irrigation water requirement refers to the amount of irrigation water needed to supplement crop water needs when the rainfall during the growth stage is insufficient. The irrigation water requirement is calculated by Equation 5.

$$I_s = MAX\left(\sum_{n=1}^{N} ET_{c_n} - \sum_{n=1}^{N} P_{e_n}, 0\right) \tag{5}$$

In the formula, N represents the number of days in the growth stage, d; I_s represents the required supplementary irrigation amount, mm/d; the remaining variables have the same meanings as previously described.

TABLE 1 Development stages of spring and summer maize.

Partition	Initial growth period①	Fast development period②	Middle growth period③	Maturity④
Shanbei (spring maize)	The last ten-day period of April	Middle of June	The first 10 days of July	The last ten-day period of August
Guanzhong area (summer maize)	Middle of June	The first 10 days of August	The first 10 days of September	The last ten-day period of September
Shannan (spring maize)	The first 10 days of April	Middle of July	The last ten-day period of July	The last ten-day period of August

TABLE 2 Revised crop coefficients at different growth stages.

Partition	①	②	③	④
Shanbei (spring maize)	0.56	0.73	0.90	1.16
Guanzhong area (summer maize)	0.61	0.93	1.27	1.07
Shannan (spring maize)	0.55	0.80	1.18	1.18

TABLE 3 Variation trend of water requirement of maize at different growth stages.

Parameter		①	②	③	④
Dr (percentage)	—	1.80%	1.40%	2.40%	9.50%
H	—	0~20 cm	10~30 cm	30~50 cm	40~50 cm
λ	Spring maize	0.19	0.3	0.55	0.1
	Summer maize	0.11	0.17	0.26	0.25

3.4 Optimization model of irrigation scheduling

3.4.1 Objective function

$$\min f = \sum_{i=1}^{L} (Y_m - Y_a) \tag{6}$$

where,

$$\frac{Y_a}{Y_m} = \prod_{i=1}^{N_2} \left(\frac{ETa^i}{ETm^i}\right)^{\lambda^i} \tag{7}$$

$$ETa^i = Ks^i ETc^i \tag{8}$$

$$ETc^i = Kc^i ET0^i \tag{9}$$

$$Ks^i = \frac{TAW^i - Dr^i}{TAW^i - RAW^i} = \frac{TAW^i - Dr^i}{(1 - p^i) TAW^i} \tag{10}$$

$$p^i = p' + 0.4\left(5 - \frac{ETc^i}{N^i}\right) \tag{11}$$

$$TAW^i = 1000 H^i (\theta_{FC} - \theta_{WP}) \tag{12}$$

$$RAW = p' TAW \tag{13}$$

The process of solving Y_a is described in Equations 6–13. In the formula, f represents a function of yield, Y_a is the actual crop yield, kg/km^2; Y_m is the maximum crop yield under sufficient water supply condition, kg/km^2; n is the number of reproductive stages; ETa^i is the actual crop evapotranspiration in the ith growth stage, mm; ETm^i is the potential crop evapotranspiration at the ith growth stage under sufficient water supply, mm; λ^i is the water sensitivity coefficient of the ith crop growth stage, which is used to characterize the sensitivity of different crops to water shortage in each growth stage. The water sensitivity coefficients of initial growth period, middle growth period, milky and mature stages are shown in Table 3. $ET0^i$ is the reference crop evapotranspiration at the ith growth stage, mm; ETc^i is the crop water requirement in the ith growth stage, mm; Ks^i is the water stress coefficient of the ith crop growth stage characterizing the water supply for crop; Kc^i is the crop coefficient in the ith growth stage; TAW^i is the total available soil water in the root zone in the ith crop growth stage, mm; RAW^i is the readily available soil water in the root zone in the ith crop growth stage, mm; Dr^i is the root zone depletion in the ith crop growth stage, mm; p^i is the fraction of TAW that a crop can extract from the root zone without suffering water stress; p' is the reference value recommended by FAO (0.55 for summer maize); N^i is the days of ith crop growth stage; H^i is the crop root zone dep that the ith growth stage; θ_{FC} is the field capacity, cm^3/cm^3; θ_{WP} and is the crop wilting coefficient, cm^3/cm^3 , which can be determined according to the soil water content at wilting point of different crop growth stages. The soil effective water content values of typical sites are shown in Table 4.

3.4.2 Constraint condition

a. Available irrigation water

In the process of optimizing agricultural irrigation water and adjusting water resources allocation, the available irrigation water was determined according to statistical yearbook with the constraints are shown in Equation 14.

$$\sum SW_t \le W_a \tag{14}$$

TABLE 4 Soil available water content at typical sites.

Typical sites	θ_{FC} (%)	θ_{WP} (%)	Effective water volume (mm)
Yulin	13	2.9	148.92
Suide	15.8	3.66	180.74
Yan'an	20.4	5.08	171.3
Luochuan	20.2	6.1	171.1
Pucheng	21.5	6.68	169.2
Weinan	22.4	7.37	161.07
Wugong	20.2	8.4~8.8	127.8
Ankang	24.4	15.99	129.2

where S is the planting area of crops, ha; W_t is the irrigation water use in unit area, m^3/ha; and W_a is the amount of agricultural irrigation water in Shaanxi Province, m^3.

b. Maximum irrigation quota constraint

If the irrigation water amount is less than the calculated maximum irrigation quota, the irrigation depth is not enough and irrigation water is insufficient for crop growth, which will increase the irrigation times. If the irrigation amount is greater than this calculated quota, deep percolation or surface runoff loss will occur. The constraint equation for irrigation water demand is given in Equation 15.

$$\sum SW_t < W_{\max}, \text{Supplemental irrigation} \tag{15}$$

where $W_{\max}$ is the maximum irrigation quota, m^3/ha.

3.4.3 Situation setting

In this study, six scenarios were set up to study the optimal allocation of irrigation water under different water shortage conditions, including agricultural full irrigation (AI), irrigation water reduced by 10% (IWS10), irrigation water reduced by 20% (IWS20), irrigation water reduced by 30% (IWS30), irrigation water reduced by40% (IWS40), and irrigation water reduced by 50% (IWS50).

3.4.4 Model solving principle

The objective function being single-target, the model primarily employs a Genetic Algorithm with enhanced elitism preservation strategy for optimization. Genetic Algorithm is an optimization algorithm that simulates principles from natural selection and genetics. It explores the solution space efficiently by mimicking operations like selection, crossover, and mutation, akin to biological evolution, to find the optimal solution to a problem. When solving single-target problems, Genetic Algorithm efficiently explores the solution space and gradually converges to the optimal solution through iterations. However, standard Genetic Algorithms may encounter slow convergence or get trapped in local optima when solving complex problems. To overcome these issues, this paper adopts the enhanced elitism preservation strategy in the Genetic Algorithm. Elitism preservation strategy is an effective optimization technique that preserves a portion of excellent individuals in each generation, directly passing them to the next-generation, thereby avoiding the loss of excellent genes and accelerating the convergence speed of the algorithm.

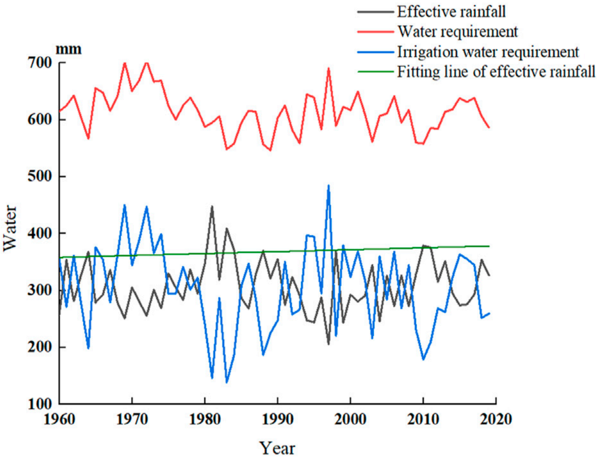

FIGURE 5
The change process of effective rainfall, water requirement and irrigation water requirement during the corn fertility period in Shaanxi Province.

By combining the global search capability of Genetic Algorithm with the rapid convergence characteristic of the elitism preservation strategy, it becomes more efficient in solving single-target problems. This algorithm not only finds the global optimal solution in large solution spaces but also completes the solution process in a shorter time, providing strong support for practical problem-solving.

In terms of the preset parameters of the NSGA-algorithm. The preset population number N (popsize) is 130; the number of iterations $Gen_{\max}$ (Maxgen) is 500; the cross probability P_c (ProC) is 1; the variation probability P_m (ProM) is $\frac{1}{Max-Size}$; the simulated binary cross parameter (DisC) is 20; the polynomial variation parameter (DisM) 20.

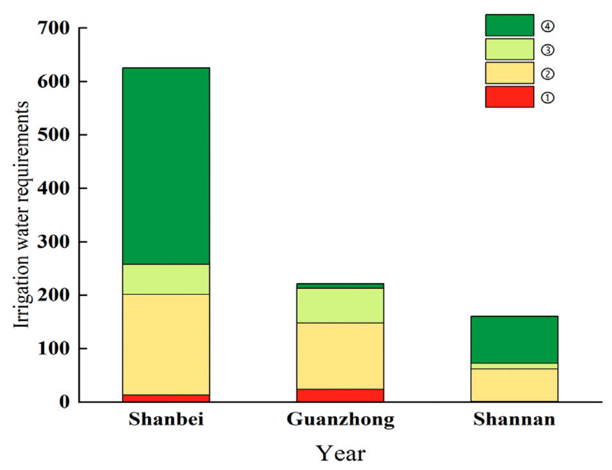

FIGURE 6
Water needs for irrigation in the stage of corn fertility in various regions of Shaanxi Province (①Initial growth period; ②Fast development period; ③Middle growth period; ④Maturity).

4 Results

4.1 Temporal and spatial analysis of maize effective rainfall, water requirement and irrigation water requirement

As the main maize planting region, the water resources situation during the growth process of maize in Shaanxi Province is of significant importance for the stability and sustainability of agricultural production. Based on the time distribution of effective rainfall, water requirement, and irrigation water requirement during the maize growing period in Shaanxi Province from 1960 to 2019 (as shown in Figure 5), this paper provides a detailed analysis of the trends of these indicators.

Effective rainfall has shown a slight increase trend over the past 60 years. Although this trend is not significant, it reflects to some extent the subtle changes in the climate conditions of Shaanxi Province. The increase in effective rainfall helps meet the water requirement during the maize growth process, but due to the small magnitude of the growth, its impact on maize growth is relatively limited.

From the perspective of water requirement, there has been a significant downward trend from 1960 to 2019. This trend may be related to the progress of agricultural technology and adjustments in planting structure. With the continuous development of agricultural technology, the optimization of maize varieties and improved drought resistance have gradually reduced the water requirement during maize growth. In addition, adjustments in planting structure may also affect water requirement, such as increasing the proportion of water-saving crops.

The trend of irrigation water requirement is similar to that of water requirement, showing a downward trend as well. This indicates that irrigation water has been more effectively utilized in the maize planting process in Shaanxi Province. This may be related to advancements in irrigation technology, improvements in water resource management strategies, and increased awareness of water conservation among farmers. It is worth noting that the maximum value of irrigation water requirement occurred in 1997, reaching 476.45 mm. This may be due to exceptionally dry weather that year, leading to a significant increase in irrigation water requirement for maize growth. The minimum value occurred in 1983, only 139.02 mm, which may be related to abundant rainfall and sufficient soil moisture that year.

According to Figure 6, there are significant differences in the irrigation water requirements during various stages of the growth period between spring maize and summer maize. These differences not only manifest in different growth stages, but also vary with different sowing times. For spring maize, the distribution of its irrigation water requirements shows a certain regularity. During the maturity stage, as the growth of maize plants tends to be perfect, the requirement for water reaches its peak, resulting in the largest irrigation water requirement. In the rapid growth stage, maize plants are in a phase of rapid growth and also have a relatively strong requirement for water, with the irrigation water requirement following closely behind. In contrast, the irrigation water requirements in the middle and initial growth stages are relatively small. Unlike spring maize, the distribution of irrigation water requirements for summer maize exhibits a different pattern. During the rapid growth stage, the irrigation water requirement for summer maize is the largest, as the high temperature and frequent rainfall in summer promote rapid maize growth and high water requirement. The irrigation water requirements in the middle and initial growth stages are relatively small, while the irrigation water requirement in the maturity stage drops to the lowest level. There are also significant differences in the irrigation water requirements of maize in different regions. Due to the dry climate and relatively scarce water resources in Shanbei, the irrigation water requirement of maize during the middle growth stage accounts for a large proportion to compensate for the lack of soil moisture. In the Guanzhong region, the climate is relatively humid, and water resources are relatively abundant, so the irrigation water requirement of maize during the rapid growth stage accounts for a higher proportion. In Shannan, due to the complex terrain and diverse climate conditions, the distribution of maize irrigation water requirements shows certain regional characteristics.

The proportions of the initial growth stage, rapid development stage, middle growth stage, and maturity stage vary among different regions during the total growth period. In Shanbei, the proportions are 2.08%, 30.08%, 9.02%, and 58.81%, respectively. In the Guanzhong region, the proportions are 10.66%, 56.09%, 29.32%, and 3.93%, respectively. In Shannan, the proportions are 0.74%, 37.98%, 6.60%, and 3.93%, respectively. These variations in proportions reflect the differences in climate conditions in different regions.

The irrigation water requirement for the entire growth period and each growth stage of maize is illustrated in Figure 7. As shown in Figure 7A, there are significant spatial differences in the average irrigation water requirement for maize crops in Shaanxi Province over multiple years throughout the entire growth period. Overall, high-value areas are mainly concentrated in the northern regions of Yulin and northern Yan'an cities. These areas are typically located in the Loess Plateau, characterized by arid climate and scarce rainfall, leading to a higher reliance on irrigation during the maize growth process. Therefore, irrigation becomes a critical factor in ensuring normal maize growth and yield in these regions. In contrast, low-value areas are distributed in Ankang

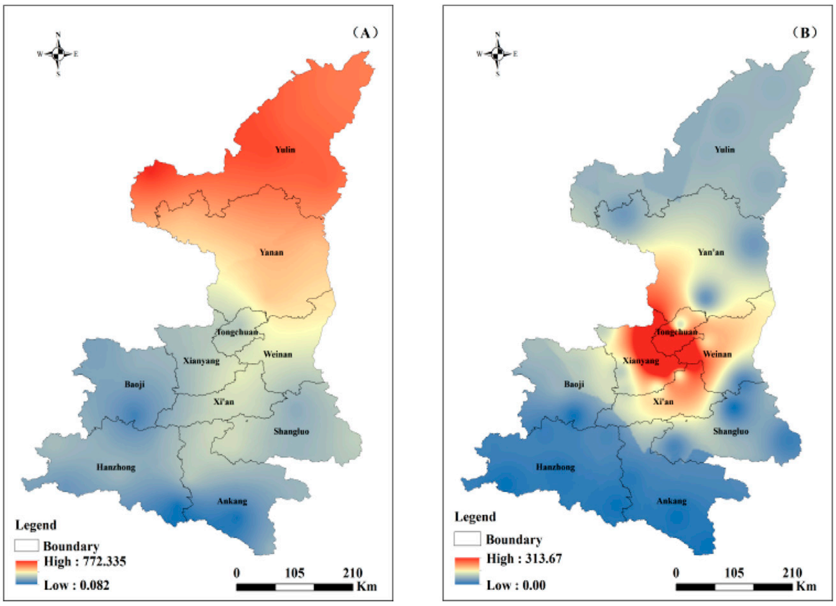

(A) Full fertility period

(B) Seedling stage

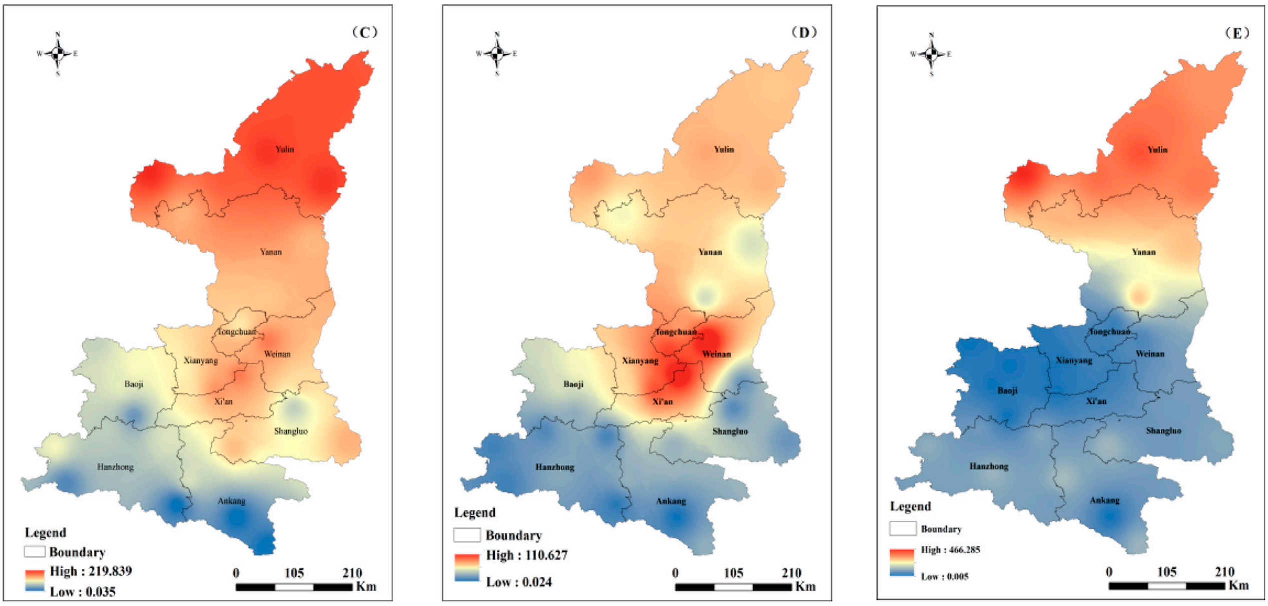

(C) Pull out the holiday period

(D) Draw the season

(E) Maturity

FIGURE 7
Spatial distribution map of the amount of water required for corn irrigation in Shaanxi Province. **(A)** Full fertility period **(B)** Seedling stage **(C)** Pull out the holiday period **(D)** Draw the season **(E)** Maturity.

city in Shannan. The climate in Shannan is humid with abundant rainfall, resulting in relatively sufficient natural water supply during maize growth. Consequently, irrigation water requirement is relatively low in these areas. The spatial distribution of irrigation water requirement for maize in Shaanxi Province aligns with the trend of maize water requirement, both showing a decreasing trend from north to south. This distribution pattern is closely related to the climatic conditions, topography, and maize planting structure in Shaanxi Province.

Furthermore, there is a close relationship between the irrigation water requirement of crops in planting areas and their effective rainfall and crop water requirement. Effective rainfall is one of the important factors influencing irrigation water requirement. In areas with abundant rainfall, most of the water needed for maize growth comes from natural rainfall, resulting in relatively low irrigation water requirement. In arid areas where rainfall is insufficient, crop water requirement is high, and irrigation becomes a necessary means of supplementing water. Crop water requirement reflects the water needs of maize at different growth stages. During periods of vigorous

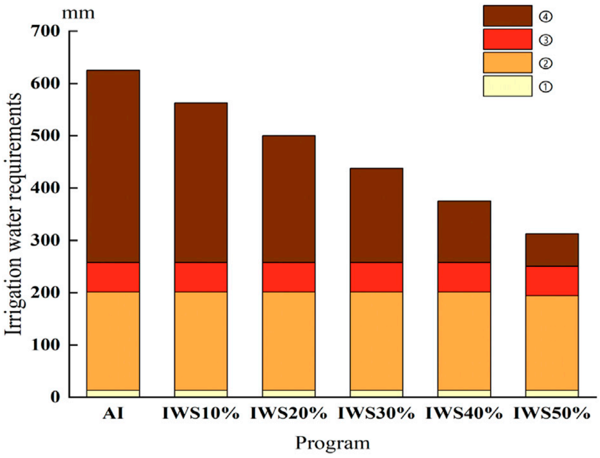

FIGURE 8
Optimization plan for irrigation water in Shanbei (①Initial growth period; ②Fast development period; ③Middle growth period; ④Maturity).

growth, such as rapid development stages, maize requires a large amount of water, leading to increased irrigation water requirement. Conversely, during the early growth or maturation stages, crop water requirement is relatively low, and irrigation water requirement decreases accordingly.

Based on Figures 7B–E, significant spatial distribution characteristics of irrigation water requirement for different growth stages of maize in Shaanxi Province can be observed. When formulating irrigation strategies, factors such as climate, soil, and planting structure in various regions should be fully considered to ensure adequate water supply for maize at each growth stage. Additionally, efforts should be made to strengthen the research and application of water resource management and water-saving technologies to improve water resource utilization efficiency and promote the sustainable development of agricultural production.

4.2 Irrigation scheduling optimization results

The article has calculated the optimal irrigation water allocation for various growth stages of spring maize in Shanbei under different water shortage conditions. The specific optimal water allocation for each growth stage is shown in Figure 8.

Under the IWS10% water shortage scenario, adjustments have been made to the irrigation strategy for spring maize. During the initial growth period, since the plants are still small and have low water requirements, irrigation water accounts for only 2.32% of the total irrigation volume. As the maize enters the fast development period and experiences rapid growth, the water requirement increases, with irrigation water accounting for 33.42% of the total. The middle growth period, crucial for reproductive growth, requires some water support, with irrigation water accounting for 10.03%. By the time maize reaches maturity and starts fruit formation and biomass accumulation, irrigation water requirement peaks at 54.23%. Compared to full irrigation (AI scenario), irrigation water volume is reduced by 62.52 mm during the maturity stage, while remaining unchanged in other stages.

As water shortage intensifies to IWS20%, further adjustments occur in irrigation water allocation for each growth stage. The initial growth period irrigation water percentage slightly increases to 2.89%, while the fast development period rises to 41.78%, and the middle growth period to 12.53%. However, irrigation water percentage during the maturity stage decreases to 42.79%. Compared to the AI scenario, irrigation water volume during the maturity stage reduces by 175.05 mm, indicating stricter water management during this critical growth phase under water shortage conditions.

At IWS30%, irrigation water allocation continues to adjust for each growth stage. The initial growth period irrigation water percentage rises to 3.31%, fast development period to 47.75%, and middle growth period to 14.33%, while decreasing to 34.62% during the maturity stage. Compared to the AI scenario, irrigation water volume during the maturity stage decreases by 231.31 mm, highlighting greater restrictions on water supply during the most severe water shortage conditions.

Under the water deficit scenario of IWS40%, the allocation of irrigation water becomes even more strained. The proportion of irrigation water used during the initial growth period reaches 3.86%, increases to 55.70% during the fast development period, and further increases to 16.71% during the middle growth period, while it is only 23.72% during the maturity stage. Compared to the AI scenario, the irrigation water volume during the maturity stage decreases by 287.58 mm, indicating that under extreme water scarcity conditions, to ensure the basic growth of maize, a significant reduction in irrigation water during the maturity stage is necessary.

Under the most severe IWS50% scenario, irrigation water allocation becomes extremely stringent. The initial growth period irrigation water percentage reaches 4.63%, fast development period 56.05%, and middle growth periodsurges to 20.06%, while dropping to 19.26% during the maturity stage. Compared to the AI scenario, not only does irrigation water volume during the maturity stage significantly decrease by 313.49 mm, but there's also a noticeable decrease in irrigation water volume during the middle growth period. This suggests that under extreme water shortage conditions, significant reductions in irrigation water volume during both the maturity and middle growth period are necessary to ensure basic reproductive growth of maize.

From the above data, it is evident that as irrigation water shortage increases, significant changes occur in the irrigation water allocation for various growth stages of spring maize in Shanbei. With milder water shortages, reductions in irrigation water volume mainly focus on the maturity stage. However, as water shortage becomes more severe, not only does irrigation water volume during the maturity stage decrease significantly, but irrigation water volume during the middle growth periodalso starts to be affected. This underscores the need for more precise irrigation water allocation and management to ensure the basic growth and yield of spring maize under water shortage conditions.

The optimal water allocation for different growth stages of summer maize in the Guanzhong region under various water shortage conditions is depicted in Figure 9.

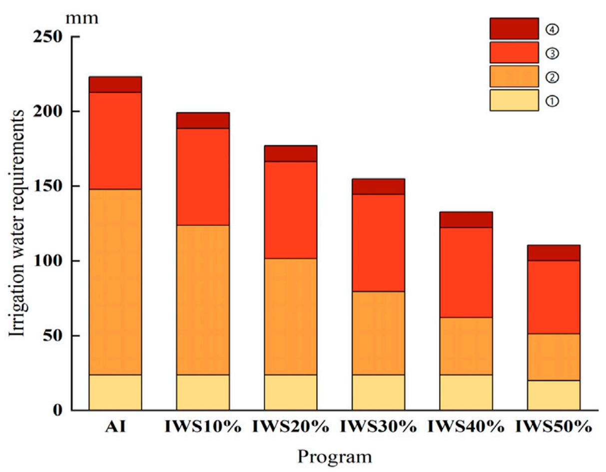

FIGURE 9
Optimization plan for irrigation water in Guanzhong (①Initial growth period; ②Fast development period; ③Middle growth period; ④Maturity).

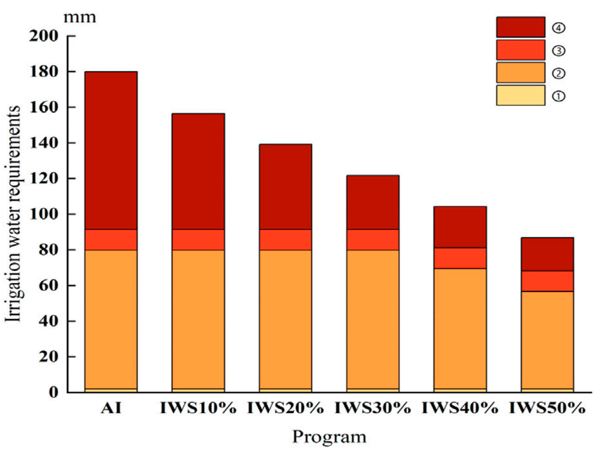

FIGURE 10
Optimization plan for irrigation water in Shannan (①Initial growth period; ②Fast development period; ③Middle growth period; ④Maturity).

Under the IWS10% scenario, irrigation management for summer maize is relatively lenient. The irrigation water percentages during the initial growth period, fast development period, middle growth period, and maturity stages respectively account for 11.91%, 50.22%, 32.57%, and 5.30% of the total irrigation volume. Compared to the AI scenario, the irrigation water volume remains unchanged for the initial growth period but decreases by 24.1 mm for the fast development period, with no change for the middle growth period and maturity stages. Summer maize needs a lot of water during its fast development period, which is very important for its growth. The irrigation percentages during the middle growth period and maturity stages are 32.57% and 5.30%, respectively. While irrigation water volume decreases for each growth stage compared to the AI scenario, overall, normal growth of summer maize can still be ensured.

As the degree of water shortage increases, significant changes occur in irrigation water allocation. Under the IWS20% scenario, the irrigation water percentages during the initial growth period, fast development period, middle growth period, and maturity stages respectively become 14.89%, 37.77%, 40.72%, and 6.63% of the total irrigation volume. Compared to the AI scenario, irrigation water volume decreases by 63.94 mm for the fast development period, with no change for other stages. Under the IWS30% scenario, the irrigation water percentages during the initial growth period, fast development period, middle growth period, and maturity stages respectively become 17.01%, 29.42%, 46.53%, and 7.57% of the total irrigation volume. Compared to the AI scenario, irrigation water volume decreases by 83.11 mm for the fast development period, with no change for other stages. The irrigation volume gradually decreases during the fast development period while increasing during the middle growth period, as summer maize becomes more reliant on irrigation during the middle growth periodto ensure normal development of the ears under reduced water availability.

When the water shortage scenario reaches IWS40%, the irrigation water percentages during the initial growth period, fast development period, middle growth period, and maturity stages respectively become 18.10%, 28.51%, 44.56%, and 8.83% of the total irrigation volume. Compared to the AI scenario, irrigation water volume decreases by 90.06 mm for the fast development period and shows noticeable decreases for the initial growth period and middle growth period. This indicates severe restrictions on summer maize growth under severe water shortage conditions, necessitating strict control over irrigation water volume during each growth stage.

In the extreme water shortage scenario of IWS50%, the irrigation water percentages during the initial growth period, fast development period, middle growth period, and maturity stages respectively become 17.75%, 27.96%, 43.70%, and 10.60% of the total irrigation volume. Compared to the AI scenario, irrigation water volume decreases by 96.29 mm for the fast development period and shows significant decreases for the middle growth period. This demonstrates the need for stringent control over irrigation water volume during each growth stage to ensure the basic growth requirements of summer maize under extreme water shortage conditions.

Under different water shortage conditions, the optimal water allocation for each growth stage of spring maize in the Shannan region is illustrated in Figure 10.

Under the IWS10% scenario, irrigation water for the initial growth period, fast development period, middle growth period, and maturity stages respectively accounts for 1.24%, 49.76%, 7.44%, and 41.56% of the total irrigation volume. Compared to full irrigation, there is no reduction in irrigation water for the initial growth period, fast development period, and middle growth period, while irrigation water during the maturity stage decreases by 23.41 mm. As the water shortage intensifies to IWS20%, irrigation water for the initial growth period, fast development period, middle growth period, maturity respectively becomes 1.55%, 62.20%, 9.31%, and 26.95% of the total irrigation volume. Compared to full irrigation, irrigation water during the maturity stage decreases by 54.71 mm, while irrigation water for other stages remains unchanged. With further increase in water

TABLE 5 Optimal allocation of irrigation water under different water shortage rates (unit:mm).

	Partition	①	②	③	④	Yield reduction rate
AI	Shanbei	7.63	116.60	30.66	220.29	—
	Guanzhong	23.72	124.13	64.88	10.56	—
	Shannan	1.94	77.88	11.65	88.45	—
IWS10	Shanbei	7.63	116.60	30.66	182.76	1.92%
	Guanzhong	23.72	100.03	64.88	10.56	3.54%
	Shannan	1.94	77.88	11.65	65.04	3.14%
IWS20	Shanbei	7.63	116.60	30.66	145.25	4.22%
	Guanzhong	23.72	77.90	64.88	10.56	7.49%
	Shannan	1.94	77.88	11.65	47.65	6.22%
IWS30	Shanbei	7.63	116.60	30.66	107.73	7.14%
	Guanzhong	23.72	55.76	64.88	10.56	12.51%
	Shannan	1.94	77.88	11.65	30.26	10.54%
IWS40	Shanbei	7.63	116.60	30.66	70.21	11.16%
	Guanzhong	23.72	38.44	60.07	10.56	19.42%
	Shannan	1.94	67.54	11.65	23.21	16.63%
IWS50	Shanbei	7.63	111.04	30.66	38.24	17.81%
	Guanzhong	19.87	31.30	48.93	10.56	27.57%
	Shannan	1.94	54.60	11.65	18.76	23.53%

shortage to IWS30%, irrigation water for the initial growth period, fast development period, middle growth period, maturity respectively becomes 1.77%, 65.20%, 10.63%, and 22.40% of the total irrigation volume. Compared to full irrigation, irrigation water for the fast development period decreases by 6.45 mm, and for the maturity stage by 63.91 mm. When the water shortage reaches IWS40%, irrigation water for the initial growth period, fast development period, middle growth period, maturity respectively becomes 2.06%, 63.66%, 12.41%, and 21.87% of the total irrigation volume. Compared to full irrigation, irrigation water for the fast development period decreases by 18.10 mm, and for the maturity stage by 67.91 mm. Under the IWS50% scenario, irrigation water for the initial growth period, fast development period, middle growth period, maturity respectively becomes 2.48%, 61.51%, 14.89%, and 21.13% of the total irrigation volume. Compared to full irrigation, irrigation water for the fast development period decreases by 29.75 mm, and for the maturity stage by 71.91 mm.

In summary, under mild water shortage conditions, irrigation strategies mainly focus on meeting the water requirement during the maturity stage. However, as the water shortage worsens, irrigation strategies adjust by reducing water usage during other growth stages, prioritizing the water requirement during the fast development period and maturity stages.

When analyzing the impact of different irrigation water shortages on the yield of spring maize in the Shaanxi region, significant differences in yield reduction rates were observed among Shanbei, Guanzhong, and Shannan, as shown in Table 5. These differences are not only related to the extent of reduction in irrigation water but also closely related to the crop growth characteristics, sensitive periods to water, and adjustments in irrigation strategies in each region.

Under the IWS10% scenario, the reduction rates in the Shanbei, Guanzhong, and Shannan are relatively low, at 1.92%, 3.54%, and 3.14%, respectively. This indicates that under mild water shortages, the impact on spring maize yield is minimal. However, as the irrigation water shortage increases, the reduction rates gradually rise. When the irrigation water shortage reaches IWS20%, the reduction rates in the Shanbei, Guanzhong, and Shannan increase to 4.22%, 7.49%, and 6.22%, respectively. It can be observed that the increase in reduction rate in the Guanzhong region is significant, which may be due to the higher sensitivity of summer maize in this region to water. With further exacerbation of the water shortage to the IWS30% scenario, the reduction rates in Shanbei, Guanzhong, and Shannan reach 7.14%, 12.51%, and 10.54%, respectively. At this point, the reduction rate in the Guanzhong region is significantly higher than that in Shanbei and Shannan, indicating a stronger sensitivity of spring maize to water shortage in this region. Under even more severe water shortage conditions, namely IWS40% and IWS50%, the reduction rates in the Shanbei, Guanzhong, and Shannan continue to increase. Particularly in the Guanzhong region, under the IWS50% scenario, the reduction rate reaches 27.57%, becoming the most severely affected area among the three regions.

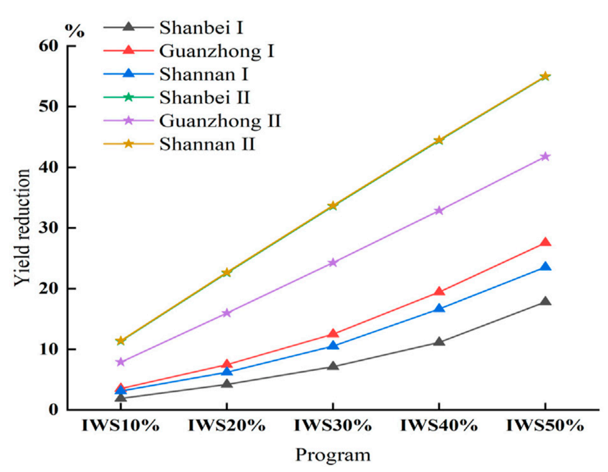

FIGURE 11
Changes in the reduction rate of corn in different regions of Shaanxi Province.

As shown in Figure 11, “I” represents the optimized model, while “II” represents the unprocessed model. The maize reduction rates after model processing are much lower than those without model processing, where irrigation water is proportionally allocated. This indicates that through scientific adjustments and optimization of irrigation strategies, it is possible to effectively reduce maize reduction rates under the same reduced irrigation water conditions. The optimal solutions obtained after model processing show that, under water shortage conditions, the Guanzhong region suffers the most severe reduction in yield. This is mainly because the summer maize in the Guanzhong region has a high sensitivity index to water, especially during the fast development period, where the requirement for water and sensitivity are significant. Therefore, under water shortage conditions, the yield of summer maize in the Guanzhong region is more easily affected. In comparison, spring maize in Shanbei and Shannan can adjust irrigation strategies to prioritize the water supply for growth stages with higher water requirement, thereby mitigating the impact of water shortage on yield to some extent.

In summary, the application of irrigation optimization models can effectively reduce reduction rates while also allowing for the development of more scientifically reasonable irrigation strategies tailored to the characteristics of different regions and maizes to address the challenge of water scarcity. This is of great significance for ensuring food security and improving the efficiency of agricultural water resource utilization.

5 Discussions

5.1 Feasibility analysis

Factors affecting maize water requirements in the field include meteorological conditions (Msowoya et al., 2016; Zakaria, 2017), soil properties (Silva et al., 2020; Balnco-Canqui et al., 2012), maize cultivation structure (Zhang et al., 2020; Huang et al., 2017), field management measures (Shinde et al., 2020), and so on. The water requirements of maizes vary greatly at different growth stages. In Shaanxi Province, spring maize and summer maize planting face significant seasonal climate differences due to different sowing times. Spring maize is planted at the end of March or early April, when precipitation is generally low in spring, resulting in a greater requirement for water during the initial growth period. Summer maize is planted in early June, when summer precipitation is abundant, which to some extent reduces the water requirement of maizes. Therefore, in the initial growth period, the irrigation water requirement of summer maize planted in the Guanzhong region is significantly lower than that of spring maize planted in the northern and southern regions of Shaanxi due to more precipitation. This difference is not only reflected in the irrigation water requirements but also in the overall growth condition of maizes. In Shanbei and Shannan, due to insufficient spring precipitation, spring maize often requires more irrigation during the initial growth period to ensure normal growth. In the Guanzhong region, however, summer maize benefits from abundant summer precipitation and relatively higher soil moisture content, resulting in better growth conditions.

The difference in sowing time leads to differences in the number of days, rainfall, evapotranspiration, and other factors during the growth stages. This, in turn, results in significant differences in the proportion of irrigation water in the entire growth stage for the same growth stage. Taking summer maize in the Guanzhong region and spring maize in Shanbei and Shannan as examples, although they all go through the maturity stage, the irrigation requirement during this stage varies significantly due to different sowing times. During the maturity stage, summer maize in the Guanzhong region requires only 4.8% of the total irrigation water due to abundant summer rainfall and relatively high soil moisture content. In contrast, spring maize in Shanbei and Shannan requires 58.8% and 50.9% of the total irrigation water, respectively, due to less spring precipitation and lower soil moisture content. This difference in irrigation requirement should take into account the difference in water sensitivity index and sowing time when allocating irrigation water. The water sensitivity index reflects the sensitivity of maizes to water at different growth stages, while sowing time differences determine the rainfall, evapotranspiration, and other conditions at different growth stages. Only by considering these two factors comprehensively can we formulate more scientifically sound irrigation plans to ensure that maizes receive adequate water supply at all growth stages, thereby achieving high yields and efficiency.

According to the “Water Consumption Quota for Industrial Water Use in Shaanxi Province” data, the calculated irrigation water requirement in this paper is close to the data in the quota, particularly in the 75% hydrological year. However, there is a significant difference in the 25% hydrological year. This is mainly because some areas in the quota have zero irrigation quotas, while actual investigations have found that these areas still require partial supplementary irrigation. Therefore, the calculated results in this paper are relatively larger than those in the quota. Other research results (Shang et al., 2022; Liu et al., 2021) also show that the calculated irrigation water requirement in this paper is similar to the results of existing studies, indicating that the research results in this paper are relatively reliable and can provide basic support for the formulation and management of irrigation quotas in maize planting areas in Shaanxi Province.

5.2 Policy recommendations

(1) In Shaanxi Province, maize production accounts for 49.51% of agricultural grain production. When facing a shortage of irrigation water and aiming to minimize the reduction in yield, the optimal allocation of irrigation water should prioritize ensuring water supply during the middle growth period, fast development period, and initial growth period for spring maize in Shanbei and Shannan, while for summer maize in the Guanzhong region, irrigation water should be ensured during the initial growth period, middle growth period, and maturity stages.

(2) The maize planting area in Shaanxi Province accounts for 24.30% of the sown area of grain maizes, with the majority of suitable planting areas located in the Guanzhong region. Under the same water shortage conditions, the Guanzhong region has the highest reduction rate in yield, followed by Shannan, and the lowest in Shanbei. To ensure the maize yield in Shaanxi Province, irrigation water for maize in the Guanzhong region must be prioritized.

(3) The advancement of science and technology drives the continuous improvement of water-saving irrigation techniques. Combining the climatic characteristics, geological conditions, and hydrological conditions of different regions in Shaanxi Province, suitable irrigation techniques should be selected to promote the increase in maize yield and quality, thus achieving efficient water-saving in the region and high yield and production of maizes.

5.3 Outlook

The article analyzes the spatial and temporal distribution of effective rainfall, water requirement, and irrigation water requirement in Shaanxi Province. It also explores the optimal allocation of irrigation water under conditions of insufficient water supply, aiming to minimize grain yield reduction. This analysis provides some theoretical support for maize cultivation in Shaanxi Province to cope with drought to a certain extent. However, in calculating the overall water requirement for maize cultivation in the province, the impact of terrain and topography in different regions of Shaanxi Province has not been considered, nor have factors such as cropping structure, crop rotation techniques, and the use of agrochemicals on soil water structure, soil nutrient content, and their influence on crop growth trends. Further research is needed to delve into these aspects in future studies.

6 Conclusion

The study analyzed the spatiotemporal distribution characteristics of effective rainfall, water requirement, and irrigation water requirement for maize in Shaanxi Province, based on meteorological data from 34 weather stations in the province combined with the crop coefficient method. The ideal water quantity under full irrigation in Shaanxi Province was obtained from the basic data. However, considering the scarcity of water resources in the region, agricultural water shortages are a challenge. Therefore, this study, based on the ideal irrigation water quantity, set different water scarcity scenarios. It employed the Jensen model to construct an optimization model with the objective of minimizing grain yield reduction, and solved it using a genetic algorithm to obtain optimized irrigation regimes for maize under different water scarcity scenarios. The main conclusions are as follows:

(1) The effective rainfall during the maize growing seasons in Shaanxi Province from 1960 to 2019 ranged from 206.05 to 447.93 mm, showing a slight increasing trend. The water requirement for maize ranged from 546.46 to 703.42 mm, showing a decreasing trend, similar to the trend observed for irrigation water requirement, which also decreased over time. The maximum irrigation water requirement occurred in 1997, reaching 476.45 mm, while the minimum was in 1983, at only 139.02 mm. This variation may be attributed to abundant rainfall and sufficient soil moisture in 1983.

The spatial distribution of irrigation water requirement for maize in Shaanxi Province showed a decreasing trend from north to south. High-demand areas were mainly located in the northern parts of Yulin and Yan'an cities in northern Shaanxi. These areas are typically located on the Loess Plateau, characterized by arid climates and scarce rainfall, leading to a high dependency on irrigation for maize growth. Low-demand areas were distributed in Ankang City in Shannan. The humid climate and abundant rainfall in Shannan provide relatively sufficient natural water supply for maize growth, resulting in lower irrigation water requirement in these areas. This distribution pattern is closely related to the climate conditions, topography, and maize planting structure in Shaanxi Province.

(2) For spring maize in Shanbei and Shannan, it is crucial to ensure water supply during the middle growth period, fast development period, and initial growth periods, while irrigation water during the maturation stage can be moderately reduced. When irrigation water is reduced by 30%, Shannan needs to reduce irrigation water during the fast development period and maturation stages, while for summer maize in the Guanzhong region, irrigation during the fast development period is reduced first under water shortage conditions. When facing severe water shortages, irrigation during the initial growth period, fast development period, and middle growth period is successively reduced. Under the same water scarcity conditions, the reduction in yield in the Guanzhong region is much greater than in Shanbei and Shannan.

(3) From the analysis of yield reduction rates, under the same water scarcity conditions, the Guanzhong region had the highest reduction rate, followed by Shannan, and Shanbei had the lowest reduction rate. This is because when facing water shortages, spring maize in Shanbei and Shannan first reduces irrigation during the maturation stage with a water sensitivity index of 0.10, while summer maize in the Guanzhong region reduces irrigation during the fast

development period with a water sensitivity index of 0.17. The higher the water sensitivity index, the higher the reduction in yield under water scarcity conditions. Therefore, under the conditions of IWS30% (30% irrigation water shortage), IWS40% (40% irrigation water shortage), and IWS50% (50% irrigation water shortage), the reduction rate in Shannan is significantly higher than in Shanbei, even though both regions plant spring maize.

Data availability statement

The original contributions presented in the study are included in the article/supplementary material, further inquiries can be directed to the corresponding author.

Author contributions

KC: Conceptualization, Data curation, Methodology, Resources, Validation, Visualization, Writing–original draft. KL: Software, Supervision, Validation, Writing–review and editing. XF: Conceptualization, Formal Analysis, Writing–review and editing.

Funding

The author(s) declare financial support was received for the research, authorship, and/or publication of this article. This work was supported by Scientific Research Project of the PowerChina ChongQing Engineering Corporation Limited [QKY2023-CQ-02-03].

Acknowledgments

We sincerely thank all individuals and institutions that have contributed to this research. Special thanks go to PowerChina ChongQing Engineering Corporation Limited for providing the (QKY2023-CQ-02-03) project funding, which is crucial to our research. We are deeply grateful for the use of NSGA-II in our article; it has made us more efficient in solving single-objective problems and has provided strong support for exploring the optimization of corn irrigation scheduling in Shaanxi Province. We appreciate the technical support throughout the research process, which played a key role in the successful completion of the article. Finally, we express our sincere gratitude to the editors and reviewers of Frontiers for their valuable comments and suggestions, which greatly improved the quality of our paper.

Conflict of interest

Authors KC, KL, and XF were employed by PowerChina HuaDong Engineering Corporation Limited. Authors KC, KL, and XF were employed by PowerChina ChongQing Engineering Corporation Limited.

Publisher's note

References

Allen, R. G., Pereira, L. S., Raes, D., and Smith, M. (1998). *Crop evapotranspiration-guidelines for computing crop water requirements-FAO irrigation and drainage paper 56.* Rome: Fao.

Ashkan, T., Naghi, A. Z., and Mohammadreza, S. N. (2023). Irrigation scheduling of walnut seedlings using HYDRUS-1D and Taguchi optimization approach. *J. Irrigation Drainage Eng.* 149 (1). doi:10.1061/(ASCE)IR.1943-4774.0001735

Blanco-Canqui, H., Claassen, M. M., and Presley, D. R. (2012). Summer cover crops fix nitrogen, increase crop yield, and improve soil–crop relationships. *Agron. J.* 104 (1), 137–147. doi:10.2134/agronj2011.0240

Gao, F. K., Wang, L., Li, X. G., Ning, H. F., Han, Q. S., Liu, H., et al. (2023). Effects of spring lrrigation on water and salt distribution in soil and cotton growth in southern Xinjiang. *J. Irrigation Drainage* 42 (01), 54–63. doi:10.13522/j.cnki.ggps.2022404

Gu, X., Liu, K., Gao, J., and Liu, L. J. (2022). Research advances of water-saving lrrigation methods and their influences on rice yield. *Hybrid. Rice* 37 (02), 7–13. doi:10.16267/j.cnki.1005-3956.20210715.256

Guo, Y. B., Feng, H., and Wu, P. T. (2007). Research progress on deficit irrigation diagnosis index of crop. *Chin. Agric. Sci. Bull.* (08), 520–525. doi:10.3969/j.issn.1000-6850.2007.08.114

Guo, Y. F., Huo, Y. Z., and Wang, W. D. (2017). A study on water consumption law and lrrigation regime for alfalfa. *Water Sav. Irrig.* (03), 8–10+13. doi:10.3969/j.issn.1007-4929.2017.03.003

Huang, S. B., Gao, Y. B., Li, Y. B., Xu, L. N., Tao, H. B., Wang, P., et al. (2017). Influence of plant architecture on maize physiology and yield in the Heilonggang River valley. *Crop J.* 5 (1), 52–62. doi:10.1016/j.cj.2016.06.018

Kang, S. Z., Zhang, X. L., He, Z. Z., and Zhang, X. (1990). Research on the isoline map of corn water requirement and division of irrigation zone in shaanxi povince. *J. Water Resour. Water Eng.* (03), 19–34.

Li, H. M., and Fan, J. Z. (2015). Analysis on meteorological drought characteristics of corn growing period in Guanzhong Summer. *J. Shaanxi Meteorology* (04), 1–5.

Li, T., Kang, S. Z., and Su, X. L. (2005). Advances in research on the crop optimal irrigation scheduleand water allocating models. *J. Northwest A and F Univ. Sci. Ed.* (12), 148–152+158. doi:10.13207/j.cnki.jnwafu.2005.12.031

Liang, W. Q., Cai, H. J., and Wang, J. (2011). Experimental study on crop coefficient of maize in Guanzhong region of shaanxi province. *Water Sav. Irrig.* (12), 1–4.

Liu, H., Zhang, X. L., Wang, Y. X., Guo, Y., Luo, J. M., and Shen, Y. J. (2021). Spatio-temporal characteristics of the hydrothermal conditions in the growth period andvarious gro wth stages of maize in China from 1960 to 2018. *Chin. J. Eco-Agriculture* 29 (08), 1417–1429. doi:10.13930/j.cnki.cjea.201009

Ma, C., Wu, T. A., Zhang, W. Z., Li, J., and Jiao, X. Y. (2024). Optimization of multi-objective irrigation schedule for rice based on AquaCrop model. *J. Irrigation Drainage* 43 (01), 9–16. doi:10.13522/j.cnki.ggps.2023279

Martínez-Romero, A., López-Urrea, R., Montoya, F., Pardo, J. J., and Domínguez, A. (2021). Optimization of irrigation scheduling for barley crop, combining AquaCrop and MOPECO models to simulate various water-deficit regimes. *Agric. Water Manag.* 258, 107219. doi:10.1016/J.AGWAT.2021.107219

Msowoya, K., Madani, K., Davtalab, R., Mirchi, A., and Lund, J. R. (2016). Climate change impacts on maize production in the warm heart of africa. *Water Resour. Manag.* 30 (14), 5299–5312. doi:10.1007/s11269-016-1487-3

Qin, X. J., Wang, Y., and HangFu, H. L. (2016). Summary of comparative experiment of spring maize with different sowing dates in Weibei upland of Shaanxi province. *Agric. Technol.* 36 (02), 77. doi:10.11974/nyyjs.20160133062

Reta, B. G., Hatiye, S. D., and Finsa, M. M. (2024). Crop water requirement and irrigation scheduling under climate change scenario, and optimal cropland allocation in lower kulfo catchment. *Heliyon* 10 (10), e31332. doi:10.1016/J.HELIYON.2024.E31332

Shang, M. F., Zhao, J. C., Han, T., Li, S., Wang, K. C., Gao, Z. Z., et al. (2022). Temporal and spatial variation of maize water requirement and water surplus and deficitin China from 1961 to 2020. *J. China Agric. Univ.* 27 (04), 22–30. doi:10.11841/j.issn.1007-4333.2022.04.02

Shinde, M. G., Pawar, D. D., Kale, K. D., and Dingre, S. K. (2020). Performance of cabbage at different irrigation levels under drip and microsprinkler irrigation systems. *Irrigation Drainage* 70 (4), 581–592. doi:10.1002/IRD.2557

Silva, P. C. G., Tiritan, C. S., Echer, F. R., Cordeiro, C. F. S., Rebonatti, M. D., and Santos, C. H. (2020). No-tillage and crop rotation increase crop yields and nitrogen stocks in sandy soils under agroclimatic risk. *Field Crops Res.* 258, 107947. doi:10.1016/j.fcr.2020.107947

Wang, B., Fan, C., Bai, L. Q., Wang, J., and Wu, C. L. (2022). Precise management mode of controlled rice irrigation in Changgang lrrigationDistrict of Heilongiiang Province. *Water Resour. Dev. Res.* 22 (09), 35–40. doi:10.13928/j.cnki.wrdr.2022.09.008

Wang, H. B., Tian, J. C., Song, L. L., and Wang, C. J. (2014). Research on the theories and process of crop optimal lrrigation schedules. *China Rural Water Hydropower* (06), 21–25. doi:10.3969/j.issn.1007-2284.2014.06.006

Wang, J. X., Xing, X. J., Zhang, L. J., and Liu, Y. K. (2011). Empirical research on the change of irrigation management patterns and its impacts on crop water use. *Geogr. Res.* 30 (09), 1683–1692. doi:10.11821/yj2011090012

Wang, K. Q., Fu, Q., Ji, F., and Xu, S. Q. (2007). Study on rice water production function and optimization of lrrigation schedule of semiarid area of western Heilongjiang province. *Water Sav. Irrig.* (08), 48–51. doi:10.3969/j.issn.1007-4929.2007.08.017

Wang, X. D., Ma, X. Q., Xu, Y., and Chen, C. (2013). Temporal analysis of the crop water surplus deficit indexfor the whole growth period in the huaihe basin. *Resour. Sci.* 35 (03), 665–672.

Xiao, J. F., Liu, Z. D., and Chen, Y. M. (2008). Study on the water requirement and water requirement regulation of maize in China. *J. Maize Sci.* (04), 21–25.

Yao, D. L., Gao, F., Li, Z. J., and Hu, T. T. (2018). Water supply and requirement of winter wheat and summer maize in Yangling. *Agric. Res. Arid Areas* 36 (01), 115–120+163. doi:10.7606/j.issn.1000-7601.2018.01.18

Zakaria, M. S. (2017). Climatic variables:Evaporation, sunshine, relative humidity,soil and air temperature and its adverse effects on cotton production. *Inf. Process. Agric.* 5 (1). doi:10.1016/j.inpa.2017.09.006

Zhang, J., Zhang, H., Chen, D. D., Li, G. L., Zhang, J. T., Zang, H. Z., et al. (2020). Spatial and temporal distribution characteristics of effective rainfall and water requirement of summer maize growth period in henan province. *J. Henan Agric. Sci.* 49 (09), 173–180. doi:10.15933/j.cnki.1004-3268.2020.09.022

Zhang, L., Chen, F., and Lei, Y. (2020). Climate change and shifts in cropping systems together exacerbate China's water scarcity. *Environ. Res. Lett.* 15 (10), 104060. doi:10.1088/1748-9326/abb1f2

Zhang, L., Zhou, W., and Li, D. X. (2019). Research progress in irrigation mode selection of high-efficiency water-saving agriculture. *J. Drainage Irrigation Mach. Eng.* 37 (05), 447–453. doi:10.3969/j.issn.1674-8530.18.0135

Zhang, X., and Hu, B. G. (2021). Application of agricultural water-saving irrigation technology in China:research progress. *Chin. Agric. Sci. Bull.* 37 (26), 153–158. doi:10.11924/j.issn.1000-6850.casb2021-0010

frontiers | Frontiers in Environmental Science

TYPE Original Research
PUBLISHED 13 January 2025
DOI 10.3389/fenvs.2024.1519807

OPEN ACCESS

EDITED BY
Xudong Huang,
North China University of Water Conservancy and Electric Power, China

REVIEWED BY
Brian Njoroge,
Chinese Academy of Sciences (CAS), China
Putu Aryastana,
Universitas Warmadewa, Indonesia

*CORRESPONDENCE
Limin Yuan,
✉ nmgyuanlm@163.com

RECEIVED 30 October 2024
ACCEPTED 24 December 2024
PUBLISHED 13 January 2025

CITATION
Bao Z, Yuan L, Meng Z, Zhang E, Zhu L and Liu J (2025) Soil moisture partitioning strategies in blowouts in the Hulunbeier grassland and response to rainfall.
Front. Environ. Sci. 12:1519807.
doi: 10.3389/fenvs.2024.1519807

Soil moisture partitioning strategies in blowouts in the Hulunbeier grassland and response to rainfall

Zhixin Bao[1], Limin Yuan[2,3,4]*, Zhongju Meng[1], Ezhen Zhang[1], Lei Zhu[1] and Jinwang Liu[1]

[1]College of Desert Control Science and Engineering, Inner Mongolia Agricultural University, Hohhot, Inner Mongolia, China, [2]Inner Mongolia Science and Technology Innovation Center of Forestry and Grassland, Hohhot, Inner Mongolia, China, [3]Inner Mongolia Autonomous Region Key Laboratory of Sandy (Desert) Ecosystem and Ecological Engineering, Hohhot, Inner Mongolia, China, [4]Key Laboratory of Conservation and Cultivation of Biological Resources in Sandy Land, National Forestry and Grassland Administration, Hohhot, Inner Mongolia, China

Introduction: Soil moisture and soil water retention capacity are key influencing factors for the normal growth and development of vegetation. Understanding the dynamic change characteristics of soil moisture in blowouts and soil water retention capacity is of great significance for the management of blowouts.

Methods: This study employs drying and *in situ* monitoring methods to select typical blowouts in different regions (sand pits, fringe zones, sand accumulation zones, and sand-grass transition zones) on the Hulunbuir Grassland. A large area of natural grassland surrounding these regions was chosen as the control (CK). Soil moisture at depths of 20, 40, 60, 100 and 200 cm below the surface was measured along the soil profile using the ECH$_2$O-10HS soil moisture automatic monitoring instrument. The HOBO-RG3-M self-recording rain gauge was used to monitor rainfall. Soil water storage, coefficient of variation, and Pearson's correlation coefficient were calculated to study the differences in soil moisture and the dynamic change regularity in soil moisture under different rainfall conditions. This research provides important theoretical support for the soil moisture distribution and vegetation restoration in the blowouts of the Hulunbuir Grassland.

Results and discussion: The volumetric water content of the soil in the blowouts was 15.95%, the volumetric soil water content in different parts of the soil varied from low to high as follows: sand pit-I < sand-grass transition zone-IV < fringe zone-II < CK < sand accumulation zone-III. The soil volumetric water content of the 0–40 cm soil layer of the blowout was higher than 17.47%, and the soil volumetric water content of the 40–200 cm soil layer ranged from 12.13% to 17.47%. The volumetric water content of soil in various parts of the blowouts under different rainfall amounts had significant differences, with rainstorms and heavy rainfall effectively recharging the blowouts to a depth of 200 cm, and the blowouts responded strongly to heavy rainfall (71.5 mm). A gradual recovery of the pre-rainfall volumetric soil moisture content was seen approximately a week after rainstorms. The water retention and storage capacity of blowout soils was significantly higher than that of CK, the soil water storage capacity of different zones ranked in descending order as the sand accumulation zone (1875.38 mm) > edge zone (1373.22 mm) > CK (1188.36 mm) > sand pit (1000.39 mm) >

sand–grass transition zone (803.90 mm). The correlation coefficient of sand pits and sand cover was 0.5612, and that of sand accumulation zones and sand cover was 0.5845, which confirmed that sand cover enhanced the water retention capacity of the localized area of blowouts (sand accumulation zones).

KEYWORDS

soil volumetric water content, rainfall, soil water storage, blowouts, soil

1 Introduction

Grassland blowouts represent the beginning stage of the formation of grassland mobile dunes. As multiple adjacent blowouts develop, they overlap to form sand bands (Malakouti et al., 1978). The conversion of grassland landscapes to sandy landscapes occurs under the dual action of wind erosion and sand burial (Byrne, 1997). Blowouts form when wind erodes the surface of the grassland and sand accumulates and spreads on the downwind side of the pit under the action of the wind. This results in the "breaching" of the moisture in the grassland soil, which leads to blowouts and extremely dry soil on the downwind side of the soil surface. However, after the rainy season, the area of sand accumulation on the downwind side of the blowouts has the function of water storage. Therefore, studying the changes in soil water content in different parts of these blowouts under rainfall is of great significance to the investigation of the water conservation and storage capacity of such blowouts. Currently, related research on blowouts mainly focuses on their morphological classification (Deren, 2016; Deren et al., 2017; Gares and Nordstrom, 1995; Jungerius, 1984; Kejun et al., 2022; Yanguang et al., 2023; Zhang, 2007; Zhang, 2009; Zhang et al., 2006), mechanical composition (Ruru et al., 2019), airflow field (Ruru et al., 2019), erosion and accumulation characteristics, and influencing factors (Zhang et al., 2007a; Zhang et al., 2007b). Research on the distribution of soil moisture in blowouts and the response of blowouts to rainfall is of great significance to the in-depth understanding of the dynamic changes of soil moisture in blowouts and the water retention capacity of the soil for the management of blowouts. However, its investigation is relatively weak.

Soil water is an important component and key link in terrestrial ecosystems (Wang et al., 2019). Soil moisture dynamics are influenced by rainfall, runoff, evapotranspiration processes, and land-use practices (Luo, 2019). The recharge effect and transport process of soil water content may exhibit significant differences in different regions (Wei et al., 2022). Rainfall is the most important source of soil moisture recharge, and rainfall entering the surface soil water through the process of infiltration alters the original soil moisture distribution pattern, thus affecting the soil water storage capacity (Chen-Mao et al., 2022; Yinglan et al., 2018; Xinle et al., 2019). It is therefore important to study the response mechanism of soil moisture to rainfall. In recent years, many scholars have conducted research in this field. For example, by analyzing the graded response of soil water content to rainfall under different vegetation cover conditions, Chunheng et al. (2020) found that under the same precipitation conditions, the corresponding soil moisture varied greatly depending on the vegetation cover condition, and there was a precipitation threshold for initiating the soil water content response process. Daly and Porporato (2005) illustrated the relationship between rainfall and soil moisture using the Richards equation and the Green–Ampt model. Min et al. (2019) explored the seasonal variation rules and vertical distribution characteristics of soil water content in different land-use types in gently sloping windy and sandy areas of loess hills and found that the soil water content exhibited obvious vertical distribution characteristics. It has been shown that ground cover can insulate surface air, causing changes in surface soil properties that affect water transport (Qi, 2022). Juan (2020) explored the response of desert steppe soil moisture to precipitation and concluded that different classes of single precipitation had significant effects on the soil moisture content under different land cover types and that the timing of heavy precipitation dominated soil moisture, with a resonance relationship between time and soil moisture ranging from 5 to 8 months and 9–16 months. In the Maowusu sand land, precipitation of >8.8 mm can rehydrate the soil layer to a depth of 10 cm, and precipitation of >40 mm can infiltrate the soil layer to a depth of 110 cm (Guangyu et al., 2021). In their study of the response of moisture of the 0–200 cm soil layer to precipitation pulsation in the oil *Artemisia* scrub in the Kubuchi Desert, Bo et al. (2020) found that >8.6 mm rainfall recharged the soil layer to a depth of 30 cm and that 11.8 mm rainfall recharged the soil layer to a depth of 50 cm; the lag of feedback to precipitation was enhanced with the depth of the soil layer In summary, the response of soil moisture to rainfall varies under different vegetation cover conditions.

Blowouts are composed of two main parts: the depression sand pit and the sand material accumulation area. In their sub-part management research on blowouts, Na et al. (2020) proposed the combined use of sand barriers + plant sand fixation in blowout side slopes, edges, and sand accumulation areas. This combined approach increased the wind erosion pit slope vegetation coverage to 27.0%, and the number of plant species in the sand accumulation area reached six. Furthermore, the study of Qu et al. showed that in the rainy season, there was an artificial spread of poplar firewood and sand *Artemisia*, and a natural vegetation cover was formed in response to the integrated sand fixation technology. Thus, it is important to study the dynamic changes of soil moisture and rainfall response of blowouts for blowout management and vegetation restoration. In their study of the heterogeneous effect of soil moisture in wind erosion pits, Liman et al. (2022) showed that after the rainy season, the sand accumulation area of wind erosion pits had a certain "water storage" effect, while the sand pits and the edge area showed a serious "water loss" effect, and the soil was in an extremely dry state, creating conditions conducive for the expansion of wind erosion of sand pits. Wind erosion pits form large areas of quicksand, and the bare sand surface replaces the vegetation cover, which reduces the water loss by vegetation and surface

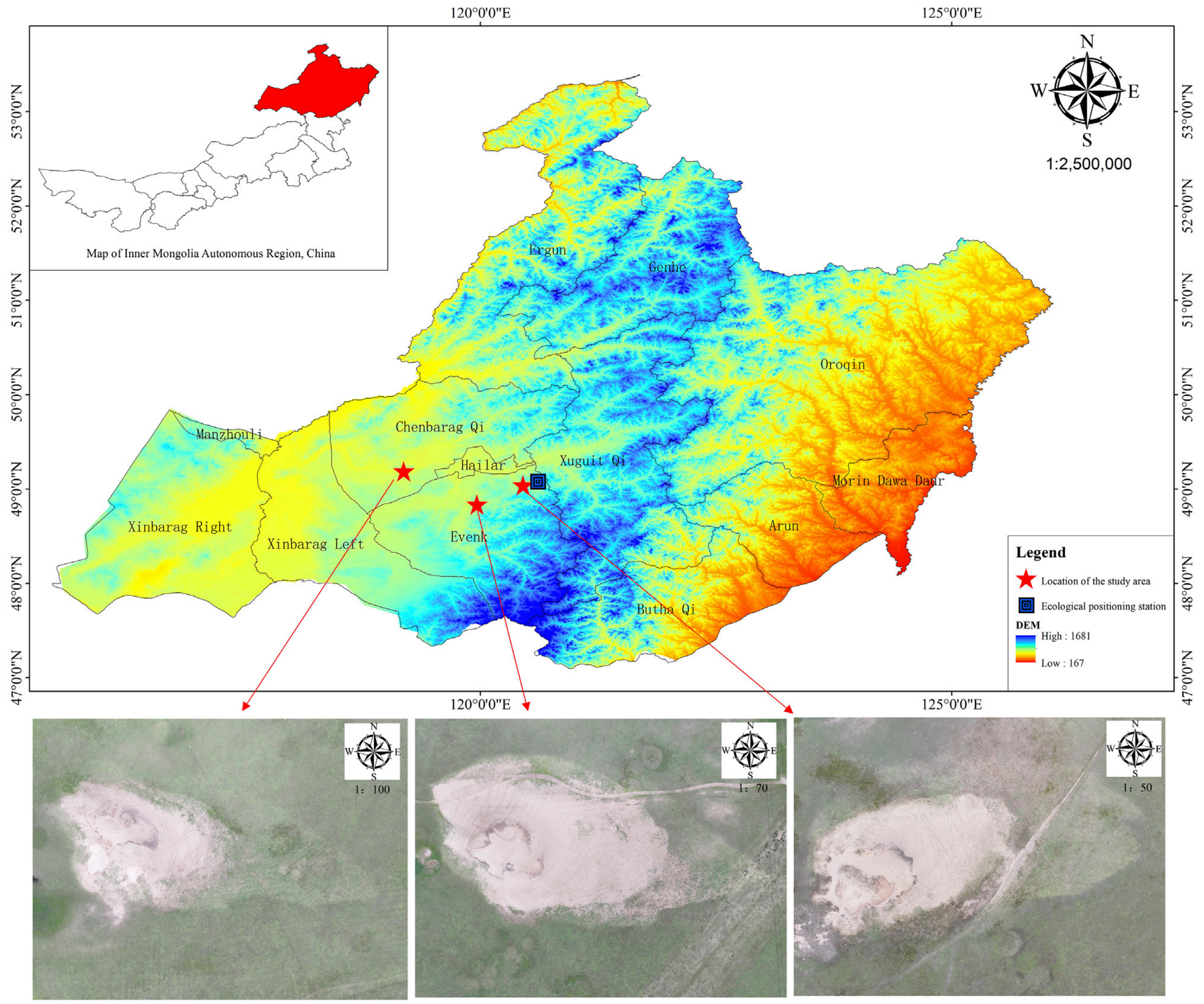

FIGURE 1
Study area location.

runoff, and the dry sand layer effectively locks the deep water. However, further studies are required to find out whether wind erosion pits have a positive effect on the deep water of the grassland under rainfall conditions. To clarify the distribution of the soil moisture content in blowouts and its response to rainfall, the present study selected four representative parts of the blowouts in the Hulunbeier grassland (sand pits, edge zones, sand accumulation zones, and sand–grass transition zones) as the research objects. Then, this study analyzed the dynamic changes of soil moisture in blowouts with natural grassland as the control (CK), compared the differences in soil moisture between different parts of the pits under different rainfall types, and clarified the response mechanism of blowouts to rainfall to determine whether wind pits have a water conservation benefit. This study aimed to (1) compare the differences in soil moisture in different parts of the blowouts under a variety of rainfall conditions; (2) understand the response mechanism of blowouts to rainfall; (3) explore whether blowouts provide the function of water retention; and (4) clarify the effect of blowouts on grassland soil moisture.

2 Material and methods

2.1 Study area

The study area is located in the Hulunbeier sandy grassland (Figure 1). The administrative area belongs to the territory of Ewenke Autonomous Banner, Hulunbeier City, Inner Mongolia Autonomous Region, in the center of the Hulunbeier grassland, south of the Daxing'anling Mountains, with an altitude of 691.10 m. The geographic coordinates of the study area are 120°45′30″–120°45′47″E, 49°03′67″–49°03′73″N. Ewenke Autonomous Banner has a temperate semi-arid continental climate, with dry and windy winters, mild and short summers, and precipitation concentrated in June–September. The average annual temperature ranges from −3.9°C to 1.2°C, and the average annual precipitation is 332.2 mm. The study area is located in the eastern part of Ewenke Autonomous Region, where black calcareous soil predominates, and the interior of the study area is dominated by sandy and windy soils, with residual

TABLE 1 Basic situation of blowouts.

Typical areas	Serial number	Sand thickness (cm)	Vegetation cover (%)	Soil water capacity (g·cm^{-3})	Total porosity (%)
Sand pit	I	80–84	0	1.61	32.51
Edge	II	0	40	1.60	35.01
Sand belt	III	40–50	3	1.61	31.48
Sand–grass transition zone	IV	6–10	50	1.61	34.11
CK	V	0	60	1.63	32.94

TABLE 2 Mechanical composition of blowouts.

Typical areas	Sand pit	Edge	Sand belt	Sand–grass transition zone	CK
Serial number	I	II	III	IV	V
Sticky particles/%	0.65 ± 0.08c	0.75 ± 0.05bc	0.75 ± 0.02bc	0.97 ± 0.01a	0.89 ± 0.23ab
Powdery grain/%	5.65 ± 0.73c	7.23 ± 0.75c	7.23 ± 0.37c	16.72 ± 1.77b	23.2 ± 3.78a
Very fine sand/%	0 ± 0b	0 ± 0b	0 ± 0b	0.18 ± 0.09a	1.37 ± 0.88b
Fine sand/%	21.1 ± 0.61a	16.55 ± 1.09bc	16.7 ± 0.51c	14.97 ± 0.47b	13.58 ± 1.43b
Medium sand/%	60.65 ± 0.33a	60.88 ± 0.45a	61.06 ± 0.39a	54.75 ± 1.3b	48.8 ± 2.16c
Coarse sand/%	12.04 ± 1.41b	14.58 ± 1.6a	13.99 ± 0.5ab	12.41 ± 0.36b	12.16 ± 0.69b
Very coarse sand/%	0 ± 0a	0 ± 0a	0 ± 0a	0 ± 0a	0 ± 0a

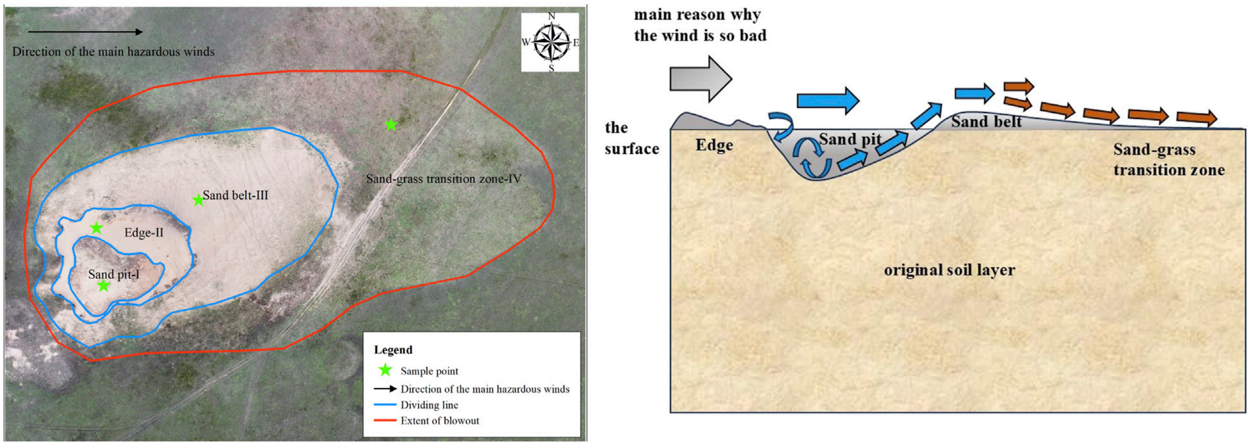

FIGURE 2
Schematic of blowout zoning.

black calcareous soils in some areas. The vegetation is dominated by thyme (*Thymus mongolicus*), stemless cinquefoil (*Potentilla acaulis*), the perennial grass *Cleistogenes squarrosa*, and needleleaf sedge (*Carex duriuscula* subsp. *rigescens*). Sand plants such as wolfsbane (*Stellera chamaejasme*) and fringed sagewort (*Artemisia frigida*) are scattered. The mechanical composition of soils in the area is dominated by medium and fine sands.

Natural grassland (CK) and blowouts in the study area were selected for investigation, the basic conditions of the blowouts were obtained using a field survey (Table 1), and the mechanical composition of the soil is shown in Table 2.

2.2 Sample plot selection and instrument setup

Blowouts are composed of two main parts: the depression sand pit and the sand material accumulation area (Shaoyun and Yuxing,

TABLE 3 Characteristics of different types of rainfall in the study area.

Type of rainfall	Rainfall criteria (mm)	Number of rainfall events	Proportion of total number of rainfall events (%)	Total rainfall (mm)	Proportion of total rainfall (%)
Light rain	0–10	20	60.61	43.50	16.00
Moderate rain	10–25	5	30.30	84.80	31.20
Heavy rain	25–50	2	6.06	72.00	26.49
Torrential rain	50–100	1	3.03	71.50	26.31
Total	0–100	28	100.00	271.80	100.00

2019). As a result, blowouts in the active stage of development can be divided into four typical parts, and the differentiation of each site is significant (Figure 2). According to the characteristics of each area of the investigated blowouts, the soil type, and the vegetation cover condition, the blowouts investigated in this study were divided into four typical parts from inside to outside: the sand pits (I), the edge zone (II), the sand accumulation zone (III), and the sand–grass transition zone (IV). The blowouts in the upwind direction and the natural grassland on the periphery were set as the control (CK). Using the drying method and *in situ* monitoring, the ECH$_2$O-10HS soil moisture automatic monitoring instrument was inserted horizontally along the soil profile to determine the volumetric moisture content and temperature of each soil layer in five sample plots at depths of 20 cm, 40 cm, 60 cm, 100 cm, and 200 cm from the surface in July 2023, with a monitoring frequency of 10 min. The HOBO-RG3-M type self-calculating rain gauge was installed in an open area of the study area to monitor the rainfall, with a data recording interval of 10 min and a measurement accuracy of 0.2 mm. Three blowouts were selected as replicates. The observation period was from 27 July 2023, to 25 September 2023, which was the plant growth period.

2.3 Rainfall characteristics

Rainfall with a large interval of at least 24 h was classified as a separate rainfall event (Ferrarezi et al., 2020). The 24-h rainfall was classified into five categories (Shengyuan, 2015): 0–10 mm was considered light rain; 10–25 mm was considered moderate rain; 25–50 mm was considered heavy rain; and 50–100 mm was considered torrential rain. From July 25 to 25 September 2023, a total of 28 rainfall events occurred in the study area (Table 3). The total rainfall was 271.80 mm, with a single-event minimum of 0.1 mm and a maximum of 71.50 mm. Light rain occurred 20 times, accounting for 60.61% of the total number of rainfall events, and contributed a total of 43.50 mm of the total rainfall, or 16%. Moderate rain occurred 5 times, accounting for 30.30% of the total number of rainfall events, with a total of 84.80 mm, or 31.20% of the total rainfall. Heavy rain occurred twice, accounting for 6.06% of the total number of rainfall events, contributing a total of 72.00 mm of precipitation, or 26.49% of the total. Torrential rainfall occurred the fewest number of times at only one heavy rainfall event, accounting for 3.03% of the total number of rainfall events and contributing 71.50 mm of precipitation, which accounted for 26.31% of the total rainfall. Rainfall data for the observation period (25 July 2023 to 25 September 2023) were obtained from the Hulunbeier Sand Observatory meteorological station near the study area.

2.4 Soil water storage

The amount of water stored in each layer of the soil, as well as the total amount of water stored, can be calculated using the following formula: (Wenfei et al., 2017)

$$SWS = SWC_i \times H_i \times 10$$

where *SWS* is the soil water storage capacity at the measurement depth (mm), SWC_i is the volumetric soil water content at the measurement depth (%), H_i is the thickness of the soil layer (cm), and 10 is the unit conversion factor (mm/cm).

2.5 Calculation of the coefficient of variation (CV)

The CV is a statistical measure of the degree of variability of each observation in the data, defined as the ratio of the sample standard deviation to the mean. In this paper, this index was used to examine the degree of variability of soil moisture between different months. CV < 10% was considered weak variability, 10% ≤ CV ≤ 100% was considered moderate variability, and CV > 100% was considered strong variability. The calculation formula is as follows: (Xueting et al., 2023)

$$CV = \left(\frac{SD}{MN}\right) \times 100\%,$$

where *CV* is the coefficient of variation (%), *SD* is the standard deviation, and *MN* is the mean.

2.6 Calculation of Pearson's correlation coefficient

Pearson's correlation coefficient was proposed by British statistician Pearson in the 20th century, and its formula is as follows: (Guozheng et al., 2023)

$$\rho = \left(\frac{COV(X,Y)}{\sqrt{D(X)}\,\sqrt{D(Y)}}\right)$$

where ρ is the correlation coefficient; COV(X,Y) is the covariance of variables X and Y; and D(X) and D(Y) are the variances of X and Y, respectively

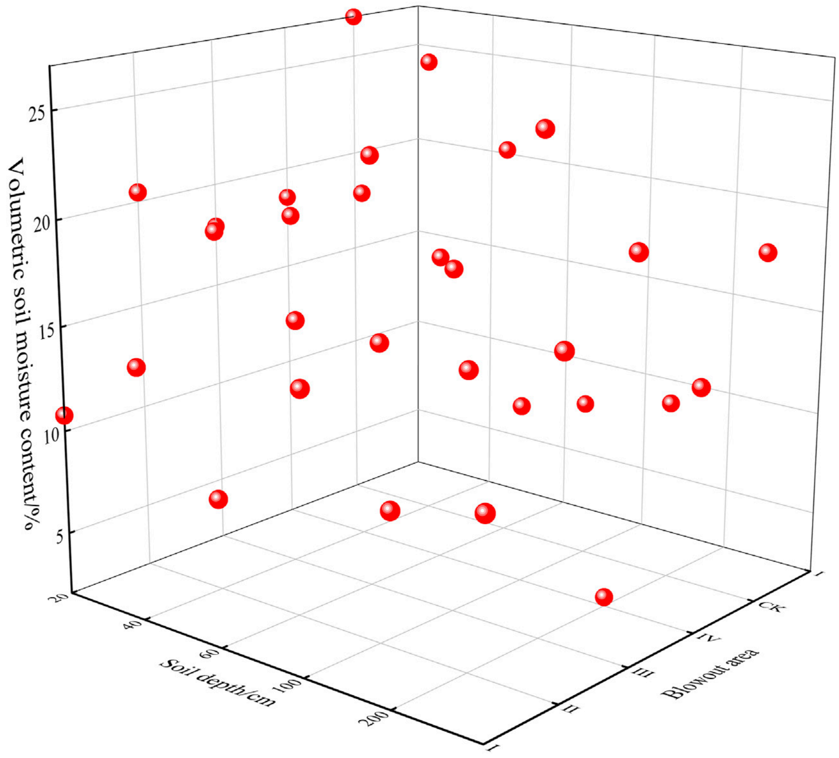

FIGURE 3
Volumetric water content of blowouts and CK soils.

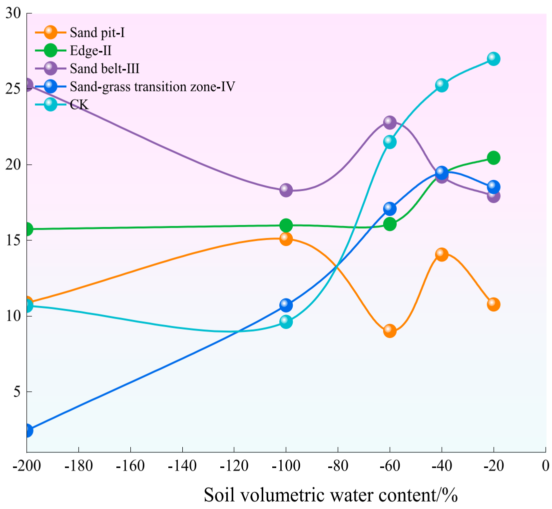

FIGURE 4
Soil volume water content in the vertical profiles of different parts of blowouts.

3 Results

3.1 Soil moisture heterogeneity in various parts of blowouts

Figure 3 displays the soil water content in the 0–200 cm soil layer in typical areas with blowouts. The soil volumetric water content did not differ significantly in different parts of the blowouts. The soil volumetric water contents in different parts of the pit were ranked from lowest to highest as follows: sand pit (I) < sand–grass transition zone (IV) < edge zone (II) < CK < sand accumulation zone (III). The soil volumetric water content of the sand accumulation zone (III) increased by 10.09% compared with CK, whereas the soil volumetric water contents of the sand pit (I), edge zone (II), and sand–grass transition zone (IV) decreased by 36.38%, 6.80%, and 27.45%, respectively, compared with CK. The mean value of the volumetric water content of blowout soil was 15.95%, which was decreased by 15.13% compared with CK.

With the deepening of the soil layer, the volumetric water content of the soil from 0 to 200 cm in different parts of the blowouts exhibited different degrees of changes (Figure 4). The soil volumetric water content of the sand pit (I) exhibited an M-shaped curve, with peaks of 14.06% and 15.09% at 40 cm and 100 cm, respectively, and the lowest volumetric water content at 60 cm, which was 9.02%. The volumetric water content of the edge zone (II) soil gradually decreased from shallow soil to deeper soil, declining from 20.44% to 15.74%. The volumetric water content of the sand accumulation zone (III) showed an N-shaped curve, with the lowest and highest values of 17.93% and 25.26%, respectively, found at 20 cm and 200 cm, respectively. The volumetric water content of the sand–grass transition zone (IV) gradually decreased below 40 cm, from 19.46% to 2.43%. The soil volumetric water content curve of the CK soil was similar to that of the sand–grass transition zone, but with similar curves found for all soil layers except for the soil at 100 cm, which contained much higher soil volumetric water content than the corresponding layer in the sand–grass transition zone (IV).

TABLE 4 Vertical profile of soil moisture variation in typical areas of blowouts.

Soil depth (cm)	Coefficient of variation (%)				
	Sand pit (zone I)	Edge (zone II)	Sand belt (zone III)	Sand–grass transition (zone IV)	CK
20	21.60	10.26	12.46	8.96	3.79
40	17.63	7.28	16.60	8.68	13.92
60	16.40	11.59	6.19	7.84	6.85
100	11.75	13.95	11.70	14.48	15.27
200	14.39	13.27	4.47	47.00	16.32
Average	16.35	11.27	10.28	17.39	11.23

As can be seen from Table 4, among the different soil layers in different parts of the blowouts, the CV was higher in the 20 cm layer of the sand pit (I) and the sand–grass transition zone (IV), which exhibited CV values of 21.60% and 47.00%, respectively. This result indicates that these two soil layers had a higher degree of dispersion and greater soil moisture fluctuation than the other layers. The soil volumetric water content of the sand pit (I) was moderately variable at all soil layers, and the degree of variability showed a decreasing trend with increasing depth. The soil volumetric water content at 40 cm in the blowout edge zone (II) was weakly variable, while the soil volumetric water contents of the remaining layers were moderately variable, and the degree of variation of the soil volumetric water content rose with the increase in soil depth from 40 cm downward. In the sand accumulation zone (III), the CV from 20 to 40 cm was moderate, the CV in the remaining layers was weak, and the highest CV was 16.60% at 40 cm. The sand–grass transition zone was weakly variable from 20 to 60 cm and moderately variable at 100 cm and 200 cm, but the soil layer at 200 cm had a higher CV, 47.00%, and was the soil layer with the highest CV among all parts of the blowout.

3.2 Response of soil moisture to rainfall in various parts of blowouts

The rainfall amount of 8.2 mm was analyzed as a representative light rainfall event, 15.7 mm was considered a representative moderate rainfall event, 45.3 mm was used as a representative heavy rainfall event, and 71.5 mm was considered a representative torrential rainfall event. Because the response time of each soil layer to rainfall differed, the maximum soil water content within 1 d after the end of rainfall was selected as the post-rainfall data.

The soil volumetric water content in different parts of the blowouts was significantly different under varying amounts of rainfall (Figure 5). The soil volumetric water content in different parts of the blowouts did not change significantly after receiving 8.2 mm of precipitation (Figure 5), and the rainfall only recharged to the 20 cm soil layer. The soil volumetric water content in zones I, II, III, and IV increased by 2.30%, 3.03%, 3.09%, and 2.67%, respectively, which were all higher than the corresponding increases in CK, and the soil layers below 20 cm did not display significant changes. This indicates that different parts of the blowouts below 20 cm did not exhibit a significant response to light rainfall events.

After 15.7 mm of rainfall, the soil volumetric water content of the soil layers at 0–40 cm changed significantly. At 20 cm, the soil volumetric water content of zones I, II, III, and IV increased by 1.85%, 6.44%, 3.51%, and 1.2%, respectively. At 40 cm, the soil volumetric water content of zones I, II, III, and IV increased by 0.91%, 0.95%, 0.51%, and 0.83%, respectively. At 60–200 cm, different parts of the blowouts were not significantly affected by rainfall, and the recharge was below 0.20%. These results indicate that different parts of the blowouts had a significant response to moderate rainfall from 0 to 40 cm.

After 45.3 mm of rainfall, the soil volumetric water content in different parts of the blowouts responded to different degrees. The soil volumetric water content at 200 cm in zones I, II, and IV responded strongly to rainfall, with increases of 4.40%, 8.70%, and 3.01%, respectively. Furthermore, the soil volumetric water content at 20 cm and 40 cm in the sand accumulation zone (III) exhibited a marked response to rainfall, with increases of 11.63% and 8.83%, respectively. The soil volumetric water content of the blowouts, except for the sand pit area, was recharged by rainfall by more than 13.58%. This was higher than the CK rainfall recharge, indicating that the soil of blowouts from 0 to 200 cm displayed a greater response to rainfall under heavy rainfall conditions and effectively recharged the soil layer at 200 cm.

After 71.5 mm of rainfall, the soil volumetric water content in different parts of the blowouts increased and exhibited a strong response. The response intensity of different parts of the blowouts from low to high was ranked as follows: CK (27.97%) < sand–grass transition zone (28.18%) < sand pit (34.75%) < sand accumulation zone (5.54%) < edge zone (42.81%). The soil layers in different parts of the blowouts were recharged by more than 3.00%, and the soil volumetric water content at 100 cm in zones I, II, III, and IV responded strongly to rainfall, with increases of 9.31%, 10.87%, 8.83%, and 9.59%, respectively, compared with the pre-rainfall period.

3.3 Effect of rainfall on soil water storage in blowouts

As can be seen from Figure 6, the soil volumetric water content of the blowouts can be roughly divided into three parts: the shallow soil layer at 0–40 cm, the medium-depth soil layer at 40–100 cm, and

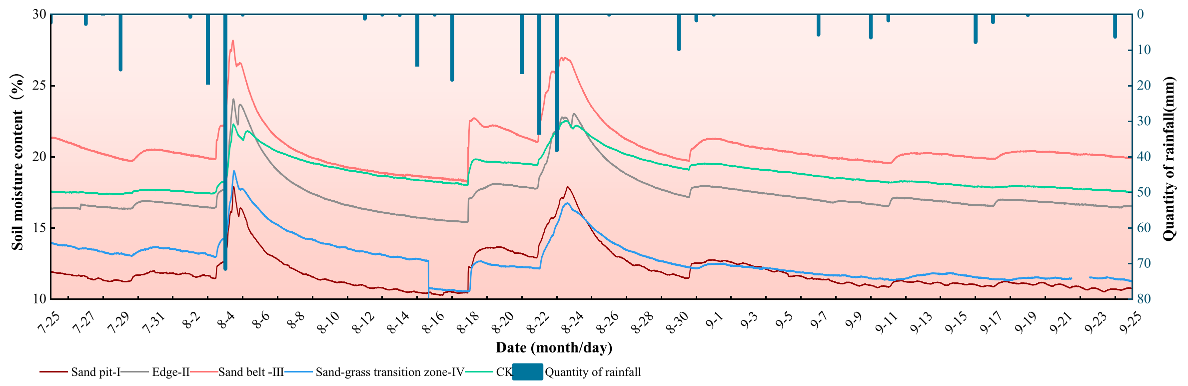

FIGURE 5
Dynamic changes of soil water content in different parts of blowouts.

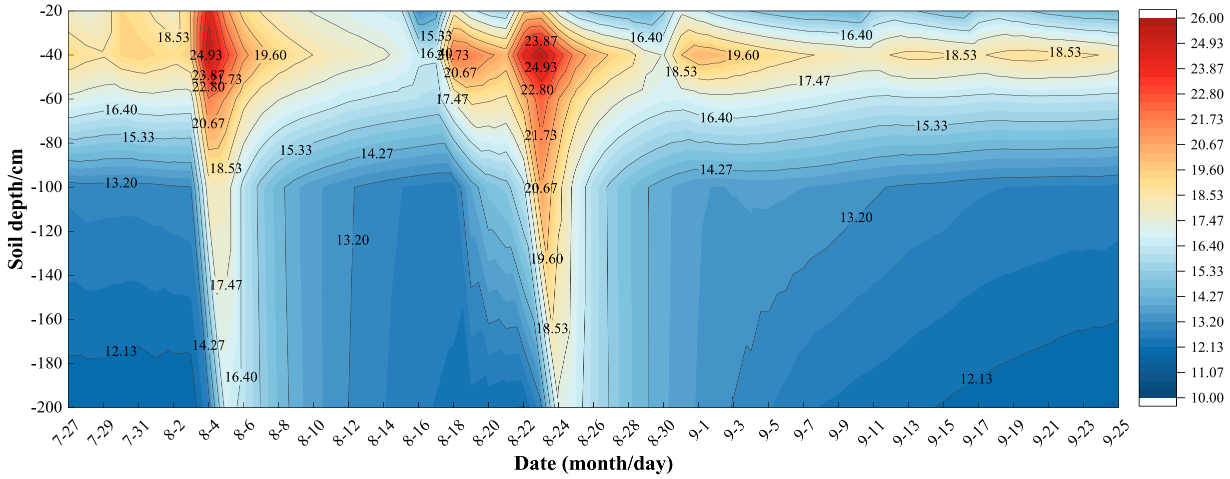

FIGURE 6
Dynamic contour plot of the soil volumetric water content of blowouts.

the deep soil layer from 100 to 200 cm. The volumetric water content of the soil at 0–40 cm was higher than that of other soil layers, with an average of more than 17.47%. The analysis of the response of the blowouts to rainfall indicated that the 0–40 cm soil layer displayed a stronger response to rainfall than the other soil layers and was easily recharged by water. This soil layer was recharged by light and moderate rainfall, but the volumetric water content of the soil decreased with time in the absence of rainfall. The volumetric water content of the soil in the middle-depth layer of 40–100 cm was 13.20%. The soil volumetric water content in the middle and deep soil layers from 40 to 100 cm ranged from 13.20% to 17.47%, which was increased by rainfall recharge and did not change significantly over time in the absence of rainfall recharge. The soil volumetric water content in the deep soil layers from 100 to 200 cm ranged from 12.13% to 15.55%.

Figure 7 depicts the dynamic changes of soil water storage in the 0–200 cm soil layer in different parts of the blowouts during the observation period. During the observation period, the cumulative rainfall was 278 mm. The soil water storage capacity in different parts of the blowouts showed fluctuations of different degrees, and the soil water storage capacity rose basically 1 d after the rainfall, which indicated that the absorption of rainfall exhibited hysteresis. As shown in Figure 7, the total soil water storage capacity of the blowouts was 1249.58 mm, which was 5.15% higher than that of CK. However, the water storage capacity of the blowouts was not as good as that of CK after sustained rainfall, water loss occurred more rapidly, and the overall total soil water storage capacity trend continued to decrease. Therefore, the soil water storage capacity of the blowouts was high, but their water retention and storage capacity was poor. Among the different parts of the blowouts, the soil water storage capacity ranked in descending order as zone III (1875.38 mm) > zone II (1373.22 mm) > CK (1188.36 mm) > zone I (1000.39 mm) > zone IV (803.90 mm). This result suggests that the water retention and storage capacity of the sand accumulation zone (III) is stronger than that of other zones, helping to preserve water, which may be because the surface layer of the sand accumulation zone (III) has a certain thickness, thereby enhancing the water retention and storage capacity of the sand accumulation zone.

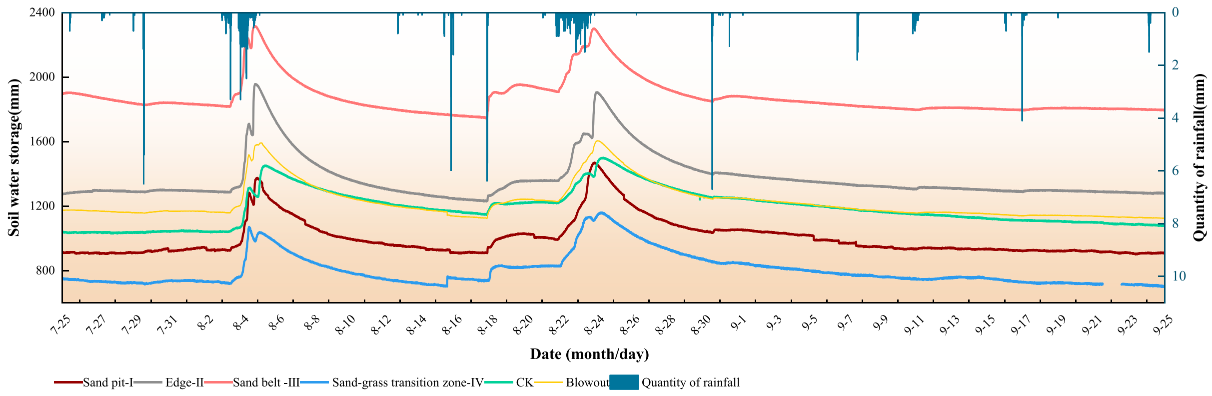

FIGURE 7
Dynamic changes of soil water storage in different parts of blowouts.

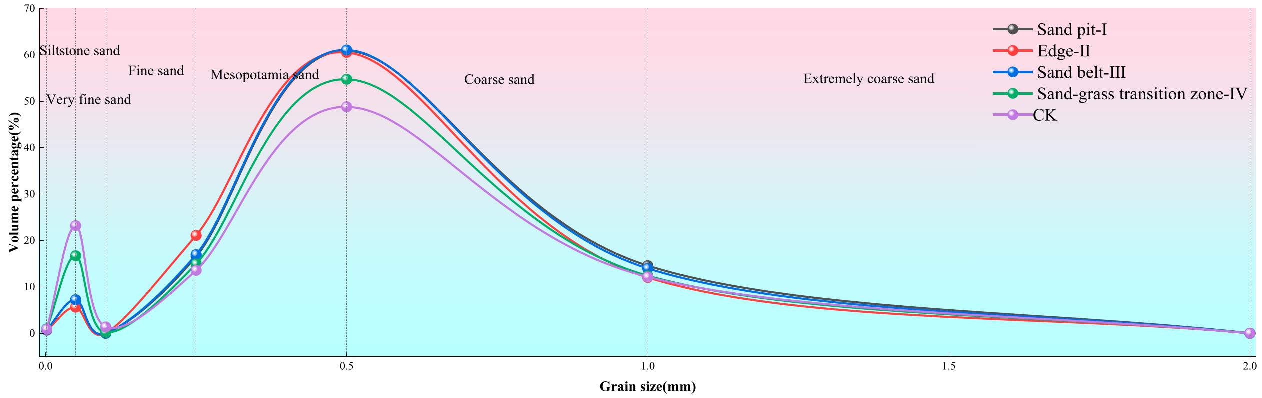

FIGURE 8
Soil particle size frequency distribution curve of wind-eroded crater soil.

4 Discussion

4.1 Influence of soil mechanical composition on soil moisture in blowouts

Soil moisture is closely related to the mechanical composition of the soil; the more loose and porous the soil, the lower the bulk density, and the more permeable the soil (Yun, 2013; Yanli, 2018). Xiwei (2018) investigated the evolution of sandy grassland blowout and suggested that the mechanical composition of blowout soils in the Hulunbeier sandy grassland is mostly dominated by fine sand, followed by medium sand. In contrast, the blowouts investigated in the present study were dominated by medium sand, followed by fine sand (Figure 8). This was consistent with Wang et al. (2008) conclusions regarding the mechanical composition of soils based on the study of trough-type blowouts in the Hulunbeier sandy grassland. Zhaungzhuang et al. (2020) suggested that soil macropores accelerate water infiltration and that soil macropores and rainfall intensity jointly influence the water infiltration process. Shenghua et al. (2019) conducted a study on the relationship between the soil water content and soil particle size distribution in desert grasslands and found that the soil water content was positively correlated with soil clay and fine particles. Honglian et al. (2022) and Honglian, 2022 research on the characteristics of deep soil moisture seepage in the Maowusu sandland suggested that soil texture is the main influencing factor affecting deep soil moisture seepage. In the present study, there was a linear fit between the soil moisture content and soil mechanical composition of blowouts, and the results indicated that the soil mechanical composition of different parts of the blowouts had different correlations to soil moisture. The correlations between soil moisture and clayey, powdery, very fine sand, and fine sand were positive, while the correlations between soil moisture and medium sand, coarse sand, and very coarse sand were negative.

4.2 Effect of sand cover thickness on the soil moisture content in blowouts

The dry sand layer has good permeability and can effectively recharge groundwater under heavy rainfall conditions (Dong et al., 2013). However, Jiansheng et al. (2014) suggested in their isotopic tracer study of moisture sources in the wet sand layer of the Alashan Desert that simulation experiments and natural rainfall observations

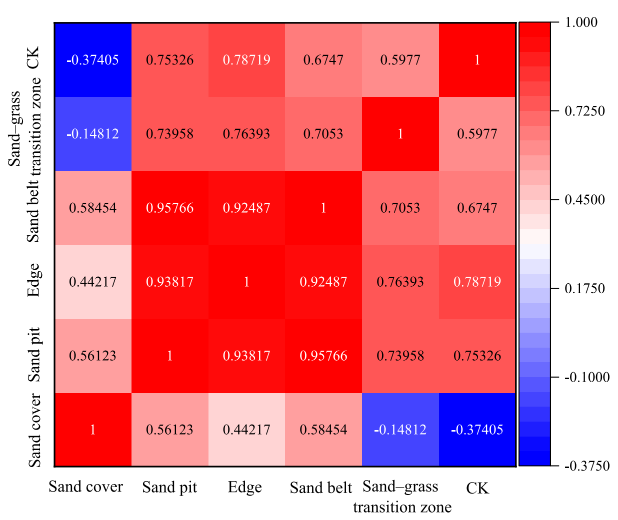

	Sand cover	Sand pit	Edge	Sand belt	Sand–grass transition zone	CK
CK	-0.37405	0.75326	0.78719	0.6747	0.5977	1
Sand–grass transition zone	-0.14812	0.73958	0.76393	0.7053	1	0.5977
Sand belt	0.58454	0.95766	0.92487	1	0.7053	0.6747
Edge	0.44217	0.93817	1	0.92487	0.76393	0.78719
Sand pit	0.56123	1	0.93817	0.95766	0.73958	0.75326
Sand cover	1	0.56123	0.44217	0.58454	-0.14812	-0.37405

FIGURE 9
Correlation between the sand cover layer of blowouts and the soil water content of different soil layers.

indicated that rainfall could not effectively recharge groundwater. Precipitation first infiltrates the dry sand layer, where the infiltrated precipitation forms a thin film water layer. The water molecules continue to infiltrate deeper soil only when the content of the dry sand layer reaches its maximum water holding capacity. Because the dry sand layer is recharged by rainfall and the soil water content is close to the limiting value, the soil water is unlikely to infiltrate deeper layers substantially over time.

Different sand and wind processes, such as wind erosion and sand burial, occur in different parts of the blowout, and the thickness of the sand overburden layer varies from one part to another. Limin et al. (2022) investigated the heterogeneous effect of soil moisture in the blowouts in the Hulunbeier grassland and suggested that the soil moisture exhibited heterogeneity in five typical parts of blowouts. Based on further analyses, it was concluded that the sand-covered layer was effective in retaining the deeper layer of moisture. Therefore, in the present study, the correlation between the thickness of sand cover and the soil moisture in different parts of the blowouts was analyzed (Figure 9). The correlation coefficients between sand pits and sand cover and between sand accumulation zones and sand cover were 0.5612 and 0.5845, respectively, and the soil moisture content was higher in sand pits and sand accumulation zones with sand cover than in CK. This finding implies that the sand cover has a positive effect on the water retention capacity of localized areas of blowouts. Yinling et al. (2023) conducted a study on the relationship between soil moisture and topographic vegetation factors in fixed dunes at the southern edge of the Gurbantunggut Desert and found that the soil moisture at different depths showed a consistent unimodal distribution, with the order of soil moisture content in different soil layers being deep layer > middle layer > surface layer, exhibiting significant differences. In the present study, the soil moisture content of different soil layers in the blowouts was markedly different. This was probably because the blowouts evolved from grassland under the action of wind erosion and sand formation, which led to ecological disruption. The examination of the soil profile revealed that the thickness of the underlying black soil layer beneath the sand layer in different parts of the blowouts varied, leading to great differences in soil moisture.

4.3 Effect of rainfall on the water storage capacity of blowouts

Rainfall has a recharging effect on soil moisture, and the only source of moisture in desert areas is usually precipitation that infiltrates deep into the soil (Wenbin et al., 2014; XueYong et al., 2006). The deeper layers of dunes hold a large amount of water, but the surface soil moisture is low due to rapid evapotranspiration and wind erosion (Yuxing et al., 2020; Yun-zhu et al., 2021). However, the soil water content from 0 to 60 cm is more strongly affected by rainfall, making it more variable than other soil layers (Haiqin et al., 2020; Dongmei et al., 2005). In the present study, we examined the water retention and storage capacity of the blowouts and their different parts before and after rainfall. The results showed that the water storage capacity of the blowouts differed from that of the CK by 61.22 mm, and the overall soil moisture of the blowouts was higher than that of the CK. However, the water storage capacity of the blowouts was not as good as that of the CK after sustained rainfall, the loss of water was more rapid, and the overall soil moisture trend continued to decrease. As a result, blowout soils have a high water storage capacity but a poor water retention and storage capacity. The water retention and storage capacity of the sand accumulation zone was strong, which was consistent with the conclusion of the previous study (Xiwei et al., 2018).

5 Conclusion

This study investigated the response of soil moisture to rainfall in different parts of the blowouts in the Hulunbeier grassland and analyzed the changes in soil moisture in the pits. The main conclusions are as follows:

(1) The volumetric water content of the soil in different parts of the blowouts varied from low to high as follows: sand pit-I < sand-grass transition zone-IV < fringe zone-II < CK < sand accumulation zone-III. The soil volumetric water content in the 0–40 cm soil layer of the blowout was high, averaging more than 17.47%; the volumetric water content in the middle and deep soil layers at a depth of 40–100 cm ranged from 13.20% to 17.47%; and the volumetric water content in the soil layer at a depth of 100–200 cm ranged from 12.13% to 15.55%.
(2) The soil volumetric water content of the blowouts differed significantly under different rainfall amounts, and rainstorms effectively recharged the pits to a depth of 200 cm (i.e., the pits responded strongly to rainstorms). The volumetric water content of the soil gradually recovered approximately a week after the rainstorm.
(3) The water storage capacity of blowout soils was significantly higher than that of CK. The soil water storage capacity of different parts of the blowouts was in the order of sand accumulation zone (1875.38 mm) > edge zone

(1373.22 mm) > CK (1188.36 mm) > sand pit (1000.39 mm) > sand–grass transition zone (803.90 mm).

(4) The correlation analysis of the thickness of the sand cover layer and the soil moisture content in different parts of the blowouts demonstrated that the correlation coefficient of the sand pit and sand cover and that of the sand accumulation zone and sand cover layer were 0.5612 and 0.5845, respectively. In addition, the soil moisture content of the sand pit and sand accumulation zone was higher than that of the sand pit and sand accumulation zone in which the natural grassland had a sand cover layer, which indicated that the sand cover layer had a positive effect on the water retention capacity of the blowouts in the local area. However, in this study, we did not thoroughly investigate how much thickness is needed in the sand cover layer for it to have enough of a water retention effect to promote plant growth.

(5) The area of the blowouts investigated in this study was small, and blowout development occurs slowly; thus, the data did not represent all stages of blowout development. Therefore, in the follow-up study, the water storage capacity of different soil layers should be investigated in each blowout development stage (the bare sand, activation stage, fixation stage, extinction stage, and re-activation stage) to provide more rigorous theoretical support regarding whether blowouts have a positive effect on the soil moisture in grasslands.

Data availability statement

The original contributions presented in the study are included in the article/supplementary material, further inquiries can be directed to the corresponding author.

Author contributions

ZB: Writing–original draft, Writing–review and editing, Conceptualization, Data curation, Formal Analysis, Funding acquisition, Investigation, Methodology, Project administration. LY: Project administration, Resources, Supervision, Writing–review and editing. ZM: Supervision, Writing–review and editing. EZ: Data curation, Methodology, Writing–original draft. LZ: Data curation, Writing–original draft. JL: Data curation, Writing–original draft.

Funding

The author(s) declare that financial support was received for the research, authorship, and/or publication of this article. “Integration and Demonstration of Ecological Restoration Technologies for Hulunbeier Sandy Land” of the Inner Mongolia Key R&D and Achievement Transformation Program (2022YFDZ0055).

Acknowledgments

We thank LetPub (www.letpub.com.cn) for its linguistic assistance during the preparation of this manuscript.

Conflict of interest

The authors declare that the research was conducted in the absence of any commercial or financial relationships that could be construed as a potential conflict of interest.

Generative AI statement

The author(s) declare that no Generative AI was used in the creation of this manuscript.

Publisher’s note

References

Bo, W., Yuxi, D., Weifeng, W., Li, X. J., Liu, Y., and Liu, Z. Q. (2020). Responses of shallow soil water content in Artemisia ordosica community to different rainfall patterns. *Chin. J. Appl. Ecol.* 31 (05), 1571–1578. doi:10.13287/j.1001-9332.202005.011

Byrne, M. L. (1997). Seasonal sand transport through a trough blowout at pinery provincial park, ontario. *Can. J. Earth Sci.* 34 (11), 1460–1466. doi:10.1139/e17-118

Chunheng, Z., Hongsong, C., Zhiyong, F., Huimin, R., and Xiu, L. (2020). Effect of soil macropore structures on soil and water loss progress in karst areas. *J. Soil Water Conservation* 34 (06), 70–76. doi:10.13870/j.cnki.stbcxb.2020.06.011

Chun-Mao, S., Ya, L., Sheng-Tian, Y., Qiu-Wen, Z., Jun-Lin, Y., and Liu, Y. (2022). Responses of soil moisture at different slope positions to rainfall in dry-hot valley. *J. Appl. Ecol.* 33 (05), 1352–1362. doi:10.13287/j.1001-9332.202202.018

Daly, E., and Porporato, A. (2005). A review of soil moisture dynamics: from rainfall infiltration to ecosystem response. *Environ. Eng. Sci.* 22 (1), 9–24. doi:10.1089/ees.2005.22.9

Deren, Y. (2016). Impact factors and morphological characteristics of blowoutss in hunshandake sandland. *Scientia Geogr. Sin.* 36 (04), 637–642.

Deren, Y., Haiguang, H., Xiaolong, H., and Limin, Y. (2017). Wind speed character in different parts of blowouts in fixed dunes. *J. Inn. Mong. For. Sci. Technol.* 43 (03), 10–13.

Dong, Z. B., Qian, G. Q., Lyu, P., and Guangyin, H. (2013). Investigation of the sand sea with the tallest dunes on earth: China’s badain jaran sand sea. *Earth-Sci. Rev.* 120, 20–39. doi:10.1016/j.earscirev.2013.02.003

Dongmei, Y., Jiaqi, Q., Shengli, H., Youliang, T., and Liansheng, G. (2005). Studies on the soil water dynamic and the characteristics of soil water potential in the drifting sand dunes in wulanbuhe desert. *J. Arid Land Resour. Environ.* (03), 126–130. doi:10.3969/j.issn.1003-7578.2005.03.024

Ferrarezi, S. R., Nogueira, R. A. T., and Zepeda, C. G. S. (2020). Performance of soil moisture sensors in Florida sandy soils. *Water* 12 (2), 358. doi:10.3390/w12020358

Gares, P. A., and Nordstrom, K. F. (1995). Acyclic model of foredune blowouts evolution for a leeward coast: island Beach. *NJ. Ann. Assoc. Am. Geogr.* 85, 1–20.

Guangyu, H., Xiaojiang, W., Guohou, L., Xiaowei, G., Lei, Z., Zhuofan, L., et al. (2021). Response of soil moisture to different rainfall patterns in hedysarum leave in mu us sandy land. *Bull. Soil Water Conservation* 41 (02), 76–83+121.

Guozheng, W., Chunyan, Q., Yuanyuan, Z., Yanfang, B., and Yan, Z. (2023). *Probability theory and mathematical statistics*. Chongqing, China: Chongqing University Press.

Haiqin, Q., Xiuli, Z., and Ping, Z. (2020). Temporal and spatial variation of soil moisture in the shallow dune fixed on baijitan in ningxia. *J. Yunnan Agric. Univ. Nat. Sci.* 35 (01), 156–163.

Honglian, L. (2022). *Spatio-temporal dynamics of soil water and deep seepage of the four land use types in the Mu Us Sandy L*. Hohhot, China: Agricultural University of Inner Mongolia.

Honglian, L., Hairong, L., Hongjiao, X., Gaowa, B., Gaowa, X., Hua, W., et al. (2022). Characteristics of deep leakage of soil water in Four land types in MU Us Sandy land. *J. Inn. Mong. For. Sci. and Technol.* 48 (04), 17–20+39.

Jiansheng, C., Xixi, C., and Ting, W. (2014). Isotopes tracer research of wet sand layer water sources in Alxa Desert. *Adv. Water Sci.* 25 (02), 196–206.

Juan, C. (2020). *Response of soil moisture to precipitation in desert steppe*. Yinchuan, China: Ningxia University.

Jungerius, P. D. (1984). A simulation model of blowout development. *Earth Surf. Process. Landforms.* 9, 509–512. doi:10.1002/esp.3290090604

Kejun, C., Shengyu, L., Haifeng, W., and Jinglong, F. (2022). Three dimensional flow field characteristics of two typical blowouts in the dry lake basin of Taitema Lake and their influence on wind erosion. *Arid. Land Geogr.* 45 (06), 1784–1794.

Limin, Y., Zhiguo, Y., Bo, X., Haiyan, G., and Zhaorigetu, H. (2022). Heterogeneity of soil moisture of blowouts in HulunBuir grassland. *Arid Zone Res.* 39 (05), 1598–1606. doi:10.13866/j.azr.2022.05.24

Luo, Y. (2019). *Moisture dynamics of a near-surface desert soil*. Las Vegas: University of Nevada.

Malakouti, M. J., Lewis, D. T., and Stubbendieck, J. (1978). Effect of grasses and soil properties on wind erosion in sand blowouts. *J. Range Manag.* 31 (6), 417–420. doi:10.2307/3897198

Min, Z., Shuang, L., Yong, L., and Hong, Z. (2019). Soil moisture variation characteristics of different land use types in the moderate slope sandy area of loess hilly region. *J. Soil Water Conservation* 33 (03), 115–120+128. doi:10.13870/j.cnki.stbcxb.2019.03.018

Na, Q., Ting, Y., Haiguang, H., Deren, Y., and Zhiguo, Y. (2020). Sand-fixing technology with sand barrier in activated blowout land vegetation restoration. *J. Inn. Mong. For. Sci. and Technol.* 46 (01), 1–7. doi:10.3969/j.issn.1007-4066.2020.01.001

Qi, S. (2022). *Study on the law of soil water movement under the conditions of different sand covering thickness and mixed straw*. Lanzou, China: Lanzhou University of Technology.

Ruru, X., Qing, A., Qi, Z., Tianyuan, C., Lvping, Y., and Ping, A. (2019). Grain size characteristics of aeolian sediments at different locations of blowoutss in the eastern margin of qaidam basin. *J. Chengdu Normal Univ.* 35 (09), 91–97.

Shaoyun, Z., and Yuxiang, D. (2019). Research progress on morphodynamics of coastal sandy blowouts. *Adv. Earth Sci.* 34 (10), 1028–1037.

Shenghua, M., Yingzhong, X., Haiying, H., and Biao, N. (2019). Relationship between soil moisture content and soil particle size distribution under two typical community types in desert steppe. *Soil Water Conservation China* (07), 61–65.

Shengyuan, B. (2015). *Study on progress of soil moisture changing in loess soil column*. Xian, China: Northwest A&F University.

Shuai, W., and Eerdun, H. (2008). Particle size variation in trough blowouts on sandy grassland. *Bull. Soil Water Conservation* 28 (06), 122–125.

Wang, C., Fu, B., Zhang, L., and Xu, Z. (2019). Soil moisture–plant interactions: an ecohydrological review. *J. Soils Sediments* 19 (1), 1–9. doi:10.1007/s11368-018-2167-0

Wei, C., Yaxin, L., Hongyang, W., Jia, W., and Congjian, S. (2022). Dynamic response characteristics of soil moisture on slope cultivated land and abandoned land to different rainfall intensities in Loess hilly region. *Acta Ecol. Sin.* 42 (01), 332–339. doi:10.5846/stxb202011303064

Wenbin, Y., Jinnian, T., Hairong, L., Hongzhong, D., and Wei, L. (2014). Deep soil water infiltration and its dynamic variation in the shifting sandy land of typical deserts in China. *Sci. China:Earth Sci.* 44 (9), 2052–2061.

Wenfei, Z., Xing, W., Youke, W., Jingxiao, Z., and Qian, H. (2017). Growth and water consumption of jujube with water-saving pruning in deep dried soil of Loess Hilly Area. *Trans. Chin. Soc. Agric. Eng.* 33 (07), 140–148.

Xinle, L., Bo, W., Jianping, Z., Xin, Z., Dong, X., and Duan, R. (2019). Dynamics of shallow soil water content in Nitraria tangutorum nebkha and response to rainfall. *Acta Ecol. Sin.* 39 (15), 5701–5708. doi:10.5846/stxb201808121721

Xiwei, Z. (2018). *Study on evolution process and development mechanism of blowoutss in typical sandy grassland*. Hohhot, China: Agricultural University of Inner Mongolia.

Xiwei, Z., Ji, W., Chunxing, H., Yanlong, D., and Cheng, B. (2018). Structure of drifting sand flow over the surface of blowoutss in the hulun buir sandy grasslands. *Arid Zone Res.* 35 (06), 1505–1511.

Xuehua, C., Wanyin, L., Mei, S., and Zhongyuan, W. (2021). Form-flow feedback within blowoutss at different developing stages in the gonghe Basin,Qinghai province. *Adv. Earth Sci.* 36 (01), 95–109.

Xueting, L., Muxing, L., Shiguo, L., Weijie, W., Jun, Y., and Jinhong, W. (2023). Spatial distribution characteristics of soil moisture on tea garden slope and its response to rainfall replenishment in the three gorges reservoir area. *J. Soil Water Conservation* 37 (05), 137–144. doi:10.13870/j.cnki.stbcxb.2023.05.017

XueYong, Z., XiaoAn, Z., HaLin, Z., Tonghui, Z., Yuqiang, L., and Xaioyong, Y. (2006). Spatial variability of soil moisture after rainfall in different type sands of Horqin Sand. *Arid. Land Geogr.* (02), 275–281. doi:10.3321/j.issn:1000-6060.2006.02.018

Yanguang, Z., Huizhong, C., Chao, G., Hongyue, L., Xingfen, Q., and Eerdun, H. (2018). Grain size characteristics of the blowouts and its environmental significance in the hulun buir sandy land,China. *J. Desert Res.* 38 (04), 724–733. doi:10.7522/j.issn.1000-694X.2018.00006

Yanguang, Z., Zhuoran, W., Damuni, Q., Rina, H., Jie, Y., Zifeng, W., et al. (2023). Morphological changes and dynamic mechanism of blowoutss on fixed dunes in the Otingdag sandy land, China. *Chin. Sci. Bulletin-Chinese* 68 (11), 1298–1311.

Yanli, L. (2018). *Study on deep soil recharge characteristics and response for irrigation of the irrigation farmland in ulan buh desert*. Beijing, China: Chinese Academy of Forestry.

Yanling, Z., Dinghai, Z., Ting, N., Zhishan, Z., Lishan, S., Guopeng, C., et al. (2023). Relationship between soil moisture and topography-vegetation factors on fixed dunes in the southern margin of the Gurbantunggut Desert. *J. Soil Water Conservation* 37 (04), 258–266+277. doi:10.13870/j.cnki.stbcxb.2023.04.032

Yinglan, A., Wang, G., Sun, W., Xue, B., and Kiem, A. (2018). Stratification response of soil water content during rainfall events under different rainfall patterns. *Hydrol. Process.* 32 (20), 3128–3139. doi:10.1002/hyp.13250

Yun, A. (2013). *Analysis og eco-efficiency on 4 kinds of typical vegetation restoration mode in Mu Us Sandy land*. Beijing, China: Beijing Forestry University.

Yun-zhu, Z., Xin, Z., Chao, Z., Xiaofei, T., Sheng, Z., and Shuchen, S. (2021). Temporal stability characteristics of surface soil moisture of fixed dunes in the mu us sandy land. *Water Sav. Irrig.* (11), 41–46. doi:10.3969/j.issn.1007-4929.2021.11.008

Yuxiang, W., Tingxi, L., Limin, D., Xin, T., and Haiying, W. (2020). Temporal and spatial variation characteristics of soil moisture and environmental impact factors in different types of dunes in horqin. *J. Soil Water Conservation* 34 (06), 125–134+142. doi:10.13870/j.cnki.stbcxb.2020.06.019

Zhang, A. (2007). HulunBuir sandy grassland blowoutss: influence of human activities. *J. Desert Res.* (02), 214–220.

Zhang, A. (2009). Morphology and developmental mode of blowoutss in hulun buir sandy grassland. *China. J. Desert Res.* 29 (02), 212–218.

Zhang, A., Hongwei, S., Xiaoke, W., and Zong-Wei, F. (2007a). HulunBuir sandy grassland blowoutss (II): process of development and landscape evolution. *J. Desert Res.* (01), 20–24+170–171.

Zhang, A., Xiaoke, W., Hongwei, S., Jia-Ming, Z., Xiu, L., and Zong-Wei, F. (2006). HulunBuir sandy grassland blowoutss: geomorphology, classification, and significances. *J. Desert Res.* (06), 894–902+1052–1058.

Zhang, A., Xiaoke, W., Hurrle, U., and Zongwei, F. (2007b). HulunBuir sandy grassland blowoutss (III): influfnce of soil layer and microrelief. *J. Desert Res.* (01), 25–31.

Zhuangzhuang, Z., Zongping, R., Peng, L., Mengyao, X., Zhanbin, L., and Guoce, X. (2020). Response of soil moisture content to precipitation under different vegetation coverages. *Sci. Soil Water Conservation* 18 (06), 62–71. doi:10.16843/j.sswc.2020.06.008

Frontiers in Environmental Science

TYPE Original Research
PUBLISHED 14 April 2025
DOI 10.3389/fenvs.2025.1515739

OPEN ACCESS

EDITED BY
Jing Zhang,
North China University of Water Conservancy and Electric Power, China

REVIEWED BY
Peter Lehmann,
ETH Zürich, Switzerland
Abdallah Alaoui,
University of Bern, Switzerland

*CORRESPONDENCE
Xiaoyan Wang,
✉ wangxy@cnu.edu.cn

RECEIVED 23 October 2024
ACCEPTED 01 April 2025
PUBLISHED 14 April 2025

CITATION
Du Y, Wang X, Nan Z, Li T, Tang Y and Huang L (2025) Assessment of the vertical preferential flow characteristics and flow types on a slope in a small headwater catchment.
Front. Environ. Sci. 13:1515739.
doi: 10.3389/fenvs.2025.1515739

Assessment of the vertical preferential flow characteristics and flow types on a slope in a small headwater catchment

Yi Du[1,2,3], Xiaoyan Wang[2]*, Zhe Nan[4], Tingting Li[1,2,3], Yi Tang[1,3] and Longsheng Huang[1,3]

[1]School of Emergency Management, Institute of Disaster Prevention, Sanhe, China, [2]College of Resources, Environment and Tourism, Capital Normal University, Beijing, China, [3]Hebei Key Laboratory of Resource and Environmental Disaster Mechanism and Risk Monitoring, Sanhe, China, [4]School of Environment and Resource, Xichang University, Xichang, Sichuan, China

This study investigated preferential flow infiltration patterns at three slope positions (upslope, mid-slope and downslope) of typical slopes in the Miyun Reservoir Basin. The evaluation was conducted by combining the multi-index evaluation method and the macropore flow classification method, based on the profile images obtained from dye tracer experiments. Multi-index analysis shows that preferential flow infiltration depth is 400 mm, and the average uniform infiltration depth is 56.6 mm. The preferential flow fraction quantified as the deviation from a perfectly homogeneous infiltration process on up, middle and down slopes are 56.6%, 74.8% and 67.5% respectively. Middle slope has higher preferential flow level due to higher weights of peak value, stained area and stable infiltration depth. Macropore flow classification results indicate at three slope positions, preferential flow is mainly macropore flow with mixed interaction with soil matrix. It is one of the five flow types and its proportion increases as elevation drops (79.31% on upper, 86.88% on middle and 95.31% on lower slope). With soil layer depth increasing, low-interaction macropore flow proportion rises and its interaction with matrix soil decreases. Correlation analysis reveals that macropore flow with low interaction negatively correlates with soil volumetric water content, porosity, but positively with soil bulk density. Macropore flow with high interaction positively correlates with soil volumetric water content. Matrix flow and fingering positively correlate with silt content. Matrix flow significantly positively correlates with soil saturated hydraulic conductivity. The difference between multi-index method and macropore flow classification lies in analysis scale. Since the calculation scale of the multi-index method encompasses the entire profile and treats the staining characteristics as a whole, it might result in an underestimation of preferential flow outcomes. On the other hand, the preferential flow classification method considering the interaction with soil matrix at pixel scale may lead to an overestimation of the calculated preferential flow results. Combining these two methods can help judge macropore flow characteristics and its interaction with soil matrix more accurately.

KEYWORDS

preferential flow, dye tracer, image analysis, flow type, hillslope

Highlights

Statistical methods are integrated with image processing to investigate the characteristics of preferential flow.

The vertical infiltration characteristics of the preferential flow were analyzed by stained path width.

The fraction of vertical preferential flow on the slope ranges between 56.6% and 74.8%, with variations observed at different slope positions.

1 Introduction

Soil preferential flow is a concept within the realm of soil hydrology. It refers to an inhomogeneous flow of water that infiltrates rapidly bypass the soil matrix (Beven and Germann, 1982). It is widely acknowledged and encompasses various types, such as macropore flow (which involves water moving through biopores, erosion cavities, cracks, or fissures), finger flow (characterized by non-uniform water movement driven by hydraulic instability or heterogeneity), and funnel flow (representing lateral flow along textural boundaries within the subsurface) (Allaire et al., 2009; Guo and Lin, 2018). Preferential flow exerts a significant influence on water loss, soil erosion as well as nutrient transport (Fuhrmann et al., 2019; Julich et al., 2017). Since the 1970s, preferential flow has garnered considerable attention, leading to a surge of studies delving into its mechanisms, the factors that influence it, and its implications for nutrient transport (Makowski et al., 2020; Simard et al., 2000; Toor et al., 2005) and hydrological response (Beven and Germann, 1982; Jarvis, 2007). Various scholars from diverse disciplines have offered their perspectives on the concept of preferential flow. Firstly, preferential flow is characterized by the rapid downward movement of water through macropores, bypassing the soil matrix (Beven and Germann, 1982). This concept narrowly attributes preferential flow to macropore flow. Second, based on the mechanism of soil water movement, Hendrickx and Flury (2001) proposed the concept of preferential flow relative to the equilibrium infiltration flow. The specific movement path bypasses some porous media and infiltrates downward, which also is a sign of the movement of soil water from homogeneous to heterogeneous areas. The third concept emerges from the perspective of scale quantification. Upon reviewing preferential flow quantification methods, it is proposed that preferential flow refers to flow mechanisms where transport of water together with dissolved or suspended matter is primarily associated with a smaller fraction of the total pore network, at any scale much larger than the microscopic (μm) scale (Allaire et al., 2009). The phenomenon consist of transmission in multiple pores. This perspective offers valuable insights into preferential flow by drawing comparisons from the vantage point of spatial network scale analysis. Currently, hydrologists widely acknowledge preferential flow as a distinctive soil water movement phenomenon where water or dissolved substances bypass the porous soil matrix, navigating through specific, spatially and temporally variable pathways within the soil (Demand et al., 2019; Guo and Lin, 2018).

Numerous investigations have consistently demonstrated that preferential flow is a ubiquitous phenomenon across diverse soils and landscapes, exhibiting notable heterogeneity across various spatial and temporal scales (Demand et al., 2019; Legout et al., 2009; Mälicke et al., 2019; Wiekenkamp et al., 2016). At present, research on preferential flow mainly focuses on field study to investigate the formation mechanism (Zhang et al., 2022; Ding et al., 2023; Chen et al., 2021; Cai et al., 2024; Hou et al., 2024) and modeling studies to explore influencing factors (Yi et al., 2023; Wang et al., 2017; Santra et al., 2021). Various factors are divided into two groups according to variability over time (Guo and Lin, 2018). One group is static factors that have little change with time, including soil properties, topography, and geological background and others (Wiekenkamp et al., 2016). The second group is dynamic factors which are greatly affected by changes over time, such as the chemical environment (Liu et al., 2021), land use and land cover (Demand et al., 2019), initial soil moisture conditions (Ding et al., 2023; Bogner et al., 2012), and input water characteristics (Wiekenkamp et al., 2016; Bogner et al., 2012), changes in the rhizosphere (Luo et al., 2018; Luo et al., 2019; Zhang et al., 2015), physical changes (e.g., freeze-thaw and wetting-drying processes) (Mao et al., 2024; Chen et al., 2024), biogenic factors (earthworks, burrowing animals) (Li et al., 2018), and others.

Researchers have conducted an in-depth exploration of the characteristics and influencing factors of preferential flow in a wide range of ecosystems, including semi-arid grasslands (Wu et al., 2022) and farmlands in the northern region (Zhang et al., 2022), vegetation cover in the Loess Plateau (Cai et al., 2024), karst rocky desertification areas (Ding et al., 2023; Bogner et al., 2012; Chen et al., 2024), tropical rainforest in the southwest (Chen et al., 2021), arid mountainous regions in the northwest (Xue et al., 2024), and the upper reaches of the Heihe River (Kang et al., 2022). Preferential flow within hillslopes plays a pivotal role in shaping the hydrological regime. Due to its open structure, which includes cracks and voids, soil particles can preferentially be carried into the drains, ultimately causing erosion (Øygarden et al., 1997). Soil conservation practices that treat surface runoff process alone may be ineffective if preferential flow is contributing (Wilson et al., 2008). Dai et al. (2020) pointed out that where preferential pathways were rich, that is, where hydrological connectivity was strong. "Hydrological connectivity" here refers to a characteristic that the soil pores, preferential flow channels (such as macropores formed by plant roots and other channels that allow water to flow rapidly), as well as the surrounding soil matrix and other elements related to water movement are interconnected and integrated with each other, enabling water to migrate in the soil relatively smoothly. Distinct from surface runoff, preferential flowpaths, can significantly increase the subsurface water flow and solute transport velocities and amounts in forested hillslopes (Laine-Kaulio et al., 2014; Jarvis, 2007; Anderson et al., 2009). Preferential flow in soils is widely acknowledged and encompasses various types, such as macropore flow, fingering flow, and funnel flow (Allaire et al., 2009; Guo and Lin, 2018). For macropore flow, it occurs through larger pores in the soil, such as those created by stones, roots, earthworms, or cracks. These macropores allow water to move more rapidly through the soil, bypassing the soil matrix in some cases (Beven and Germann, 1982). Regarding fingering flow, it is a form of unstable flow where water moves in finger - like patterns through the soil. This often happens when there are differences in soil properties, the water breaks into the subjacent layer through fingers (preferential flow paths) rather than uniformly through the entire layer (Liu et al., 2023; de Rooij, 2000; Rezanezhad et al., 2006). Funneled flow is an unique category of flow phenomena referring to the situation in which a capillary barrier develops above a coarse layer which underlies a relatively fine soil (Walter et al., 2000).

As the primary drinking water source for Beijing, supplying over 70% of the municipal demand, Miyun Reservoir is Beijing's important water source and ecological conservation area. Mountainous areas account for over 80% of the Miyun reservoir Watershed. It faces significant soil-water challenges in its surrounding rocky mountainous areas. In the mountainous areas, the soil depth is around 20–60 cm, and in the soil there is a high proportion of gravel and the bottom part is mainly a gravel layer or mother rock. The well-developed fissures within the bedrock facilitate significant groundwater storage, serving as preferential flow pathways that respond promptly to precipitation events (Tian and Xu, 2024). Rainfall-driven application of pesticides and fertilizers facilitates the transport of nutrients and pollutants into subsurface systems or water bodies via preferential flow pathways. Given the critical role of Miyun Reservoir as a primary water source for Beijing, characterizing preferential flow dynamics in its upstream watershed is essential for developing effective water security strategies. Investigating the infiltration mechanisms of preferential flow and their interactions with soil properties enhances our understanding of hydrological processes governing the migration and distribution of water, nutrients, and contaminants in the ecosystem.

Dye tracer experiments, which facilitate the direct visualization of flow pathways within soils, have become a standard methodology for characterizing preferential flow phenomena (Widemann and Bogner, 2012). The image processing technique utilized in staining tracer experiments successfully emphasizes variations in the preferential flow pathways, however, it lacks the capability to quantitatively differentiate between the various types of preferential flow. Therefore, based on the analysis of the stain path and the width of the dyeing path, it is essential to further analyze the type and distribution of preferential flow (Bargués Tobella et al., 2014; Alaoui et al., 2011; Weiler and Naef, 2003). The objectives of this experimental investigation were as follows: (1) to quantitatively evaluate the preferential flow characteristics on a slope using image analysis and stained path width (SPW); (2) to uncover the characteristics of preferential flow at varying slope positions; and (3) to identify the influencing factors within a small watershed upstream of a drinking water reservoir. The findings of this study may provide valuable insights into the water quality, soil erosion and nutrient transportation.

2 Materials and methods

2.1 Study area

The Xitaizi Experimental Watershed (XEW) is situated in the mountainous northern region of Huairou District, Beijing, upstream of the Miyun Reservoir. It covers an area of 6.7 square kilometers and lies at an elevation ranging from 676 to 1,202 m above sea level. This region features a semi-humid continental climate with an annual average precipitation of 625 mm, predominantly occurring between May and September (Peng et al., 2016a; Zhao et al., 2019). The predominant soil type within the watershed is brown loam, ranging in thickness from absent to 1.5 m deep. Granite is the primary rock type found in this area. With a forest coverage rate of 98%, the watershed comprises 54.2% broad-leaved forest, 2.3% coniferous forest, 10.5% mixed coniferous and broad-leaved forest, and 33% shrubs (Zhao et al., 2019; Tie et al., 2018). The annual mean air temperature was 11.5°C from 2014 to 2023, with soils remaining frozen between late November and mid-March when the daily mean air temperature remained below 0°C (Cui et al., 2024). A typical hillslope in XEW was chosen as the study hillslope (named SH1, see Figure 1). The experimental site is a north-facing hillslope located at an elevation of 780–805 m above sea level, covered by a broad-leaf forest consisting of pure stands of Aspen. Based on actual measurements, the slope of the experimental terrain has an inclination of 38°. Dye tracer experiments were conducted at three sampling locations: downslope, mid-slope, and upslope.

2.2 Dye tracer experiment

Dyes serve as valuable tracers for visualizing flow patterns and pathways within soil. On 27 October 2019, a dye tracer experiment was conducted at the downslope, mid-slope, and upslope locations, with five profiles established at each position. Prior to the experiment, litter from the surface layer was carefully removed to avoid any disruption to the surface layer structure. As shown in Figure 2, a 1 m^2 square area surrounded by a self-made PVC board on the slope is used as an area to simulate rainfall. To mimic natural rainfall and eliminate any uneven distribution of the surface water head, a pressure-controlled sprayer was utilized. A 40-L dye tracer solution was crafted by dissolving 160 g of Brilliant Blue FCF powder in ordinary tap water, yielding a solution with a concentration of 4 g L^{-1} (Flury and Flühler, 1995; Alaoui et al., 2011; Guan et al., 2024) and was evenly sprayed on the test area at a height of 1 m for about 1 h. The spray flow was adjusted to ensure no water accumulation or confluence, serving as the benchmark for its control. Immediately after dye application, the upper layer of the test area was shielded with a waterproof plastic cover to prevent water evaporation. After 24 h, in order to check whether there is a parallel preferential flow along the slope, we dig a blank quadrate. The blank quadrate had the same size with the stained quadrate (1 m × 1 m),it is located downhill neighbor the stained quadrate. We assume that if a parallel flow is created, then this location will be the convergence region. If there is dyeing, it means that the parallel preferential flow happened along the slope, but we did not find any stained soil when digging 1 m depth of the blank quadrate. The vertical dyed profiles were excavated at intervals of 20 cm to a depth of 1 m, and five stained sections were excavated at each point as repeated controls. During the excavation process, boulders were handled with care; however, some were too large to be moved and were thus left in place. The excavated section was photographed using a Canon EOS 350D camera, with efforts made to minimize shadows caused by uneven lighting.

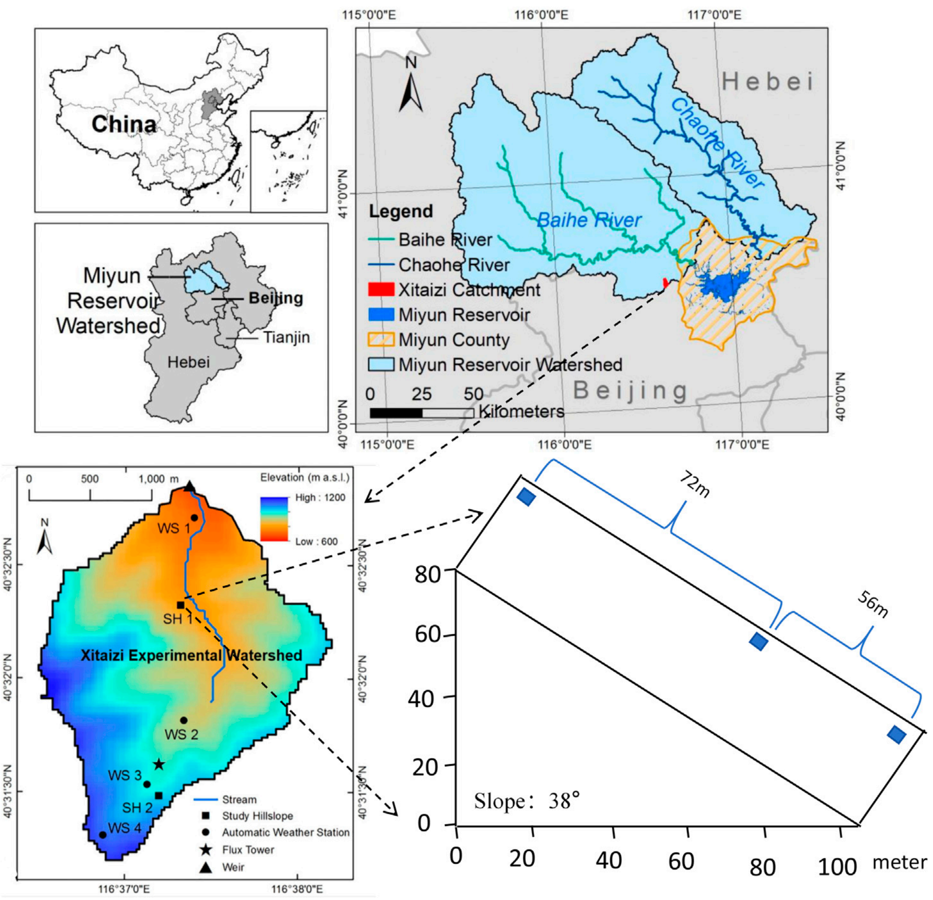

FIGURE 1
Location of the study area and schematic diagram of sampling points (Tie et al., 2018).

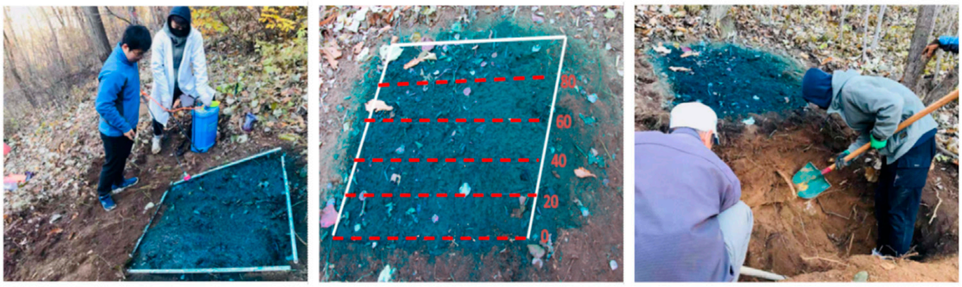

FIGURE 2
Field experiment of dye trace.

2.3 Site description

The length of the slope is about 130 m. The distance between the up slope and the mid-slope is about 72 m, and the distance between the mid-slope and the down slope is about 56 m. The corresponding contents have been added to the 2.1 study area. Table 1 presents the average values of soil properties, which were determined by taking three parallel soil samples 30 cm apart from each soil horizon at all three slope with the depth 0–10, 10–30, and 30–40 cm. Samples were collected using a 100-cubic-centimeter cylinder to determine bulk density and saturated hydraulic conductivity. For each soil depth, six parallel samples were prepared, with three used for measuring bulk density and three for measuring saturated hydraulic conductivity. Additionally, 500 g soil horizon samples were stored in PE self-sealing bags for soil texture analysis.

After a 12-h drying in an oven at 105°C, soil bulk density was determined as the dry weight per unit volume of soil core. The soil particle size was analyzed in the laboratory utilizing the Microtrac

TABLE 1 Basic properties of soils at the slope sites.

Site	Depth (cm)	Particle size distribution (%)						Bulk density (g cm^{-3})	Saturated hydraulic conductivity (ksat) (mm min^{-1})	Total porosity (%)	Volumetric moisture content (%)
		Sand% (>60 μm)	Average	Silt% (2–60 μm)	Average	Clay % (<2 μm)	Average				
Down slope	0–10	7.27	6.31	75.24	71.92	17.49	21.76	0.8 ± 0.3	5.89 ± 2.27	70.3 ± 11.9	49.5 ± 5.4
	10–30	6.41		66.82		26.77		1.0 ± 0.4	2.79 ± 0.77	61.5 ± 14.7	44.7 ± 7.1
	30–40	5.26		73.7		21.03		1.2 ± 0.4	1.28 ± 0.05	55.2 ± 15.8	39.8 ± 9.5
Mid slope	0–10	6.5	5.99	77.09	73.41	16.41	20.59	0.9 ± 0.1	1.45 ± 0.04	67.6 ± 3.8	43.8 ± 4.9
	10–30	10.56		72.25		17.18		0.8 ± 0.2	1.68 ± 0.45	68.2 ± 8.1	41.1 ± 3.7
	30–40	0.92		70.9		28.17		1.1 ± 0.3	1.24 ± 0.02	59.9 ± 12.2	39.3 ± 6.7
Up slope	0–10	4.3	3.17	76.87	72.67	18.83	24.17	0.8 ± 0.2	6.21 ± 0.65	69.8 ± 5.7	43.8 ± 1.0
	10–30	3.15		73.23		23.62		0.9 ± 0.2	1.29 ± 0.97	66.3 ± 5.8	44.1 ± 5.2
	30–40	2.05		67.9		30.05		1.1 ± 0.2	0.30 ± 10.17	59.8 ± 8.2	41.1 ± 7.1

Note: For bulk density, saturated hydraulic conductivity (Ksat), total porosity, and volumetric moisture content, the mean value and standard deviation are given.

S3500 (United States) laser particle size meter after sample dispersion treatment. The saturated hydraulic conductivity (Ksat) was measured through the constant head method. In the laboratory, a cutting ring is used to measure the amount of water that passes through a unit area per unit time under a unit water potential gradient. The soil volume moisture content was determined through a Spectrum TDR350 (United States) during excavation. Total porosity is derived from bulk density. Both were determined directly for each undisturbed sample after drying at 105°C for 24 h, assuming a particle density of 2.65 g cm^{3} (Alaoui, 2023; Benegas et al., 2014).

According to the international system of soil texture classification, the soil on this slope is characterized as silty loam, with a texture dominated by silt, comprising 66.82%–77.09% of its composition. The soil bulk density exhibits a range of 0.8–1.2 g cm^{-3}. The saturated hydraulic conductivity ranges from 0.3 to 6.21 mm min^{-1}. Total porosity ranges from 55.2% to 70.3% and volumetric moisture content ranges from 39.3% to 49.5%. As soil depth increased, soil bulk density showed an upward trend, whereas volumetric moisture content exhibited a downward trend.

2.4 The image processing

To determine an accurate measure of the stained areas, the processing of the dyed image is divided into four steps: geometric correction, white balance correction, color correction, and image denoising (Figure 3) (Forrer et al., 2000). In the first step, the image was corrected with DxO Optics Pro 11, the pixels of each profile image are 1,600 × 640 (1,000 mm × 400 mm). In the second step, the color was replaced with GIMP 2.10.14, replacing the dyed part with white and the undyed part with black. The Gaussian filter method is adopted for the process of Image Denoising in image processing. The mineral soil, organic soil, stones, roots, and stained areas were then manually identified in order to enhance the image truth of the analysis. In the third step, Matlab was used to convert the image into a TXT file of "0.255″through Raster Calculator and the Raster Converter Tool. Based on the TXT file, Excel were used to calculate the feature data of preferential flow path.

The original dyed profiles of the three points are presented in Figure 4, where numerous roots and rocks can be observed in the stained areas of the profiles. Nimmo (2020) pointed out that macropore flow can be observed through simple observation. Its characteristic lies in continuity rather than the size of the aperture. As shown in Figure 4, stones and root systems can be observed with in the soil profile. To better characterize the distribution of stones, root systems, and macropores in soil profiles, we performed digital image processing using morphological operations (erosion and dilation) on binary images. After identifying the features of stones, roots, and macropores, we calculated the percentage of area they occupy in the soil layer.

2.5 Characteristic indexes of preferential flow

To analyze the degree of preferential flow in soils, the dye coverage, total stained area, uniform infiltration depth,

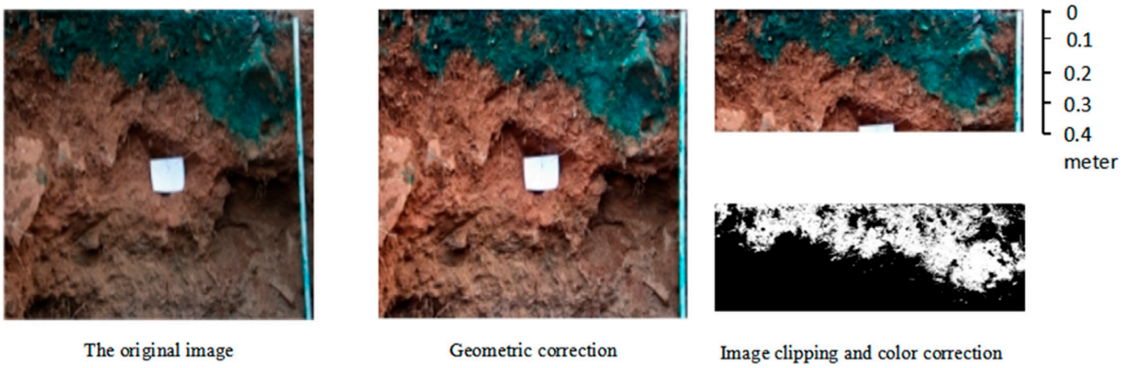

FIGURE 3
Image processing process.

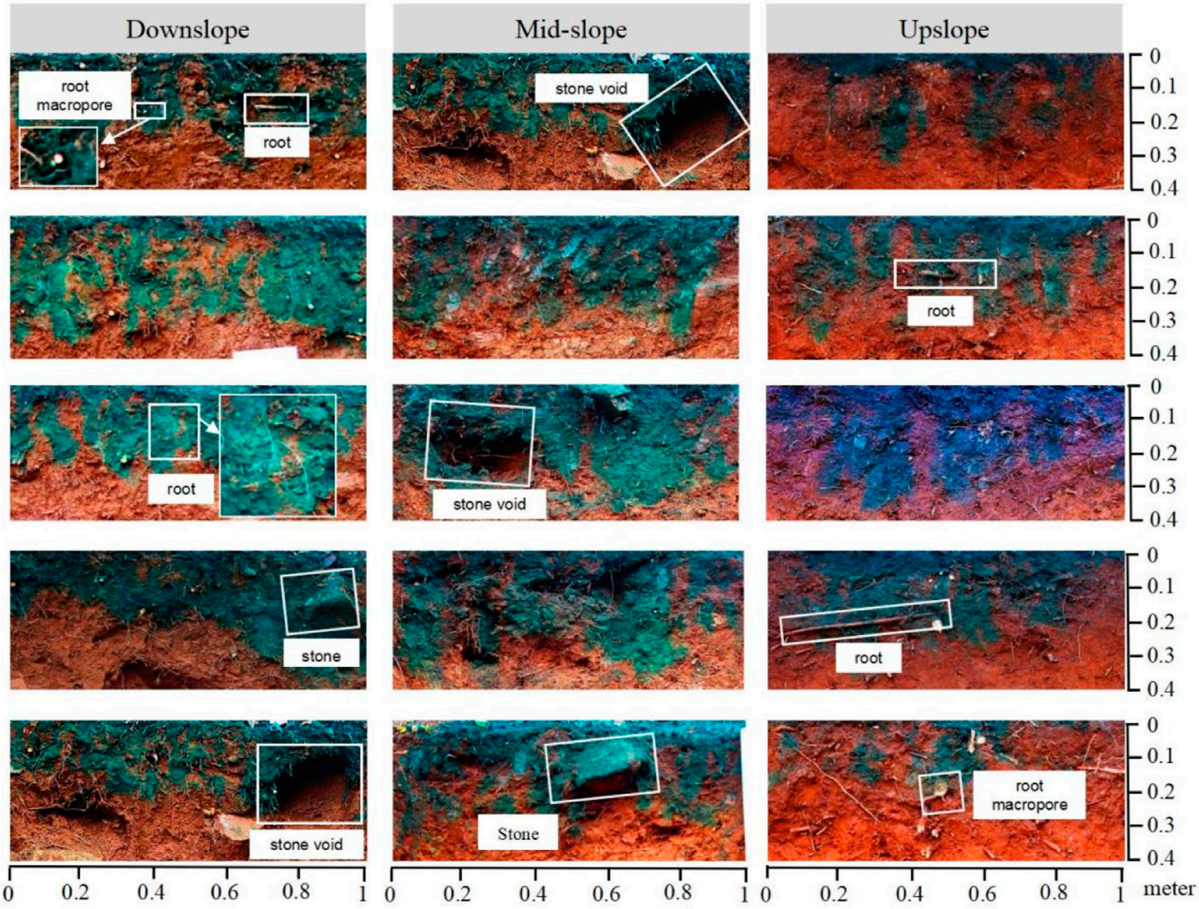

FIGURE 4
Profiles of three slope positions.

preferential flow fraction, coefficient of variation, length index, and peak index are commonly used as the indexes extracted from stained profiles (Bargués Tobella et al., 2014; Benegas et al., 2014; Zhang et al., 2017; Zhu et al., 2020). Five vertical profiles were excavated for each slope position. The parameters of each section are calculated as follows. The presented parameters are the average values of the five vertical soil profiles for each sampling location.

2.5.1 Dye coverage (DC)

It is calculated as the ratio of the dye-stained area to the sum of the dye-stained area and the non-stained area. Mathematically, this can be expressed as Equation 1 (Hendrickx and Flury, 2001).

$$DC = \left(\frac{D}{D + ND}\right) \cdot 100 \tag{1}$$

Here, DC is the percentage of dye coverage, D signifies the area that has been stained by the dye, and ND represents the area that remains unstained. The DC depends on the maximum dyed depth that is 640 pixels.

2.5.2 Total stained area (TSA)

TSA defines as the sum of the cumulative areas of all dye units within a profile that is 100 cm wide and 40 cm deep (Cai et al., 2024).

2.5.3 Uniform infiltration depth (UID)

The uniform infiltration depth is where the stained area drops sharply below 80% and a clear infiltration front is visible. When the matrix's infiltration capacity is not exceeded, macropore infiltration remains low. Therefore, matrix infiltration is key to triggering macropore flow (van Schaik, 2009).

2.5.4 Preferential flow fraction (PFF)

PFF is defined as the proportion of the total infiltration volume that specifically flows through preferential flow paths within the system or medium under consideration (Equation 2) (Benegas et al., 2014; van Schaik, 2009). This fraction quantifies the significance of preferential flow in the overall infiltration process.

$$PFF = 100 \times \left(1 - \frac{UID \times 100}{TSA}\right) \tag{2}$$

where PFF is the preferential flow fraction (%), UID is the uniform infiltration depth (cm), which is multiplied by the width of the profile (100 cm).

2.5.5 Length index (LI)

LI refers to the cumulative measure of the absolute variations in dye coverage values as they vary with depth across a given profile (Equation 3). It represents the total deviation from uniformity or homogeneity in dye penetration along the depth profile. Stain patterns from soils where infiltration is dominated by preferential flow are more heterogeneous than those where uniform flow is predominant. Therefore, soils with a higher development of preferential flow tend to exhibit higher values of the length index (Bargués Tobella et al., 2014).

$$LI = \sum_{i=1}^{n} \left| DC_{i+1} - DC_i \right| \tag{3}$$

where LI is the length index; and i represents a given depth interval (or zone) in which dye coverage, same as the stained area (DC (%)) was calculated, and DC_i and DC_{i+1} represent the dye area ratio corresponding to layer i and layer i+1, respectively, of the soil profile. n is the vertical pixel, which is 639.

2.5.6 Peak value (PV)

The number of times a vertical line based on total dye coverage (the maximum depth of staining is 640 pixel) intersects the dye coverage profile. This parameter reflects the heterogeneity of stained patterns; higher values suggest a greater degree of preferential flow (Bargués Tobella et al., 2014).

2.5.7 Coefficient of variation (CV)

CV is a measure of heterogeneity of the soil profile staining (Equation 4) (Zhang et al., 2017).

$$CV = \frac{\sqrt{\frac{1}{n-1}\sum_{i=1}^{n}\left(DC_i - \overline{DC}\right)^2}}{\frac{1}{n}\sum_{i=1}^{n} DC_i} \tag{4}$$

where $\overline{DC}$ is the average ratio of the dye area. n is the vertical pixel, which is 640.

2.6 Multi-index evaluation of preferential flow

To accurately reflect the varying degrees of soil preferential flow across different slope positions and neutralize discrepancies among diverse indices, the range method was employed to standardize the preferential flow index, yielding a dimensionless value. This standardized value was then utilized to compute the mean square deviation for each index. Ultimately, the weight coefficients for each index were assigned through the mean square error decision-making approach (Zhang et al., 2017). The weights are calculated for seven indicators on three slopes, each indicator is calculated through 15 profiles, so i is the number of copies of the indicator (1–15) when standardizing, and j is the serial number (1–7) of the given indicator.

Utilizing the standardized values and respective weight coefficients, an evaluation index for preferential flow is derived. This integrated result encapsulates the contributions of all indices, effectively mirroring the extent of preferential flow development within the soil. A higher value signifies a high degree of preferential flow development.

Index normalization (Equation 5):

$$Z_{ij} = \frac{\left| X_{ij} - X_{\min-j} \right|}{X_{\max-j} - X_{\min-j}} \tag{5}$$

where Z_{ij} is the standardized value of the index; X_{ij} is the actual value of the preferential flow index; $X_{\max-j}$ is the maximum value of the indicator j; $X_{\min-j}$ is the minimum value of the indicator j.

The mean of the normalized index $E(G_j)$ (Equation 6):

$$E\left(G_j\right) = \frac{1}{15}\sum_{i=1}^{15} Z_{ij} \tag{6}$$

Mean square deviation of each index $\sigma(G_j)$ (Equation 7):

$$\sigma\left(G_j\right) = \sqrt{\frac{1}{15}\sum_{i=1}^{15}\left(Z_{ij} - E\left(G_j\right)\right)^2} \tag{7}$$

Calculate the weight coefficient of each index W_j (Equation 8):

$$W_j = \frac{\sigma\left(G_j\right)}{\sum_{j=1}^{7}\sigma\left(G_j\right)} \tag{8}$$

Preferential flow evaluation index P_{FI} (Equation 9):

$$P_{FI} = \sum_{j=1}^{7}\sum_{i=1}^{15} Z_{ij}W_j \tag{9}$$

2.7 Classification of preferential flow

According to the SPW profiles, preferential flows were categorized into five distinct types, each representing a unique pattern of water movement within the soil. Five distinct vertical water transport patterns were characterized by specific soil properties and SPW distributions (Weiler and Flühler, 2004).

1. Macropore flow with low interaction, occurring in low-permeability or saturated soil matrices, exhibits greater than 50% SPW in sub-20 mm zones and less than 20% SPW in zones exceeding 200 mm, indicative of limited pore-matrix connectivity.
2. Macropore flow with mixed interaction (combining high and low interactions), observed in heterogeneous soils or variable macropore networks, demonstrates 20%–50% SPW in sub-20 mm zones while maintaining less than 20% SPW above 200 mm, reflecting transitional flow dynamics.
3. Macropore flow with high interaction in permeable soil matrices (textured or aggregated) shows less than 20% SPW in sub-20 mm zones and under 30% SPW beyond 200 mm, consistent with strong hydraulic exchanges between macropores and the matrix.
4. Heterogeneous matrix flow and fingering, driven by spatial variability in texture/aggregation, water repellency, or flow instability, retains less than 20% SPW in sub-20 mm zones but displays 30%–60% SPW in zones surpassing 200 mm, suggesting preferential flow pathway formation.
5. Homogeneous matrix flow in permeable soils exhibits less than 20% SPW in sub-20 mm zones and over 60% SPW in zones greater than 200 mm, aligning with classical Darcian flow behavior. These patterns quantitatively link soil structural heterogeneity to transport mechanisms through systematic SPW signature analysis.

Three of them are related to macropore flow, including macropore flow and surrounding soil matrix with low interaction, mixed interaction, and high interaction; and two of them involve matrix flow, including heterogeneous matrix flow and fingering and homogeneous matrix flow. Interaction is defined as vertical water flow from preferential into the surrounding soil matrix.

2.8 Statistical analysis

2.8.1 Multiple comparison method

A statistical technique used to compare the mean values of multiple indicators simultaneously. Its aim is to identify significant differences among the mean values of indicators from different slope positions through a series of statistical tests, thereby providing a more precise understanding of the variations and relationships among slope positions.

2.8.2 Correlation analysis

A statistical method that assesses whether two variables change in the same direction (positive correlation) or opposite directions (negative correlation). The closer the correlation coefficient value is to 1 or −1, the stronger the relationship between the variables; whereas, a value closer to 0 indicates a weaker correlation. The Pearson correlation analysis assume that the variables follow a normal distribution. We performed tests for normality with the Shapiro - Wilk (Small - data samples generally refer to those with a sample size of less than 5,000) test on our data. If the data does not pass the normality test, appropriate methods were selected to transform the data so that it conforms to the normal distribution, and then perform Pearson correlation analysis.

3 Results

3.1 Analysis of preferential flow stained images

The qualitative visual analysis of flow patterns was conducted based on the binary images produced. The infiltration patterns are assessed semiquantitatively by analyzing the dye coverage distributions (Flury and Flühler, 1995). This involves counting the number of stained pathways that contribute to preferential flow, which provides a quantifiable measure of the extent and nature of preferential flow within the system. Figure 5 reveals that the soil preferential flow dye depth is similar at three locations on the slope. A distinct and pronounced staining of the upper soil layer was consistently observed across all positions. The dye depth is about 400 mm and the dye area decreases with the depth. At the upslope and mid-slope locations, with the increase of the depth, the dye area shows a trend of first decreasing, then keeping stable, and finally decreasing. The stabilization stage is between 150 and 250 mm. While, at the downslope location, the overall trend of the dye area is first decreasing, then increasing, and finally decreasing. The increasing stage was found between 100 and 125 mm. In stained profiles from 0 to 400 mm, upslope has higher dye coverage, i.e., total stain area is 1,962.1 cm^2, accounting for 49%, where mid-slope and downslope have lower dye coverage, total stain areas are 1,879.7 and 1,917.4 cm^2, accounting for 47% and 48%, respectively. But overall the differences in the total stain areas are not substantial.

Uniform infiltration depths are highest on upslope reaching to 70 mm and relatively lower at mid-slope and downslope, reaching 44.8 and 55 mm, respectively. So the average infiltration depth is 56.6 mm. High uniform infiltration depth indicates that there is a high matrix flow upslope. Accordingly, the result of the preferential flow fraction (PFF) is opposite to that of the uniform infiltration depth. The PFF is lowest at upslope accounting for 56.6%, while mid-slope and downslope have a relatively higher PFF, accounting for 74.8% and 67.5%, respectively. The elevated length index and peak value signify a considerable degree of preferential flow development. At mid-slope, the LI and PV are 431 and 7, respectively, indicating that the preferential flow development is more pronounced in the mid-slope region compared to the upslope and downslope areas. This is consistent with the PFF result at mid-slope.

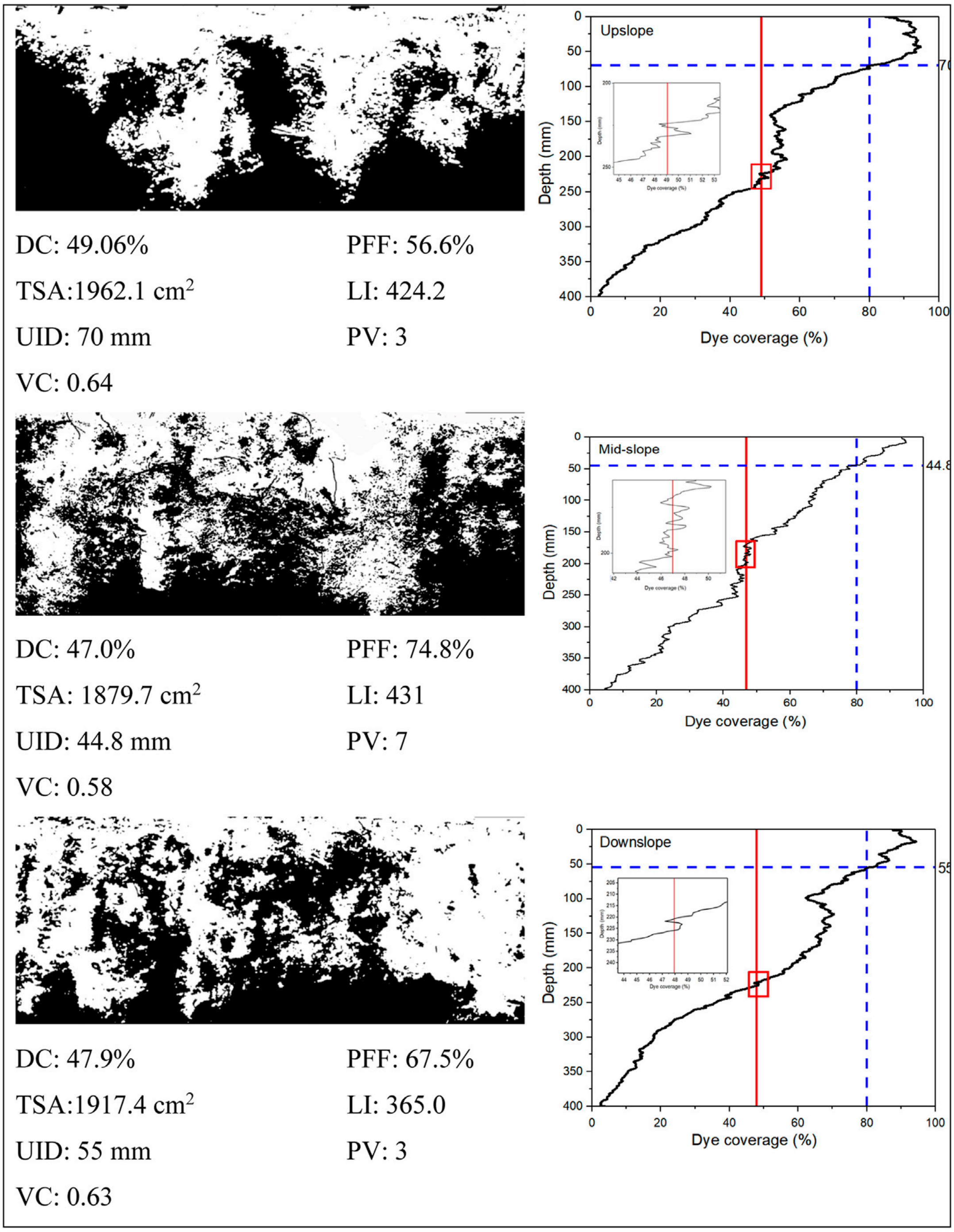

FIGURE 5
Images of examples vertical stained profiles and preferential flow parameters (White: stained area; black: unstained area; the blue line is the soil depth corresponding to DC = 80% (UID); the red line is the profile DC; the peak value can be seen in the red rectangle, and the details are shown to the left of the red rectangle).

Spatial variations in macropore flow potential across slope positions were linked to soil structural and hydraulic properties (Tables 1, 2). The mid-slope exhibited the highest potential for macropore-dominated flow, driven by its elevated stone content (17.01% in 0–10 cm) and silt-dominated matrix (73.41% silt), which promoted preferential pathways through inter-stone voids despite low matrix hydraulic conductivity (Ksat: 1.45 ± 0.04 mm min^{-1}). The downslope showed intermediate potential, with higher sand content (6.31% sand) and Ksat (5.89 ± 2.27 mm min^{-1}) supporting moderate macropore connectivity, yet compaction (bulk density: 1.0 ± 0.4 g cm^{-3} at 10–30 cm) likely restricted lateral flow continuity. In contrast, the upslope, despite the highest root density (12.68%) and macropore abundance (9.10%), prioritized vertical infiltration due to elevated Ksat (6.21 ± 0.65 mm min^{-1}) and clay-enriched

TABLE 2 Distribution of rocks, roots and large holes in soil layer.

Position	Soil depth (cm)	Stones (%)	Macropores (%)	Roots (%)
Up slope	0–10	4.34	9.10	12.68
	10–30	3.06	2.31	11.60
	30–40	0.60	0.38	0.40
Mid slope	0–10	17.01	3.00	10.95
	10–30	1.36	1.34	4.21
	30–40	0.32	0.13	0.17
Down slope	0–10	5.22	5.01	9.54
	10–30	2.43	2.28	4.64
	30–40	0.16	0.44	0.00

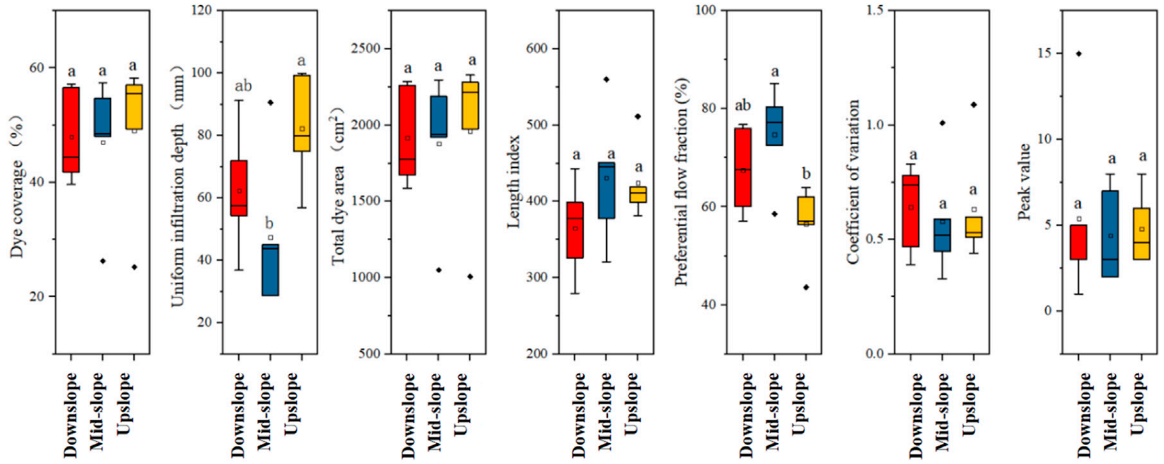

FIGURE 6
Boxplots of preferential flow parameters at each sampling position. Note: Within each indicator, if the boxes are labeled with different letters, it indicates that there are significant differences among slope positions; otherwise, there are no significant differences. The calculation of each slope position's indicator is derived from the analysis of five profiles.

texture (24.17% clay), which enhanced water retention (volumetric moisture: 43.8% ± 1.0%) but limited lateral macropore activation. Vertical heterogeneity was evident across all positions, with macropore-related parameters (e.g., Ksat, roots) declining sharply below 10 cm depth.

3.2 Multi-indicator evaluation

The PFF and UID represent preferential flow and matrix flow, respectively. LI and PV indicate the heterogeneity of the flow pattern. Compared to the other slope positions, at mid-slope, high preferential flow fraction (PFF = 74.8%), low uniform infiltration depth (UID = 44.8 mm), high length index (LI = 431), and high peak value (PV = 7) are present. Figure 6 shows that uniform infiltration depth and preferential flow fraction have significant differences at mid-slope and upslope while downslope has no significant difference with the other two sites. The uniform infiltration depth upslope has the highest value and variation indicating that matrix flow is relatively well developed, but high variability indicates developmental instability, and preferential flow at mid-slope is well developed and stable. At the mid-slope, the preferential flow fraction exhibits significant differences compared to the upslope, whereas no significant differences are observed when compared to the downslope.

To calculate the weight of each indicator, we calculated the preferential flow indicator for 15 profiles at three locations according to Section 2.6. The calculation results of the standardized mean value, mean square deviation and weight coefficient of each indicator are listed in Table 3. It is evident that the weight of the uniform infiltration depth (0.16) and peak value (0.18) is higher when evaluating the development degree of the preferential flow, indicating that these two indicators play an important role in the evaluation of preferential flow. However, the distribution of the parameter weight coefficient is relatively uniform, and there is no decisive factor for excessive weight, which is related to the large variation of the distribution characteristics of preferential flow.

TABLE 3 The standardized mean value, mean square error, and weight coefficient of each index.

Indicators	Mean value	Mean square error	Weight coefficient
Dye coverage, DC	0.69	0.33	0.15
Uniform infiltration depth, UID	0.49	0.35	0.16
Total stain area, TSA	0.69	0.33	0.15
Length index, LI	0.45	0.26	0.11
Preferential flow fraction, PFF	0.55	0.27	0.12
Coefficient of Variation, CV	0.38	0.30	0.13
Peak value, PV	0.35	0.40	0.18

TABLE 4 The preferential flow evaluation index at three slope positions.

Slope position	Evaluation index of preferential flow			
	Minimum value	Maximum value	Standard deviation	Mean value
Upslope	0.23	0.62	0.14	0.48
Mid-slope	0.41	0.73	0.10	0.61
Downslope	0.36	0.54	0.16	0.44

There are five soil profiles at each slope position. The preferential flow evaluation index at different slope positions was calculated according to the normalized value and weight coefficient of each index. As can be seen from Table 4, the evaluation index of preferential flow at upslope is between 0.23 and 0.62, with a mean value of 0.48 and standard deviation of 0.14. At mid-slope, the evaluation index of the preferential flow was between 0.41 and 0.73, with a mean value of 0.61 and a standard deviation of 0.10. The evaluation index of preferential flow at downslope ranged from 0.36 to 0.54, with an average value of 0.33 and a standard deviation of 0.16. Thus, it could be concluded that the preferential flow developed best at mid-slope followed by downslope. The development degree of preferential flow at upslope was the lowest.

3.3 Classification of preferential flow

As we defined in Section 2.4, the preferential flow in this study is mainly macropore flow. According to Weiler and Flühler (2004), the SPW profile for each experiment is constructed by integrating all the vertical dye patterns obtained within that specific experiment. What is striking in Figure 7 is that the stain widths of the three experimental locations showed heterogeneity with the change of depth. With the increase of depth, the proportion of dye width less than 20 mm gradually increases, while the proportion of dye width greater than 200 mm tends to decrease. The proportion of dye width from 20 to 200 mm first increases and then decreases. The macropore flow width can be categorized into three distinct sections based on depth, with dividing points occurring at 100 and 275 mm (horizontal lines in Figure 7), respectively. In the depth ranges of 0–100 mm, the SPW greater than 200 mm has a certain advantage, but the advantage downslope is lower. In the range of 100–275 mm, the macropore flow with width of 20–200 mm is absolutely dominant. When the soil depth is greater than 275 mm the dye width mainly is less than 20 mm and macropore flow with a width greater than 200 mm seldom occurs.

Both matrix flow and macropore flow were observed at the three sampling locations (downslope, mid-slope, and upslope). Matrix flow, when present, occurred in the top 50 mm of the soil profile and no matrix flow was observed below this in either soil texture. Figure 8a shows that the macropore flow changes from matrix flow to macropore flow with the increase of depth, and the interaction between macropores and surrounding soil matrix decreases gradually indicating the degree of macropores increased. The three slope positions at 0–100 mm depth are mainly homogeneous matrix flow and finger flow. Macropore flow with mixed interaction (both high and low) is dominant at depths ranging from 100–275 mm, while macropore flow with mixed interaction primarily occurs between depths of 275–400 mm. As the depth increases, the types of macropore flow become more dispersed, particularly at the downslope location. The macropore flow regime transitions sequentially from mixed-interaction to high-interaction dominance, followed by a gradual shift toward low-interaction dynamics. At mid-slope and upslope, vertical macropore flow with mixed interaction is relatively homogeneously distributed.

Figure 8b shows vertical macropore flow especially with mixed interaction dominates the macropore flow on the slope and matrix flow is less prevalent. The total percentage of matrix flow at three slope position increases with the increase of elevation, accordingly accounting for 4.7, 13.2, and 18.8%, respectively. Accordingly, macropore flow accounts for 95.3, 86.8, and 81.2% when moving up the slope. As elevation increases, the proportion of vertical macropore flow characterized by high interaction with surrounding soil matrix decreases, with 22.1% observed at the downslope location and a negligible amount (0.6%) found at the upslope location. The proportion of vertical macropore flow

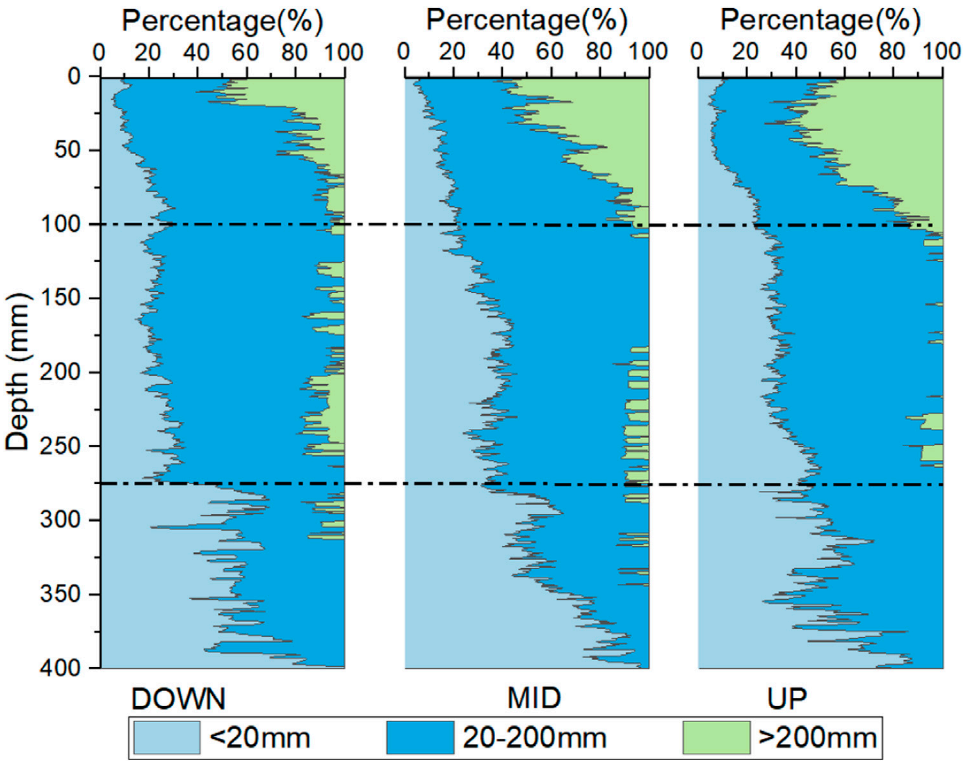

FIGURE 7
The distribution of soil stain width with depth (Weiler and Flühler, 2004).

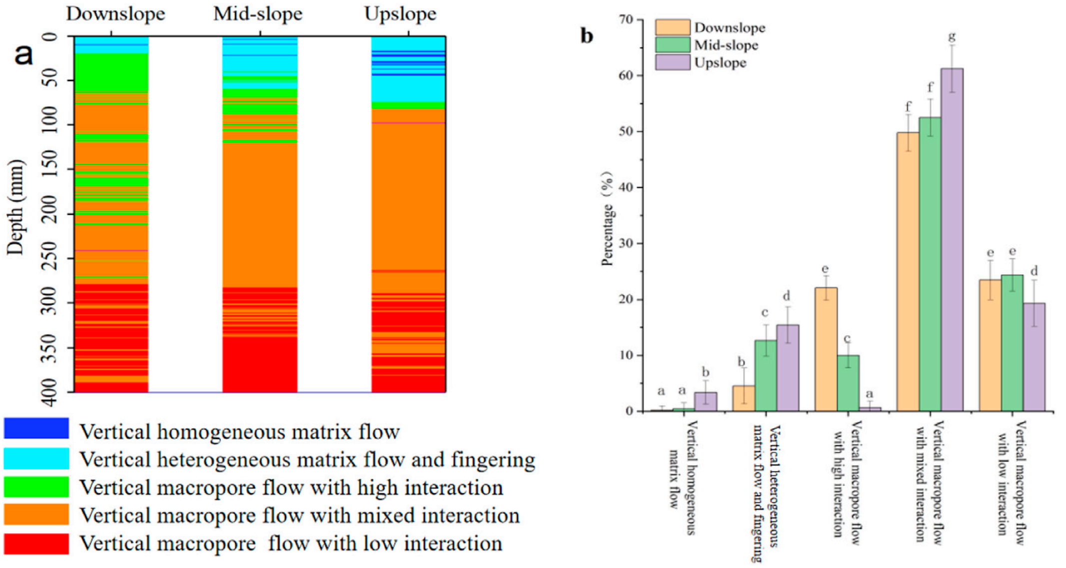

FIGURE 8
Macropore flow types at different slope locations. Note: **(a)** represents the change of macropore flow type with depth, and **(b)** represents the percentage of each macropore flow type at different positions. There is a significant difference between bar charts containing different lowercase letters.

featuring mixed interaction exhibits an upward trend with increasing elevation, comprising 49.8% at the downslope location, 52.5% at the mid-slope, and peaking at 61.3% at the upslope position.

Table 5 displayed the percentages of the five flow types within the soil layers. As depicted in Figure 8a, the vertical macropore flow with low interaction predominantly took place in the deep soil layer (ranging from 30 to 40 cm). Specifically, it accounted for 16.88%,

TABLE 5 The percentage of the five flow types for the soil layers (%).

Site	Depth (cm)	Vertical macropore flow with low interaction	Vertical macropore flow with mixed interaction (high and low)	Vertical macropore flow with high interaction	Vertical heterogeneous matrix flow and fingering	Vertical homogeneous matrix flow	Proportion of macropore flow
Down slope	0–10	0.00	8.28	12.03	4.53	0.16	95.31
	10–30	5.00	35.00	10.00	0.00	0.00	
	30–40	18.59	6.41	0.00	0.00	0.00	
Mid slope	0–10	0.00	3.44	8.44	12.66	0.47	86.88
	10–30	4.22	44.22	1.56	0.00	0.00	
	30–40	20.16	4.84	0.00	0.00	0.00	
Up slope	0–10	0.00	3.48	0.83	15.01	5.68	79.31
	10–30	1.88	48.13	0.00	0.00	0.00	
	30–40	16.88	8.13	0.00	0.00	0.00	

TABLE 6 Correlation between macropore flow type and soil properties.

Soil properties	Vertical macropore flow with low interaction	Vertical macropore flow with mixed interaction	Vertical macropore flow with high interaction	Vertical heterogeneous matrix flow and fingering	Vertical homogeneous matrix flow
Volumetric water content of the soil	**−0.767***	0.064	**0.786***	0.336	0.145
Bulk density	**0.960****	−0.429	−0.502	−0.42	−0.265
Saturated hydraulic conductivity (Ksat)	−0.583	−0.18	0.311	0.629	**0.804****
Porosity	**−0.939****	0.498	0.467	0.361	0.188
Sand	−0.548	0.363	0.485	0.096	−0.073
Silt	−0.505	−0.342	0.081	**0.747***	0.519
Clay	0.666	0.034	−0.333	−0.579	−0.323

*Significant correlation at 0.05 level. **Significant correlation at 0.01 level. The bold font is used to emphasize significant relations.

20.16%, and 18.59% at the down slope, mid slope, and up slope respectively. The vertical macropore flow with mixed interaction (both high and low) mainly occurred in the middle part of the stained soil layer (from 10 to 30 cm). At the down slope, mid slope, and up slope, its proportions were 48.13%, 44.22%, and 35% respectively. Elevational gradients positively correlate with both the progressive deepening of infiltration depths and the proportional increase of high-interaction macropore flow. On the contrary, the proportion of the matrix flow experiences a continuous decline. Matrix flow only occurred in topsoil (0–10 cm).

As can be seen from Table 5, excluding the vertical heterogeneous matrix flow and fingering and vertical homogeneous matrix flow, the proportions of preferential flow related to macropores are 79.31%, 86.88%, and 95.31%, respectively, as the altitude decreases. Correspondingly, the percentages of preferential flow obtained by the multi-index evaluation method are 56.6%, 74.8%, and 67.5% (Figure 4), respectively. Both methods indicate that the upslope position has less pronounced preferential flow characteristics compared to the other positions.

3.4 The potential relationship between macropore flow types and soil properties

Based on the depth of soil property sample collection (0–10, 10–30, 30–40 cm), we have categorized and quantified the various types of macropore flow observed within distinct soil horizons. A Pearson correlation analysis (presented in Table 6) was conducted to investigate the association between the proportion of these macropore flow types and the soil properties. There's a positive correlation between volumetric water content of the soil and vertical macropore flow with high interaction, while a negative one with low interaction. Higher high-interaction proportion means more matrix flow and higher moisture content; higher low-interaction proportion leads to more macropore flow but lower moisture content. The greater the soil bulk density, the smaller the porosity, and the greater the degree of soil compaction, which restricts water infiltration through the soil matrix (Karahan and Erşahin, 2017; Luo et al., 2020). In this case, once macropores (such as roots, stones, etc.) exist in the soil, these macropores will be relatively stable. When water flows through, the interaction with the surrounding soil is relatively small, resulting in a relatively high proportion of macropore flow with low interaction. Saturated hydraulic conductivity (Ksat) has a significant positive correlation with homogeneous matrix flow. High Ksat promotes matrix flow as large pores mainly handle water transport under saturation, causing uniform downward water movement. The silt content in the soil significantly affects the formation of heterogeneous matrix flow and fingering.

4 Discussion

4.1 Dye patterns: hydrometeorological controls on preferential flow

Image analysis revealed distinct spatial heterogeneity in macropore flow characteristics across the slope profile, with differential flow classifications between slope positions. In this study, dye penetration depths consistently reached ~400 mm, exceeding the <400 mm staining depth recorded under 250 mm simulated rainfall in Mount Maka (Zhang and Xu, 2016). Dye-tracing experiments demonstrated contrasting preferential flow penetration depths across ecosystems: 55 cm under 40 mm rainfall in Finland's forested slopes (Laine-Kaulio et al., 2015) versus 300 mm with 88 mm rainfall in Chinese loess plantations (Mei et al., 2018). These studies collectively indicate that staining depth is governed by rainfall intensity and vegetation-soil interactions. In our silt loam slope, measured dye depths (~400 mm) aligned with Grant et al. (2019), who reported 433–632 mm penetration in silt loam with no moisture-dependent variation. Preferential flow occurrence in this region exhibits strong hydrometeorological dependence, the average occurrence probability is 41%, surging to 71% when the rainfall events exceed 20 mm (Hu et al., 2019). This rainfall-intensity modulation amplifies with antecedent soil moisture, as demonstrated by Peng et al. (2016b) who documented 17.9%–74.3% frequency variations controlled by storm characteristics (amount/duration/intensity). Our measurements align with this pattern, showing 56.6%–74.8% preferential flow when soil moisture reached 40%–50%. Such moisture thresholds likely reflect macropore network interactions that elevate hydraulic pressure gradients, driving matrix-to-macropore water redistribution (Nieber and Sidle, 2010).

4.2 Slope position modulates preferential flow pathways

In our study, according to the applied quantification schemes, the flow at upslope position is less preferential compared to the mid-slope and downslope direction. Study on the effect of slope position on the spatial distribution of soil preferential flow paths in a subtropical evergreen broad-leaved forest area revealed that the middle slope was more likely to generate preferential flow than those at the upslope and the downslope (Li et al., 2024). The research on the slopes of tropical rainforest mountains also found that, combined with the infiltration capacity, the preferential flow increased with increasing hillslope elevation (Chen et al., 2021). While, some findings are opposite. In semiarid loess hillslopes, abundant rock fragments in the downslope locations resulted in higher preferential flow and infiltration variability (Mei et al., 2018). These results indicate that not only hillslope position but also other factors, such as soil type, properties, lithology and soil structure can influence the preferential flow (Tang et al., 2020). The multi-index evaluation of the entire soil profile revealed that the mid-slope position had the highest silt content (73.41%), which contributed to significant shrink-swell dynamics in the soil matrix. Frequent wet-dry cycles promoted macropores genesis at this position, potentially explaining the elevated preferential flow occurrence (74.8%). The relatively stable saturated hydraulic conductivity observed at mid-slope, compared to upslope and downslope areas, likely contributed to the maximum preferential flow peak (7) and highest preferential flow fraction. Stable saturated hydraulic conductivity values enhance structural connectivity through macropores and gravel, intensifying preferential flow through hydraulically efficient pathways.

4.3 Soil porosity and particle size dictate flow interaction

The correlation analysis shows that there is a significant negative correlation between soil porosity and macropore flow with low interaction. In stony soils of a small mountain catchment, assessed via Poiseuille's equation, the number of macropores decreased with soil depth (Hlavácіková et al., 2019), which may be the direct reason for the decrease of macropore flow interaction with depth. Table 1 indicates that as the soil depth increases, the soil porosity decreases. Correspondingly, Table 5 shows that as the soil depth increases, the proportion of macropore flow with high interaction decreases, while the proportion of macropore flow with low interaction increases. The relationship between particle size and preferential flow revealed that in clay loam or sandy clay loam soil, they were prone to macropore and finger flow (Liu et al., 2021), sandy soil favours the flow of water from macropores to the surrounding sandy matrix, and that preferential flow was more prevalent in clays than in silt loams (Grant et al., 2019).

4.4 Methodological trade-offs in preferential flow quantification

The flow type profiles demonstrate the persistence of individual flow types and the prevalence of transitions between distinct flow types. Furthermore, they reveal both differences and similarities among the experiments (Weiler and Flühler, 2004). Traditional digital image analysis is well suited for visualizing and quantifying water infiltration into soil (Persson, 2005), thereby identifying various infiltration mechanisms in the soil, but cannot be directly used to distinguish the different flow processes of each soil layer (Weiler and Naef, 2003). This paper combines the evaluation indicators extracted from the dye tracer image and the preferential flow path classification standard proposed by Weiler and Flühler (2004) to identify and classify the preferential flow. Quantifying preferential flow using a dye tracer experiment, various sources contributed to the overall error. The detailed examination of the precision of various correction methodologies and their consequences on outcomes remains unexplored. Moreover, the selection of camera, lens, and camera settings plays a pivotal role in determining image quality, which subsequently impacts the accuracy with which preferential flow is evaluated (Persson, 2005). The results calculated by the preferential flow fraction (Equation 2) indicate that the proportion of preferential flow is 56.6% on the upper slope, 74.8% on the middle slope, and 67.5% on the lower slope. This index is relatively single. Thus, we evaluated the preferential flow through seven indexes. Among them, the length index, peak value, and coefficient of variation are all related to the heterogeneity of the stained images. Since the preferential flow is a non-uniform flow, the staining changes in the regions through which it flows are more obvious. These three indexes can accurately reflect the degree of change in the staining patterns among different soil layers. The larger the preferential flow evaluation index value obtained based on multiple indexes is, the higher the development degree of the preferential flow will be. The preferential flow evaluation index derived through the standardized treatment of indexes and the mean square deviation analysis method can only evaluate the relative development among different slope positions and cannot quantify the proportion of preferential flow in the soil. On the other hand, the multi-index evaluation method is an overall evaluation of the stained area and can reflect the development of the degree of the preferential flow in soil. However, it cannot reflect the interaction between the preferential flow and the soil during infiltration process due to a lack of rigorous calibration when conducted the dye tracer experiment. Flow type classification can make up for this deficiency. By calculating the staining width and staining proportion of each soil layer (at the pixel level), the macropore flow was divided into five types. Through flow type classification, the relationship between macropore flow and the soil matrix was further investigated. Finally, the flow type classification method shows that the proportion of macropore flow is 79.31% on the upper slope, 86.88% on the middle slope, and 95.31% on the lower slope. Our findings indicate that the occurrence of heterogeneous matrix flow and fingering flow in the forest topsoil during infiltration processes is primarily driven by spatial variations in soil texture, water repellency, and flow instability (Weiler and Flühler, 2004). Textural analysis across soil horizons revealed that the silt percentage in the 0–10 cm layer at three slope positions consistently exceeded that in the 10–30 cm layer. This vertical textural differentiation establishes a soil structure with finer-textured horizons overlying coarser-textured substrates, creating a positive matric potential gradient at the interface that promotes flow instability and subsequent fingering development (Baker and Hillel, 1990; Selker et al., 1992).

However, the proportion of preferential flow obtained by the preferential flow classification method is higher than that by the multi-index method. The main reason lies in the difference in the scale of analysis. In the multi-index evaluation method, the proportion of preferential flow is derived by subtracting the dyed area of the matrix flow region from the dyed area of the entire profile. The calculation process is relatively straightforward and reflects more the overall summative effect of the profile. During the operations such as large-scale integration and averaging at the macroscopic level, the advantages of local macropore flow will be weakened. In contrast, the preferential flow classification method takes the dyed width as the core judgment basis, it can precisely capture macropore flow at the microscopic level by carrying out analysis at the soil layer scale (pixel level). Consequently, it is more likely to present higher values in the results. By combining these two methods, the characteristics of macropore flow and its interaction with the soil matrix can be judged more accurately.

4.5 Limitations: lateral vs. vertical preferential flow dynamics

The limitations of the current study is the relationship between slope lateral preferential and vertical preferential flow. A pivotal challenge within hillslope hydrology lies in the conceptual framing and parameterization of the impacts exerted by lateral preferential flow (Weiler and McDonnell, 2007). Current research indicates that as the input intensity increases at sites with comparatively large macropores, the production of vertical preferential flow also intensifies, whereas the contribution of parallel macropores to slope runoff remains minimal (Buttle and McDonald, 2002). In relation to soil structure, subsurface lateral preferential flow typically arises when percolating water within a soil profile encounters a hydrologically constraining layer, for instance, an impeding soil stratum, a soil profile characterized by differing textures, or a bedrock of low permeability (Guo et al., 2014). With regards to soil moisture content and rainfall intensity, lateral flow generation was observed exclusively when the soil's large storage capacity became saturated in conjunction with a minimum precipitation event exceeding a specific threshold amount (Todd et al., 2010). What's more, from the perspective of research methods, dye tracer experiment are more direct for visualizing vertical preferential flow than lateral preferential flow. Hydrological connectivity resulting from such pathways may be overlooked unless a pronounced diffusion phenomenon is observed at a greater depth. This type of lateral hydrological connectivity is characterized by its instability and complexity (Dai et al., 2020). The intricate characteristics of lateral preferential flow, coupled with the absence of a suitable investigation methodology, have posed obstacles to direct observation of this phenomenon in the field (Guo et al., 2014).

5 Conclusion

In this study, the characteristics of preferential flow on the slope and the relationship between macropore flow and soil properties were determined through the multi-index evaluation method and the macropore flow classification method. The details are as follows:

(1) The multi-index analysis method shows that the infiltration depth of preferential flow is 400 mm, while that of the average

uniform infiltration depth is 56.6 mm. It showed no significant difference from the average uniform infiltration depth of 56.6 mm obtained using the 80% stained area ratio. The proportion of the preferential flow component is 56.6% on the upper slope, 74.8% on the middle slope, and 67.5% on the lower slope. Through comprehensive analysis with multiple indexes, it is found that the level of preferential flow on the middle slope is higher than that on the upslope and downslope. The main reason is that the weights of the peak value, the stained area, and the stable infiltration depth are relatively high.

(2) The results of macropore flow classification show that the macropore flow at the three slope positions is mainly dominated by macropore flow with mixed interaction. As the elevation decreases, the proportion of macropore flow gradually increases. Specifically, the proportion of macropore flow is 79.31% on the upslope, 86.88% on the mid-slope, and 95.31% on the downslope. With the increase in the depth of the soil layer, the proportion of macropore flow with low interaction increases, and the interaction between macropore and the surrounding matrix soil decreases. Correlation analysis shows that macropore flow with low interaction has a significant negative correlation with soil volumetric water content and porosity, and a significant positive correlation with soil bulk density. Macropore flow with high interaction has a significant positive correlation with soil volumetric water content. Matrix flow and fingering have a significant positive correlation with the silt content in soil texture. Matrix flow has a significantly positive correlation with soil saturated hydraulic conductivity.

(3) The multi - index method and preferential flow classification method differ in analysis scales. The multi - index method gets the preferential flow proportion by subtracting the matrix flow dyed area from the whole profile dyed area. It is one sided in depicting preferential flow features and cannot well portray its dynamic changes in soil. In contrast, the preferential flow classification method, by calculating the proportion of different dyed widths at the pixel level, can more accurately judge macropore flow characteristics and its relationship with the soil matrix.

Data availability statement

The raw data supporting the conclusion of this article will be made available by the authors, without undue reservation.

Author contributions

YD: Conceptualization, Funding acquisition, Methodology, Visualization, Writing – original draft, Writing – review and editing. XW: Conceptualization, Funding acquisition, Project administration, Supervision, Writing – review and editing. ZN: Software, Writing – review and editing. TL: Validation, Visualization, Writing – review and editing. YT: Formal Analysis, Supervision, Validation, Writing – review and editing. LH: Validation, Visualization, Writing – review and editing.

Funding

The author(s) declare that financial support was received for the research and/or publication of this article. Funding for this research has been provided by the National Key Research and Development Program (No. 2018YFD0800902), Special fund for basic scientific research in central universities (No. ZY20220211, ZY20240227, ZY20220214), the Langfang City Science and Technology Bureau Scientific Research and Development Plan Self-funded Project (No. 2022013088, 2023013092), the Beijing Natural Science Fund - Beijing Municipal Education Commission jointly funded key projects (No. KZ201810028047), National Natural Science Foundation of China (No. 41271495), and the Sino-German PPP program (China Scholarship Council and German Academic Exchange Service).

Acknowledgments

The author would like to thank Professor Fuqiang Tian of Tsinghua University in particular for providing access to the Xitaizi Clean small watershed. The authors would like to thank Professor Charles S. Melching from Melching Water Solutions, Greenfield, Wisconsin, U.S for an internal review of the draft manuscript and for many useful comments and edits. The authors acknowledge the comments made by two reviewers which improve the quality of this paper.

Conflict of interest

The authors declare that the research was conducted in the absence of any commercial or financial relationships that could be construed as a potential conflict of interest.

Generative AI statement

The author(s) declare that no Generative AI was used in the creation of this manuscript.

Publisher's note

References

Alaoui, A. (2023). A simple method to assess key soil hydraulic properties. *Water* 15 (3), 467. doi:10.3390/w15030467

Alaoui, A., Caduff, U., Gerke, H. H., and Weingartner, R. (2011). Preferential flow effects on infiltration and runoff in grassland and forest soils. *Vadose Zone J.* 10 (2), 367–377. doi:10.2136/vzj2010.0076

Allaire, S. E., Roulier, S., and Cessna, A. J. (2009). Quantifying preferential flow in soils: a review of different techniques. *J. Hydrology* 378 (1-2), 179–204. doi:10.1016/j.jhydrol.2009.08.013

Anderson, A. E., Weiler, M., Alila, Y., and Hudson, R. O. (2009). Dye staining and excavation of a lateral preferential flow network. *Hydrology Earth Syst. Sci.* 13 (4), 935–944. doi:10.5194/hess-13-935-2009

Baker, R. S., and Hillel, D. (1990). Laboratory tests of a theory of fingering during infiltration into layered soils. *Soil Sci. Soc. Am. J.* 54 (1), 20–30. doi:10.2136/sssaj1990.03615995005400010004x

Bargués Tobella, A., Reese, H., Almaw, A., Bayala, J., Malmer, A., Laudon, H., et al. (2014). The effect of trees on preferential flow and soil infiltrability in an agroforestry parkland in semiarid Burkina Faso. *Water Resour. Res.* 50 (6), 3342–3354. doi:10.1002/2013WR015197

Benegas, L., Ilstedt, U., Roupsard, O., Jones, J., and Malmer, A. (2014). Effects of trees on infiltrability and preferential flow in two contrasting agroecosystems in Central America. *Agric. Ecosyst. and Environ.* 183, 185–196. doi:10.1016/j.agee.2013.10.027

Beven, K., and Germann, P. (1982). Macropores and water flow in soils. *Water Resour. Res.* 18 (5), 1311–1325. doi:10.1029/WR018i005p01311

Bogner, C., Borken, W., and Huwe, B. (2012). Impact of preferential flow on soil chemistry of a podzol. *Geoderma* 175-176, 37–46. doi:10.1016/j.geoderma.2012.01.019

Buttle, J. M., and McDonald, D. J. (2002). Coupled vertical and lateral preferential flow on a forested slope. *Water Resour. Res.* 38 (12). doi:10.1029/2001WR000773

Cai, L., Wang, F., Lin, Y., Long, Q., Zhao, Y., Han, J., et al. (2024). Changes in preferential flow caused by root effects in black locust plantations of different stand ages in the semi-arid region of the Loess Plateau. *J. Hydrology* 634, 131086. doi:10.1016/j.jhydrol.2024.131086

Chen, C., Zou, X., Singh, A. K., Zhu, X., Zhang, W., Yang, B., et al. (2021). Effects of hillslope position on soil water infiltration and preferential flow in tropical forest in southwest China. *J. Environ. Manag.* 299, 113672. doi:10.1016/j.jenvman.2021.113672

Chen, L., Yang, C., Wang, J., Meng, Q., and Tarolli, P. (2024). Variation in preferential flow features induced by desiccation cracks in physical crusts. *J. Hydrology* 634, 131118. doi:10.1016/j.jhydrol.2024.131118

Cui, Z., Tian, F., Zhao, Z., Xu, Z., Duan, Y., Wen, J., et al. (2024). Bimodal hydrographs in a semi-humid forested watershed: characteristics and occurrence conditions. *Hydrology Earth Syst. Sci.* 28 (15), 3613–3632. doi:10.5194/hess-28-3613-2024

Dai, L., Zhang, Y., Liu, Y., Xie, L., Zhao, S., Zhang, Z., et al. (2020). Assessing hydrological connectivity of wetlands by dye-tracing experiment. *Ecol. Indic.* 119, 106840. doi:10.1016/j.ecolind.2020.106840

Demand, D., Blume, T., and Weiler, M. (2019). Spatio-temporal relevance and controls of preferential flow at the landscape scale. *Hydrology Earth Syst. Sci. Discuss.* doi:10.5194/hess-2019-80

de Rooij, G. H. (2000). Modeling fingered flow of water in soils owing to wetting front instability: a review. *J. Hydrology* 231-232, 277–294. doi:10.1016/s0022-1694(00)00201-8

Ding, B., Cai, X., Wang, Y., Li, H., Zhao, X., Xiao, M., et al. (2023). Secondary vegetation succession following reforestation intensifies preferential flow by improving soil structure in the Chinese Karst region. *Ecol. Indic.* 156, 111166. doi:10.1016/j.ecolind.2023.111166

Flury, M., and Flühler, H. (1995). Tracer characteristic of brilliant blue FCF. *Soil Sci. Soc. Am. J.* 59 (1), 22–27. doi:10.2136/sssaj1995.03615995005900010003x

Forrer, I., Papritz, A., Kasteel, R., Flühler, H., and Luca, D. (2000). Quantifying dye tracers in soil profiles by image processing. *Eur. J. Soil Sci.* 51 (3), 313–322. doi:10.1046/j.1365-2389.2000.00315.x

Fuhrmann, S., Maarastawi, J., Neumann, J., Amelung, W., Frindte, K., Knief, C., et al. (2019). Preferential flow pathways in paddy rice soils as hot spots for nutrient cycling. *Geoderma* 337, 594–606. doi:10.1016/j.geoderma.2018.10.011

Grant, K. N., Macrae, M. L., and Ali, G. A. (2019). Differences in preferential flow with antecedent moisture conditions and soil texture: implications for subsurface P transport. *Hydrol. Process.* 33, 2068–2079. doi:10.1002/hyp.13454

Guan, N., Cheng, J., Bi, H., and Shi, X. (2024). Laboratory and field characterization of preferential flow under consideration of geometric fracture features in a karst region in Southwest China. *J. Hydrology* 631, 130851. doi:10.1016/j.jhydrol.2024.130851

Guo, L., Chen, J., and Lin, H. (2014). Subsurface lateral preferential flow network revealed by time-lapse ground-penetrating radar in a hillslope. *Water Resour. Res.* 50, 9127–9147. doi:10.1002/2013WR014603

Guo, L., and Lin, H. (2018). Addressing two bottlenecks to advance the understanding of preferential flow in soils. *Adv. Agron.* 147, 61–117. doi:10.1016/bs.agron.2017.10.002

Hendrickx, J. M. H., and Flury, M. (2001). "Uniform and preferential flow mechanisms in the vadose zone," in *Conceptual model of flow and transport in fractured vadose zone*. Washington, DC: The National Academies Press. doi:10.17226/10102

Hlaváčiková, H., Holko, L., Danko, M., and Novák, V. (2019). Estimation of macropore flow characteristics in stony soils of a small mountain catchment. *J. Hydrol.* 574, 1176–1187. doi:10.1016/j.jhydrol.2019.05.009

Hou, F., Cheng, J., Zhang, H., Wang, X., Shi, D., and Guan, N. (2024). Response of preferential flow to soil-root-rock fragment system in karst rocky desertification areas. *Ecol. Indic.* 165, 112234. doi:10.1016/j.ecolind.2024.112234

Hu, H., Wen, J., Peng, Z., Tian, F., Tie, Q., Lu, Y., et al. (2019). High-frequency monitoring of the occurrence of preferential flow on hillslopes and its relationship with rainfall features, soil moisture and landscape. *Hydrol. Sci. J.* 64, 1385–1396. doi:10.1080/02626667.2019.1638513

Jarvis, N. J. (2007). A review of non-equilibrium water flow and solute transport in soil macropores: principles, controlling factors and consequences for water quality. *Eur. J. Soil Sci.* 58, 523–546. doi:10.1111/j.1365-2389.2007.00915.x

Julich, D., Julich, S., and Feger, K. (2017). Phosphorus fractions in preferential flow pathways and soil matrix in hillslope soils in the Thuringian Forest (Central Germany). *J. Plant Nutr. Soil Sci.* 180 (4), 407–417. doi:10.1002/jpln.201600305

Kang, W., Tian, J., Lai, Y., Xu, S., Gao, C., Hong, W., et al. (2022). Occurrence and controls of preferential flow in the upper stream of the Heihe River Basin, Northwest China. *J. Hydrology* 607, 127528. doi:10.1016/j.jhydrol.2022.127528

Karahan, G., and Erşahin, S. (2017). Relating macropore flow to soil parametric and morphological variables. *Soil Sci. Soc. Am. J.* 81 (5), 1014–1024. doi:10.2136/sssaj2016.10.0327

Laine-Kaulio, H., Backnäs, S., Karvonen, T., Koivusalo, H., and Lauren, A. (2015). Dye tracer visualization of flow patterns and pathways in glacial sandy till at a boreal forest hillslope. *Geoderma* 249-260, 23–34. doi:10.1016/j.geoderma.2015.05.004

Laine-Kaulio, H., Backnäs, S., Karvonen, T., Koivusalo, H., and McDonnell, J. J. (2014). Lateral subsurface stormflow and solute transport in a forested hillslope: a combined measurement and modeling approach. *Water Resour. Res.* 50, 8159–8178. doi:10.1002/2014WR015381

Legout, A., Legout, C., Nys, C., and Dambrine, E. (2009). Preferential flow and slow convective chloride transport through the soil of a forested landscape (Fougères, France). *Geoderma* 151 (3-4), 179–190. doi:10.1016/j.geoderma.2009.04.002

Li, M., Yao, J., Yan, R., Fan, Y., and Liu, S. (2024). Effect of slope position on the spatial distribution of soil preferential flow paths based on point pattern analysis. *PLoS One* 19 (12), e0315660. doi:10.1371/journal.pone.0315660

Li, T., Shao, M. A., Jia, Y., Jia, X., and Huang, L. (2018). Small-scale observation on the effects of the burrowing activities of mole crickets on soil erosion and hydrologic processes. *Agric. Ecosyst. Environ.* 261, 136–143. doi:10.1016/j.agee.2018.04.010

Liu, Y., Zhang, S., and Liu, H. (2023). The relationship between fingering flow fraction and water flux in unsaturated soil at the laboratory scale. *J. Hydrology* 622, 129695. doi:10.1016/j.jhydrol.2023.129695

Liu, Y., Zhang, Y., Xie, L., Zhao, S., Dai, L., and Zhang, Z. (2021). Effect of soil characteristics on preferential flow of Phragmites australis community in Yellow River delta. *Ecol. Indic.* 125, 107486. doi:10.1016/j.ecolind.2021.107486

Luo, L., Lin, H., and Schmidt, J. (2020). Quantitative relationships between soil macropore characteristics and preferential flow and transport. *Soil Sci. Soc. Am. J.* 74 (6), 1929–1937. doi:10.2136/sssaj2010.0062

Luo, Z. T., Niu, J. Z., Xie, B. Y., Zhang, L. N., Chen, X. W., Berndtsson, R., et al. (2019). Influence of root distribution on preferential flow in deciduous and coniferous forest soils. *Forests* 10 (11), 986. doi:10.3390/f10110986

Luo, Z. T., Niu, J. Z., Zhang, L., Chen, X. W., Zhang, W., Xie, B. Y., et al. (2018). Roots-enhanced preferential flows in deciduous and coniferous forest soils revealed by dual-tracer experiments. *J. Environ. Qual.* 48 (1), 136–146. doi:10.2134/jeq2018.03.0091

Makowski, V., Julich, S., Feger, K. H., Breuer, L., and Julich, D. (2020). Leaching of dissolved and particulate phosphorus via preferential flow pathways in a forest soil: an approach using zero-tension lysimeters. *J. Plant Nutr. Soil Sci.* 183 (2), 238–247. doi:10.1002/jpln.201900216

Mälicke, M., Hassler, S., Blume, T., Weiler, M., and Zehe, E. (2019). Soil moisture: variable in space but redundant in time. *Hydrology Earth Syst. Sci. Discuss.*, 1–28. doi:10.5194/hess-2019-574

Mao, Z., Ma, X., Geng, M., Wang, M., Gao, G., and Tian, Y. (2024a). Development characteristics and quantitative analysis of cracks in root-soil complex during different growth periods under dry-wet cycles. *Biogeotechnics* 3, 100121. doi:10.1016/j.bgtech.2024.100121

Mei, X., Zhu, Q., Ma, L., Zhang, D., Wang, Y., and Hao, W. (2018). Effect of stand origin and slope position on infiltration pattern and preferential flow on a Loess hillslope. *Land Degrad. and Dev.* 29 (5), 1353–1365. doi:10.1002/ldr.2928

Nieber, J. L., and Sidle, R. C. (2010). How do disconnected macropores in sloping soils facilitate preferential flow? *Hydrol. Process.* 24 (12), 1582–1594. doi:10.1002/hyp.7633

Nimmo, J. R. (2020). The processes of preferential flow in the unsaturated zone. *Soil Sci. Soc. Am. J.* 85, 1–27. doi:10.1002/saj2.20143

Øygarden, L., Kværner, J., and Jenssen, P. D. (1997). Soil erosion via preferential flow to drainage systems in clay soils. *Geoderma* 76 (1-2), 65–86. doi:10.1016/S0016-7061(96)00099-7

Peng, Z., Hu, H., Tian, F., Tie, Q., and Zhao, S. (2016a). Impacts of rainfall features and antecedent soil moisture on occurrence of preferential flow: a study at hillslopes using high-frequency monitoring. *Hydrology Earth Syst. Sci. Discuss.* 2016, 1–22. doi:10.5194/hess-2016-112

Peng, Z., Tian, F., Hu, H., Zhao, S., Tie, Q., Sheng, H., et al. (2016b). Spatial variability of soil moisture in a forest catchment: temporal trend and contributors. *Forests* 7, 154. doi:10.3390/f7080154

Persson, M. (2005). Accurate dye tracer concentration estimations using image analysis. *Soil Sci. Soc. Am. J.* 69, 967–975. doi:10.2136/sssaj2004.0186

Rezanezhad, F., Vogel, H.-J., and Roth, K. (2006). Experimental study of fingered flow through initially dry sand. *Hydrology Earth Syst. Sci. Discuss.* 3, 2595–2620. doi:10.5194/hessd-3-2595-2006

Santra, P., Kumar, M., and Kumawat, R. N. (2021). Characterization and modeling of infiltration characteristics of soils under major land use systems in hot arid region of India. *Agric. Res.* 10 (3), 417–433. doi:10.1007/s40003-020-00511-1

Selker, J., Parlange, J. Y., and Steenhuis, T. S. (1992). Fingered flow in two dimensions: 2. Predicting finger moisture profile. *Water Resour. Res.* 28 (9), 2523–2528. doi:10.1029/92WR00962

Simard, R. R., Beauchemin, S., and Haygarth, P. M. (2000). Potential for preferential pathways of phosphorus transport. *J. Environ. Qual.* 29, 97–105. doi:10.2134/jeq2000.00472425002900010012x

Tang, Q., Duncan, J. M., Guo, L., Lin, H., Xiao, D., and Eissenstat, D. M. (2020). On the controls of preferential flow in soils of different hillslope position and lithological origin. *Hydrol. Process.* 34, 4295–4306. doi:10.1002/hyp.13883

Tian, F., and Xu, Z. (2024). Streamflow diurnal fluctuation and driving mechanism of headwater stream in a semi-humid mountainous region. *J. Hydrology* 641, 131803. doi:10.1016/j.jhydrol.2024.131803

Tie, Q., Hu, H., Tian, F., and Holbrook, N. M. (2018). Comparing different methods for determining forest evapotranspiration and its components at multiple temporal scales. *Sci. Total Environ.* 633, 12–29. doi:10.1016/j.scitotenv.2018.03.082

Toor, G. S., Condron, L. M., Cade-Menun, B. J., Di, H. J., and Cameron, K. C. (2005). Preferential phosphorus leaching from an irrigated grassland soil. *Eur. J. Soil Sci.* 56, 155–167. doi:10.1111/j.1365-2389.2004.00656.x

van Schaik, N. L. M. B. (2009). Spatial variability of infiltration patterns related to site characteristics in a semi-arid watershed. *Catena* 78 (3), 36–47. doi:10.1016/j.catena.2009.02.017

Walter, M., Kim, J., Steenhuis, T., Parlange, J., Heilig, A., Braddock, R., et al. (2000). Funneled flow mechanisms in a sloping layered soil: laboratory investigation. *Water Resour. Res.* 36 (4), 841–849. doi:10.1029/1999WR900328

Wang, T., Stewart, C. E., Ma, J., Zheng, J., and Zhang, X. (2017). Applicability of five models to simulate water infiltration into soil with added biochar. *J. Arid Land* 9 (5), 701–711. doi:10.1007/s40333-017-0025-3

Weiler, M., and Flühler, H. (2004). Inferring flow types from dye patterns in macroporous soils. *Geoderma* 120 (1-2), 137–153. doi:10.1016/j.geoderma.2004.08.014

Weiler, M., and McDonnell, J. J. (2007). Conceptualizing lateral preferential flow and flow networks and simulating the effects on gauged and ungauged hillslopes. *Water Resour. Res.* 43 (3), W03403. doi:10.1029/2006WR004867

Weiler, M., and Naef, F. (2003). An experimental tracer study of the role of macropores in infiltration in grassland soils. *Hydrol. Process.* 17 (3), 477–493. doi:10.1002/hyp.1136

Widemann, B. T. Y., and Bogner, C. (2012). "Image analysis for soil dye tracer infiltration studies," in 2012 3rd International Conference on Image Processing Theory, Tools and Applications, 409–414. doi:10.1109/IPTA.2012.6469517

Wiekenkamp, I., Huisman, J. A., Bogena, H. R., Lin, H. S., and Vereecken, H. (2016). Spatial and temporal occurrence of preferential flow in a forested headwater catchment. *J. Hydrology* 534, 139–149. doi:10.1016/j.jhydrol.2015.12.050

Wilson, G. V., Cullum, R. F., and Römkens, M. J. M. (2008). Ephemeral gully erosion by preferential flow through a discontinuous soil-pipe. *Catena* 73 (1), 98–106. doi:10.1016/j.catena.2007.09.005

Wu, X., Dang, X., Meng, Z., Fu, D., Cong, W., Feiyan, Z., et al. (2022). Mechanisms of grazing management impact on preferential water flow and infiltration patterns in a semi-arid grassland in northern China. *Sci. Total Environ.* 813, 152082. doi:10.1016/j.scitotenv.2021.152082

Xue, D., Tian, J., Zhang, B., Kang, W., Zhou, Y., and He, C. (2024). Effects of vegetation types on soil wetting pattern and preferential flow in arid mountainous areas of northwest China. *J. Hydrology* 641, 131849. doi:10.1016/j.jhydrol.2024.131849

Yi, L., Jiaming, Z., Zhi, Z., and Victor, C. (2023). Modelling preferential flow induced by dynamic changes of desiccation cracks: a comparative numerical study. *Geoderma* 433, 116471. doi:10.1016/j.geoderma.2023.116471

Zhang, D., Zhang, H., and Cheng, J. (2017). Quantitative analysis of preferential flow in slope farmland soils based on multi-index evaluation and fractional dimension. *Trans. Chin. Soc. Agric. Mach.* 48 (12), 214–220. doi:10.6041/j.issn.1000-1298.2017.12.025

Zhang, J., Sun, Q., Wen, N., Horton, R., and Liu, G. (2022). Quantifying preferential flows on two farmlands in the North China plain using dual infiltration and dye tracer methods. *Geoderma* 428, 116205. doi:10.1016/j.geoderma.2022.116205

Zhang, J., and Xu, Z. (2016). Dye tracer infiltration technique to investigate macropore flow paths in Maka Mountain, Yunnan Province, China. *J. Central South Univ.* 23 (8), 2101–2109. doi:10.1007/s11771-016-3266-y

Zhang, Y. H., Niu, J. Z., Zhu, W. L., Du, X. Q., and Li, J. (2015). Effects of plant roots on soil preferential pathways and soil matrix in forest ecosystems. *J. For. Res.* 26 (2), 397–404. doi:10.1007/s11676-015-0023-2

Zhao, S., Hu, H., Harman, C. J., Tian, F., Tie, Q., Liu, Y., et al. (2019). Understanding of storm runoff generation in a weathered, fractured granitoid headwater catchment in northern China. *Water* 11 (1), 123. doi:10.3390/w11010123

Zhu, Z., Liu, B., Liu, C., and Si, R. (2020). Characteristics of preferential flow and water infiltration in desert oasis wetland. *Acta Ecol. Sin.* 40 (8), 1–12. doi:10.5846/stxb201901150

frontiers | Frontiers in Environmental Science

TYPE Original Research
PUBLISHED 24 April 2025
DOI 10.3389/fenvs.2025.1564047

EDITED BY
Jing Liu,
University of Birmingham, United Kingdom

REVIEWED BY
Vanessa Otero Jimenez,
University of Idaho, United States
Yumin Cai,
Northeastern University, United States

*CORRESPONDENCE
Jehangir H. Bhadha,
✉ jango@ufl.edu

RECEIVED 21 January 2025
ACCEPTED 07 April 2025
PUBLISHED 24 April 2025

CITATION
Melkani S, Manirakiza N, Rabbany A, Medina-Irizarry N, Smidt S, Braswell A, Martens-Habbena W and Bhadha JH (2025) Understanding the mechanisms of hydrolytic enzyme mediated organic matter decomposition under different land covers within a subtropical preserve.
Front. Environ. Sci. 13:1564047.
doi: 10.3389/fenvs.2025.1564047

Understanding the mechanisms of hydrolytic enzyme mediated organic matter decomposition under different land covers within a subtropical preserve

Suraj Melkani[1], Noel Manirakiza[1], Abul Rabbany[1], Natalia Medina-Irizarry[2], Samuel Smidt[3], Anna Braswell[2,4], Willm Martens-Habbena[5] and Jehangir H. Bhadha[1]*

[1]Department of Soil, Water, and Ecosystem Sciences, Everglades Research and Education Center, University of Florida, Belle Glade, FL, United States, [2]School of Forest, Fisheries, and Geomatics Sciences, University of Florida, Gainesville, FL, United States, [3]American Farmland Trust, Washington, DC, United States, [4]Florida Sea Grant, University of Florida/IFAS, Gainesville, FL, United States, [5]Department of Microbiology and Cell Science, Fort Lauderdale Research and Education Center, Institute of Food and Agricultural Sciences, University of Florida, Davie, FL, United States

Soil Organic Matter (SOM) decomposition, vital to the carbon cycle, is influenced by land cover, hydrological conditions, and soil properties. However, understanding of how hydrolytic enzymes involved in SOM turnover vary under these factors remains limited. To address this, a study was conducted in a sub-tropical preserve in South Florida to assess hydrolytic enzyme activities across 23 diverse land covers (Categorized into five ecosystems: A-Upland Forests, B-Wetland ecosystems, C-Shrub ecosystems, D-Range Areas, and E-Barren ecosystems) during wet and dry seasons. The assessed enzymes were β-1,4 glucosidase (βG), β-1,4-N-acetyl glucosaminidase (β-NAG), Acid Phosphatase (AP), and Aryl Sulfatase (AS). A weighted index termed the Hydrolytic Enzyme Decomposition Indicator (HEDI) was derived using principal component analysis to summarize overall enzymatic activity as an indicator of decomposition. The results showed that among the land covers, βG, β-NAG, AP, and AS activities during the dry season ranged from 18.40 to 327.20, 14.71–351.90, 302.89–10,185.80, and 26.51–1,745.75 μg PNP/g soil/hr, respectively, while in the wet season, the activities for all enzymes except AS were higher, ranging from 4.08 to 398.66, 21.72–1,118.97, 372.38–11,960.36, and 28.26–1,475.09 μg PNP/g soil/hr. Among ecosystems, βG and β-NAG showed seasonal variability, with β-NAG consistently higher in A-Upland Forests, B-Range Areas, and C-Shrub. AP and AS showed minimal variation, with all enzymes showing lower activity in D-Barren ecosystems. HEDI values in the dry season A-Upland Forests exhibited the widest range (–0.962–1.613), indicating diverse decomposition rates, while Barren ecosystems showed consistently low activity (–0.928 to –0.916), suggesting lower decomposition. Correlation analysis revealed positive relationships between enzymatic activities and soil properties such as SOM (0.51–0.59), active carbon (0.46–0.58), soil protein (0.27–0.40), and cation exchange capacity (0.28–0.40), while bulk density showed negative correlations (–0.31 to –0.50). Overall, this study highlights the necessity of considering the complex interactions between soil properties, vegetation, moisture, and enzymatic activity in understanding SOM decomposition.

KEYWORDS

soil organic matter, decomposition, hydrolytic enzymes, land covers, wet season, dry season

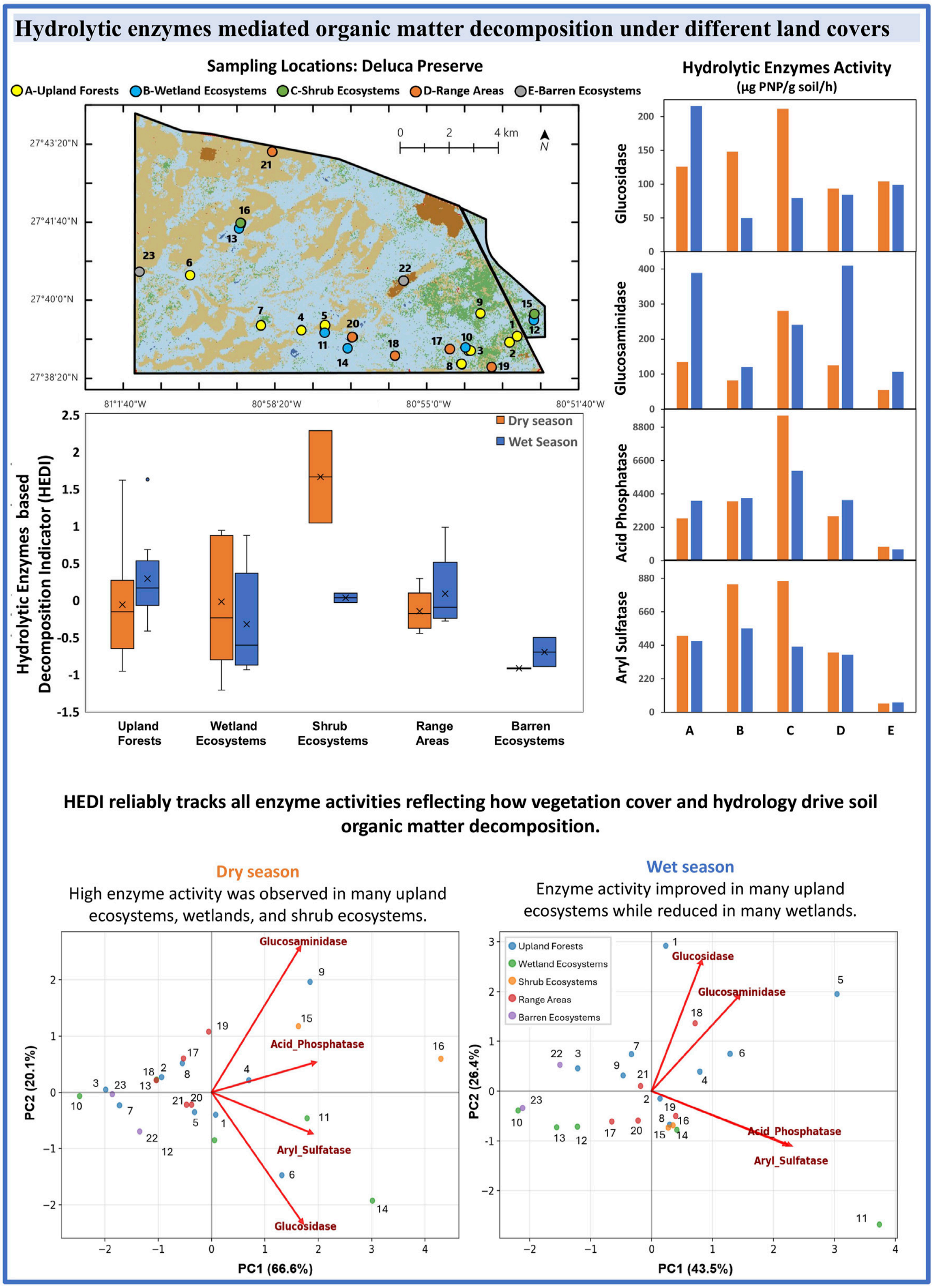
Hydrolytic enzymes mediated organic matter decomposition under different land covers

HEDI reliably tracks all enzyme activities reflecting how vegetation cover and hydrology drive soil organic matter decomposition.

Dry season
High enzyme activity was observed in many upland ecosystems, wetlands, and shrub ecosystems.

Wet season
Enzyme activity improved in many upland ecosystems while reduced in many wetlands.

GRAPHICAL ABSTRACT

1 Introduction

Soil Organic Matter (SOM) is an essential component of soil (Osman and Osman, 2013; Körschens, 2002) undergoing several transformative processes, including mineralization, immobilization, and decomposition (Filipović et al., 2024; Paul, 2016). Each of these processes plays a crucial role in the functioning of soil ecosystems, directly influencing soil fertility, structure, and overall soil health

(Murphy, 2015; Fageria, 2012). Mineralization is the process through which soil microbes convert SOM releasing inorganic forms of nutrients and making them available to plants. Immobilization on the other hand is the process, where inorganic forms of nutrients are converted back into organic forms, making them temporarily unavailable to plants (Mohammadi et al., 2011; Nieder and Benbi, 2008; Rice, 2002; Haynes, 1986). Decomposition which involves the breakdown of SOM by soil microorganisms is considered the most crucial process within the soil because it directly influences both mineralization and immobilization (Carter and Tibbett, 2008). During decomposition, the SOM can either undergo mineralization by soil microorganisms or be reincorporated into microbial biomass through immobilization (Findlay, 2021; Robertson and Paul, 2000; Haynes, 1986). Decomposition of SOM is a fundamental ecological process, vital for the recycling of nutrients, maintenance of soil structure and regulation of the carbon cycle (Raza et al., 2023; Nair et al., 2021; Angst et al., 2021; Paul and Collins, 2020). The rate at which SOM is decomposed also determines the balance between the carbon sequestered in soils and the carbon released into the atmosphere (Prescott, 2010; Swift, 2001), a balance with direct implications for climate change mitigation and the sustainability of diverse ecosystems (Goebel et al., 2011; Anderson, 1991).

The decomposition of SOM is a complex phenomenon influenced by several factors, including land cover, hydrological conditions, soil properties, climate, microbial community composition, nutrient availability, and human activities (Adl, 2003; Guo and Gifford, 2002; Robertson and Paul, 2000). Each factor contributes to the complex dynamics of SOM breakdown, affecting the rate and efficiency with which organic materials are decomposed (Cotrufo and Lavallee, 2022; Paul, 2016). For example, the nature of the land cover plays a significant role, with different vegetation and land uses providing varying SOM inputs and thus influencing the microbial consortia specialized for decomposition in these microhabitats (Ramesh et al., 2019; Moghimian et al., 2017; Deng et al., 2016; Muñoz-Rojas et al., 2015; Guo and Gifford, 2002). Soil type also directly influences the rate of SOM decomposition, affecting factors such as aeration, moisture retention, and nutrient cycling. These variations in soil properties create distinct microenvironments that impact microbial activity, enzyme production, and ultimately the efficiency of SOM decomposition and carbon turnover (Rittl, et al., 2020; Zheng et al., 2019; Frøseth and Bleken, 2015; Tumer et al., 2013; Dijkstra and Cheng, 2007; Scott et al., 1996). Biological properties, including microbial biomass and enzymatic activity, play a crucial role in driving decomposition processes (Wang and Allison, 2019; Glassman et al., 2018; Don et al., 2017 Condron, et al., 2010; Van Veen and Kuikman, 1990). Moreover, hydrological conditions, encompassing wet and dry seasons, particularly in humid sub-tropical climates like that of Central Florida (Lascody and Melbourne, 2002; Black, 1993) also play a crucial role in the decomposition of SOM (Harrison-Kirk et al., 2014; Zhu and Cheng, 2013; Lohse et al., 2009 Denef et al., 2001). For example, during wet periods, increased moisture levels can enhance microbial activity by improving the mobility of enzymes and substrates, thus potentially accelerating decomposition rates (Harrison-Kirk et al., 2014; Xiang et al., 2008; Williams and Rice, 2007). Conversely, dry periods may lead to a reduction in microbial activity due to moisture stress, which can slow down the decomposition process (Schimel, 2018; Ouyang and Li, 2013; Boddy, 1986).

Understanding the role of discussed factors in SOM decomposition is essential. However, to understand the mechanisms of SOM decomposition more comprehensively it is important to consider the effects of these factors on indicative soil parameters that can define SOM decomposition. Central to this understanding are a variety of enzymes that work synergistically to break down complex organic compounds. These include both hydrolytic enzymes such as β-1,4-glucosidase (βG), β-1,4-N-acetyl glucosaminidase (β-NAG), Acid Phosphatase (AP), and Aryl Sulfatase (AS) whichserve as critical mediators in the decomposition process (Bautista-Cruz and Ortiz-Hernández, 2015) and oxidative enzymes, like peroxidases and phenol oxidases, which are essential for degrading more recalcitrant components such as lignin (Hassan et al., 2013; Beckett et al., 2013). In this study, we specifically focus on hydrolytic enzymes due to their well-established role in catalyzing the breakdown of labile SOM fractions and their rapid responsiveness to environmental changes (Bautista-Cruz and Ortiz-Hernández, 2015). These enzymes are directly involved in the mineralization of key nutrients and are therefore considered sensitive indicators of microbial nutrient transformations under varying ecological conditions (Shi, 2010; Sinsabaugh et al., 2008). These enzymes, crucial for microbial nutrient transformations, significantly influence the rate-limiting steps of SOM decomposition (Koch et al., 2007; Speir et al., 2002) as theytarget specific substrates within the soil organic complex, facilitating the breakdown of SOM. βG plays a pivotal role in the carbon cycle by catalyzing the final step in cellulose compound breakdown and enabling the release of simple glucose to microorganisms (Tischer et al., 2015; Piotrowska and Koper, 2010). β-NAG, on the other hand, is vital for hydrolyzing N-acetylglucosamine from fungal chitin and bacterial murein, linking it to microbial turnover of carbon and nitrogen (Tischer et al., 2015). AP and AS contribute to the cycling of phosphorus and sulfur, respectively (Wang et al., 2019; Kang and Freeman, 1999). Despite the significant role of hydrolytic enzymes in SOM decomposition, more research is needed to understand how enzyme activities vary across different hydrological conditions and land cover types, as well as their implications for SOM decomposition. Current studies have primarily focused on controlled environments, leaving a gap in understanding enzyme activities under natural conditions with varying, soil types, and land covers (Burns et al., 2013). Moreover, there is a limited understanding of enzyme activity fluctuations across different hydrological periods, such as wet and dry seasons, which can significantly impact microbial activity and enzyme activity (Henry, 2013). These research gaps hinder our ability to understand SOM decomposition dynamics accurately and develop effective land management strategies for carbon sequestration and soil health improvement. Therefore, investigating these enzyme activities across different hydrological periods, soil types and land covers can provide insights into the temporal and spatial aspects of SOM decomposition. Furthermore, exploring how soil properties influence hydrolytic enzyme activity will enhance our understanding of the factors affecting SOM decomposition, supporting conservation efforts and carbon sequestration in less managed ecosystems.

The Deluca preserve, with its diverse ecosystems and well-defined wet and dry seasons, offers a prime setting for the investigation of all these research gaps. The preserve's location within a humid subtropical climate zone in central Florida, characterized by distinct hydrological patterns, and its diverse array of ecosystems, from woodlands to wetlands offer a microcosm through which the complex relationship between hydrolytic enzyme activity and SOM decomposition can be observed. This study explores how hydrolytic enzyme activities differ across various land covers and between wet and dry seasons within the DeLuca Preserve, aiming to uncover patterns in enzyme activity that may influence SOM decomposition. Additionally, it investigates the associations between hydrolytic enzyme activities and soil physicochemical properties, seeking to understand how these relationships contribute to SOM dynamics in different environmental contexts within the preserve. The study was conducted with the following objectives. (i) To investigate the variations in hydrolytic enzyme activities in different land covers in dry and wet seasons and their implications on SOM decomposition and (ii) to examine the relationship between soil physiochemical properties and hydrolytic enzyme activities in dry and wet season, and how these interactions affect SOM decomposition.

2 Materials and methods

2.1 Study location

This study was conducted on the Deluca preserve located in Central Florida (South of SR 60, West of FL Turnpike) about 11 km east of the Kissimmee River, geographically located between 27°38′ 20′′ to 27°44′ 10′′ N, and 80°51′ 40′′ to 81°1′ 40′′ W (Figure 1). The site is located in a tropical climate zone with an average annual high and low temperature of 28.89°C, and 17.22°C, and a mean yearly rainfall of approximately 1,204 mm. The preserve is characterized by cyclical patterns of a wet rainy season from June to September and a dry, cool winter season beginning from December to February, which are referred to as the "wet" and "dry" seasons, respectively (Figure 1). This natural hydroperiod of seasonally flooded and desiccated conditions on an annual basis is the major driver creating a favorable condition for the diverse land covers on the preserve (Exum, 2020).

2.2 Soil sampling and processing

Based on the major vegetation categories in the Deluca preserve, 23 unique land covers were selected for the study (Figure 2; Table 1). Topsoil samples (0–15 cm) were collected from these land covers during two seasons: the dry season (January 2021) and the wet season (August 2022). To capture spatial variability and minimize the impact of sampling point selection on soil properties, composite samples were taken from three locations within each land cover type. At each location, soil was collected within a 1-m diameter and mixed to form a single composite sample, ensuring representativeness for each sample (Supplementary Table S1 in the Supplementary Material for geographic coordinates of sampling locations).

Considering the overall ecological setting, including dominant vegetation type, hydrological characteristics, land management and land-use history, these 23 land covers were further classified into five distinct ecosystems (Table 1; Supplementary Figure S1 in the Supplementary Material for more detailed views of land cover and ecosystems). This classification aimed to facilitate a more structured analysis of regional ecological patterns and to minimize the impact of sampling point selection on observed soil properties. The collected soil samples were oven-dried at 50°C for chemical analysis and air-dried for enzymatic analysis. All samples were then sieved to 2 mm prior to laboratory analysis.

2.3 Ecological setting

The Deluca preserve, across 109.05 square kilometers (km^2), is a mix of diverse ecosystems and land uses (Figure 3). The area distribution includes several diverse ecosystems as described below:

i. *Wetland, Watercourse, and Waterbody Areas (27.02 km^2):* Encompassing herbaceous prairies, marshes, and forested wetlands, these areas are essential for water purification, groundwater recharge, and providing habitats for species such as the eastern indigo snake and Florida sandhill crane.
ii. *Upland Forests (21.61 km^2):* Consisting of mesic hammocks, Florida scrub, mesic flatwoods, and scrubby flatwoods, these forests support a wide range of flora and fauna, including rare habitats for the red-cockaded woodpecker and gopher tortoise.
iii. *Native Range Areas (30.02 km^2):* Dominated by dry prairie habitats with indigenous vegetation, these areas are vital for the conservation of species like the Florida grasshopper sparrow, maintained through light grazing and regular fires.
iv. *Cultivated Agricultural Areas (3.28 km^2):* Including active citrus groves and lands previously utilized for row crops, these areas are now mainly used for cattle grazing on bahiagrass, reflecting the agricultural heritage of the preserve.
v. *Improved Pasture Areas (26.68 km^2):* Primarily used for cattle grazing, these pastures have been enhanced for forage with bahiagrass, aiding in the conservation and agricultural management of the landscape.
vi. *Intensive Use Areas (0.44 km^2):* These areas are allocated for more concentrated activities, likely including the infrastructure and facilities essential for the management and operations of the preserve.

2.4 Soils geology and hydrology

Based on the NRCS soil survey for Osceola County, a comprehensive analysis has identified a total of 38 distinct soil types and 6 soil orders within the DeLuca Preserve (Exum, 2020), as detailed in Figure 4 and summarized in Table 2. Table 3, derived from the Soil Survey Geographic Database (National Resources Conservation Service, 2024), provides key soil hydrological properties across various land cover types, including parameters such as available water storage, water table depth, saturated hydraulic conductivity, and moisture content. These parameters

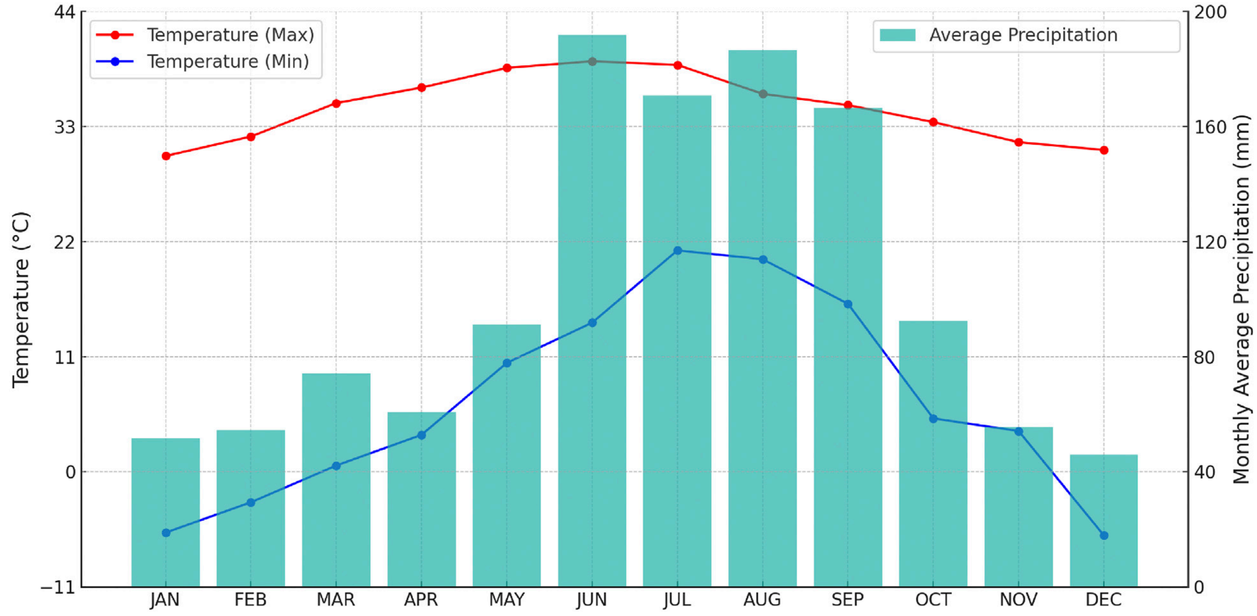

FIGURE 1
Monthly Temperature and Precipitation Averages for DeLuca preserve (1981–2023) Source: NASA/POWER CERES/MERRA2 Climatology Data 2024.

remain relatively stable and serve as a comprehensive source of information, offering a detailed description of hydrological attributes for different land cover and ecosystems. Wetland and poorly drained soils have higher water retention capacities and hydric soil presence, while xeric and sandy soils, such as those in hammocks and abandoned citrus groves, exhibit lower available water capacities and higher drainage. Additional details on specific soil types and their distributions can be found in Supplementary Materials S2, S3.

2.5 Laboratory analysis

All soil samples were subjected to physicochemical analyses following standard procedures. For Enzymatic analysis, air-dried soil samples were sieved through a 2 mm sieve for analysis of βG and β-NAG, AP, and AS by the method described by Tabatabai (1994). Enzyme activities were expressed in μg PNP/g dry soil/h, representing the micrograms of p-nitrophenol released per gram of dry soil per hour. To examine the relationship between soil physiochemical properties and hydrolytic enzyme activities, ten soil properties were analysed: pH, bulk density (BD), maximum water holding capacity (MWHC), cation exchange capacity (CEC), SOM, active carbon (AC), soil protein (SP), total phosphorus (TP), total potassium (TK), and total Kjeldahl nitrogen (TKN). Soil pH (soil/water suspension of 1.5:15) was determined using a pH meter (Amgain, Martens-Habbena, and Bhadha, 2022). BD was measured by filling a 25 mL graduated cylinder with oven-dry soil and dividing the soil mass by the cylinder volume (25 cm^3) (Xu et al., 2022). MWHC was measured following a modified protocol by Jenkinson and Polson (1976). SOM was determined using the loss on ignition method at 550°C. CEC was determined using the ammonium acetate method (Sumner, Miller, and Sparks, 1996). AC was measured using the Potassium Permanganate ($KMnO_4$) method (Schindelbeck et al., 2016). SP was measured using the sodium citrate extraction method under autoclaving at high temperature and pressure (Schindelbeck et al., 2016). TP and TK were measured by ashing samples at 550°C in a muffle furnace for at least 5 h (not exceeding 16 h), followed by extraction with 6 M HCl and analysis using ICP-OES. TKN was analyzed using the Kjeldahl method (Bremner and Mulvaney, 1982).

2.6 Statistical analysis

All statistical analyses were performed using statistical software R-4.4.0 (R Development Core Team, 2024). Data were tested for normality, and transformations were applied as necessary to meet assumptions. For the first objective, a two-way ANOVA was conducted with land cover and season as factors to examine their interaction and main effects on the response variables. Mean comparisons were conducted using Bonferroni adjustments at a 5% significance level, separately between land covers and between seasons. Similarly a two-way ANOVA was also performed with the five ecosystems and years as factors to provide an overall understanding of SOM decomposition across a broader scale, reflecting the aggregated ecosystem groups from the 23 distinct land covers. Mean comparisons were conducted using Bonferroni adjustments at a 5% significance level, separately between ecosystems and between seasons.

Principal Component Analysis (PCA) was performed on all four hydrolytic enzymes to determine their combined effect on SOM decomposition. Using the results from the PCA, an index termed the PCA-based hydrolytic enzymes decomposition indicator (HEDI)

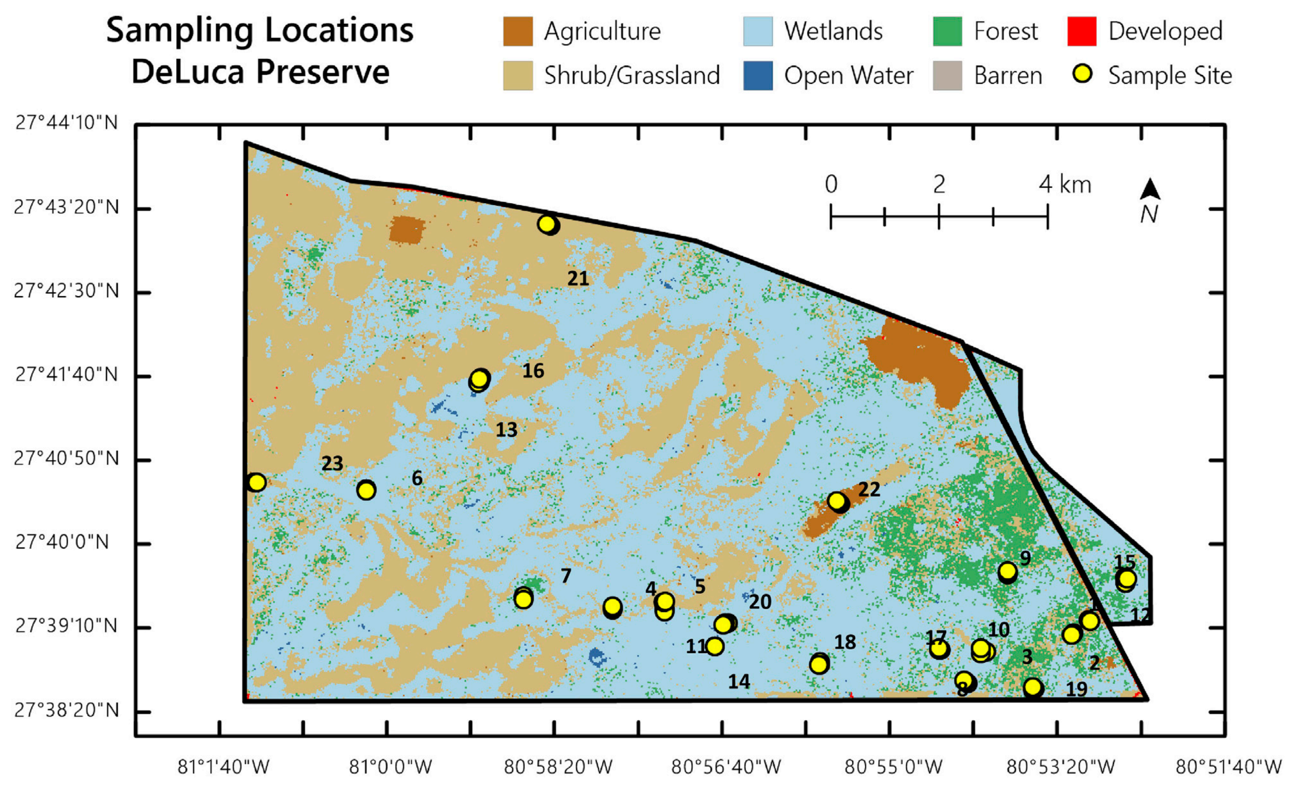

FIGURE 2
Deluca preserve, Florida with sampling locations.

was calculated to represent the overall enzymatic activity which can act as an indicator of decomposition. This index incorporates the weighted methodology that considers the principal components (PC) scores. The weight of each PCs score is given by the proportion of variance it explains. HEDI was calculated with the following equation:

$$\mathbf{HEDI} = (\mathbf{PC1} \times \mathbf{V1}) + (\mathbf{PC2} \times \mathbf{V2}) + \ldots + (\mathbf{PCn} \times \mathbf{Vn})$$

Where PCn is the score for principal component n, and Vn is the variance explained by that component. Similar approaches of using weighted PCA scores has been employed to assess soil quality and variability, where PCA scores, weighted by explained variance, serve as critical indicators (Martin-Sanz et al., 2022; Karaca et al., 2021; Kumar et al., 2012). This study adapts and modifies these established methodologies to develop HEDI. Seasonal comparisons using the HEDI are not feasible because the index is calculated based on distinct principal components derived from the dry and wet seasons, which prevents a direct comparison of enzymatic activity between these periods. However, to facilitate relative comparisons of enzymatic activity across seasons, the activities in each season were classified into quartiles. PCA scores for the dry and wet seasons are provided in Supplementary Tables S2A, B, and the PCA Biplot is illustrated in Supplementary Figure S4.

For second objective, Spearman correlation analysis was conducted to explore the interactions between hydrolytic enzyme activities and the soil parameters across different land covers. This method was directly applied due to its suitability for non-normal, non-transformed data and its ability to capture both monotonic and non-linear relationships. Multiple regression analyses were performed for each of the four enzymes, using all soil physicochemical properties and other enzyme activities as predictors. Standardized coefficients were calculated for each equation to identify significant predictors and compare their relative effects on soil hydrolytic enzymes.

3 Results

3.1 Variations in hydrolytic enzyme activities in different land covers in dry and wet seasons and their implications on SOM decomposition

3.1.1 Hydrolytic enzyme activities across land covers

Distinct patterns in hydrolytic enzyme activities emerged from seasonal comparisons across various land covers, with a significant interaction ($p < 0.05$) observed between land cover and season for all enzymes (Figures 5–8).

Among different land covers during the dry season, βG activity ranged from 18.40 to 327.20 μg PNP/g soil/hr (Figure 5) with highest values observed in 14-Wetland-4, which was not significantly different ($p > 0.05$) from nine other land cover types, reflecting consistent enzymatic activity across multiple ecosystems. On the other hand, in the wet season, βG activity showed a wider range, from 4.02 to 398.66 μg PNP/g soil/hr, with the highest value in 1-

TABLE 1 Characterization of the 23 land covers present at the Deluca preserve.

S.No	Land cover	Vegetation cover	Soil order	T[a] (°C)	P[a] (mm)	Texture	Ecosystems
1	Flatwood	Oak (*Quercus virginiana*)	Spodosols	23	1,245	Sandy	Group A Upland Forests (Forested ecosystems/ Natural Tree Cover)
2	Mesic flatwood	Saw palmetto (*Serenoa repens*)/Gall berry (*Ilex glabra*)/Slash pine *(Pinus elliottii)*	Spodosols	23	1,245	Sandy	
3	Dry hammock	Sabal palm (*Sabal palmetto*)/Live oak *(Quercus virginiana)*	Alfisols	23	1,372	Loamy	
4	Xeric hammock	Live oak *(Quercus virginiana)*/Sabal palm (*Sabal palmetto*)	Alfisols	23	1,295	Loamy	
5	Palm hammock (Xeric)	Oak (Quercus *sp.*)	Spodosols	23	1,245	Sandy	
6	Cypress	Natural tree cover	Spodosols	23	1,320	Sandy	
7	Pinewood-1	Slash pine *(Pinus elliottii)*/Sabal palm (*Sabal palmetto*)	Entisols	23	1,270	Sandy	
8	Hammock	Oak (*Quercus virginiana*), pines (*Pinus*), palmettos	Spodosols	23	1,245	Sandy	
9	Pinewood-2	Pine (*Pinus*)/saw palmetto (*Serenoa repens*)/ Gall berry (*Ilex glabra*)	Spodosols	23	1,320	Sandy	
10	Canal (wet)	Cattails (*Typha*)/Pickerelweed (*Pontederia cordata*)	Alfisols	23	1,372	Loamy	Group B Wetland ecosystems (Wetland, Watercourse, and Waterbody Areas)
11	Wetland-1	Aquatic plants	Entisols	22	1,282	Sandy	
12	Wetland-2	Aquatic plants, 15-inch depth	Entisols	22	1,320	Loamy	
13	Wetland-3	Juncus/hypericum/Panicum	Alfisols	23	1,265	Loamy	
14	Wetland-4	Sawgrass (*Cladium*), 8-inch depth	Entisols	22	1,320	Loamy	
15	Sawtooth palmetto	Sawtooth palmetto (*Serenoa repens*)/Gallberry (*Ilex glabra*)	Entisols	22	1,320	Loamy	Group C Shrub ecosystems
16	Sabal palmetto	Saw palmetto (*Serenoa repens*)/Sabal palm (*Sabal palmetto*)/black berry (*Rubus* sp.)	Alfisols	23	1,265	Loamy	
17	Dry Prairie-1	Gall berry (*Ilex glabra*)/Saw palmetto (*Serenoa repens*)/Running oak (*Quercus* sp.)	Entisols	23	1,321	Sandy	Group D Range Areas (Grassland and Prairie ecosystems)
18	Dry Prairie-2	Andropogon (*Andropogon*)/wiregrass (*Aristida stricta*)	Entisols	23	1,321	Sandy	
19	Dry Prairie-3	Slash pine *(Pinus elliottii)*/Saw palmetto (*Serenoa repens*)	Spodosols	23	1,245	Sandy	
20	Native pasture	Panic grass (*Panicum*)	Spodosols	23	1,245	Sandy	
21	Improved pasture	Bahia grass (*Paspalum notatum*)/ Andropogon (*Andropogon*)	Spodosols	23	1,320	Sandy	
22	Abandoned citrus grove	Abandoned Citrus Plantation	Spodosols	23	1,320	Sandy	Group E Barren ecosystems
23	Sandy spoil	No vegetation	Entisols	23	1,282	Loamy	

[a] *T* stands for Mean Annual Air Temperature in degrees Celsius, and *P* stands for Mean Annual Precipitation in millimetres.

Flatwood which was not significantly different ($p > 0.05$) from ten other land cover types. For β-NAG activity, values during the dry season ranged from 14.71 to 351.90 µg PNP/g soil/hr (Figure 6), with the highest levels observed in 9-Pinewood-2, which were not significantly different ($p > 0.05$) from 16 other land covers. In the wet season, however, β-NAG activity showed a broader range of 21.72 to 1,118.97 µg PNP/g soil/hr, with the highest value observed in 17-Dry Prairie-1. These values were not significantly different ($p > 0.05$) from 1-Flatwood and 5-Palm Hammock (Xeric) but were statistically higher than other land covers, indicating more variability among land covers compared to the dry season. AP activity showed the largest range of activity among all enzymes. During the dry season, AP ranged from 302.89 to 10,185.80 µg PNP/g soil/hr (Figure 7), with the highest levels observed in 16-Sabal Palmetto. These values were not significantly different ($p > 0.05$) from those in 11-Wetland-1, 14-Wetland-4, and 15-Sawtooth Palmetto. In the wet season, AP activity displayed a broader range, from 372.38 to 11,960.36 µg PNP/g soil/hr, with 11-

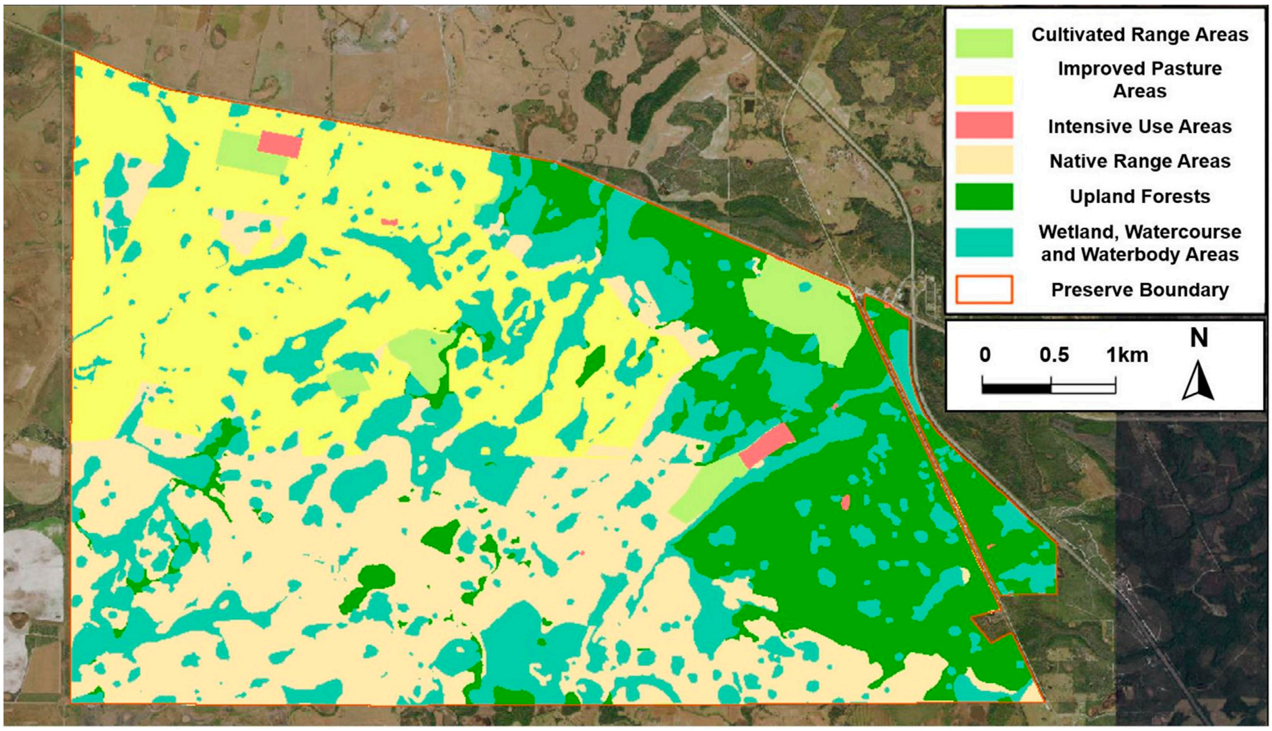

FIGURE 3
Land use categories and distribution within the DeLuca preserve.

Wetland-1 recording statistically higher value ($p < 0.05$) than all other land covers. In contrast to βG, β-NAG and AP, AS activity showed opposite trends from the dry to wet season. In the dry season, AS activity ranged from 26.51 to 1,745.75 µg PNP/g soil/hr (Figure 8), with the highest levels observed in 14-Wetland-4 not significantly different ($p > 0.05$) from 16-Sabal Palmetto, 9-Pinewood-2 and 10-Canal (wet). In the wet season, AS activity exhibited a narrower range, from 28.26 to 1,475.09 µg PNP/g soil/hr, with the highest levels observed in 11-Wetland-1 not significantly different ($p > 0.05$) from 6-Cypress. Overall, the highest enzymatic activity exhibited variable trends between the dry and wet seasons, while the lowest enzymatic activity remained consistently lowest in 10-Canal (wet) across all enzymes during the dry season. This trend was similar in the wet season with minimum values of β-NAG and AS in 10-Canal (wet).

3.1.2 Hydrolytic enzyme activities across seasons

For pairwise seasonal comparisons for each land cover, hydrolytic enzyme activities displayed variable patterns for different enzymes. βG activity increased significantly in 5-Palm hammock (Xeric) and 10-Canal (wet), while decreased significantly in 11-Wetland-1, 12-Wetland-2, 14-Wetland-4, 16-Sabal palmetto, and 17-Dry Prairie-1. For β-NAG, only a significant increase was recorded in 1-Flatwood, 2-Mesic flatwood, 3-Dry hammock, and 18-Dry Prairie-2. AP activity exhibited significant increases in 5-Palm hammock (Xeric), 7-Pinewood-1, 10-Canal (wet), and 19-Dry Prairie-3, while decreased significantly in 9-Pinewood-2, 12-Wetland-2, 16-Sabal palmetto, and 23-Sandy spoil. Additionally, AS activity showed a significant increase in 3-Dry hammock and decreased significantly in 9-Pinewood-2, 12-Wetland-2, and 16-Sabal palmetto. Other land covers such as 6-Cypress, 8-Hammock, 15-Sawtooth Palmetto, 20-Native Pasture, 21-Improved Pasture, and 22-Abandoned Citrus Grove, exhibited no significant seasonal differences in enzymatic activity.

3.1.3 Ecosystems comparison

Across different ecosystems, a visible pattern emerged with the transition from dry to wet conditions (Figure 9). Overall, the C-Shrub ecosystems demonstrated the highest range of enzymatic activity, spanning from 79.42 to 9,561.07 µg PNP/g soil/hr, while the D-Barren ecosystems exhibited the lowest range, from 54.94 to 106.58 µg PNP/g soil/hr.

Among different ecosystems in the dry season, βG activity showed no significant differences; however, it varied more in the wet season, with βG being highest in A-Flatwoods, not statistically different ($p > 0.05$) to the C-Shrub and D-Barren ecosystems. For β-NAG, the highest activity in the dry season was observed in the C-Shrub ecosystems, not statistically different ($p > 0.05$) to the B-Range Areas and A-Upland Forests. Similarly, in the wet season, β-NAG was highest in the B-Range Areas not statistically different ($p > 0.05$) to A-Flatwoods C-Shrub ecosystems. The results indicated that β-NAG activity was consistently higher in these three ecosystems (A-Upland Forests, B-Range Areas, and C-Shrub ecosystems) across both seasons. AP activity was significantly higher in the C-Shrub ecosystems during the dry season.

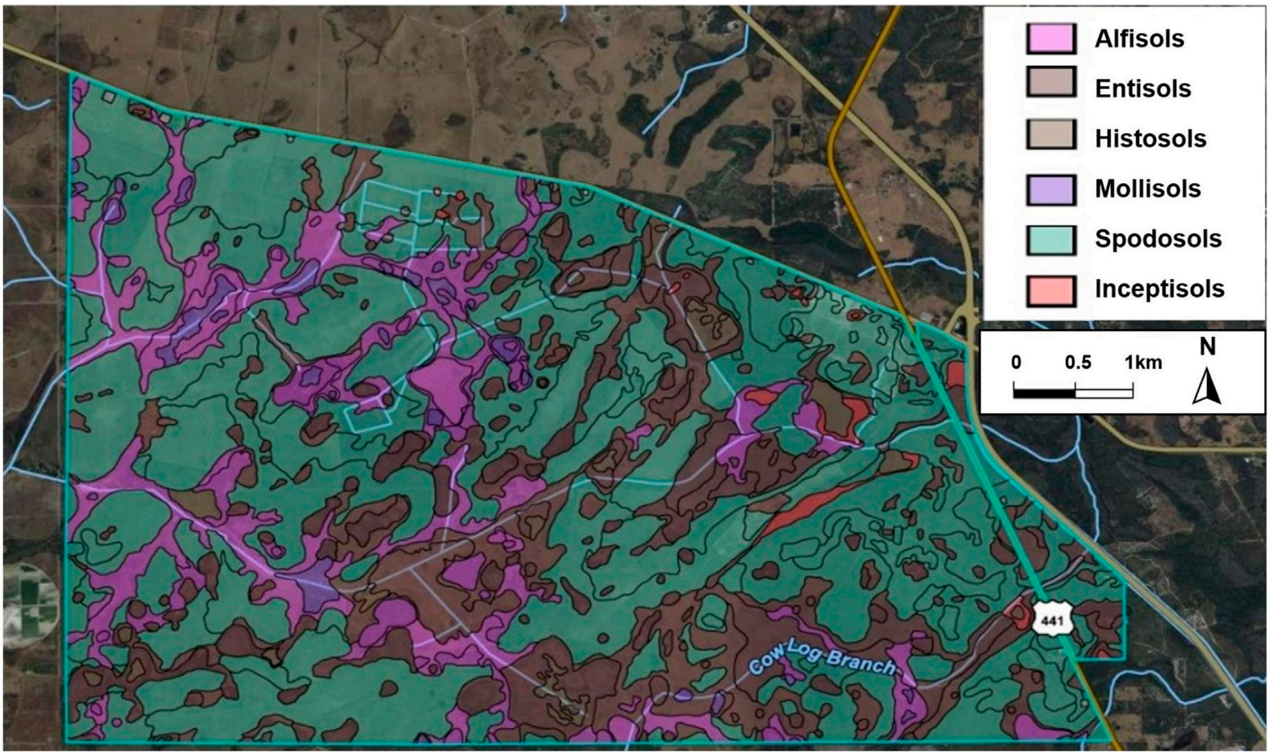

FIGURE 4
Soil taxonomy map of soil orders across the preserve. Source: (U.S. Department of Agriculture, [USDA]-NRCS, 2024).

TABLE 2 Soil Characteristics in the DeLuca preserve.

Soil texture	Area (km^2)	Percent	Soil order	Area (km^2)	Percent	Soil type	Area (km^2)	Percent
Fine Sand	105.57	96.43	Spodosols	61.72	61.7	Smyrna fine sand	33.17	30.4
Muck	2.00	1.82	Entisols	27.86	27.9	Myakka fine sand	11.46	10.5
Loamy Fine Sand	1.07	0.98	Alfisols	15.38	15.4	Eaugallie fine sand	11.37	10.4
Sand	0.84	0.77	Histosols	1.99	2.0	Basinger fine sand, depressional	11.02	10.1
			Mollisols	1.62	1.6	Basinger fine sand	9.22	8.5
			Inceptisols	0.86	0.9	Others	33.19	30.1

However, in the wet season, AP activity showed no significant differences, except for the D-Barren ecosystems, which showed significantly lower values. AS showed minimal variation among ecosystems in both seasons, with no statistical difference ($p > 0.05$) among all ecosystems except for the D-Barren ecosystems which showed significantly lower activity in both seasons. Overall, the results indicate that both AP and AS activities remained relatively stable across most ecosystems, highlighting the distinct differences in enzymatic responses based on seasonal changes.

From dry to wet seasons, βG increased significantly in A-Flatwoods, while it decreased significantly in both B-Wetlands and C-Shrub ecosystems. β-NAG showed significant increases in A-Flatwoods and B-Range Areas, with no significant decreases observed in any ecosystem. Both AP and AS demonstrated no significant changes from dry to wet season across all ecosystems.

3.1.4 HEDI across different land covers and ecosystems

The HEDI values demonstrated significant variability across different land covers and seasons (Table 4). Among different land covers during the dry season, HEDI values ranged from a minimum of −1.217 in 10-Canal (wet) to a maximum of 2.281 in 16-Sabal palmetto, indicating a spectrum of enzymatic activity. In the wet season however, the HEDI values exhibited a narrower range, with the lowest value at −0.943 again in 10-Canal (wet) and the highest at 1.623 in 5-Palm Hammock (Xeric). Land covers such as 1-Flatwood, 6-Cypress, 11-Wetland-1, 15-Sabal palmetto, and 16-Sawtooth palmetto consistently showed higher HEDI values, classifying in the highest quartile classes (I or II) in both seasons, which reflects overall higher enzymatic activity. In contrast, several land covers, including 3-Dry hammock, 10-Canal (wet), 12-Wetland-2, 13-

TABLE 3 Soil hydrological characteristics of the 23 land covers present at the Deluca preserve.

S.No	Land cover	Available water storage (cm)				Water table depth annual minimum (cm)	Drainage class - dominant condition	Hydric soils presence (%)	Saturated hydraulic conductivity (μm/s)	Water content, 15 bar (%)	Water content, 0.33 bar (%)	Available water capacity (cm/cm)	Moisture Subclass
		0–25	0–50	0–100	0–150								
1	Flatwood	2.03	4.09	10.38	14.51	31	Poorly drained	5	23.0	4.4	11.2	0.08	Aeric
2	Mesic flatwood	2.01	4.20	10.35	14.44	15	Poorly drained	90	92.0	3.0	9.5	0.08	Typic
3	Dry hammock	2.01	4.03	8.12	12.16	0	Very poorly drained	99	92.0	5.3	12.2	0.08	Typic
4	Xeric hammock	1.45	2.90	6.51	10.95	31	Poorly drained	9	20.0	2.2	6.6	0.06	Typic
5	Palm hammock (Xeric)	2.03	4.09	10.38	14.51	31	Poorly drained	5	23.0	4.4	11.2	0.08	Aeric
6	Cypress	2.06	4.05	10.08	14.79	15	Poorly drained	86	28.2	2.3	8.4	0.08	Typic
7	Pinewood-1	1.45	2.90	6.51	10.95	31	Poorly drained	9	20.0	2.2	6.6	0.06	Typic
8	Hammock	1.85	4.08	7.84	11.47	0	Very poorly drained	97	91.7	8.6	15.0	0.07	Typic
9	Pinewood-2	2.00	4.69	8.85	13.05	31	Poorly drained	6	28.2	4.9	11.7	0.08	Aeric
10	Canal (wet)	2.01	4.03	8.12	12.16	0	Very poorly drained	99	92.0	5.3	12.2	0.08	Typic
11	Wetland-1	1.85	4.08	7.84	11.47	0	Very poorly drained	97	91.7	8.6	15.0	0.07	Typic
12	Wetland-2	1.85	4.08	7.84	11.47	0	Very poorly drained	97	91.7	8.6	15.0	0.07	Typic
13	Wetland-3	2.01	4.02	8.10	14.09	0	Very poorly drained	100	28.2	5.3	12.2	0.08	Typic
14	Wetland-4	1.85	4.08	7.84	11.47	0	Very poorly drained	97	91.7	8.6	15.0	0.07	Typic
15	Sawtooth palmetto	2.03	4.09	10.38	14.51	31	Poorly drained	5	23.0	4.4	11.2	0.08	Aeric
16	Sabal palmetto	2.01	4.20	10.35	14.44	15	Poorly drained	90	92.0	3	9.5	0.08	Typic
17	Dry Prairie-1	2.00	4.69	8.85	13.05	31	Poorly drained	6	28.2	4.9	11.7	0.08	Aeric

(Continued on following page)

TABLE 3 (*Continued*) Soil hydrological characteristics of the 23 land covers present at the Deluca preserve.

S.No	Land cover	Available water storage (cm)				Water table depth annual minimum (cm)	Drainage class - dominant condition	Hydric soils presence (%)	Saturated hydraulic conductivity (µm/s)	Water content, 15 bar (%)	Water content, 0.33 bar (%)	Available water capacity (cm/cm)	Moisture Subclass
		0–25	0–50	0–100	0–150								
18	Dry Prairie-2	2.01	4.20	10.35	14.44	15	Poorly drained	90	92.0	3.0	9.5	0.08	Typic
19	Dry Prairie-3	2.00	4.69	8.85	13.05	31	Poorly drained	6	28.2	4.9	11.7	0.08	Aeric
20	Native pasture	2.01	4.20	10.35	14.44	15	Poorly drained	90	92.0	3.0	9.5	0.08	Typic
21	Improved pasture	2.00	4.69	8.85	13.05	31	Poorly drained	6	28.2	4.9	11.7	0.08	Aeric
22	Abandoned citrus grove	1.07	2.14	4.48	6.70	76	Somewhat poorly drained	4	210.0	2.2	8.2	0.04	Aquic
23	Sandy spoil	2.00	4.01	8.09	14.15	15	Poorly drained	96	28.2	5.3	12.2	0.08	Typic

Source: (USDA-NRCS, 2024).

Wetland-3, 21-Improved pasture, 22-Abandoned citrus grove, and 23-Sandy spoil, remained in the lower quartile classes (III and IV) for HEDI values, indicating minimal enzymatic activity.

Among different ecosystems in the dry season, A-Upland Forests showed the widest range of HEDI values, ranging from −0.962 to 1.613, indicating a wide variation of enzymatic activity. C-Shrub ecosystems demonstrated the highest values of HEDI ranging from 1.035 to 2.280, suggesting high hydrolytic enzyme activity. In contrast, E-Barren ecosystems showed lowest HEDI values between −0.928 and −0.916, emphasizing limited enzymatic activity. In the wet season, A-Upland Forests again showed a wide range of HEDI values, from −0.421 to 1.623, along with B-Wetland ecosystems ranging from −0.942 to 0.870, indicating a diverse enzymatic activity across these ecosystems. Similarly, E-Barren ecosystems remained consistent with low HEDI of −0.897 to −0.505 in the wet season as well, indicating persistently limited enzymatic activity across both seasons.

3.2 Relationship between soil physiochemical properties and hydrolytic enzyme activities in wet and dry seasons

The analysis of the relationship between soil biogeochemical properties and hydrolytic enzyme activities revealed significant insights, particularly in understanding the differences between wet and dry seasons (Figure 10). SOM, SP, AC, CEC, and MWHC showed positive correlations with all enzymes in both seasons, while BD showed consistently negative correlations, and pH showed no significant correlations. Other parameters, such as TP, TKN, and TK, showed more variable correlation values. During the dry season, SOM and AC showed significant positive correlations at $p < 0.001$ with all enzymes. The correlations for SOM were 0.59, 0.54, 0.51, and 0.55, and for AC, were 0.58, 0.58, 0.46, and 0.50, with βG, β-NAG, AP, and AS, respectively. In the wet season, although SOM and AC retained positive correlations with enzymatic activities, they showed greater variability, with significant correlations at $p < 0.001$ observed only with AS (0.51 with SOM and 0.50 with AC). A general trend of decreasing correlation strength was observed from the dry to wet season for most relationships, with exceptions such as SP with AP (Dry: 0.27, $p < 0.05$; Wet: 0.32, $p < 0.01$) and AS (Dry: 0.30, $p < 0.05$; Wet: 0.40, $p < 0.001$), MWHC with AS (Dry: 0.28, $p < 0.05$; Wet: 0.61, $p < 0.001$), and CEC with AS (Dry: 0.28, $p < 0.05$; Wet: 0.28, $p < 0.01$). Other important correlations included SP, TKN and TP, which exhibited positive relationships during dry seasons which was more variable during wet season. The correlations between enzymes were all positive and generally exhibited significant reduction from the dry to wet season, with exceptions for AP and AS (Dry: 0.60, $p < 0.001$; Wet: 0.63, $p < 0.001$) and β-NAG and AP (Dry: 0.50, $p < 0.001$; Wet: 0.39, $p < 0.001$), with no significant reduction.

Based on the Multiple Linear regression analysis (Table 5), the predictors influencing enzyme activities varied between the dry and wet seasons, reflecting dynamic soil-enzyme interactions. For βG and β-NAG, the R^2 values decreased between seasons, with βG dropping from 0.71 in the dry season to 0.41 in the wet season and β-NAG declining from 0.48 to 0.31 ($p < 0.001$). Conversely, for AP and AS, the R^2 values increased between seasons. AP rose from 0.51 in

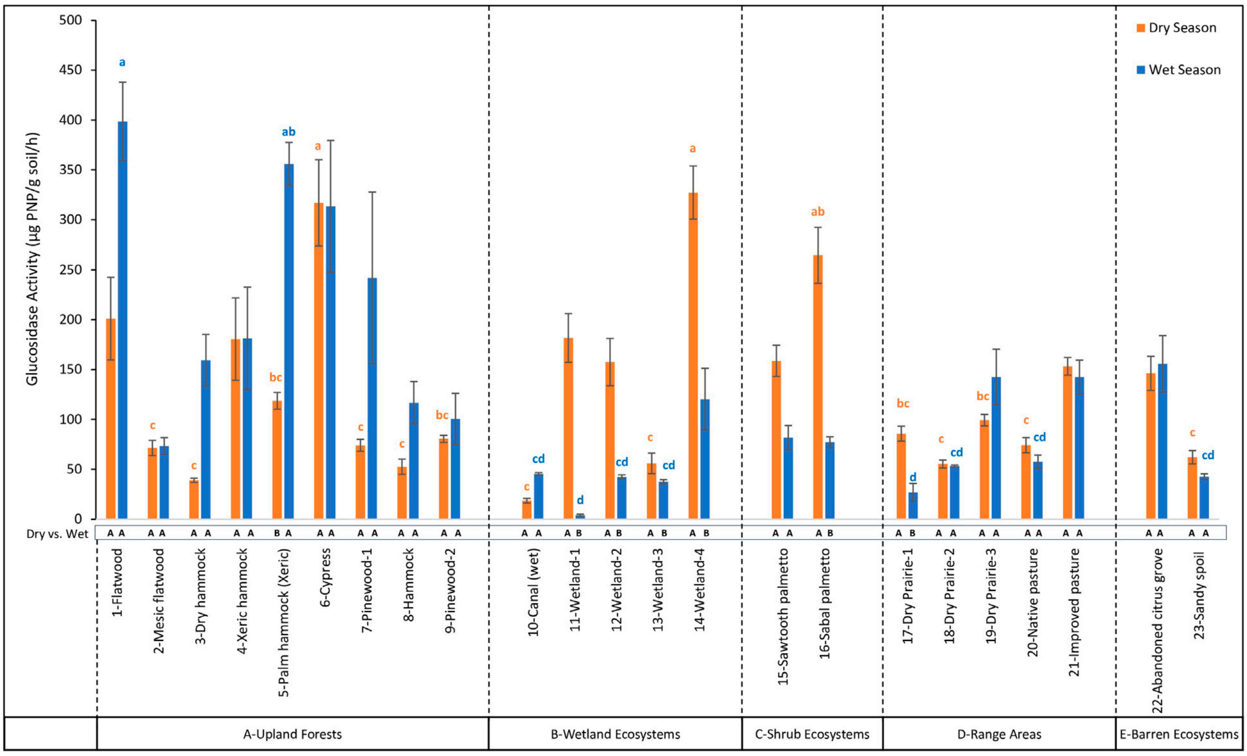

FIGURE 5
Comparison of β-1,4 glucosidase (βG) activity across 23 land cover types at the DeLuca Preserve in wet and dry seasons (Error bars represent ±standard error of the mean. Lowercase letters above bars indicate significant differences among land covers within each season (Bonferroni-adjusted, $p < 0.05$), with blue letters denoting differences in the wet season and orange letters in the dry season. Capital letters below bars denote significant seasonal differences (dry vs wet) within each land cover type (Bonferroni-adjusted, $p < 0.05$). To enhance clarity, only the extreme significance labels are displayed; detailed comparisons are provided in the Supplementary Table S3. Land cover types are grouped by ecosystem categories (A–E), separated by dashed lines).

the dry season to 0.74 in the wet season, while AS increased from 0.56 to 0.71 ($p < 0.001$). HEDI, representing overall enzymatic activity, had a high R^2 of 0.80 in the dry season and was predicted by a broader range of soil properties, including AP, β-NAG, AS, MWHC, CEC, and AC. In the wet season, HEDI had a slightly lower R^2 of 0.72, with fewer significant predictors, including β-NAG, AP, and pH.

4 Discussion

4.1 Variations in hydrolytic enzyme activities in different land covers in wet and dry seasons and their implications on SOM decomposition

4.1.1 Hydrolytic enzyme activities across land covers

Among different enzymes the observed activities for βG in both seasons and β-NAG in the dry season demonstrate consistently high activity across several land covers, likely driven by the combined effects of vegetation type, hydrological, and soil properties regulating microbial activity and enzyme production (Wang et al., 2020; Simpson et al., 2019; Salazar et al., 2011). This suggests that βG and β-NAG enzymes play a key role in stabilizing decomposition processes across these land covers (Sherene, 2017), facilitating consistent SOM turnover under varying environmental conditions. Additionally, environmental factors such as rainfall and temperature (Mariscal-Sancho et al., 2018; Rastin et al., 1988), along with soil characteristics like substrate availability (Mir et al., 2023), likely influenced the βG and β-NAG activities, contributing to the observed results. β-NAG activity exhibits greater variability among land covers during the wet season compared to the dry season, suggesting that increased moisture availability may contribute to the broader range of β-NAG activity and decomposition processes (Borowik and Wyszkowska, 2016; Zhang et al., 2011). AP and AS exhibited different trends compared to βG and β-NAG during the dry season, with their activities showing greater variability across land covers, possibly because these enzymes are more influenced by factors such as land cover characteristics (Mayor et al., 2016; Salam et al., 2001) and soil type (Nedyalkova et al., 2020) indicating varying levels of SOC decomposition. Overall, all enzymes exhibited increased activity ranges from the dry to wet season, indicating enhanced SOC decomposition, except for AS, which showed an opposite trend. This divergence may result from AS's regulation by sulfate availability and its sensitivity to wetting and drying cycles, which can suppress activity (Kunito et al., 2022; Cooper, 1972). In contrast,

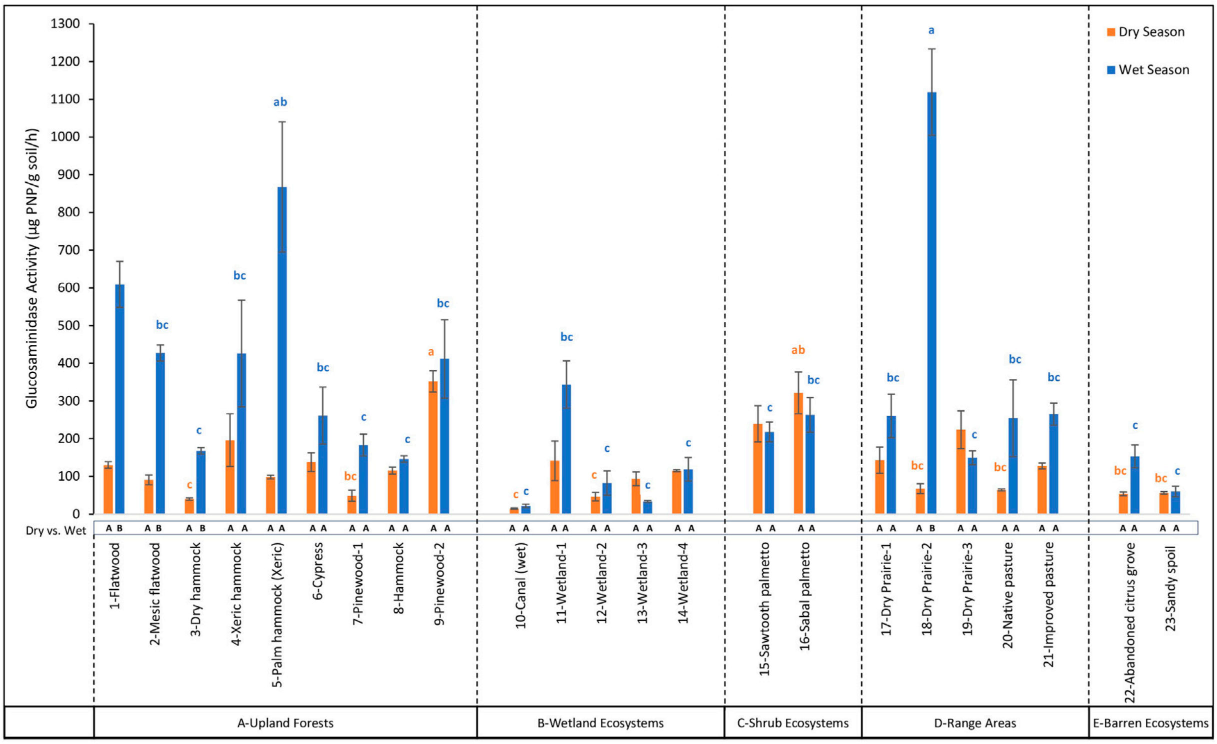

FIGURE 6
Comparison of β-1,4-N-acetyl glucosaminidase (β-NAG) activity across 23 land cover types at the DeLuca Preserve in wet and dry seasons (Error bars represent ±standard error of the mean. Lowercase letters above bars indicate significant differences among land covers within each season (Bonferroni-adjusted, $p < 0.05$), with blue letters denoting differences in the wet season and orange letters in the dry season. Capital letters below bars denote significant seasonal differences (dry vs wet) within each land cover type (Bonferroni-adjusted, $p < 0.05$). To enhance clarity, only the extreme significance labels are displayed; detailed comparisons are provided in Supplementary Table S3. Land cover types are grouped by ecosystem categories (A–E), separated by dashed lines).

βG, β-NAG, and AP activities were positively influenced by increased moisture, consistent with studies showing enhanced enzyme activities during wet seasons or after rewetting (Hammerl et al., 2019; Kapila et al., 2017; Liao et al., 2016). These results emphasize the critical role of hydrology in regulating enzyme-mediated SOC decomposition.

Among land covers in the dry season, 11-Wetland-1, 14-Wetland-4, 15-Sawtooth palmetto, and 16-Sabal palmetto generally showed higher enzymatic activity. This could be attributed to specific characteristics of these land covers, such as very poorly drained loamy soils, which are known to enhance water retention and support microbial activity (Kim, 2015). Additionally, these soils are typically associated with a high moisture class and high available water storage capacity, creating favourable conditions for microbial processes and enzyme production (Kim, 2015; Wu et al., 2021). These conditions may have maintained sufficient soil moisture even during dry periods, supporting microbial activity and enzyme production (Sinsabaugh et al., 2008). Whereas the lowest enzymatic activities during the dry season in the 10-Canal (wet) ecosystem for all enzymes could have resulted from over-saturated conditions, which may hinder oxygen diffusion and microbial activity necessary for enzyme production (Furtak et al., 2020; Borowik and Wyszkowska, 2016). The persistence of minimum values for β-NAG and AS in 10-Canal (wet) across both seasons, again suggests that prolonged wetland conditions might consistently inhibit these enzymes. This inhibition could be due to factors such as reduced oxygen availability or changes in substrate accessibility under saturated conditions (Veres et al., 2015; Daunoras et al., 2024). Moreover, the 23-Sandy spoil land cover also showed consistently lower enzymatic activity, which could be attributed to lower substrate availability in this type of soil (Allison et al., 2011; Babcock and Esen, 1994).

4.1.2 Hydrolytic enzyme activities across seasons

Insignificant seasonal differences in the enzymatic activity across several land covers like 6-Cypress, 8-Hammock, 15-Sawtooth Palmetto, 20-Native Pasture, 21-Improved Pasture, and 22-Abandoned Citrus Grove could be a result of the interactions of several soil and environmental factors with a diverse range of vegetation (Shao et al., 2015; Ullah et al., 2013; Wallenstein et al., 2009; Boerner et al., 2005; Kang and Freeman, 1999). This interaction might have resulted in insignificant changes in enzyme activity from dry to wet season enzymatic activity, minimally influencing SOM decomposition rates and the turnover of SOM components. The presence of aeric moisture subclass in most of these ecosystems is characterized by a well-aerated soil environment (Soil Survey Staff, 2003; Soil Survey Staff, 1999) potentially could also cause these results. The sufficient

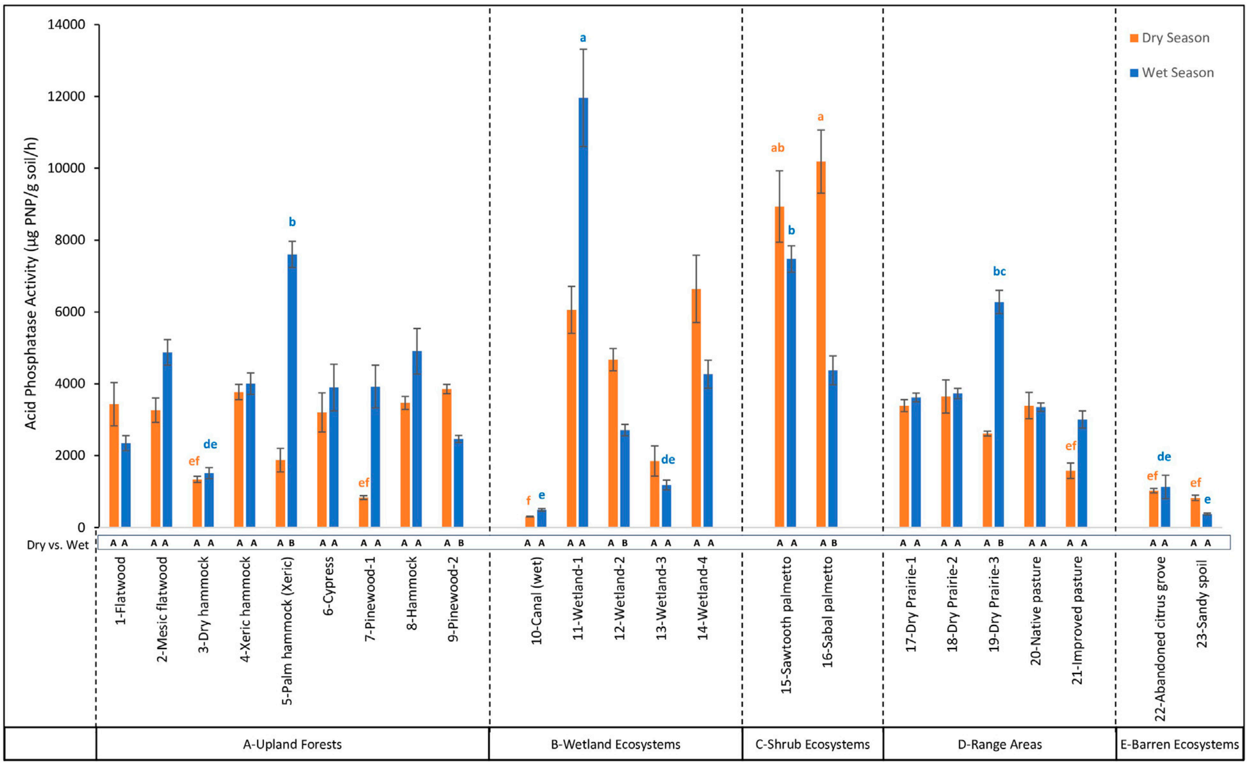

FIGURE 7
Comparison of Acid Phosphatase (AP) activity across 23 land cover types at the DeLuca Preserve in wet and dry seasons (Error bars represent ±standard error of the mean. Lowercase letters above bars indicate significant differences among land covers within each season (Bonferroni-adjusted, $p < 0.05$), with blue letters denoting differences in the wet season and orange letters in the dry season. Capital letters below bars denote significant seasonal differences (dry vs wet) within each land cover type (Bonferroni-adjusted, $p < 0.05$). To enhance clarity, only the extreme significance labels are displayed; detailed comparisons are provided in Supplementary Table S3. Land cover types are grouped by ecosystem categories (A–E), separated by dashed lines).

aeration could have led to consistent enzymatic activity, making the transition to wetter conditions less impactful on enzymatic processes and SOM decomposition (Wang et al., 2022; Ge et al., 2020). Moreover, the presence of Spodosols soil order with sandy texture (McKeague et al., 1983) and poor drainage capacity in most of these ecosystems may have promoted consistent hydrological conditions resulting in insignificant changes in enzyme activity.

The increase in some specific enzymatic activity in land covers like 1-Flatwood, 2-Mesic flatwood, 3-Dry hammock, 5-Palm hammock (Xeric) and 7-Pinewood-1 A- Upland ecosystems, during the transition from dry to wet season can be attributed to the inherent attributes of trees and their environmental interactions, enhancing SOM decomposition (Błońska et al., 2021). Trees such as oaks and pines contribute rich SOM through leaf litter, enhancing substrate availability for microbes and facilitating the decomposition of both labile and stable SOM components thereby promoting enzymatic activity (Prescott and Vesterdal, 2021; Prescott and Grayston, 2013; Hättenschwiler, 2005). Similarly diverse root exudates from species like sabal palm can stimulate microbial communities to produce enzymes further enhancing SOM decomposition (Zhang, et al., 2019; Grayston et al., 1997). The presence of adequate moisture in this resource-rich environment in wet season could also have increased enzymatic activity (Brockett, et al., 2012). On the other hand, the nonsignificant differences among the majority of land covers within this ecosystem demonstrate that the forest canopy creates a stable microclimate, maintaining consistent conditions that protect microbial enzymatic activity from seasonal extremes ensuring stable SOM decomposition rates (De Frenne, et al., 2021; Breshears et al., 1998). Contrarily to this, 9-Pinewood-2 land cover despite having similar vegetative and soil conditions as other upland forests, showed a significant reduction in AP and AS. This reduction may stem from unique interactions between pine root exudates, microbial communities, and other soil and environmental factors under wet conditions (Prescott and Grayston, 2013; Shi et al., 2011). The composition of root exudates, particularly organic acids, significantly influences soil bacterial community structure and diversity (Shi et al., 2011), and some pine root exudates may reduce soil enzyme activity (Zhang et al., 2015). For instance, certain exudates may favor microbes that produce fewer extracellular enzymes, thereby decreasing the breakdown of organic matter (Kawasaki et al., 2021; Ferreira et al., 2024). These factors, along with some other soil and environmental factors, could have affected AP and AS activity uniquely in wet conditions (Huang et al., 2011; Baligar et al., 2005). The decline in enzymatic activities among land covers like 11-Wetland-1, 12-Wetland-2, and 14-Wetland-4 within Group B Aquatic and Wetland ecosystems could be attributed to the saturated conditions of these ecosystems, which may hinder oxygen diffusion and microbial activity necessary for

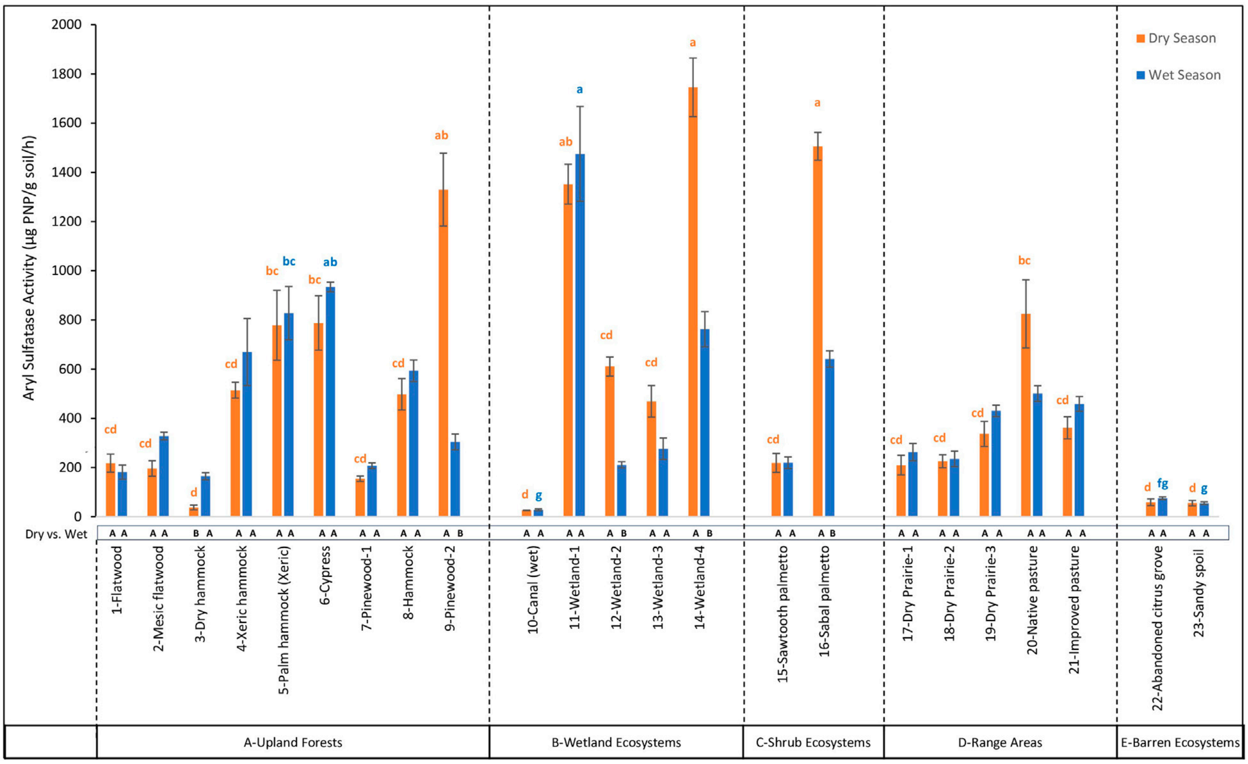

FIGURE 8
Comparison of Aryl Sulfatase (AS) activity across 23 land cover types at the DeLuca Preserve in wet and dry seasons. (Error bars represent ± standard error of the mean. Lowercase letters above bars indicate significant differences among land covers within each season (Bonferroni-adjusted, $p < 0.05$), with blue letters denoting differences in the wet season and orange letters in the dry season. Capital letters below bars denote significant seasonal differences (dry vs. wet) within each land cover type (Bonferroni-adjusted, $p < 0.05$). To enhance clarity, only the extreme significance labels are displayed; detailed comparisons are provided in Supplementary Table S3. Land cover types are grouped by ecosystem categories (A–E), separated by dashed lines).

enzyme production thus detrimentally affecting decomposition of SOM (Borowik and Wyszkowska, 2016; de Macedo et al., 2002; Eswaran, 1982). Aquatic plants typically thrive in water-saturated soils, which may experience enzymatic dilution or washout due to excessive wetness leading to a significant reduction in βG activity in the wet season also indicating a decline in the decomposition rates (Długosz et al., 2023; Xue et al., 2018). However, the significant increase in βG and AP activities in the 10-canal (wet) land cover, with similar conditions highlights the fact that wetland plants like Cattails and Pickerelweed growing in land cover might have enhanced the microbial substrate (Mallison et al., 2001; Sistani et al., 1999) and conditions conducive to enzymatic reactions during wet seasons (Rejmánková and Sirová, 2007). These land covers, along with some others exhibiting decreased enzymatic activity, was observed to fall under Alfisols or Entisols, suggesting soil orders may play a role in enzymatic responses to moisture changes. Alfisols, with their finer textures and higher nutrient contents, tend to retain moisture but may become waterlogged in wet conditions, inhibiting oxygen flow and reducing the activity of aerobic microbes responsible for enzymatic production (de Maced eta al., 2002; Russell, 1978; Rust, 1983). Entisols, conversely, are often sandy and well-drained, leading to rapid moisture percolation. In wet seasons, this could have resulted in the leaching of nutrients necessary for microbial activity, thus reducing enzymatic activity (Grossman, 1983). These all observations emphasize the critical roles of vegetation, soil type, and hydrological conditions in regulating enzymatic activities, reflecting the complex ecological processes that govern SOM decomposition. Vegetation influences enzyme activity through the type and quality of organic inputs, including litter and root exudates, which act as substrates for microbial metabolism. For instance, flatwood ecosystems dominated by pine, oak and palms, wetlands with aquatic plants, prairie grasses, and shrublands each contribute distinct litter chemistry and root exudates, thereby shaping microbial communities and enzyme production (Zhang et al., 2022; Schroeter et al., 2022; Meena and Rao, 2020). These plant-soil-microbe interactions directly influence the expression of enzymes involved in nutrient cycling. Soil type further modulates enzymatic activity through its inherent physical and chemical properties. Soils classified as Entisols and Alfisols, which dominate large portions of the study area, differ in their development, organic matter content, and nutrient-holding capacity. In particular, loamy textured soils typically provide higher water retention and improved aeration (Zega, 2024). Compared to sandy soils, supporting more stable microbial habitats and enhancing enzyme activity (Kim, 2015; Schnecker et al., 2014; Sinsabaugh et al., 2008). Hydrological conditions, especially the contrast between wet and dry seasons, strongly influence soil enzyme dynamics. In dry conditions, moderate moisture and aerobic environments enhance microbial respiration and promote the activity of hydrolytic enzymes. In

TABLE 4 HEDI with corresponding Quartile class among different land covers and ecosystems in dry and wet season.

Land cover	Dry season		Wet season		Ecosystems	HEDI value	
	HEDI value	Quartile class	HEDI value	Quartile class		Dry season	Wet season
1-Flatwood	−0.160	II	0.678	I	Group A Upland Forests	−0.962 to 1.613	−0.421 to 1.623
2-Mesic flatwood	−0.394	III	0.160	II			
3-Dry hammock	−0.962	IV	−0.421	III or IV			
4-Xeric hammock	0.374	I or II	0.337	I or II			
5-Palm hammock (Xeric)	−0.209	III	1.623	I			
6-Cypress	0.152	II	0.375	I			
7-Pinewood-1	−0.913	IV	−0.029	II			
8-Hammock	−0.085	II	−0.099	III			
9-Pinewood-2	1.613	I	−0.048	II or III			
10-Canal (wet)	−1.217	IV	−0.943	IV	Group B Wetland ecosystems	−1.217 to 0.937	−0.942 to 0.870
11-Wetland-1	0.797	I	0.870	I			
12-Wetland-2	−0.242	III	−0.610	IV			
13-Wetland-3	−0.397	III	−0.813	IV			
14-Wetland-4	0.937	I	−0.151	III			
15-Sawtooth palmetto	1.036	I	0.092	II	Group C Shrub ecosystems	1.035 to 2.280	0.092 to −0.035
16-Sabal palmetto	2.281	I	−0.036	II			
17-Dry Prairie-1	−0.102	II	−0.286	III	Group D Range Areas	−0.454 to 0.288	−0.286 to 0.978
18-Dry Prairie-2	−0.454	III or IV	0.979	I			
19-Dry Prairie-3	0.289	II	0.035	II			
20-Native pasture	−0.184	II or III	−0.210	III			
21-Improved pasture	−0.314	III	−0.099	III			
22-Abandoned citrus grove	−0.916	IV	−0.505	IV	Group E Barren ecosystems	−0.928 to −0.916	−0.897 to −0.505
23-Sandy spoil	−0.928	IV	−0.898	IV			

contrast, wet conditions, especially in poorly drained wetland systems can lead to waterlogging, reduce oxygen availability, and lower redox potential, thereby suppressing enzyme production and microbial function (Hammerl et al., 2019; Kapila et al., 2017; Liao et al., 2016). Together, these interrelated factors along with other environmental variables shape the biochemical and microbial environment, ultimately driving the decomposition of SOM across diverse ecosystems.

4.1.3 Comparison across ecosystems

Among different ecosystems, the broad range of enzymatic activity in C-Shrub ecosystems in dry season can be attributed to dense and diverse shrub vegetation, such as Saw palmetto and Gal berry, which contribute significant plant debris to the soil. This debris serves as a rich source of SOM, enhancing a variety of enzymes necessary for decomposing plant material (Charlebois, et al., 2010; Archibold and Archibold, 1995). On the other hand, the absence of vegetation in barren ecosystems might also contribute to the lowest enzymatic activities observed (Minick et al., 2022).

Across different ecosystems, higher βG activities in the wet season under A-Flatwoods and C-Shrub ecosystems can be attributed to the combined influence of higher available water storage capacity and sufficient substrate availability (Diédhiou et al., 2020; Bracho et al., 2008), which are favorable conditions indicative of high SOM decomposition (Blonska et al., 2020; Weintraub et al., 2013). For β-NAG, higher activities in A-Upland Forests, B-Range Areas, and C-Shrub ecosystems during both seasons can be attributed to optimal moisture levels (Borowik and Wyszkowska, 2016) combined with sufficient substrate availability (Song et al., 2021; Yao et al., 2019), conditions that promote SOM decomposition (Blonska et al., 2020; Blonska et al., 2020; Weintraub et al., 2013). Moreover, higher AP activity in C-Shrub ecosystems during the dry season could be attributed to the role of shrubs in maintaining soil moisture and stimulating microbial activity under dry conditions (Diédhiou et al., 2020; Bach and Hofmockel, 2016), which likely enhances enzymatic activity in these ecosystems. AS showing minimal variation in both seasons indicates its relatively insensitive nature (Moreira et al., 2017;

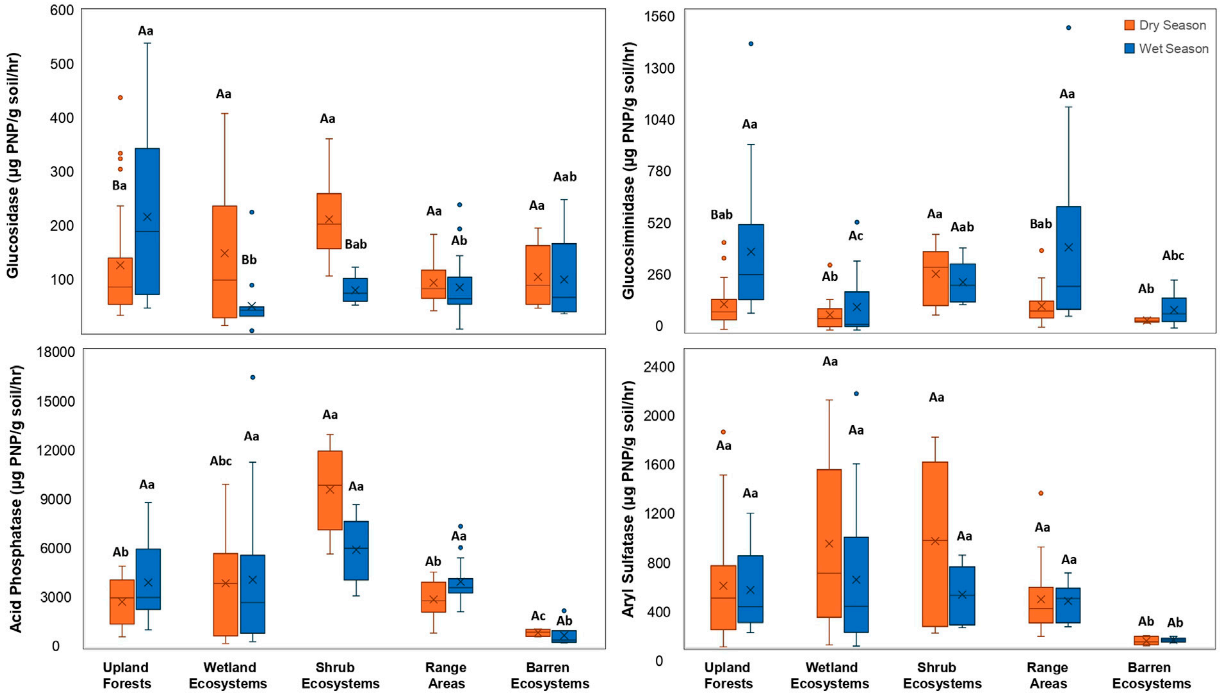

FIGURE 9
Comparison of hydrolytic enzyme activities- β-glucosidase, β-1,4-N-acetylglucosaminidase (β-NAG), acid phosphatase (AP), and arylsulfatase (AS) across five ecosystem categories at the DeLuca Preserve in wet and dry seasons. (Error bars represent ±standard error of the mean. Each ecosystem comprises multiple land cover types (Table 1). Capital letters above each box indicate significant seasonal differences within an ecosystem (dry vs. wet), while lowercase letters denote significant differences among ecosystems within each season (Bonferroni-adjusted, $p < 0.05$).

Wyszkowska et al., 2010). Several studies suggest that while some enzymes are sensitive to environmental changes, AS often exhibits stability under varying conditions (Moreira et al., 2017; Wyszkowska et al., 2010; Ekenler and Tabatabai, 2003; Bergstrom et al., 1998).

From dry to wet seasons the increase in βG and β-NAG activity in A-Upland Forests possibly due to the presence of Spodosols. These soils, with their sandy texture, can retain moisture without becoming waterlogged (New York State College of Agriculture and United States Soil Management Support Services, 1985). This moist yet aerated environment, enriched with organic material from varied vegetation (Prescott and Vesterdal, 2021; Prescott and Grayston, 2013; Hättenschwiler, 2005), likely encouraged microbial proliferation and enzymatic activity during the wet season. The decline in βG activity from the dry to the wet season within the B-Wetlands and C-Shrub ecosystems may be attributed to reduced microbial activity during the wet season, as during the dry season the presence of aeric and typic moisture subclasses likely promote greater microbial activity due to higher oxygen availability (Soil Survey Staff, 2003; Dekker et al., 1984). Conversely, in the wet season, the loamy soils with very poorly drained textures might lead to anaerobic, water-logged conditions, diminishing microbial activity and, consequently, enzymatic activities (Bogati et al., 2023; Steinweg et al., 2012).

4.1.4 HEDI across different land covers and ecosystems

The observed variability in the HEDI across different land covers and seasons shows the complex interplay of ecological factors influencing soil enzymatic activity and subsequent SOM decomposition (Wang, et al., 2020; Simpson et al., 2019). Low HEDI values, particularly in Canal (wet), indicate environments where conditions might be limiting for enzymatic processes, potentially due to factors like water saturation which could impede oxygen diffusion and thus microbial activity (Borowik and Wyszkowska, 2016).

The variation within ecosystems, particularly the contrast between the broad variability in Upland Forests and the consistently low activity in Barren ecosystems, highlights the role of vegetation (Li et al., 2015; Yin et al., 2014; Caldwell, et al., 1999) and soil characteristics (Błońska et al., 2017) in shaping enzymatic activity. Upland Forests, with a mix of vegetation supplying sufficient SOM, create conditions that can either foster or inhibit microbial activity depending on seasonal changes (Prescott and Vesterdal, 2021; Prescott and Grayston, 2013). For example, in favorable conditions, such as during moderate moisture and temperature, this vegetation-derived SOM provides abundant substrates that stimulate microbial growth and enzyme production (Osman, 2013; Baldrian and Štursová, 2010). However, in wet conditions, excess organic matter can lead to reduced oxygen availability or the accumulation of inhibitory compounds (e.g., polyphenols), which may suppress microbial processes (Zak et al., 2019; Zak et al., 2015; Myers et al., 2001). In Barren ecosystems, the minimal fluctuation in HEDI values suggests that the lack of vegetation and potentially poor soil conditions provide limited organic substrates for microbial decomposition, leading to consistently low enzymatic activity regardless of season (De Varennes and Torres, 2011; Badiane et al., 2001).

The observed shift towards higher HEDI values in A-Upland Forests, D-Range Areas and E-Barren ecosystems and lowering

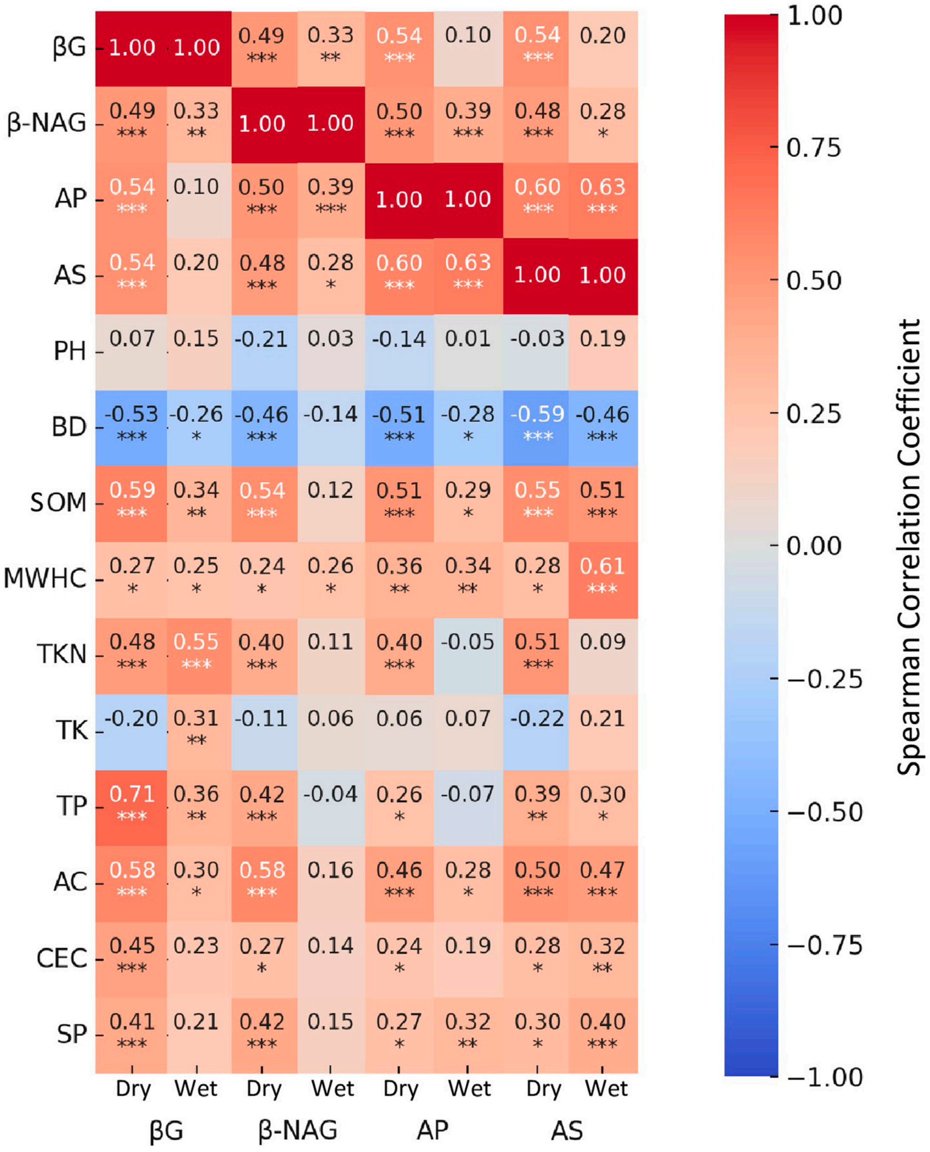

FIGURE 10
Spearman correlation heatmaps showing the relationships between hydrolytic enzyme activities- β-glucosidase, β-1,4-N-acetylglucosaminidase (β-NAG), acid phosphatase (AP), and arylsulfatase (AS) and soil physicochemical parameters under dry and wet season conditions at the DeLuca Preserve. Each cell displays the Spearman correlation coefficient (ρ) between a given enzyme and soil property. Statistical significance is denoted by asterisks: ***$p < 0.001$, **$p < 0.01$, *$p < 0.05$. Non-significant correlations are unmarked. Abbreviated soil variables: bulk density (BD), soil organic matter (SOM), maximum water holding capacity (MWHC), total nitrogen (TKN), total potassium (TK), total phosphorus (TP), active carbon (AC), cation exchange capacity (CEC), and soil protein (SP).

down in B-Wetland ecosystems and C-Shrub ecosystems during the wet season, underlines the complexity of SOM decomposition dynamics (Lehmann and Kleber, 2015; Schnitzer and Khan, 1975). While moisture is generally favorable for decomposition but only in optimum amount, it can also lead to conditions that may not always benefit enzymatic activity, as seen in the Range Areas where excessive moisture may not yield increased enzymatic action (Brockett et al., 2012; Hinojosa et al., 2004).

4.2 Relationship between soil physiochemical properties and hydrolytic enzyme activities in wet and dry seasons

The study revealed significant seasonal variations in soil enzyme-property relationships, emphasizing the dynamic nature of soil enzymes. Enzyme activities, strongly associated with microbial activity, showed positive correlations with OM (Kouchou et al., 2017; Madejón et al., 2001), SP (Theng, 2012; Ladd, 1985), and AC (Bhaduri et al., 2016; Zhongmei and Changchun, 2008), highlighting their roles in substrate availability and SOC decomposition (Smith et al., 2018; Kumar and Sharma, 2019). Additionally, enzyme activities are influenced by nutrient concentration and cycling (Ndlovu et al., 2023), as nutrients regulate microbial metabolism and enzyme synthesis (Liu et al., 2022; Chettri et al., 2020), aligning with the positive correlation observed with CEC. MWHC, meanwhile, improves water retention and provides essential nutrients for soil microorganisms (Mohammadi et al., 2011). The negative correlation between bulk density and enzyme activities across seasons supports Wang et al.'s

TABLE 5 Regression equations for hydrolytic enzyme activities across seasons.

Enzyme	Season	Equation	R^2
βG	Dry	$\beta G = 0.43 + 0.51TP + 0.34AP - 0.12TK$	0.71
	Wet	$\beta G = 0.08 + 0.49TKN + 0.18CEC$	0.41
β-NAG	Dry	$\beta\text{-}NAG = -0.09 + 0.32AC + 0.36AP$	0.48
	Wet	$\beta\text{-}NAG = -0.53 + 0.67AP + 0.24\beta G$	0.31
AP	Dry	$AP = 1.91 + 0.33AS + 0.35\beta\text{-}NAG$	0.51
	Wet	$AP = 2.41 + 0.50AS - 0.35TP + 0.19AC$	0.74
AS	Dry	$AS = 1.23 + 0.77AP - 1.43BD - 0.63TK$	0.56
	Wet	$AS = -2.69 + 0.76AP + 1.24MWHC + 0.30TP - 0.08CEC$	0.71
HEDI	Dry	$HEDI = -3.23 + 0.86AP + 0.59\ \beta\text{-}NAG + 0.51AS - 1.18MWHC + 0.24CEC - 0.21AC$	0.80
	Wet	$HEDI = -6.34 + 0.62\beta\text{-}NAG + 0.69AP + 3.46pH$	0.72

All predictors were significant at $p < 0.05$. The R^2 values represent the proportion of variance explained by the regression equation.

(2019) conclusions on the impact of soil compaction on microbial processes. Moreover, BD is negatively related to SOM (Tanveera et al., 2016; Ahad et al., 2015; Chaudhari et al., 2013; Angers and Simard, 1986), a key driver of enzymatic activity, further emphasizing the negative correlation between BD and enzyme activity. Seasonal shifts in enzyme correlations with reduction from the dry to wet season suggest changes in microbial resource allocation strategies, consistent with observations by Merino et al. (2016) regarding microbial adaptations to environmental fluctuations and nutrient demands in wet conditions.

The multiple linear regression analysis reveals dynamic seasonal shifts in soil-enzyme interactions, highlighting the complex nature of these relationships (Lee et al., 2021; Weintraub et al., 2013). The decreased R^2 values for βG and β-NAG in the wet season suggest that these carbon and nitrogen-cycling enzymes may be more sensitive to changes in soil moisture and associated environmental conditions. This aligns with the findings by Steinweg et al. (2012), who observed that soil moisture can significantly affect hydrolytic enzyme activities. Conversely, the increased R^2 values AP and AS in the wet season indicate that phosphorus and sulfur-cycling enzymes may be more strongly regulated by moisture-related factors. This could be due to increased substrate availability or changes in microbial community composition under wetter conditions, as suggested by Burns et al. (2013). The HEDI values showed strong associations with a broader range of soil properties in the dry season, where substrate availability and microbial activity were key drivers (Sistla and Schimel, 2013) but became more streamlined to fewer predictors in the wet season, where soil hydrology played a dominant role (Sistla and Schimel, 2013; Weintraub et al., 2013). This shift indicates that dominant controlling factors for overall enzyme activity may change between seasons, reflecting alterations in substrate availability, microbial community dynamics, or physicochemical soil properties (Wallenstein and Burns, 2011).

5 Conclusion

The investigation into the variations of hydrolytic enzyme activities between dry and wet conditions across different land covers has provided significant insights into the underlying mechanisms driving SOM decomposition in various land covers during wet and dry season. The study underlines the complex interaction between soil biogeochemical properties, vegetation types, moisture levels, and enzymatic activity, highlighting their collective impact on the dynamics of SOM decomposition. The higher βG activities observed during the wet season in A-Flatwoods and C-Shrub ecosystems emphasize the importance of adequate water storage and substrate availability in facilitating SOM decomposition under hydrologically favourable conditions. Similarly, the consistently elevated β-NAG activities across A-Upland Forests, B-Range Areas, and C-Shrub ecosystems indicate that optimal moisture levels and sufficient substrates are critical drivers of microbial activity and SOM decomposition. The increased AP activity in C-Shrub ecosystems during the dry season reflects the adaptive role of shrubs in maintaining soil moisture and promoting microbial processes under arid conditions. Conversely, the minimal seasonal variation in AS activity suggests its relative insensitivity to environmental fluctuations, highlighting its potential as a stable indicator of soil enzymatic functionality. Moreover, among ecosystems, B-Wetlands demonstrated consistently low enzymatic activity in wet season due to water saturation hindering oxygen diffusion and microbial activity. In contrast, upland forests and shrub ecosystems showed higher enzyme activities due to favourable conditions such as adequate substrate availability and well-aerated soils. The HEDI further highlighted these patterns, with variability across ecosystems reflecting the interplay of vegetation, soil type, and moisture conditions.

The correlations and regression analyses provide a deeper understanding of how soil properties such as OM, SP, and AC consistently correlate positively with enzyme activity, reflecting their central roles in enhancing substrate supply and promoting microbial growth. Similarly, CEC and MWHC foster an environment conducive to enzymatic functions by improving nutrient retention and water availability. On the other hand, high BD and waterlogging in wetland or canal ecosystems restrict oxygen diffusion and reduce enzymatic activity, inhibiting SOM turnover. This variability indicates the adaptive strategies of microbial communities in response to changing environmental conditions, particularly in maintaining the balance between the decomposition of labile and stable SOM. The variability in HEDI values, serving as a proxy for soil enzymatic processes governing SOM decomposition, across land covers and seasons provides critical insights into ecological functioning within this subtropical preserve. These findings emphasize the necessity of tailored conservation strategies to enhance ecosystem resilience and functionality. For instance, in wetland systems, managing hydroperiods to reduce waterlogging can improve oxygen diffusion and enzymatic activity. In shrub ecosystems, preserving native vegetation supports adaptive processes during dry seasons by maintaining soil moisture. Similarly, in upland forests, optimizing substrate availability through organic matter inputs sustains βG and β-NAG driven decomposition. HEDI offers a novel, integrative index that combines the activity of key hydrolytic enzymes involved in SOM breakdown, enabling a more holistic understanding of microbial decomposition potential. Unlike traditional approaches that assess enzymes individually, HEDI provides a composite measure that reflects microbial functioning across diverse ecosystems and seasons. Moreover, integrating HEDI into a monitoring framework and accounting for the complex interactions among soil properties, vegetation, and moisture can help track early shifts in soil functionality and enable the design of conservation practices that can maintain the crucial balance between labile and stable carbon turnover in SOM.

Moreover, the land covers in this study were not evenly distributed across the five major ecosystems; however, the sampling design still allowed us to capture representative variability within and across land cover types. While the current sampling density revealed meaningful patterns in enzyme activity and SOM dynamics, future studies with more balanced representation and increased sampling intensity alongside consideration of additional environmental could further strengthen these insights. Importantly, the findings of this study offer a transferable framework for understanding SOM decomposition and soil functioning in other subtropical or ecologically similar landscapes, supporting informed soil management and conservation strategies beyond the DeLuca Preserve.

Data availability statement

The original contributions presented in the study are included in the article/Supplementary Material, further inquiries can be directed to the corresponding author.

Author contributions

SM: Conceptualization, Data curation, Formal Analysis, Investigation, Methodology, Validation, Visualization, Writing – original draft. NM: Conceptualization, Data curation, Formal Analysis, Investigation, Methodology, Writing – review and editing. AR: Formal Analysis, Investigation, Methodology, Writing – review and editing. NM-I: Conceptualization, Investigation, Methodology, Writing – review and editing. SS: Conceptualization, Funding acquisition, Investigation, Methodology, Project administration, Supervision, Writing – review and editing. AB: Conceptualization, Funding acquisition, Investigation, Methodology, Project administration, Supervision, Writing – review and editing. WM-H: Conceptualization, Funding acquisition, Investigation, Methodology, Project administration, Supervision, Writing – review and editing. JB: Conceptualization, Funding acquisition, Investigation, Methodology, Project administration, Supervision, Validation, Visualization, Writing – original draft.

Funding

The author(s) declare that financial support was received for the research and/or publication of this article. This work was supported by the University of Florida/Institute of Food and Agricultural Sciences DeLuca Preserve/Forest Systems Jumpstart Funding.

Acknowledgments

Additional support was provided by Bai Xue, Md. Anik Mahmud for their valuable discussions, technical assistance, and help with data interpretation. Special thanks to Salvador and Carolina for their help with lab analysis and ensuring the accuracy of experimental procedures.

Conflict of interest

The authors declare that the research was conducted in the absence of any commercial or financial relationships that could be construed as a potential conflict of interest.

The author(s) declared that they were an editorial board member of Frontiers, at the time of submission. This had no impact on the peer review process and the final decision.

Generative AI statement

The authors declare that no Generative AI was used in the creation of this manuscript.

Publisher's note

Supplementary material

The Supplementary Material for this article can be found online at: https://www.frontiersin.org/articles/10.3389/fenvs.2025.1564047/full#supplementary-material

References

Adl, S. M. (2003). *The ecology of soil decomposition*. Wallingford, Cambridge: CABI. doi:10.1079/9780851996615.0000

Ahad, T., Kanth, T. A., and Nabi, S. (2015). Soil bulk density as related to texture, organic matter content and porosity in kandi soils of district Kupwara (Kashmir Valley), India. *Int. J. Sci. Res.* 4 (1), 198–200.

Allison, S. D., Weintraub, M. N., Gartner, T. B., and Waldrop, M. P. (2011). Evolutionary-economic principles as regulators of soil enzyme production and ecosystem function. *Soil Enzym.*, 229–243. doi:10.1007/978-3-642-14225-3_12

Amgain, N. R., Martens-Habbena, W., and Bhadha, J. H. (2022). Effect of dry and flooded rice as cover crops on soil health and microbial community on histosols. *Agric. Res.* 11 (4), 40. doi:10.5539/sar.v11n4p40

Anderson, J. M. (1991). The effects of climate change on decomposition processes in grassland and coniferous forests. *Ecol. Appl.* 1 (3), 326–347. doi:10.2307/1941761

Angers, D. A., and Simard, R. R. (1986). Relations entre la teneur en matière organique et la masse volumique apparente du sol. *Can. J. soil Sci.* 66 (4), 743–746. doi:10.4141/cjss86-074

Angst, G., Pokorný, J., Mueller, C. W., Prater, I., Preusser, S., Kandeler, E., et al. (2021). Soil texture affects the coupling of litter decomposition and SOM formation. *Soil Biol. Biochem.* 159, 108302. doi:10.1016/j.soilbio.2021.108302

Archibold, O. W., and Archibold, O. W. (1995). Terrestrial wetlands. *Ecol. World Veg.*, 319–353. doi:10.1007/978-94-011-0009-0_10

Babcock, G. D., and Esen, A. (1994). Substrate specificity of maize β-glucosidase. *Plant Sci.* 101 (1), 31–39. doi:10.1016/0168-9452(94)90162-7

Bach, E. M., and Hofmockel, K. S. (2016). A time for every season: soil aggregate turnover stimulates decomposition and reduces carbon loss in grasslands managed for bioenergy. *Gcb Bioenergy* 8 (3), 588–599. doi:10.1111/gcbb.12267

Badiane, N. N. Y., Chotte, J. L., Pate, E., Masse, D., and Rouland, C. (2001). Use of soil enzyme activities to monitor soil quality in natural and improved fallows in semi-arid tropical regions. *Appl. soil Ecol.* 18 (3), 229–238. doi:10.1016/s0929-1393(01)00159-7

Baldrian, P., and Štursová, M. (2010). *Enzymes in forest soils*. Berlin, Heidelberg: Springer, 61–73. doi:10.1007/978-3-642-14225-3_4

Baligar, V. C., Wright, R. J., and Hern, J. L. (2005). Enzyme activities in soil influenced by levels of applied sulfur and phosphorus. *Commun. soil Sci. plant analysis* 36 (13-14), 1727–1735. doi:10.1081/CSS-200062431

Bautista-Cruz, A., and Ortiz-Hernández, Y. D. (2015). Hydrolytic soil enzymes and their response to fertilization: a short review. *Comun. Sci. Hortic. J.* 6 (3), 255–262. doi:10.14295/CS.V6I3.962

Beckett, R. P., Zavarzina, A. G., and Liers, C. (2013). Oxidoreductases and cellulases in lichens: possible roles in lichen biology and soil organic matter turnover. *Fungal Biol.* 117 (6), 431–438. doi:10.1016/j.funbio.2013.04.007

Berg, B. (2014). Decomposition patterns for foliar litter–a theory for influencing factors. *Soil Biol. Biochem.* 78, 222–232. doi:10.1016/j.soilbio.2014.08.005

Bergstrom, D. W., Monreal, C. M., and King, D. J. (1998). Sensitivity of soil enzyme activities to conservation practices. *Soil Sci. Soc. Am. J.* 62 (5), 1286–1295. doi:10.2136/sssaj1998.03615995006200050020x

Bhaduri, D., Saha, A., Desai, D., and Meena, H. N. (2016). Restoration of carbon and microbial activity in salt-induced soil by application of peanut shell biochar during short-term incubation study. *Chemosphere* 148, 86–98. doi:10.1016/j.chemosphere.2015.12.130

Black, R. J. (1993). Florida climate data. *Univ. Fla. Coop. Ext. Serv. Inst. Food Agric. Sci.*, 1–4. EDIS. doi:10.32473/edis-ep108-2002

Blonska, E., Lasota, J., da Silva, G. R. V., Vanguelova, E., Ashwood, F., Tibbett, M., et al. (2020). SOM stabilization and carbon-cycling enzyme activity are affected by land management. *Ann. For. Res.* 63 (1), 71–86. doi:10.1016/j.foreco.2019.05.040

Błońska, E., Lasota, J., and Zwydak, M. (2017). *The relationship between soil properties, enzyme activity and land use*. doi:10.1515/frp-2017-0004

Błońska, E., Piaszczyk, W., Staszel, K., and Lasota, J. (2021). Enzymatic activity of soils and soil organic matter stabilization as an effect of components released from the decomposition of litter. *Appl. Soil Ecol.* 157, 103723. doi:10.1016/j.apsoil.2020.103723

Boddy, L. Y. N. N. E. (1986). "Water and decomposition processes in terrestrial ecosystems," in *Water, fungi and plants* (Cambridge: Cambridge University Press), 375–398. doi:10.1525/9780520407114-003

Boerner, R. E. J., Brinkman, J. A., and Smith, A. (2005). Seasonal variations in enzyme activity and organic carbon in soil of a burned and unburned hardwood forest. *Soil Biol. Biochem.* 37 (8), 1419–1426. doi:10.1016/j.soilbio.2004.12.012

Bogati, K., Sewerniak, P., and Walczak, M. (2023). Effect of changes in soil moisture on agriculture soils: response of microbial community, enzymatic and physiological diversity. *Ecol. Quest.* 34 (4), 1–33. doi:10.12775/eq.2023.043

Borowik, A., and Wyszkowska, J. (2016). Soil moisture as a factor affecting the microbiological and biochemical activity of soil. *Plant Soil Environ.* 62 (6), 250–255. doi:10.17221/158/2016-PSE

Bracho, R., Powell, T. L., Dore, S., Li, J., Hinkle, C. R., and Drake, B. G. (2008). Environmental and biological controls on water and energy exchange in Florida scrub oak and pine flatwoods ecosystems. *J. Geophys. Res. Biogeosciences* 113 (G2). doi:10.1029/2007JG000469

Bremner, J. M., and Mulvaney, C. S. (1982). "Nitrogen-total," in *Methods of soil analysis. Part 2. Chemical and microbiological properties*. Editor A. L. Page (New York: American Society of Agronomy, Soil Science Society of America), 595–624. doi:10.2134/agronmonogr9.2.2ed.c31

Breshears, D. D., Nyhan, J. W., Heil, C. E., and Wilcox, B. P. (1998). Effects of woody plants on microclimate in a semiarid woodland: soil temperature and evaporation in canopy and intercanopy patches. *Int. J. Plant Sci.* 159 (6), 1010–1017. doi:10.1086/297622

Brockett, B. F., Prescott, C. E., and Grayston, S. J. (2012). Soil moisture is the major factor influencing microbial community structure and enzyme activities across seven biogeoclimatic zones in western Canada. *Soil Biol. Biochem.* 44 (1), 9–20. doi:10.1016/j.soilbio.2011.09.003

Burns, R. G., DeForest, J. L., Marxsen, J., Sinsabaugh, R. L., Stromberger, M. E., Wallenstein, M. D., et al. (2013). Soil enzymes in a changing environment: current knowledge and future directions. *Soil Biol. Biochem.* 58, 216–234. doi:10.1016/j.soilbio.2012.11.009

Caldwell, B. A., Griffiths, R. P., and Sollins, P. (1999). Soil enzyme response to vegetation disturbance in two lowland Costa Rican soils. *Soil Biol. Biochem.* 31 (12), 1603–1608. doi:10.1016/s0038-0717(99)00067-x

Carter, D. O., and Tibbett, M. (2008). "Cadaver decomposition and soil: processes," in *Soil analysis in forensic taphonomy*. Boca Raton, USA: (CRC Press), 41–64. doi:10.1201/9781420069921.ch2

Charlebois, D., Byers, P. L., Finn, C. E., and Thomas, A. L. (2010). Elderberry: botany, horticulture, potential. *Hortic. Rev.* 37 (37), 213–280. doi:10.1002/9780470543672.ch4

Chaudhari, P. R., Ahire, D. V., Ahire, V. D., Chkravarty, M., and Maity, S. (2013). Soil bulk density as related to soil texture, organic matter content and available total nutrients of Coimbatore soil. *Int. J. Sci. Res. Publ.* 3 (2), 1–8.

Chettri, B., Jang, W., and Seo, T. (2020). Adhaeribacter rhizoryzae sp. nov., a fibrillar matrix-producing bacterium isolated from the rhizosphere of rice plant. *Int. J. Syst. and Evolu. Micro.* 70 (10), 5382–5388. doi:10.1099/ijsem.0.004422

Condron, L., Stark, C., O'Callaghan, M., Clinton, P., and Huang, Z. (2010). The role of microbial communities in the formation and decomposition of SOM. *Soil Microbiol. Sustain. crop Prod.*, 81–118. doi:10.1007/978-90-481-9479-7_4

Cooper, P. J. M. (1972). Aryl sulphatase activity in northern Nigerian soils. *Soil Biol. Biochem.* 4 (3), 333–337. doi:10.1016/0038-0717(72)90029-6

Cotrufo, M. F., and Lavallee, J. M. (2022). Soil organic matter formation, persistence, and functioning: a synthesis of current understanding to inform its conservation and regeneration. *Adv. Agron.* 172, 1–66. doi:10.1016/bs.agron.2021.11.002

Daunoras, J., Kačergius, A., and Gudiukaitė, R. (2024). Role of soil microbiota enzymes in soil health and activity changes depending on climate change and the type of soil ecosystem. *Biology* 13 (2), 85. doi:10.3390/biology13020085

De Frenne, P., Lenoir, J., Luoto, M., Scheffers, B. R., Zellweger, F., Aalto, J., et al. (2021). Forest microclimates and climate change: importance, drivers and future research agenda. *Glob. Change Biol.* 27 (11), 2279–2297. doi:10.1111/gcb.15569

Dekker, L. W., Wösten, J. H. M., and Bouma, J. (1984). Characterizing the soil moisture regime of a Typic Haplohumod. *Geoderma* 34 (1), 37–42. doi:10.1016/0016-7061(84)90004-1

de Macedo, J. R., Meneguelli, N. D. A., Ottoni Filho, T. B., and de Sousa Lima, J. A. (2002). Estimation of field capacity and moisture retention based on regression analysis involving chemical and physical properties in Alfisols and Ultisols of the state of Rio de Janeiro. *Commun. soil Sci. plant analysis* 33 (13-14), 2037–2055. doi:10.1081/css-120005747

Denef, K., Six, J., Bossuyt, H., Frey, S. D., Elliott, E. T., Merckx, R., et al. (2001). Influence of dry–wet cycles on the interrelationship between aggregate, particulate organic matter, and microbial community dynamics. *Soil Biol. Biochem.* 33 (12-13), 1599–1611. doi:10.1016/s0038-0717(01)00076-1

Deng, L., Zhu, G. Y., Tang, Z. S., and Shangguan, Z. P. (2016). Global patterns of the effects of land-use changes on soil carbon stocks. *Glob. Ecol. Conservation* 5, 127–138. doi:10.1016/j.gecco.2015.12.004

De Varennes, A., and Torres, M. O. (2011). Post-fallow tillage and crop effects on soil enzymes and other indicators. *Soil use Manag.* 27 (1), 18–27. doi:10.1111/j.1475-2743.2010.00307.x

Diedhiou, S., Assigbetsee, K. B., Goudiaby, A. O. K., Diedhiou, I., Badiane, A. N., Sène, M., et al. (2020). *Arid agroecosystem shrubs enhance enzyme activities during the dry season*. doi:10.4236/ajps.2020.112014

Dijkstra, F. A., and Cheng, W. (2007). Moisture modulates rhizosphere effects on C decomposition in two different soil types. *Soil Biol. Biochem.* 39 (9), 2264–2274. doi:10.1016/j.soilbio.2007.03.026

Długosz, J., Piotrowska-Długosz, A., and Breza-Boruta, B. (2023). The effect of differences in soil water content on microbial and enzymatic properties across the soil profiles. *Ecohydrol. Hydrobiology*. doi:10.1016/j.ecohyd.2023.06.010

Don, A., Böhme, I. H., Dohrmann, A. B., Poeplau, C., and Tebbe, C. C. (2017). Microbial community composition affects soil organic carbon turnover in mineral soils. *Biol. Fertil. soils* 53 (4), 445–456. doi:10.1007/s00374-017-1198-9

Ekenler, M., and Tabatabai, M. A. (2003). Responses of phosphatases and arylsulfatase in soils to liming and tillage systems. *J. Plant Nutr. Soil Sci.* 166 (3), 281–290. doi:10.1002/jpln.200390045

Eswaran, H. (1982). "Alfisols and ultisols," in *Proceedings of South pacific regional forum on soil taxonomy, suva, Fiji, 2-13 november 1981*. Editors R. J. Morrison, and D. M. Leslie (Suva, Fiji: Institute of Natural Resources, University of the South Pacific), 1982. doi:10.25082/ree.2020.02.001

Exum, J. H. (2020). *Conservation easement baseline documentation report DeLuca preserve Osceola county*. Florida: Exum Associated Inc. doi:10.3133/ofr791595

Fageria, N. K. (2012). Role of soil organic matter in maintaining sustainability of cropping systems. *Commun. soil Sci. plant analysis* 43 (16), 2063–2113. doi:10.1080/00103624.2012.697234

Ferreira, M. I., Marais, A., Botha, A., Reinhardt, C. F., and Rijst, M. (2024). Root exudates from weedy ryegrass hybrid type and selected crop plants affect soil microbial communities in two soil types of the Western Cape, South Africa. *West. Cape, S. Afr.* 4, 2378. doi:10.54517/ama.v4i2.2378

Filipović, A., Perčin, A., Hadžiabulić, A., and Mandić, A. (2024). "Transformation of SOM and impact on the ecosystem," in *Agroforestry for carbon and ecosystem management* (Academic Press), 311–329. doi:10.1016/b978-0-323-95393-1.00018-x

Findlay, S. E. (2021). "SOM decomposition," in *Fundamentals of ecosystem science* (Academic Press), 81–102. doi:10.1016/b978-0-12-812762-9.00004-6

Frøseth, R. B., and Bleken, M. A. (2015). Effect of low temperature and soil type on the decomposition rate of soil organic carbon and clover leaves, and related priming effect. *Soil Biol. Biochem.* 80, 156–166. doi:10.1016/j.soilbio.2014.10.004

Furtak, K., Gałązka, A., and Niedźwiecki, J. (2020). Changes in soil enzymatic activity caused by hydric stress. *Pol. J. Environ. Stud.* 29 (4), 2653–2660. doi:10.15244/pjoes/112896

Ge, M., Zhou, H., Shen, Y., Meng, H., Li, R., Zhou, J., et al. (2020). Effect of aeration rates on enzymatic activity and bacterial community succession during cattle manure composting. *Bioresour. Technol.* 304, 122928. doi:10.1016/j.biortech.2020.122928

Glassman, S. I., Weihe, C., Li, J., Albright, M. B., Looby, C. I., Martiny, A. C., et al. (2018). Decomposition responses to climate depend on microbial community composition. *Proc. Natl. Acad. Sci.* 115 (47), 11994–11999. doi:10.1073/pnas.1811269115

Goebel, M. O., Bachmann, J., Reichstein, M., Janssens, I. A., and Guggenberger, G. (2011). Soil water repellency and its implications for SOM decomposition–is there a link to extreme climatic events? *Glob. Change Biol.* 17 (8), 2640–2656. doi:10.1111/j.1365-2486.2011.02414.x

Grayston, S. J., Vaughan, D., and Jones, D. (1997). Rhizosphere carbon flow in trees, in comparison with annual plants: the importance of root exudation and its impact on microbial activity and nutrient availability. *Appl. soil Ecol.* 5 (1), 29–56. doi:10.1016/s0929-1393(96)00126-6

Grossman, R. B. (1983). Chapter 2 Entisols. *Dev. soil Sci.* 11, 55–90. doi:10.1016/s0166-2481(08)70613-5

Guo, L. B., and Gifford, R. M. (2002). Soil carbon stocks and land use change: a meta analysis. *Glob. change Biol.* 8 (4), 345–360. doi:10.1046/j.1354-1013.2002.00486.x

Hammerl, V. B., Grant, K., Pritsch, K., Jentsch, A., Schloter, M., Beierkuhnlein, C., et al. (2019). Seasonal effects of extreme weather events on potential extracellular enzyme activities in a temperate grassland soil. *Front. Environ. Sci.* 6, 157. doi:10.3389/fenvs.2018.00157

Harrison-Kirk, T., Beare, M. H., Meenken, E. D., and Condron, L. M. (2014). Soil organic matter and texture affect responses to dry/wet cycles: changes in soil organic matter fractions and relationships with C and N mineralisation. *Soil Biol. Biochem.* 74, 50–60. doi:10.1016/j.soilbio.2014.02.021

Hassan, W., Chen, W., Cai, P., and Huang, Q. (2013). Oxidative enzymes, the ultimate regulator: implications for factors affecting their efficiency. *J. Environ. Qual.* 42 (6), 1779–1790. doi:10.2134/jeq2013.05.0204

Hättenschwiler, S. (2005). "Effects of tree species diversity on litter quality and decomposition," in *Forest diversity and function: temperate and boreal systems* (Berlin, Heidelberg: Springer Berlin Heidelberg), 149–164. doi:10.1007/3-540-26599-6_8

Haynes, R. J. (1986). The decomposition process: mineralization, immobilization, humus formation, and degradation. *Mineral nitrogen plant-soil Syst.*, 52–126. doi:10.1016/b978-0-12-334910-1.50006-6

Henry, H. A. (2013). Reprint of "Soil extracellular enzyme dynamics in a changing climate". *Soil Biol. Biochem.* 56, 53–59. doi:10.1016/j.soilbio.2012.10.022

Hinojosa, M. B., Carreira, J. A., García-Ruíz, R., and Dick, R. P. (2004). Soil moisture pre-treatment effects on enzyme activities as indicators of heavy metal-contaminated and reclaimed soils. *Soil Biol. Biochem.* 36 (10), 1559–1568. doi:10.1016/j.soilbio.2004.07.003

Huang, W., Liu, J., Zhou, G., Zhang, D., and Deng, Q. (2011). Effects of precipitation on soil acid phosphatase activity in three successional forests in southern China. *Biogeosciences* 8 (7), 1901–1910. doi:10.5194/bg-8-1901-2011

Jenkinson, D. S., and Polson, D. S. (1976). The effects of biocidal treatments on metabolism in soil-I. Fumigation with chloroform. *Soil Biol. Biochem.* 8 (3), 167–177. doi:10.1016/0038-0717(76)90001-8

Kang, H., and Freeman, C. (1999). Phosphatase and arylsulphatase activities in wetland soils: annual variation and controlling factors. *Soil Biol. Biochem.* 31 (3), 449–454. doi:10.1016/s0038-0717(98)00150-3

Kapila, S., Devi, K., Thakur, S., and Rao, A. (2017). Acid phosphatase activity in some Indian Liverworts. *Cryptogam. Bryol.* 38 (3), 325–331. doi:10.7872/cryb/v38.iss3.2017.325

Karaca, S., Dengiz, O., Turan, İ. D., Özkan, B., Dedeoğlu, M., Gülser, F., et al. (2021). An assessment of pasture soils quality based on multi-indicator weighting approaches in semi-arid ecosystem. *Ecol. Indic.* 121, 107001. doi:10.1016/j.ecolind.2020.107001

Kawasaki, A., Dennis, P. G., Forstner, C., Raghavendra, A. K. H., Mathesius, U., Richardson, A., et al. (2021). Manipulating exudate composition from root apices shapes the microbiome throughout the root system. *Plant Physiol.* 187, 2279–2295. doi:10.1093/plphys/kiab337

Kim, H. (2015). A review of factors that regulate extracellular enzyme activity in wetland soils. *Korean J. Microbiol.* 51 (2), 97–107. doi:10.7845/kjm.2015.4087

Koch, O., Tscherko, D., and Kandeler, E. (2007). Temperature sensitivity of microbial respiration, nitrogen mineralization, and potential soil enzyme activities in organic alpine soils. *Glob. Biogeochem. Cycles* 21 (4). doi:10.1029/2007gb002983

Körschens, M. (2002). Importance of soil organic matter (SOM) for biomass production and environment (a review). *Archives Agron. Soil Sci.* 48 (2), 89–94. doi:10.1080/03650340214162

Kouchou, A., Rais, N., Thoisy, J. C., Duplay, J., Ghazi, M., Elsass, F., et al. (2017). Behavior of enzyme activities exposed to contamination by heavy metals and dissolved organic carbon in calcareous agricultural soils. *Soil Sediment Contam. Int. J.* 26 (3), 259–276. doi:10.1080/15320383.2017.1289499

Kumar, A., and Sharma, S. (2019). *Microbes and enzymes in soil health and bioremediation*. Singapore: Springer, 353–366. doi:10.1007/978-981-13-9117-0

Kumar, S., Lal, R., and Lloyd, C. D. (2012). Assessing spatial variability in soil characteristics with geographically weighted principal components analysis. *Comput. Geosci.* 16, 827–835. doi:10.1007/s10596-012-9290-6

Kunito, T., Kurita, H., Kumori, M., Sakaguchi, K., Nishizawa, S., Fujita, K., et al. (2022). Microbial synthesis of arylsulfatase depends on the soluble and adsorbed sulfate concentration in soils. *Eur. J. Soil Biol.* 111, 103418. doi:10.1016/j.ejsobi.2022.103418

Ladd, J. N. (1985). "Soil enzymes," in *Soil organic matter and biological activity*. Dordrecht: Springer Netherlands, 175–221. doi:10.1007/978-94-009-5105-1_6

Lascody, R., and Melbourne, N. (2002). *The onset of the wet and dry seasons in East Central Florida, a subtropical wet-dry climate*. Melbourne, USA: National Weather Service Weather Forecast Office Melbourne, FL. doi:10.3334/ornldaac/723

Lee, J., Kim, H. S., Jo, H. Y., and Kwon, M. J. (2021). Revisiting soil bacterial counting methods: Optimal soil storage and pretreatment methods and comparison of culture-dependent and -independent methods. *PLOS ONE* 16 (2), e0246142. doi:10.1371/journal.pone.0246142

Lehmann, J., and Kleber, M. (2015). The contentious nature of soil organic matter. *Nature* 528 (7580), 60–68. doi:10.1038/nature16069

Li, J., Zhou, X., Yan, J., Li, H., and He, J. (2015). Effects of regenerating vegetation on soil enzyme activity and microbial structure in reclaimed soils on a surface coal mine site. *Appl. Soil Ecol.* 87, 56–62. doi:10.1016/j.apsoil.2014.11.010

Liao, X., Inglett, P. W., and Inglett, K. S. (2016). Seasonal patterns of nitrogen cycling in subtropical short-hydroperiod wetlands: effects of precipitation and restoration. *Sci. Total Environ.* 556, 136–145. doi:10.1016/j.scitotenv.2016.02.203

Liu, C., Ma, J., Qu, T., Xue, Z., Li, X., Chen, Q., et al. (2022). Extracellular enzyme activity and stoichiometry reveal nutrient dynamics during microbially-mediated plant residue transformation. *Forests* 14 (1), 34. doi:10.3390/f14010034

Lohse, K. A., Brooks, P. D., McIntosh, J. C., Meixner, T., and Huxman, T. E. (2009). Interactions between biogeochemistry and hydrologic systems. *Annu. Rev. Environ. Resour.* 34, 65–96. doi:10.1146/annurev.environ.33.031207.111141

Madejón, E., Burgos, P., Murillo, J. M., and Cabrera, F. (2001). Phytotoxicity of organic amendments on activities of select soil enzymes. *Commun. soil Sci. plant analysis* 32 (13-14), 2227–2239. doi:10.1081/CSS-120000279

Mallison, C. T., Stocker, R. K., and Cichra, C. E. (2001). Physical and vegetative characteristics of floating islands. *J. Aquatic Plant Manag.* 39, 107–111. doi:10.1577/m03-043.1

Mariscal-Sancho, I., Ball, B., and McKenzie, B. (2018). Influence of tillage practices, organic manures and extrinsic factors on β-glucosidase activity: the final step of cellulose hydrolysis. *Soil Syst.* 2 (2), 21. doi:10.3390/soilsystems2020021

Martin-Sanz, J. P., de Santiago-Martin, A., Valverde-Asenjo, I., Quintana-Nieto, J. R., Gonzalez-Huecas, C., and Lopez-Lafuente, A. L. (2022). Comparison of soil quality indexes calculated by network and principal component analysis for carbonated soils under different uses. *Ecol. Indic.* 143, 109374. doi:10.1016/j.ecolind.2022.109374

Mayor, A. G. , Goirán, S. B., Vallejo, V. R., and Bautista, S. (2016). Variation in soil enzyme activity as a function of vegetation amount, type, and spatial structure in fire-prone Mediterranean shrublands. *Sci. Total Environ.* 573, 1209–1216. doi:10.1016/j.scitotenv.2016.03.139

McKeague, J. A., DeConinck, F., and Franzmeier, D. P. (1983). "Chapter 6 Spodosols," in *Developments in soil science* (Elsevier), 11, 217–252. doi:10.1016/s0166-2481(08)70617-2

Meena, A., and Rao, K. S. (2020). Assessment of soil microbial and enzyme activity in the rhizosphere zone under different land use/cover of a semi-arid ecosystem. *India*. doi:10.21203/rs.3.rs-42033/v1

Merino, C., Godoy, R., and Matus, F. (2016). Soil enzymes and biological activity at different levels of SOM stability. *J. Soil Sci. plant Nutr.* 16 (1), 14–30. doi:10.4067/s0718-95162016005000002

Minick, K. J., Aguilos, M., Li, X., Mitra, B., Prajapati, P., and King, J. S. (2022). Effects of spatial variability and drainage on extracellular enzyme activity in coastal freshwater forested wetlands of Eastern North Carolina, USA. *Forests* 13 (6), 861. doi:10.3390/f13060861

Mir, Y. H., Ganie, M. A., Shah, T. I., Bangroo, S. A., Mir, S. A., Shah, A. M., et al. (2023). Soil microbial and enzyme activities in different land use systems of the Northwestern Himalayas. *PeerJ* 11, e15993. doi:10.7717/peerj.15993

Moghimian, N., Hosseini, S. M., Kooch, Y., and Darki, B. Z. (2017). Impacts of changes in land use/cover on soil microbial and enzyme activities. *Catena* 157, 407–414. doi:10.1016/j.catena.2017.06.003

Mohammadi, K., Heidari, G., Khalesro, S., and Sohrabi, Y. (2011). Soil management, microorganisms and SOM interactions: a review. *Afr. J. Biotechnol.* 10 (86), 19840. doi:10.5897/ajbx11.006

Moreira, R. S., Chiba, M. K., Nunes, S. B., and Maria, I. D. (2017). Air-drying pretreatment effect on soil enzymatic activity. *Plant Soil Environ.* 63, 29–33. doi:10.17221/656/2016-PSE

Muñoz-Rojas, M., Jordán, A., Zavala, L. M., De la Rosa, D., Abd-Elmabod, S. K., and Anaya-Romero, M. (2015). Impact of land use and land cover changes on organic carbon stocks in Mediterranean soils (1956–2007). *Land Degrad. Dev.* 26 (2), 168–179. doi:10.1002/ldr.2194

Murphy, B. W. (2015). Impact of soil organic matter on soil properties—a review with emphasis on Australian soils. *Soil Res.* 53 (6), 605–635. doi:10.1071/sr14246

Myers, R. T., Zak, D. R., White, D. C., and Peacock, A. D. (2001). Landscape-level patterns of microbial community composition and substrate use in upland forest ecosystems. *Soil Sci. Soc. Am. J.* 65 (2), 359–367. doi:10.2136/SSSAJ2001.652359X

Nair, P. R., Kumar, B. M., Nair, V. D., Nair, P. R., Kumar, B. M., and Nair, V. D. (2021). Soil organic matter (SOM) and nutrient cycling. *Introd. Agrofor. Four Decades Sci. Dev.*, 383–411. doi:10.1007/978-3-030-75358-0_16

National Resources Conservation Service (2024). *Soil survey geographic Database (SSURGO)*. United States Department of Agriculture. Available online at: https://www.nrcs.usda.gov.

Ndlovu, S., Suinyuy, T. N., Pérez-Fernández, M. A., and Magadlela, A. (2023). Encephalartos natalensis, their nutrient-cycling microbes and enzymes: a story of successful trade-offs. *Plants* 12 (5), 1034. doi:10.3390/plants12051034

Nedyalkova, K., Donkova, R., and Malinov, I. (2020). Acid phosphatase activity under the impact of erosion level in agricultural soils of different type and land use. *Bulg. J. Agric. Sci.* 26 (6).

New York State College of Agriculture, Life Sciences. Department of Agronomy, and United States. Soil Management Support Services (1985). Keys to soil taxonomy: Alfisols, aridisols, Entisols, histosols, inceptisols, mollisols, oxisols, Spodosols, ultisols, vertisols, soil family (No. 6). *Soil Manag. Support Serv.* doi:10.21474/ijar01/12414

Nieder, R., and Benbi, D. K. (2008). Carbon and nitrogen transformations in soils. *Carbon nitrogen Terr. Environ.*, 137–159. doi:10.1007/978-1-4020-8433-1_5

Osman, K. T. (2013). *Organic matter of forest soils*. Cham: Springer, 63–76. doi:10.1007/978-3-319-02541-4_4

Osman, K. T., and Osman, K. T. (2013). *Soil organic matter (SOM). In Soils: principles*. Dordrecht, Netherlands: Properties and Management, 89–96. doi:10.1007/978-94-007-5663-2_7

Ouyang, Y., and Li, X. (2013). Recent research progress on soil microbial responses to drying–rewetting cycles. *Acta Ecol. Sin.* 33 (1), 1–6. doi:10.1016/j.chnaes.2012.12.001

Paul, E. A. (2016). The nature and dynamics of soil organic matter: plant inputs, microbial transformations, and organic matter stabilization. *Soil Biol. Biochem.* 98, 109–126. doi:10.1016/j.soilbio.2016.04.001

Paul, E. A., and Collins, H. P. (2020). "The characteristics of SOM relative to nutrient cycling," in *Methods for assessment of soil degradation* Boca Raton, USA: (CRC Press), 181–197. doi:10.1201/9781003068716-9

Piotrowska, A., and Koper, J. (2010). Soil beta-βG activity under winter wheat cultivated in crop rotation systems depleting and enriching the soil in SOM. *J. Elem.* 15 (3), 593–600. doi:10.5601/jelem.2010.15.3.593-600

Prescott, C. E. (2010). Litter decomposition: what controls it and how can we alter it to sequester more carbon in forest soils? *Biogeochemistry* 101, 133–149. doi:10.1007/s10533-010-9439-0

Prescott, C. E., and Grayston, S. J. (2013). Tree species influence on microbial communities in litter and soil: current knowledge and research needs. *For. Ecol. Manag.* 309, 19–27. doi:10.1016/j.foreco.2013.02.034

Prescott, C. E., and Vesterdal, L. (2021). Decomposition and transformations along the continuum from litter to soil organic matter in forest soils. *For. Ecol. Manag.* 498, 119522. doi:10.1016/j.foreco.2021.119522

Ramesh, T., Bolan, N. S., Kirkham, M. B., Wijesekara, H., Kanchikerimath, M., Rao, C. S., et al. (2019). Soil organic carbon dynamics: impact of land use changes and management practices: a review. *Adv. Agron.* 156, 1–107. doi:10.1016/bs.agron.2019.02.001

Rastin, N., Rosenplänter, K., and Hüttermann, A. (1988). Seasonal variation of enzyme activity and their dependence on certain soil factors in a beech forest soil. *Soil Biol. Biochem.* 20 (5), 637–642. doi:10.1016/0038-0717(88)90147-2

Raza, T., Qadir, M. F., Khan, K. S., Eash, N. S., Yousuf, M., Chatterjee, S., et al. (2023). Unraveling the potential of microbes in decomposition of organic matter and release of carbon in the ecosystem. *J. Environ. Manag.* 344, 118529. doi:10.1016/j.jenvman.2023.118529

R Development Core Team (2023). *R: a language and environment for statistical computing (Version 4.3.2)*. Vienna, Austria: R Foundation for Statistical Computing. [Computer software]. doi:10.1201/9780203738672-4

Rejmánková, E., and Sirová, D. (2007). Wetland macrophyte decomposition under different nutrient conditions: relationships between decomposition rate, enzyme activities and microbial biomass. *Soil Biol. Biochem.* 39 (2), 526–538. doi:10.1016/j.soilbio.2006.08.022

Rice, C. W. (2002). SOM and nutrient dynamics. *Encycl. soil Sci.* 2, 1180–1183. doi:10.1081/e-ess3-120002258

Rittl, T. F., Canisares, L., Sagrilo, E., Butterbach-Bahl, K., Dannenmann, M., and Cerri, C. E. (2020). Temperature sensitivity of soil organic matter decomposition varies with biochar application and soil type. *Pedosphere* 30 (3), 336–342. doi:10.1016/s1002-0160(20)60013-3

Robertson, G. P., and Paul, E. A. (2000). "Decomposition and SOM dynamics," in *Methods in ecosystem science* (New York, NY: Springer New York), 104–116. doi:10.1007/978-1-4612-1224-9_8

Russell, M. B. (1978). "Profile moisture dynamics of soil in Vertisols and Alfisols," in *Proceedings, international workshop on the agroclimatological research needs of the semi-arid tropics*, 22–24. doi:10.2134/asaspecpub34.c6

Rust, R. H. (1983). Chapter 7 Alfisols. *Dev. Soil Sci.* 11, 253–281. doi:10.1016/s0166-2481(08)70618-4

Salam, A. K., Afandi, Sriyani, N., and Kimura, M. (2001). Soil enzymatic activities in a hilly coffee plantation in Lampung Province, South Sumatra, Indonesia, under plant cover management. *J. Soil Sci. Plant Nutr.* 47 (4), 695–702. doi:10.1080/00380768.2001.10408434

Salazar, S., Sánchez, L. E., Alvarez, J., Valverde, A., Galindo, P., Igual, J. M., et al. (2011). Correlation among soil enzyme activities under different forest system management practices. *Ecol. Eng.* 37 (8), 1123–1131. doi:10.1016/j.ecoleng.2011.02.007

Schimel, J. P. (2018). Life in dry soils: effects of drought on soil microbial communities and processes. *Annu. Rev. Ecol. Evol. Syst.* 49, 409–432. doi:10.1146/annurev-ecolsys-110617-062614

Schindelbeck, R. R., Moebius-Clune, B. N., Moebius-Clune, D. J., Kurtz, K. S., and van Es, H. M. (2016). *Cornell University comprehensive assessment of soil health laboratory standard operating procedures*. Ithaca, NY: Cornell Univ. doi:10.2134/jeq2016.05.0182

Schnecker, J., Wild, B., Hofhansl, F., Eloy Alves, R. J., Bárta, J., Čapek, P., et al. (2014). Effects of soil organic matter properties and microbial community composition on enzyme activities in cryoturbated arctic soils. *PLoS One* 9 (4), e94076. doi:10.1371/journal.pone.0094076

Schnitzer, M., and Khan, S. U. (1975). *Som*. Elsevier. doi:10.1016/s0166-2481(08)70015-1

Schroeter, S. A., Eveillard, D., Chaffron, S., Zoppi, J., Kampe, B., Lohmann, P., et al. (2022). Microbial community functioning during plant litter decomposition. *Dent. Sci. Rep.* 12 (1), 7451. doi:10.1038/s41598-022-11485-1

Scott, N. A., Cole, C. V., Elliott, E. T., and Huffman, S. A. (1996). Soil textural control on decomposition and soil organic matter dynamics. *Soil Sci. Soc. Am. J.* 60 (4), 1102–1109. doi:10.2136/sssaj1996.03615995006000040020x

Shao, X., Yang, W., and Wu, M. (2015). Seasonal dynamics of soil labile organic carbon and enzyme activities in relation to vegetation types in Hangzhou Bay tidal flat wetland. *PLoS One* 10 (11), e0142677. doi:10.1371/journal.pone.0142677

Sherene, T. (2017). Role of soil enzymes in nutrient transformation: a review. *Bio Bull.* 3 (1), 109–131.

Shi, S., Richardson, A. E., O'Callaghan, M., DeAngelis, K. M., Jones, E. E., Stewart, A., et al. (2011). Effects of selected root exudate components on soil bacterial communities. *FEMS Microbiol. Ecol.* 77 (3), 600–610. doi:10.1111/j.1574-6941.2011.01150.x

Shi, W. (2010). *Agricultural and ecological significance of soil enzymes: soil carbon sequestration and nutrient cycling*. Berlin, Heidelberg: Springer, 43–60. doi:10.1007/978-3-642-14225-3_3

Simpson, R. M., Mason, K., Robertson, K., and Müller, K. (2019). Relationship between soil properties and enzyme activities with soil water repellency. *Soil Res.* 57 (6), 689–702. doi:10.1071/sr18199

Sinsabaugh, R. L., Lauber, C. L., Weintraub, M. N., Ahmed, B., Allison, S. D., Crenshaw, C., et al. (2008). Stoichiometry of soil enzyme activity at global scale. *Ecol. Lett.* 11 (11), 1252–1264. doi:10.1111/j.1461-0248.2008.01245.x

Sistani, K. R., Mays, D. A., and Taylor, R. W. (1999). Development of natural conditions in constructed wetlands: biological and chemical changes. *Ecol. Eng.* 12 (1-2), 125–131. doi:10.1016/s0925-8574(98)00058-5

Sistla, S. A., and Schimel, J. P. (2013). Seasonal patterns of microbial extracellular enzyme activities in an arctic tundra soil: identifying direct and indirect effects of long-term summer warming. *Soil Biol. Biochem.* 66, 119–129. doi:10.1016/j.soilbio.2013.07.003

Smith, P., Lutfalla, S., Riley, W. J., Torn, M. S., Schmidt, M. W., and Soussana, J. F. (2018). The changing faces of soil organic matter research. *European Journal of Soil Science* 69 (1), 23–30. doi:10.1111/ejss.12500

Soil Survey Staff (1999). "Soil taxonomy: a basic system of soil classification for making and interpreting soil surveys," in *U.S. Department of agriculture, natural resources conservation Service*. 2nd ed. (Agriculture Handbook No. 436). doi:10.1111/j.1475-2743.2001.tb00008.x

Soil Survey Staff (2003). *Keys to soil taxonomy*. 9th ed. Washington, DC: United States Department of Agriculture, Natural Resources Conservation Service. doi:10.1111/j.1475-2743.2001.tb00008.x

Song, Y., Jiang, L., Song, C., Wang, X., Ma, X., Zhang, H., et al. (2021). Microbial abundance and enzymatic activity from tussock and shrub soil in permafrost peatland after 6-year warming. *Ecol. Indic.* 126, 107589. doi:10.1016/j.ecolind.2021.107589

Speir, T. W., and Ross, D. J. (2002). *Hydrolytic enzyme activities to assess soil degradation and recovery. Enzymes in the environments: activity, ecology and applications*, 407–431. doi:10.1201/9780203904039.ch16

Steinweg, J. M., Dukes, J. S., and Wallenstein, M. D. (2012). Modeling the effects of temperature and moisture on soil enzyme activity: linking laboratory assays to continuous field data. *Soil Biol. Biochem.* 55, 85–92. doi:10.1016/j.soilbio.2012.06.015

Sumner, M. E., Miller, W. P., and Sparks, D. (1996). *Methods of soil analysis. Part 3. Chemical methods. Cation exchange capacity, and exchange coefficients*. Madison: Soil Science Society of America and American Society of Agronomy, 65–94.

Swift, R. S. (2001). Sequestration of carbon by soil. *Soil Sci.* 166 (11), 858–871. doi:10.1097/00010694-200111000-00010

Tabatabai, M. A. (1994). Soil enzymes. *Methods soil analysis Part 2 Microbiol. Biochem. Prop.* 5, 775–833. doi:10.2136/sssabookser5.2.c37

Tanveera, A., Kanth, T. A., Tali, P. A., and Naikoo, M. (2016). Relation of soil bulk density with texture, total organic matter content and porosity in the soils of Kandi Area of Kashmir valley, India. *Int. Res. J. Earth Sci.* 4 (1), 1–6. doi:10.9734/JGEESI/2016/21344

Theng, B. K. G. (2012). Proteins and enzymes. *Dev. Clay Sci.* 4, 245–318. doi:10.1016/B978-0-444-53354-8.00008-6

Tischer, A., Blagodatskaya, E., and Hamer, U. (2015). Microbial community structure and resource availability drive the catalytic efficiency of soil enzymes under land-use change conditions. *Soil Biol. Biochem.* 89, 226–237. doi:10.1016/j.soilbio.2015.07.011

Tumer, A. R., Karacaoglu, E., Namli, A., Keten, A., Farasat, S., Akcan, R., et al. (2013). Effects of different types of soil on decomposition: an experimental study. *Leg. Med.* 15 (3), 149–156. doi:10.1016/j.legalmed.2012.11.003

Ullah, R., Lone, M. I., Ullah, K. S., Mehdi, S. M., and Qazi, M. A. (2013). Effect of cropping system and seasonal variation on soil microbial biomass and enzymatic activities in arid soils. doi:10.1007/s12665-014-3376-5

U.S. Department of Agriculture, Natural Resources Conservation Service (2024). Web soil survey. Available online at: https://websoilsurvey.sc.egov.usda.gov/.

Van Veen, J. A., and Kuikman, P. J. (1990). Soil structural aspects of decomposition of organic matter by micro-organisms. *Biogeochemistry* 11, 213–233. doi:10.1007/bf00004497

Veres, Z., Kotroczó, Z., Fekete, I., Tóth, J. A., Lajtha, K., Townsend, K., et al. (2015). Soil extracellular enzyme activities are sensitive indicators of detrital inputs and carbon availability. *Appl. Soil Ecol.* 92, 18–23. doi:10.1016/j.apsoil.2015.03.006

Wallenstein, M. D., and Burns, R. G. (2011). Ecology of extracellular enzyme activities and organic matter degradation in soil: a complex community-driven process. *Methods of soil enzymology* 9, 35–55. doi:10.2136/sssabookser9.c2

Wallenstein, M., Steinweg, J. M., and McMahon, S. (2009). Recent advancements in understanding the ecology of soil extracellular enzymes. *Nat. Precedings*. doi:10.1038/npre.2009.4115

Wang, B., and Allison, S. D. (2019). Emergent properties of organic matter decomposition by soil enzymes. *Soil Biol. Biochem.* 136, 107522. doi:10.1016/j.soilbio.2019.107522

Wang, C., Dippold, M. A., Blagodatskaya, E., and Dorodnikov, M. (2022a). Oxygen matters: short-and medium-term effects of aeration on hydrolytic enzymes in a paddy soil. *Geoderma* 407, 115548. doi:10.1016/j.geoderma.2021.115548

Wang, L., Pang, X., Li, N., Qi, K., Huang, J., and Yin, C. (2020). Effects of vegetation type, fine and coarse roots on soil microbial communities and enzyme activities in eastern Tibetan plateau. *Catena* 194, 104694. doi:10.1016/j.catena.2020.104694

Wang, S., Zhou, K., Mori, T., Mo, J., and Zhang, W. (2019). Effects of phosphorus and nitrogen fertilization on soil aryl sulfatase activity and sulfur availability of two tropical plantations in southern China. *For. Ecol. Manag.* 453, 117613. doi:10.1016/j.foreco.2019.117613

Weintraub, S. R., Wieder, W. R., Cleveland, C. C., and Townsend, A. R. (2013). Organic matter inputs shift soil enzyme activity and allocation patterns in a wet tropical forest. *Biogeochemistry* 114, 313–326. doi:10.1007/s10533-012-9812-2

Williams, M. A., and Rice, C. W. (2007). Seven years of enhanced water availability influences the physiological, structural, and functional attributes of a soil microbial community. *Appl. Soil Ecol.* 35 (3), 535–545. doi:10.1016/j.apsoil.2006.09.014

Wu, D., Chi, Q., Sui, X., Zhang, M., Zhang, M., Jia, H., et al. (2021). Metabolic diversity and seasonal variation of soil microbial communities in natural forested wetlands. *J. For. Res.* 32 (6), 2619–2631. doi:10.1007/S11676-021-01326-8

Wyszkowska, J., Kucharski, M., and Kucharski, J. (2010). Activity of beta-glucosidase, arylsulfatase and phosphatases in soil contaminated with copper. *J. Elem.* 15 (1), 213–226. doi:10.5601/jelem.2010.15.1.213-226

Xiang, S. R., Doyle, A., Holden, P. A., and Schimel, J. P. (2008). Drying and rewetting effects on C and N mineralization and microbial activity in surface and subsurface California grassland soils. *Soil Biol. Biochem.* 40 (9), 2281–2289. doi:10.1016/j.soilbio.2008.05.004

Xu, N., Amgain, N. R., Rabbany, A., Capasso, J., Korus, K., Swanson, S., et al. (2022). Interaction of soil health indicators to different regenerative farming practices on mineral soils. *Agrosystems, Geosciences Environ.* 5 (1), e20243. doi:10.1002/agg2.20243

Xue, W. L., Pan, W., Lu, Q., Xu, Q. R., Wu, C. N., and Du, S. T. (2018). Aquatic plant debris changes sediment enzymatic activity and microbial community structure. *Environ. Sci. Pollut. Res.* 25, 21801–21810. doi:10.1007/s11356-018-2310-x

Yao, Y., Shao, M., Fu, X., Wang, X., and Wei, X. (2019). Effects of shrubs on soil nutrients and enzymatic activities over a 0–100 cm soil profile in the desert-loess transition zone. *Catena* 174, 362–370. doi:10.1016/j.catena.2018.11.031

Yin, R., Deng, H., Wang, H. L., and Zhang, B. (2014). Vegetation type affects soil enzyme activities and microbial functional diversity following re-vegetation of a severely eroded red soil in sub-tropical China. *Catena* 115, 96–103. doi:10.1016/j.catena.2013.11.015

Zak, D., Roth, C., Gelbrecht, J., Fenner, N., and Reuter, H. (2015). Polyphenols as enzyme inhibitors in different degraded peat soils: implication for microbial metabolism in rewetted peatlands. Available online at: https://ui.adsabs.harvard.edu/abs/2015EGUGA.1714824Z/abstract.

Zak, D., Roth, C., Unger, V., Goldhammer, T., Fenner, N., Freeman, C., et al. (2019). Unraveling the importance of polyphenols for microbial carbon mineralization in rewetted riparian peatlands. *Front. Environ. Sci.* 7. doi:10.3389/FENVS.2019.00147

Zega, N. D. (2024). Pengaruh tekstur dan struktur tanah terhadap distribusi air dan udara di profil tanah. *J. Ilmu Pertan. Dan. Perikan.* 1 (2), 1–6. doi:10.70134/penarik.v1i2.52

Zhang, X., Dippold, M. A., Kuzyakov, Y., and Razavi, B. S. (2019). Spatial pattern of enzyme activities depends on root exudate composition. *Soil Biol. Biochem.* 133, 83–93. doi:10.1016/j.soilbio.2019.02.010

Zhang, Y., Chen, L., Wu, Z., and Sun, C. (2011). Kinetic parameters of soil β-glucosidase response to environmental temperature and moisture regimes. *Rev. Bras. Ciência do Solo* 35, 1285–1291. doi:10.1590/S0100-06832011000400022

Zhang, Y. Q., Chen, L., Pang, D., He, W., Li, X.-B., Wu, M.-Y., et al. (2022). Responses of soil microbial community structure to litter inputs. *Chin. J. Appl. Ecol.* 33 (11), 2943–2953. doi:10.13287/j.1001-9332.202211.031

Zhang, Z., Qiao, M., Li, D., Zhao, C., Li, Y., Yin, H., et al. (2015). Effects of two root-secreted phenolic compounds from a subalpine coniferous species on soil enzyme activity and microbial biomass. *Chem. Ecol.* 31 (7), 636–649. doi:10.1080/02757540.2015.1075515

Zheng, Q., Hu, Y., Zhang, S., Noll, L., Böckle, T., Dietrich, M., et al. (2019). Soil multifunctionality is affected by the soil environment and by microbial community composition and diversity. *Soil Biol. Biochem.* 136, 107521. doi:10.1016/j.soilbio.2019.107521

Zhongmei, W., and Changchun, S. (2008). Vertical dynamics of soil enzyme activities and its relationship with active organic carbon indicators in Calamagrostis angustifolia wetland. *Wetl. Sci.* 6 (2), 249–257.

Zhu, B., and Cheng, W. (2013). Impacts of drying–wetting cycles on rhizosphere respiration and soil organic matter decomposition. *Soil Biol. Biochem.* 63, 89–96. doi:10.1016/j.soilbio.2013.03.027

Frontiers in
Environmental Science

Explores the anthropogenic impact on our natural world

An innovative journal that advances knowledge of the natural world and its intersections with human society. It supports the formulation of policies that lead to a more inhabitable and sustainable world.

Discover the latest Research Topics

See more →

Frontiers

Avenue du Tribunal-Fédéral 34
1005 Lausanne, Switzerland
frontiersin.org

Contact us

+41 (0)21 510 17 00
frontiersin.org/about/contact

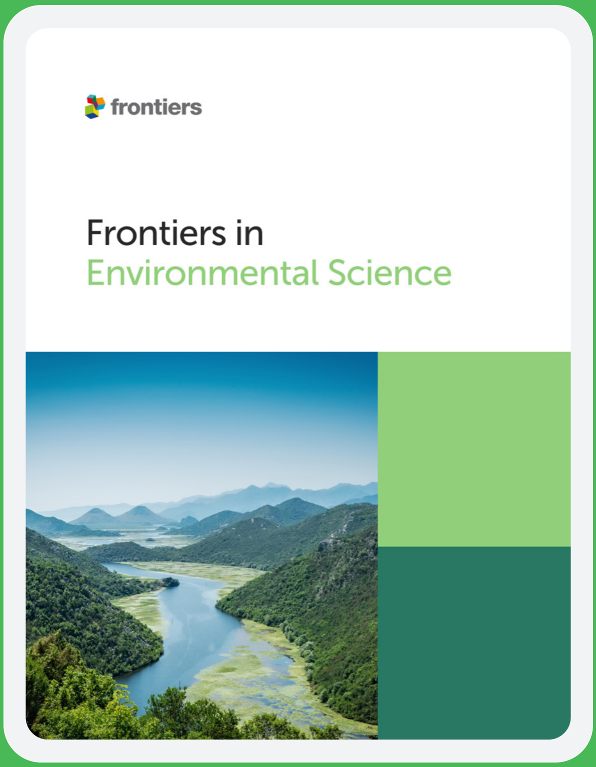

frontiers

Frontiers in
Environmental Science